NUREG/CP-0097
Vol. 5
R1, R4, R5, RD

Proceedings of the U.S. Nuclear Regulatory Commission

Sixteenth Water Reactor Safety Information Meeting

Volume 5
- NUREG-1150
- Accident Management
- Recent Advances in Severe Accident Research
- TMI-2
- BWR Mark I Shell Failure

Held at
National Institute of Standards and Technology
Gaithersburg, Maryland
October 24-27, 1988

Date Published: March 1989

Compiled by: Allen J. Weiss

Office of Nuclear Regulatory Research
U.S. Nuclear Regulatory Commission
Washington, DC 20555

Proceedings prepared by
Brookhaven National Laboratory



ABSTRACT

This five-volume report contains 141 papers out of the 175 that were presented at the Sixteenth Water Reactor Safety Information Meeting held at the National Institute of Standards and Technology, Gaithersburg, Maryland, during the week of October 24-27, 1988. The papers are printed in the order of their presentation in each session and describe progress and results of programs in nuclear safety research conducted in this country and abroad. Foreign participation in the meeting included twenty different papers presented by researchers from Germany, Italy, Japan, Sweden, Switzerland, Taiwan and the United Kingdom. The titles of the papers and the names of the authors have been updated and may differ from those that appeared in the final program of the meeting.

PROCEEDINGS OF THE
16th WATER REACTOR SAFETY INFORMATION MEETING

October 24-27, 1988

Published in Five Volumes

GENERAL INDEX

VOLUME 1
- Plenary Session
- Decontamination and Decommissioning
- License Renewal
- Human Factors
- Generic Issues
- Risk Analysis/PRA Applications
- Innovative Concepts for Increased Safety of Advanced Power Reactors

VOLUME 2
- Industry Safety Research
- Non-Destructive Evaluation
- Materials Engineering
  - Pressure Vessel Research
  - Radiation Effects
  - Degraded Piping

VOLUME 3
- Nuclear Plant Aging
- Structural and Seismic Engineering
- Mechanical Research
- Environmental Effects in Primary Systems

VOLUME 4
- Code Uncertainty for ECCS Rule
- International Code Assessment Program
- Thermal Hydraulics
- 2D/3D Data Applications

VOLUME 5
- NUREG-1150
- Accident Management
- Recent Advances in Severe Accident Research
- TMI-2
- BWR Mark I Shell Failure

REGISTERED ATTENDEES (NON-NRC)
16th WATER REACTOR SAFETY INFORMATION MEETING

J. A. ADAM
STONE & WEBSTER
245 SUMMER ST
BOSTON MA 02107
USA

S. L. ADDITON
TENERA
2011 EYE STREET N.W., SUITE 300
WASHINGTON DC 20006
USA

M. J. ADES
SAVANNAH RIVER LABORATORY
BLDG. 773-43A
AIKEN SC 29808
USA

D. W. AKERS
EG&G IDAHO INC.
P.O. BOX 1625
IDAHO FALLS ID 83415
USA

H. AKIMOTO
JAPAN ATOMIC RESEARCH INST.
TOKAI-MURA, NAKA-GUN
IBARAKI-KEN 319-11
JAPAN

N. S. AKSAN
PAUL SCHERRER INSTITUTE
WUERENLINGEN CH5300
SWITZERLAND

R. P. ALLEN
PACIFIC NORTHWEST LABORATORY
P.O. BOX 999
RICHLAND WA 99352
USA

R. A. ALLEN
SAVANNAH RIVER LABORATORY
AIKEN SC 29808
USA

K. ALMENAS
UNIVERSITY OF MARYLAND
COLLEGE PARK MD 20742
USA

A. ALONSO
MADRID POLYTECHNIC UNIVERSITY
JOSE GUTIERREZ ABASCAL,2
MADRID 28006
SPAIN

H. ALSMEYER
KERNFORSCHUNGSZENTRUM, IRB/PRS
POSTFACH 3640
7500 KARLSRUHE 1
FRG

J. G. ANDERSEN
GENERAL ELECTRIC CO.
175 CURTNER AVE
SAN JOSE CA 95125
USA

J. M. ANDERSON
BECHTEL POWER CORP.
15740 SHADY GROVE ROAD
GAITHERSBURG MD 20874
USA

K. B. ANDERSSON
SWEDISH NUCLEAR POWER INSPECTORATE
BOX 27016
STOCKHOLM SW S-10252
SWEDEN

C. E. APPERSON
SAVANNAH RIVER LABORATORY
1635 ALPINE DR.
AIKEN SC 29801
USA

K. J. ARAJ
BDM
7915 JONES BRIDGE DRIVE
MCLEAN VA 22102
USA

W. C. ARCIERI
ENSA
15825 SHADY GROVE ROAD
ROCKVILLE MD 20850
USA

W. W. ASCROFT-HUTTON
HMNI
BAYNARDS HOUSE/WESTBOURNE GROVE
LONDON ENGLAND W2 4TF
UK

B. ATEFI
SCIENCE APPLICATIONS INT'L CORP.
1710 GOODRIDGE DR.
MCLEAN VA 22102
USA

N. I. AVDOSHKIN
USSR EMBASSY
1125 16TH ST NW
WASHINGTON DC 20036

S. M. BAJOREK
WESTINGHOUSE POWER SYSTEMS DIVISION
P.O. BOX 355
PITTSBURGH PA 15230-2728
USA

K. K. BANDYOPADHYAY
BROOKHAVEN NATIONAL LABORATORY
BLDG 129
UPTON NY 11973
USA

R. A. BARI
BROOKHAVEN NATIONAL LABORATORY
BLDG. 197C
UPTON NY 11973
USA

G. P. BAROIS
FRAMATOME
TOUR FIAT - CEDEX 16
PARIS LA DEFENSE FR 92084
FRANCE

J. H. BARON
MADRID POLYTECHNICAL UNIVERSITY
JOSE GUTIERREZ ABASCAL,2
MADRID 28006
SPAIN

B. R. BASS
OAK RIDGE NATIONAL LABORATORY
PO BOX 2003
OAK RIDGE TN 37831
USA

J. A. BAST
GENERAL ELECTRIC CO.
P.O. BOX 1072, BLDG. F3-8
SCHENECTADY NY 12301
USA

P. D. BAYLESS
EG&G IDAHO INC.
P.O. BOX 1625
IDAHO FALLS ID 83415
USA

P. BEDNARIK
SCIENCE & TECHNOLOGY
3900 LINNEAN AVE., NW
WASHINGTON DC 20008
CZECHOSLOVAKIA

K. D. BERGERON
SANDIA NATIONAL LABS.
P.O. BOX 5800
ALBUQUERQUE NM 87185
USA

R. F. BEYER
WESTINGHOUSE
206 NAVAJO RD.
PITTSBURGH PA 15241
USA

V. M. BHARGAVA
VIRGINIA POWER
5000 DOMINION BLVD.
GLEN ALLEN VA 23060
USA

W. BINNER
AUSTRIAN RESEARCH CENTER
SEIBERSDORF A-2444
AUSTRIA

D. P. BIRMINGHAM
BABCOCK & WILCOX CO.
1562 BEESON STREET
ALLIANCE OH 44601
USA

D. BIZZAK
CARNEGIE-MELLON UNIVERSITY
386 HUNTINGDON AVENUE
N. HUNTINGDON PA 15642
USA

R. J. BOHL
LOS ALAMOS NATIONAL LABORATORY
P.O. BOX 1663, MS K560
LOS ALAMOS NM 87545
USA

T. C. BORDINE
CONSUMERS POWER COMPANY
1945 WEST PARNALL RD.
JACKSON MI 49201
USA

R. B. BORSUM
BABCOCK & WILCOX CO.
1700 ROCKVILLE PIKE, #525
ROCKVILLE MD 20852
USA

B. E. BOYACK
LOS ALAMOS NATIONAL LAB
PO BOX 1663
LOS ALAMOS NM 87545
USA

D. R. BRADLEY
SANDIA NATIONAL LABS.
P.O. BOX 5800
ALBUQUERQUE NM 87185
USA

R. J. BRANDON
GE NUCLEAR CORP
6728 LOOKOUT BEND
SAN JOSE CA 95120
USA

P. A. BRATBY
NATIONAL NUCLEAR CORP.
BOOTHS HALL, CHELFORD ROAD
KNUTSFORD
UK

R. J. BREEDING
SANDIA NATIONAL LABS., DIV. 6410
P.O. BOX 5800
ALBUQUERQUE NM 87185
USA

S. J. BRETT
CEGB, GENERATION DEV. & CONSTRUCTION
GEN. DEV. & CONST. DIV., BARNWOOD
GLOUCESTER GL47RS
UK

I. BRITTAIN
UKAEA/AEE WINFRITH
DOERCHESTER
DORSET DT28DH
UK

J. M. BROUGHTON
EG&G IDAHO INC.
P.O. BOX 1625
IDAHO FALLS ID 83415
USA

S. BRYANT
CENTRAL ELECTRICITY GENERATING BD.
BOOTHS HALL, CHELFORD RD
KNUTSFORD, CHESHIRE WA16BQG
UK

C. E. BUCHHOLZ
GENERAL ELECTRIC CO.
175 CURTNER AVE
SAN JOSE CA 95125
USA

B. BUESCHER
EG&G IDAHO INC.
P.O. BOX 1625
IDAHO FALLS ID 83415
USA

L. C. BUFFARDI
GEORGE MASON UNIVERSITY
4400 UNIVERSITY DRIVE
FAIRFAX VA 22030
USA

J. D. BYRON
ELECTRIC POWER RESEARCH INSTITUTE
3412 HILLVIEW AVE.
PALO ALTO CA 94303
USA

J. I. CALVO
CONSEJO SEGURIDAD NUCLEAR
SOR ANGELA DE LA CRUZ 3
MADRID 28020
SPAIN

A. L. CAMP
SANDIA NATIONAL LABS. DIV. 6412
P.O. BOX 5800
ALBUQUERQUE NM 87185
USA

D. D. CARLSON
SANDIA NATIONAL LABS, DIV. 6513
P.O. BOX 5800
ALBUQUERQUE NM 87185
USA

R. CARO
CONSEJO DE SEGURIDAD NUCLEAR
C/SOR ANGELA DE LA CRUZ, 3
MADRID 28020
SPAIN

D. E. CARROLL
SANDIA NATIONAL LABS.
P.O. BOX 5800
ALBUQUERQUE NM 87185
USA

R. CARUSO
NUCLEAR ENERGY AGENCY
38 BLVD. SUCHET
PARIS 75016
FRANCE

D. A. CASADA
OAK RIDGE NATIONAL LABORATORY
PO BOX 2009, BLDG. 9104-1
OAK RIDGE TN 37831
USA

J. H. CHA
KOREA ADVANCED ENERGY RESEARCH INST.
PO BOX 7, DAEDUK-DANJI
TAEJON CHUNG-NAM
KOREA

S. CHAKRABORTY
PAUL SCHERRER INSTITUTE
WUERENLINGEN CH5303
SWITZERLAND

R. CHAMBERS
EG&G IDAHO INC.
P.O. BOX 1625
IDAHO FALLS ID 83415
USA

Y. I. CHANG
ARGONNE NATIONAL LABORATORY
9700 S. CASS AVE.
ARGONNE IL 60439
USA

D. CHAPIN
MPR ASSOCIATES, INC.
1050 CONNECTICUT AVENUE, N.W.
WASHINGTON DC 20036
USA

S. C. CHENG
TAIWAN POWER COMPANY
TAIPEI

ROC

L. Y. CHENG
BROOKHAVEN NATIONAL LABORATORY
BLDG 703
UPTON NY 11973
USA

R. D. CHEVERTON
OAK RIDGE NATIONAL LABORATORY
PO BOX 2009
OAK RIDGE TN 37831
USA

W. G. CHOE
TU ELECTRIC
400 N. OLIVE STREET
DALLAS TX 75201
USA

O. K. CHOPRA
ARGONNE NATIONAL LABORATORY
9700 S. CASS AVE., BLDG 335
ARGONNE IL 60439
USA

B. CHUNG
KOREA ADVANCED ENERGY RESEARCH INST.
NSC, DAE DUK DAN-JI, BOX 7
CHOONG-NAM
KOREA

D. T. CHUNG
SCIENTECH
11821 PARKLAWN DR.
ROCKVILLE MD 20878
USA

H. CHUNG
ARGONNE NATIONAL LABORATORY
9700 S. CASS AVE.
ARGONNE IL 60439
USA

J. P. CHURCH
SAVANNAH RIVER LABORATORY
BLDG. 773-41A
AIKEN SC 29808
USA

D. B. CLAUSS
SANDIA NATIONAL LABS. DIV. 6442
P.O. BOX 5800
ALBUQUERQUE NM 87122
USA

M. COLAGROSSI
ENEA/DISP
VIA VITALIANO BRANCATI, 48
ROME 00144
ITALY

M. W. CONEY
CENTRAL ELECTRICITY GENERATING BD.
C.E.R.L., KELVIN AVENUE
LEATHERHEAD SURREY KT227SE
UK

W. R. CORWIN
OAK RIDGE NATIONAL LABORATORY
PO BOX 2009
OAK RIDGE TN 37831
USA

D. CROUCH
BROOKHAVEN NATIONAL LABORATORY
BLDG. 130
UPTON NY 11973
USA

W. H. CULLEN
MATERIALS ENGINEERING ASSOCIATES
9700-B M. L. KING HIGHWAY
LANHAM MD 20706
USA

G. E. CUMMINGS
LAWRENCE LIVERMORE NATIONAL LAB
P.O. BOX 808, L-198
LIVERMORE CA 94526
USA

H. D. CURET.
ADVANCED NUCLEAR FUELS
2101 HORN ROAD
RICHLAND WA 99352
USA

B. D. CURRY
PHILADELPHIA ELECTRIC CO.
PO BOX A SARATOGA BR.
POTTSTOWN PA 19464
USA

R. A. CUSHMAN
NIAGRA MOHAWK POWER CORP.
301 PLAINHELD ROAD
SYRACUSE NY 13212
USA

D. A. DAHLGREN
SANDIA NATIONAL LABS., ORG. 6440
P.O. BOX 5800
ALBUQUERQUE NM 87123
USA

J. DALLMAN
EG&G IDAHO INC.
P.O. BOX 1625
IDAHO FALLS ID 83415
USA

R. DAMERON
ANATECH
10975 TORREYANA RD., SUITE 301
SAN DIEGO CA 92121
USA

J. DARLASTON
CENTRAL ELECTRICITY GENERATING BD.
BERKLEY NUCLEAR LABS
GLOUCESTER GL139PB
UK

W. L. DAUGHERTY
SAVANNAH RIVER LABORATORY
PO BOX A
AIKEN SC 29808
USA

N. W. DAVIES
UKAEA, RISLEY LABORATORY
WARRINGTON
CHESHIRE WA3 6AT
UK

M. A. DAYE
BECHTEL POWER CORP.
15740 SHADY GROVE RD.
GAITHERSBURG MD 20877
USA

J. A. DE MASTRY
FLORIDA POWER AND LIGHT CO.
BOX 14000
JUNO BEACH FL 33408
USA

L. O. DeIGEORGE
COMMONWEALTH EDISON
P.O. BOX 767
CHICAGO IL 60690
USA

L. V. DeWITT
SAVANNAH RIVER LABORATORY
1313 WILLIAMS DR.
AIKEN SC 29801
USA

M. DIMARZO
UNIVERSITY OF MARYLAND
MECHANICAL ENGINEERING DEPT.
COLLEGE PARK MD 20016
USA

M. R. DINSEL
BECHTEL POWER CORP.
15740 SHADY GROVE ROAD
GAITHERSBURG MD 20874
USA

S. R. DOCTOR
PACIFIC NORTHWEST LABORATORY
P.O. BOX 999
RICHLAND WA 99352
USA

C. V. DODD
OAK RIDGE NATIONAL LABORATORY
PO BOX 2008
OAK RIDGE TN 37831
USA

T. F. DORIAN
DOUB, MUNTZING & GLASGOW, CHARTERED
808 17TH STREET, N. W., SUITE 400
WASHINGTON DC 20006
USA

J. DRCEC
NPP KRSKO
PO VRBINA 12
KRSKO 68270
YUGOSLAVIA

S. S. DUA
GENERAL ELECTRIC
M/C 769, 175 CURTNER AVE.
SAN JOSE CA 95125
USA

S. W. DUCE
EG&G IDAHO INC
P.O. BOX 1625
IDAHO FALLS ID 83415
USA

J. J. DUCO
CEA FRENCH ATOMIC ENERGY COMMISSION
DAS/SASC,CEN/FAR, BP NO. 6
FONTENAY-AUX-ROSES 92265
FRANCE

R. B. DUFFEY
EG&G IDAHO INC.
P.O. BOX 1625
IDAHO FALLS ID 83415
USA

K. K. DWIVEDY
VIRGINIA POWER
5000 DOMINION BLVD.
GLEN ALLEN VA 23060
USA

J. L. EDSON
EG&G IDAHO INC.
P.O. BOX 1625
IDAHO FALLS ID 83415
USA

G. R. EIDAM
BECHTEL/GPUN
P.O. BOX 72
MIDDLETOWN PA 17057
USA

D. M. EISSENBERG
OAK RIDGE NATIONAL LABORATORY
PO BOX 2009, BLDG. 9104-1
OAK RIDGE TN 37831
USA

Z. J. ELAWAR
ARIZONA NUCLEAR POWER PROJECT, 7202
P.O. BOX 52034
PHOENIX AZ 85072
USA

G. ELETTI
ENEA/DISP
VIA VITALIANO BRANCATI, 48
ROME 00144
ITALY

F. A. ELIA
STONE AND WEBSTER
PO BOX 2325
BOSTON MA 02014
USA

G. T. EMBLEY
GENERAL ELECTRIC
BOX 1092
SCHENECTADY NY 12301
USA

T. C. ENG
DEPARTMENT OF ENERGY
EH-35, MAIL STOP F-137
WASHINGTON DC 20545
USA

R. G. ESPEFALT
SWEDISH STATE POWER BD.
VATTENFALL
VALLINGBY S-16287
SWEDEN

C. R. FARRAR
LOS ALAMOS NATIONAL LAB.
MS J576
LOS ALAMOS NM 87545
USA

H. E. FILACCHIONE
SCIENTECH
11821 PARKLAWN DR.
ROCKVILLE MD 20878
USA

S. R. FISCHER
MIDDLE SOUTH UTILITIES
188 E. CAPITOL STREET, SUITE 600
JACKSON MS 39201
USA

R. G. FITZPATRICK
BROOKHAVEN NATIONAL LABORATORY
BLDG 130
UPTON NY. 11973
USA

C. W. FORSBERG
OAK RIDGE NATIONAL LABORATORY
P.O. BOX 2008, BLDG 4500N
OAK RIDGE TN 37831
USA

E. FOX
OAK RIDGE NATIONAL LABORATORY
P.O. BOX 2009
OAK RIDGE TN 37831-8063
USA

G. FREI
SIEMENS
HAMMERBACHERSTR. 12
ERLANGEN 852
FRG

B. C. FRYER
ADVANCED NUCLEAR FUELS
1930 CYPRESS
RICHLAND WA 99352
USA

H. FUJIMOTO
COMPUTER SOFTWARE DEVELOPMENT CO.
4-1,SHIBAKOUEN 2-CHOME,MINATO-KU
TOKYO 105
JAPAN

P. J. FULFORD
NUS CORPORATION
910 CLOPPER ROAD
GAITHERSBURG MD 20878
USA

R. R. FULLWOOD
BROOKHAVEN NATIONAL LABORATORY
BLDG 130
UPTON NY 11973
USA

F. M. GANTENBEIN
CEA FRENCH ATOMIC ENERGY COMMISSION
CEN-SACLAY DEMT/SMTS/EMSI
GIF-SUR-YVETTE 91191
FRANCE

F. GELBARD
SANDIA NATIONAL LABS.
P.O. BOX 5800
ALBUQUERQUE NM 87185
USA

D. I. GERTMAN
EG&G IDAHO INC.
P.O. BOX 1625
IDAHO FALLS ID 83415
USA

T. GINSBERG
BROOKHAVEN NATIONAL LABORATORY
BLDG 820
UPTON NY 11973
USA

T. GINZBURG
APPLIED BIOMATHEMATICS INC.
100 NORTH COUNTRY ROAD
SETAUKET NY 11733
USA

B. GITNICK
ENSA, INC.
15825 SHADY GROVE RD., STE. 120
ROCKVILLE MD 20850
USA

H. G. GLAESER
GESELLSCHAFT FUR REAKTORSICHERHEIT
FORSCHUNGSGELANDE
D-8046 GARCHING
FRG

J. GLEASON
WYLE LABORATORY
7800 GOVERNORS DRIVE WEST
HUNTSVILLE AL 35807
USA

D. W. GOLDEN
EG&G IDAHO INC.
P.O. BOX 1625
IDAHO FALLS ID 83415
USA

M. GOMOLINSKI
CEA FRENCH ATOMIC ENERGY COMMISSION
CEN/FAR, BP NO. 6
FONTENAT-AUX-ROSES 92265
FRANCE

C. GONZALEZ
MADRID POLYTECHNICAL UNIVERSITY
JOSE GUTIERREZ ABASCAL,2
MADRID 28006
SPAIN

E. D. GORHAM-BERGERON
SANDIA NATIONAL LABS.
P.O. BOX 5800
ALBUQUERQUE NM 87185
USA

T. C. GORRELL
SAVANNAH RIVER LABORATORY
RX TECH, DU PONT (SRP)
AIKEN SC 29808
USA

G. A. GREENE
BROOKHAVEN NATIONAL LABORATORY
BLDG. 820M
UPTON, NY 11973
USA

P. GRIFFITH
MIT
ROOM 7-044
CAMBRIDGE MA 02139
USA

F. GRIMM
SIEMENS
HAMMERBACHERSTR. 12
ERLANGEN 852
FRG

C. GRIMSHAW
BROOKHAVEN NATIONAL LABORATORY
BLDG. 130
UPTON NY 11973
USA

W. W. GUNTHER
BROOKHAVEN NATIONAL LABORATORY
BLDG 130
UPTON NY 11973
USA

S. HABER
BROOKHAVEN NATIONAL LABORATORY
BLDG. 130
UPTON NY 11973
USA

D. R. HAFFNER
WESTINGHOUSE HANFORD CO.
P.O. BOX 1970 A3-30
RICHLAND WA 99352
USA

F. M. HAGGAG
OAK RIDGE NATIONAL LABORATORY
P.O. BOX 2008, BLDG 4500-S
OAK RIDGE TN 37831-6151
USA

A. N. HALL
HM NUCLEAR INSTALLATIONS INSPECTORATE
ST PETER'S HOUSE, BALLIOL RD
BOOTLE,MERSEYSIDED L203LZ
UK

R. J. HAMMERSLEY
FAUSKE & ASSOCIATES
16W070 WEST 83RD STREET
BURR RIDGE IL 60521
USA

A. M. HASHIMOTO
JAPAN INST. OF NUCLEAR SAFETY
3-17-1 TOYANOMON
MINATOKU, TOKYO 105
JAPAN

Y. A. HASSAN
DEPT OF NUCL ENERGY, TEXAS A & M
COLLEGE STATION TX 77843
USA

J. R. HAWTHORNE
MATERIALS ENGINEERING ASSOCIATES
9700-B M. L. KING HIGHWAY
LANHAM MD 20706
USA

H. D. HAYNES
OAK RIDGE NATIONAL LABORATORY
PO BOX 2009, BLDG. 9201-3
OAK RIDGE TN 37831
USA

J. HAZELTINE
WYLE LABORATORY
7800 GOVERNORS DRIVE WEST
HUNTSVILLE AL 35807
USA

R. E. HENRY
FAI
16W070 WEST 83RD STREET
BURR RIDGE IL 60521
USA

G. F. HEWITT
UKAEA/HARWELL LABORATIRY
THERMAL HYDRAULICS DIV, BLDG 392
OXON OX11 ORA
UK

J. HIBBARD
MPR ASSOCIATES, INC.
1050 CONNECTICUT AVENUE, N.W.
WASHINGTON DC 20036
USA

D. E. HIDINGER
GENERAL ELECTRIC
14 CORONET CT.
SCHENECTADY NY 12309
USA

J. C. HIGGINS
BROOKHAVEN NATIONAL LABORATORY
BLDG 130
UPTON NY 11973
USA

C. J. HIGGINS
APPLIED RESEARCH ASSOCIATES, INC.
4300 SAN MATEO NE, STE B 380
ALBUQUERQUE NM 87111
USA

P. R. HILL
PENNSYLVANIA POWER & LIGHT CO.
2 N. NINTH STREET
ALLENTOWN PA 18101
USA

J. E. HINTON
DU PONT DE NEMOURS
SRP 707-C, RM. 329
AIKEN SC 29808
USA

T. J. HIRONS
LOS ALAMOS NATIONAL LABORATORY
P.O. BOX 1663, MS E561
LOS ALAMOS NM 87545
USA

M. HIROSE
NUCLEAR POWER ENG'G TEST CTR
FUJITA KMKO BLDG., TORANOMON, MINATO-
TOKYO 105
JAPAN

S. A. HODGE
OAK RIDGE NATIONAL LABORATORY
PO BOX 2009; BLDG. 9104-1
OAK RIDGE TN 37831
USA

P. G. HOFMANN
KERNFORSCHUNGSZENTRUM, IMF
POSTFACH 3640
7500 KARLSRUHE
FRG

C. H. HOFMAYER
BROOKHAVEN NATIONAL LABORATORY
BLDG 129
UPTON NY 11973
USA

G. S. HOLMAN
LAWRENCE LIVERMORE NATIONAL LAB
P.O. BOX 808, L-197
LIVERMORE CA 94550
USA

K. R. HOOPINGARNER
PACIFIC NORTHWEST LABORATORY
P.O. BOX 999
RICHLAND WA 99352
USA

R. G. HOPPE
WESTINGHOUSE ELECTRIC CORP.
P.O. BOX 79
W MIFFLIN PA 15122
USA

K. G. HORNBERGER
OAK RIDGE NATIONAL LABORATORY
P.O. BOX 2009
OAK RIDGE TN 37831-8056
USA

P. J. HOSEMANN
PAUL SCHERRER INSTITUTE
WUERENLINGEN CH5303
SWITZERLAND

B. J. HSEIH
ARGONNE NATIONAL LABORATORY
9700 SO CASS AVE.
ARGONNE IL 60439
USA

A. H. HSIA
URA
240 MONROE STREET
ROCKVILLE MD 20854
USA

H-N HSIAU
TAIWAN POWER COMPANY
TAIPEI TAIWAN
ROC

K. HU
BROOKHAVEN NATIONAL LABORATORY
BLDG. 475B
UPTON NY 11973
USA

D. S. HUMPHRIES
SCIENTECH
11821 PARKLAWN DR.
ROCKVILLE MD 20852
USA

M. L. HYDER
SAVANNAH RIVER LABORATORY
AIKEN SC 29808
USA

C. R. HYMAN
OAK RIDGE NATIONAL LABORATORY
PO BOX 2009, BLDG. 9104-1
OAK RIDGE TN 37831
USA

T. IGUCHI
JAPAN ATOMIC RESEARCH INST.
TOKAI-MURA, NAKA-GUN
IBARAKI-KEN 319-11
JAPAN

R. L. IMAN
SANDIA NATIONAL LABS. DIV 6415
P.O. BOX 5800
ALBUQUERQUE NM 87185
USA

J. R. IRELAND
LOS ALAMOS NATIONAL LAB
PO BOX 1663, MSK 551
LOS ALAMOS NM 87544
USA

M. ISHII
PURDUE UNIVERSITY
WEST LAFAYETTE ID
USA

S. K. ISKANDER
OAK RIDGE NATIONAL LABORATORY
P.O. BOX 2008
OAK RIDGE TN 37831-6151
USA

R. IVANY
COMBUSTION ENGINEERING, INC.
1000 PROSPECT HILL RD.
WINDSOR CT 06095
USA

J. M. IZQUIERDO
CONSEJO SEGURIDAD NUCLEAR
SOR ANGELA DE LA CRUZ 3
MADRID 28020
SPAIN

M. J. JACOBUS
SANDIA NATIONAL LABS., DIV. 6447
P.O. BOX 5800
ALBUQUERQUE NM 87185
USA

J. F. JANSKY
BTB-LEONBERG
RILKESTRASSE 5
LEONBERG D-7250
FRG

D. B. JARRELL
PACIFIC NORTHWEST LABORATORY
P.O. BOX 999
RICHLAND WA 99352
USA

G. W. JOHNSEN
EG&G IDAHO INC.
P.O. BOX 1625
IDAHO FALLS ID 83415
USA

A. B. JOHNSON
PACIFIC NORTHWEST LABORATORY
P.O. BOX 999
RICHLAND WA 99352
USA

E. R. JOHNSON
WESTINGHOUSE ELECTRIC CORP.
P.O. BOX 2728
PITTSBURGH PA 15230-2728
USA

H. V. JULIAN
VOLIAN ENTERPRISES, INC.
PO BOX 410
MURRYSVILLE PA 15668
USA

J. E. KALINOWSKI
SAVANNAH RIVER LABORATORY
AIKEN SC 29808
USA

P. S. KALRA
ELECTRIC POWER RESEARCH INSTITUTE
3412 HILLVIEW AVE.
PALO ALTO CA 94303
USA

F. B. KAM
OAK RIDGE NATIONAL LABORATORY
PO BOX 2008
OAK RIDGE TN 37831
USA

H. KAMATA
JAPAN ATOMIC RESEARCH INST.
TOKAI-MURA, NAKA-GUN
IBARAKI-KEN 319-11
JAPAN

D. D. KANA
SOUTHWEST RESEARCH INSTITUTE
6220 CULEBRA ROAD
SAN ANTONIO TX 78284
USA

L. D. KANNBERG
PACIFIC NORTHWEST LABORATORY
P.O. BOX 999
RICHLAND WA 99352
USA

S. KARIMIAN
BROOKHAVEN NATIONAL LABORATORY
BLDG. 130
UPTON NY 11973
USA

W. Y. KATO
BROOKHAVEN NATIONAL LABORATORY
BLDG 197C
UPTON NY 11973
USA

K. R. KATSMA
EG&G IDAHO INC.
P.O. BOX 1625
IDAHO FALLS ID 83415
USA

G. KATZENMEIER
KERNFORSCHUNGSZENTRUM, PHDR
POSTFACH 3640
7500 KARLSRUHE 1
FRG

W. R. KEANEY
GENERAL ASSOCIATES CORP.
1314 OAKVIEW DR.
WORTHINGTON OH 43085
USA

J. E. KELLY
SANDIA NATIONAL LABS. DIV. 6418
P.O. BOX 5800
ALBUQUERQUE NM 87185
USA

C. R. KEMPF
BROOKHAVEN NATIONAL LABORATORY
BLDG. 197-C
UPTON NY 11973
USA

W. L. KIRK
LOS ALAMOS NATIONAL LABORATORY
P.O. BOX 1663, N-DO, MS E561
LOS ALAMOS NM 87545
USA

E. KNOGLINGER
PAUL SCHERRER INSTITUTE
WUERENLINGEN CH5303
SWITZERLAND

A. KOHSAKA
JAPAN ATOMIC RESEARCH INST.
TOKAI-MURA, NAKA-GUN
IBARAKI-KEN 319-11
JAPAN

M. J. KOMSI
IMATRAN VOIMA OY
P.O. BOX 112
VANTAA 01601
FINLAND

C. A. KOT
ARGONNE NATIONAL LABORATORY
9700 S. CASS AVE., BLDG 335
ARGONNE IL 60439
USA

G. S. KRAMER
BATTELLE COLUMBUS
505 KING AVE.
COLUMBUS OH 43201
USA

T. S. KRESS
OAK RIDGE NATIONAL LABORATORY
P.O. BOX 2009
OAK RIDGE TN 37831-8063
USA

C. A. KROPP
ENEA/DISP
VIA ANGUILLARESE K 1+300
ROME 00060
ITALY

G. A. KRUEGER
PHILADELPHIA ELECTRIC
2301 MARKET ST., N2-1
PHILADELPHIA PA 19101
USA

R. C. KRYTER
OAK RIDGE NATIONAL LABORATORY
P.O. BOX 2008
OAK RIDGE TN 37831-6010
USA

R. KUBOTA
HITACHI
SAIWAICHO 3-1-1
IBARAKI-KEN 317
JAPAN

C. A. KUKIELKA
PENNSYLVANIA POWER & LIGHT CO.
2 N. NINTH STREET
ALLENTOWN PA 18101
USA

D S. KUPPERMAN
ARGONNE NATIONAL LABORATORY
9700 S. CASS AVE.
ARGONNE IL 60439
USA

K. F. KUSSMAUL
UNIVERSITY OF STUTTGART
PFAFFENWALDRING 32
STUTTGART 80 7000
FRG

P. S. LACY
URA
51 MONROE STREET
ROCKVILLE MD 20854
USA

T. K. LARSON
EG&G IDAHO INC.
P.O. BOX 1625
IDAHO FALLS ID 83415
USA

D LEAVER
TANERA
1340 SARATOGA-SUNNYSIDE ROAD, SUITE 2
SAN JOSE CA 95129
USA

R. E. LECKENBY
UKAEA, RISLEY LABORATORY
WARRINGTON
CHESHIRE WA36AT
UK

M. LEE
BROOKHAVEN NATIONAL LABORATORY
BLDG. 130
UPTON NY 11973
USA

N. E. LEE
COMBUSTION ENGINEERING
1000 PROSPECT HILL RD
WINDSOR CT 06095
USA

J. R. LEHNER
BROOKHAVEN NATIONAL LABORATORY
BLDG. 130
UPTON NY 11973
USA

K. M. LEIGH
UKAEA/SRD
WIGSHAW LANE, CULCHETH
WARRINGTON WA34NE
UK

S. J. LEVINSON
BABCOCK & WILCOX CO.
3315 OLD FOREST RD
LYNCHBURG VA 24506
USA

P. M. LEWIS
PACIFIC NORTHWEST LABORATORY
P.O. BOX 999
RICHLAND WA 99352
USA

K. LIESCH
GESELLSCHAFT FUR REAKTORSICHERHEIT
FORSCHUNGSGELANDE
D-8046 GARCHING
FRG

J. N. LILLINGTON
UKAEA/AEE WINFRITH
DOERCHESTER
DORSET DT28DH
UK

C. L. LIN
ELECTRIC POWER RESEARCH INSTITUTE
3412 HILLVIEW AVE.
PALO ALTO CA 94303
USA

L. LINDSTROM
SWEDISH NUCLEAR POWER INSPECTORATE
BOX 27016
STOCKHOLM SW S-10252
SWEDEN

Y. Y. LIU
ARGONNE NATIONAL LABORATORY
9700 S. CASS AVE.
ARGONNE IL 60439
USA

R. LOFARO
BROOKHAVEN NATIONAL LABORATORY
BLDG. 130
UPTON NY 11973
USA

J. P. LONGWORTH
CENTRAL ELECTRICITY GENERATING BD.
COURTNEY HSE., WARWICK LA
LONDON
UK

F. J. LOSS
MATERIALS ENGINEERING ASSOCIATES
9700-B M. L. KING HIGHWAY
LANHAM MD 20706
USA

A. L. LOWE, JR.
BABCOCK & WILCOX CO.
PO BOX 10935
LYNCHBURG VA 24506
USA

T. S. LUBNOW
MPR ASSOCIATES
1050 CONNECTICUT AVE., NW
WASHINGTON DC 20036
USA

W. J. LUCKAS, JR.
BROOKHAVEN NATIONAL LABORATORY
BLDG. 130
UPTON NY 11973
USA

H. L. MAGLEBY
EG&G IDAHO INC.
P.O. BOX 1625
IDAHO FALLS ID 83415
USA

A. P. MALINAUSKAS
OAK RIDGE NATIONAL LABORATORY
P.O. BOX 2008
OAK RIDGE TN 37831-6135
USA

R. M. MANDL
SIEMENS
HAMMERBACHERSTR. 12
ERLANGEN 852
FRG

C. F. MARKUS
WESTINGHOUSE ELECTRIC CORP.
P.O. BOX 79
W. MIFFLIN PA 15122-0079
USA

C. W. MARSCHALL
BATTELLE COLUMBUS
505 KING AVE.
COLUMBUS OH 43201
USA

P. MARSILI
ENEA/DISP
VIA VITALIANO BRANCATI, 48
ROME 00144
ITALY

B. MAVKO
J. STEFAN INSTITUTE
JAMOVA 39
LJUBLJANA 61000
YUGOSLAVIA

D. E. MC CABE
MATERIALS ENGINEERING ASSOCIATES
9700-B M. L. KING HIGHWAY
LANHAM MD 20706
USA

L. D. McCANN
WESTINGHOUSE ELECTRIC CORP.
P.O. BOX 79
W. MIFFLIN PA 15122-0079
USA

R. K. McCARDELL
EG&G IDAHO INC.
P.O. BOX 1625
IDAHO FALLS ID 83415
USA

D. J. McCLOSKEY
SANDIA NATIONAL LABS.
P.O. BOX 5800
ALBUQUERQUE NM 87122
USA

K. P. McKAY
WESTINGHOUSE ELECTRIC CORP.
P.O. BOX 79
W. MIFFLIN PA 15228
USA

N. R.H. McMILLAN
UKAEA/SRD
WIGSHAW LANE, CULCHETH
WARRINGTON WA34NE
UK

C. MEDICH
SIET
VIA NINO BIXIO 27
PIACENZA ITALY 29100
ITALY

H. B. MEIERAN
H B MEIERAN ASSOCIATES
458 SOUTH DALLAS AVENUE
PITTSBURGH PA 15208
USA

M. MERILO
ELECTRIC POWER RESEARCH INSTITUTE
3412 HILLVIEW AVE.
PALO ALTO CA 94303
USA

J. G. MERKLE
OAK RIDGE NATIONAL LABORATORY
P.O. BOX 2009
OAK RIDGE TN 37831-8049
USA

J. F. MEYER
SCIENTECH
11821 PARKLAWN DRIVE
ROCKVILLE MD 20852
USA

A. MEYER-HEINE
CEA FRENCH ATOMIC ENERGY COMMISSION
CEN CADARACHE-DERS/SEMAR BP NO. 1
SAINT PAUL LEZ DURANCE 13108
FRANCE

S. M. MIHAIU
YANKEE ATOMIC ELECT. CO.
508 MAIN ST.
BOLTON MA 01740
USA

J. S. MILLER
GULG STATES UTILITIES
P.O. BOX 220
ST. FRANCISVILLE LA 70775
USA

A. MINATO
ENERGY RESEARCH LAB., HITACHI LTD.
1168 MORIYAMA-CHO
HITACHI-SHI IBARAKI-KEN 316
JAPAN

S. M. MODRO
FZS-AUSTRIA C/O EG&G
P.O. BOX 1625
IDAHO FALLS ID 83415
USA

T. MOMMA
JAERI C/O GENERAL ELECTRIC SAPS
RT. 168 S.
BEAVER PA 15077
USA

F. J. MOODY
GE NUCLEAR ENERGY
175 CURTNER AVE. MAIL CODE-769
SAN JOSE CA 95125
USA

R. J. MOORE
SAVANNAH RIVER LABORATORY
BLDG. 707C
AIKEN SC 29808
USA

F. I. MOPSIK
NAT'L INST. OF STDS. & TECH.
GAITHERSBURG MD 20899
USA

M.J. MOREAU
GENERAL ELECTRIC
P.O. BOX 1072
SCHENECTADY NY 12301
USA

V. MUBAYI
BROOKHAVEN NATIONAL LABORATORY
BLDG. 130
UPTON NY 11973
USA

Y. MURAO
JAPAN ATOMIC RESEARCH INST.
TOKAI-MURA, NAKA-GUN
IBARAKI-KEN 319-11
JAPAN

S. A. NAFF
SIEMENS AG,UB,KWU,U8S
POSTFACH 3220
ERLANGEN 8520
FRG

C. NAKAMURA
JAPAN ATOMIC RESEARCH INST.
TOKAI-MURA, NAKA-GUN
IBARAKI-KEN 319-11
JAPAN

R. K. NANSTAD
OAK RIDGE NATIONAL LABORATORY
PO BOX 2008, MS 6151
OAK RIDGE TN 37831
USA

A. NATLIZIO
ATOMIC ENERGY OF CANADA
SHERIDAN PARK RSCH. COMM.
MISSISSAUGA ONTARIO L5K1B2
CANADA

D. J. NAUS
OAK RIDGE NATIONAL LABORATORY
P.O. BOX 2009, BLDG 9204-1
OAK RIDGE TN 37831-8056
USA

E. NEGRENTI
ENEA/DISP
V. ANGUILLARESE, 301
ROME 00060
ITALY

D. B. NEWLAND
NATIONAL NUCLEAR CORP.
BOOTHS HALL, CHELFORD ROAD
KNUTSFORD ENGLAND
UK

L. Y. NEYMOTIN
BROOKHAVEN NATIONAL LABORATORY
BLDG 475B
UPTON NY 11973
USA

Y. NOGUCHI
CHUBU ELECTRIC POWER CO. INC
900 17TH ST. N.W., SUITE 714
WASHINGTON DC 20006
USA

P. NORTH
EG&G IDAHO INC.
P.O. BOX 1625
IDAHO FALLS ID 83415
USA

H. NOURBAKHSH
BROOKHAVEN NATIONAL LABORATORY
BLDG. 130
UPTON NY 11973
USA

S. P. NOWLEN
SANDIA NATIONAL LABS.
PO BOX 5800, DIV. 6447
ALBUQUERQUE NM 87185
USA

E. I. NOWSTRUP
CONSULTANT
17605 PARK MILL DR
ROCKVILLE MD 20855
USA

A. NUHM
TECHNICATOME
CEN CADARACHE
CADARACHE 13115
FRANCE

J. O'HARA
BROOKHAVEN NATIONAL LABORATORY
BLDG. 130
UPTON NY 11973
USA

K. R. O'KULA
SAVANNAH RIVER LABORATORY
BLDG. 773-41A
AIKEN SC 29808
USA

C. F. OBENCHAIN
EG&G IDAHO INC.
P.O. BOX 1625
IDAHO FALLS ID 83415
USA

T. OHNO
NUCLEAR POWER ENG'G TEST CTR
BLDG. 4-3-13, TORANOMON, MINATO-KU
TOKYO 105
JAPAN

M. OHUCHI
JAPAN SYSTEMS CORP.
NOMURA BLDG., 4-8 YOMBANCHO, CHIYODA
TOKYO 102
JAPAN

T. OKUBO
JAPAN ATOMIC RESEARCH INST.
TOKAI-MURA, NAKA-GUN
IBARAKI-KEN 319-11
JAPAN

R. C. OLSON
BALTIMORE GAS & ELECTRIC CO.
CCNPP-NGF PO BOX 1535
LUSBY MD 20657
USA

A. OMOTO
TOKYO ELECTRIC POWER
1901 L ST., NW, STE. 720
WASHINGTON DC 20036
USA

N. R. ORTIZ
SANDIA NATIONAL LABS., DIV. 6410
P.O. BOX 5800
ALBUQUERQUE NM 87185
USA

J. PAN
UNIVERSITY OF MICHIGAN
2250 G. G. BROWN BLDG., MECH. ENG.
ANN ARBOR MI 48108
USA

R. K. PAPESCH
BECHTEL-KWU ALLIANCE
15740 SHADY GROVE RD.
GAITHERSBURG MD 20877
USA

C. PARK
BROOKHAVEN NATIONAL LABORATORY
BLDG. 130
UPTON NY 11973
USA

W. R. PEARCE
CONSULTANT
6846 GLENBROOK ROAD
BETHESDA MD 20814
USA

G. A. PERTMER
UNIVERSITY OF MARYLAND
DEPT. OF CHEMISTRY & NUCLEAR ENGR.
COLLEGE PARK MD 20742
USA

G. PETRANGELI
ENEA/DISP
VIA VITALIANO BRANCATI, 48
ROME 00144
ITALY

J. L. PIERREY
CEA FRENCH ATOMIC ENERGY COMMISSION
CEN/FAR, BP-NO. 6
FONTENAT-AUX-ROSES 92265
FRANCE

A. PINI
ENEA/DISP
VIA VITALIANO BRANCATI, 48
ROME 00144
ITALY

M. G. PLYS
FAUSKE & ASSOCIATES
16W070 WEST 83RD STREET
BURR RIDGE IL 60521
USA

M. Z. PODOWSKI
RENSSELEAR POLYTECHNIC INSTITUTE
TROY NY 12180-3590
USA

A. Y. PORRACCHIA
CEA FRENCH ATOMIC ENERGY COMMISSION
CEN CADARACHE-DERS/SEMAR BP NO. 1
SAINT PAUL LEZ DURANCE 13108
FRANCE

D. A. POWERS
SANDIA NATIONAL LABS.
P.O. BOX 5800
ALBUQUERQUE NM 87185
USA

N. PRASAD
WESTINGHOUSE POWER SYSTEMS DIVISION
P.O. BOX 2728
PITTSBURGH PA 15230-2728
USA

T. PRATT
BROOKHAVEN NATIONAL LABORATORY
BLDG. 130
UPTON NY 11973
USA

D. A. PRELEWICZ
ENSA, INC.
15825 SHADY GROVE RD. (SUITE 170)
ROCKVILLE MD 20850
USA

J. G. PRUETT
OAK RIDGE NATIONAL LABORATORY
P.O. BOX 2008
OAK RIDGE TN 37831-6135
USA

J. PUGA
UNITED ELECTRICIA, S. A. (UNESA)
FRANCISCO GERVAS, 3
MADRID 28020
SPAIN

C. E. PUGH
OAK RIDGE NATIONAL LABORATORY
P.O. BOX 2009
OAK RIDGE TN 37831
USA

W. J. QUAPP
WESTINGHOUSE HANFORD CO.
PO BOX 1970
RICHLAND WA 99352
USA

P. J. QUATTRO
MBZ, INC.
1175 HERNDON PKWY., STE. 150
HERNDON VA 22070
USA

Z. H. QURESHI
SAVANNAH RIVER LABORATORY
786-5A
AIKEN SC 29808
USA

H. J. REILLY
IDAHO NATIONAL ENGINEERING LAB
PO BOX 1625
IDAHO FALLS ID 83402
USA

L. RIB
LNR ASSOCIATES
8605 GRIMSBY CT.
POTOMAC MD 20854
USA

B. RIEGEL
GESELLSCHAFT FUR REAKTORSICHERHEIT
FORSCHUNGSGELANDE
D-8046 GARCHING
FRG

D. E. ROBERTSON
PACIFIC NORTHWEST LABORATORY
P.O. BOX 999
RICHLAND WA 99352
USA

S. B. RODRIGUEZ
EG&G IDAHO INC.
1646 GRANDVIEW #1
IDAHO FALLS ID 83402
USA

U. S. ROHATGI
BROOKHAVEN NATIONAL LABORATORY
BLDG 475B
UPTON NY 11973
USA

B. ROSENSTROCH
EBASCO SERVICES INC.
2 WORLD TRADE CENTER 89E
NEW YORK NY 10048
USA

S. T. ROSINSKI
SANDIA NATIONAL LABS, DIV. 6513
P.O. BOX 5800
ALBUQUERQUE NM 87185
USA

J. C. ROUSSEAU
CEA FRENCH ATOMIC ENERGY COMMISSION
CEN/GRENOBLE
GRENOBLE 38000
FRANCE

D. RUBIO
ELECTRIC POWER RESEARCH INSTITUTE
3412 HILLVIEW AVE.
PALO ALTO CA 94303
USA

K. A. RUSSELL
EG&G IDAHO INC.
1520 SAWTELLE
IDAHO FALLS ID 83415
USA

J. RUTHERFORD
CENTRAL ELECTRICITY GENERATING BD.
BOOTHS HALL, CHELFORD ROAD
KNUTSFORD CHESHIRE WA16 806
UK

B. F. SAFFELL
BATTELLE COLUMBUS DIVISION
505 KING AVENUE
COLUMBUS OH 43201
USA

R. T. SAIRANEN
TECHNICAL RSCH CTR OF FINLAND
POB 169
HELSINKI SF-00181
FINLAND

K. SAKANA
JAPAN INST. OF NUCLEAR SAFETY
FUJITA KANKOU TORANOMON MINATO
TOKYO 105
JAPAN

K. SAKANO
JAPAN INSTITUTE OF NUCLEAR SAFETY
FUJITA KANKON TOR. BLDG. 3-17-1
TOKYO 105
JAPAN

A. SALA
HIDROELECTRICO ESPANOLA
HERMOSILLA 3
MADRID 28001
SPAIN

J. SALUJA
VIKING SYSTEMS INTERNATIONAL
2070 WM PITT WAY
PITTSBURGH PA 15238
USA

L. SCHOR
YANKEE ATOMIC ELECT. CO.
508 MAIN ST.
BOLTON MA 01740
USA

D. G. SCHRAMMEL
UFK
WEBERSTR. 5
KARLSRUHE
FRG

S. SETH
MITRE CORP.
7525 COLSHIRE DR.
MC LEAN VA 22102
USA

W. J. SHACK
ARGONNE NATIONAL LABORATORY
BLDG. 212
ARGONNE IL 60439
USA

V. N. SHAH
EG&G IDAHO INC.
P.O. BOX 1625
IDAHO FALLS ID 83415
USA

R. H. SHANNON
CONSULTING ENGINEER
P.O. BOX 2264
ROCKVILLE MD 20852
USA

R. S. SHARMA
AMERICAN ELECTRIC POWER
ONE RIVERSIDE PLAZA
COLUMBUS OH 43017
USA

D. A. SHARP
SAVANNAH RIVER LABORATORY
AIKEN SC 29801
USA

D. L. SHAW
BALTIMORE GAS & ELECTRIC COMPANY
CALVERT CLIFFS NPP, P.O. BOX 1535
LUSBY MD 20657
USA

L. SHEN
ATOMIC ENERGY COUNCIL, ROC
NO 67, LANE 144, KEELUNG RD. SEC. 4
TAIPEI TAIWAN 107
ROC

G. L. SHERWOOD
U.S. DEPT. OF ENERGY
GERMANTOWN MD 21701
USA

P. SHEWMON
ACRS
2477 LYTHAM ROAD
COLUMBUS OH 43220
USA

K. SHIBATA
JAPAN ATOMIC RESEARCH INST.
TOKAI-MURA, NAKA-GUN
IBARAKI-KEN 319-11
JAPAN

K. SHIMIZU
HITACHI, LTD.
1-1 SAIWAI-MACHI
HITACHI
JAPAN

A. SHIMIZU
OHBAYASHI CORP.
777 RIVERVIEW DR., APT. 9
ROCHESTER PA 15074
USA

J. J. SHIN
EBASCO SERVICES, INC.
2 WORLD TRADE CENTER
NEW YORK NY 10048
USA

M. S. SHINKO
EMERGENCY RESPONSE TEAM
PO BOX 129
WASHINGTON GROVE MD 20880
USA

B. S. SHIRALKAR
GENERAL ELECTRIC CO.
175 CURTNER AVE (M/C 186)
SAN JOSE CA 95125
USA

D. A. SIEBE
LOS ALAMOS NATIONAL LABORATORY
P.O. BOX 1663, MS K555
LOS ALAMOS NM 87545
USA

E. G. SILVER
OAK RIDGE NATIONAL LABORATORY
P.O. BOX 2009, BLDG 9201-3
OAK RIDGE TN 37831-8065
USA

F. A. SIMONEN
PACIFIC NORTHWEST LABORATORY
P.O. BOX 999
RICHLAND WA 99352
USA

F. B. SIMPSON
EG&G IDAHO INC.
P.O. BOX 1625
IDAHO FALLS ID 83415
USA

L. SLEGERS
SIEMENS KWU
BERLINER STR 295-303
OFFENBACH 6000
FRG

G. L. SMITH
WESTINGHOUSE HANFORD CO.
P.O. BOX 1970 XO-44
RICHLAND WA 99352
USA

A. W. SNYDER
SANDIA NATIONAL LABS., ORG. 6500
P.O. BOX 5800
ALBUQUERQUE NM 87185
USA

P. SOO
BROOKHAVEN NATIONAL LABORATORY
BLDG 830
UPTON NY 11973
USA

H. SPECTER
NEW YORK POWER AUTHORITY
123 MAIN STREET
NEW YORK NY 10601
USA

J. E. SPEELMAN
ECN
3 WESTERDUINWEG, P.O. BOX 1
PETTEN NEW HOLLAND 1755 ZG
THE NETHERLANDS

K. E. ST. JOHN
YANKEE ATOMIC ELECTRIC CO.
1671 WORCESTER RD
FRAMINGHAM MA 01701
USA

H. STADTKE
JOINT RESEARCH CENTRE-ISPRA ESTABLISH
ISPRA 21020
ITALY

D. D. STEPNEWSKI
WESTINGHOUSE HANFORD CO.
P.O. BOX 1970 NI-31
RICHLAND WA 99352
USA

E. J. STUBBE
TRACTABEL
31 RUE DE LA SCIENCE
BRUSSELS 1040
BELGIUM

R. K. SUNDARAM
YANKEE ATOMIC ELECT. CO.
508 MAIN ST.
BOLTON MA 01740
USA

J. D. SUTTON
YANKEE ATOMIC ELECTRIC CO.
580 MAIN ST.
BOLTON MA 01740
USA

T. SUZUKI
TOSHIBA
SHINSUGITA ISOGO-KU
YOKOHAMA
JAPAN

I. SZABO
C.E.A.
C.E.N CADARACHE
ST. PAUL LES DURAN 43
FRANCE

A. TAKAGI
TOSHIBA
4921 NORWALK DR., APT Y202
SAN JOSE CA 95125
USA

K. TASAKA
JAPAN ATOMIC RESEARCH INST.
TOKAI-MURA, NAKA-GUN
IBARAKI-KEN 319-11
JAPAN

J. H. TAYLOR
BROOKHAVEN NATIONAL LABORATORY
BLDG 130
UPTON NY 11973
USA

B. J. TOLLEY
COMM. OF THE EUROPEAN COMMUNITIES (CI
200 RUE DE LA LOI
BRUSSELS 1049
BELGIUM

J. S. TONG
ATOMIC ENERGY CONTROL BOARD
PICKERING NGS OPERATIONS
PICKERING ONTARIO L1V2R5
CANADA

L. S. TONG
TAI
9733 LOOKOUT PLACE
GAITHERSBURG MD 20879
USA

F. M. TOUBOUL
CEA FRENCH ATOMIC ENERGY COMMISSION
CEN-SACLAY DEMT/SMTS/RDMS
GIF-SUR-YVETTE 91191
FRANCE

H. E. TRAMMELL
OAK RIDGE NATIONAL LABORATORY
104 OGLETHORPE PL.
OAK RIDGE TN 37830
USA

J. D. TROTTER
GROVE ENGINEERING
15215 SHADY GROVE RD.
ROCKVILLE MD 20878
USA

C-K TSAI
WESTINGHOUSE POWER SYSTEMS DIVISION
P.O. BOX 355
PITTSBURGH PA 15230-2728
USA

T. TSUJINO
JAPAN ATOMIC RESEARCH INST.
TOKAI-MURA, NAKA-GUN
IBARAKI-KEN 319-11
JAPAN

B. D. TURLAND
UKAEA CULHAM
CULHAM LABORATORY
ABINGDON
UK

G. TYROR, DIRECTOR
UKAEA/SRD
WIGSHAW LANE, KNUTSFORD
WARRINGTON WA34NE
UK

R. E. UHRIG
OAK RIDGE NATIONAL LABORATORY
113 CONNORS DRIVE
OAK RIDGE TN 37830
USA

R. A. VALENTIN
ARGONNE NATIONAL LAB - BLDG. 208
9700 S. CASS AVE
ARGONNE IL 60439
USA

G. L.C.M. VAYSSIER
MINISTRY OF SOCIAL AFFAIRS
P.O. BOX 69
VOORBURG 2270MA
THE NETHERLANDS

O. VESCOVI
SIET
VIA NINO BIXIO 27
PIACENZA 29100
ITALY

G. L. VINE
ELECTRIC POWER RESEARCH INSTITUTE
3412 HILLVIEW AVE.
PALO ALTO CA 94303
USA

D. S. WALLS
OAK RIDGE NATIONAL LABORATORY
P.O. BOX 2009, MS-8057
OAK RIDGE TN 37831-8065
USA

S. F. WANG
INST. OF NUCLEAR ENERGY RSCH.
PO BOX 3-3, LUNG TAN
TAIPEI TAIWAN 32500
ROC

O. J. WANG
WESTINGHOUSE HANFORD CO.
P.O. BOX 1970 XO-44
RICHLAND WA 99352
USA

R. WANNER
PAUL SCHERRER INSTITUTE
WUERENLINGEN CH5303
SWITZERLAND

E. A. WARMAN
STONE & WEBSTER
245 SUMMER ST.
BOSTON MA 02107
USA

K. E. WASHINGTON
SANDIA NATIONAL LABS.
P.O. BOX 5800
ALBUQUERQUE NM 87185
USA

W. L. WEAVER
EG&G IDAHO INC.
P.O. BOX 1625
IDAHO FALLS ID 83415
USA

E. O. WEINER
WESTINGHOUSE HANFORD CO.
P.O. BOX 1970, L2-57
RICHLAND WA 99352
USA

P. A. WEISS
SIEMENS AG / UB KWU
HAMMERBACHERSTR. 12+14
ERLANGEN 8520
FRG

H. J. WELLAND
EG&G IDAHO INC.
442 JOAN AVENUE
IDAHO FALLS IDAHO 83401
USA

E. T. WESSEL
CONSULTANT
312 WOLVERINE STREET
HAINES CITY FL 33844
USA

H. WESTPHAL
GESELLSCHAFT FUR REAKTORSICHERHEIT
SCHWERTNERGASSE 1
D-5000 COLOGNE 1
FRG

A. M. WHITE
SAVANNAH RIVER LABORATORY
BLDG. 773-11A
AIKEN SC 29808
USA

J. D. WHITE
OAK RIDGE NATIONAL LABORATORY
P.O. BOX 2008
OAK RIDGE TN 37831-6009
USA

G. M. WILKOWSKI
BATTELLE COLUMBUS
505 KING AVE.
COLUMBUS OH 43201
USA

W. K. WINEGARDNER
PACIFIC NORTHWEST LABORATORY
P.O. BOX 999
RICHLAND WA 99352
USA

F. J. WINKLER
SIEMENS
RINGSTRASSE 19
SPARDORF
FRG

L. WOLF
KERNFORSCHUNGSZENTRUM, PHDR
POSTFACH 3640
7500 KARLSRUHE 1
FRG

A. J. WOLFORD
EG&G IDAHO INC.
P.O. BOX 1625
IDAHO FALLS ID 83415
USA

D. N. WOODY
SAVANNAH RIVER LABORATORY
AIKEN SC 29808
USA

R. O. WOOTON
BATTELLE COLUMBUS
505 KING AVE.
COLUMBUS OH 43201
USA

J. WREATHALL
SAIC
2929 KENNY RD.
COLUMBUS OH 43221
USA

D. W. WRIGHT
ANCHOR/DARLING VALVE
701 FIRST ST.
WILLIAMSPORT PA 17701
USA

W. WULFF
BROOKHAVEN NATIONAL LABORATORY
BLDG 475B
UPTON NY 11973
USA

H. XU
BROOKHAVEN NATIONAL LABORATORY
BLDG 130
UPTON NY 11973
USA

Y. YAMAMOTO
TAKENAKA CO.
21-1 8CHOME CHUO-KU
TOKYO
JAPAN

H. YASOSHIMA
JAPAN ATOMIC RESEARCH INST.
TOKAI-MURA, NAKA-GUN
IBARAKI-KEN 319-11
JAPAN

M. YOKOTA
JAPAN ATOMIC RESEARCH INST.
TOKAI-MURA, NAKA-GUN
IBARAKI-KEN 319-11
JAPAN

Y. YOSHIMOTO
HITACHI, LTD.
SAIWAI-CHO 3-H
HITACHI-SHI 316
JAPAN

R. W. YOUNGBLOOD
BROOKHAVEN NATIONAL LABORATORY
BLDG 130
UPTON NY 11973
USA

R. ZIPPER
GESELLSCHAFT FUR REAKTORSICHERHEIT
SCHWERTNERGASSE 1
D-5000 COLOGNE 1
FRG

P. C. ZMOLA
C&P ENGINEERING
5409 NEWINGTON RD.
BETHESDA MD 20816
USA

R. ZOGRAN
MPR ASSOCIATES, INC.
1050 CONNECTICUT AVENUE, N.W.
WASHINGTON DC 20036
USA

PROCEEDINGS OF THE
SIXTEENTH WATER REACTOR SAFETY INFORMATION MEETING

October 24-27, 1988

TABLE OF CONTENTS - VOLUME 5

	Page
ABSTRACT	iii
GENERAL INDEX	v
REGISTERED ATTENDEES	vii

NUREG-1150
Chairman: D. W. Pyatt (NRC)

Use of Expert Judgment in NUREG-1150 N. R. Ortiz and T. A. Wheeler (SNL), M. A. Meyer (LANL), and R. L. Keeney (USC)	1
Requantification of the Zion Risk Profile C. K. Park et al. (BNL), and S. D. Unwin (BCD)	27

ACCIDENT MANAGEMENT
Chairman: N. Lauben (NRC)

Depressurization to Mitigate Direct Containment Heating R. Chambers, D. J. Hanson and R. J. Dallman (INEL), and F. Odar (NRC)	45
Identification of Accident Management Information Needs D. J. Hanson, W. R. Nelson and L. W. Ward (INEL), and D. E. Solberg (NRC)	59
Containment Venting as an Accident Management Strategy R. J. Dallman, W. J. Galyean and K. C. Wagner (INEL)	83
ATWS Scoping Calculations for a BWR Plant Performed Using RELAP5/Mod2 and CONTAIN Codes P. Marsili, A. Pasculli and P. Camiciola (ENEA-DISP)	101
Containment and Release Management J. R. Lehner and W. T. Pratt (BNL)	123

RECENT ADVANCES IN SEVERE ACCIDENT RESEARCH
Chairman: R. B. Foulds (NRC)

Page

Revaporization of Deposited Radionuclides and the Thermal Decomposition of Cesium Iodide. 133
R. M. Elrick and D. A. Powers (SNL)

High-Pressure Melt Ejection and Direct Containment Heating Research. 143
W. W. Tarbell et al. (SNL), and T. Ginsberg and N. K. Tutu (BNL)

Particle Capture in an Experimental Ice Condenser at Low Flow Rates. 165
L. D. Kannberg et al. (PNL)

Results of the Preliminary Hydrogen Distribution Experiment at HDR and Future Experiments for Phase III 189
L. Wolf (Battelle FRG) and L. Valencia (KfK)

HMS Hydrogen Distribution Results for the PHDR Hydrogen Benchmark Experiment. 223
J. R. Travis (LANL)

Severe Accident Natural Circulation Studies Using SCDAP/RELAP5. 247
P. D. Bayless (INEL)

TMI-2
Chairman: R. Van Houten (NRC)

Summary of TMI-2 Core Sample Examinations 255
R. K. McCardell et al. (INEL)

TMI-2 Core Materials and Fission Product Inventory. 273
D. W. Akers, R. K. McCardell and M. L. Russell (INEL), and G. Worku (Grove Engrg.)

Evaluation of Selected Samples from the TMI-2 Core. 295
Y. Y. Liu, L. A. Neimark and W. D. Jackson (ANL)

Status of Disassembly of the Damaged TMI-2 Reactor Core 313
G. R. Eidam (Bechtel National)

BWR MARK I SHELL FAILURE
Chairman: T. Walker (NRC)

Experiments Relating to Drywell Shell-Core Debris Interactions. 317
R. E. Henry, R. J. Hammersley and B. Malinovic (Fauske & Assoc., and R. Sehgal and E. L. Fuller (EPRI)

BWR MARK I SHELL FAILURE
(Cont'd)

Page

Experimental Studies on Melt Spreading, Bubbling Heat Transfer, and Coolant Layer Boiling 341
G. A. Greene et al. (BNL), and S. B. Burson (NRC)

Feedwater Coast Down Measurement of a BWR 359
C. A. Kukielka, S. Seyedhosseini and M. P. Carr (PP&L)

Small Scale BWR Core Debris Eutectics Formation and Melting Experiment. 367
G. W. Parker, L. J. Ott and S. A. Hodge (ORNL)

BWRSAR Calculations of Reactor Vessel Debris Pours for Peach Bottom Short-Term Station Blackout. 377
S. A. Hodge and L. J. Ott (ORNL)

CONTAIN Calculations of Debris Conditions Adjacent to the BWR Mark I Drywell Shell During the Later Phases of a Severe Accident. 403
C. R. Hyman (ORNL)

Analysis of the Thermal Response of a BWR Mark-I Containment Shell to Direct Contact by Molten Core Materials. 429
T. S. Kress and J. C. Cleveland (ORNL)

Assessment of Models for Steam Release from Concrete and Implications for Modeling Corium Behavior in Reactor Cavities 453
K. E. Washington and D. E. Carroll (SNL)

The Influence of Conventional PRA Conservatisms on the Assessment of BWR Accident Sequences. 475
P. R. Hill and C. A. Kukielka (PP&L)

Toward Estimating Mark-I Liner-Failure Probability. 491
T. G. Theofanous, U. Ratnam and A. S. Wanniarachchi (UCSB)

Is Mark I Shell Failure Really Important? 503
H. Specter (NYPA) and P. Bieniarz (RMA)

Mark I Drywell Shell Temperature Response in a Severe Accident. 525
P. J. Moody, R. Muralidharan and S. S. Dua (GE)

Experiments to Assess the Thermal Response of the Mark I Drywell Shell 551
D. R. Bradley et al. (SNL)

SAND88-2253C

USE OF EXPERT JUDGMENT IN NUREG-1150*

by

N. R. Ortiz and T. A. Wheeler
Sandia National Laboratories

M. A. Meyer
Los Alamos National Laboratory

R. L. Keeney
University of Southern California

ABSTRACT

The explicit expert judgment process used in NUREG-1150, "Severe Accident Risks: An Assessment for Five U.S. Nuclear Plants," is discussed in this paper. The main steps of the process are described, including selection of issues and experts; elicitation training; presentation of issues to the experts; preparation of issue analyses by the experts; discussion of issue analyses and elicitation; and recomposition and aggregation of results. To demonstrate the application of the expert judgment process to NUREG-1150, an issue from the front-end system is presented. Recommendations and insights are provided to improve the use of explicit expert judgement in complex technical issues.

I. INTRODUCTION

The expert judgment process used in NUREG-1150, "Severe Accident Risks: An Assessment for Five U. S. Nuclear Plants," is an advance over those processes developed in previous probabilistic risk assessments. The new process was used to obtain expert judgment on issues expected to be the main contributors to the potential risk of five nuclear plants. The use of expert judgment helped to incorporate both the experience and the research results obtained since the Reactor Safety Study (U.S. NRC, 1975). The new process also enabled NUREG-1150 to include a comprehensive uncertainty analysis, an analysis that had been lacking in the earlier Reactor Safety Study.

* This work supported by the United States Nuclear Regulatory Commission and performed at Sandia National Laboratories, which is operated for the United States Department of Energy under Contract DE-AC04-76DP00789.

This process for gathering expert judgment was developed in response to criticisms applied to the previous Reactor Safety Study by the Lewis Committee (Lewis, 1978) and to review comments of the Kouts Committee (1987) on the draft NUREG-1150. The process is based on accepted decision analysis techniques and findings from the numerous studies involving the quantification of judgment. See, for example, EPRI (1986); Mosleh, et al. (1987); and Merkhofer (1987). The result, a formal process for eliciting and documenting expert judgment for risk assessment, is one of the major contributions of NUREG-1150.

Definition, Quality, and Use of Expert Judgment

Expert judgments are expressions of opinion, based on knowledge and experience, that experts make in responding to technical problems. Specifically, the judgments represent the expert's state of knowledge at the time of response to the technical question (Keeney and von Winterfeldt, 1988). Expert judgment is not restricted to the experts' answer but includes the experts' mental processes (definitions, assumptions, and algorithms) for arriving at answers.

The quality of expressed expert judgments can vary according to the manner in which they are gathered. Guidance on how judgments should be gathered, such as with minimal bias (Meyer, et al., 1988), comes from a large body of experiments on human cognition and communication. Much of this research has been stimulated by three fields--psychology (Hogarth, 1980), decision analysis (Spetzler and Stael von Holstein, 1975), and artificial intelligence (Mumpower, et al., 1987). The quality of expert judgment is usually evaluated in terms of the methods used to gather these judgments. For example, state-of-the-art elicitation methods should avoid any systematic bias and include consistency checks with feedback to the experts to allow for revisions of expressed judgments.

Expert judgment is necessarily used in all technical fields. Because these judgments are often implicit, they are sometimes not acknowledged as being expert judgments. For example, expert judgment is frequently used implicitly, even unconsciously, when researchers make decisions about defining problems, establishing boundary conditions, or screening data. By contrast, expert judgment is also obtained explicitly, through formal processes. The process includes selecting the experts, the problems or issues, and the methods by which the judgment will be elicited. Explicit expert judgment, as it was elicited and used in NUREG-1150, will be the focus of this paper.

Need of Expert Judgment in Risk Assessment

The use of expert judgment in risk assessment is often implicit. However, risk assessment frequently needs explicit expert judgment as a source of data, particularly if one or more of the following situations exist:

1. No other data for answering the technical problem or issue are available.

2. High variability characterizes the data.

3. Experts question the applicability of the data.

4. Existing data needs to be supplemented, interpreted, or incorporated with model or code calculations.

5. Analysts need to determine the state of knowledge about what is currently known, what is not known, and what is worth learning.

Expert judgment in risk assessment needs to be explicit rather than implicit. Although the explicit approach requires more effort, it offers several advantages. First, the procedures of the explicit approach can provide the expert with aids to processing the magnitude of information associated with complex technical questions. For example, typically the questions are broken into logical parts that can be more easily considered. Second, the explicit process is more likely than its implicit counterpart to use the body of research on human cognition and communication. This practice usually enhances the quality of the expressed judgments. Third, the procedures of the explicit approach provide a record of the experts' judgments and of their reasoning in arriving at these judgments. This documented record allows the judgments obtained by the explicit process to be more easily updated as new information becomes available. Fourth, people other than those immediately involved can scrutinize the explicit process and its results. With the implicit approach, there is little to review and, indeed, reviews are not often done. Thus, the explicit approach is more likely to advance through the process of reviews.

Expert's judgments in risk assessments should often be quantitative rather than qualitative because quantitative expressions more precisely encode the experts' knowledge (e.g., "a likelihood of 10%" versus "a small chance"). Numerical expressions of judgment allow the experts "to be precise about what they know as well as to acknowledge what they do not know" (Keeney and von Winterfeldt, 1988). Perhaps more important is the fact that systematic analysis can efficiently proceed using expert judgments represented in quantitative form.

For issues extremely difficult to quantify, due to lack of data or poorly understood phenomena, sensitivity studies were performed using fairly conservative ranges for the parameters. The results of the sensitivity analyses were not combined with the uncertainty analyses. However, the insights obtained from the sensitivity analysis are very useful to identify and focus the research required to address the issues in the future.

In Section II, we present a summary of the process used to elicit expert judgment; in Section III, an application of the process to NUREG-1150; and in Section IV, the conclusions and recommendations.

II. EXPERT JUDGMENT PROCESS

The expert judgment process used in NUREG-1150 includes steps recommended by state-of-the-art probability encoding studies (Merkhofer, 1987; Mosleh, et al., 1987). These steps are:

1. Selection of issues and experts;
2. Elicitation training;
3. Presentation of issues to the experts;
4. Preparation of issue analyses by the experts;
5. Discussion of issue analyses and elicitation of expert's judgments, and
6. Recomposition and aggregation of expert's judgments.

To cover these steps, the implementation of the expert judgment process included three meetings as shown in Figure 1. A brief discussion of each step is presented below.

Selection of Issues and Experts

The selection of safety issues and expert panels is closely related. The initial selection of issues for inclusion in the expert judgment process was made by the NUREG-1150 project staff. The expert panels were selected according to each technical area of expertise required to address the issues. The experts were given the opportunity to review all the safety issues and were encouraged to propose additions or deletions to the list of issues. There were several changes in the issues list based on the experts' recommendations. Issues were selected based on the following criteria:

- Preliminary analyses indicate that the issues could have significant impact on risk and/or uncertainty.
- Different points of view exist among the nuclear reactor community about the safety importance of the issues.
- Alternative sources of information such as experimental or observational data or validated computer models are not available or are not widely agreed upon.

It is important to recognize that for most of the cases the experts had recent analyses or experimental data. However, in most cases, the information was not directly applicable to the conditions of the issues, or there were significant differences in the interpretation of the data among the nuclear reactor community.

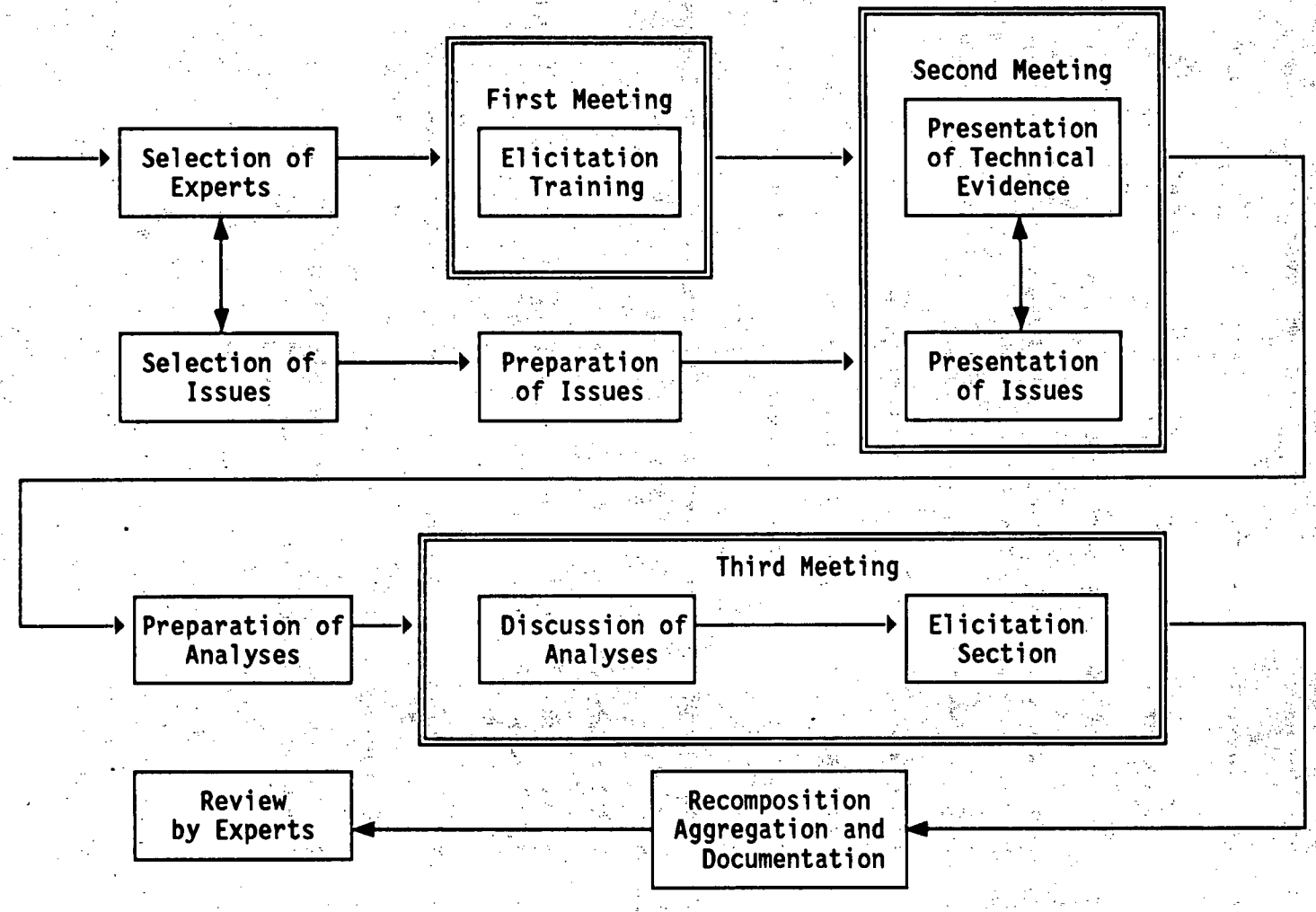


Figure 1. Expert Judgment Process

The safety issues in NUREG-1150 included the areas of systems analysis (seven issues); in-vessel accident progression analysis (six issues); structural failure analysis (five issues); molten core containment interactions (three issues); containment loading analysis (three issues) and source term analysis (eight issues). The systems analysis is called the "Front-End Analysis," the others are referred to as the "Back-End Analysis." The safety issues examined by the expert panels in the front-end systems analysis are:

- Check valve failures causing a loss of coolant accident (LOCA).
- Emergency core cooling system (ECCS) failure due to venting or containment failure.
- Reactor Coolant Pump Seal LOCA.
- Innovative recovery actions for long-term sequences involving loss of containment heat removal.
- Component cooling water pipe rupture.
- High Pressure Cooling System (HPCS) pumps failures
- Decision to spray or inject from high pressure service water.

The safety issues examined by the expert panels in the back-end analysis are listed in Table 1.

Expert panel groups were selected for each one of the five groups of issues shown in Table 1. Experts were chosen to ensure a balance of viewpoints across the nuclear reactor community. The experts were selected using the following criteria:

1. Experts should have demonstrated experience by publications, hands-on experience, consulting or managing research in the areas related to the issues.
2. Experts should represent a wide variety of experience as is obtained in universities, consulting firms, national laboratories, nuclear utilities, or government agencies.
3. The experts should be knowledgeable about the state of the art and have as wide a perspective of issues as possible.
4. The experts should be willing to have their judgments elicited for use in NUREG-1150.

It was impossible to satisfy each criterion entirely for every expert/issue combination. However, we were pleased with the high quality and objectivity of the experts that participated in this project. This was also confirmed by the positive comments received from individuals attending the expert panel meetings.

Table 1
SAFETY ISSUES FOR EXPERT ELICITATION:
ACCIDENT PROGRESSION/CONTAINMENT ANALYSIS/
SOURCE TERM ANALYSIS

In-Vessel Accident Progression Issues

Temperature-Induced Failure of the Hot Leg: Pressurized Water Reactors (PWRs)
Temperature-Induced Steam Generator Tube Failure: PWRs
In-Vessel Hydrogen Production: Boiling Water Reactors (BWRs)
In-Vessel Hydrogen Production: PWRs
Temperature-Induced Bottom Head Failure: BWRs
Temperature-Induced Bottom Head Failure: PWRs

Containment Loads Issues

Loads Due to Combustion Before Vessel Breach: Grand Gulf and Sequoyah
Loads Due to Combustion in the Reactor Building: BWRs
Loads at Vessel Breach: All Plants

Molten Core Containment Issues

Drywell Melt-through: Peach Bottom
Pedestal Failure Timing: LaSalle
Mark III Containment Failure Via Pedestal Failure: Grand Gulf

Structural Issues

Static Containment Failure Pressure and Mode: All Plants
Reactor Building Bypass Probability: Peach Bottom
Ice Condenser Failure Due to Combustible Gas Detonation: Sequoyah
Reactor Pedestal Failure Due to Erosion by Core Concrete Interactions: Grand Gulf
Drywell and Wetwell Failure Due to Combustible Gas Detonation: Grand Gulf

Source Term Issues

Fractional Fission Product Release and Retention In-Vessel: All Plants
Ice Condenser Decontamination Factor: Sequoyah
Revolatilization of Fission Products from Reactor Coolant System: All Plants
Fractional Fission Product Release During Core-Concrete Interactions (CCI): All Plants
Late Iodine Releases: Grand Gulf
Reactor Building Decontamination Factor: Peach Bottom
Fractional Fission Product Release from Direct Containment Heating: All Plants
Release of CCI Species from Containment, Aerosol Agglomeration: All Plants

There were a total of 12 experts participating in the front-end system analysis panel and 38 experts in the five panels addressing the back-end analysis.

Elicitation Training

The purpose of the training session was to help the experts become familiar with encoding their knowledge and beliefs into probabilistic expressions compatible with risk assessments. Previous studies in probability elicitation (Alpert and Raiffa, 1982) have demonstrated that training has significantly improved the quality of experts' assessments. The training session included discussion of methods used to encode probability distributions, methods to decompose complex questions, calibration training using both technical and nontechnical examples, and psychological aspects that could impact the elicitation.

The fixed value and bisection methods for encoding probabilities were discussed during the training session. In the fixed value method, the values of the variable in question are fixed and the probabilities of each interval are assessed. In the bisection method, the values of the variable in question are assessed at given cumulative probabilities. Both methods were used in the elicitation sessions.

A large number of examples of decomposition methods were discussed. These included examples of in-vessel hydrogen production, high-pressure cooling system failure and containment failure pressure, mode and size of failure. Sample problems were also discussed to address the problems of overconfidence in the accuracy of our knowledge to estimate probabilities of occurrence of events. There is the tendency to assign too much precision to values that appear to be reasonable or are calculated by computer models even when working with rare events and extremely low probabilities. Previous studies performed in decision analysis and expert judgment warn us about the bias problem (Tversky and Kahneman, 1974; von Winterfeldt and Edwards, 1986; and Meyer, et al., 1988).

The experts were required to attend the elicitation training session. The few experts that could not attend the live session were required to observe the taped video session. Most of the experts indicated that the training session was extremely useful in performing their job.

Presentation of Issues to the Experts

The issue papers were presented by the members of the NUREG-1150 team to the expert panel. The main objective was to assure that the experts obtained a clear statement and a good understanding of the safety issues. Each issue paper consisted of (1) a concise and clear statement of the issue; (2) background information with a more detailed description of the issue including data, models and analyses related to the issue; (3) a description of how the issue and subcases will be incorporated in the PRA; and (4) an example of a potential decomposition of the issue.

Issue decomposition is used in the NUREG-1150 expert judgment process as a mechanism to improve the quality and documentation of the assessment. Issue decomposition allows the experts to make a series of simpler assessments rather than one assessment of an overall complex issue. Experimental studies (Armstrong, 1985; Armstrong, et al., 1975) have shown that decomposition often improves the accuracy of the assessments. The experts were encouraged to develop their own decompositions or to modify the decompositions proposed by the plant analysts. For many of the issues, the proposed decompositions brought lively discussions of alternative ways of analyzing the main components of the issues.

The presentation of the issues provided an excellent mechanism to discuss the state-of-the-art data base for the issues. The plant analysts presented data sources, models, experimental results, reports and references relevant to the issues. Individuals performing research or studies in the relevant technical areas were invited to present their work. Presentations were made by members of the nuclear industry, utilities, universities, national laboratories, government agencies and private consultants. The detailed technical discussions in these sessions provided excellent insights and a wealth of information contributing to the resolution of the issues.

Preparation of Issue Analyses by the Experts

The expert panels were allowed a time period of two to four months to analyze the issues before the elicitation session. Each panel member analyzed two or three issues, and each issue was assigned three to six experts. Several panels arranged additional meetings to discuss alternative decompositions of the issues. They also discussed results of accident analysis, experiments, and data not covered during the presentation of the issues. Some experts requested specific computer calculations from the project staff to be performed with codes such as CONTAIN, MELCOR, and HECTR. Panel members also performed code calculations specific to their issues using other codes such as MAAP, MELPROG, BWRSAR, STCP, and MARCH-RMA. Other experts performed analytical or hand calculations to guide their judgment concerning the issues.

This part of the process compiled a significant amount of data, methods of analysis, and technical approaches to address important safety issues. Panel members prepared documentation that varied from brief reports to very extensive reports. These were circulated for information among the panel members.

Discussion of Issue Analyses and Elicitations

In the third meeting, prior to the elicitation session, project staff presented the issue, defined the elicitation variables, and proposed a decomposition of the issue summarizing the results of the second meeting. Then for each issue, the experts presented the results of their analyses and research, including the case structure and decomposition with the technical rationale. In some issues, members of the nuclear industry, universities, engineering consulting firms and project staff presented additional results of analyses

and experiments relevant to the issues. Discussion followed to ensure a common understanding of the data base, elicitation variable as well as possible decompositions. These discussions provided valuable information on applicable experiments and data, applicable computer and analytical results, agreements, or disagreements on the phenomena controlling the accidents or failure, and major sources of uncertainties on the issues.

Following the completion of these presentations and discussions, the expert panel convened to reach agreement on the exact elicitation variables and the minimum case structure required by the NUREG-1150 study. After this agreement was achieved, the normative and substantive experts met with each expert in a separate room for the elicitation session.

The substantive experts were members of the NUREG-1150 project staff and were very knowledgeable on the issues and requirements of NUREG-1150. The role of the substantive experts was to provide technical data or clarify assumptions used in NUREG-1150, document the experts' technical rationale, and to assess the technical consistency of the expert judgment. In some elicitations, the substantive expert had extensive technical discussions with the panel expert.

The normative experts were knowledgeable about probability and decision theory and the art and practice of probability elicitation for engineering problems. The role of the normative expert was to assist the experts encoding their reasoning in probabilistic terms, to ensure that the required information was obtained, to check the consistency of the experts' judgments with the laws of probability, and to document the numerical results for later aggregation.

The experts used different technical approaches to address the issues during the elicitation session. Some experts developed event trees to represent the phenomenology of the accident progression. Other experts relied on different code calculations and sensitivity analyses to determine variables and/or phenomena that were important. They usually weighted the results of several computer codes depending on their applicability to the safety issue under consideration. Still other experts relied on experiments or a combination of analytical and experimental results. While emphasizing one of the above approaches, most experts used a mix of all of them in formulating their judgment.

The information obtained in the elicitation sessions was documented by four different means. First, a tape recording was taken of the whole session. Second, the normative expert wrote down the quantitative information. Third, the substantive expert took notes on all the technical reasoning of the experts. Fourth, the materials prepared and used by the experts were made part of the documented elicitation record.

The results of the elicitations for the front-end and back-end safety issues are documented in Wheeler, et al., (1988) and NUREG/CR-4551 (1989), respectively.

Recomposition and Aggregation of Results

The experts' elicitations were recomposed to obtain the result of each specific issue. Recomposing the subjective probability distributions provided by the experts for each part of their issue decomposition was accomplished by the normative and substantive analysts using probability theory concepts varying from simple calculations to more detailed computer programs to assemble large numbers of cases.

After the recomposition, the results were aggregated to obtain a base case representation for each issue. The aggregations were done using the principle of simple averaging of the expert's probabilities, which provides equal weight to each expert. Thus, when three experts provided information for three cumulative distributions $F(x)$, $G(x)$, and $H(x)$, respectively, the resulting aggregated distribution function would be $[F(x) + G(x) + H(x)]/3$. A few issues were aggregated using Monte Carlo methods. In both cases (single averaging and Monte Carlo), the full range of values of the variables as expressed by the experts is automatically kept (Hora and Iman, 1988).

The final step of the expert judgment process was to document the analysis and results provided by each expert. The written documentation was sent to each expert for review and signature to assure that the documentation correctly reflected the judgment of each expert.

The purpose of the documentation was to provide to potential users and reviewers of NUREG-1150 a paper trail of the process followed to obtain the expert's judgments. This includes the issue descriptions and information provided to the experts; the experts' technical rationale, methods, data, computer codes, and/or experiments used to address the issue; and any manipulation of the assessment needed for aggregation. This documentation would be extremely useful to update the analyses when future research provides additional information on the safety issues.

III. APPLICATION OF THE PROCESS TO NUREG-1150

To demonstrate the application of the expert judgment process to NUREG-1150, an issue from the front-end analysis is discussed in this section.

Example Issue: Check Valve Failures Causing a Loss of Coolant Accident (LOCA)

The experts were requested to assess:

1. The failure probability (per year) for severe check valve leakage, given the scenarios in question and the available data.

2. The degree of correlation (if any) that should be used for rupture-rupture failure combinations and rupture-leakage failure combinations. The degree of correlation should include both the tendency of one valve failure to lead to the other valve failure through phenomenological factors, as well as through common causes.

Three failure scenarios are hypothesized:

1. Random, independent rupture (catastrophic leakage) of both valves.

2. Failure of one check valve to reclose upon reactor coolant system (RCS) pressurization followed by random rupture of the other valve.

3. The undetected failure of one valve during operation between test periods followed by the rupture of the other valve. This undetected failure can be caused by opening of the disk, or severe deterioration of the seat. This failure is not detected because the other valve is holding pressure. When the good valve fails, the first valve failure becomes apparent.

This issue involves the quantification of the frequency of an interfacing system LOCA between the high-pressure primary system and the low-pressure Residual Heat Removal (RHR) system. The primary concern is the reliability of the two check valves placed in series in the RHR discharge path into the primary system. At issue is in what modes and how frequently the check valves could fail to maintain a pressure barrier between the systems. Another issue involves whether or not to model common-cause failure (CCF) for check valves in series.

Compromise of the pressure boundary between high and low pressure systems is a scenario with potential for serious risk consequences. These interfacing system LOCAs represent a failure to contain the water and fuel inventory inside the primary system by introduction of a direct pathway from the reactor to the environment that bypasses the containment. The check valves under consideration separate high pressure water from low pressure piping at junctions where low pressure injection paths are linked to high pressure injection paths (Figure 2).

Elicitation:

Five experts, who will be referred to as A, B, C, D, and E, were elicited for this issue. Each expert developed a model of the frequency of interfacing system LOCA to address the three failure scenarios and the common-cause failure of the two check valves. A summary of the results provided by each expert and the aggregated results are discussed below.

The likelihood of an interfacing system LOCA was analyzed by the five experts using variations of the following models:

$$\lambda_T = \lambda_1 \, P(2|1) + 2 \, \lambda_1 \, SD \text{ or} \qquad (1)$$

$$\lambda_T = \lambda_1 \, P(2|1) + 2 \, \lambda_1 \, S'(T/2) \qquad (2)$$

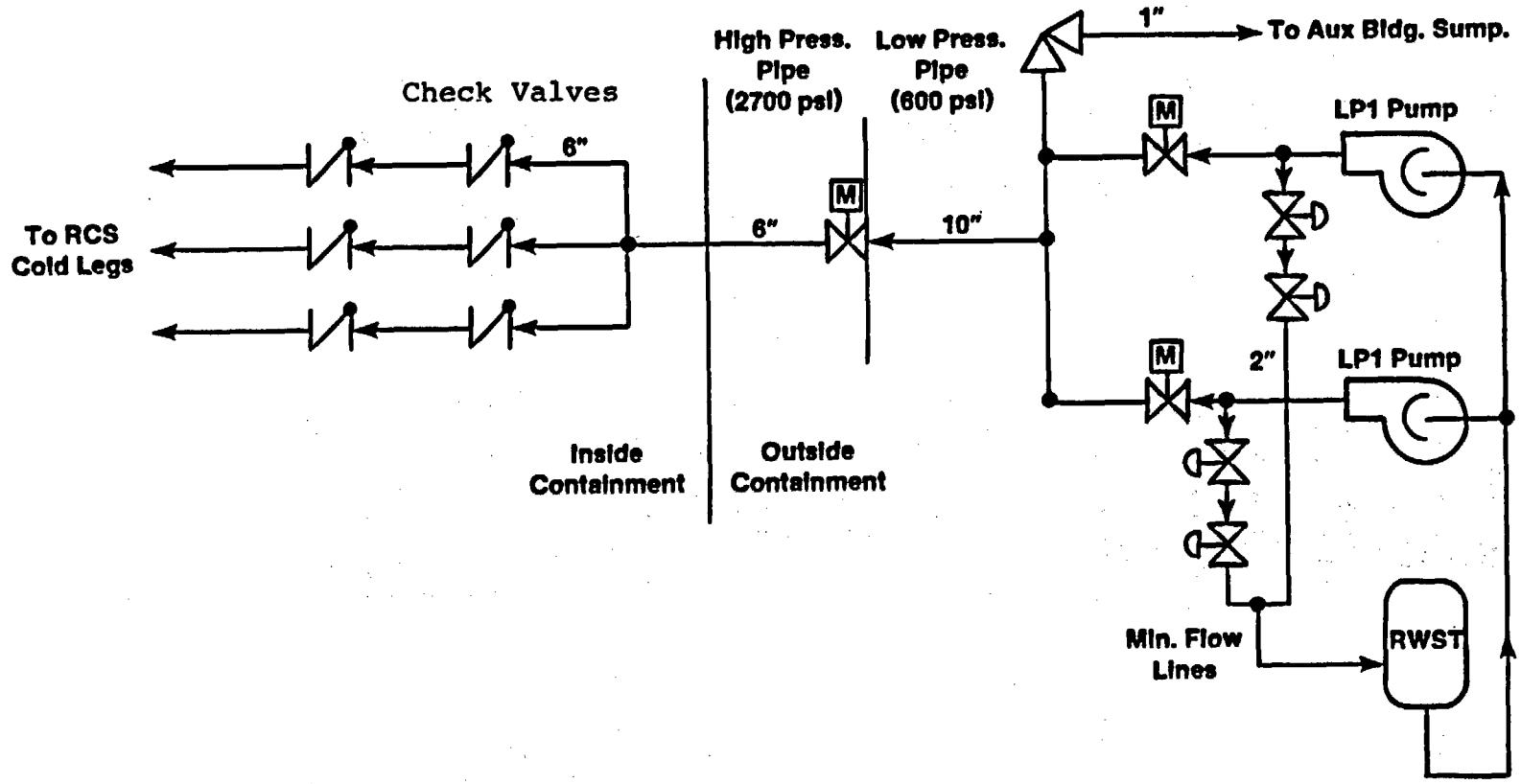


Figure 2. Check Valves Isolation Between High-Pressure and Low-Pressure Piping System.

where

λ_T = Total frequency (per year) of an interfacing system LOCA.

λ_1 = Frequency (per year) of a rupture of the RCS side check valve per unit of time.

P(2|1) = Probability of the second check valve failing given that the first check valve has failed.

S = Probability of a check valve failing to close per demand.

D = Number of demands on the check valve to close between test periods.

S' = Frequency of check valve failing to close per unit of time.

T = The test interval.

The first term corresponds to the rupture-rupture sequence where the valve ruptures when the RCS side valve ruptures. The second term represents both the open-rupture and rupture-open scenarios, which are symmetric in this assessment.

Experts' Rationale

Expert A used Equation (1) to model the interfacing systems LOCA at the Surry Nuclear Power Plant. He estimated each parameter of the equation using available information and consulting with individuals having many years of experience in valve design and operation. Three reports published by the Nuclear Regulatory Commission (NUREG/CR-4302, NUREG/CR-1363, and NUREG/CR-2770) provided information about valve failures caused by aging, service wear, and common cause faults.

The reports do not show any rupture of a check valve internal at a commercial nuclear power reactor. Several catastrophic reverse leaks have been reported but not under the conditions in this issue. Further review of the data indicated at least one valve disk cracked and one valve body with a 140° crack. In summary, the reported valve failure data shows that the causes of failure given that a failure here occurred are as follows:

CAUSE	NUREG/CR-4302	NPRDS*
Seat leakage	52%	70%
External leakage	7%	16%
Internal failures	32%	4%
Valve body failure	2%	--
Valve body rupture	--	--
Failure to open	--	2%
Failure to close	--	8%
Other	7%	--

*Nuclear Power Reliability Data System

Several valve experts were consulted in an effort to estimate check valve rupture rates. They agreed that the rupture failure mode was unlikely, but not impossible, since they could list several potential valve rupture mechanisms. Expert A used the following rationale to estimate the valve rupture frequency (λ_1). The lower bound of the distribution was obtained by assuming that a valve rupture would not occur during the full life time of the current generation of light water reactor plants (approximately a 50% chi-squared value for no events in 5000 reactor-years). The central estimate corresponds to current experience, calculated as a 50% chi-squared value for no valve rupture in 960 reactor years. The upper bound (0.90 percentile) corresponds to assuming one valve rupture in 960 reactor years. This upper bound was influenced by a presentation made by Expert E, which indicated that a leakage did not have to be extensive to cause a severe problem. Expert A recommended a cumulative probability distribution with a 0.05 percentile of 1.6E-10, a median of 1.0E-9, and a 0.95 percentile of 1.3E-8.

The second term in Equation (1) requires estimates of the probability of a check valve to fail to reclose after use(S). Expert A's review of the literature indicated a range of values similar to the frequency distribution presented by Expert E (see Figure 4). He modified the data using expert judgment to take into account potential omissions such as (1) the available data may not represent all of the failures; and (2) valve could stick open and later be dislodged back to a closed position, without being noticed by the plant staff. For the valve failure to close, he estimated a cumulative probability distribution with a 0.05 percentile of 1.0E-5, a median of 6.3E-4, and a 0.95 percentile of 2.0E-2.

The Steverson report (NUREG/CR-2770) provides data related to common-cause failure of check valves. Another data source (NUREG/CR-1363) indicated at least three common-cause failures out of 30 check valve leakage events. Some examples of common-cause failure are:

1. Six of six diesel cooling water check valves suffered complete failure, pivot-arm/disk separation at the Dresden and Quad Cities plants.

2. Three check valves experienced problems opening at the Davis Besse plant.

3. Two of four check valves in the low-pressure coolant injection system were found to have severe internal damage at the Palisades plant.

4. Both check valves closest to the reactor coolant system in the low pressure injection lines were found stuck full open at Point Beach plant.

5. The Salem turbine driven feedwater pump, steam supply check valve completely disassembled internally. The valve had cracks in the disk. Similar damage was found in the other steam supply line check valve.

Expert A concluded, based on the available evidence, that common-cause failure could be an important contributor to valve failure. He used the following approach to estimate the probability distribution for P(2|1). The lower bound value represents an independent failure of the second valve. It was calculated using the mean value for rupture rate times one-half the nine-month period. The median value is based on existing information for common-cause failures recognizing that there is some chance that the first failure could be detected, depending on the valve involved. The upper bound corresponds to the evidence that common cause occurs about 10% of other valve failure modes, which is also a general value for other mechanical equipment. Expert A recommended a cumulative probability distribution for P(2|1) with a 0.05 percentile of 1.0E-5, a median of 1.0E-2, and a 0.95 percentile of 1.0E-1.

The total frequency (per year) of an interfacing system LOCA (λ_T) was estimated by Expert A using the above data and Equation 1. The cumulative probability distribution is shown in Figure 3.

Expert B developed a model slightly different from Equation 1. He assigned different failure rates for a check valve with high-pressure differential (λ_{HP}) than one with low-pressure differential (λ_{LP}). He assumed that leakage through the upstream valve would leave the downstream valve with the high-pressure differential. His model for Surry becomes

$$\lambda_T = 0.99[\lambda_{HP}\ T/2(\lambda_{HP} + \lambda_{LP})] + 0.01[(\lambda_{HP} + \lambda_{LP})\beta] + 2(\lambda_{HP}SD)\ , \qquad (3)$$

where β is the beta factor for common-cause failure of two check valves.

The first term is the independent rupture-rupture failure mode. The second term represents rupture of the low pressure valve, followed by rupture of the high pressure valve within the remaining time before the next test (T/2). The third term is the rupture of the high pressure valve, causing the low pressure valve to be exposed and to rupture at high pressure differential. Expert B assumed that a large leakage caused effects similar to a valve ruptured based on Expert E's testimony. Therefore, he used data from large leakage rates to represent rupture rates. He estimated cumulative probability distributions for λ_{HP} and λ_{LP} with 5 percentile of 1.0E-11 and 3.2E-10, median of 1.0E-10 and 5.0E-9, and 95 percentile of 1.0E-9 and 6.8E-4, respectively.

Expert B obtained the valve failure rate to close per demand using the information provided by Expert E (see Figure 4) in his testimony. Expert B made adjustments to the upper part of the distribution because he felt that the San Onofre plant failure data did not apply to this case. He indicated that the failure at San Onofre was a defect in valve design.

Expert B assigned a weight factor of 0.99 to the rupture-rupture failure mode scenario and a 0.01 weight factor to the common-cause failure of both the high- and low-pressure valve. He assumed a log uniform distribution for the beta factor with a 5 percentile at 1.0E-6, a median of 3.2E-5, and a 95 percentile at 1.0E-3.

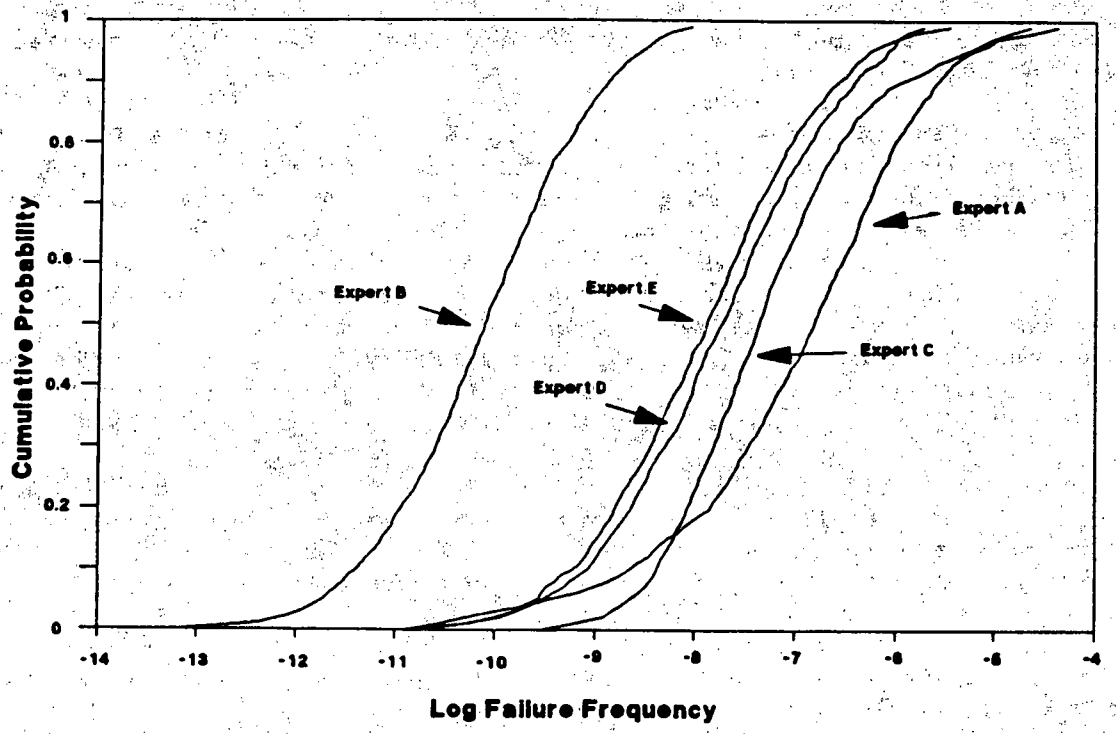


Figure 3. Interface System LOCA Frequency (per year) for Surry.

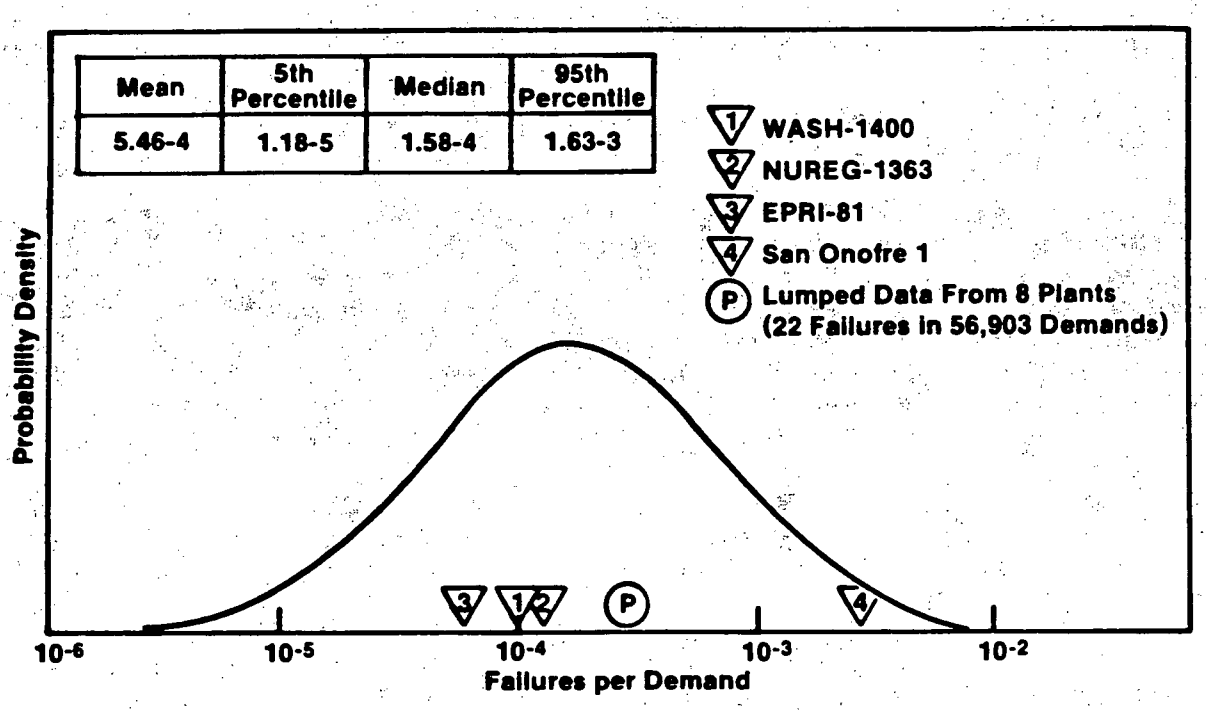


Figure 4. Generic Check Valve Failure Demand Frequency Distribution.

The total frequency (per year) of an interfacing system LOCA estimated by Expert B is shown in Figure 3.

Expert C employed the model represented by Equation 2. He estimated the valve rupture distribution using valve failure data from nuclear and non-nuclear facilities. He gave higher weight to the nuclear than to the non-nuclear experience. He made adjustments to the data from the oil industry because it was not clear that large leakage was included in the assessment of oil industry data. The lower bound of the distribution was established assuming that the valve failure rate could not be better than the reactor pressure vessel failure rate (approximately 1.0E-8/yr). Expert C estimated a cumulative probability for valve rupture with a 5 percentile of 1.0E-7, a median of 4.0E-7 and a 95 percentile of 1.0E-5.

The probability distribution of a check valve failing to close was estimated by Expert C using data from an EG&G report (EGG-EA-5816) and existing data on the frequency of large leaks and failure of the valve to reseal properly. The resulting distribution shows a 5 percentile of 1.3E-9, a median of 1.0E-8, and a 95 percentile of 8.0E-7.

Expert C estimated the probability distribution for the failure of the downstream valve given failure of the upstream valve P(2|1) by using historically beta factors for other components in a nuclear power plant. He concluded that a valve common mode failure is similar to other mechanical components (10% median value). He indicated that a rapid failure of the first valve could cause larger transient stress on the second valve aggravating any inherent weakness. The resulting distribution has a median of 1.0E-1, a 5 percentile of 1.0E-2, and a 95 percentile of 1.

Expert C estimates of the total frequency (per year) of an interfacing system LOCA is shown in Figure 3.

Expert D used the model represented by Equation 2 to calculate the frequency of an interfacing system LOCA (λ_1) using the following approach. The lower bound was selected to be the same as the rupture frequency of the reactor pressure vessel. The upper bound (99 percentile) was based on the existing data base for leaks and extrapolation from leak to large leak. The median was selected using the expert's judgment and the existing data base. The resulting cumulative probability for check valve rupture is represented by a 5 percentile of 1.0E-7, a median of 1.0E-6, and a 95 percentile of 5.0E-6.

Expert D mentioned material flaws and incorrect installation as major contributors to the conditional probability P(2|1). He assumed a cumulative probability for P(2|1) with a 5 percentile of 1.6E-4, a median of 1.0E-2 and a 95 percentile of 2.5E-1.

Expert D assessed the probability of a check valve to fail to close as a probability per hour of exposure. He estimated the 1 percentile based on ten reported events with about 1.0E+5 demands. The median was calculated using

the same ten reported events but with a number of about 1.0E+4 demands. The resulting cummulative probability for valve failure to close has a 5 percentile value of 1.3E-8, a median of 1.0E-7, and a 95 percentile of 8.0E-7. The total frequency (per year) of an interfacing system LOCA estimated by Expert D is shown in Figure 3.

Expert E provided very substantial documentation of his rationale to estimate check valve failures (Wheeler, Hora, and Cramond, 1988). He also made an extensive presentation of the available data and his decomposition of the issue. As mentioned previously, other experts in the panel used some of this data or made comparisons between their research findings and the information presented by Expert E.

Expert E decomposed the issue by defining three different types of interfacing LOCAs. These are (1) gross failure of interfacing valves; (2) gross failure of interfacing valves that lead to residual heat removal (RHR) pressure greater than design pressure; and (3) gross failure of interfacing valves that lead to overpressure and failure of RHR piping. The second case corresponds to the issue under investigation.

Expert E modeled the rupture-rupture sequence using elements of the models of all previous experts. He considered the possibility that one valve may have ruptured since the last inspection, leaving only one check valve operational. The model becomes:

$$\lambda_T = \lambda_1 P(2|1) + 2\lambda_1(\lambda_1 T/2) + 2\lambda_1 SD \qquad (4)$$

He did not differentiate between a high- and low-pressure failure rate for the two check valves as was done by Expert B (Eq. 3).

The check valve rupture frequency, λ_1, was further decomposed in terms of the leak size using the results of an analysis performed by Pickard, Lowe and Garrick for their probabilistic safety study on Seabrook (PLG-0432). The analysis provides the check valve frequency as a function of leak size, including the best fit of data as the median and 90% intervals to represent uncertainties. Expert E assumed that the interfacing system LOCA occurs when the leak rate through both check valves is greater than the flow relief capacity of the RHR in Surry (1800 gpm). He selected the median for λ_1, at the intersection of the 1800 gpm line and the best fit of data curve. He defined the 5 percentile and 95 percentile for λ_1, as the intersection of the 1800 gpm line and the 90% interval assumed curves. These values are: median = 2.4E-9, 5 percentile = 1.2E-10, and 95 percentile = 5.1E-8.

The check valve failure to close per demand, S, was calculated by Expert E using the curve in Figure 4. This curve is a generic distribution developed by Pickard, Lowe and Garrick, based on data from several reports, as noted in the figure, and lumped data from eight plants.

The conditional probability of second valve rupture given first valve rupture, P(2|1), was estimated using the following assumptions and rationale.

Expert E assumed that both valves have design pressure greater than the reactor coolant system (RCS) pressure, the peak dynamic pressure is less or equal than the RCS pressure, valves were tested for design and construction errors, common-cause failure is not significant relative to other failure possibilities, and there is high confidence of structural integrity under water solid conditions. He defined P(2|1) as the frequency of undetected operation with portions of the RHR piping not water solid due to uncertainties regarding possible water hammer effects. Expert E used experience he had from studying check valve failure due to water hammer because the fundamental problem here and with water hammer is the ability of the valve to withstand a pressure pulse. He felt the water hammer analysis was a good bound on this issue. Based on the Light Water Reactor (LWR) operating experience with RHR air ingress problems, he concluded that the median point estimate was 5.0E-5 per demand. He assigned to P(2|1) a lognormal distribution with median of 5.0E-5, 5 percentile of 5.0E-6, and 95 percentile of 5.0E-4.

The total frequency (per year) of an interfacing system LOCA estimated by expert E is shown in Figure 3.

Recomposition and Aggregation

The assessments provided by each expert were recomposed into the distribution for the frequency of an interfacing system LOCA using Monte Carlo simulation techniques. The testing period was assumed to be one year and the distribution for the number of demands to close the valve, D, provided by experts A and B, was multiplied by a factor of 4/3 to rescale from a nine-month to twelve-month period. The distributions in Figure 3 were estimated by generating 2000 values from the distributions of the various failure rates from each expert's model. The 2000 values were generated as independent random variables and then combined to produce the distribution for λ_T (Wheeler, Hora, Cramond, 1988).

The aggregated interfacing system LOCA, λ_T, was constructed by randomly generating 2000 values from the summation of the five experts' distributions. Figure 5 is the aggregated cumulative distribution function for the interfacing system LOCA for Surry. The distribution has a mean of 3.8E-7, a median of 1.6E-8, 5 percentile of 1.3E-11, and 95 percentile of 1.7E-6. The aggregation curve is for a single RCS-RHR interface pathway, it should be multiplied by 3 to cover the three RCS-RHR interfaces in the Surry plant (see Figure 2).

IV. CONCLUSION AND RECOMMENDATIONS

Introduction

The conclusions and recommendations are directed toward the expert judgment elicitation procedure and the results obtained from the procedure. As with all scientific and statistical analyses, expert judgment can be misinterpreted and misused. It is important to understand the proper use of expert judgment to reduce the likelihood of improper use.

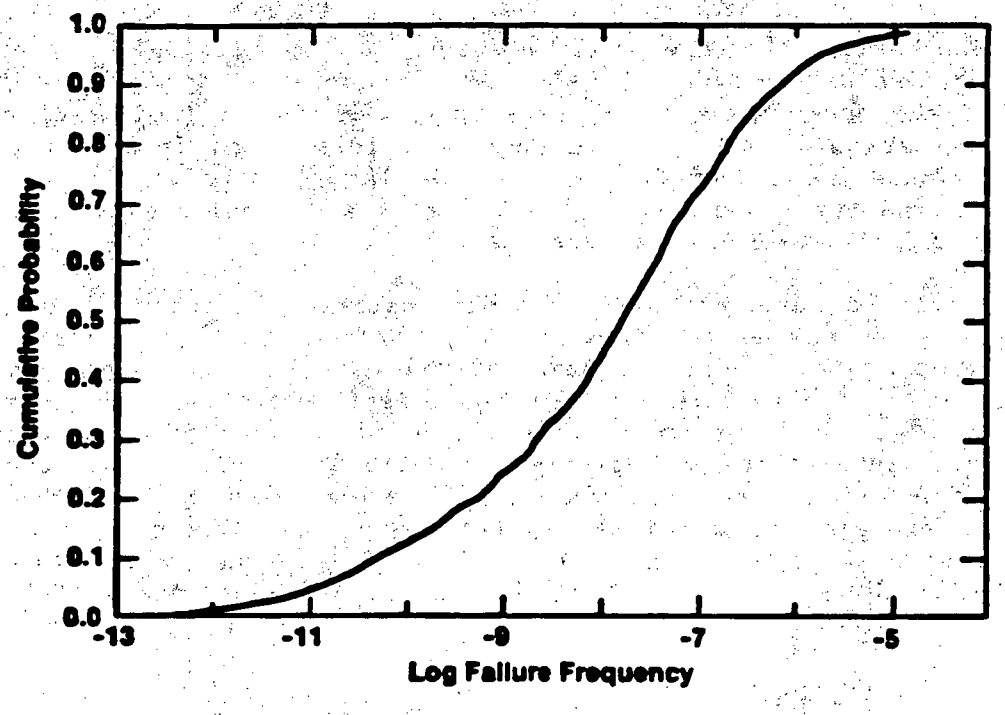


Figure 5. Aggregated Interface System LOCA Frequency (per year) for Surry.

Expert judgment should not be held as equivalent to technical calculations or models based on physical and mathematical laws or extensive data. But, expert elicitations are useful for those problems where recognized methods or sufficient data from solving the problems do not exist. They provide quantitative representations of the state-of-knowledge of such problems at the present time. These representations provide a basis for decision making and communications throughout the industrial, scientific, and regulatory communities interested in the issues. Interested parties (e.g., utility groups, regulatory agencies) who disagree with or are concerned by the results of expert assessments may become motivated to do experimentation or analysis on particular issues. If these efforts result in improved understanding of the issues and solutions that differ from the expert's assessment, then this is a contribution or success of the expert judgment process, not a failure. The expert assessments serve as the best representation of an issue until such time as the state-of-knowledge changes, and the expert assessment may be a catalyst for improved knowledge on the issue. The documentation of the experts rationale and models allows reviewing and upgrading the results, if future experiments or analyses produce new information.

Expert Judgment Elicitation

The formal process for eliciting and documenting expert judgment helped to reduce the problems of bias and overconfidence in quantifying their knowledge. Understanding of the issues was enhanced by analyses and studies performed by the experts prior to the elicitation meeting, and by the exchange

of information between the experts and observers at the meeting. Indeed, the size and expertise of the expert panel was, in a manner of speaking, enlarged beyond the expert panel members. Several panel members, in their preparation for the elicitation meeting sought advice, opinion, and information from individuals around the country who have particularly extensive knowledge and experience on specific issues. So the opinions and knowledge of many more experts were actually presented at the meeting.

The expert's elicitations provided specific analysis and technical insights to address the front-end and back-end safety issues in NUREG-1150. The expert judgment process generated state-of-the-art data base summaries that are very useful in the performance of probabilistic safety assessment and in providing guidance for future reactor severe accident research. The elicitation of complex-interrelated safety issues should be scheduled such that the results of the first panel elicitations could be used by the subsequent panels. For example, it would be helpful if the elicitations of the In-Vessel Accident Progression Panel were completed before the Containment Loads Panel performed their analyses. This was not possible under the NUREG-1150 schedule.

Expert Judgment Procedures

The elicitation methodology and procedures provided state-of-the-art expert elicitations. Because these elicitations represent part of the largest elicitation task to date, several observations can be made as conclusions and recommendations. They are the following:

1. This was a major task that was planned and coordinated in an organized manner culminating in extensive documentation with significant amount of useful information for NUREG-1150 as well as for other potential users. The needs of NUREG-1150 were met with results that are clearly understood and documented.

2. Because the elicitation format focused on detailed technical issues, the opportunity for constructive participation from all knowledgeable sources was promoted. In general, the cooperation from representatives of the industry, universities, national laboratories and government agencies was very good.

3. It is recommended that more attention be given early to the form of the questions and decompositions. The variable to be elicited should be clearly and unambiguously defined. The questions should be explicit, and the desired format of the answer should be specific. This can be done with simple, straightforward issues; however, more complex issues may need the participation of the expert panel to select the variables and questions to be elicited.

4. The discussions and presentations from different organizations and the expert panels provided a relatively open forum for the attendees to express their ideas. People who had unique views were given ample

time and the issues were explored in some detail. These discussions provided important state-of-the-art information, helped to identify the many phenomena impacting the safety issues, and identified specific technical points of disagreements among the participants.

5. The training on expert opinion elicitations was very helpful to all participants. It permitted the audience to recognize the care that was being taken and allowed the experts to translate their fundamental understanding of probability and statistics into meaningful answers representing their real opinions on each issue. Anyone preparing to do such an elicitation should devote at least one-half day to training including numerous examples.

6. The typical issue should take about one to two days, broken into thirds. The first part would be for discussions, the second for the elicitation, and the final part for documentation. All people making presentations should come with vu-graphs and copies for distribution. If information is important enough to be presented, it is also important enough to be distributed for later reference. After the formal elicitation, each expert needs time to document his rationale. Some of the experts provided their rationale in detail at the time of the elicitation. This was very helpful and efficient. In some cases, we permitted experts to mail in their detailed documentation after leaving the assessment meeting. In the long run, this was not efficient. A small amount of effort by the experts at the time of the elicitation is very beneficial.

7. We videotaped the discussion and audiotaped the elicitations. This represented a significant effort. In a few cases, much discussion occurred after the formal elicitation to finally resolve the issue. This, unfortunately, was not recorded. Nevertheless, the tapes provide a record of the expert elicitation process that can be used in the future, especially for anyone desiring to do research into the elicitation process or to investigate the technical details that were discussed. During aggregation and documentation of the results, the experts were contacted on numerous occasions to clarify their opinions.

8. While experts need the flexibility to express their opinions, they should not be permitted to modify the question unless by consensus of the panel, since they all should be addressing the same question. In cases where the issues are not well defined, we should clearly indicate to the experts their role in defining the issues.

9. Quality elicitation sessions require the use of an individual trained and experienced in assessing professional judgments from experts with technical expertise. The logical foundation for the assessments is probability theory, but applying this in practice to obtain an expert's judgments requires skill and experience.

REFERENCES

Alpert, M. and H. Raiffa (1982), "A Progress Report on the Training of Probability Assessors," in Judgment Under Uncertainty: Heuristics and Biases, Cambridge University Press.

Armstrong, J. S., (1985) Long-Range Forecasting: From Crystal Ball to Computer, John Wiley & Sons, New York.

Armstrong, J. S., et al. (1975) "The Use of the Decomposition Principle in Making Judgments," Organizational Behavior and Human Performance, 14, pp. 257-63.

Electric Power Research Institute, (1986) Seismic Hazard Methodology for the Central and Eastern United States Methodology, Vol. 1, NP-4/26.

Hogarth, R. (1980), Judgement and Choice: The Psychology of Decisions, Wiley-Interscience: Chicago.

Hora, S. and R. L. Iman (1988), "Expert Opinion in Risk Analysis: The NUREG-1150 Methodology," SAND88-0122C, presented at The American Nuclear Society Meeting, June 12-17, 1988, San Diego, CA.

Keeney, R. L. and D. von Winterfeldt (1988) "Use of Expert Judgment on Complex Technical Problems," submitted to IEEE Transactions on Engineering Management.

Kouts, H., et al. (1987), "Methodology for Uncertainty Estimation in NUREG-1150 (DRAFT): Conclusions of a Review Panel," NUREG/CR-5000.

Lewis, H. W. et al. (1978), "Risk Assessment Review Group Report to the U.S. Nuclear Regulatory Commission," NUREG/CR-0400.

Merkhofer, M. W. (1987), "Quantifying Judgmental Uncertainty: Methodology, Experiences, and Insights," IEEE Transactions on Systems, Man, and Cybernetics, SMC-17, 741-752.

Meyer, M. A. et al. (1988), "Using Three Minimally Biasing Elicitation Techniques for Knowledge Acquisition," to be published in Proceedings of the 3rd Knowledge Acquisition for Knowledge-Based Systems Workshop, Banff, Canada.

Mosleh, A. et al. (1987), "Methods for the Elicitation and Use of Expert Opinion in Risk Assessment," Pickard, Lowe & Garrick, Inc., NUREG/CR-4962, PLG-0533

Mumpower, J. L., L. D. Phillips, O. Renn, and V. R. R. Uppuluri (1987), Expert Judgment and Expert Systems, Springer-Verlag Publishers: New York.

Spetzler, C. S. and C. A. Stael von Holstein (1975), "Probability Encoding in Decision Analysis," Management Science, 22, pp. 340-358.

Tversky, A. and D. Kahneman (1974), "Judgment under Uncertainty: Heuristics and Biases," Science, 185, pp. 1124-31, 1974.

U.S. Nuclear Regulatory Commission (1988), NUREG-1150, Washington, D.C.

U.S. Nuclear Regulatory Commission (1975), Reactor Safety Study: An Assessment of Accident Risks in U.S. Commercial Nuclear Power Plants, WASH-1400 (NUREG-75/014).

von Winterfeldt, D. and W. Edwards (1986), Decision Analysis and Behavioral Research, Cambridge University Press.

Wheeler, T., et al. (1988), "Results of the Expert Judgment Elicitation on Internal Event Front-End Issues for NUREG-1150: Expert Panel," NUREG/CR-5116, Vol. 1, SAND88-0642.

REQUANTIFICATION OF THE ZION RISK PROFILE

C. K. Park, E. Cazzoli, M. Lee, C. Grimshaw, and W. T. Pratt
Brookhaven National Laboratory
Upton, NY 11973

S. D. Unwin
Battelle Columbus Laboratories
Columbus, OH 43201

ABSTRACT

In February 1987, a preliminary version of the Zion Study performed at the Brookhaven National Laboratory was published for comment. This analysis provided one of the technical bases for the draft NUREG-1150 document. Since the publication, various comments both upon general technical terms and specific calculational issues were received from industry, the public and various peer review panels. In the light of methodological and modelling deficiencies identified in the draft analysis by both internal and external reviews, extensive modifications to the preliminary Zion study were undertaken in support of the final version of NUREG-1150. The integrated analysis of Zion is a collaborative effort involving Brookhaven National Laboratory (BNL) and Idaho National Engineering Laboratories (INEL). The current paper discusses preliminary results of the requantification efforts in various stages of the Zion back-end analysis performed at BNL.

1. INTRODUCTION

Zion is one of the five plants that is currently undergoing detailed reanalysis as part of the Nuclear Regulatory Commission's NUREG-1150 effort [1]. While Sandia National Laboratories (SNL) is the primary analyst for four of the five plants, the integrated analysis of Zion [2] is a collaborative effort involving Brookhaven National Laboratory (BNL) and Idaho National Engineering Laboratory (INEL). While the contribution of INEL focuses largely upon refinement and updating of the Zion accident sequence models, BNL is performing the back-end study (containment, source term, and consequences) and the integration of the analysis within the NUREG-1150 methodological framework.

Various shortcomings of the draft Zion analysis [3], both in general technical terms, and for specific calculational issues, were recognized early by the analysts, and confirmed by external review. The final version of the Zion analysis will enjoy an equal level of modelling detail and of plant-specificity as that of the remaining reference plant studies. The primary improvements to the draft analysis are: a) greater extent and detail of the systems analysis, b) the generation of a plant-specific phenomenological data base by implementation of mechanistic severe accident analysis codes, c) the formal elicitation of expert judgement of Zion-specific issues, and d) improvement of the methodological framework for the probabilistic propagation

of uncertainties.

The current paper illustrates preliminary quantification for various stages of the Zion analysis. Section 2 overviews the current status of the Zion analysis. This section describes the modifications of computer codes for the Zion-specific calculations, development of interfacing computer routines, and information flow among the codes. Sections 3 and 4 describe the preliminary screening sensitivity analysis performed for the identification of important containment and source term parameters, respectively. Section 5 presents the aggregation results for two of the Zion-specific containment uncertainty issues, namely, containment loading and structural capacity. Finally, conclusions are given in Section 6.

2. STATUS OF THE ZION ANALYSIS[1]

Most of the analytical tools for the Zion analysis were developed by SNL and modified by BNL in order to incorporate various Zion-specific features. These features include, for example, the operation of safety grade fan coolers and a Zion-specific containment failure mode (i.e., rupture by shear at the junction between the basemat and the cylindrical wall). The source term analysis code for the Surry plant (SURSOR) was obtained from SNL and only minor modifications were necessary for the quantification of the shear failure mode source term. The PARTITION code has replaced the CLUSTER code for the interfacing between the source term calculations and the consequence calculations. The offsite consequences will be calculated by the MACCS code. The PRAMIS code is being used for the final integration of the results from various stages of the analysis to quantify the Zion risk. The PRAMIS and PARTITION codes are PWR generic so that they did not need major modifications at BNL.

A schematic diagram showing the information flow among these codes is given in Figure 1. The LHS code generates sets of random samples to be used in the uncertainty analysis. It is, however, necessary to transform the LHS sample values into a proper format to be used in each code. The EXTENDER code performs such transformations. The "FRONT END" block indicates the systems analysis being performed by INEL. The important plant damage states will be identified at INEL. Precise definitions of these plant damage states will be generated and these in turn define the initial conditions for the containment analysis. The information supplied by INEL will be in the form of a probability distribution for each plant damage state.

The Zion containment event tree (CET) is an input to the EVENTRE code, which calculates the conditional probabilities of possible containment bins characterizing the different types of possible radioactivity releases. The Zion CET is a modified Surry CET and consists of 71 top event questions. There are two Zion-specific uncertainty issues and many PWR generic issues which were

[1] Various computer codes appearing in the current paper will be described in detail in NUREG/CR-4551 series of reports. NUREG/CR-4551 is designated for a series of NRC contractors' reports related to NUREG-1150.

elicited by various expert panels. The information generated by the EVENTRE code is transferred to ZISOR for estimating the quantity of radioactivity release as well as other release characteristics. The PARTITION code is used to reduce the number of MACCS calculations. The MACCS code predicts various offsite consequence measures caused by radioactivity release to the environment. The informations from the systems analysis, containment analysis, and consequence calculations are integrated by the PRAMIS code to give the final Zion-specific risk measures.

3. THE CET SCREENING SENSITIVITY ANALYSIS

In order to identify the important containment parameters, a screening sensitivity analysis was performed using a regression technique [4]. The screening sensitivity analysis involved approximately 60 input parameters. All of the expert elicited containment uncertainty issues were included in the study. Zion-specific data were used, where available. Where little information was available, complete ignorance was assumed, i.e., either uniform or loguniform distributions over the possible ranges of the corresponding parameter variation. A partial list of the parameters and the corresponding uncertainty ranges is given in Table 1.

A 'fast' station blackout accident sequence was selected for the sensitivity analysis. Through the use of the PARTITION code, it was verified that all no-failure bins could be combined into a single bin, and basemat melt-through bins were collapsed into two bins, one with sprays, and the other without sprays. The source terms were calculated at the point estimate values. The PARTITION code was modified in order to incorporate Zion-specific population density and the weather information. The early fatalities were calibrated according to 30 MACCS calculations previously performed for the draft Zion analysis. Other release characteristics were also modified according to the expected progression of the selected core melt sequence. The LHS code was used for the generation of 150 sets of samples. The importance measures were frequency-weighted early and latent fatalities. The regression analysis was performed and the results are summarized in Figure 2. The goodness of the regression model can be indicated by the explained portion of the output uncertainties (i.e., uncertainties in the importance measures) by the model. The value was 0.75, which is relatively low compared to what would be expected for a very good model. This is due to the relatively small size of samples for more than 60 input parameters. However, the results in Figure 2 confirmed that the expert elicited containment uncertainty issues were indeed important. An additional important parameter identified by the analysis is the possibility of core damage arrest after re-establishing core cooling. The quantification of this particular parameter will be performed by in-house expert elicitation.

4. SOURCE TERM ANALYSIS

The SURSOR code for the Surry source term analysis was obtained from SNL and minor modifications were performed in order to include the Zion-specific containment failure mode, namely rupture by shear at the junction between the cylindrical wall and the basemat (the failure location is underground). Since the version of the SURSOR code obtained was not thoroughly investigated for

possible coding errors or inconsistencies between the elicited information and hard-wired numerical values inside the code, much effort was devoted at BNL to the verification of the Zion source term analysis code (ZISOR). These efforts can be subdivided into two categories, deterministic and probabilistic. The deterministic efforts were to compare the point estimate values by the current ZISOR code and the draft Zion report results. The probabilistic efforts were to determine the uncertainty importance of each source term parameter in the code by performing a limited sensitivity analysis using the given probability distributions of source term uncertainty issues. The limited sensitivity analysis was performed by adding one variable at a time to find the changes in the ranges of release fractions of nine groups of radioisotopes.

Figure 3 shows the comparison of release fractions for nine isotopic groups between the mean values from the draft Zion report and point estimate values calculated by the current ZISOR code with all parameters at the median. The selected bin was the early containment failure by rupture with a direct containment heating (DCH) contribution to release. With the exception of Noble gases, the difference between the two estimations is about an order of magnitude. Similar trends were observed for a release bin corresponding to late containment leakage without sprays operating (Figure 4).

For the limited sensitivity analysis, the accident sequence selected was a station blackout. Other conditions are listed in Table 2. The results are summarized in Figures 5 through 7. Also shown in the figures are the point estimate values (denoted by x) and the source term code package (STCP) calculational results [5]. The histograms shown in Figure 5 (and other figures) were constructed in such a way that, as one moves from left to right, another parameter was added as an uncertain variable in the source term uncertainty analysis. The contribution of each parameter to the overall uncertainty range was therefore included one parameter at a time. For example, the first histogram in Figure 5 is the uncertainty distribution for the Iodine release due to FCORE only. The next histogram shows the uncertainty distribution due to both FCORE and FVES.

The last two parameters considered in the analysis were FPART (the fraction of core participating in the CCI phenomenon) and FPME (the fraction of core ejected under high RCS pressure), respectively. The results of the limited sensitivity analysis shown in Figures 5 through 7 indicate that FPART and FPME do not significantly influence the uncertainty ranges. Since the rest of the parameters considered in the sensitivity analysis are those already elicited by the source term experts, they will remain in the final Zion uncertainty analysis.

5. THE ZION SPECIFIC CONTAINMENT UNCERTAINTY ISSUES

There are two Zion-specific uncertainty issues that were elicited by the Containment Expert Groups; namely containment loading at the time of vessel breach and the structural capacity of the Zion containment. This section will describe briefly the method used in the aggregation of each issue and the results will be shown in tabular form.

5.1 Zion Containment Loading at Vessel Breach

Five experts were involved in the elicitation of Zion containment loading. The initial case structure is shown in Table 3 along with the additional variables considered by the experts. Because of these additional variables, there are a maximum of 64 possible subcases, which is too many for the EVENTRE code to handle. The analysis of variance (ANOVA) technique and the least significant difference (LSD) test [6] were used in a process to systematically reduce the number of subcases.

Among the three additional variables considered by the experts, the amount of Zr oxidation was found not to be significant (in a statistical sense) enough to warrant making it a separate variable. Where an expert had given different loads for cases of high and low Zr oxidation, they were arithmetically averaged. Note, however, that this case condensation process does not reduce the information given by the experts because this information is used by other top event questions in the containment event tree. That is, the case condensation applies only to this top event question in the containment event tree.

The least significant difference (LSD) test was used in the case reduction process, and the ANOVA was applied again to collapse the subcases within the condensed case structure. The final result of the case condensation process is shown in Table 4. Each expert's data was rearranged according to this final case structure and then aggregated. The aggregation result is given in Table 5 showing the pressure increments at different percentiles for all 17 new cases.

5.2 The Zion Containment Capacity

The second Zion-specific containment issue relates to the capacity of containment. Initially the experts were asked to provide information on the capacity of the containment to withstand three different types of pressure rise, i.e., pressure spike at vessel breach, late Hydrogen deflagration, and late gradual pressure rise. The experts, however, were not able to distinguish between these various pressure rises because they felt that there was not a sufficiently developed knowledge base. Instead, they each gave one probability distribution for the Zion containment capacity assuming a "static" pressurization. However, four different failure modes were identified by the experts for the Zion containment; namely, leakage, rupture by hoop stress, catastrophic rupture, and rupture by shear. Only one expert believed that the shear failure mode is possible. He also gave a much wider failure pressure range than the other two experts. The other experts favored the hoop tendon failure modes with relatively narrow uncertainty ranges.

The final aggregated result is shown in Table 6. At lower containment pressures, the leakage failure mode dominates. The median failure pressure is about 140 psig, which is about the same failure pressure estimated by the Zion Probabilistic Safety Study (ZPSS) [7].

6. CONCLUSIONS

The preliminary Zion analysis included in draft NUREG-1150 differed in

various respects from other plant studies performed at SNL. The current paper described various efforts directed to improving the Zion analysis. These efforts include: a) the formal elicitation of expert judgement of Zion-specific issues, b) improvement of the methodological framework for the probabilistic propagation of uncertainties, and c) inclusion of Zion-specific features at various stages of the analysis.

7. REFERENCES

1. Severe Accident Risks: An Assessment for five U.S. Nuclear Power Plants, U.S. Nuclear Regulatory Commission, NUREG-1150, December 1988.

2. C. K. Park, et al., Evaluation of Severe Accident Risks: Zion Unit 1, Brookhaven National Laboratory, NUREG/CR-4551, Vol. 7, December 1988.

3. M. Khatib-Rahbar, et al., Evaluation of Severe Accident Risks and Potential for Risk Reduction: Zion Plant, Draft for Comment, Brookhaven National Laboratory, NUREG/CR-4551, Vol. 5, February 1987.

4. R. Iman, et al., A FORTRAN 77 Program and User's Guide for the Calculation of Partial Correlation and Standardized Regression Coefficients, Sandia National Laboratory, NUREG/CR-4122, SAND85-0044, June 1985.

5. R. Denning, et al., Radionuclide Release Calculations for Selected Severe Accident Scenarios: PWR, Large Dry Containment, Battelle Columbus Laboratories, NUREG/CR-4624, BMI-2139, Vol. 5, July 1986.

6. SAS User's Guide: Basics, Vol. 5, SAS Institute Inc., 1985.

7. Zion Probabilistic Safety Study, Commonwealth Edison Co., September 1981.

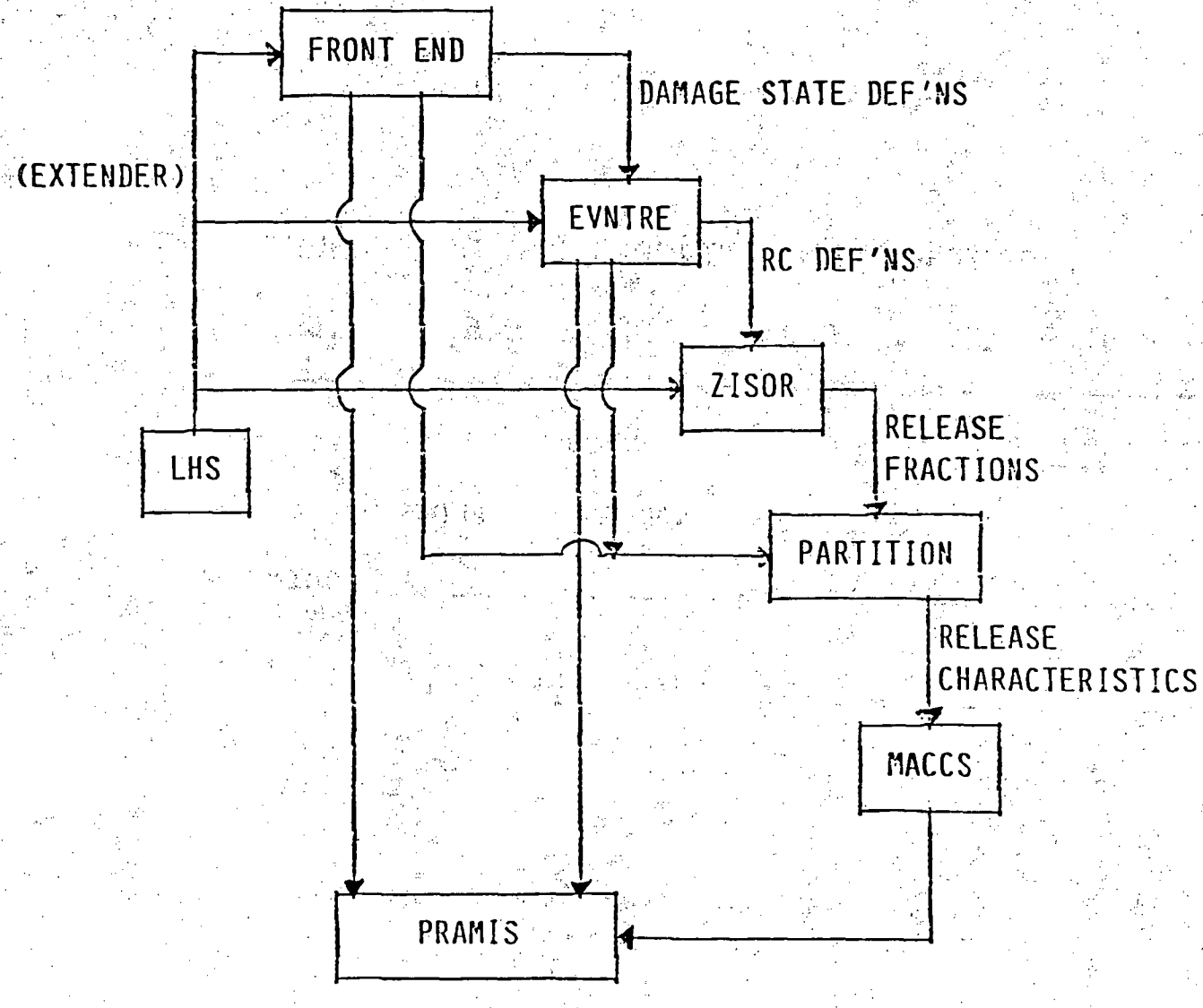


Figure 1 Zion risk rebaselining study: information flow.

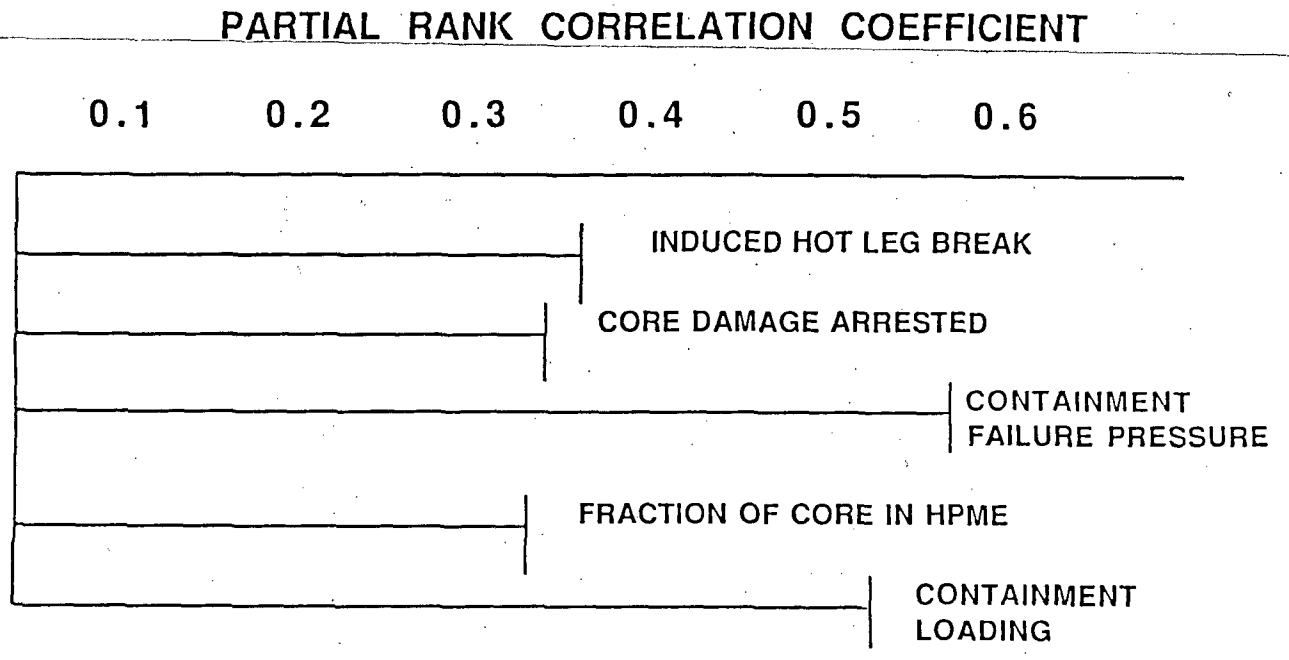


Figure 2 Screening sensitivity analysis results.

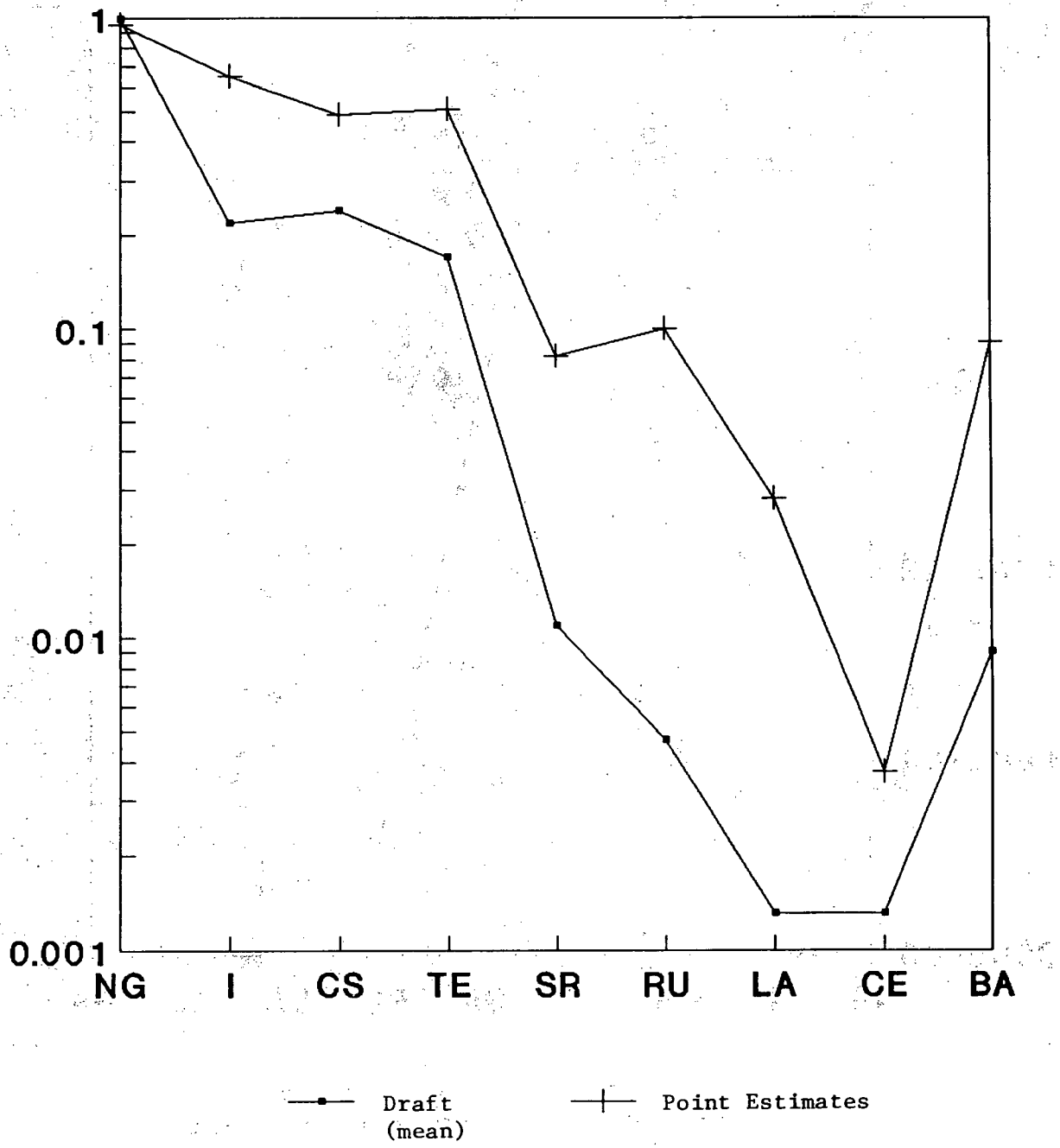


Figure 3 Source term quantification (rupture, early, DCH).

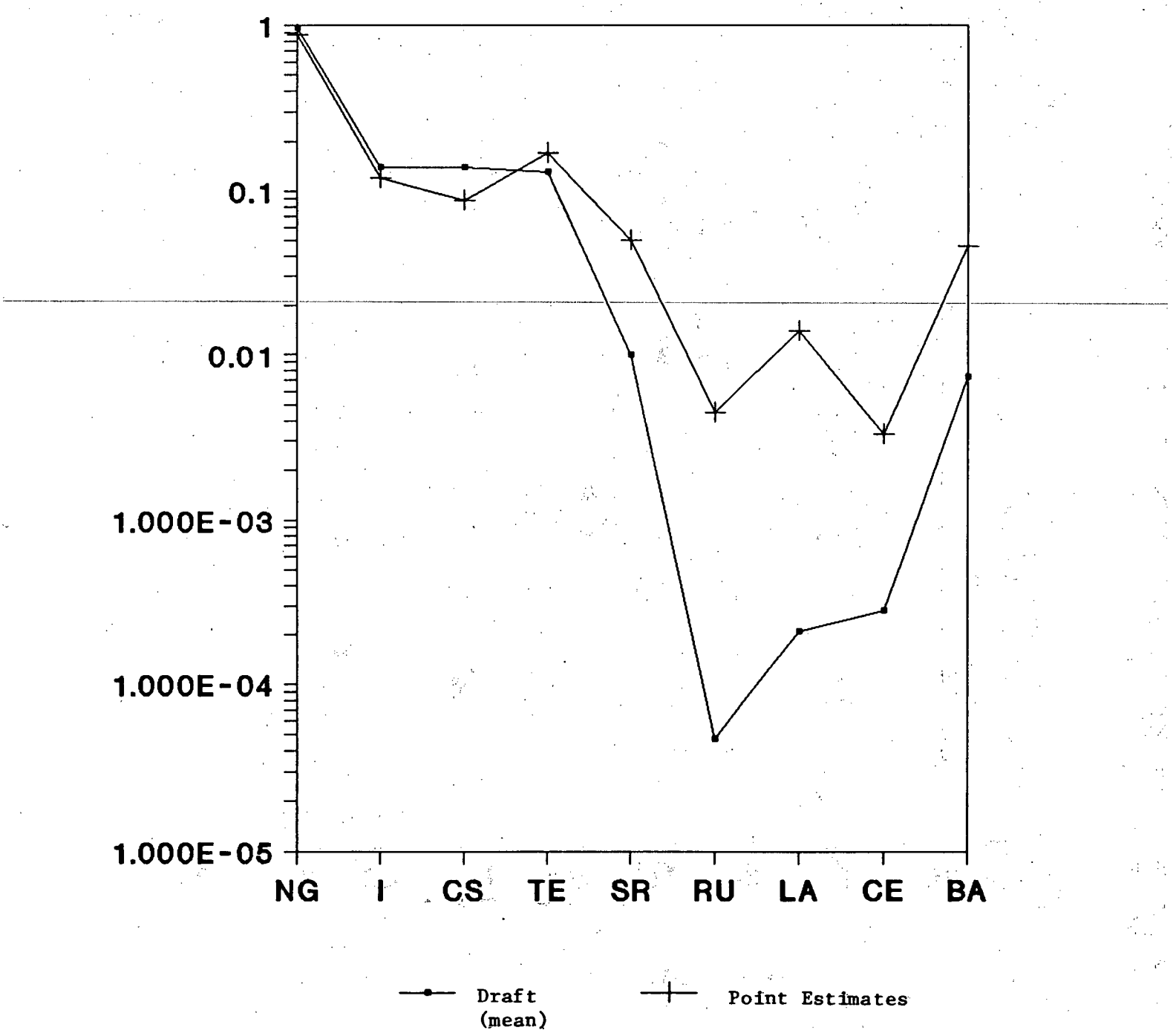


Figure 4 Source term quantification (leak, late, no spray).

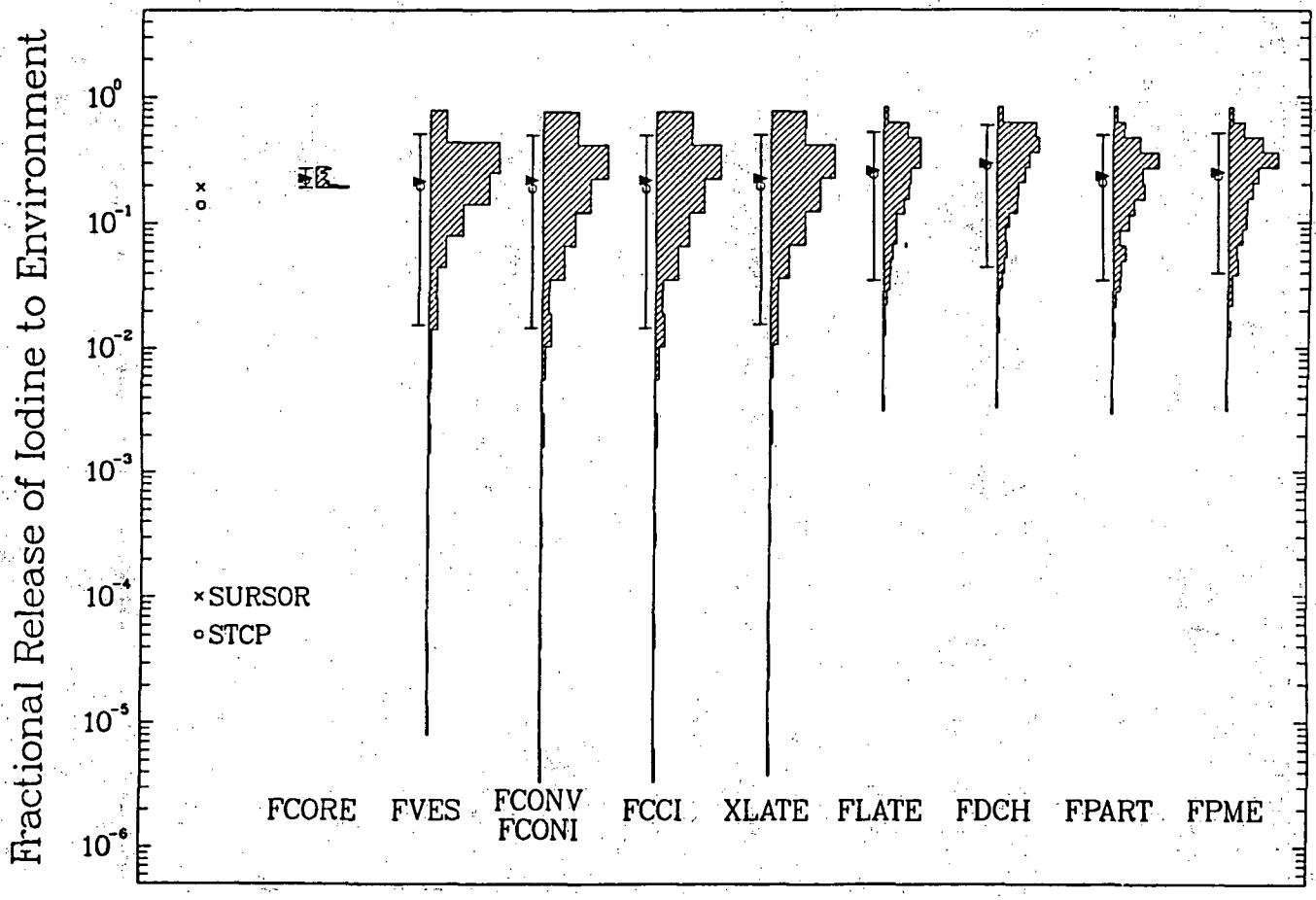


Figure 5 Changes in the uncertainty range for iodine release.

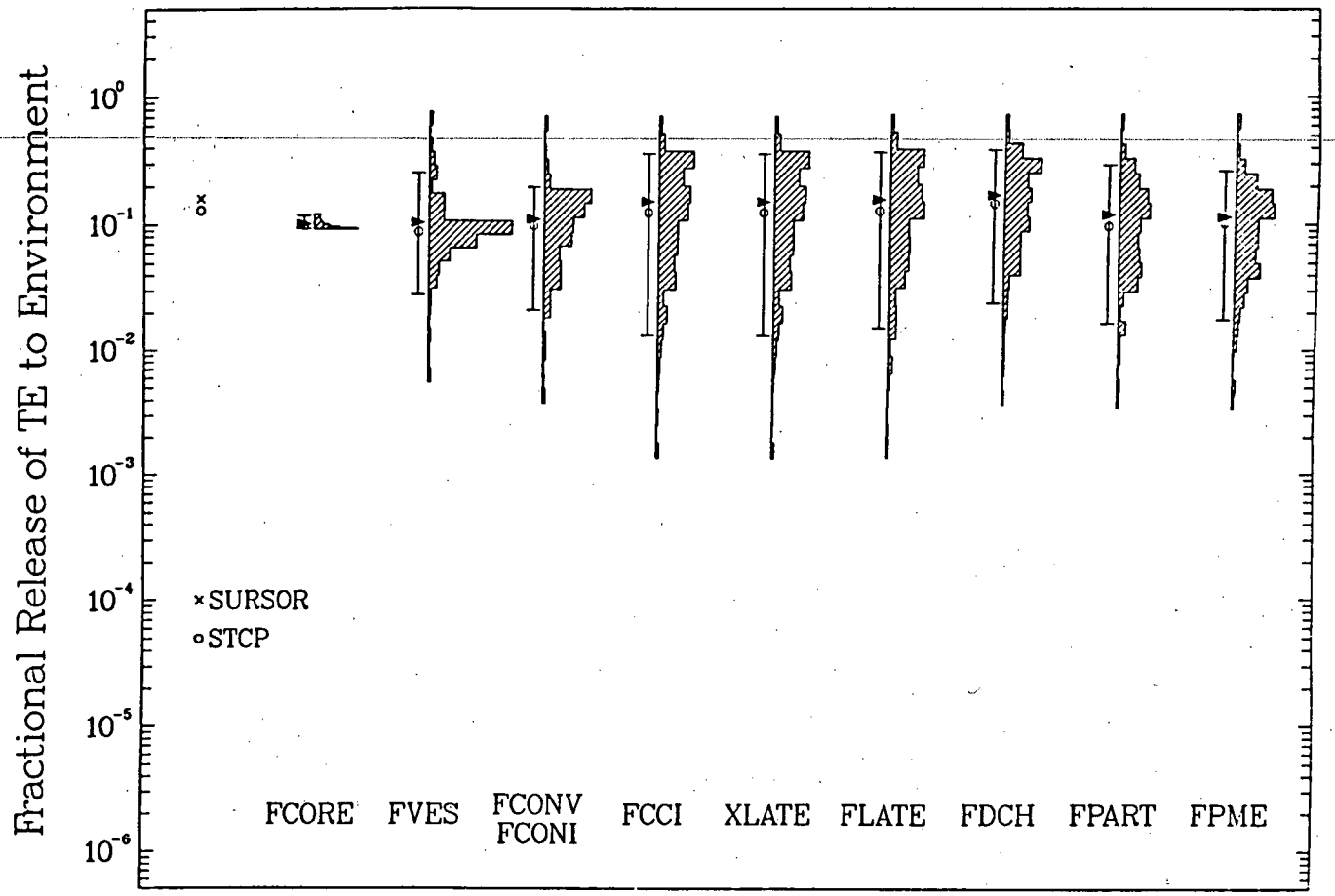


Figure 6 Changes in the uncertainty range for Te release.

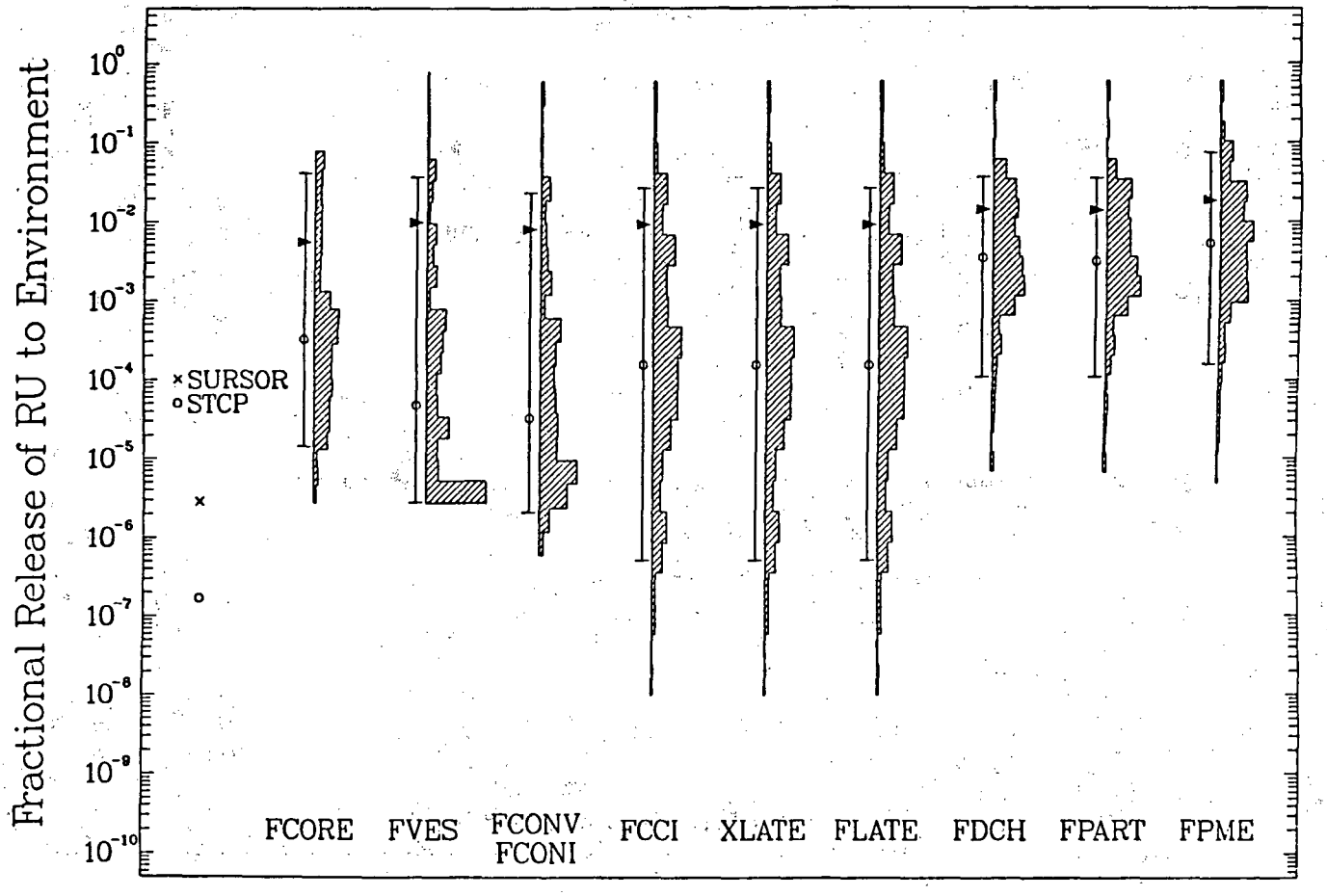


Figure 7 Changes in the uncertainty range for Ru release.

Table 1 A Partial Listing of CET Parameters and Ranges

Question No.	Question Type	Range
Q15	Temperature induced RCP seal failure	0 - 1
Q16	Temperature-induced hot leg break, in-vessel issue:	
	High Pressure	0 - 1
	Pressure around 2000 psia	0 - 1
Q19	Core cooling reestablished after power recovery:	
	Yes	.9 - 1
Q20	Core damage arrested	0 - 1
Q31	Fraction of core participating in HPME	.1 - .65
Q34	Alpha Mode	loguniform 10^{-6} - 10^{-2}
Q35	Rocket	loguniform 10^{-5} - 10^{-1}
Q37, 38	Pressure rise at vessel breach Surry load curves used for all cases	
Q40	Containment failure pressures	uniform 50-200 psia*
Q47	FCCI	0 - 1
Q57	H_2 produced in CCI	37.5 - 189.5
	H_2 produced in CO_2	250 - 1200
	Sprays and fan coolers at various times	0 - 1

*Preliminary

Table 2 Source Term Bin Analyzed (TMLB)

Containment failure near RPV failure
No spray
Prompt Dry MCCI
RPV pressure at system set point
With HPME
No STGR
Large amount of MCCI
Low Zr oxidation
Low HPME
Containment rupture
Two large hole in RCS

Table 3 Cases for Consideration by the Experts

Case	RCS Pressure (psia)	Cavity Water	Sprays Operating
1	2000-2500	Full	Yes
1a	2000-2500	Half	No
1b	2000-2500	Dry	No
3	500-1000	Full	Yes
3a	500-1000	Half	No
3b	500-1000	Dry	No
3c	500-1000	Full	No
4	50- 200	Full	No

Additional Variables

Description	Word	Letter	Nominal	Range
Core Fraction Ejected	High	HI	75%	> 50%
	Low	LO	33%	< 50%
Vessel Hole Size	Large	HI	2 m^2	> .5 m^2
	Small	LO	.1 m^2	< .5 m^2
In-Vessel Zr Oxidation	High	HI	60%	40-80%
	Low	LO	25%	10-40%

Table 4 Combined Cases for Containment Event Tree

Case	RCS Pressure	Cavity Water	Sprays Operating	Core Fraction Ejected	Vessel Hole Size
1	High[a]	Full	Yes	High[b]	Large[c]
2	High	Full	Yes	High	Small[d]
3	High	Full	Yes	Low[e]	Large
4	High	Full	Yes	Low	Small
5	High	Half/Dry	No	High	Large
6	High	Half/Dry	No	High	Small
7	High	Half/Dry	No	Low	Large
8	High	Half/Dry	No	Low	Small
9	Med[f]	Full	Yes	High	Large
10	Med	Full	Yes	High	Small
11	Med	Full	Yes	Low	Large
12	Med	Full	Yes	Low	Small
13	Med	--	No	High	Large
14	Med	--	No	High	Small
15	Med	--	No	Low	Large
16	Med	--	No	Low	Small
17	Low[g]	Full	No	--	--

[a] 2000-2500 psia
[b] 75%
[c] 2 m^2
[d] .1 m^2
[e] 33%
[f] 500-1000 psia
[g] 50-200 psia

Table 5 Aggregated Results for the Pressure Loads at Vessel Breach at Zion (Pressure Increments in Bars)

	Fractiles								
Case	0.01	0.05	0.10	0.25	0.50	0.75	0.90	0.95	0.99
1	1.33	2.39	3.23	5.12	6.68	7.95	9.57	10.67	12.11
2	1.24	2.09	2.69	4.05	6.03	7.10	8.25	9.67	11.17
3	1.20	2.03	2.49	3.51	4.55	5.60	6.48	6.97	7.66
4	1.11	1.82	2.20	2.94	4.05	4.86	5.63	6.43	7.62
5	1.91	2.85	3.77	5.83	7.38	8.52	9.66	10.27	11.30
6	1.84	2.56	3.18	4.75	6.72	7.80	8.60	9.26	10.64
7	1.85	2.43	2.94	4.02	4.97	5.86	6.82	7.26	7.96
8	1.48	2.03	2.43	3.36	4.51	5.40	6.14	6.52	7.30
9	1.19	1.97	2.54	3.66	5.32	6.45	7.34	8.14	9.60
10	0.96	1.67	2.06	2.93	4.48	6.00	6.90	7.71	9.57
11	1.04	1.63	1.99	2.70	3.65	4.49	5.14	5.48	5.92
12	0.91	1.25	1.52	2.21	3.13	3.97	4.46	4.73	5.22
13	2.00	2.50	3.00	4.14	5.99	7.13	7.92	8.50	9.62
14	1.42	2.08	2.48	3.36	5.02	6.59	7.41	7.79	9.04
15	1.67	2.07	2.31	2.96	4.02	4.78	5.26	5.58	5.99
16	1.07	1.67	1.96	2.46	3.48	4.34	4.88	5.16	5.64
17	0.45	0.75	0.92	1.22	1.75	2.48	3.02	3.34	4.28

Table 6 Structural Issue 1--Zion Static Failure Pressure
The Joint Probability Distribution of Containment Failure Mode

AGGREGATE

Pressure Psig	Failure Mode				Marginal
	Leak	Rupture (Hoop)	Rupture (Shear)	Catastrophic Rupture	
50	0.000	0.000	0.000	0.000	0.000
60	0.007	0.000	0.000	0.000	0.007
70	0.007	0.000	0.000	0.000	0.007
80	0.008	0.000	0.000	0.000	0.008
90	0.009	0.000	0.001	0.000	0.010
100	0.009	0.000	0.001	0.000	0.010
110	0.022	0.000	0.001	0.000	0.023
120	0.059	0.007	0.001	0.000	0.007
130	0.146	0.023	0.003	0.007	0.179
140	0.110	0.151	0.005	0.194	0.460
150	0.045	0.010	0.005	0.053	0.113
160	0.019	0.000	0.008	0.000	0.027
170	0.019	0.000	0.008	0.000	0.027
180	0.013	0.000	0.007	0.000	0.020
190	0.008	0.000	0.005	0.000	0.013
200	0.008	0.000	0.005	0.000	0.013
225	0.008	0.000	0.008	0.000	0.016
Marginal	0.497	0.191	0.058	0.254	1.000

DEPRESSURIZATION TO MITIGATE DIRECT CONTAINMENT HEATING[a]

Rosanna Chambers
Duane J. Hanson
R. Jack Dallman
Idaho National Engineering Laboratory
EG&G Idaho, Inc.

Frank Odar
U.S. Nuclear Regulatory Commission

ABSTRACT

Calculations are being performed to bound the system pressure and the time of lower head failure during a station blackout sequence in a 3-loop pressurized water reactor using the SCDAP/RELAP5 computer code. Failure of the pressurizer surge line from creep rupture was predicted prior to lower head failure. To bound the system pressure response from a pressure boundary failure, calculations, extending to the time the accumulators had emptied, have been performed. Calculations bounding in-core damage progression prior to relocation of molten material to the lower plenum have also been completed. Heat transfer to the coolant was maximized and minimized by varying in-core relocation and fragmentation parameters within their uncertainty ranges. The system pressure was lowered significantly, but core damage was extensive. The system pressure was not strongly influenced by the progression of core melt. However, the extent of the molten pool was strongly affected by variation of in-core damage progression parameters. Calculations are planned to bound the pressure and timing of lower head failure by applying reasonable bounds to the porosity of the debris as it moves into the lower plenum.

INTRODUCTION

Direct containment heating (DCH) can potentially occur during certain pressurized water reactor (PWR) severe accidents after core melt and high pressure melt ejection from the reactor pressure vessel (RPV). Molten core material is dispersed into the containment and a rapid transfer of energy to the containment atmosphere follows. The resultant rise in the temperature and pressure could cause the containment to fail relatively early in the accident sequence.

Depressurization of the reactor coolant system (RCS) is a proposed accident management strategy to reduce the DCH contribution to early containment failure. An analysis evaluating the effectiveness of this strategy is being conducted at the Idaho National Engineering Laboratory.

ANALYSIS DESCRIPTION

The capability to depressurize a 3-loop PWR during a TMLB' sequence (loss of ac power and feedwater) using the pressurizer power operated

---

a. Work supported by the U.S. Nuclear Regulatory Commission, Office of Nuclear Regulatory Research under DOE Contract No. DE-AC07-76ID01570.

relief valves (PORVs) and the RPV head vent is being analyzed using the SCDAP/RELAP5 computer code[1]. The TMLB' sequence (loss of ac power and feedwater) was identified in draft NUREG-1150 analyses[2] as an important contributor to the probability of early containment failure.

Calculations to bound the system pressure and the time of lower head failure are being performed. These calculations are listed in Table 1 along with the parameter values associated with fuel relocation, reflood fragmentation, and debris porosity.

Calculation 1 was performed to assess the system behavior when the fuel rods remained essentially intact through the time when the accumulators had emptied, maximizing cladding oxidation and heat transfer to the coolant. Calculation 2 presents the pressure sensitivity to failure of the RCS pressure boundary at the surge line. Calculations 1 and 2 did not include improved code models for UO_2 dissolution and fragmentation of oxidized cladding by quenching. Further calculations, as described below, were then performed with these models.

Calculations 3-5 were performed in order to determine the parameter values that maximize fuel dissolution and relocation. In these calculations, two input parameters were varied within their uncertainty ranges; the Zircaloy oxide failure temperature and the percent of Zircaloy oxidation above which relocation will not take place. The Zircaloy oxide failure temperature is between the melting point of Zircaloy (2123 K) and of ZrO_2 (2973 K). When this temperature is reached, the oxide shell (if thin enough) will fail, allowing molten Zircaloy with chemically dissolved UO_2 to relocate downward. If the cladding is sufficiently oxidized, however, the Zircaloy oxide shell is able to contain the molten core material and downward relocation is precluded. The second input parameter is the fraction of cladding oxidation above which the oxide shell will not fail. The uncertainties in these two parameters have not been quantified, but, using a failure temperature of 2680 K and maximum oxide thickness for failure that corresponds to 60% cladding oxidation, results are obtained that are in agreement with the PBF SFD 1-4 experiment[3]. Calculation 3 was performed with these parameters. In calculations 4 and 5, temperatures of 2300 K and 2400 K were used and relocation was allowed until the Zircaloy was 99.9% oxidized. By thus varying the input failure temperature, a maximum amount of UO_2 that can be dissolved by the molten Zircaloy before the cladding is almost completely oxidized can be determined. Fuel relocation is, therefore, maximized.

The four remaining calculations are being performed to establish bounds on system pressure and time of lower head failure. These calculations do not extend over the full transient, but will establish the influence of important modeling uncertainties. As shown on Figure 1, the calculations will establish the envelope of behavior along two damage progression pathways. The upper pathway is expected to result in the maximum increases in system pressure, but should produce the longest time from accident initiation to lower head failure. This pathway results from the selection of bounds on modeling options that maximize the heat transfer from the damaged core and debris to the coolant. The lower pathway is the opposite extreme. In this pathway, modeling bounds are selected that minimize the transfer of heat so the maximum energy goes into heating the core material rather than the coolant.

Table 1. Depressurization Calculations

Calculation	Relocation parameters		Fragmentation parameters		Debris Porosity[a]
	ZrO_2 temperature[b]	Percent oxidized[c]	Cladding temperature[d]	Beta layer thickness[e]	
Pressure boundary sensitivities					
1 - Intact surge line	2500 K	60	f		
2 - Failed surge line	2500 K	60	f		
Relocation sensitivities					
3	2680 K	60	Tsat+200 K	0.0001 m	
4	2300 K	99.9	Tsat+200 K	0.0001 m	
5	2400 K	99.9	Tsat+200 K	0.0001 m	
Core configuration sensitivities					
6 - Maximize fragmentation	2680 K	60	1273 K	0.0001 m	
7 - Maximize metallic U-Zr-O relocation	2400 K	99.9	Tsat+90 K	0.0001 m	
Steam interaction sensitivities					
8 - Maximize steam interactions					0.5
9 - Minimize steam interactions					0.001

a. Ratio of volume of molten material interstices to volume of its mass.
b. Temperature at which ZrO_2 shell fails.
c. Percent of Zr oxidation above which relocation will not take place until ZrO_2 melting.
d. Temperature at which ZrO_2 will shatter.
e. Thickness of the beta-Zr layer above which ZrO_2 will not shatter.
f. Fragmentation not calculated.

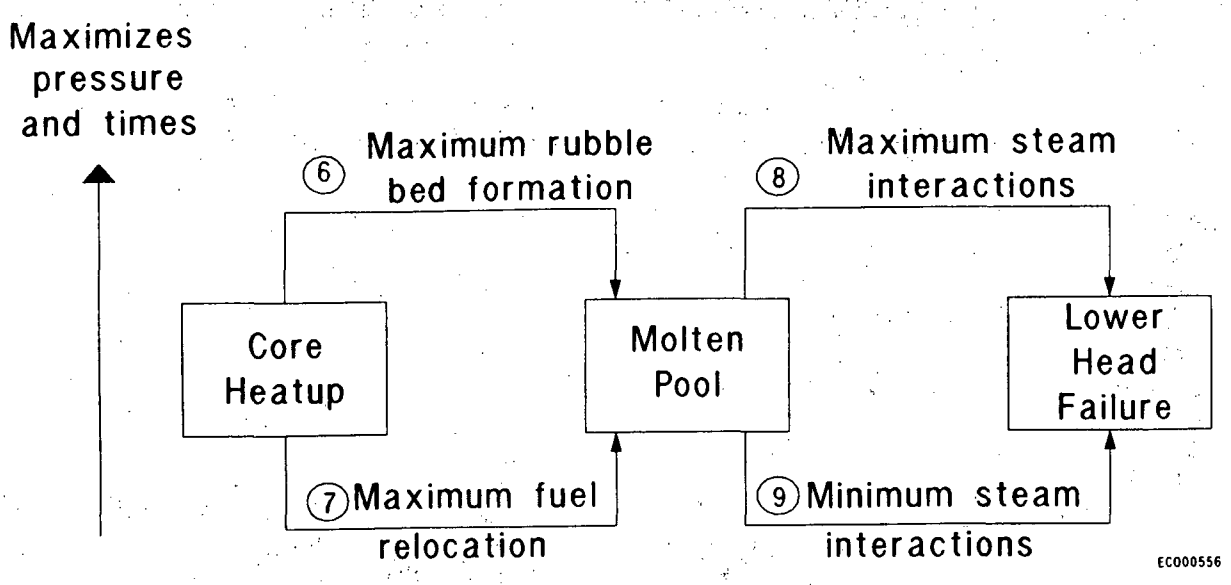


Figure 1. Logic diagram for calculations 6 through 9.

In the first branch of the upper and lower pathways, two possible mechanisms for in-core fuel relocation were bounded. The first is the relocation of mostly ceramic $(U,Zr)O_2$ resulting from the melting of UO_2 and ZrO_2. Zircaloy oxidation is allowed to proceed as far as possible prior to melt relocation. The second mechanism is the relocation of mostly metallic U-Zr-O resulting from the melting of Zircaloy and chemical dissolution of UO_2. Also, the timing and amount of cladding embrittlement and fragmentation by quenching were bounded. In the upper pathway, maximum rubble bed formation, relocation of metallic U-Zr-O mixtures were minimized, allowing in-place oxidation of the cladding to proceed as long as possible, thus maximizing the oxidation heat generation. The criteria for rubble formation were set so that a reasonable upper bound for cladding oxide embrittlement was used, resulting in the shattering of the maximum amount of ZrO_2 and an increased surface area for heat transfer to the coolant. In the lower pathway, maximum metallic U-Zr-O relocation, input parameters were chosen to maximize relocation of metallic mixtures of U-Zr-O. Because this process is highly non-linear, with the maximum mass of liquefied material occurring between the melting point of Zircaloy and of ZrO_2, calculations 3 through 5 were performed to find the maximum mass relocated. The criteria for rubble bed formation were set so that a reasonable lower bound for cladding embrittlement and core quenching was used. Thus, heat transfer to the coolant was minimized.

In the second branch, the behavior of molten material as it moves into the lower plenum is bounded. The upper pathway, maximum steam interactions, results from the selection of modeling options that allow

the molten material, emerging from an in-core molten pool, to quench as it moves into the lower plenum. Consequently, the heat transfer to the coolant is also maximized during this event but the lower head debris is cooled prior to interaction with the lower head. The lower pathway is the bounding behavior for the penetration of molten material into the lower plenum where steam generation is minimized. Thus, there is little pressurization, but the debris bed in the lower plenum is still molten when it first contacts the lower head.

In calculations 6 and 7, in-core relocation and reflood fragmentation parameters were varied. The in-core relocation parameters are described above. The fragmentation parameters are the Zircaloy oxide temperature at which shattering occurs and the beta-Zr layer thickness below which the oxide will shatter. The oxide temperatures are 1273 K (the temperature of a phase change in the oxide - above which the oxide is too pliable to fragment[4]) and Tsat + 90 K (a lower limit on this temperature). The beta-Zr layer is unoxidized Zircaloy, so, the smaller the thickness, the more the cladding has oxidized. The uncertainty in the beta-Zr layer thickness is very small. Therefore, this parameter was not varied from the best-estimate value of 0.0001 m. Using the results of calculations 3-5, the parameters giving a maximum rubble bed formation with a minimum metallic U-Zr-O relocation (calculation 6) and a maximum metallic U-Zr-O relocation with a minimum rubble red formation (calculation 7) were determined. Calculations 6 and 7 were performed up to the time a molten pool was formed and had begun relocating to the lower plenum.

After the time of molten pool formation and relocation to the lower plenum, calculations 8 and 9 will be performed, respectively maximizing and minimizing the molten pool/steam interactions. These sensitivities will bound the time and pressure at vessel meltthrough. In calculation 8, the porosity of the relocating molten material will be set to 0.5 (the maximum porosity of particles from the TMI lower head debris examination[5]), maximizing the surface area of the molten material and the transfer of stored energy from the molten material to the coolant. This will cause an increase in the system pressure, but will partially cool the molten debris and delay the time of lower head failure. Conversely, the stored energy will be retained in the molten pool in calculation 9 by setting the porosity of the relocating molten material to 0.001 (simulating minimal break up of the molten material). The pressure effect will be less than in calculation 8; but heat will be retained in the debris, causing lower head failure to occur earlier.

RESULTS

Calculations 1 and 2

Calculation 1 was performed to assess the system behavior during core degradation with essentially intact rods. Cladding oxidation was allowed to proceed as far as possible, providing the maximum oxidation heat production and high heat transfer to the coolant. The pressurizer surge line was predicted by SCDAP/RELAP5 to fail by creep rupture near the hot leg connection. Calculation 2 was performed to investigate sensitivity of system pressure to failure of the reactor coolant system pressure boundary. In calculation 1, the surge line failure was not simulated. Calculation 2 assumed the surge line to fail, with a break area equal to

the pipe cross-sectional area. Depressurization was initiated when the steam generator secondaries were dry, by latching open the PORVs and the RPV head vent. The calculations were terminated when the accumulators were empty.

The calculated results were identical until surge line failure. The RCS pressure response is plotted in Figure 2. The RCS rapidly depressurized when the PORVs and head vent were opened. The pressure then increased when boiling began in the core and the pressurizer became liquid full. This increase continued until the PORVs began venting steam again.

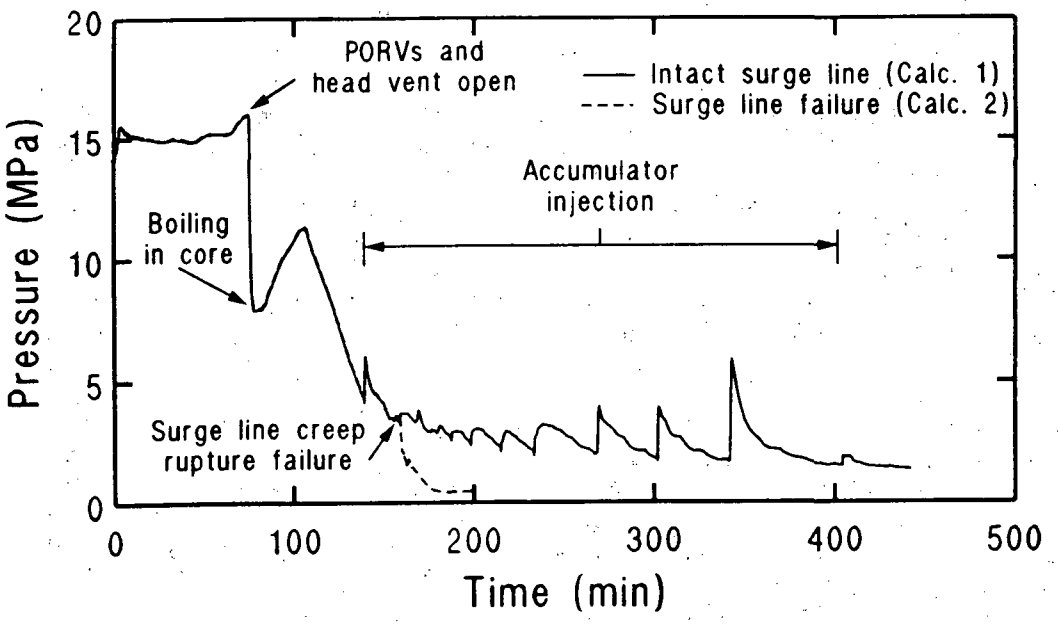


Figure 2. Primary system pressures from calculations 1 and 2.

Figure 3 contains plots of the cladding surface temperature in the top-center of the core. Core heatup began at 114 min - about 45 min earlier than during a TMLB′ sequence with no depressurization[6]. Complete oxidation of the cladding in the top of the core was calculated. The thick oxide shell prevented relocation of metallic U-Zr-O_2 and resulted in a mostly rod-like geometry throughout the calculation. However, limited relocation of ceramic $(U,Zr)O_2$ resulted from the melting of UO_2 and ZrO_2. Accumulator injection provided core cooling, but temporarily caused the pressure to increase. The core began to heatup again, but after a delay of about 200 minutes. Fragmentation of ZrO_2 during accumulator injection was not calculated to occur in these simulations.

For the intact surge line calculation (calculation 1), cyclic accumulator injection caused cooling of more than half the core and it remained partially cooled for about 3 hours. The pressure decreased to 1.3 MPa after the accumulators emptied. Oxidation of 73% of the Zircaloy in the core was calculated producing 515 kg of hydrogen.

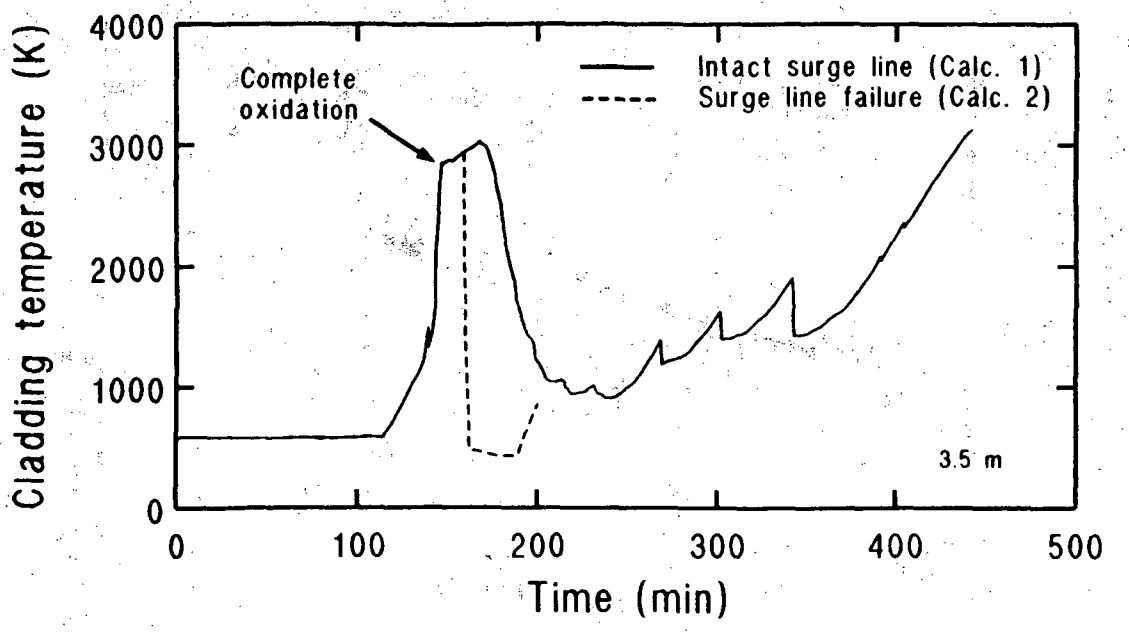


Figure 3. Maximum cladding surface temperatures from calculations 1 and 2.

In calculation 2, when the surge line failed, the RCS depressurized rapidly to 0.4 MPa. The core was covered by accumulator water and a complete core quench resulted. However, heatup started again about 20 minutes later.

Calculations 3, 4, and 5

The purpose of these calculations was to determine the values of the input parameters that maximize metallic relocation of cladding and dissolved fuel. The calculations were initiated at the time cladding heatup began, using conditions from calculation 1. They were terminated after melting and relocation of core material had occurred.

Figure 4 is a plot of cladding surface temperatures at the top-center of the core from calculations 3, 4 and 5. The peak temperature at this elevation was calculated at about 150 min. The highest cladding temperature at this elevation occurred in calculation 3. The peak temperature was reached when the fuel rod cladding at this elevation became completely oxidized and oxidation heat generation was no longer possible. The cladding did not fail because it was more than 60% oxidized when cladding temperatures reached the failure temperature. Relocation of fuel rod material was, therefore, prevented. Zircaloy was relocated, but came from control rod guide tubes. However, in calculations 4 and 5, the peak temperatures were reached when the failure temperature was calculated. These temperatures were 2300 K for calculation 4 and 2400 K for calculation 5. In these two calculations, relocation of fuel rod material occurred, because the rods were not oxidized above 99.9% when the failure temperature was calculated.

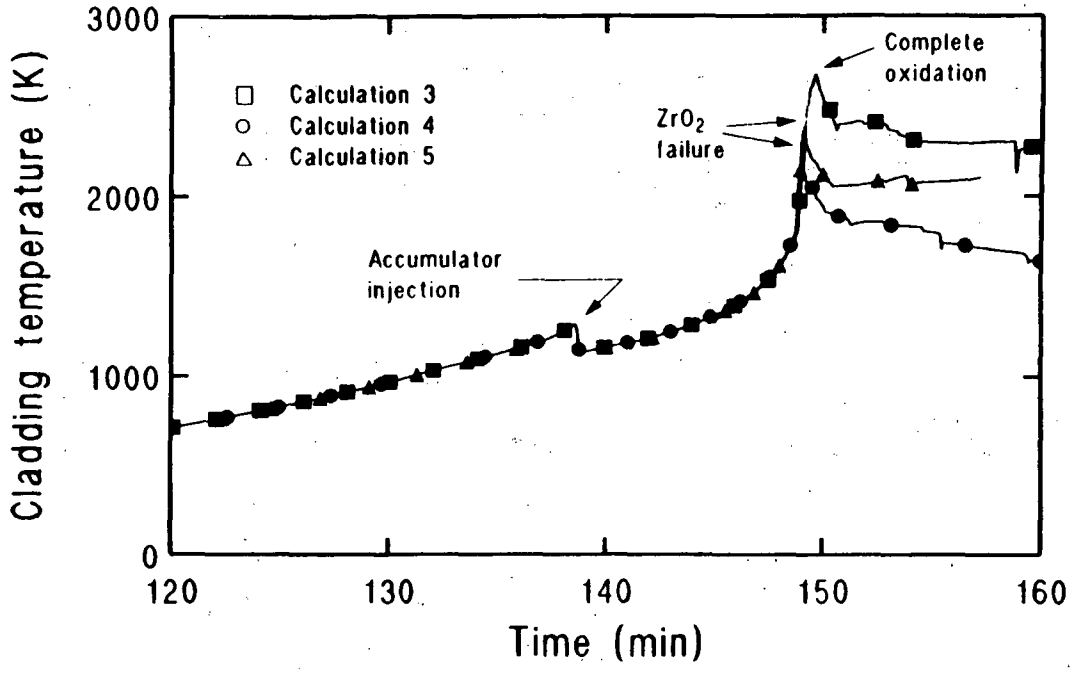


Figure 4. Maximum cladding surface temperatures from calculations 3, 4, and 5.

Table 2 presents the masses of uranium, Zircaloy, and control rod material that were relocated during the three calculations. For this transient, the maximum fuel relocation occurred in calculation 5, when the input failure temperature was 2400 K and the maximum oxide thickness for relocation corresponded to 99.9% cladding oxidation.

Table 2. Core Material Relocated (kg)

Calculation	Time (min)	UO_2	Zr[a]	Control material	Stainless steel
3	170	0	275	770	190
4	170	470	395	200	50
5	160	2280	585	435	105

a. Includes control rod Zircaloy

The information gained from calculation 3 (highest fuel rod temperatures and maximum cladding oxidation) and from calculation 5 (maximum fuel relocation) were used to generate input for calculations 6 and 7, respectively.

Calculations 6 and 7

Calculations 6 and 7 were performed to bound the system pressure and the timing of events before relocation of molten pool material to the lower plenum. The calculations were initiated when cladding heatup began using conditions from calculation 1, and were terminated when molten core material had begun relocating to the lower plenum.

Table 3 presents a sequence of events from calculations 6 and 7. Modelling differences caused timing differences in the calculations. For instance, fragmentation by quenching occurred earlier in calculation 6 and relocation of molten U-Zr-O occurred much earlier and to a much larger extent in calculation 7. The difference in timing of two other phenomena are also related to differences in modelling assumptions. First, the timing of surge line failure is attributable to these modelling differences. Since metallic U-Zr-O relocation did not occur until very late in the transient in calculation 6, more cladding oxidation was calculated before 166 min than in calculation 7. Therefore, more heat was generated and transferred to the coolant, causing the surge line to fail earlier in calculation 6 than in calculation 7. A second difference is the timing of the relocation of molten material to the lower plenum. The molten pool in calculation 6 was much larger than in calculation 7 and extended from the bottom to the top of the center of the core. It extended to a lower elevation because metallic U-Zr-O relocation occurred at a higher temperature. Relocation of material to the lower plenum in calculation 6 began when the lower crust supporting this molten pool failed. However, in calculation 7, because the lowest elevation of cohesive debris was more than 1 m above the bottom of the core, metallic U-Zr-O from fuel rods in the bottom 1 m of the core relocated into the lower head without encountering blockage.

Table 3. Sequence of Events for Core Configuration Sensitivities

Event	Time (min)	
	Calc 6	Calc 7
Loss of ac power	0	0
PORVs and head vent open	75	75
Cladding heatup	114	114
Cladding oxidation	131	131
Cladding ballooning	< 133	< 133
Cladding failure	137	137
Accumulator injection	139	139
Control rod slumping	< 150	< 150
Surge line failure prediction	166	172
Fragmentation by quenching	183	193
In-core metallic U-Zr-O relocation	366	149
Accumulators empty	367	348
Molten pool formation (ceramic melting)	400	378
Molten material to lower plenum	452	390
Failure of lower support crust	452	

The system pressure response is plotted in Figure 5 for both calculations 6 and 7. The two pressures are similar, both increasing temporarily each time accumulator injection occurred. Differences in core damage had little effect on the system pressure. When material began relocating to the lower plenum, the pressure from calculation 6 was 1.06 MPa and that from calculation 7 was 1.23 MPa. Liquid was still boiling in the core in calculation 7, causing the pressure to be slightly higher.

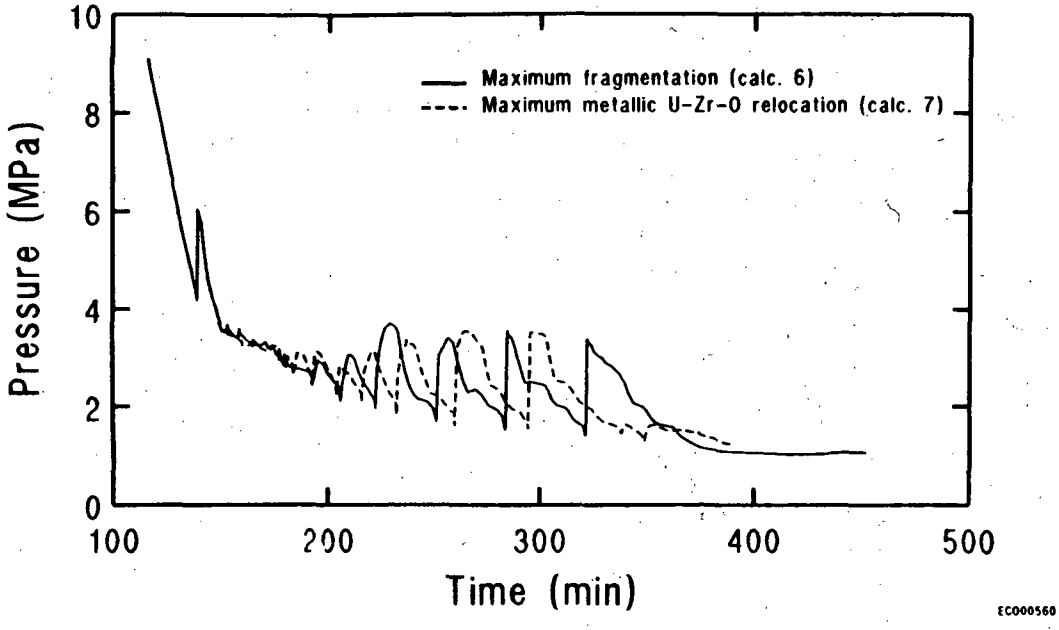


Figure 5. Primary system pressures from calculations 6 and 7.

Figure 6 is a plot of cladding surface temperatures near the top of the core from calculations 6 and 7. The initial temperature responses are similar to those from calculations 3 through 5. The peak cladding surface temperature at this elevation in calculation 6 was reached when the cladding had completely oxidized and heat was no longer being generated. The cladding in calculation 7 reached 2400 K at a slightly earlier time and the oxide shell was breached and slumping of Zircaloy and dissolved fuel occurred. The mixture relocated to a lower elevation and froze, resulting in a flow restriction. The cladding surface temperature decreased shortly after that time, but began increasing again because cladding oxidation was occurring at lower elevations. The temperature decreased in both calculations when the system pressure became low enough for accumulator injection. This decrease continued until about 230 min. Injection of water from the accumulators provided sufficient cooling to delay further core damage for about 200 minutes. At about 180 min, fragmentation of cladding occurred in the top 40% of the center of the core in calculation 6. The flow resistance through the top 40% the core increased significantly and coolant flow decreased. An increase in temperature resulted. The cladding in calculation 7, however, did not shatter until later. When shattering did occur, a similar temperature

increase was not calculated. The power was lower at this elevation in calculation 7 than in calculation 6 because a significant fraction of the fuel had relocated from this elevation. The temperatures at this elevation increased to 3590 K and 2920 K for calculations 6 and 7, respectively.

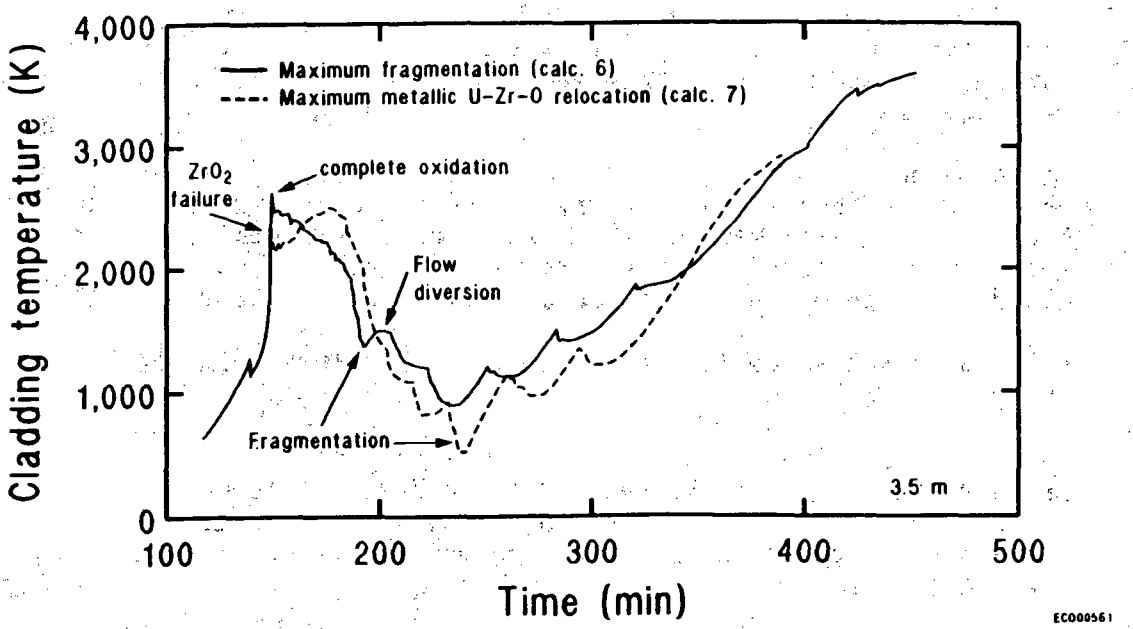


Figure 6. Maximum cladding surface temperatures from calculations 6 and 7.

Core damage progressed differently in the two calculations. In calculation 6, complete oxidation of the top 40% of the fuel rods occurred. Relocation of metallic U-Zr-O did not occur until very late, and only at lower elevations in the center of the core. Instead, the highly oxidized rods were fragmented when water from the accumulators was injected. Eventually, melting of ZrO_2 contributed ceramic $(U,Zr)O_2$ to the debris. Heatup of the debris bed thus formed continued in this mixture of fragmented cladding and molten ZrO_2 until its melting temperature was reached. The temperature continued to increase until UO_2 melting temperature was calculated. The entire center and the upper portions of the periphery of the core were molten when relocation to the lower plenum began in calculation 6. This relocation was caused by failure of the supporting crust. The molten pool contained 81120 kg of material, representing about 77% of the material in the core. On the other hand, in calculation 7, much of the core material, including dissolved UO_2, had already relocated from its original position by the time fragmentation of the oxide in the upper core occurred. Most of the center portion of the core, but none of the periphery was part of the molten pool when relocation to the lower plenum began. The relocated

material came from below the lower support crust. 51700 kg of material were in the molten pool - about 50% of the core. In calculation 6, 45% of the Zircaloy in the core was oxidized and 318 kg of hydrogen had been produced, while 42% was oxidized in calculation 7 producing 295 kg of hydrogen.

CONCLUSIONS

For the described calculations, the following observations were made:

- Depressurizing the primary system shortens the time to core damage, but accumulator injection delays substantial core melting.

  The time until the beginning of core damage was shortened by about 45 min because the primary system was depressurized. But because the system was depressurized, the accumulator pressure setpoint was reached and the core was cooled. Heatup of the cladding began again, but after a delay of about 200 min.

- Failure of the surge line prior to vessel failure from creep rupture is probable.

  In all calculations, the surge line was predicted to fail by creep rupture between 159 and 172 min. When modelling of the surge line failure was not included, the surge line metal temperature reached and exceeded the melting temperature of stainless steel.

- Relocation of molten core materials into the lower plenum occurs between 6.5 and 7.5 hours after the loss of power.

  Molten pool formation and relocation to the lower plenum occurred later, but applied a much greater challenge to the lower head when modelling assumptions for core damage progression were chosen that maximized oxidation and fragmentation and minimized fuel relocation. Conversely, an earlier relocation occurred when fuel relocation was maximized, but oxidation and fragmentation were minimized.

- System pressure is not significantly influenced by the progression of core damage prior to melt relocation to the lower plenum.

  Calculations bounding core damage phenomena resulted in little difference in the system pressure response. Relocation of molten materials to the lower plenum occurred near the pressure of the final accumulator injection.

- The extent of the molten pool is strongly affected by variation of in-core damage progression.

  The size of the molten pool varied from 50% to 77% of the core.

FUTURE WORK

The following tasks are planned to complete the analysis of primary system depressurization to mitigate DCH.

- Complete the assessment of the influence of core relocation to the lower plenum on system pressure.

  Calculations bounding the heat transfer to the coolant in the lower plenum will be performed. The timing and system pressure at vessel failure can, therefore, be bounded.

- Investigate the effect of secondary water addition and secondary side depressurization.

  As an alternative to primary system depressurization, an accident management strategy determining whether feed and bleed of the secondary system using mobile pump systems, e.g. fire trucks, to prevent core damage or prevent or mitigate DCH will be assessed.

- Investigate the effect of later initiation of depressurization.

  A determination will be made of whether depressurization at a time later than steam generator dryout, e.g. when upper plenum thermocouples read 1200^{o}F, would mitigate DCH.

- Evaluate the influence of the PORV size on the depressurization rate.

  A study of other PWRs will be performed to ascertain the feasibility of extending Surry results to other PWR plants which have different PORV relief capacities.

- Evaluate the influence of hydrogen generated during core degradation on the containment response.

  Since a large amount of hydrogen was discharged from the PORVs during core degradation, further study of the disposition of hydrogen in the containment should be performed.

REFERENCES

1. C. M. Allison et al., SCDAP/RELAP5/MOD1 Code Manual, EG&G Idaho Draft Preliminary Report, February 1988.

2. A. S. Benjamin et al., Evaluation of Severe Accident Risks and the Potential for Risk Reduction: Surry Power Station, Unit 1, Vol. 1, NUREG/CR-4551, SAND86-1309, (Draft), February 1987.

3. D. A. Petti, et al., PBF Severe Fuel Damage Test 1-4 Test Results Report (Draft), NUREG/CR-5163, EGG-2542, September 1988.

4. R. J. Ackermann, S. P. Garg, and E. G. Rauh, "High-Temperature Phase Diagram for the System Zr-O", Journal of the American Ceramic Society, Vol. 60, No. 7-8, July-August 1977.

5. C. S. Olsen, D. W. Akers, and R. K. McCardell, Examination of Debris From the Lower Head of the TMI-2 Reactor, GEND-INF-084, January 1988.

6. P. D. Bayless, Analysis of Natural Circulation During a Surry Station Blackout Using SCDAP/RELAP5, NUREG/CR-5214, EGG-2547, to be published (manuscript completed September 1988).

IDENTIFICATION OF ACCIDENT MANAGEMENT INFORMATION NEEDS

Duane J. Hanson William R. Nelson
Leonard W. Ward
Idaho National Engineering Laboratory
Idaho Falls, ID 83415

Donald E. Solberg
U.S. Nuclear Regulatory Commission
Washington D.C. 20555

ABSTRACT

An assessment of the information needs of plant operating personnel during severe accidents is being performed to support accident management research conducted by the U. S. Nuclear Regulatory Commission. The objectives of this research are to identify: (1) the information needs for a broad range of severe accidents, (2) those existing measurements capable of supplying these needs, (3) potential limitations on the capabilities of existing systems to function under severe accident conditions, and (4) areas where the information systems may mislead plant personnel. A three step approach has been developed to first identify the relationships between the safety objectives of accident management and the strategies for accomplishing them and then to use these relationships as a tool to determine the information needs and the capabilities of existing measurements to supply these needs. The information needs developed using this approach will form the basis for more comprehensive information needs developed through detailed strategy analysis. This paper provides a progress report of a "proof of principle" application of this approach to a Pressurized Water Reactor with a large dry containment.

INTRODUCTION

The U.S. Nuclear Regulatory Commission (NRC) is conducting an Accident Management Research Program that emphasizes the application of severe accident research results to enhance the capability of plant operating personnel to effectively manage severe accidents. These plant operating personnel, (including reactor operators, shift technical advisors, and technical support center personnel) are responsible for diagnosing an accident, determining its safety significance, monitoring performance of automatic systems, selecting corrective actions, and implementing these actions. Without proper information and guidance, these operating personnel cannot fulfill their roles. Hence, it is vital to ensure that plant information systems adequately support the plant personnel during severe accidents.

The information needs of the plant operating personnel during severe accidents are being addressed as an issue in the Accident Management Research Program Plan. A research project has been developed to aid in resolving this issue by identifying (1) the information needs of the plant

personnel during a broad range of accident conditions, (2) the existing plant measurements capable of supplying these information needs and what, if any, minor additions to instrument and display systems would enhance the capability to manage accidents, (3) known limitations on the capability of these measurements to function properly under the conditions that will be present during a wide range of postulated severe accidents, and (4) areas in which the information systems could mislead plant personnel.

A three step approach has been developed for identifying accident management information needs. The first step identifies the relationships between the high level safety objectives that have been identified for severe accident management and the potential strategies for accomplishing these objectives. The second step uses these relationships to identify the information needed by the operating personnel to understand what objectives are not being met and what strategies may be effective. The final step examines the capability of existing or proposed measurements to supply these information needs. The information needs developed using this approach will form the basis for more comprehensive information needs developed through detailed strategy analysis. This paper provides initial results from a "proof of principle" application of the first step of this approach to a Pressurized Water Reactor (PWR) with a large dry containment. Example results from portions of the second step are also provided as well as a brief description of future work.

APPROACH

The initial step in the three step approach utilizes a "top down" evaluation that starts with the overall objectives of accident management and relates these objectives to the various strategies using a hierarchical tree structure. The role of the plant operating personnel during the management of an accident is to reach certain safety objectives. In order to reach these safety objectives, certain critical plant safety operations, i.e., safety functions, must be maintained. An accident can present challenges to the safety functions which may result from different physical mechanisms. Finally, the operating crew can implement various strategies for dealing with the mechanisms that result in safety function challenges. The operating crew thus fulfills its role to reach the safety objectives by:

1. Monitoring the status of the safety functions
2. Detecting challenges to the safety functions.
3. Identifying, if possible, the specific mechanisms that could be causing the safety function challenges.
4. Selecting and implementing strategies for maintaining or restoring challenged safety functions.
5. Monitoring the performance of the strategies to determine if they are having the desired effects in maintaining or restoring the safety functions.

The categories described above: safety objectives, safety functions, challenges, mechanisms, and strategies, form a natural hierarchy that defines the role of the operating crew for accident management. For convenience of analysis, this hierarchy can be arranged in a tree structure. It is then possible to evaluate the tree structure for specific severe accident scenarios to determine the effects of the scenario on the safety objectives, what challenges are presented to the safety functions, what strategies are disabled by the event, and what remaining strategies are appropriate for use to mitigate safety function challenges.

The Safety Objective Trees developed initially are used in the second and third steps of the approach as a tool to systematically determine the operating crew's information and measurement needs. To identify information needs, the branch points at various levels in these trees were examined to decide what information is necessary to: (1) determine the status of the safety operations (functions) in the plant, i.e., whether the safety functions are being adequately maintained, (2) identify plant behavior (mechanisms) or precursors to this behavior that will indicate a challenge to plant safety is occurring or is imminent, and (3) select strategies that will prevent or mitigate this plant behavior and monitor the implementation and success of these strategies. Measurements that have the potential to supply the identified information needs are then determined and compared to the measurements available in a plant. Ranges of operation of the existing measurements and their qualification requirements can then be compared to parameters calculated during the analysis of severe accidents and judgements made regarding the capability of the existing measurements to supply accurate, unambiguous information.

SAFETY OBJECTIVE TREE DEVELOPMENT

The Accident Management Research Program Plan subdivides the issues into those associated with in-vessel accident management and those associated with containment and release management. Based on this subdivision, the following safety objectives were selected for analysis: prevent reactor vessel failure, prevent containment failure, and mitigate fission product release. The safety objective trees developed for each of the three safety objectives assume that the accident management strategies aimed at preventing core damage have failed and that core damage has occurred, or is imminent. Hence, prevention of core damage is not included in the development of the trees. The strategies shown on each tree are a preliminary set that generally require further evaluation to determine whether they adequately prevent of mitigate the appropriate mechanisms. Following is a brief description of the trees for the three safety objectives selected.

Prevent Vessel Failure Safety Objective Tree

The safety objective for preventing vessel failure is important in both short and long term accident management because the strategies and actions for managing a degraded core would be less complicated if the core material could be retained within the boundary of the reactor vessel. In

addition, there are relatively large uncertainties in the response of the containment when molten core material exits the vessel and interacts with the containment structures. These uncertainties can be avoided if the core can be maintained indefinitely within the reactor vessel.

The structure of the Prevent Vessel Failure safety objective tree, shown in Figure 1, is the least complicated of the three safety objective trees because there are a relatively small number of strategies identified that will prevent vessel failure. For this safety objective, two safety functions were identified that would contribute to preventing vessel failure: preventing further core degradation to maintain the core within its boundaries, or maintaining the relocated core within the vessel boundary if all or some of the core relocates. These two safety functions are designated as, "Maintain Core Boundary" and "Maintain Vessel Boundary" on Figure 1. For ease in relating the discussion to the various levels of the tree, each level has been assigned a unique identifier that is descriptive of its position on the tree. Thus, the Maintain Core Boundary safety function has an identifier V1 and a mechanism causing a challenge to this safety function is identified by V1A1. The letter "V" identifies this safety function as relating to the Prevent Vessel Failure safety objective tree.

Maintain Core Boundary Safety Function.

There are two challenges that influence the capability to maintain the fuel within the core boundaries. The least severe challenge would be a Mechanical Failure (V1A) of the fuel rods which could result in loss of fuel from the rod and dispersal across the core boundary. The second challenge, Material Melt/Relocation (V1B), could be expected to result in the transport of major amounts of core material if the progression of core degradation is not arrested by accident management strategies.

Mechanical Failure Challenge. The mechanisms that would contribute to the Mechanical Failure challenge are Clad Rupture/Relocation (V1A1) and Rubble Bed Formation (V1A2). Clad rupture and fuel relocation would result from ballooning the fuel rod cladding followed by rod burst which could spew some fuel pellet fragments from the clad boundaries. In addition, some fuel would be leached from the fuel rods over a period of time. In either case, the fuel could settle or be carried in water or steam across the core boundaries. This mechanism would be expected to be a minor contributor to fuel relocation during a severe accident and the strategies associated with this mechanism may be considered to be a lower priority unless they compliment other strategies for higher priority mechanisms. Four potential strategies have been identified to control or prevent this mechanism:

Pumped RCS Flow - This strategy would involve use of the RCS pumps to force flow through the core if there is sufficient RCS inventory and pump motive power. Studies may indicate that the flow should be controlled within a specific range to minimize entrainment of fuel particles and their transport out of the core region.

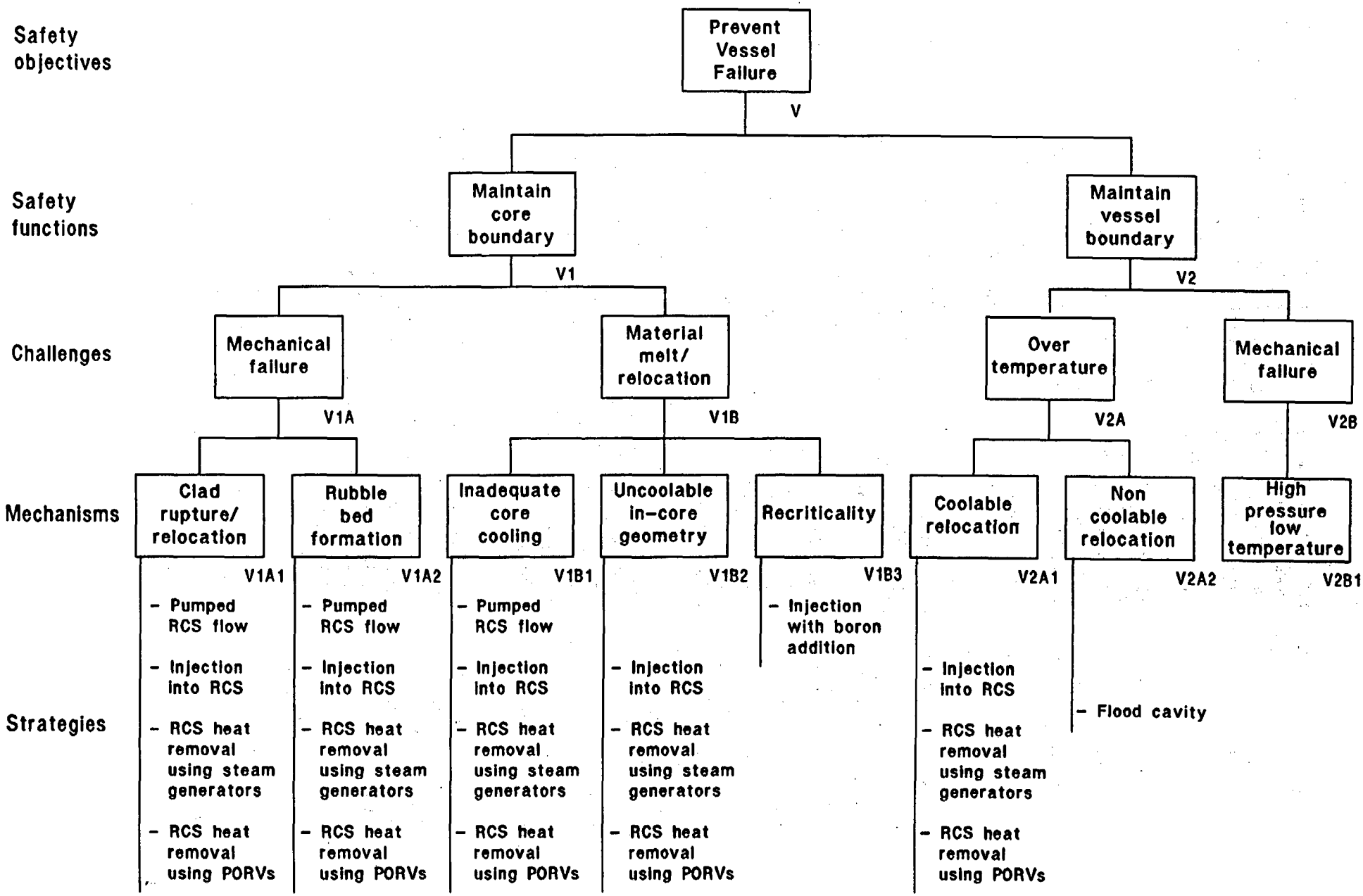


Figure 1. Prevent Vessel Failure Safety Objective Tree

Injection into RCS - This strategy would involve injection of coolant into the RCS to increase inventory. It is most likely that alternate injection methods would be required although there are some accident situations where normal injection modes would be available if proper anticipatory actions, e.g. RCS depressurization, were implemented. Alternate sources of water for injection would also be included.

RCS Heat Removal Using Steam Generators - The effectiveness of this strategy is highly dependant on the primary side conditions. Alternate means of feeding the steam generators are included in this strategy, e.g., steam generator depressurization and use of low head fire pumps or mobile pumps, as well as alternate sources of feedwater.

RCS Heat Removal Using PORVs - This strategy is feed and bleed of the RCS including use of identification of alternate injection means and water sources.

The second mechanism, Rubble Bed Formation (V1A2), represents the next level of severity in the progression of a severe accident. For this mechanism the accident has advanced to the stage where fuel clad temperatures are sufficiently high to initiate significant oxidation which can embrittle the cladding. The cladding temperature rise is sufficiently slow that melting has not become a dominant process. The cladding is therefore very brittle and susceptible to shattering as a result of applied loading or thermal shock. Shattering of the cladding could result in the formation of a rubble bed and transport of material across the core boundary. If the condition of the cladding could be established, the strategies discussed previously could be adjusted in an attempt to prevent or delay the mechanical collapse of the core, for example, control of the coolant injection rates to prevent rapid cooling or excessive loads on the core. However, employment of this strategy is not likely without further study because: (1) it could product the much more serious condition of undercooling and core melting, and (2) there is a high likelihood that the operator can not accurately assess either the conditions calling for initiation of this strategy or the status of the core to determine whether the strategy is successful.

Material Melt/Relocation Challenge. The mechanisms that influence the Material Melt/Relocation (V1B) challenge include Inadequate Core Cooling (V1B1), Uncoolable In-core Geometry (V1B2), and Recriticality (V1B3). If there is insufficient flow through the core or if there is insufficient inventory for a relatively long period of time, the core structure will continue to degrade and eventually relocate outside the core boundary. Strategies similar to those discussed previously for mechanical failure would be applicable for the Inadequate Core Cooling and Uncoolable In-core Geometry mechanisms.

Core flow and inventory addition strategies may not be effective in preventing relocation if the core has degraded beyond certain states. If this condition could be detected or anticipated, the strategy for Uncoolable In-core Geometry would involve injection into the RCS to ensure that there was water in the lower plenum to provide cooling to the relocated core material. The systems used would be similar to the previously discussed

injection strategy. The strategies associated with RCS heat removal have also been listed since continued heat removal would help control RCS pressure and temperature.

The mechanism shown as Recriticality (V1B3) may occur if the core temperatures are sufficiently high to allow the control rod material to melt and relocate followed by an addition of water that is insufficiently borated. Since water must be present to cause recriticality and raise the power levels, cooling would also take place and this mechanism would not likely result in significant relocation of additional core material across the core boundary. However, recriticality is not considered to be an acceptable core condition. Presence of the unborated water necessary to cause recriticality would only be possible if normal sources of injection water had been exhausted and an alternate unborated source was being used. The strategy for this mechanism would involve providing a means of adding boron to water being injected either at the source or directly in the injection lines.

Maintain Vessel Boundary Safety Function

If cooling of the core cannot be established sufficiently early in the accident, relocation of the core beyond its boundaries will occur. At this stage of the accident, the safety function related to maintaining the core within its boundaries cannot be achieved and accident management efforts should be directed toward preserving the integrity of the vessel lower head, shown as the safety function Maintain Vessel Boundary (V2) on Figure 1.

The challenges that would influence the capability to the maintain a relocated core within the vessel boundary are identified as Over Temperature (V2A) and and Mechanical Failure (V2B). The Over Temperature challenge is considered to be the most challenging during a severe accident. The Mechanical Failure challenge has been examined during extensive studies of pressurized thermal shock sponsored by the NRC and the nuclear industry and, as a result, is not discussed further in this report.

Over Temperature Challenge. The mechanisms that would contribute to the Over Temperature challenge are Coolable Relocation (V2A1) and Non Coolable Relocation (V2A2). These mechanisms are intended to reflect the status of the core following relocation. If the core relocates in a coolable geometry, a challenge would occur if there was insufficient inventory and RCS heat removal to provide long term cooling. If upon relocation the core material breaks up into very fine particles and forms a mass that is relatively impermeable to water, or very large pieces that are too large to transfer all the energy generated within, or if the material forms a pool on the bottom of the vessel head, the core material may not be easily cooled. Unfortunately there are no existing measurements that have the capability to determine whether the core is in a coolable geometry. Therefore, although different strategies are identified for these two mechanisms, it is doubtful that there is sufficient information available to distinguish which strategies are needed.

If the core relocates in a coolable geometry, the potential strategies should include a continuation of inventory addition to maintain water in the lower plenum and removal of the energy being generated by the relocated core. Since this mechanism would occur late in the course of a severe accident, these strategies would be an extension of the injection and RCS heat removal strategies discussed previously. It is most likely that alternate injection methods would be required although there would be a significant amount of time elapsed for recovery of the normal injection modes. Strategies for RCS heat removal may require assessment of the specific equipment available and the plant conditions. Since the RCS may be highly voided, the steam generators may not be capable of providing adequate heat removal. It appears that feed and bleed of the RCS would provide the highest likelihood of successfully mitigating the core melt progression if properly sized equipment was available.

If the core relocates in a non coolable geometry, the only strategy identified that has the potential to prevent vessel failure would be to flood the cavity.

Flood cavity - This strategy would rely on energy removal through the lower head to prevent the vessel from overheating. There are large uncertainties in the likelihood of success for this strategy resulting from the thermal resistance of the vessel material and the vessel insulation and the capability to flood the cavity due to its size and shape. The large inventory required to fill the cavity up to the level of the lower head would compete with the need for water in the vessel. Using this mode of vessel energy removal would also require that containment heat removal systems were operable to prevent eventual overpressurization of the containment building.

PREVENT CONTAINMENT FAILURE SAFETY OBJECTIVE TREE

The second accident management safety objective is designated as "Prevent Containment Failure". This safety objective is important because the containment building is the final barrier that can prevent the spread of fission products to the surrounding environment in the event of a severe accident. The tree for the Prevent Containment Failure safety objective, shown in Figure 2, describes the safety functions that must be maintained, the challenges to the safety functions, and the strategies that could potentially be employed to respond to these challenges.

For this safety objective three safety functions were identified which would contribute to preventing containment failure and assuring containment integrity: (1) maintain overpressure control to prevent structural damage and eventual rupture of the containment, (2) maintain overtemperature control to prevent failure of the containment structures from the effects of excessive temperature, and (3) maintain control of internally generated missiles to prevent penetration of the containment shell. These safety functions are respectively designated Maintain Overpressure Control (C1), Maintain Overtemperature Control (C2), and Maintain Missile Control (C3) and are discussed below.

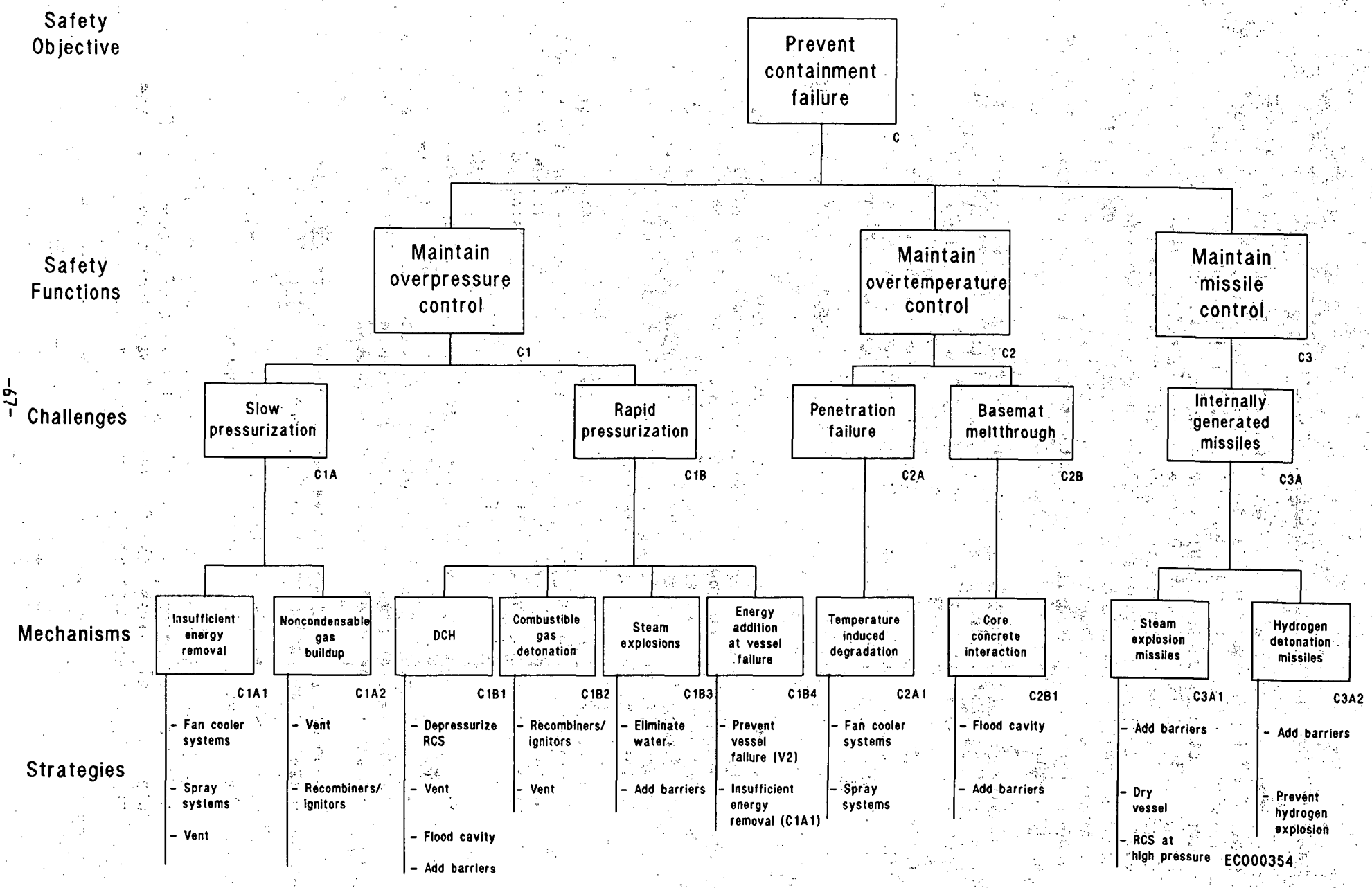


Figure 2. Prevent Containment Failure Safety Objective Tree

Maintain Overpressure Control Safety Function

There are two challenges that influence the capability to maintain control of the pressure in the containment. These two challenges were identified as a result of the potential information sources and the potential strategies that could be employed. In general, a Slow Pressurization (C1A) challenge would generally require less information to detect and implement strategies that would prevent a late containment failure. A Rapid Pressurization (C1B) challenge would require significantly more information to diagnose and, in most cases, would need preventative strategies to be implemented prior to the occurrence of the challenge. In general the rapid pressurization challenge could lead to an early containment failure.

Slow Pressurization Challenge. Two mechanisms were identified as contributing to the Slow Pressurization challenge, Insufficient Energy Removal (C1A1) which would occur when heat removal systems failed to operate or could not operate at the required capacity, and Noncondensable Gas Buildup (C1A2) from gases such as hydrogen, carbon monoxide and carbon dioxide. Under some accident conditions these mechanisms could act simultaneously to cause an overpressurization of the containment.

Three potential strategies have been identified for the Insufficient Energy Removal (C1A1) mechanism:

Spray systems - Use of this strategy may require use of alternate systems capable of spraying into the containment atmosphere and removing heat from the spray water, or use of alternate sources of spray or cooling water. Knowledge of the conditions under which sprays could potentially lead to burns of the combustible gases and information that could be used to identify these conditions should be an integral part of this strategy.

Fan cooler systems - Restoration of the normal fan cooler system functions or use of alternate means of to supply these functions would be the principle activities for this strategy. As with sprays, the potential effects on combustible gases should be considered in the development of this strategy.

Vent - A containment venting strategy could be used to remove sufficient energy from the containment to maintain overpressure control. However, both the positive and negative aspects of releasing the containment atmosphere to the environment and information necessary to make the decision to vent would be needed.

Two potential strategies have been identified for the slow pressurization mechanism of Noncondensable Gas Buildup (C1A2):

Vent - This strategy is identical to the vent strategy described for the mechanism of insufficient energy removal.

Recombiners/Igniters - The effectiveness of this strategy for overpressure control would depend on the rate of production of noncondensable gases, the fraction that were combustible, and the capacity and location of the recombiners or igniters.

Rapid Pressurization Challenge. Prevention of containment failure during a rapid pressurization challenge (C1B) could, in most cases, be difficult since there may not be sufficient time for operations personnel to implement mitigating strategies. For these cases, identification of precursor conditions would be needed to effectively invoke strategies prior to the beginning of a rapid pressurization. Four potential mechanisms have been identified that would cause rapid containment pressurization: (1) high pressure melt ejection with sufficient force to disperse the molten core material and cause direct containment heating (DCH), (2) the buildup and detonation of combustible gases, (3) steam explosions that may occur in the containment, and (4) energy addition to the containment from the steam and water that is expelled when the vessel boundary fails. These mechanisms are designated: DCH (C1B1), Combustible Gas Detonation (C1B2), Steam Explosions (C1B3), and Energy Addition at Vessel Failure (C1B4).

The mechanism of DCH (C1B1) has the potential to cause containment failure, particularly if the containment is at an elevated pressure when core melt ejection occurs. The potential strategies that have been identified to mitigate the effects of DCH are:

Depressurize RCS - The potential for DCH to significantly raise containment pressure is greater if the molten material is ejected into the containment when the RCS is at a high pressure. This strategy would use RCS equipment to depressurize the system prior to failure of the lower vessel head so that the molten core material is not ejected at high pressure conditions.

Vent - There are two potential strategies for the use of venting to mitigate the overpressurization threat from DCH. A small vent system could be used to minimize the initial containment pressure so that the pressure increase associated with DCH does not exceed the containment design pressure. The second strategy would use a relatively large vent system to relieve enough of the energy generated during DCH that overpressurization will not occur even though the initial pressure may be high. Further studies on the practicality of these strategies are needed.

Barriers - Barriers or structures could be installed in and around the reactor vessel cavity which would retard the dispersion of core debris into the containment atmosphere to limit the extent of the heat transfer and exothermic chemical reactions that could take place.

Flood Cavity - This strategy would rely on the capability of a pool of water in the reactor cavity to break up and cool the molten core material ejected from the reactor vessel.

The mechanism of Combustible Gas Detonation (C1B2) can result in large pressure increases in a relative short period of time. Although the large size of a large dry containment makes the probability of containment failure due to the burning of combustible gases relatively low, several strategies for mitigating this mechanism have been identified:

Recombiners/Igniters - For this strategy recombiners/igniters would be installed that have the capability to burn the combustible gases while

concentrations are low thereby eliminating the potential for large scale detonations.

Vent - Containment venting could be used to reduce the concentration of combustible gases to a level below the detonation or deflagration limits.

The likelihood is very small that the steam explosion mechanism in the containment would cause sufficient pressurization to rupture a large dry containment. Potential strategies that could be used to deal with this low probability event are:

Eliminate Water - The potential for steam explosions within the containment could be significantly reduced by eliminating water sources or pools in the cavity region. This strategy would be in conflict with other strategies that include addition of water to the cavity so a prioritization would be required based on effectiveness.

Barriers - Local barriers could be installed in the cavity region that would restrict the contact and spreading of the molten material with the water in the cavity. The effectiveness of this strategy would need to be weighed against the potential consequences and the cost.

The final mechanism for the rapid pressurization challenge is a rapid Energy Addition at Vessel Failure (C1B4) This energy addition would result from high pressure and temperature water entering the containment from the RCS and would only cause excessive pressure if the large dry containment was already near its failure limit The most effective strategies would be those used for the Maintain Vessel Boundary (V2) safety function on the Prevent Vessel Failure tree and those associated with the Insufficient Energy Removal (C1A1) mechanism of the Prevent Vessel Failure tree. These strategies were discussed earlier.

Maintain Overtemperature Control Safety Function

There are two challenges that have been identified as contributing to the Maintain Overtemperature Control (C2) safety function. These two challenges represent different ways in which a large dry containment can fail from overtemperature. Overtemperature would be expected to cause Penetration Failure (C2A) and Basemat Meltthrough (C2B). The possibility of contact of molten material with the containment wall during a high pressure melt ejection was considered but rejected due to the low likelihood of this occurrence in a large dry containment.

Penetration Failure Challenge. Penetration failure resulting from localized strains in the liner could be induced by the combination of high temperature conditions and containment pressure at levels somewhat higher than ambient. The mechanism of Temperature Induced Degradation (C2A1) could affect a range of penetration locations and types but would most likely have the largest affect on electrical penetrations. Two potential strategies were identified. These strategies both rely on existing plant systems to cool the containment atmosphere. Strategies using Spray Systems and Fan

Cooler Systems would be similar to the strategies described for Insufficient Energy Removal (C1A1). The sprays could be even more effective if the location of the nozzles provided direct cooling for exposed penetrations.

Basemat Melt-Through Challenge. Basemat melt-through could occur if sufficient molten core material collected in the vessel cavity. The mechanism for melt-through is Core Concrete Interaction (C2B1). The strategies aimed at mitigating the core concrete interaction are:

Flood Cavity - Experiments indicate that if there is sufficient water covering the concrete or if sufficient water is added within a short time following the initiation of attack, the effects of the molten material on the concrete can be mitigated.

Barriers - The use of "core catchers" has been widely studied for preventing basemat melt-through. Costs were estimated to be very high.

Maintain Missile Control Safety Function

The third safety function for the Prevent Containment Failure safety objective is Maintain Missile Control (C3). This safety function is intended to indicate that containment integrity can be challenged by a penetration of the containment wall with an internally generated missile. The mechanisms that are included are in-vessel Steam Explosion Missiles (C3A1) and Hydrogen Detonation Missiles (C3A2). Both of these mechanisms are considered to have a low probability of occurrence. Missiles from rotating machinery were not considered since they have been investigated extensively and their generation is not considered to be a severe accident issue.

The mechanism of in-vessel steam explosions can result in the generation of missiles that could cause containment failure. This mechanism is generally referred to as an alpha-mode containment failure. In this situation a steam explosion in the reactor vessel causes the impact of material on the reactor vessel upper head. Failure of the vessel causes the upper head to become a missile that fails the containment. Strategies to control this form of missile generation are:

Barriers - Barriers could be designed into the containment to prevent the vessel upper head from striking the containment wall in the event of an in-vessel steam explosion. This strategy would be expensive.

Dry Vessel - Steam explosions could be eliminated by ensuring that there was no water in the vessel for the molten core to fall into. However, this strategy would be in direct opposition to strategies intended to cool the core which are much higher priority and implementation is not considered to be practical.

RCS at High Pressure - The potential for in-vessel steam explosions could be mitigated by maintaining the RCS pressure sufficiently high so as to eliminate the triggering and propagation phenomena leading to the rapid generation of steam. This strategy would be in conflict with other strategies since high RCS pressures would enhance the potential for DCH and therefore is not considered to be practical.

The last mechanism for missile generation is due to hydrogen detonation, which was identified in Draft NUREG-1150 as having the potential to generate missiles. This mechanism would seem to be low probability since there should be a limited source of missiles that could be generated through hydrogen detonation. The strategies include using barriers if potential missiles can be identified and elimination of the threat of combustible gas detonation using the same strategies discussed in the Combustible Gas Detonation (C1B2) mechanism for the Rapid Pressurization Challenge.

Mitigate Fission Product Release Safety Objective

The third accident management safety objective is "Mitigate Fission Product Release". This safety objective is important since it is intended to minimize the quantity of fission products released and to delay the release as long as possible if there is a failure of the containment boundary. The strategies associated with this safety objective would generally be worked in conjunction with the strategies for the other two safety functions and, in most situations, would enhance the effectiveness of these other strategies. The tree for the Mitigate Fission Product Release safety objective, shown in Figure 3, details the safety functions that must be maintained, the challenges to the safety functions, and the strategies that could potentially be employed to respond to these challenges.

Three safety functions were identified which would contribute to mitigating the release of fission products: (1) maintain control of the fission products that may be dispersed either to the containment or directly outside of the containment, (2) maintain control of the inventory of fission products suspended in the containment atmosphere, and (3) maintain control of the release of fission products that reside in the water inside of the containment. These safety functions are respectively designated Maintain Control of FP Dispersion (F1), Maintain Control of FP Inventory in Containment Atmosphere (F2), and Maintain Control of FP Release From Containment Water (F3). A brief description of each of the safety functions follows.

Maintain Control of Fission Product Dispersion Safety Function

This safety function is concerned with mitigating the effect of releasing fission products from the RCS to locations where they could spread further to the environment. Two challenges were identified, Transport to Containment (F1A) where the fission products would become part of the mass within the containment, and Transport Outside Containment (F1B) where the containment is bypassed and the fission products are dispersed outside of the containment.

Transport From RCS to Containment Atmosphere Challenge. Three mechanisms were identified as influencing the Transport to Containment safety function, PORV/SRV Flow (F1A1), RCS Boundary Failure (F1A2), and Lower Head Failure (F1A3) which is a special case of RCS boundary failure that has the potential to use a unique strategy.

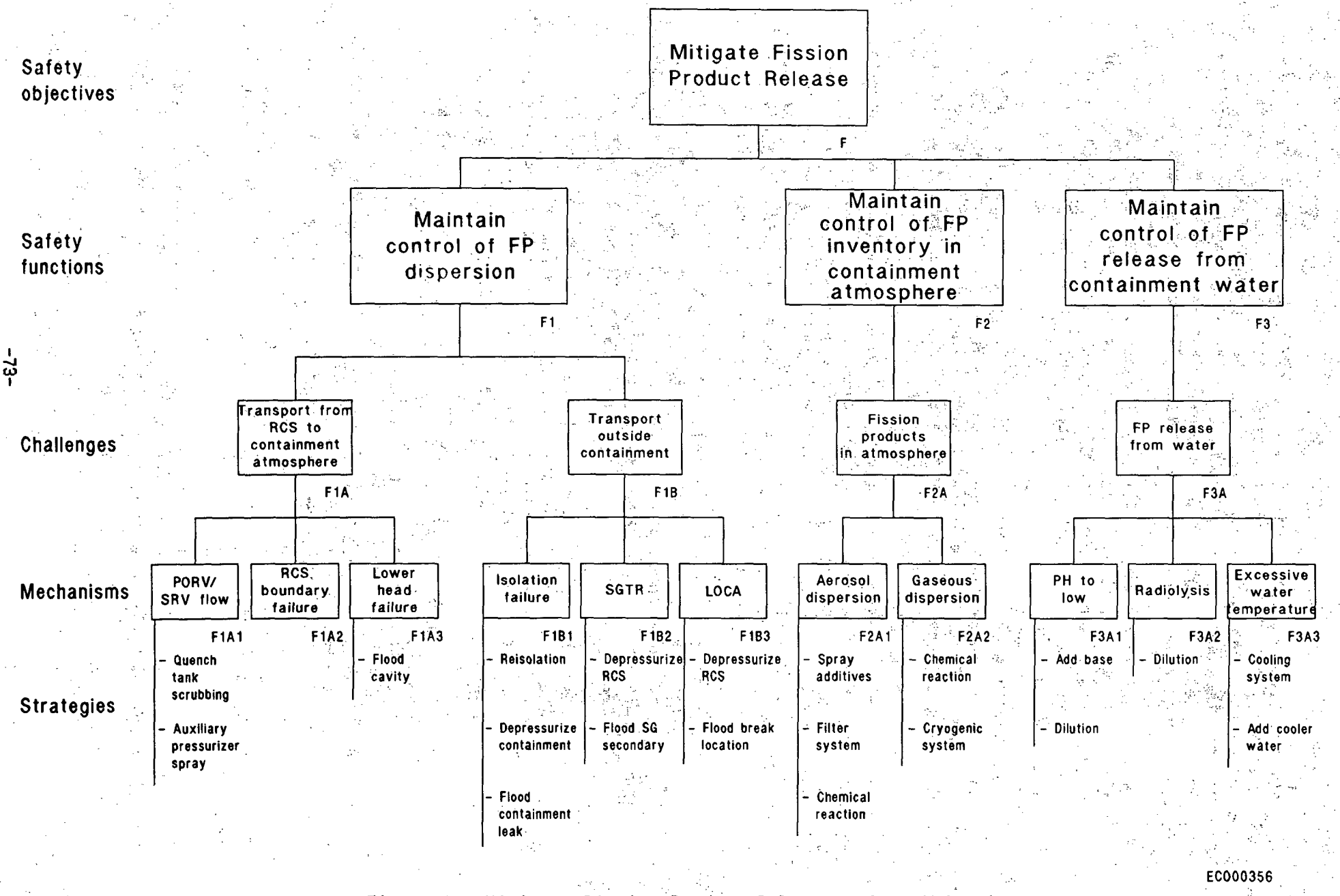


Figure 3. Mitigate Fission Product Release Safety Objective Tree

For the first mechanism, if fission products have been released to the RCS, opening of the PORV or SRV will cause the fission products to be transported to a quench tank for these relief paths and then to the containment atmosphere if the pressure setpoint of the rupture discs in the tank is exceeded. The potential strategies that can be employed to mitigate fission product release through the PORVs or SRVs are as follows:

Quench Tank Inventory - Sufficient inventory should be maintained in the quench tank during the release of fission products to ensure that effluent released through the PORVs or SRVs is introduced to the quench tank underwater, providing some scrubbing of fission products and retention in the liquid.

Auxiliary Pressurizer Spray - Those plants which have an auxiliary pressurizer spray system could use this spray capability to scrub fission products before release through the PORV or SRV, and to reduce RCS pressure which would result in a decrease in flow through the valves.

The second mechanism that may cause fission products to be transported from the core region to the containment atmosphere is RCS Boundary Failure (F1A2). Failure of RCS piping or other RCS components in the system pressure boundary, e.g. RCS pump seals, will cause the blowdown of the RCS into the containment atmosphere and with the potential to release fission products. A potential strategy that could be effective in mitigating the release of fission products for some accident conditions would be:

Directed System Flow - For certain long term transients it would be possible to direct at least some of the RCS inventory containing fission products through the PORVs to the quench tank. This strategy would only be feasible if the break in the RCS boundary was small, so that a meaningful fraction of RCS inventory could be redirected.

The third mechanism that can result in the transport of fission products to the containment atmosphere is Lower Head Failure (F1A3). Failure of the lower head results in the release of core debris into the reactor cavity, from which fission products can be transported to the containment atmosphere. A potential strategy for this mechanism would be:

Flood Cavity - Implementation of this strategy would be similar to those previously described resulting in partial scrubbing of the fission products and retention in the water.

Transport Outside Containment Challenge. The second challenge to the Maintain Control of Fission Product Dispersion safety function is the transport of fission products directly from the RCS or containment to the outside atmosphere. Three mechanisms have been identified that would contribute to this challenge: Isolation Failure (F1B1), Steam Generator Tube Rupture (SGTR) (F1B2), and a loss-of-coolant accident (LOCA) outside of containment (F1B3).

The mechanism of Isolation Failure can cause fission products to pass from the containment either as a result of failure of the containment isolation system (CIS) or as a result of failures within the containment.

The strategies that have been identified are aimed at mitigating the effect of fission product dispersal to the environment either by reestablishing control of failed components or by reducing the driving force causing flow from the containment or by flooding the leak location to reduce the inventory of fission products in the effluent leaving the containment.

Re-isolation - This strategy would include those actions that could be taken by the operations personnel to identify the cause of containment leakage and reestablish containment isolation.

Depressurize Containment - Reduction of the driving force across the leak path would decrease the flow of fission products from the containment. There are several strategies that could be effective in depressurizing the containment which are discussed for the Slow Pressurization Challenge (C1A) for the Prevent Containment Failure safety objective.

Flood Leak Location - This strategy would only be effective if the location of the penetration could be flooded to sufficient depth that significant fission product scrubbing would occur.

The second mechanism that can result in the transport of fission products directly to the outside environment is a steam generator tube rupture. Strategies identified to mitigate this mechanism are primarily aimed at reducing fission product release assuming the RCS remains intact. These strategies are:

Depressurize RCS - The strategy involving depressurization of the RCS in the event of a steam generator tube rupture is generally employed in current emergency operating procedures.

Flood Steam Generator Secondary - Submerging the break would cause the partial scrubbing of the fission products because the steam leaving the RCS must pass through the water before being released to the atmosphere through the secondary system relief valves.

If the SGTR accident progresses to the point that the vessel is breached, previously discussed strategies involving containment depressurization and reducing the containment fission product inventory would be effective.

The third mechanism would contribute to transport of fission products outside the containment would be a LOCA outside of the containment boundary (a V sequence). The strategies identified to mitigate this mechanism are nearly identical to those identified for the steam generator tube rupture and include Depressurization of the RCS and Flooding of the Break Location. If the accident progresses to the point that vessel failure occurs, the strategies of Depressurizing Containment and Reducing Fission Product Inventory, discussed previously, could be employed. Since Depressurization of the RCS was discussed for the previous mechanism, only the Flood Break Location strategy will be discussed further.

Flood Break Location - Fission product scrubbing could be accomplished for some LOCAs discharging outside containment if the break location could be flooded.

Maintain Control Of Fission Product Inventory In Containment Atmosphere Safety Function

This safety function is aimed at controlling the concentration of fission products in the containment atmosphere. By reducing the quantity of fission products in the containment atmosphere, the amount available for release as a result of containment leakage or failure is also reduced. The challenge to this safety function is the presence of fission products in the atmosphere within the containment. Two mechanisms were identified that represent the types of fission products that could be dispersed within the containment during a severe accident; Aerosol Dispersion (F2A1), and Gaseous Dispersion (F2A2).

The quantity of fission products suspended in the containment atmosphere in an aerosol form can be reduced through several strategies that take advantage of the physical structure and nature of aerosol particles. These strategies rely on both passive and active devices for the removal of aerosols.

Spray/Additives - Containment spray with chemical additives has historically been considered as a primary means of removing some of the fission product aerosols from the containment atmosphere.

Filter System - A filter system could be used to process the containment gases to remove fission product aerosols prior to release to the environment. This system could be included entirely within the containment or it could be included in the design of a venting system.

Chemical Reactions - The installation of chemically reactive materials (paints, foils, etc.) could be used to enhance deposition and prevent resuspension of deposited fission product aerosols from the containment surfaces.

The second mechanism that influences the availability of fission products for release is Gaseous Dispersion in the containment atmosphere. These gaseous fission products behave differently from aerosols and therefore require a different set of strategies. Potential strategies that could be used to reduce the concentration of gaseous fission products in the atmosphere are described as follows:

Chemical Reactions - Chemically reactive materials would be used to remove some of the gaseous fission products from the containment atmosphere. Means of circulating the containment atmosphere though the chemically reactive materials would be required.

Cryogenic System - A cryogenic system could be used to cool the gases in the containment until at least the fission product gases liquefy. This strategy would be expensive and difficult to implement under severe accident conditions.

Maintain Control of Fission Products in Containment Water Safety Function

This safety function is aimed at preventing the release of fission products present in the water inside the containment. If the fission

products are held within the water, they are not available for release to the environment through the containment atmosphere and would be less of a threat if the water was inadvertently diverted to a location outside of the containment, e.g. the Auxiliary Building. The challenge to this safety function is the release of fission products from the water.

There are three mechanisms identified that can cause the release of fission products from the containment water: (1) if the pH of the water is to low the capability to retain fission products is reduced, (2) radiolysis can cause the release of fission products from water, and (3) excessive water temperature will reduce the retention capability of the water. These mechanisms are shown in the Mitigate Fission Product Release safety objective tree respectively as: pH Too Low (F3A1), Radiolysis (F3A2), and Excessive Water Temperature (F3A3).

The strategies that can be used to address the first mechanism, a low pH in the containment water, are as follows.

Add Base - To inhibit the escape of iodine from the containment water, a basic solution could be added to raise its pH.

Dilution - The containment water could be diluted by adding neutral or basic pH water in order to raise the effective pH and inhibit the release of fission products.

The second mechanism that can result in the release of fission products from the containment water is radiolysis of the water in a high radiation field. The strategy identified as being capable of inhibiting radiolysis of the containment water is:

Dilution - The fission product content of the containment water could be diluted by adding water to reduce the rate at which radiolysis was occurring.

The third mechanism that results in the release of fission products from the containment water is excessive water temperature. Excessive water temperature can result in the vaporization of fission products. For example, excessive water temperature could have a large influence on the effect of the containment spray systems if the containment atmosphere or structures were at a sufficiently high temperature to cause some or all of the spray droplets to evaporate. Strategies that could be used to reduce the effects of excessive water temperature on this mechanism are:

Cooling System - Cooling systems for the containment water would likely be in use as a result of other strategies, e.g. use of containment sprays. However, if the heat exchangers were not in use or were not effective in removing the generated heat, alternate equipment with the capability for cooling the containment water should be identified.

Add Cooler Water - Dilution of the containment water with additional cooler water from alternate sources outside the containment would be effective in reducing the likelihood of excessive containment water temperatures.

INFORMATION NEEDS

The Safety Objective Trees were examined to identify the information that is needed to determine:

- o The status of the safety function.
- o The presence of plant conditions (a mechanism) that would challenge a plant safety function, or the presence of a precursor that would indicate the approach of plant conditions that would lead to a challenge in the future.
- o Which criteria have been met for selecting the strategy or strategies that will prevent or mitigate the conditions (mechanisms) that challenge the safety functions.
- o Whether the selected strategies have been initiated,
- o The effectiveness of the implemented strategies in controlling the safety function challenge.

The information needs for the challenges to the safety functions were not included in this examination since the combined information needs for the mechanisms associated with a challenge are the same as the information needs for the challenge itself.

A table based format has been developed to help in the systematic identification and display of the accident management information needs. This format provides a comprehensive picture of accident management information needs across the spectrum of safety functions. Sections that form rows on the table correspond to levels of the Safety Objective Trees and contain the information needs for that level. The columns show the categories of information needs, measurements that would supply the needed information, and a comment column. Table 1 is an example, for the proof of principle application to a PWR with a large dry containment, of the first branch of Prevent Vessel Failure safety objective tree including the first strategy. The preliminary tables developed to describe the three trees discussed previously total about 85 pages.

The first section (row) of the table contains the information needs that relate to the safety function. This section is used to describe the information needed to determine the status of the safety function, i.e., whether the safety function is being maintained within the accepted safety limits. The second section (row) of the table displays the information needed to identify a specific mechanism that is a challenge to a safety function. Two categories of information are given: indicators and precursors. The indicators category identifies the information needed to determine when a mechanism is actually present. The precursor category gives the information needs for determining whether the mechanism would be expected to occur in the future if appropriate strategies were not implemented. The third section (row) of the table shows the information needed to select and implement strategies for preventing or mitigating a challenge to one of the safety functions. Three categories of information needs are presented in this row. The "selection criteria" category

Table 1 Prevent Vessel Failure (V) - Clad Rupture/Relocation Mechanism (V1A1)

	Information Needs	Direct Information Source	Indirect Information Source	Available Instruments	Potential Instruments	Comments
Maintain Core Boundary Safety Function (V1)	Passage of Core Material Across Boundary	None		None		Source Range Monitors May Not be Effective for All Plants
			Radiation Levels Outside Core Region	Source Range Monitors and/or SPNDs		
Clad Rupture/ Relocation Mechanism (V1A1)	Indicator Fuel Rod Cladding Condition	None		None		Presence or Absence of Cladding Rupture
			Fuel Rod Internal Pressure	None	Fuel Rod Pressure Sensor	
			Cladding Temperature	None	Cladding Temperature Thermocouple	
			RCS Coolant Activity	RCS Sampling System		
			Core Exit Temperature History	Core Exit Thermocouples		
	Precursor Core Temperature (High)	Cladding Temperature		None	Cladding Temperature Thermocouple	
			Core Exit Temperature	Core Exit Thermocouples		
			Reactor Vessel Inventory	RVLMS		Dependent on RCS Pump Operation Status

Table 1 Prevent Vessel Failure (V) - Clad Rupture/Relocation Mechanism (V1A1) (Cont.)

	Information Needs	Direct Information Source	Indirect Information Source	Available Instruments	Potential Instruments	Comments
Injection Into RCS Strategy	Selection Criteria					
	RCS Pressure History	RCS Pressure		RCS Pressure		
	RCS Inventory (Trend)	None		None		
			Pressurizer Inventory	Pressurizer Level		
			Reactor Vessel Inventory	RVLMS		Dependent on RCS Pump Operation Status
	Injection Water Availability	RCS Injection Water Tanks Inventories		Tank Levels		
		Containment Sump Inventory		Sump Levels		
	Strategy Initiation					
	Injection Pump Flow HPSI/LPSI/CP	Injection Pump Flow Rate		Flow Indication		
				Pump Outlet Pressure & Motor Current		
	Injection Water Inventory (Decreasing)	RCS Injection Water Tanks Inventories		Tank Level		
	Strategy Effectiveness					
	RCS Inventory History	None		None		Conditions In RV Head, Core, And Flow
			Pressurizer Inventory	Pressurizer Level		
			Reactor Vessel Inventory	RVLMS		Dependent on RCS Pump Operation Status
	Cladding Temperature	None		None		
			Core Exit Temperature	Core Exit Thermocouples		

identifies the information needed to determine which strategies should be selected for a given situation, including consideration of the plant conditions under which the strategy can operate and be effective. Since hardware for the implementation of strategies and information indicating the status of this hardware is plant specific, information on the operability of systems including availability of support systems, e.g. electrical power, cooling water, etc., was generally not listed in this row although it is recognized as being needed. The "strategy initiation" category gives the information needed for the operating crew to determine whether a strategy has been implemented as intended. The position and status of equipment was generally not included in this row due to the plant specific nature of this information. The "strategy effectiveness" row describes the information needed to determine whether the strategy is having its intended effect, that is, whether implementation of the strategy is having a beneficial effect on the status of the safety function that is being challenged.

As stated previously, the columns of the table are used to provide the characteristics of the information needs for each level of the safety objective tree. The first column lists the levels of the Safety Objective Tree and the second column summarizes the needed information for each of these levels. The third column lists potential direct sources of information that could supply the needed information. A direct information source is one that can be used to provide information that will determine positively the presence or absence of a certain condition on the safety objective tree. In addition, potential indirect sources of information are listed in the fourth column. An indirect information source is one that can be used to infer the needed information, but there may be conditions for which the information may be ambiguous. For example, core exit temperature may provide reasonable information on the fuel cladding temperatures for some system conditions but would not be a good indicator for all system flow and inventory situations. The fifth column lists types of measurements that are currently available in PWRs with large dry containments that could be used to provide the needed information. The list of measurements in this column in Table 1 is preliminary and potentially incomplete and will be the subject of additional work. The final column provides space for comments.

SUMMARY AND FUTURE WORK

A methodology to identify and assess the information needs of the operating crew of a nuclear power plant during a severe accident has been developed and application of this methodology to a PWR with a large dry containment is underway. Safety objective trees have been developed to relate the plant safety objectives to potential strategies and these trees have been used in identifying information needs. A tabular format has been used to show the relationship between the safety functions, mechanisms, and strategies and the information needs and information sources. A preliminary identification of the availability of existing measurements to fulfill the identified information needs has been completed.

The capability of currently available measurements in a PWR with a large dry containment to supply the identified information needs is being assessed. The results of this work will indicate the diversity and depth of measurements available for each information need and may also identify

alternate means of supplying information needs. An assessment of the potential ranges and environmental qualification conditions for severe accident conditions is also being conducted to identify limitations in the measurements based on existing severe accident information. Areas where the information systems may mislead plant operating personnel are being evaluated by examining the types of information available to the operator. Information needs that rely solely on indirect sources of information could provide ambiguous results and increase the difficulty of implementing effective accident management strategies.

CONTAINMENT VENTING AS AN ACCIDENT MANAGEMENT STRATEGY[a]

R. Jack Dallman
William J. Galyean
K. C. Wagner

EG&G Idaho, Inc.
Idaho National Engineering Laboratory

Introduction

The idea of primary containment venting to prevent or mitigate the consequences from a severe accident is not new. Research has been conducted on filter effectiveness for over thirty years. United States production reactors have had containment filter systems and applications to commercial facilities have been studied over the same period. In Europe, the countries with the largest nuclear power production (France, Germany, and Sweden) all have filtered containment venting systems installed or planned on their nuclear power plants (NPPs). Boiling water reactors (BWRs) in the United States are operated based in part on Emergency Procedure Guidelines (EPGs)[1] which call for wetwell and drywell venting under some circumstances. With increased interest in the management of severe accidents, containment venting as an accident management strategy has experienced new interest, and more detailed evaluations are being performed. Areas being investigated include the capability to reduce hydrogen concentrations, the effect on other systems or proposed modifications, the cost-effectiveness of venting, and its net risk benefit.

One of the most comprehensive studies of containment venting[2] was performed on the Peach Bottom Atomic Power Station, a BWR with a Mark I containment. A main conclusion from that study was that based on the draft procedures and equipment in place at the time of the analysis, containment venting had limited potential for further reducing the risk

a. Work supported by the U. S. Nuclear Regulatory Commission, Office of Nuclear Regulatory Research under DOE Contract No. DE-AC07-76ID01570.

associated with accident sequences currently identified as being important to risk. In the draft Reactor Risk Reference Document, NUREG-1150[3], venting along with consideration of alternate injection sources was credited with lowering the core damage frequency due to accident sequences, which include a loss of long-term decay heat removal, to less than 1E-8 per reactor year. That result made these sequences (which were identified as dominant contributors in WASH-1400[4]) insignificant compared to other risk contributors for Peach Bottom.

Design and Operational Considerations

Containment venting is used at U. S. reactors for a number of purposes. These include purging during operation, ventilation during shutdown, and for accident management. Two classes of U. S. reactors (24 BWR Mark I units and 9 BWR Mark II units) utilize nitrogen inerting as the primary defense against hydrogen ignition during degraded core accidents. For these plants, filtered exhaust systems are used during operation to control containment nitrogen concentrations, and for purge and ventilation purposes.

Venting in U. S. commercial reactors is generally not contemplated during accidents up to the severity of design basis accidents. Such accidents are generally associated with single failure events, and are not believed to result in any fuel melting or containment breach. The accompanying fission product releases to the containment would be the noble gases, and iodine that had been dissolved in the coolant and from some fuel pins. This release from the fuel pins is often referred to as gap activity. Release of fission products to the environment from such events would occur due to containment leakage. Much of the containment leakage, however, would be processed through filtered discharge systems. These same systems could be used to purge containments of residual fission products during and after more serious accidents when containment pressures and temperatures were low enough not to challenge the structural integrity of the filtered vent systems. They could also be used in accidents with greater challenges, which could result in their failure. Failures within the reactor building could cause contamination of spaces and equipment, and the ability to reclose the vent(s) could be compromised.

Accidents involving fuel melting can produce large quantities of fission products, hydrogen and other non-condensibles. The result could cause significant containment pressure and temperature challenges. U. S. studies have indicated there are a number of important challenges to containment arising from severe accident conditions, each with its associated failure modes:

a) containment bypass (including failure to isolate containment on demand, suppression pool bypass, and interfacing system LOCAs);
b) early overpressure failures both before or after core melting (including those from direct containment heating, non-condensible gas generation and combustible gas (hydrogen) ignition, and ex-vessel molten core/water interactions);
c) early overtemperature challenges from core debris attack on steel containment liners;
d) late overpressure/overtemperature failure, primarily from core-concrete interactions and non-condensible gas buildup; and
e) late basemat failures resulting from core-concrete interactions.

The feasibility and potential benefits of containment venting have been studied by the Nuclear Regulatory Commission (NRC) and its contractors as well as the nuclear industry. These studies indicate that potential benefits depend upon the specific accident sequence and upon plant hardware and procedures. Venting may have positive benefits for those sequences in which the rate of containment pressure rise is relatively slow. Venting is less feasible, however, for those sequences resulting in containment failure challenges by early overtemperature or overpressure conditions. This is because the relatively rapid increase in containment pressure requires large containment penetrations for successful pressure relief. Venting has also been shown to have the possibility of preventing core melting for accident sequences involving loss of long-term decay heat removal capability and for some anticipated transient without scram sequences. For other sequences, venting has been postulated to increase the likelihood of core damage by causing pump cavitation and the eventual loss of injection to the reactor coolant system. Finally, venting is not

regarded as effective in sequences involving containment bypass, although some have argued that venting could be beneficial in reducing the driving force for such bypass and thus lowering the energy of the release.

Venting as an accident management strategy, has been shown to require considerations of the ability of the vent path (size and timing) to release sufficient energy to influence the course of accidents, the ability to open and reclose valves, the effects of reactor building releases on equipment and operator actions, and protection against inadvertent or unnecessary operation.

Within the United States, the only commercial reactors approved to vent during severe accidents are boiling water reactors having pressure suppression pools. The water pool serves to scrub and retain radionuclides. The degree of effectiveness has generated some debate within the technical community. The decontamination factor (DF) associated with suppression pool scrubbing can range anywhere from one (no scrubbing) to well over 1000 (99.9% effective). This wide band is a function of the accident scenario and composition of the fission products, the pathway to the pool (through spargers, downcomers, etc.), and the conditions in the pool itself. Conservative DF values of five for scrubbing in Mark I suppression pools, and 10 for MARK II and Mark III suppression pools, have recently been proposed for licensing review purposes. These factors, of course, exclude considerations of noble gases, which would not be retained in the pool.

Emergency Procedure Guidelines (EPGs)[1], have been developed by industry and approved by the NRC staff for use at U.S. BWRs. These EPGs were developed in direct response to operating problems identified as a result of the TMI-2 accident, and provide guidance for the development of plant specific emergency operating procedures (EOPs). The EPGs are generic to a range of General Electric designs from BWR 1 through BWR 6, and apply to the Mark I, II, and III containment types. By design, they are mostly symptom-based and call for actions which strive to maintain plant safety regardless of the initiating event.

Primary containment venting is called for by the EPGs for two situations. The first is for hydrogen control (note that Mark III containments have their own special features and procedures in this area). The second situation is for venting to prevent overpressurization and to maintain primary containment integrity. For the latter, the operator is instructed to vent the primary containment to reduce and maintain the pressure below the primary containment pressure limit (PCPL). The PCPL is defined to be the lesser of either (1) the pressure capability of the containment, (2) the maximum containment pressure at which vent valves can be opened and closed to reject decay heat from the containment, (3) the maximum containment pressure at which safety relief valves (SRVs) can be opened, or (4) the maximum containment pressure at which vent valves can be opened and closed to vent the reactor pressure vessel. Venting could be from the drywell or wetwell, but wetwell venting is preferred to allow for fission product (excluding noble gases) scrubbing in the suppression pool.

Venting procedures as used within the EPGs are intended as a "last resort" operator action. Uncontrolled increases in the containment temperature or pressure will result in containment failure with unknown results. Therefore, it is felt that a controlled action with defined consequences is preferable to no operator action. The methodology to establish the venting pressure is an equally important consideration. Ideally, the venting pressure could be established solely on the actual pressure capability of the containment. That would delay venting until the latest possible time and minimize unnecessary releases. However, considerations associated with actual operating plant constraints tend to reduce the venting pressure (based on the PCPL). As a result, there are plant-to-plant differences in EOPs. This is best demonstrated by looking at the selection of the valves that are in the flow paths to be used for venting. The accepted philosophy is to begin opening valves in the smallest flow path, starting with wetwell penetrations. Failing successful control of the transient, the operator is to increase the diameter of valves that are opened sequentially until even drywell

penetrations (resulting in an unscrubbed release) would become candidates. It has also been proposed to vent the wetwell through the spent fuel pool to enhance fission product scrubbing after core damage.

Pressurized water reactors (PWRs) also contain systems that could be used for venting to prevent containment overpressurization. The feasibility of utilizing them for that purpose, however, has not been extensively explored. Certain engineered systems such as fan coolers and containment sprays could also enhance the trapping and retention of fission products over and above the effects of natural deposition processes.

Risk Reduction Potential From Venting

The conclusions drawn from an analysis of containment venting are plant-specific, sequence-specific, and dependent on assumptions made by the analysts. To properly assess the impacts of venting requires the definition of a venting strategy[5]. That strategy should include specific information related to hardware, phenomena, and operational considerations.

An approach to quantify the risk reduction potential from venting for BWR Mark I containments was developed for the NRC's Containment Performance Improvement Program that evaluates current designs and hard pipe modifications. Additional filters were not considered because of the previously explained effectiveness of pool scrubbing on reducing the source term. Simplified containment event trees (S-CETs) were developed to simulate the Peach Bottom plant response during short and long-term station blackout sequences as described in draft NUREG-1150. The station blackout sequences represented approximately 85% of the core melt frequency for the Peach Bottom plant and nearly 100% of the risk. Therefore, any potential containment improvement should be operable during station blackout conditions. The next most dominant plant damage state at the Peach Bottom was the anticipated transient without scram (ATWS). Although the ATWS constituted most of the remaining 15% of the plant damage frequency, it contributed less than 1% to any of the overall plant

risk measures (i.e., early fatalities, 50 mile population dose, latent cancers, or economic costs). During the ATWS sequence, ac power availability and operator mitigative actions made the consequences less severe than the station blackout sequences.

A final class of accidents, loss of long-term decay heat removal (TW sequence), was not considered an important contributor to the total core melt frequency or plant risk in draft NUREG-1150. Containment venting along with a "realistic" assessment of the availability of alternate injection systems such as the condensate system, high pressure service water system, and the control rod drive injection system were credited with reducing the frequency of the TW core melt sequences by three orders of magnitude, from approximately 1E-5 to <1E-8 per year. This reduction is primarily due to an assessed probability of 0.999 for successful venting given the long time period available during the TW sequence (greater than 10 hours)[6]. For perspective, the median core melt frequency listed in the draft NUREG-1150 evaluation of Peach Bottom is 8.2E-6. If venting had not reduced the TW core melt sequence probability, the total core melt frequency would be double the estimated value and TW would be the most dominant plant damage state.

Potential Modifications to Existing Equipment

In the case of an ATWS, high core power and steaming rates to the containment cause the containment to pressurize quickly. Based upon existing hardware and procedures at Peach Bottom, the ability of venting to successfully prevent containment failure during a worst case ATWS was determined to be unlikely[2]. In addition, if the vessel water injection sources are not changed from the pressure suppression pool, flashing in the pressure suppression pool during venting could cause the pumps to fail and lead to core damage. It should be noted, however, that the BWR EPGs would instruct the operators to change the vessel injection sources prior to venting. For both the TW and the ATWS sequences, venting would be attempted to relieve containment pressure prior to core damage. Venting prior to core damage would only release steam (with coolant activity) and nitrogen, rather than large amounts of fission products.

Utilizing existing equipment to perform containment venting has been studied in detail[2]. A main conclusion from that study for Peach Bottom was that "based on the draft procedures and equipment in place at the time of the analysis, containment venting has limited potential for further reducing risk associated with accident sequences currently identified as being important to risk." Numerous problems were noted in that study. First, the existing vent system could not be operated automatically from the control room during station blackout sequences. This is a major limitation based upon the core melt frequency for Peach Bottom. Second, the existing system discharged into ventilation ductwork and would fail the ductwork during venting operations. Failure of the ductwork would cause the effluent to be discharged into reactor building. This would limit repair efforts and could damage equipment vital to recovering the accident. Third, the existing system required approximately 22 minutes to connect jumper cables and open the vent valve. Consequently, operator response time was significant during fast containment pressurization sequences such as ATWS. A hard-pipe vent system with dedicated dc valve actuators would (a) permit operation during station blackout sequences, (b) vent through hard piping to the plant stack for an elevated release, (c) permit repair efforts to continue during venting operations, (d) permit quick actuation of the vent system from the control room, (e) minimize inadvertent venting via a rupture disk in the line, and (f) assure the valves can be operated under severe accident conditions.

A dedicated vent system could be potentially beneficial for all the plant damage states. For the TW sequences, the containment could be successfully vented to prevent core melting while not affecting repair operations. Similarly, during station blackout sequences, the vent system could be safely opened from the control room. With existing systems, the valve can only be opened manually during station blackouts. If core damage had occurred, the radiation environment near some of the vent valves would inhibit manual operation. In other cases, opening the vent line would expose the operator to a dangerous environment after the ductwork ruptures[7]. Finally, the dedicated vent system would be important for ATWS sequences since the vent line could be opened quickly and on-going repair efforts would not be effected.

The final considerations for an enhanced vent system are pertinent to thermal-hydraulic performance issues. For the vent system to be successful, it must be able to maintain the containment pressure below the PCPL. Figures 1 and 2 show the normalized steam energy that could be removed by various size vent systems as a function of containment pressure. Figure 1 is based on the choke plane size for the vent system whereas Figure 2 has a discharge coefficient of 0.772 (to account for line losses; see Reference 2) applied to the results. During scrammed accidents, such as the TW or station blackouts, the decay heat energy in the core is less than 1.5% of the rated thermal core power at one hour. Therefore, an 8 to 10 inch vent line (see Figure 1) should be able to remove the decay heat energy from a plant with the same thermal power rating as Peach Bottom. If core melting and/or core-concrete interactions have occurred, the vent system would need to remove decay heat plus the chemical energy from metal-water reactions. The energy from metal-water reactions can represent several times the amount of decay energy. However, it is expected that an 18 inch line, which can remove approximately 7% of the rated thermal core power, could adequately depressurize the system. This was confirmed by calculations performed for the Peach Bottom venting study[2].

During a high pressure ATWS sequence with plant automatic response, a typical BWR will add energy to the containment at approximately 30% of full power[8]. To vent 30% of the rated thermal power at the Peach Bottom plant at the containment design pressure (60 psig), critical flow calculations show that a 30.6" diameter choke plane is required. Even at lower power levels indicative of successful operator actions, relatively large flow areas are needed. For instance, to vent 14% of the rated thermal power at Peach Bottom, a 21" diameter choke plane is required at a containment pressure of 60 psig. Therefore, unless a multi-valve vent system is used, it is only likely that venting would slow the containment pressurization rate and delay core damage. A dedicated vent system, however, could open as soon as it was needed to provide additional time for repair operations in the reactor building, which could continue during venting operations.

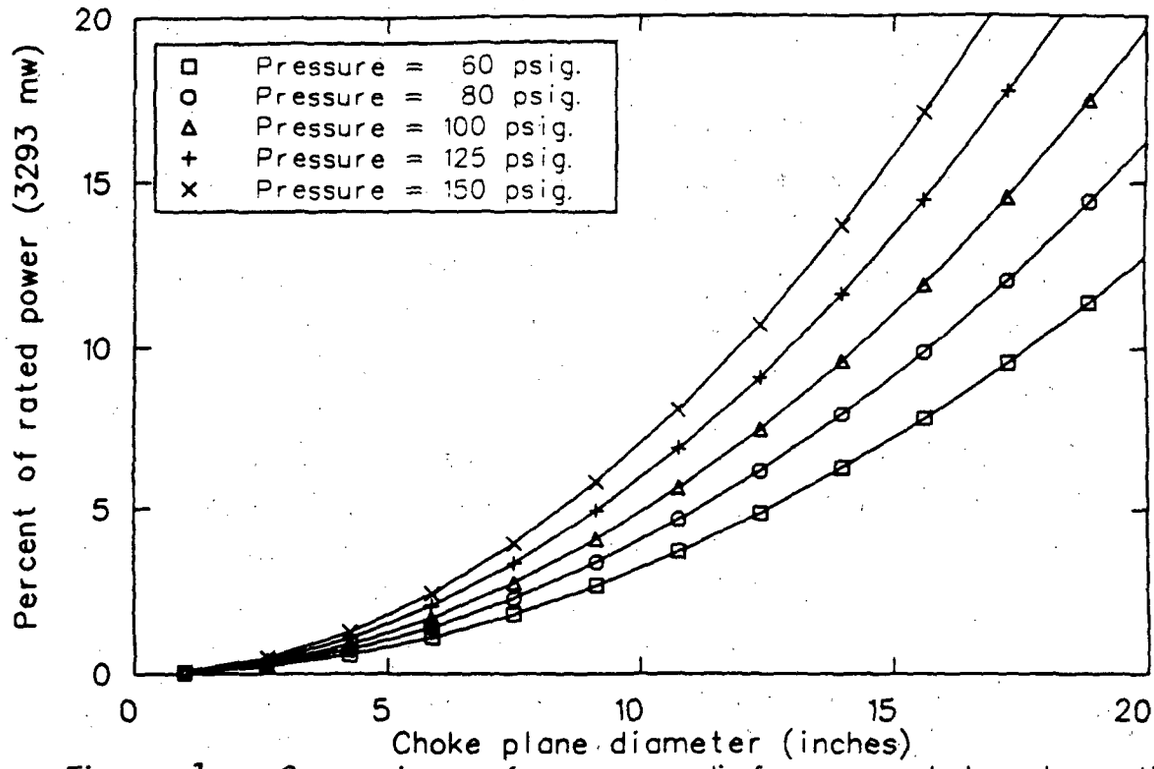


Figure 1. Comparison of energy relief versus choke plane diameter for dry steam as a function of containment pressure.

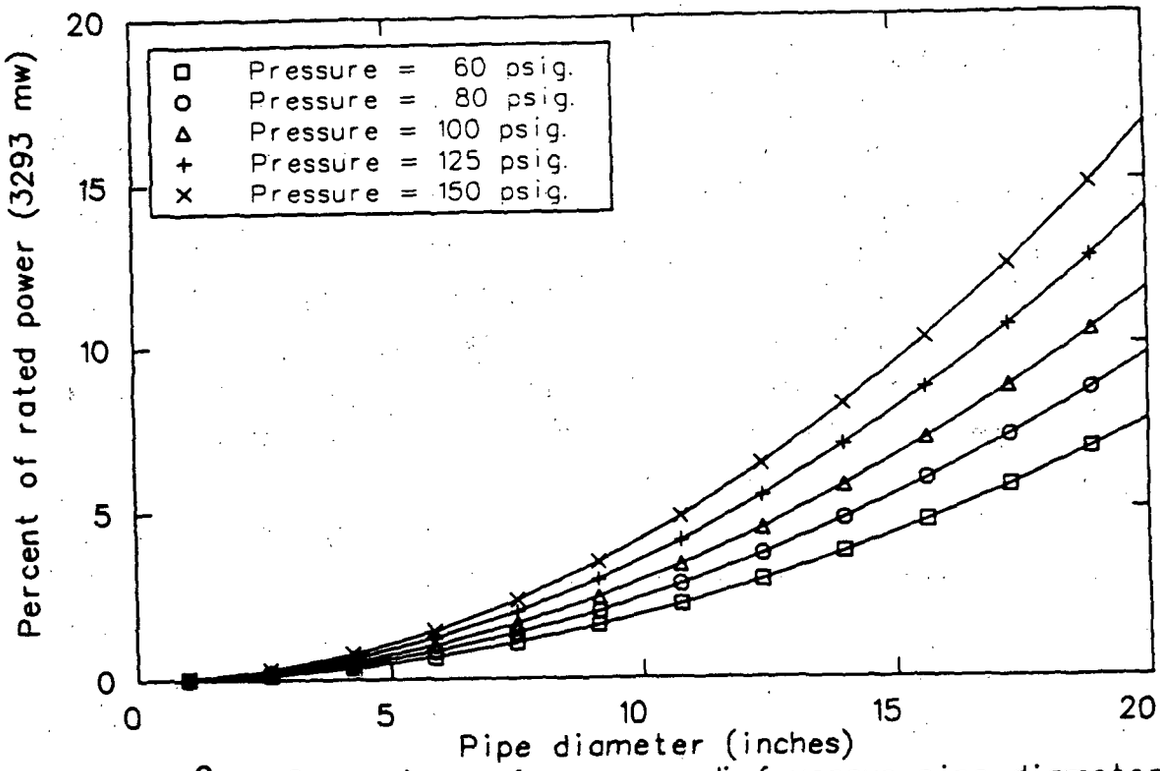


Figure 2. Comparison of energy relief versus pipe diameter for dry steam as a function of containment pressure using a discharge coefficient of 0.772.

Simplified Containment Event Tree Results

The simplified containment event tree methodology is described in detail in Reference 9. The philosophy driving the development was to produce reasonable results quickly, while relying on the vast amount of information generated in support of the NUREG-1150 effort. For application to the station blackout sequences at Peach Bottom, event trees were developed that required 15 to 20 top events. This is compared to the 107 questions used for the draft NUREG-1150 work (Reference 10). The reduction is possible by describing only those containment events and phenomena that were identified as being significantly important to risk. Off-the-shelf software specifically designed for developing, editing, and analyzing event trees were used. This facilitated both the construction of the S-CET and subsequent changes to reflect contemplated modifications in hardware or procedures. The development of the S-CET and corresponding branch point split-fractions relies heavily on the data and insights generated by the NUREG-1150 effort. However, instead of trying to consider the entire range of possibilities and their uncertainties, the S-CET assigned best-estimate branch probabilities. While this approach produced a point estimate of the risk and does not identify the range of uncertainty in the calculations, it provides a concise and flexible model which can easily be executed for a large number of sensitivities. The output from the S-CET is a table identifying each event tree end state (i.e. the unique accident scenarios identified by each specific path through the event tree) and its associated probability.

After the end states were determined from the S-CET, they were assigned to the various accident progressions from the list of Peach Bottom accident progression bins. This was done by comparing their characteristics and assigning them to the best-match accident progression bins from the draft NUREG-1150 data base. This process reduced the number of source terms that need to be considered.

Each source term that is identified requires corresponding consequence measures produced by that source term. Since the source terms were taken directly from the draft NUREG-1150 work, the consequences were treated likewise. In those few instances where a new source term may be defined to reflect a parameter not explicitly included in the original analysis,

the resulting consequences can be calculated using MACCS[11]. To maintain a consistent set of consequence measures, any new ones would be generated by modifying an existing source term bin and using a MACCS input deck consistent with the original calculations. Once the new bin probabilities are generated, the new risk is calculated by multiplying the plant damage state (PDS) frequency, the conditional bin probability and the consequences of the bin together using the following equation:

$$Risk_{PDS} = \sum_{i}^{N} F_{PDS} \times (P_{bin_i} \times C_{bin_i})$$

where: F_{PDS} = frequency of PDS.

P_{bin_i} = conditional probability of bin_i given PDS.

C_{bin_i} = consequences of bin_i.

The simplified containment event trees results were benchmarked against the draft NUREG-1150 results and then modified to reflect new ac power recovery factors. A comparison of station blackout population dose is shown in Figure 3. Comparison of the first two columns is an illustration that the total risk from all sequences in NUREG-1150 was dominated by station blackout. The third column compares the S-CET results. All of the individual risk measures calculated by the S-CETs compared well to the draft NUREG-1150 results. Column 4 shows the impact of using more recent probabilities for ac power recovery[12]. These higher probabilities for recovery were used for all subsequent analyses.

Figure 4 illustrates two key results from the S-CET analyses. Shown in the figure are the population dose risks for station blackout sequences with and without venting. Those risks are calculated for four different probabilities of drywell liner melt-through (0.0, 0.25, 0.5, and 1.0). It was found that venting alone did not significantly affect the risks from station blackout. That is primarily because the Peach Bottom risk was dominated by early containment failure, where venting by itself would not help. Changing the probability of liner melt-through, however, was found to have a large impact on the risk results. It is noted that for the purposes of these analyses, liner melt-through probability was taken to be 0.5 for all of the base case and other sensitivity analyses. The draft NUREG-1150 calculations assumed that if liner melt-through failure were to occur, it would happen within minutes of reactor pressure vessel failure.

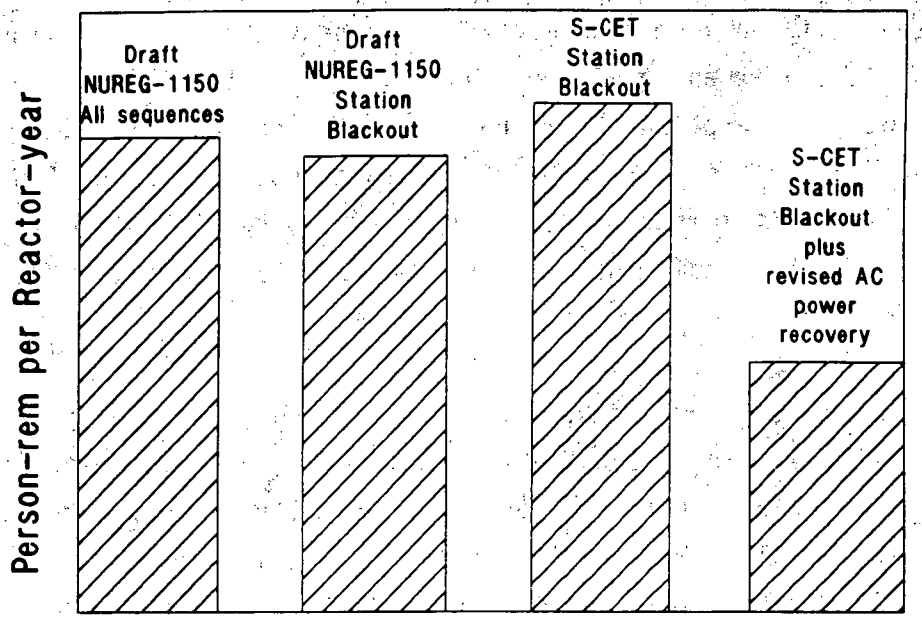


Figure 3. Comparison of Draft NUREG-1150 and S-CET station blackout risk.

EC000576

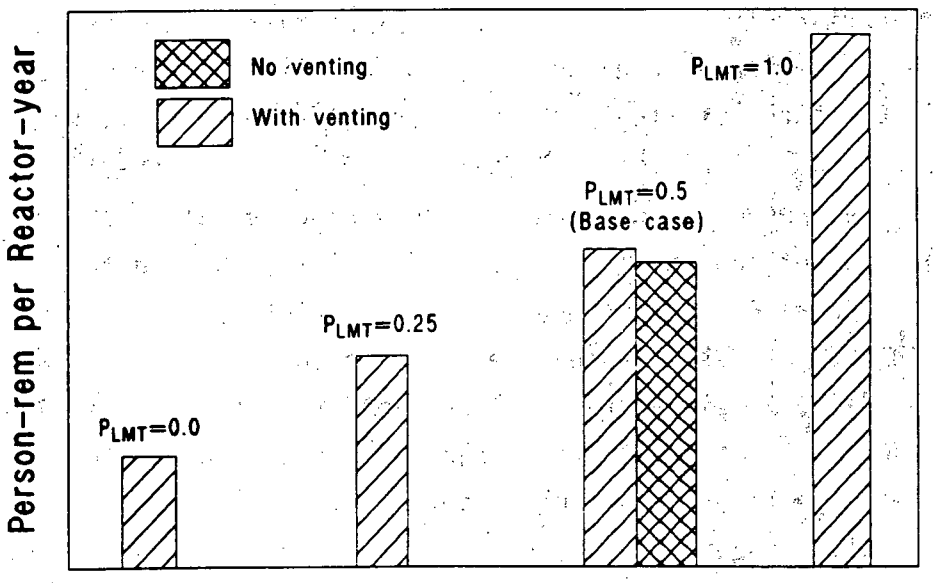


Figure 4. Effect of liner shell failure probability on risk.

EC000577

As stated above, for the station blackout applications venting by itself does not significantly reduce overall risk. Containment venting, however, is potentially an important mechanism in preventing or delaying core melting in the TW and ATWS (or TC) sequences. The ATWS and the TW represent short and long-term challenges to the reactor, respectively. However, unlike the station blackout sequences, the TW and ATWS sequences can cause a containment pressurization above the PCPL prior to core melting. High containment pressure can lead to a core melt sequence unless specific operator actions are taken.

A MACCS 1.5[11] consequence deck for Peach Bottom was developed using the draft NUREG-1150 MACCS 1.4 Peach Bottom decks and meteorology files, the MACCS 1.5 sample deck for the Sequoyah plant (similar to the deck being developed for final NUREG-1150 consequence calculations), and the WASH-1400 TW source terms (with and without reactor building bypass[4]). Using these input decks, consequences measures similar to those in draft NUREG-1150 were generated. Representative results of these analyses comparing the TW consequences and the S-CET station blackout sequences are displayed in Figure 5. It is seen that without venting, TW becomes the risk dominant sequence. As stated previously, station blackout sequences essentially represent all the risk as presented in the draft NUREG-1150 results. However, if venting was not successful, the TW sequence would be a significant contributor to the total plant risk. The risk shown is based on: a sequence frequency of 1E-5 (approximated from draft NUREG-1150 without venting), the WASH-1400 TW source term, and consequences as calculated by MACCS 1.5. Different assumptions on the sequence frequency, source term, or consequence parameters would change the magnitude of the importance. As an example, the probability of TW is varied in Figure 6. For reference, the value of 3E-4 is the value in the Cooper PRA[13]. As described earlier, vent flow paths utilizing ductwork would most likely release the effluent into the reactor building. While it is plant-dependent and not quantified, there is a finite probability that release to the reactor building would fail equipment or instrumentation required to maintain reactor pressure vessel integrity. That effect on risk can be envisioned by comparing the risk shown on Figure 6 for TW probability of 1E-4 to that for 1E-5. That comparison illustrates the reduction in risk from venting where reactor building release causes failures 10% of the time for a TW frequency of 1E-4.

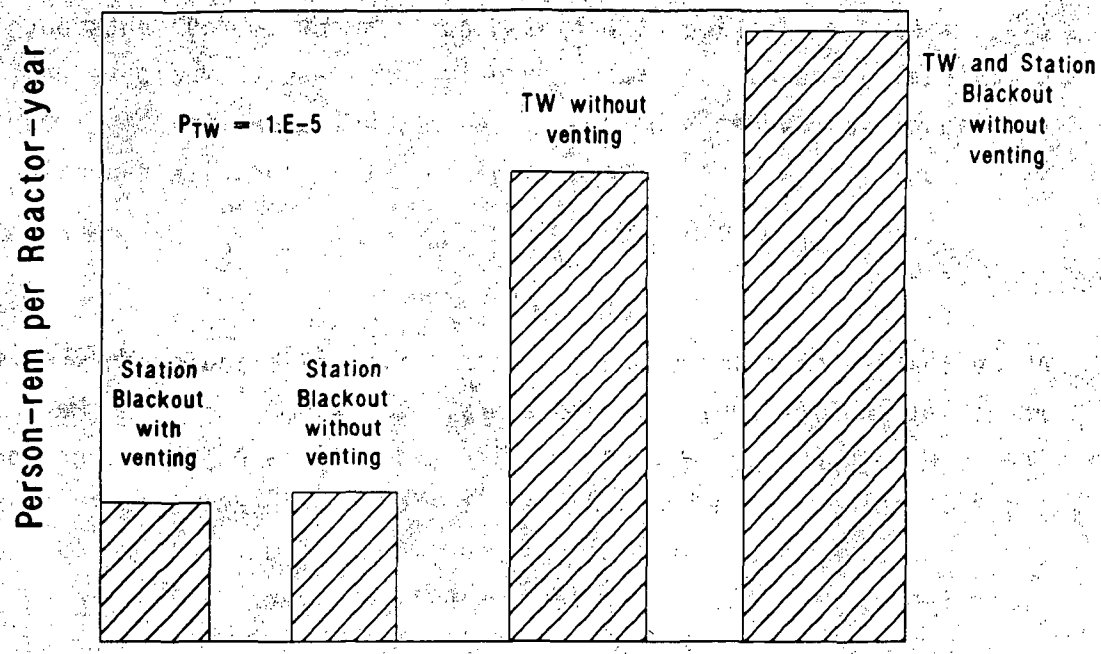


Figure 5. Comparison of station blackout and TW risk without venting.

EC000578

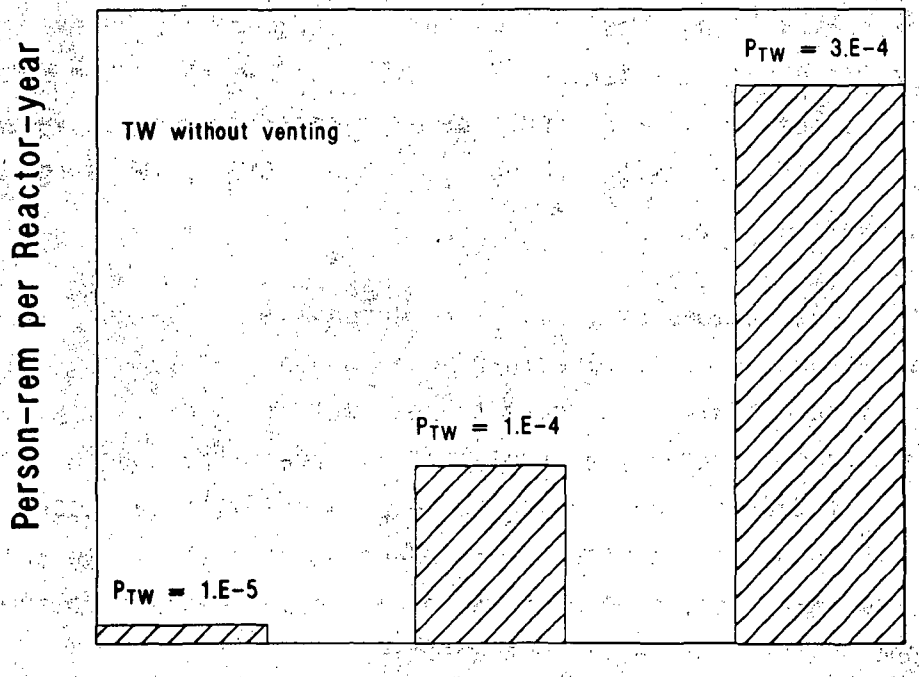


Figure 6. Effect of different TW probabilities on risk.

EC000579

Sensitivity studies are in progress to assess different assumptions and new information emerging from other research activities. These evaluations are looking at proposed containment improvements both individually and as a package. Preliminary results indicate that while individual improvements by themselves may not significantly impact risk, taken together they can have a large potential for risk reduction.

Conclusions

An evaluation of primary containment venting is being performed at the Idaho National Engineering Laboratory. Containments of the Mark I type are receiving current attention, with evaluations of the other containment types to follow. The Peach Bottom Atomic Power Station is the subject of study, to take advantage of the large amount of data and analysis generated on Peach Bottom by the NUREG-1150 effort.

Evaluations to date indicate that venting, as described by the BWROG EPGs, has little effect on the risk from station blackouts at Peach Bottom. Changes in risk are dominated by phenomena causing early containment failure. Uncertainties in phenomena such as drywell liner melt-through can change calculated risks significantly.

For sequences involving loss of long-term decay removal, however, venting can have a big effect on risk. This is illustrated for Peach Bottom, where with successful venting and continued reactor pressure vessel injection, TW risk is insignificant. Without venting, TW is the risk dominant sequence.

Quantitative evaluations of venting are dependent on the definition of a venting strategy, which involves hardware, phenomena, and operations. The results from such evaluations have to be scrutinized carefully, since the assumptions used by individual analysts can affect the conclusions. Sensitivity studies are continuing to help identify those uncertainties that have the biggest impact on risk reduction potential. In addition, the risk reduction potential of venting when combined with potential containment improvements will be quantified.

References

1. General Electric Company, BWR Owner's Group Emergency Procedure Guidelines, Revision 4, NEDO-31331, March 1987.

2. D. J. Hanson, et al., Containment Venting Analysis for the Peach Bottom Nuclear Power Plant, NUREG/CR-4696, EGG-2464, December 1986.

3. U. S. NRC Office of Nuclear Regulatory Research, Reactor Risk Reference Document, NUREG-1150 (Draft), February 1987.

4. U. S. NRC, Reactor Safety Study--An Assessment of Accident Risks in U.S. Commercial Nuclear Power Plants, WASH-1400 (NUREG-75/014), October 1975.

5. R. J. Dallman, L. G. Hulman, and J. A. Kudrick, "Filtered Venting Considerations in the United States," Specialist Meeting on Filtered Venting Systems, Paris, France, May 17-18, 1988.

6. A. Kolacykowski, et al., Analysis of Core Damage Frequency From Internal Events: Peach Bottom, Unit 2, Draft NUREG CR/4550, Volume 4, October 1986.

7. R. M. Harrington, "Containment Venting as a Mitigation Technique for BWR Mark I Plant ATWS," Nuclear Engineering and Design, 108, June 1988, pp. 55-70.

8. R. J. Dallman, et al., Severe Accident Sequence Analysis Program - Anticipated Transient Without Scram Simulations for Browns Ferry Nuclear Plant Unit 1, NUREG/CR-4165, EGG-2374, May 1987.

9. R. J. Dallman letter to J. N. Ridgely, Preliminary Report on Potential Mark I Containment Improvements, RJD-42-88, October 4, 1988.

10. C. N. Amos, et al., Containment Event Analysis for Postulated Severe Accidents: Peach Bottom Atomic Power Station, Unit 2, NUREG/CR-4700 Volume 3, Draft Report for Comment, May 1987.

11. D. I. Chanin, et al., MELCOR Accident Consequence Code System (MACCS Version 1.5), Volume 1, User's Guide, Sandia National Laboratories Report, to be published.

12. R. N. Inman, S. C. Hora, Modeling Time to Recovery and Initiating Event Frequency for Loss of Offsite Power Incidents at Nuclear Power Plants, NUREG/CR-5032, SAND87-2428, January 1988.

13. S. W. Hatch, et al., Shutdown Decay Heat Removal Analysis of a General Electric BWR/4 Mark I, NUREG/CR-4767, SAND86-2419, July 1987.

ATWS scoping calculations for a BWR plant performed using Relap5/Mod2 and CONTAIN codes

P. Marsili - A. Pasculli - P. Camiciola
ENEA-DISP, Rome, Italy

Abstract

In the frame of the licensing process for ALTO LAZIO nuclear power plant (a BWR/6 - MARK III design) some calculations have been performed for evaluating the plant response and the effectiveness of the safety systems during an ATWS transient.
Furthermore the containment behaviour and the containment venting effectiveness have been evaluated.
Two best estimate codes have been used for this study:
- Relap5/Mod2 for the Reactor Cooling System (RCS) behaviour calculation;
- CONTAIN 1.1 for the containment response calculation.

The initiating event has been determined as a Main Steam Isolation Valve (MSIV) closure because of its severity and, in order to assess the relative effect, three different Stand-by Liquid Control System (SLCS) actuation modes have been considered:
a) NOSLCS-case: it is supposed no intervention of SLCS;
b) SLCS2-case: the SLCS starts two minutes after the initiating event;
c) SLCS10-case: the SLCS is supposed to start ten minutes after the initiating event.

The calculation results have been evaluated in terms of core and containment T/H conditions.

Introduction

The ATWS event gives the most contribution to the core melt probability for BWR plants. In order to face this event, some additional safety systems and operator actions have been requested for ALTO LAZIO. In particular should be mentioned the Alternate Rod Insertion system (ARI), the Recirculation Pump Trip system, the Feedwater Runback features and the SLCS (injecting into the RCS a 13% concentration sodium pentaborate).
In the case of ATWS with no ARI available, there are no systems other than SLCS to shut down the reactor.
Consequently in this case it is very important to evaluate:
- the effectiveness and the intervention time of the SLCS;
- how to mitigate the consequences in case of an ATWS without intervention of SLCS.
- the time at which the High Pressure Core Spray (HPCS) and RCIC may be considered no longer operating because of the high temperature in

Suppression Pool (SP);
- the effectiveness and magnitude of containment venting in the worst case.

For these reasons it is interesting to analyze three cases related to the SLCS availability.
The first case, related to no SLCS intervention (NOSLCS-case), implies the plant evolution not affected by the operator action (the systems as Reactor Core Isolation Cooling (RCIC), Control Rode Drive (CRD) and High Pressure Core Spray System (HPCS) are supposed operating in automatic mode).
The second case is related to the automatic start of the SLCS for which the SLCS can be supposed to start two minutes after the initiating event (SLCS2-case).
The third mode is related to the manual activation of the SLCS (SLCS10-case) and the starting time of SLCS can be evaluated in 10 minutes after the initiating event.
In order to get realistic results best-estimate codes (RCS dedicated and containment dedicated) can be used. Having two separate codes as Relap5/Mod2 and Contain 1.1, the calculations can be performed in two different phases:

phase 1): The Reactor Cooling System (RCS) evolution calculated by Relap5/Mod2 code, considering no containment feedback on the RCS safety systems

phase 2): The Relap5/Mod2 and CONTAIN 1.1 codes alternatively used determining the mutual boundary conditions.

RCS model general description

Fig. 1 gives a schematic representation of the BWR vessel considered in the calculations.
The nodalization of the RCS (fig. 1) has been determined by:
- 122 volumes
- 131 junctions
- 153 heat structures

representing most of all important component of the RCS (valves, pipes, pumps, core, downcomer, jet pumps, ...).
The HPCS, SLCS and RCIC systems have been also simulated and the downcomer level control system has been considered operating during the transient and it allows the HPCS and RCIC to inject when the downcomer level is inside a well determined range (level 2 ÷ level 8).
The Safety Relief Valves (SRVs) were divided into five groups depending on their opening/closure set points and their actuation logic.
It should be noticed that the SLCS injects into the Reactor Vessel (RV) by the HPCS injection line.

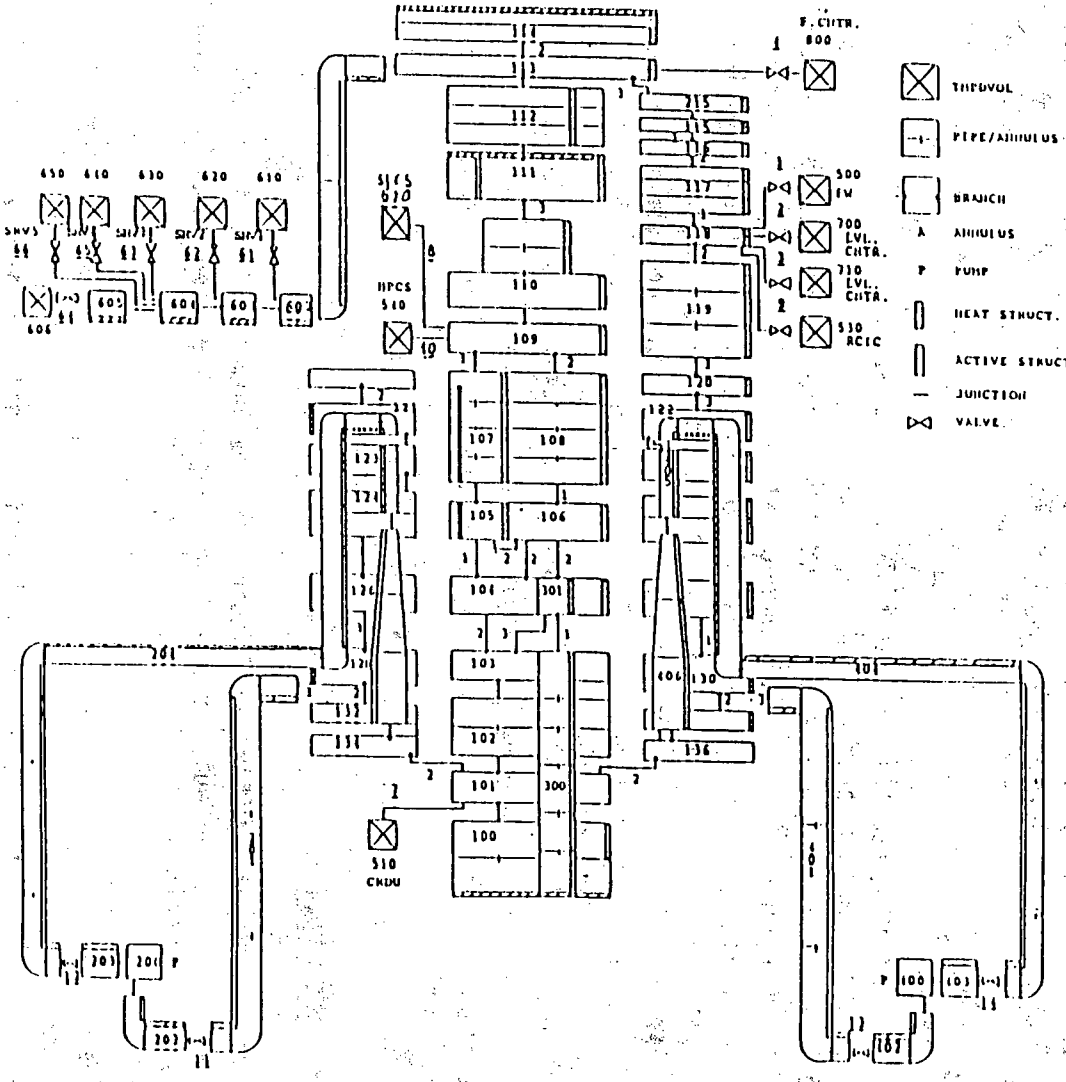


FIG. 1

RCS Relap nodalization

Containment model description

The design of Alto Lazio Plant is that of a typical 218/624 BWR/6 MARK III with a double containment building: a primary free standing steel containment and a secondary concrete structure containment. There is an air gap (Annulus) between the two ones.
As this work regards only the accident evolution in the short time (up to the second hour after the initiation) it has been considered only the primary containment for the heat exchange between the building and the external environment. The primary containment has been divided into three compartment: upper dome, wetwell and drywell. The main characteristics of the nodalization (fig. 2) can be summarized in:

- 10 nodes,
- 17 junctions,
- 29 heat sinks,
- 2 pools: a refueling pool and the MARK III suppression pool.

Furthermore we have considered:

- a break valve between the wetwell and the drywell (that opens when a pressure difference of 2 psi is reached between the two compartments);
- two train of Residual Heat Removal (RHR) of 80 Megawatt capability which starts operating ten minutes after the accident initiation;
- one train of Special Emergency Heat Removal System (SEHR) of 40 Megawatt capability which starts working when a suppression pool temperature of 333 K is reached;
- a vent between the primary containment and the external enviroment.

The vent diameter size for base calculations is 40 inches;

- HPCS system (whose characteristics have been determined by Relap and Contain iterative calculations).

Calculation description

In order to obtain the effect evaluation of the some actions that can be taken (by the operator or automatically) during the transient the following cases have been selected:

- NOSLCS-case
- SLCS2-case
- SLCS10-case.

As mentioned the MSIV closure is the initiating event for all cases and the ARI is considered not available.
The NOSLCS-case is related to the situation of mitigative actions being limited to the Recirculation Pump Trip (RPT) Feed Water (FW) pump runback containment venting, RHR, SEHR and HPCS the SLCS considered not available. This case was chosen to have an evaluation of both the worst consequences and the mitigation capability during an ATWS event. For this case alternate Relap5/Mod2 and Contain calculations have been done in the following sequence:

a) A first calculation by Relap5/Mod2 code was done to calculate the discharged enthalpy from the RCS to the Containment.
b) Taking into account the discharged enthalpy the containment conditions

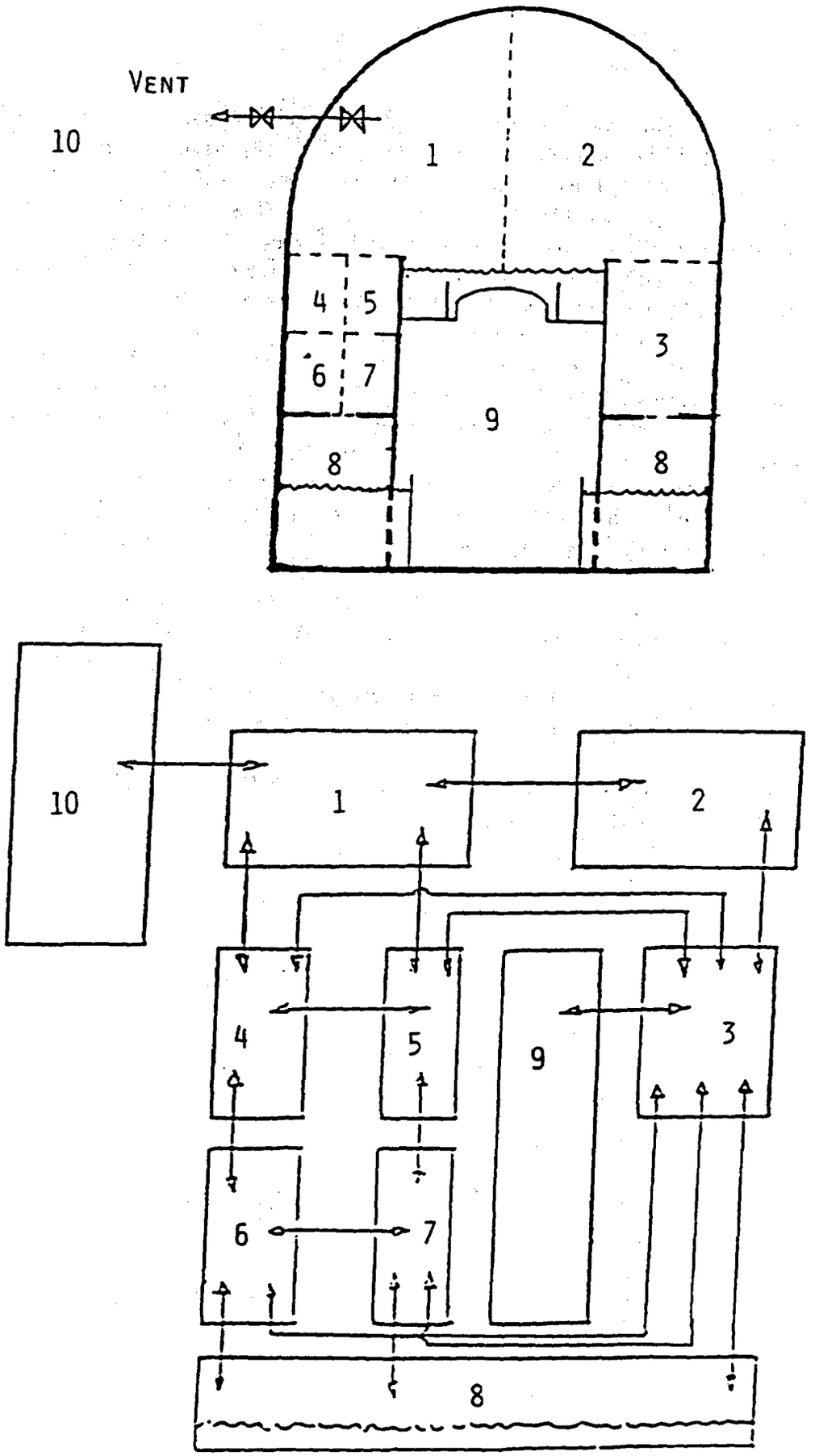


Fig. 2

MARK III Contain nodalization

were evaluated by the Contain code and the time, 2650 sec., at which the Suppression Pool (SP) temperature reached 120°C, was determined.

c) A second Relap5/Mod2 calculation starting at time = 2650 sec. was done considering no longer available the RCIC and HPCS and from that time a new discharged enthalpy from the RCS to the SP was calculated.

d) Finally a new Contain calculation was performed from the time 2650 sec. (using the new discharged enthalpy calculated under point C) and a new containment behaviour was evaluated.

e) Sensitivity studies were done by Contain in order to evaluate the containment venting effects. Three different diameter size were considered: 20", 30" and 40". For each calculations, the pressure set point opening of the containment venting was supposed to be 0.4 Mpa.

In the SLCS2-case the SLCS was assumed to intervene at two minutes after the initiating event. This case simulates the automatic actuation of the SLCS because two minutes is the time evaluated to start that system in automatic mode.

In order to evaluate the relative effect of the SLCS actuation time, the SLCS10-case was calculated. The actuation time was defined at 10' after the initiating event because 10' is the time evaluated for the operator to perform all the requested actions in order to start the SLCS injection.

In both cases the automatic start of both RPT and the Feedwater Runback was assumed.

Table 1 and Table 2 summarize for all cases the boundary conditions and the sequence of the event respectively.

QUANTITY	UNITS	VALUE
Vessel height	(m)	21.309
Vessel diameter	(m)	5.586
Power	(Mwt)	3014.
Liquid inventory into the Vessel	(Kg)	192.10^3
Number of fuel bundles	(-)	624.
Number of rods per fuel bundle	(-)	62.
Active height of bundles	(m)	3.801
Number of recirculation lines	(-)	2.
Number of jet pumps	(-)	20.
Core flow	(Kg/s)	11160.
Recirculation flow	(Kg/s)	1800.
Steam flow	(Kg/s)	1640.
Upper plenum quality	(-)	0.14
Feedwater temperature	(°K)	485.
Lower plenum temperature	(°K)	552.
Steam dome pressure	(MPa)	7.15
Overall axial peak factor	(-)	1.4
Overall radial peak factor	(-)	1.4

Table 1
Boundary conditions and plant characteristics

	NOSLCS (s)	SLCS2 (s)	SLCS10 (s)
MSIV closure: start	0	0	0
open	4	4	4
Recirculation Pump Trip	1	1	1
SRV opening	2.5	2.5	2.5
HPCS and RCIC start	165	165	165
FW runback start	75	75	75
FW stop	90	90	90
SLCS start	*NA	120	600
SLCS stop	*NA	2620	3100
Containment venting start	4580.	*NA	*NA

Table 2
Sequence of events

*NA = Not Applicable

RCS Calculation results

It should be noticed that the initiating event is supposed to happen at t = 100 s in the time scale of the diagrams.

- NOSLCS-case t = 0 ÷ 2650 sec

  The MSIV closure at t = 100 sec causes the first pressure peak (fig. 3) with a consequent power peak (fig. 4) due to the decrease of void fraction inside the core.
  The Safety Relief Valves (SRV) open quickly 2,5 sec after the initiating event producing a pressure and power decrease.
  The power has some oscillations due to the SRV opening/closure switching, but the mean value decreases up to 25% at t = 300 sec of the rated value as the core mass flow rate strongly drops after the RPT.
  Later on the power and pressure oscillations are stabilized around 25% and 90% of the respective rated values.
  The discharged energy into the SP by the SRV (fig. 5) increases quite constantly after 500 sec.
  The core bundle level remains quite constant (fig. 6) and there is no temperature rising at the fuel clad (fig. 7).

- NOSLCS-case t = 2650 ÷ 4100 sec

  At t = 2650 the SP temperature reached 120°C. From that time two different calculations were performed.
  The first calculation is related to the case with HPCS and RCIC available in spite of the high SP temperature. This assumption is supported by the last conclusions of NUREG 1150 that considers HPCS and RCIC working independently from the temperature of water in the SP.
  In this case the fuel clad does not experiment any heat up during the transient (fig. 7), but as will be shown later, the containment experiences the most severe conditions.
  In case of HPCS and RCIC not operating, the behaviour of RCS is quite different.
  In fact, after the HPCS and RCIC stop, the core power decreased quickly (fig. 8), the pressure oscillations were around a lower value (fig. 9) and the discharged energy into the SP stopped increasing (fig. 10).
  The core level decreased (fig. 11) and the fuel clad experimented dry-out (fig. 12).

- SLCS2-case

  The SLCS is supposed to start 2 minutes after the initiating event. The plant behaviour is the same as in NOSLCS-case up to 220 sec.
  At that time the boron injection determines a faster power decreasing (fig. 13) and the RCS pressure after some oscillations at t = 250 sec decreases (even if the SRV are closed) because of the strong condensation effect of the HPCS.
  At t = 300 sec the downcomer water level starts increasing again

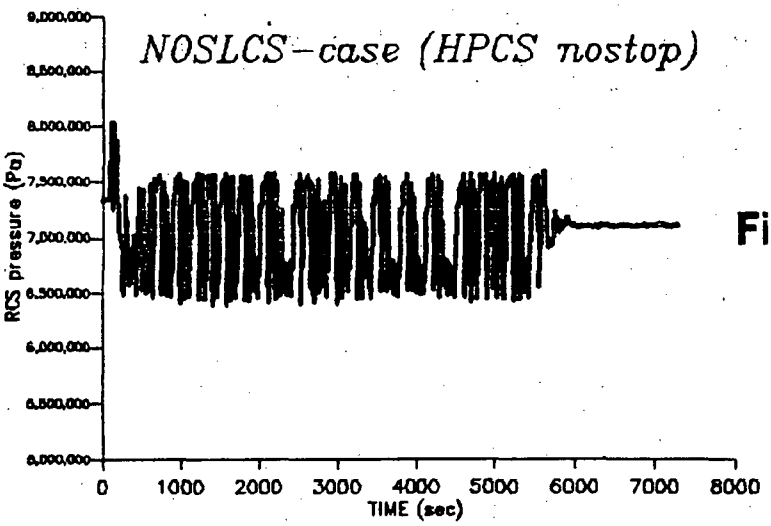


Fig.3

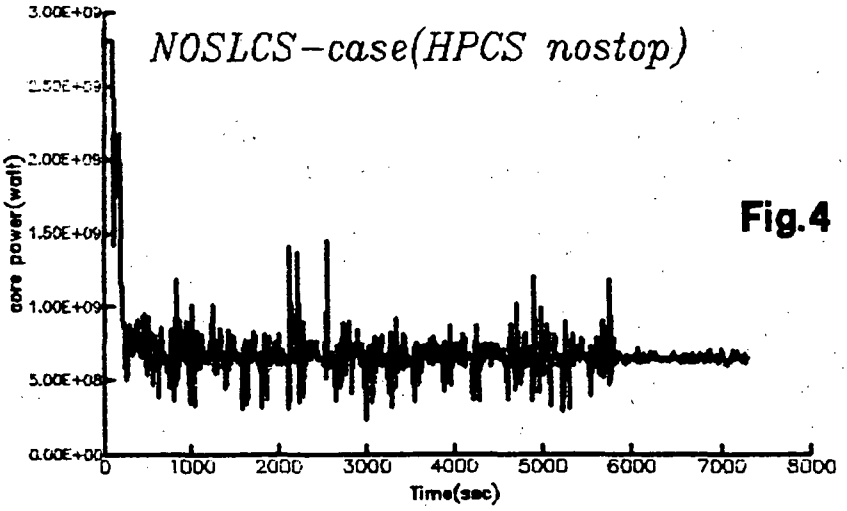


Fig.4

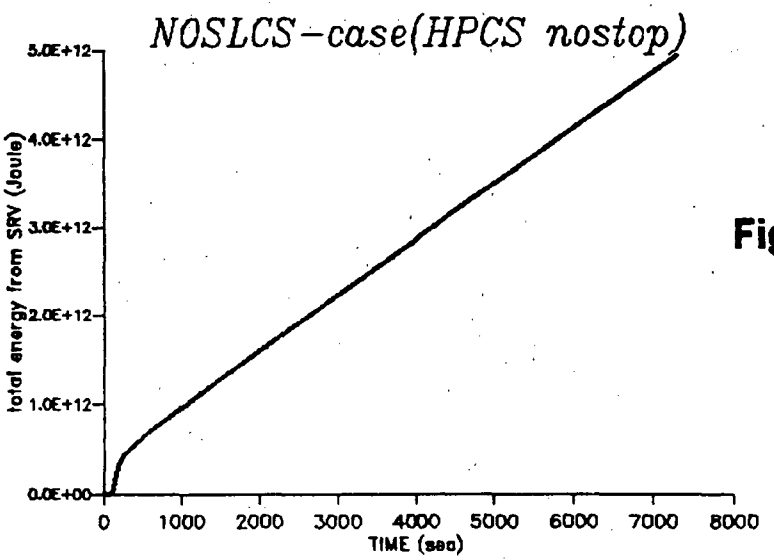


Fig.5

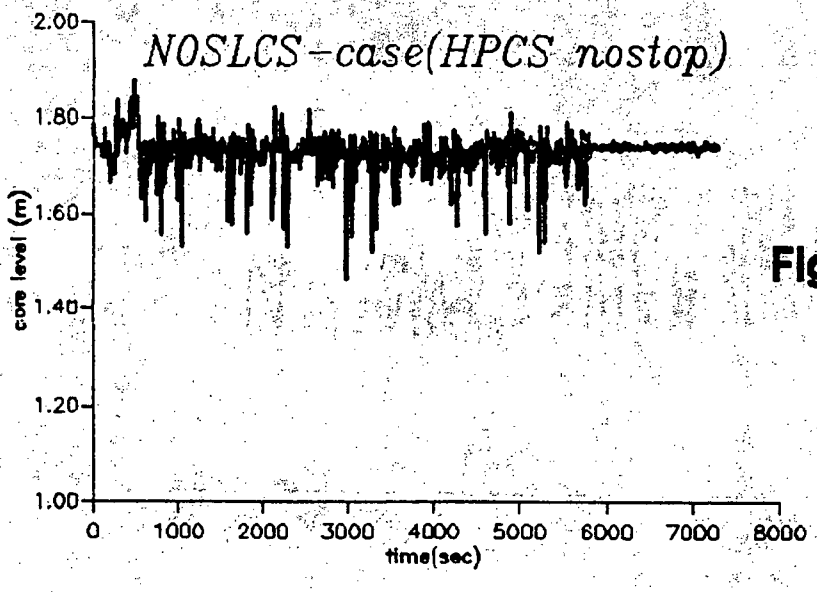


Fig.6

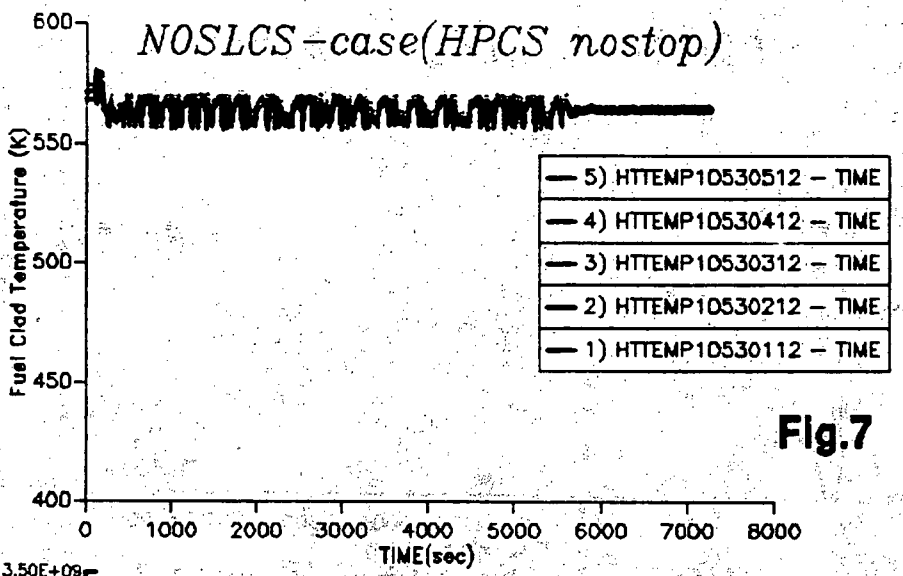


Fig.7

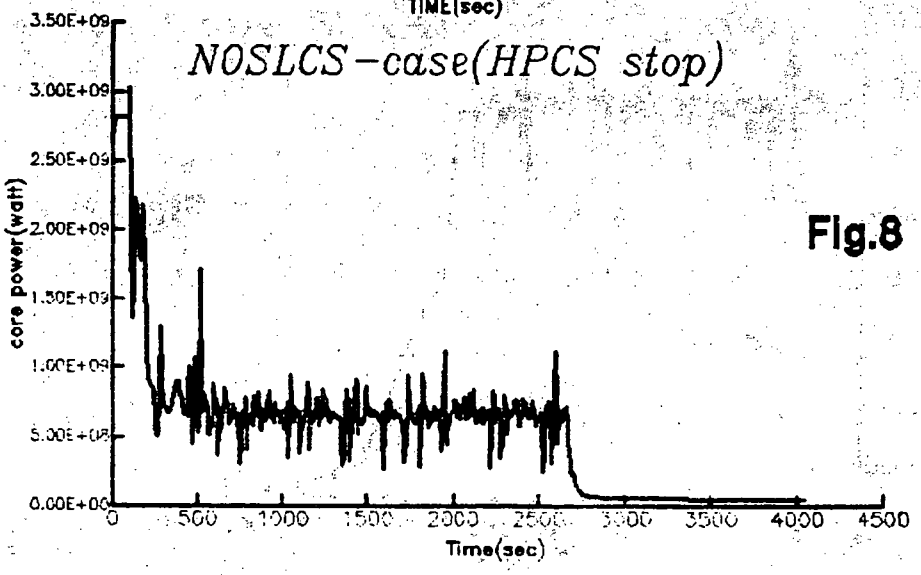


Fig.8

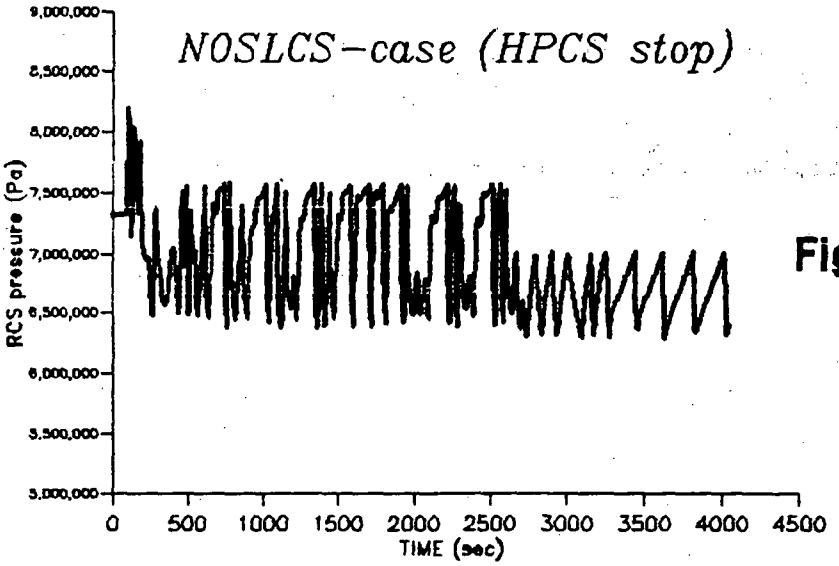


Fig.9

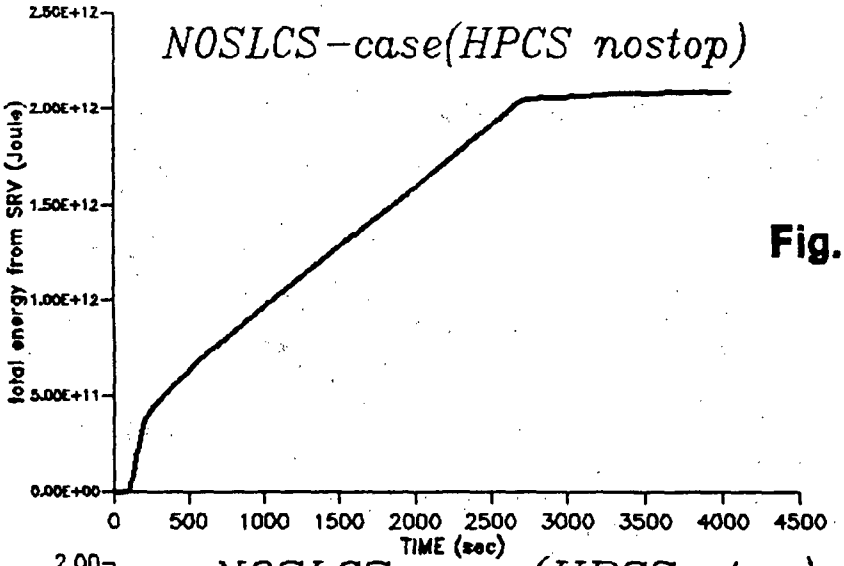


Fig.10

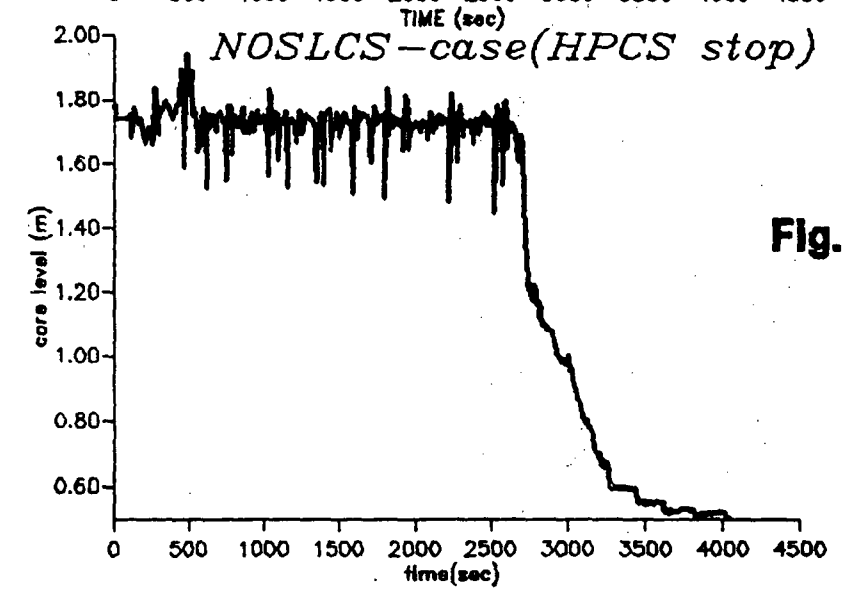


Fig.11

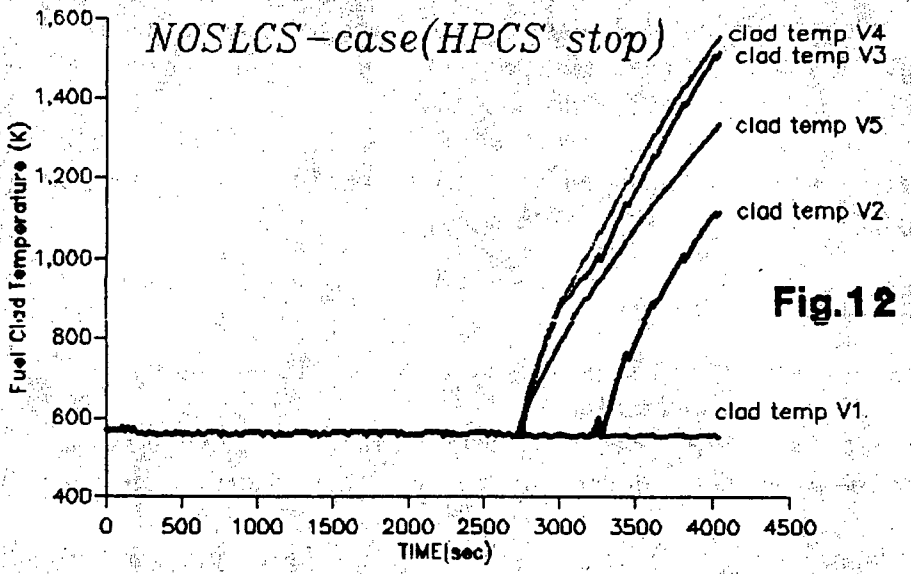


Fig.12

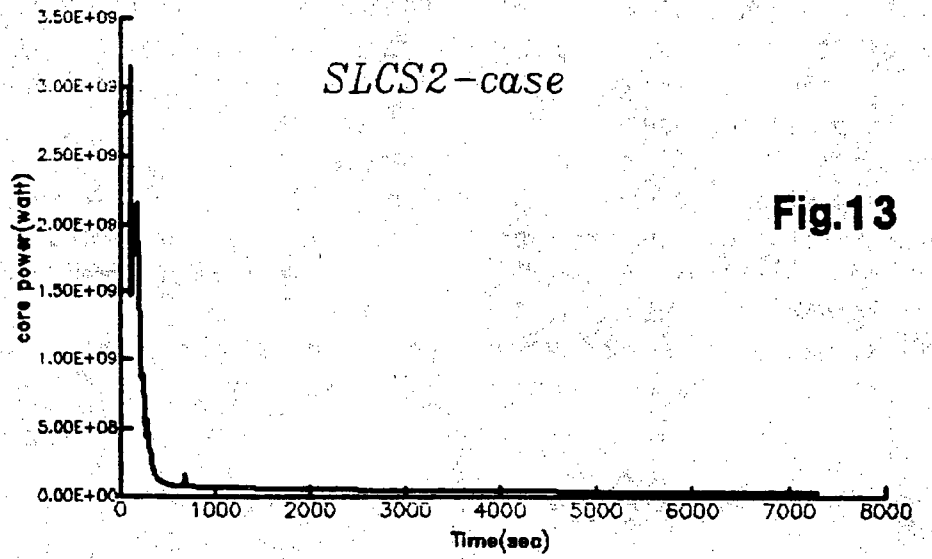


Fig.13

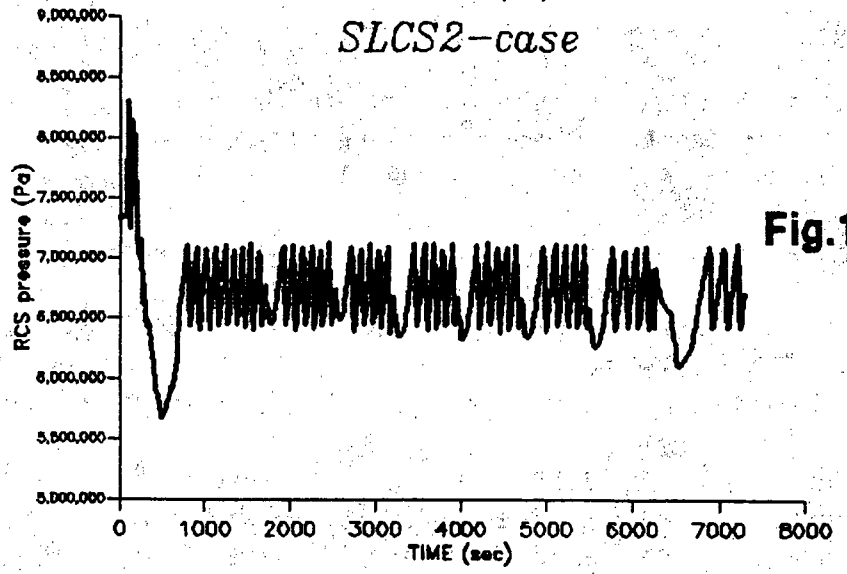


Fig.14

(fig. 17) because of SLCS effect and when reaches level-8 (at about 620 sec) the level control system stops HPCS and RCIC. Due to the HPCS stop the RCS pressure increases producing a power peak at t = 650 sec (fig. 13). After that the reactor power is at decay heat values and the reactor can be considered shut-down.
Figg. 14, 15 give the trend of RCS pressure and discharged energy into the SP. Fig. 16 shows an high core bundle level and so no core uncovery is experimented in this case.

- SLCS10-case

The plant behaviour is similar to the NOSLCS-case up to t = 700 sec when the SLCS starts injecting.
At that time the reactor power (fig. 18) decreases more rapidly and consequently the depressurization is faster than in NOSLCS-case (fig. 3).
The downcomer water level starts increasing just after SLCS injection initiation (fig. 20) and at t = 1200 sec it reaches level-8 at which the control level system inhibits HPCS and RCIC injection. Consequently a quite strong RCS repressurization is observed and a power peak (fig. 18) is determined because of the void collapsing.
After this perturbation the plant reaches a quasi-steady condition with one group of SRVs opened. The reactor power is at decay-heat values and so the reactor can be considered to stay at shut down condition.
The core water level remains higher than in normal condition and so no core uncovery is experimented in this case.
In figg. 19, 21 and 22 are reported the RCS pressures, the downcomer water level and the core bundle level respectively.

Containment calculation results

- NOSLCS-case

The containment response is shown in fig. 23 and fig. 24 where the SP temperature and the containment pressure, respectively, are represented. The results show a slight increase of both the temperature and the pressure up to 1500 seconds.
At that time these parameters experiment a quite rapid increase due to the pool mass bulk boiling.
At t = 2650 sec the SP temperature and containment pressure grow up to 120°C and 0.21 MPa respectively (figg. 25 and 23) and from that time on the containment conditions are strongly depending on HPCS and RCIC systems.
In fact in case of unavailability of these systems the reactor power decreases rapidly and the discharged energy (fig. 10) from the SRV does not increase any more. In figg. 23 and 24 curves labeled by the number 4 show the containment conditions following the unavailability of HPCS. So in this case the containment does not experiment severe conditions before the clad temperature reaches 1200°C.

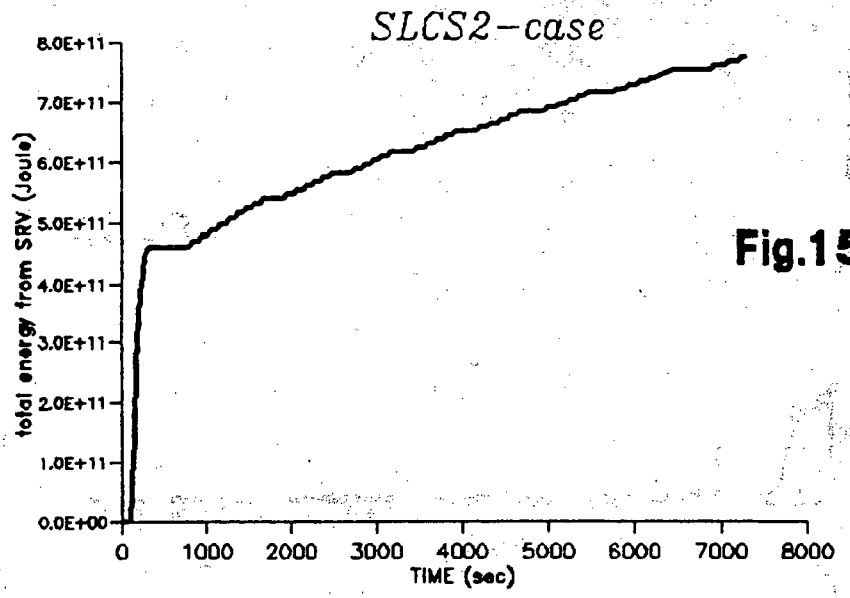


Fig.15

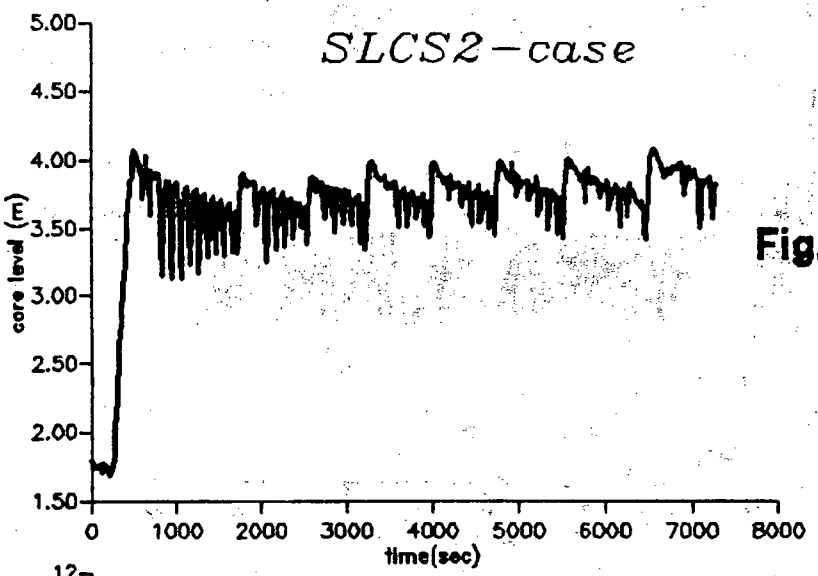


Fig.16

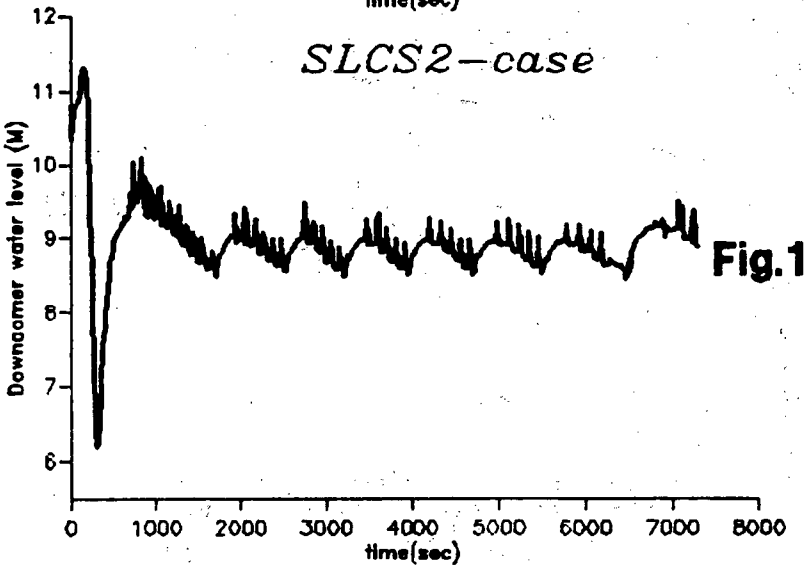


Fig.17

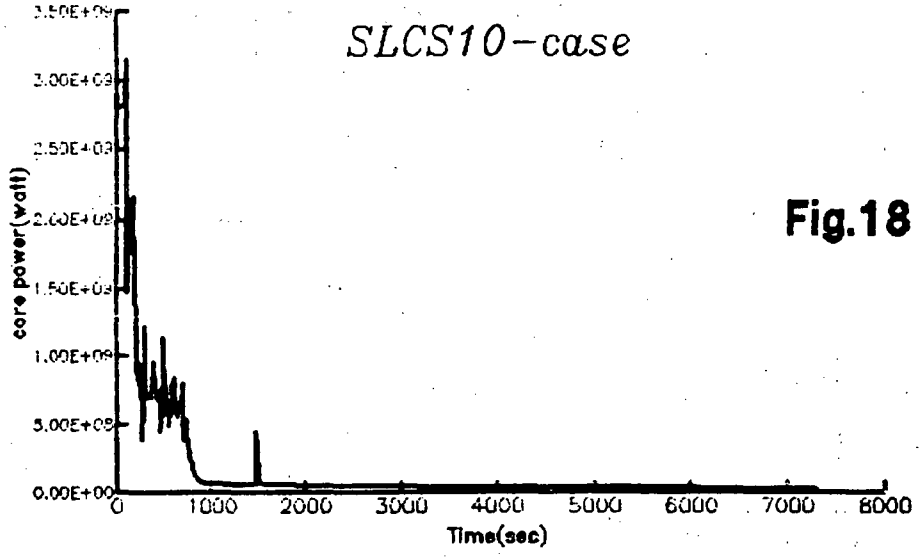


Fig.18

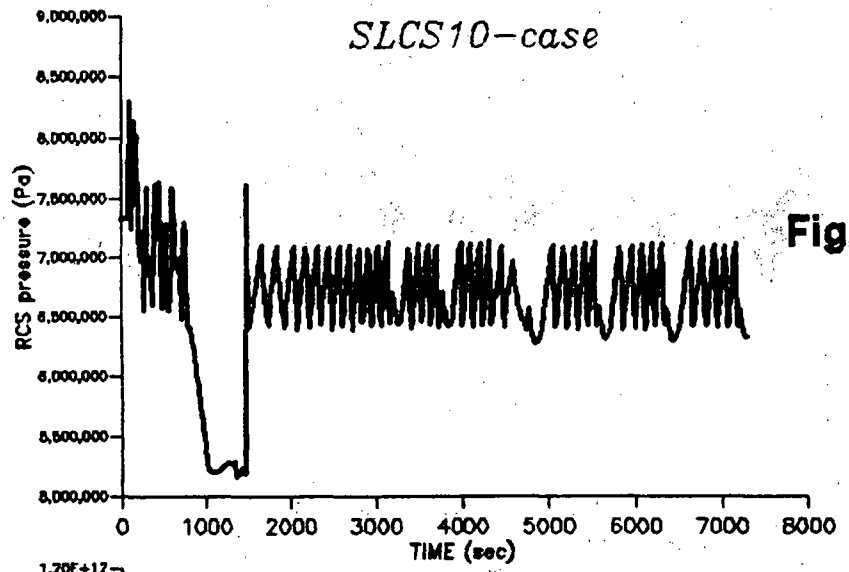


Fig.19

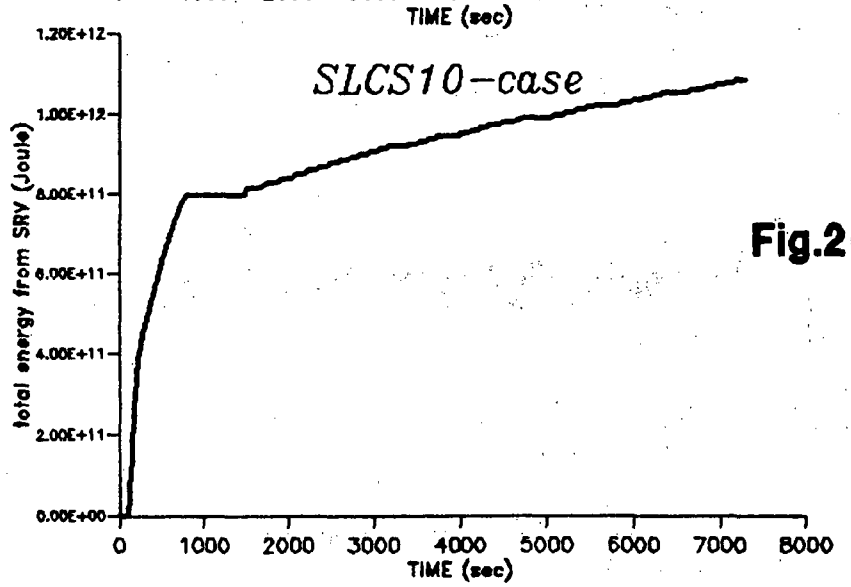


Fig.20

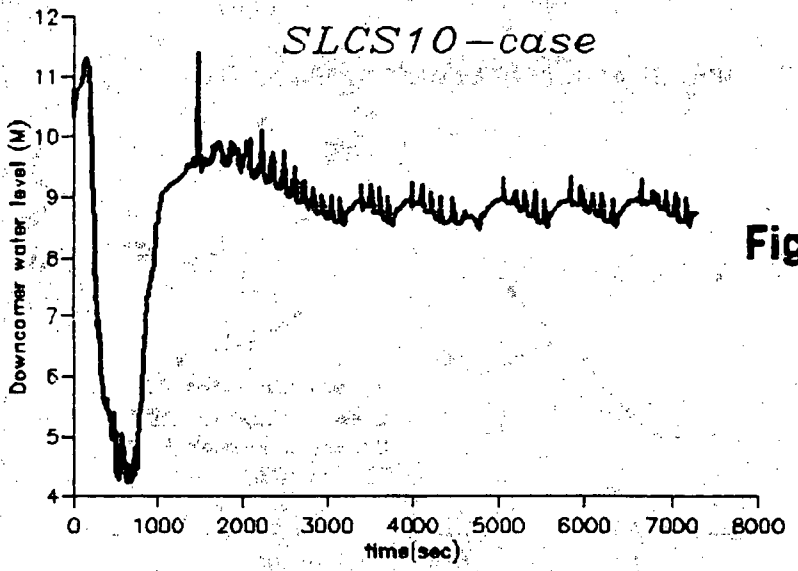


Fig.21

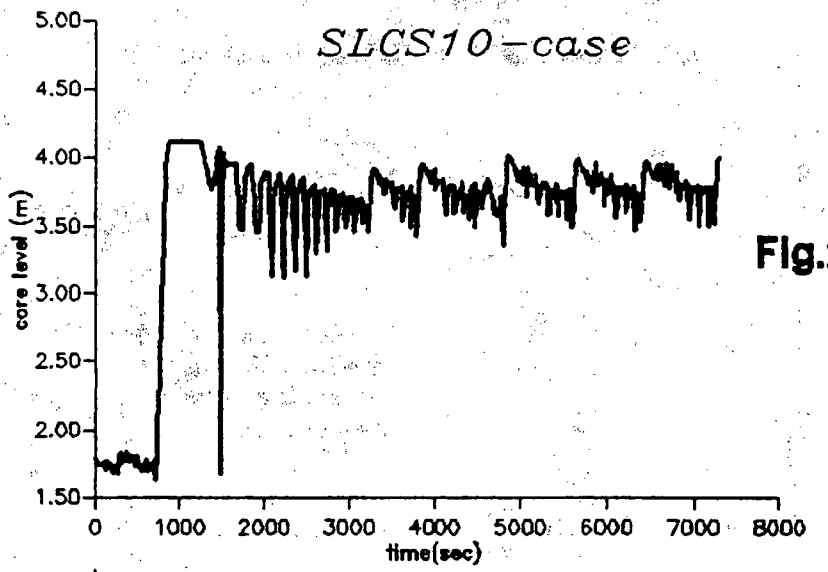


Fig.22

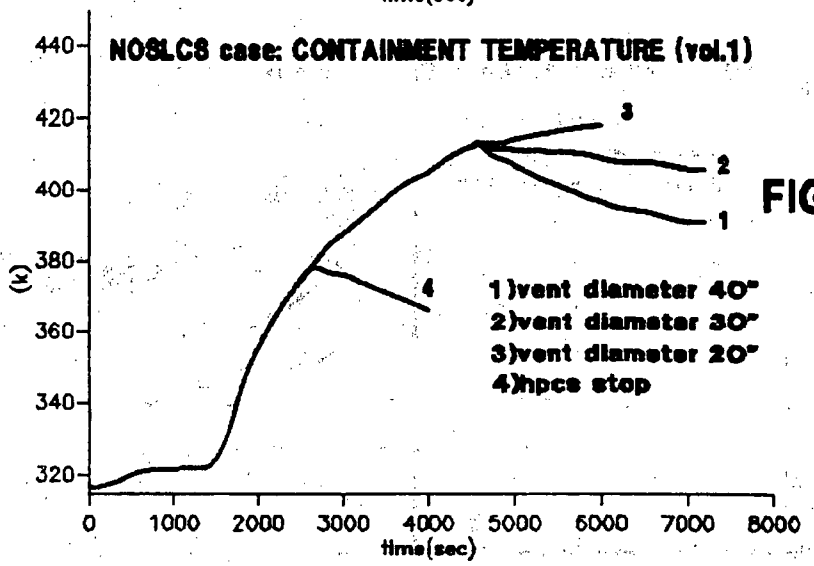


FIG.23

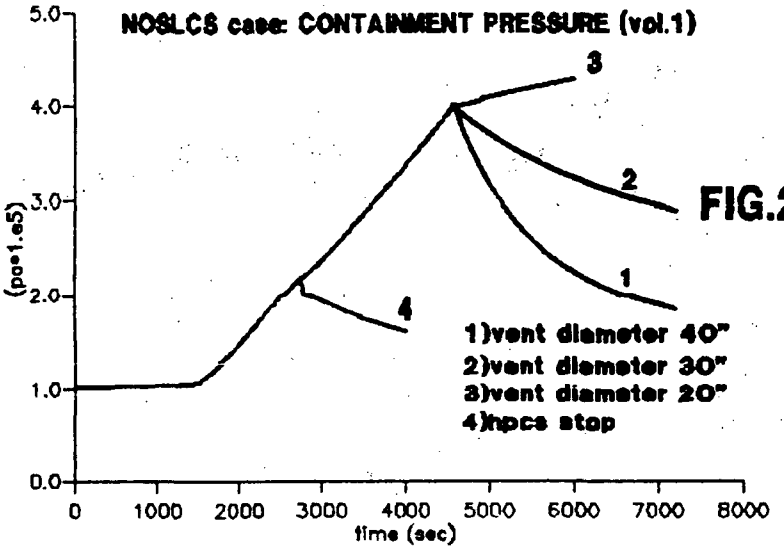


FIG.24

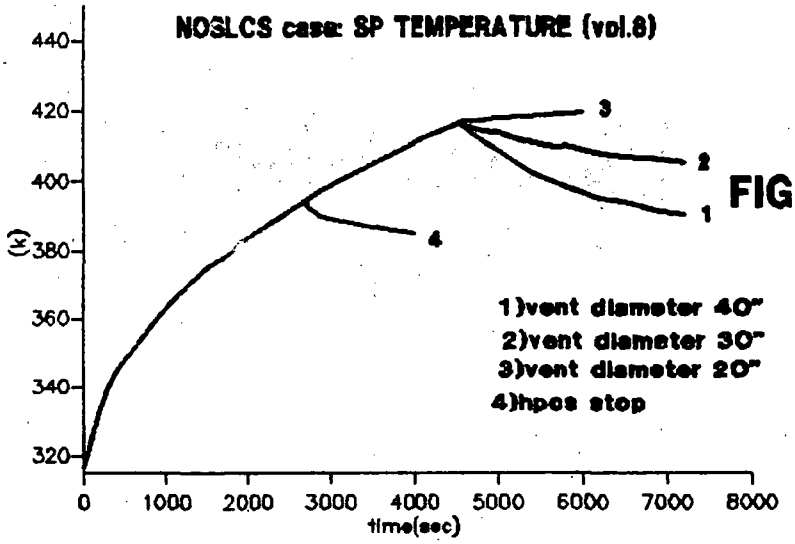


FIG.25

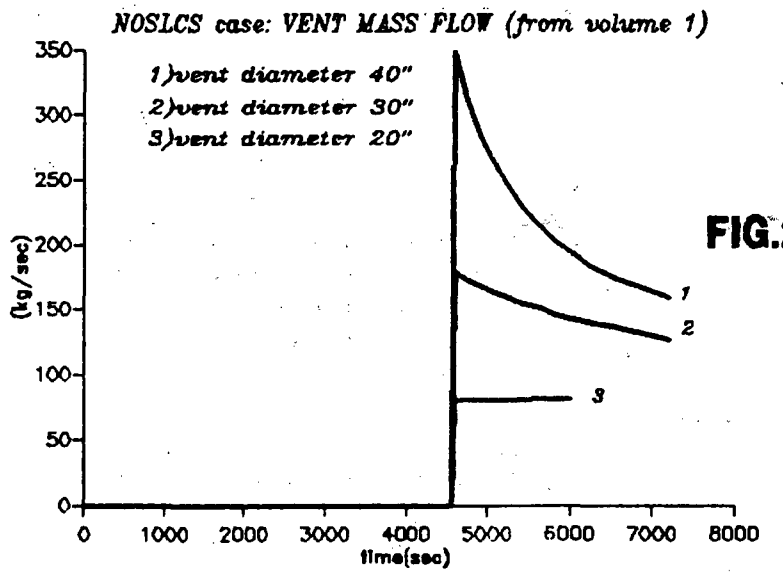


FIG.26

On the contrary, if HPCS and RCIC systems are considered operating during all the time, the containment conditions become severe and at t = 4580 sec the absolute containment pressure reaches 4 ata and venting becomes necessary in order to avoid containment ruptures.
In order to have an estimation of the vent diameter some sensitivity studies were performed with Contain code.
The diameters chosen for this study were: 20", 30" and 40". The calculation results show (fig. 22 curved labeled by number 3) that 20" is not sufficient to guarantee the containment integrity while 30" and mainly 40" produce a good pressure decreasing. The vent flow rate (fig. 26) depends on the balance between the boiled mass flow from the suppression pool and the mass flow discharged from the containment vent. As it is shown in fig. 26 the mass flows equilibrium is reached 2000 sec. after the vent opening for the case 1 and 2, while, for the case 3, the equilibrium is reached just after the vent opening.

- SLCS2-case
  SLCS10-case

  The figg. 27 and 28, 29 show that the SLCS, is sufficient, if available, to face the ATWS. Anyway the SLCS injection has to start no later than 10 min after the initiating event. In fact these figures show that for SLCS10-case both the SP temperature and containment pressure increase much faster than in SLCS2-case.

Conclusions

The tab. 3 summarizes the calculated value of some important parameters relating to the cases considered in this study.
From these data the following conclusion can be taken:
- the SLCS is very effective to shut down the reactor;
- the starting time for the SLCS should not overcome 10' after the initiating event;
- the HPCS and RCIC availability can guarantee the fuel integrity but makes more severe containment conditions;
- 30" is the minimum size of the vent diameter for limiting the pressure increase inside the containment.

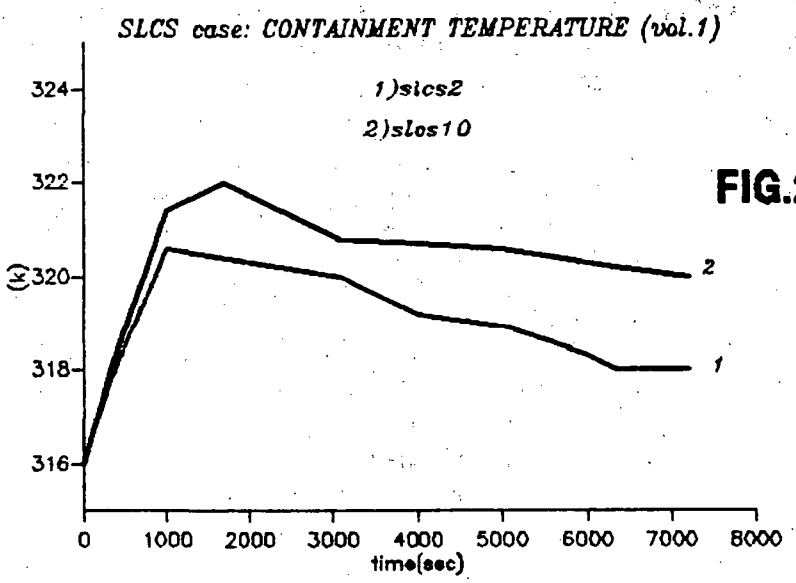


FIG.27

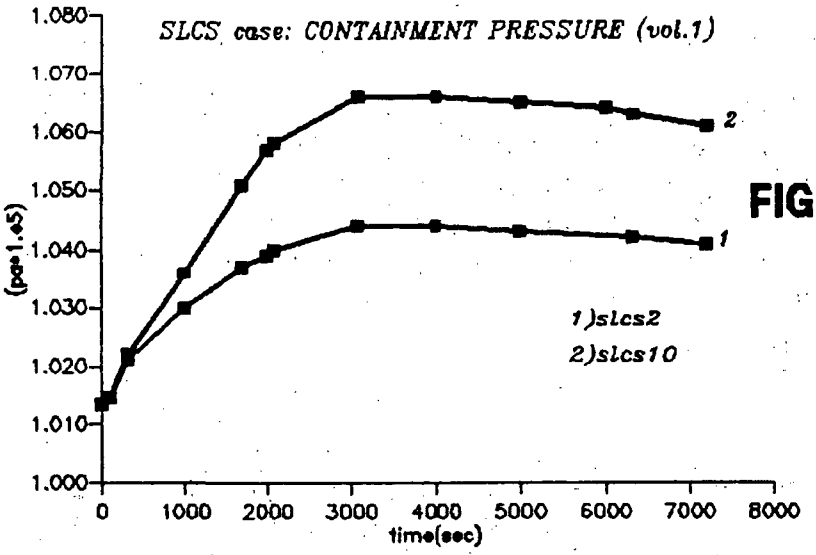


FIG.28

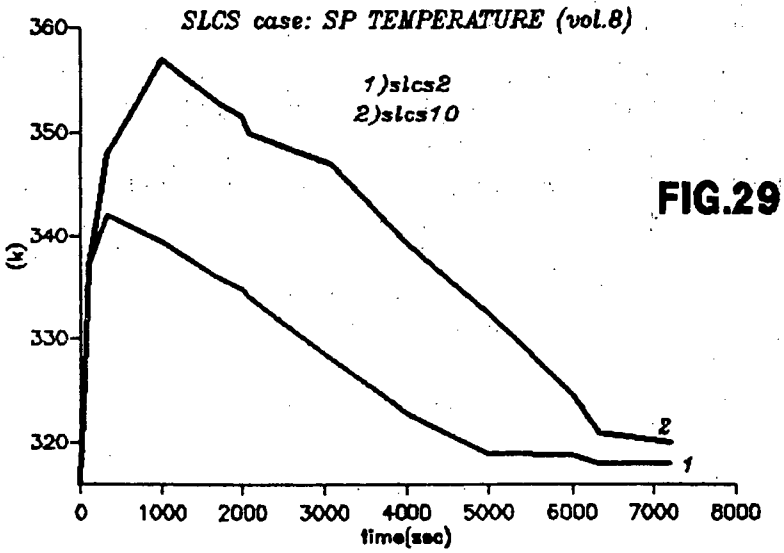


FIG.29

	NOSLCS		SLCS2	SLCS10
	with HPCS RCIC	without HPCS RCIC after 2650 sec		
Long term Reactor power (MW)	639	30	30	30
Long term RCS mean pressure (MPa)	7.0	6.6	6.7	6.7
Start time HPCS e RCIC (sec)	200	200	166	200
Discharged Energy into SP at t = 4000 sec (GJ)	2860	2100	600	950
Minimum down corner level (m)	4.2	4.2	6.2	4.3
Reactor shut down time (sec)	-	2800	760	1315
Tclad Max (K)	580	1560	580	580
Max containment pressure (MPa)	0.4*		0.1044	0.1066
Max SP temperature (K)	416*		342	357

* at time of venting initiation

Table 3
Main parameters calculation results

References

C.J. Hsu, L. Neymotin, P. Saha: "Analysis of a Typical BWR/4 MSIV Closure A.T.W.S. Using RAMONA-3B and TRAC-B01 Codes" ASME-TRANS-84-NE-10.

C.E. Peterson et alii: "Reducing BWR Power by Water Level Control during an A.T.W.S.: a Transient Analysis" NSAC/70.

R.I. Dallman, W.C. Jouse: "A.T.W.S.. Analysis for Browns Ferry Nuclear Plant Unit 1" Proceedings of Thirteenth Water Reactor Safety Research Information Meeting, Gaithersburg, October 22-25 1985.

NEDO-24222: "Assesssment of the BWR Mitigtion of ATWS "Vol. I e II, G.E., December 1979.

P. Camiciola, R. Caporali, P. Marsili, C. Tricoli, G. Sgalambro: "Risposta della centrale di Alto Lazio alle sequenze ATWS" - ENEA/DISP ACO/PROCS 13/RT(87).

V.H. Ransom et alii: "Relap5/Mod2 Code Manual" Vol. I e II, NUREG/CR-4312 EGG-2396, August 1985.

P. Camiciola, P. Marsili: "Analisi della risposta dell'impianto ALTO LAZIO a seguito di un evento ATWS" - ENEA/DISP ACO/PROCS 1/RT(88).

K.D. Bergeron et alii: "User's Manual for Contain 1.1, A Computer Code for Severe Nuclear Reactor Accident Containment Analysis".
NUREG/CR-4085 SAND 84-1204, May 1985.

CONTAINMENT AND RELEASE MANAGEMENT*

J.R. Lehner and W.T. Pratt
Department of Nuclear Energy
Brookhaven National Laboratory
Upton, New York 11973

ABSTRACT

Reducing the risk from potentially severe accidents by appropriate accident management strategies is receiving increased attention from the international reactor safety community. Considerable uncertainty still surrounds some of the physical phenomena likely to occur during a severe accident. The USNRC, in developing its research plan for accident management, wants to ensure that both the developers and implementors of accident management strategies are aware of the uncertainty associated with the plant operators ability to correctly diagnose an accident, as well as the uncertainties associated with various preventive and mitigative strategies. The use of a particular accident management strategy can have both positive and negative effects on the status of a plant and these effects must be carefully weighed before a particular course of action is chosen and implemented.

By using examples of severe accident scenarios, initial insights are presented here regarding the indications plant operators may have to alert them to particular accident states. Insights are also offered on the various management actions operators and plant technical staff might pursue for particular accident situations and the pros and cons associated with such actions. The examples given are taken for the most part from the containment and release phase of accident management since this is the current focus of the effort in the accident management area at Brookhaven National Laboratory.

1. Background

Although severe accidents in nuclear power plants are viewed as very unlikely events, history has shown that their occurrence cannot be ruled out completely. In recent years there has been an increased international interest in the risk arising from potential severe accidents and the role management of such accidents can play in reducing risk.

A useful way of grouping accident management strategies is by their emphasis on preventing core damage, arresting core damage (in-vessel management), or preserving containment integrity (ex-vessel management). The

*This work was performed under the auspices of the U.S. Nuclear Regulatory Commission. This paper does not necessarily express the opinion of the USNRC.

latter, termed containment and release management is the focus of our present discussion and is concerned with maintaining containment integrity as long as possible and minimizing the consequences of offsite releases. Usually containment and release management strategies apply to situations where core debris has penetrated the reactor vessel so that the containment is the only barrier between fission products and the environment. However, some containment strategies involve measures to be implemented before vessel failure and even prior to core damage.

2. Objective

The objective of this paper is to highlight some of the important considerations regarding severe accident management that need to be addressed by the NRC research program in this area. While specific examples of management strategies cited here deal for the most part with the containment and release phase, in-vessel and ex-vessel strategies are of necessity closely coupled and often dependent on each other. Therefore many of the insights cited here apply to preventing or arresting core damage as well as to preserving containment integrity.

A significant amount of uncertainty still limits our understanding of many of the physical processes associated with severe accidents. This is especially true of phenomena occurring at reactor vessel penetration and subsequent stages of the accident. High pressure melt ejection, core-concrete interaction, and debris coolability are a few prominent examples of events where comprehension remains limited by uncertainty.

Despite this uncertainty, there is a wide consensus in the reactor safety community that a significant benefit can be obtained by carefully developing accident management strategies and preparing reactor personnel for implementing them. However, the use of a particular strategy can have negative as well as positive effects on the status of the plant. Both the developers and the implementors of a strategy must be aware of the pros and cons associated with it and have confidence that, in the specific situation in which the strategy is applied, the benefits outweigh the disadvantages. The previously mentioned uncertainties make such an assessment more difficult and can themselves influence the selection of a strategy. (For instance a more costly or less efficient strategy, but one with less uncertain "side-effects," may be preferable to a less costly or more efficient strategy which has more uncertainty attached to it.)

Two key questions for conceiving and evaluating any accident management strategy are, first, what will the operators and other responsible plant personnel know, and second, what can they do based on the information available? Often, when the progression of a theoretical severe accident is analyzed and various outcomes postulated, the implicit assumption is made that the status of the core, the conditions in the primary system, the reactor cavity, and the rest of the containment are all known and various safety systems can be called on to fulfill their function at the appropriate time. In reality, lack of information, or erroneous information regarding the status of plant systems may be the biggest obstacle in arresting or mitigating a severe accident.

Therefore, to adequately address the two questions stated above, an accident management research program must focus on the following items:

1) information the operating staff can acquire during a severe accident with the instruments and information systems currently existing within the various containment types;
2) how these symptoms can be correlated to different severe accident phenomena and plant damage states;
3) preventive and mitigative actions that are possible, contingent on the functioning engineered safety features and other available systems;
4) which among these options is the optimum choice under particular containment conditions, and
5) any obviously cost-effective enhancement of instruments and other systems or procedural changes which could improve the accident management response.

In addition, human factors involving the training, staffing and performance of operational and technical personnel, as well as plant organization and lines of responsibility will affect accident management, but in the present discussion we will restrict ourselves to presenting some initial insights related to the first four items listed above. Many of these insights are based on the work done in assembling the five volumes of NUREG/CR-4920[1] and some of them have previously been discussed in NUREG/CR-5132.[2]

By means of examples we want to illustrate how a particular severe accident scenario can be diagnosed from the information the operating staff is likely to have, what strategies could be implemented, and the positive and negative aspects of each strategy.

3. Insights

As a number of studies have shown, one way in which containment integrity can be impaired is via an isolation failure or bypass. Therefore, as a first example illustration we want to consider the situation where an interfacing systems LOCA occurring during a severe accident causes the containment to be bypassed.

An interfacing systems LOCA can occur in both BWRs and PWRs due to a failure of the barriers between the high-pressure reactor coolant system and connected low-pressure systems, resulting in the failure of some components outside of primary containment. Although such sequences have been found to be relatively low frequency events, they may lead to potentially high radiological releases because these events provide a direct path for release of fission products to the atmosphere.

The symptoms of an interfacing systems LOCA that an operator is likely to see on his control panel indicators are several. Primary system pressure level will drop. A loss of primary system inventory will occur without a corresponding increase in containment sump level indication. Since the breach of the low-pressure system outside of the primary containment boundary will occur

in the reactor building of BWRs or the auxiliary building or safeguards building in PWRs there may be an indication of water level in these buildings. Furthermore, if some fuel damage has occurred, radiation levels in the auxiliary or reactor building may also provide strong indication that an interfacing systems LOCA is taking place.

Assuming the plant operators have received some of the signals mentioned, have interpreted them correctly, and have realized what is happening, what actions can the operators and plant technical staff take to arrest this accident or mitigate its consequences?

If an interfacing systems LOCA is in progress the operator may be able to arrest it by isolating the component or section of piping where the failure occurred. In many cases adequate additional valves exist to isolate the affected section of the low-pressure system if it can be located precisely. If isolation of the failed component is not feasible it may be possible to flood the location of the break in the auxiliary or reactor building with water and mitigate the consequences of the LOCA by scrubbing any fission products which are being released. If flooding is not possible, the operator may be able to turn on fire sprays in the BWR reactor building or the PWR auxiliary building to reduce the pressures and temperatures and decontaminate the atmosphere. Finally, in some situations it may be feasible to depressurize the high-pressure system to reduce the driving force and thereby the flow and amount of fission products bypassing the containment.

However, there are serious concerns associated with all these strategies except isolation of the affect low-pressure system component, and even in this case, if the system is an essential one, its isolation may solve the immediate problem but have detrimental implications for the future progress of the accident. Trying to flood the location of the break can lead to excessive flooding and impair other systems. The use of fire sprays can have very detrimental effects on electrical apparatus or other sensitive equipment. Deliberate additional depressurization of the high-pressure reactor coolant system will lead to further depletion of the primary system inventory and may, in some accident scenarios, hasten the onset of core damage or aggravate the progression of core melt.

As further examples of the kinds of information operators can expect and the actions plant personnel can take when faced with a severe accident we will describe a severe accident progression in a PWR and identify operator actions which may reduce the severity of such an accident but we will also indicate the risks that may accompany such actions. Both high-pressure sequences as well as situations where the reactor coolant system has been depressurized will be considered and the accident will be followed from core damage to reactor vessel penetration and through the ex-vessel phase.

Many studies have predicted that most severe accidents would be started by transients or small breaks in the primary system pressure boundary. Under these circumstances, the primary system would remain at high pressure unless the plant operators take actions to reduce the pressure. If such an accident starts and high-pressure injection is not available, and heat removal through

the steam generators is not effective, then core damage will occur unless the plant operators restore high-pressure injection, reestablish heat removal through the steam generators or depressurize the primary or secondary systems to take advantage of any available low-pressure injection systems.

As long as the primary system has not been breached a major objective of plant personnel must be to maintain water flow to the core. If coolant injection can be restored before core damage the accident is terminated, but it is also possible that plant operators may restore the coolant injection systems only after the start of core damage. The water will cool the reactor core, prevent further degradation, and could prevent the core from melting through the reactor pressure vessel. While supplying water to the damaged core is a major objective of the plant operators, there are phenomena associated with mixing water and high temperature molten core materials that are difficult to predict. It is possible that by adding water additional steam will be produced which in turn could generate more hydrogen before the core materials are cooled. It is also possible that more violent interactions may occur between the hot core debris and water and additional fission products may be released. In addition, adding relatively cool water to hot fuel could shatter the fuel into rubble, impeding further coolant flow through the core.

If high-pressure injection cannot be restored depressurization of the reactor coolant system will allow low-pressure systems to inject. The preferred way of accomplishing this would appear to be depressurization using the steam generators. After the primary system has been depressurized via secondary heat removal, the accumulators will inject and the low-pressure injection systems can be actuated. To attain success in this procedure, the operator must open the steam generator atmospheric steam dump valves, maintain auxiliary feedwater, main feedwater, or special makeup (e.g., fire pumps) to the steam generators, and have one of the low-pressure injection systems available. Although these procedures may improve cooling capabilities, the secondary side depressurization and reflood may induce thermal shock and hence increase the possibility of steam generator tube rupture, which may aggravate the accident sequence. In addition, depressurization of the steam generators will cause loss of steam that could otherwise be used for the steam-driven pumps. Both the nuclear industry and the NRC are studying this emergency procedure further.

If primary system depressurization cannot be achieved by heat removal through the steam generators, direct depressurization may be possible by opening relief valves in the primary system. If successful, the procedure will allow the accumulators to inject, and available low-pressure injection systems can be actuated. Although this procedure has obvious advantages, it is not clear to what extent existing systems in various reactors are capable of meeting such an objective. Depending on the particular strategy, it is also possible that for some accidents the time to core damage could be reduced relative to time that it would have taken with the primary system at high pressure. In addition, pressure relief will also vent hydrogen to the containment atmosphere early in the accident, with the possibility of a burn or detonation. Therefore before implementing this procedure the advantages and

disadvantages have to be carefully assessed. It is also being investigated by both NRC and the nuclear industry.

If water flow to the core cannot be restored and the primary system is not depressurized, then core relocation (into the lower plenum) and subsequent lower vessel head failure at high pressure will follow. Upon vessel failure, violent melt ejection could produce large-scale core debris dispersal. The containment integrity could be threatened by any or all of the following: direct containment heating, large, energetic releases of hydrogen, and direct melt-through from contact with core debris. Which, if any, of these threats apply depends on the exact scenario and the particular containment design.

In general, if the accident has progressed to this point there appears to be very little that can be done by the plant operators to mitigate the effects of a high-pressure failure of the reactor vessel during the blowdown phase. However, it is possible for the plant operators to manage containment-related safety features prior to reactor vessel penetration to minimize the effects of high pressure melt ejection. If fan coolers or sprays are available they will keep the containment pressure low so that any pressure increase generated at the time of reactor pressure vessel failure will have less impact than if these containment systems were not operating. In addition, if fan coolers are able to maintain a low containment pressure, spray operation could be saved until the plant operators have an indication of core damage. Spray operation after core damage and fission product release could aid in removing aerosol fission products from the containment atmosphere. However, it has also been suggested that it is an advantage to have water in the reactor cavity prior to the release of the core debris from the reactor pressure vessel. For some containment designs, water will only be available in the reactor cavity after the sprays have injected all of the water from the refueling water storage tank into containment. Thus, the advantages and disadvantages of early or late spray operation depend on the containment design.

If the accident sequence is one which causes a reactor coolant system pressure drop (such as a large LOCA) or if the system has been depressurized by one of the techniques mentioned above a number of additional systems can be made available to inject water into the core. Even if no low-pressure injection systems can be made available and core damage eventually occurs, depressurization may still be advantageous because vessel failure with the primary system depressurized represents much less of a challenge to containment integrity. However, it has again been suggested that it would also be an advantage to have water in the cavity prior to vessel failure for low-pressure accidents to mitigate core-concrete interactions. It is also an advantage to have spray operation during core degradation and vessel failure. Therefore, it is again necessary to optimize spray operation to ensure the most effective mitigation of the accident.

In our discussion so far we have skipped over the question of how the plant operators will know that core damage has occurred. With the present instrumentation in commercial nuclear reactors there are not very many indicators of core damage and those that exist are not very precise. Readings of prolonged low water level in the reactor vessel should alert the staff that

damage may have occurred. The same is true of high temperature readings from exit thermocouples. Abnormal containment radiation levels are another sign that fuel has been damaged. Beyond such circumstantial evidence however the operators information regarding core damage is very limited. Not only is it difficult for the operating staff to determine if core damage has occurred and the extent of damage, the operators may not know whether the core is still essentially in the vessel or whether some or all of it has penetrated the primary system. The indicators of vessel meltthrough seen in the control room are ambiguous: Rapid depressurization of the primary system may be caused by the core melting through the vessel or by a high temperature failure somewhere in the primary system boundary. High containment temperatures may be due to core penetration but could also be caused by other phenomena such as a hydrogen burn. Likewise high radiation levels in containment and large quantities of noncondensibles may be due to an ex-vessel core which is reacting with concrete, but may also occur if the primary system has failed but the core still remains in the vessel.

Once the core debris has exited the reactor vessel the principal objectives of the plant staff must be to flood the debris with water and to maintain or restore containment heat removal systems. Even if the containment has failed, it is advantageous to flood and cool the core debris to prevent further fission product release from the damaged fuel and to keep the containment atmosphere at a low pressure to minimize the driving force for fission product release to the environment. Although these objectives are well defined, in practice they may be difficult to achieve and may have side effects that have to be carefully considered.

When trying to flood the core debris with water, the plant operators may have to decide to restore water flow to the primary system or directly to the containment atmosphere via the spray system. If the core debris has been released from the reactor vessel, there are advantages and disadvantages to using either system. However as just discussed above, the plant operators will probably not be able to determine whether or not the core debris has actually been released from the vessel or know the extent to which it is dispersed within the containment. Thus, the first priority would be to restore water flow to the primary system in an attempt to retain the core debris in the vessel. If the core debris has already penetrated the bottom head, the water would flow through the break onto the top of the core debris in the reactor cavity. The subsequent interactions between the water and core debris depend on the containment design and the details of the accident prior to vessel failure.

If the core debris melts through the vessel with the primary system at high pressure, it is possible that a large fraction of the core debris could be blown out of the reactor cavity. It is therefore possible that limited quantities of core debris would be left in the cavity and thus minimum concrete attack would occur. However, at the other extreme, if the primary system is depressurized when the core debris melts through the vessel, most if not all the core debris would likely be retained in the reactor cavity. If the cavity is initially dry and the core debris forms a deep bed, it could remain hot for a relatively long time and extensive concrete attack would

occur. Under these circumstances, pouring water on top of the core debris may have the effect of rapidly cooling the core and stopping concrete attack. However, experiments have shown that a crust can form on top of the molten core debris and effectively prevent the water from mixing with and cooling the core. These experiments were performed at small scale and the stability of the crusts under the conditions of a severe accident in a power plant have not been established. Thus, the effect of pouring water on top of the core debris is uncertain. Therefore, even though water flow is restored to the core debris continued concrete attack with the generation of more combustible gases and fission products is still possible. The presence of water above the debris does have the advantage, however, of trapping a fraction of the fission-product aerosols generated during the concrete attack, which would otherwise have reached the containment atmosphere.

Core debris attack of concrete in a dry cavity will pressurize the containment relatively slowly. However, concrete attack will generate large quantities of aerosols (nonradioactive and radioactive), combustible and non-condensible gases, all at relatively high temperatures. If water cools the core debris and all the decay heat goes to boiling water, containment pressurization will be significantly faster. However, containment temperatures will remain relatively low and concrete attack will be slowed or prevented.

Restoration of containment heat removal systems such as containment sprays after significant amounts of steam and hydrogen have entered the containment must also be approached with caution. Condensation of the steam by the spray system in a previously steam-inerted containment could result in the formation of a combustible mixture of possible detonable gases in containment and, if an ignition source is available, a potentially damaging combustion event could occur.

If containment heat removal cannot be restored, containment pressurization may very well continue until structural failure. Under these circumstances, controlled containment venting has been suggested as a way of preventing the uncontrolled release of radioactivity that would accompany structural failure of the containment. However, there are questions regarding venting that must be answered prior to implementing such a procedure. Combustion could occur in the vent line, which in turn could produce an uncontrolled release. Venting at some predetermined pressure level significantly below the containment ultimate capacity means that radioactivity release is certain whereas if the accident had been allowed to proceed structural failure may not occur. Isolation valve performance during venting is also uncertain and, if the valves fail open, could result in an uncontrolled release. Finally, restoration of containment heat removal to a vented containment could condense residual steam, and produce a vacuum in containment, with the attendant possibility of implosion.

4. Summary

Initial insights were presented here regarding the information available to plant operators and technical personnel during a severe accident and the interpretation of that information. Insights were also given regarding some

of the preventive and mitigative actions plant personnel might take when confronted with a severe accident and the benefits and concerns associated with these actions.

More detailed insights will be developed under the NRC sponsored accident management program now under way as part of an integrated approach to severe accident resolution.

5. References

1. "Assessment of Severe Accident Prevention and Mitigation Features," NUREG/CR-4920, Volumes 1 through 5, Brookhaven National Laboratory, July 1988.

2. "Severe Accident Insights Report," NUREG/CR-5132, Brookhaven National Laboratory, April 1988.

REVAPORIZATION OF DEPOSITED RADIONUCLIDES AND THE THERMAL DECOMPOSITION OF CESIUM IODIDE

R. M. Elrick
D. A. Powers

ABSTRACT:

Uncertainty analyses of the potential revaporization of radionuclides in the reactor coolant system are presented. These results indicate deposited Cs, I, Te and to some extent Ru and Ba have significant probabilities of revaporizing from the reactor coolant system once the reactor coolant system has been breached and natural convection causes a flow from the reactor containment building through the coolant system. The magnitude of the revaporization depends critically on the chemical form of the deposited material. Experimental studies of CsI transport behavior in high temperature steam indicate CsI may decompose yielding a volatile form of iodine and leaving cesium bound to structural surfaces in a form substantially less volatile than CsI or CsOH. A factorial design test series considering the variables of flow velocity, surface area, cesium iodide-to-steam concentration ratio, and oxygen potential has been conducted to establish the kinetics of cesium iodide decomposition. A model of the kinetic processes is suggested.

THE REVAPORIZATION ISSUE

Modern reactor accident analyses [1] consider the possibility that radionuclides will deposit in the reactor coolant system following release from the reactor fuel during a severe reactor accident. This natural attenuation of radionuclide release is especially effective in accidents involving slow flows through the reactor core as fuel degrades and such accidents are often among the more risk dominant severe accidents hypothesized for a nuclear plant [2]. Predictions of the attenuation indicate that over 90% of the cesium, iodine, and tellurium may be trapped during transport through the reactor coolant system and consequently would not be available for release from the reactor plant.

Deposited radionuclides would continue to radioactively decay and consequently heat themselves and any underlying structures. This

* This work was supported by the U. S. Nuclear Regulatory Commission and performed at Sandia National Laboratories which is operated for the U. S. Department of Energy under Contract Number DE-AC04-76DP00789.

decay heating together with convective heating could be sufficient to produce substantial vapor pressures over the deposited radionuclides. The possibility that deposited radionuclides may not be permanently retained in the reactor coolant system is then raised. Analyses [3-5] have indeed shown that long after reactor core degradation is complete, deposited radionuclides can be revaporizing from the reactor coolant system. This revaporization is especially severe when a natural convection flow develops coming from the containment atmosphere and passing through the reactor coolant system--the so-called "chimney effect". Since the revaporization takes place late in an accident, it is more likely that containment integrity will have been lost and consequently it may be possible for the revaporized radionuclides to escape the plant.

Analyses of revaporization have to date focused on the behaviors of cesium and iodine. These analyses have invoked rather simple chemistry. Cesium is hypothesized to be deposited as CsOH or CsI and iodine is hypothesized to be deposited as CsI. Recent in-pile studies of fission product release from irradiated fuel have shown that the chemistries of these and other radionuclides released from the reactor fuel into the reactor coolant system may not be so simple [6,7]. Cesium deposited in the reactor coolant system may not be present as pure CsOH or CsI. At the very minimum, the deposits will be mixtures. The dilution created by mixing will certainly reduce the vapor pressures of the deposited materials and may alter their abilities to revaporize [8]. Cesium may react to form cesium molybdates, cesium borates, and cesium tellurium compounds with vapor pressures very different than CsOH or CsI.

UNCERTAINTY ANALYSIS OF REVAPORIZATION

Revaporization--even with simple chemistry--is not uniformly addressed by severe accident analysis codes. The complications posed by questions of the chemical forms of deposited radionuclides and flows through the reactor coolant system make revaporization an uncertain issue even for those analyses that do treat the subject.

A major effort to quantitatively evaluate the phenomenological uncertainties in severe accident analysis has been under way for the last two years [2]. Revaporization is one of the phenomenological uncertainties being addressed in this work. As one part of the analysis of revaporization uncertainties, a model of the revaporization process during natural circulation through the reactor coolant system was formulated [9]. Uncertain "parameters" defined in the model included descriptions of the chemistries of deposited radionuclides as well as physical and geometrical properties that affect flow through the reactor coolant system. Uncertainty ranges and probability density functions for the many parameters in the model were defined based on available literature, accident calculations and, only where absolutely necessary, engineering judgement. The revaporization model was then repetitively executed using values of the parameters randomly selected in accordance with the parametric probability densities. Results of the calculations are shown in

Figure 1 as plots of the probability that a greater fraction of the radionuclide in question would revaporize against the fraction of the radionuclide revaporized.

From the uncertainty analyses, it is evident that deposited cesium, iodine, tellurium and to a more limited extent ruthenium and barium can revaporize significantly from the reactor coolant system. The uncertainty in the extent of revaporization arises because of uncertainties in the flow and because of uncertainties in the chemistry of the deposited materials. The revaporization of iodine (assumed to be deposited in mixtures as CsI) is of particular interest because (1) substantial releases of iodine from fuel during core degradation are expected, (2) there is a very high probability of extensive revaporization of deposited iodine, and (3) the radiological consequences of extensive iodine release even late in an accident could be quite large. Experiments were conducted to examine cesium iodide behavior under reactor accident conditions and to address in particular whether there would be cesium iodide present to revaporize.

CESIUM IODIDE DECOMPOSITION

Cesium iodide has, for some time, been expected to be the preferred chemical form adopted by iodine released from reactor fuel [13]. Past analyses have often assumed, for conservative purposes, that iodine would form more volatile species. But, modern accident analyses, especially those done since the accident at Three Mile Island, have been based on the assumption cesium iodide is the chemical form adopted by released iodine and that this chemical form is so stable it endures the hostile environment created during a reactor accident. Elrick and Powers [10], however, have observed that cesium iodide can decompose in steam over stainless steel. The decomposition involved entrapment of the cesium-bearing product on surfaces and the continued transport of a volatile iodine-bearing product of decomposition. Though originally this was thought to be a radiation-induced process and indeed radiation induced decomposition of CsI is known [11], it is now established that the decomposition of cesium iodide observed by Powers and Elrick is a thermal process that proceeds independently of the radiation field. The importance of the decomposition to reactor accident analyses depends then on the kinetics of the decomposition. Rapid decomposition to yield a volatile iodine-bearing product and deposited cesium would mean that there would be little deposited iodine to revaporize late in an accident. There would, of course, be a heavier burden of iodine injected into containment during core degradation, but it is expected natural and engineered mechanisms would attenuate this burden early in an accident.

DECOMPOSITION KINETICS EXPERIMENTS

Experiments to establish the kinetics of cesium iodide decomposition were conducted in the Fission Product Reaction Facility, which has been described extensively elsewhere [12] and is shown schematically in Figure 2. In brief, the facility permits injection

of CsI vapors into flowing steam that passes over stainless steel surfaces along a 75 cm length of 2.5 cm diameter pipe. The steam exiting the reaction pipe is condensed and the ratio of Cs^+ to I^- in the condensate is measured to establish the extent of CsI decomposition. Temperatures along the pipe were constant to +0, -7°C and could be reproduced to ±5°C. Pressure within the system was kept higher (1kPa) than ambient to avoid in-leakage of air. The gas phase was continuously monitored by mass spectrometry to establish the hydrogen-to-steam partial pressure ratio and to detect contaminant gases present in the system.

The tests were factorially arranged with the variables being flow velocity, stainless steel surface area, cesium iodide concentration at input to the system and the hydrogen-to-steam partial pressure ratio as shown in Table 1. Prior to injection of cesium iodide vapors, the system was exposed to steam at the test temperature (1180 K) for three hours to partially oxidize the stainless steel. Steel within a reactor coolant system would be expected to have sustained some oxidation prior to the onset of iodine release in a severe accident. Then, cesium iodide vapors were injected under constant conditions for three hours -- a period sufficient to establish quasi-steady state conditions. Then, the hydrogen-to-steam partial pressure ratio was increased and a new steady state established for three hours. Finally, conditions were returned to those during the initial three hours of cesium iodide exposure to see if the original steady state could be re-established. Condensates collected during the tests were analyzed for cesium ion, iodine ions, and a variety of other species by ion chromatography, and ion selective electrodes. The Cs^+/I^- ratios found for the samples are accurate to ±7%.

RESULTS OF THE TESTS

Typical data from a test are shown in Figure 3. The hydrogen-to-steam ratio decreases with time to a steady state value as the pre-oxidation phase progresses. At about 12:00 clock time a 0.010 cm diameter critical orifice was inserted to control flow. Then a 6 cm^3/min flow of helium was initiated over a crucible of CsI heated to 863 K to inject cesium iodide vapors into the system. At 4:00 clock time additional hydrogen was injected and the hydrogen-to-steam partial pressure ratio rose. The rise was not, however, to the level expected based on simple addition of flows because the additional hydrogen caused some chemical reduction of the oxides on the stainless steel. This reduction consumed hydrogen and produced additional water vapor. This transient condition prevailed for about 1 hour. At 7:00 clock time the original conditions were re-established and at 10:00 clock time the experiment was terminated.

Cesium iodine ratios observed in the condensate samples collected in the various tests are listed in Table 2. The ratios vary from less than 0.05, indicative of nearly complete decomposition, to essentially 1.0, indicative of almost no decomposition, depending on the conditions of the test. It is also apparent that addition of hydrogen leads to generally higher cesium-to-iodine ratios in the condensates.

Even when original conditions are re-established, the cesium ion to iodine ion ratios do not, in general, fall to values observed before introduction of additional hydrogen.

Results of the test could be empirically correlated with the test variables and the coefficients of the correlations subjected to statistical tests to establish the levels of significance. Different, statistically meaningful correlations were obtained for each of the quasi-steady states in the tests. During the first three hour period of exposure to CsI vapors, the cesium ion to iodide ion ratio was correlated by

$$\frac{Cs^+}{I^-} = 0.400 - 0.130A + 0.0915V + 0.119C + 0.0540AC + 0.0350AVC$$

where

A = area of stainless steel exposed to the vapors (cm^2),
V = flow velocity (cm/s), and
C = initial ratio of moles CsI to moles H_2O input to the system.

This correlation reflects the experimental finding that the extent of decomposition increases with the surface area exposed to vapors, and decreases with cesium iodide concentration and flow velocity. When additional hydrogen is introduced, the statistically meaningful correlation is

$$\frac{Cs^+}{I^-} = 0.496 + 0.138V - 0.0409AV + 0.0411AVC$$

That is, flow velocity is the major variable affecting CsI decomposition. When the original conditions are re-established,

$$\frac{Cs^+}{I^-} = 0.418 + 0.171V - 0.0716C - 0.0781VC$$

The disparity between this correlation and that derived from data for the initial exposure of CsI to stainless steel suggests that addition of hydrogen produces changes in the oxidized stainless steel surfaces that are not reversed during the three hours of final exposure to CsI vapors.

Physical Modeling of CsI Decomposition

Physical interpretation of CsI decomposition begins with the recognition that at the elevated temperatures present in the reactor coolant system during an accident and in the tests, cesium iodide reacts with steam:

$$CsI + H_2O = CsOH + HI$$

The extent of this homogeneous gas phase reaction is a strong function of temperature as shown in Figure 4. Were this reaction all that

happened, no net decomposition of importance to reactor accident analysis would be observed since the reaction products (CsOH and HI) would recombine to form CsI as the vapors cool. Vapor phase CsOH is, however, a reactive species [12]. If this cesium hydroxide vapor encounters reactive materials such as aerosols or structural surfaces, it will be trapped and net decomposition will be observed since insufficient cesium will be available to recombine with HI when the vapors cool. In the tests, the reactive surfaces appear to be the oxide films on stainless steel. Tests with pure CsOH vapors [12] have shown that reaction is with SiO_2 from silicon impurities in the stainless steel (typically there is about 0.3-1.0 weight percent Si in stainless steel) to form $Cs_2Si_4O_9$ which has a much lower vapor pressure than CsOH. Limitations on the rate of reaction are 1) gas phase mass transport to the structural surface, 2) gaseous or Knudsen diffusion across the outer, magnetite, oxide layer on stainless steel, and 3) the kinetics of chemical reaction with silica in the inner, spinel oxide layer on stainless steel. A model of these kinetic processes, parameterized with data from the tests, is being formulated [14] and accounts for test observations during the first period of CsI exposure to stainless steel in the tests.

CONCLUSIONS

Revaporization of Cs, I, Te, and possibly Ru and Ba deposited in the reactor coolant system is possible and constitutes a source term not universally recognized in accident analysis. The importance of this source term depends on the chemical forms adopted by the deposited radionuclides. Little information has been developed on the chemical forms of the deposited radionuclides except to show they are more complicated than pure CsOH and pure CsI assumed in accident analyses. Experiments have shown that CsI may decompose in the environment of a reactor accident freeing iodine as a volatile species and leaving cesium retained in a low volatility form. If decomposition is extensive, no iodine will be available in the reactor coolant system for revaporization late in an accident.

REFERENCES

1. M. Silberberg, J. A. Mitchell, R. O Meyer, and C. P. Ryder, Reassessment of the Technical Bases for Estimating Source Terms, NUREG-0956, U.S. Nuclear Regulatory Commission, Washington, DC, July 1986.

2. Office of Nuclear Regulatory Research, Reactor Risk Reference Document, NUREG-1150 Draft for Comment, U.S. Nuclear Regulatory Commission, Washington, DC, February 1987.

3. P. P. Bieniarz and R. E. Deem, "Analysis of a BWR Mk 1 Utilizing Advanced BMI-2104 Computational Techniques to Calculate Source Terms," paper IAEA-SM-281/48 Source Term Evaluation for Accident Conditions, International Atomic Energy Agency, Vienna, Austria, 1986.

4. M. Donahue, M. Hazzan, J. Metcalf and E. Warman, "An Analysis of Retention/Revaporization in a BWR Mark II Power Plant," paper IAEA-SM-281/23, ibid.

5. Industry Degraded Core Rulemaking Project, Peach Bottom Atomic Power Station, IDCOR Task 23.1 Integrated Containment Analysis, Atomic Industrial Forum, Bethesda, MD, 1984.

6. B. J. Schlenger, Characterization of Deposits on Select Coupons from Source Term Experiments Project (STEP) Tests, ANL/RAS/STEP 86-1, Argonne National Laboratory, Argonne, IL, March 1986.

7. J. D. Baker, D. H. Meikrantz and O. D. Simpson, "Fission Product Deposition Behavior," Proc. Symp. Chemical Phenomena Associated with Radioactivity Releases During Severe Nuclear Plant Accidents, NUREG/CP-0078, U.S. Nuclear Regulatory Commission, Washington, DC, June 1987.

8. D. A. Powers and P. P. Bieniarz, "Influence of Chemical Form on Cesium Revaporization from the Reactor Coolant System," ibid.

9. D. A. Powers and R. C. Schmidt, "Analysis of Revaporization of Deposited Radionuclides - An Uncertainty Analysis for NUREG-1150," in press.

10. R. M. Elrick and D. A. Powers, "Effects of Ionizing Radiation on the Transport Chemistry of Cesium Iodide," Proc. Specialists' Workshop on Iodine Chemistry in Reactor Safety, AERE R 11974, Harwell Laboratory, Oxfordshire, United Kingdom January 1986.

11. M. Yamawaki, T. Yoneoka, H. Kaneko, and K. Konashi, J. Nucl. Materials 154 (1988) 47.

12. R. M. Elrick, R. A. Sallach, A. L. Ouellette, S. C. Douglas, Reactions Between Some Cesium-Iodine Compounds and the Reactor Materials 304 Stainless Steel, Inconel 600 and Silver: Volume I Cesium Hydroxide Reactions, NUREG/CR-3197/1 of 3, SAND83-0395, Sandia National Laboratories, Albuquerque, NM, June 1984.

13. U.S.N.R.C., Reactor Safety Study - An Assessment of Accident Risks in U.S. Commercial Nuclear Power Plants, WASH-1400, NUREG-75/014, Washington, DC, October 1975.

14. D. A. Powers and R. M. Elrick, A Model of CsI Decomposition, in preparation.

Table 1
Conditions of the Tests

Test #	Surface Area (cm^2)	Velocity (cm/s)	CsI/H_2O (molar)	H_2/H_2O (molar)
64	610	1.3	1×10^{-5}	0.12/5.7/2.6*
61	4830	1.3	1.5×10^{-5}	0.62/1.9/1.6
74	610	14.1	0.7×10^{-5}	0.024/0.85/0.013
62	4830	14.1	0.8×10^{-5}	0.042/0.59/0.01
69	610	1.3	1.4×10^{-4}	0.2/9.3/--
67	4830	1.3	1.6×10^{-4}	0.50/3.0/2.0
63	610	14.1	0.6×10^{-4}	0.013/0.65/0.013
71	4830	14.1	0.7×10^{-4}	0.10/0.77/0.053
72	2720	6.2	2.2×10^{-5}	0.20/0.17/0.067
73	2720	7.4	2.1×10^{-5}	0.10/1.3/0.024

* Initial Exposure Period/Increased Hydrogen/Initial Conditions Re-Established

Table 2
Test Results

Test	Cs^+/I^- Ratio: Initial Exposure Period	Increased Hydrogen	Initial Conditions Re-established
64	0.352	0.303	0.196
61	<0.04	0.477	0.406
74	0.577	0.741	0.735
62	0.144	0.587	0.623
69	0.527	0.339	--
67	0.302	0.310	0.289
63	0.661	0.618	0.555
71	0.581	0.590	0.445
72	0.466	0.582	0.343
73	0.426	0.770	0.450

Figure 1. Uncertainty Range for Revaporization of Deposited Radionuclides [9]

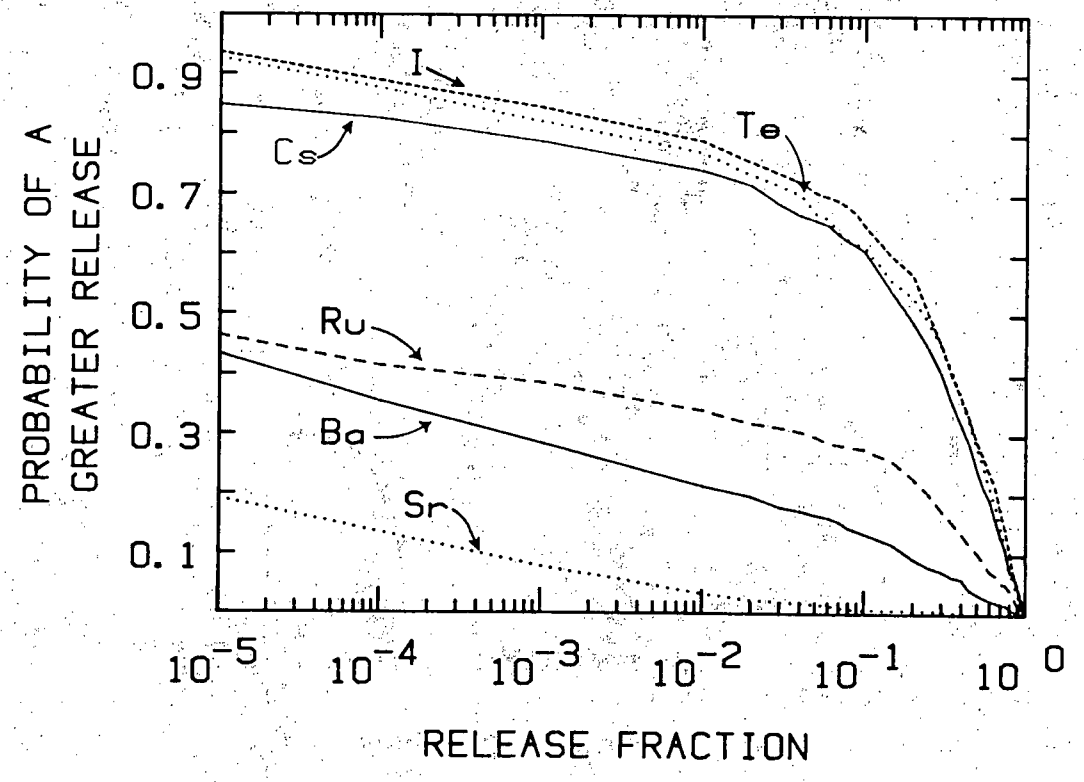


Figure 2. Schematic Diagram of the Fission Product Reaction Facility

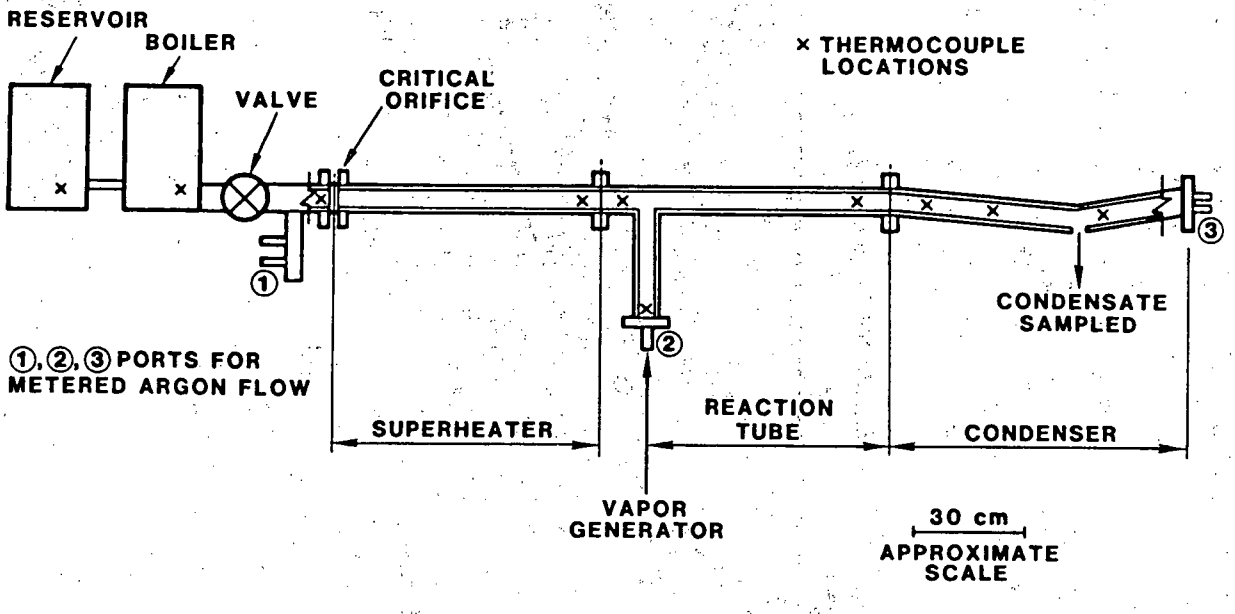


Figure 3. Time Line for Result of Test 61 Showing Condensate Rate (bar), Hydrogen Generation Rate (Curve) and Hydrogen Added (dashed line)

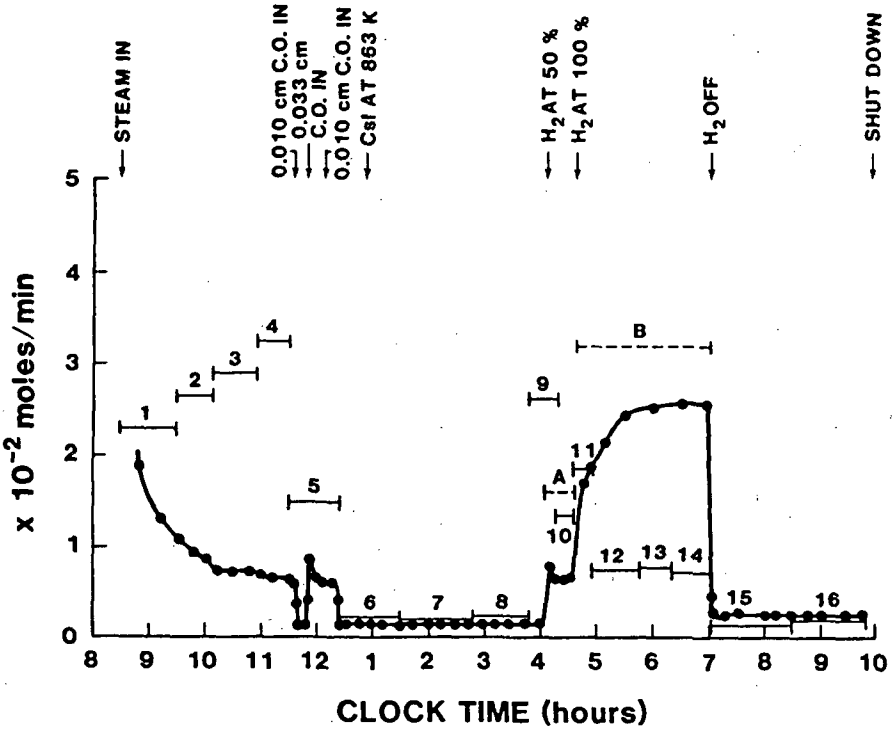
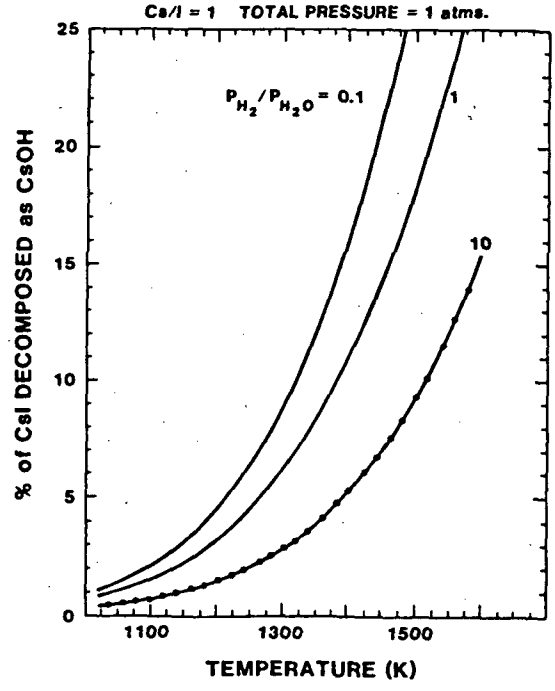


Figure 4. Speciation of CsI in Steam as a Function of Temperature



SAND88-2977C

High-Pressure Melt Ejection and Direct Containment Heating Research *

William W. Tarbell, Marty Pilch, Kenneth E. Washington, John E. Brockmann
Sandia National Laboratories
Albuquerque, NM

T. Ginsberg and N. K. Tutu
Brookhaven National Laboratory
Upton, NY

ABSTRACT

Reactor accidents that involve localized failure of the lower head of the pressure vessel while the primary system is at elevated pressure may result in debris dispersal from the cavity region and direct heating of the containment atmosphere. Results from calculations suggest that the pressure level achieved in some accidents could exceed the strength of the reactor containment. Programs are underway at Sandia National Laboratories and Brookhaven National Laboratory to investigate the phenomena associated with direct containment heating and to develop predictive tools to reduce the uncertainty involved with these accidents. Results are discussed from current experimental programs that involve the use of low-temperature core debris simulants to study the character of debris dispersal from scale models of reactor cavities. Descriptions are given of phenomelogical models that are being created to describe the observed behavior. Calculations of recent tests in the Surtsey facility with system-level codes are discussed.

Brookhaven National Laboratory

Debris dispersal experiments were performed with the objective of determining the maximum permissible primary system pressure at vessel failure ("low-pressure cutoff for debris dispersal") that yields negligible dispersal of core melt from the Surry reactor cavity.

A series of debris dispersal experiments using a 1/42-scale model of the Surry cavity without internal structure were performed in the apparatus shown schematically in Figure 1. The parameters that were varied were: (a) the melt simulant (water, molten Wood's metal), (b) the driver gas, and (c) the size of the hole through which the melt simulant and the driver gas are discharged into the cavity model. To begin an experiment, a volumetrically scaled quantity of the melt simulant is placed in the melt holder (MH) and the pressure vessels are charged with the simulant gas to the appropriate pressure. The experiment is initiated by opening a ball valve (BV) that results in the rupture of a thin foil diaphragm at the bottom of the melt

* This work was supported by the U.S. Nuclear Regulatory Commission and performed at Sandia National Laboratories which is operated for the U.S. Department of Energy under Contract Number DE-AC04-76DP00789.

holder. Thus, a known mass of melt simulant is injected into the cavity model from an orifice above the cavity floor. This is followed immediately by the blowdown gas from the pressure vessels. At the end of the experiment, the fraction of melt simulant mass trapped within the cavity, f, is measured.

The experimental data suggested that the fraction of melt trapped is a function of the Kutateladze number (based upon the area averaged gas velocity), the hole size, d_o, and the density of the driver gas, ρ_g. As an initial attempt to correlate the experimental data, the data were plotted against a combination of three dimensionless groups.

Figure 2 shows the experimental data plotted against the quantity:

$$G = N_5(L/d_o)^2\sqrt{(\rho_g/\rho_L)}$$

Where the group N_5 is defined as:

$$N_5 = (\text{Kutateladze Number})^2 = \rho_g u_g^2/(\rho_L g\sigma)^{0.5}$$

where ρ_L is the density of the melt simulant, u_g is the reference value of the gas velocity within the cavity, g is the acceleration due to gravity, σ is the surface tension of the melt simulant, and L is the length scale of the cavity.

The threshold for debris dispersal from the reactor cavity is approached as the quantity f approaches unity. It is noted that the quantity G correlates the data reasonably well in the range of the dispersal threshold, i.e., $G < 10$.

Based upon these results, we select the following preliminary criterion for the low-pressure cutoff for debris dispersal from the Surry cavity:

$$G = N_5 \left(\frac{L}{d_o}\right)^2 \left(\frac{\rho_g}{\rho_L}\right)^{0.5} = 7 \qquad \text{Eq. 1}$$

This low-pressure cutoff criteria has been used to obtain estimates of the low-pressure cutoff for the full-scale Surry cavity for various assumed hole sizes in the reactor pressure vessel (RPV).

Equation (1) is used to estimate the value of the primary system pressure P_o, below which negligible melt dispersal from the full-scale Surry cavity will take place. Assuming the hole size, d_o, and the steam temperature in the cavity, Equation (1) is used to calculate N_5. Then, the definition of N_5 is used together with the equation for the cavity gas velocity to calculate the low-pressure cutoff for P_o. Table 1 lists the estimates of low-pressure cutoff for various values of vessel hole sizes and two assumed values of steam temperature within the cavity. The first case assumes that due to efficient melt-steam heat transfer, the steam temperature within the cavity is equal to

the melt temperature. In the other case, it is assumed that the steam-melt heat transfer within the cavity is poor, and therefore a value of 500 K for the steam temperature is used. To obtain these low-pressure cutoff estimates, the value of the surface tension of molten core material was assumed to be 0.5 N/m.

The above criterion and procedure for estimation of the low-pressure cutoff should be viewed as preliminary. Modeling of reactor cavity dispersal phenomena is underway, directed towards prediction of the low-pressure cutoff. The experiments described above are now being performed with internal cavity structure in place. A model of the internal structure was fabricated using drawings obtained from Stone and Webster. Water experiments have been completed. Wood's metal experiments are currently being performed.

Table 1. Estimates of Low-Pressure Cutoff for Debris Dispersal for the Full-Scale Surry Cavity Without Internal Structure

Steam Temperature = 2533 K		Steam Temperature = 500 K	
Diameter of Hole in Reactor Pressure Vessel (m)	Low-Pressure Cutoff, P'_o (MPa)	Diameter of Hole in Reactor Pressure Vessel (m)	Low-Pressure Cutoff, P'_o (MPa)
0.1	5.88	0.1	8.33
0.2	3.12	0.2	4.54
0.4	1.61	0.4	2.38
0.5	1.30	0.5	1.92
1.0	0.66	1.0	0.98

For full-scale Surry cavity, $L = 4.14$ m, $A_R = 12.62$ m^2

Sandia National Laboratories

I. Low-Pressure Debris Dispersal Experiments

Studies in the areas of HPME (High Pressure Melt Ejection) and DCH (Direct Containment Heating) have traditionally assumed the primary system pressure to be above the accumulator set point (~4 MPa).[1,2] At this pressure debris dispersal from some cavity configurations may be virtually assured.[3,4] For this reason, research has been concentrated on DCH phenomena and less on questions concerning debris ejection from the cavity. There are at least two accident scenarios, however, in which debris may be ejected from the RPV under low pressure conditions. In the first case, the primary system is at low

pressure prior to instrument tube expulsion because of a failure in another location of the system. Secondly, intentional depressurization of the primary system may be employed as an option for accident management, to avoid the possible consequences of DCH. Thus, interest has developed in the important aspects of low-pressure driven debris dispersal: the fraction of debris dispersed from the cavity as a function of driving pressure, the quality or character of the dispersal (sheets, films, or is highly fragmented particles), and the extent of hydrogen generation in the cavity during the ejection process.

Current analytical approaches for debris dispersal from the cavity rely on empirical correlations for entrainment and very simple gas flow patterns within the cavity. The work reported here is directed towards performing dimensionally scaled experiments that will develop a data base for refined scaling analyses. Extrapolations to reactor scale will be done using a mechanistic model of gas flow and debris entrainment. Such models will also be employed to correlate data from experiments at different length scales.

The test matrix has been developed to study debris dispersal from either the Zion or Surry reactor cavity at low primary system pressures. The objective is to vary key parameters to assess the effect on the physical processes of dispersal. The commonly quoted criteria for debris dispersal from a reactor cavity is the Kutateladze number, Ku.[1] The critical Kutateladze number corresponds to the threshold at which films or particles can be levitated from the cavity by the flowing gas. This dimensionless grouping is defined as (note that this representation is the square of that given in the first section above):

$$Ku = \frac{\rho_g V_g^2}{(g\ \sigma\ \rho_L)^{0.5}} \geq 9 \qquad \text{Eq. 2}$$

where,

ρ_g = Density of the gas, (kg/m^3),
V_g = Velocity of the gas,(m/s),
g = Acceleration due to gravity, (m/s^2)
σ = Liquid surface tension (N/m) and
ρ_L = Density of the liquid, (kg/m^3).

As formulated, Ku does not provide the rate of entrainment or the size of the entrained drops. In order to be useful for accident predictions, a mechanistic entrainment model must be developed to encompass variations in the condition of the primary system, RPV, cavity geometry, and the core debris at the time of HPME.

Typically, the value of V_g is determined from the blowdown of the pressure vessel assuming fully developed, isentropic flow out of the pressure vessel and into the cavity tunnel cross section. The local value of V_g in the

region where melt resides is expected to vary widely depending on the cavity geometry, the location within the cavity, and whether there are structures in the cavity to alter flow patterns. Because the dominant dispersal effect is the gas flowing in the cavity, values for the variables in the numerator ($\rho_g V_g^2$) of Equation 2 are varied in the matrix. This is done by using different driving gases (compressed air and helium) and by varying system pressure (0 to 3.5 MPa). Testing is also done with two different orifice sizes, both with and without cavity structures present.

The apparatus is dimensionally scaled based on a 1:10 reduction of the Zion or Surry reactor cavity.[5] The volume of the pressure vessel used (0.25 m^3) is an approximate 1:10 linear reduction of the Zion primary system (340 m^3). A melt simulant container and ball valve are installed within the pressure vessel to allow simulating the discharge of melt out of the RPV, ahead of the blowdown gas. The apparatus is shown in Figure 3.

The 1:10 linear scale model cavities are constructed of concrete placed in the proper geometric configuration and encased in a steel shell. The top of the tunnel region and exit chute form a weldment that is removable from the bottom portion to facilitate instrumenting and cleaning. Figure 4 shows an exploded view of the Zion cavity with internal structures. The lower portion of the cavity forms a keyway whose width tapers from the circular portion to the exit end, forming a decreasing-area duct.

The structures within the cavity are represented by models of the instrument tubes leading from the RPV to cavity exit, and their supports. The model uses forty-four 12-gauge wires that are 1:10 linear scale reductions of the external dimensions of the actual instrument tubes. The Zion plant actually has 56 instrument tubes, but the lesser number is used to account for the tubes lost with the formation of the aperture in the RPV. The instrument tubes are bolted to the pressure vessel in a roughly square pattern by means of a 6 cm thick steel plate. From the plate, the tubes are arranged in a vertically-downward direction to two support racks located on the floor of the cavity. The tubes are oriented in four horizontal planes proceeding to the exit via a ladder support located at the inclined portion of the tunnel.

Gas flow mapping testing of the Zion cavity uses driving gases at pressures of 0.52, 1.03, and 2.06 MPa. Measurements are taken with three Pitot-static tubes installed to measure differential pressure at three elevations within the cavity: 0.038 m, 0.165 m, and 0.267 m. The Pitot tube sensing tips are in a single vertical plane in the horizontal tunnel region, approximately 0.44 m from the center of the RPV simulator. The devices are aligned parallel to the longitudinal axis of the cavity with one tube in the center and other two placed on either side 5 cm from the walls. Three separate tests are needed to acquire data from each of the nine measurement locations within the cavity.

The tests are conducted by pressurizing the vessel to a predetermined value with the appropriate driving gas. The ball valve is then actuated and the gas escapes through the aperture into the cavity below. The valve opening time (<40 ms) is considered short relative to the blowdown interval (~1.5-2.0 s). The dynamic pressure sensed by the probes is measured by sensitive

differential pressure gauges whose output is recorded by a fast response data acquisition system.

The water dispersal experiments are performed in a similar fashion to the flow mapping tests except that a prescribed volume of water is initially placed in the reservoir prior to the opening of the valve mechanism. Water masses of 7, 14, and 16 kg are used in the tests. Based on volume scaling, these represent 44%, 88%, and 100%, respectively, of the total predicted melt volume for accidents at the Zion plant. The majority of the tests use 14 kg.

The water is introduced into the reservoir through an opening in the top flange cover and the vessel is then charged to the test pressure using the proper driving gas. Tests requiring helium as the driving gas are conducted by first evacuating the vessel to approximately 0.027 MPa, before pressurization begins.

Following ejection and blowdown, the water remaining in the cavity is recovered using a small suction pump and is weighed with an accurate scale. This value is then used to plot the fraction of water dispersed as a function of driving pressure. It is estimated the error in reading the mass of water recovered is ±0.5 kg. This corresponds to a 3.5% error in the 14-kg tests. Errors incurred in making pressure measurements are estimated to be ±5% of the recorded value (manufacturer's specifications).

The results from the Pitot tube measurements are very transient but can be related to Ku by assuming incompressible flow and utilizing the Pitot-tube formula:

$$V_g = \left[\frac{2\,(p_o - p_s)}{\rho_g} \right]^{0.5} \qquad \text{Eq. 3}$$

where:

V_g = Gas Velocity, (m/s),
p_o = Stagnation pressure, (Pa),
p_s = Static pressure, (Pa), and
ρ_g = Gas density, (kg/m^3).

Because the Pitot-tube positioning is critical to the accuracy of the data and because the flow is transient through the cavity, the results are interpreted primarily on a qualitative basis. Typical plots of pressure as a function of time for three vertical positions are shown in Figure 5. Positive pressure indicates gas flow from the RPV towards the cavity exit, while negative pressure is produced by recirculating gas flow. Comparing the plots, there is a strong positive flow along the floor of the cavity while the middle and upper probes indicate weaker recirculation of the gas. This suggests that the gas along the floor of the tunnel that is responsible for entrainment of

the debris is at a much higher velocity than would be predicted using an area-averaged pressure from the blowdown of the pressure vessel. Thus, entrainment calculations based on average gas velocity may underpredict the extent of dispersal.

A representation of the cross section of the cavity showing the peak velocities obtained from the dynamic pressures records is shown in Figure 6. These velocities are calculated from the differential pressure values recorded in the cavity for an initial driving pressure of 2.07 MPa in the RPV simulator. Values marked with a plus sign (+) indicate flow toward the cavity exit while minus signs (-) indicate recirculation flow toward the RPV simulator. The highest velocity in the recirculation pattern on the top row occurs in the center of the cavity cross section while weaker flow takes place along the outside walls. The recirculation velocities of the middle level are the same value across the tunnel width. For the gas flowing toward the exit along the floor the highest velocities occur along the cavity walls, while the lower value is recorded in the center.

The influence of the Zion cavity structures on the gas flow patterns is illustrated in Figure 7. The recorded differential pressure, with and without structures, is shown for the same initial conditions and at the same location within the cavity. The peak dynamic pressure without cavity structures is slightly higher and occurs later in time than the corresponding plot with structures. The area under the curve is about 20% higher in the test without the structures. The implication of the comparison of these two pressure plots and those from the other locations is that the structures have a detectable, but not significant, influence on the gas flow through the tunnel region of the cavity.

The debris dispersal experiments are all performed to develop the full response of the cavity, i.e. to establish both the lower and upper thresholds for dispersed fraction. Figure 8 shows the dispersed fraction of debris (based on the initial mass of water within the reservoir) as a function of the initial pressure in the vessel. The figure compares the results from the Zion and Surry cavities under nearly identical conditions of gas volume, gas density, orifice size, and water mass. As seen, the response of the two cavity types is nearly identical despite the fact that the Surry geometry would appear to inhibit the discharge of material.

Several aspects of the debris dispersal results are interesting. First, the lower threshold for the onset of dispersal is at a very modest pressure (~0.5 MPa). Although direct application of these results to full scale is not recommended, the cutoff for debris dispersal may be much lower than expected. Second, the data points change dramatically with increasing pressure over the range of interest. Only a slight increase in the driving pressure can result in a large increase in the extent of debris dispersed. Third, virtually all of the material is removed from the Zion cavity at pressures above 1.0 MPa. The Surry cavity shows a similar trend except that the maximum dispersed fraction is slightly lower (0.9), because of the apparent retention of material between the vessel support skirt and cavity wall and also that trapped beneath the steel plate used to simulate the steel liner of the cavity. Although not shown in this figure, the results of the tests also

indicate that the initial mass of the water (over the range of 7-16 kg) has no influence on the results.

The third curve in Figure 8 is the results from the Surry cavity where the diameter of the discharge aperture was changed from 3.8 cm to 2.5 cm. The fraction dispersed as a function of pressure behavior for this configuration is seen shifted to slightly higher pressure for the onset of dispersal, with a wider range in pressure to the the upper threshold. The shift in the threshold value is caused by the requirement to use a higher driving pressure to achieve the equivalent mass flow into the cavity.

Figure 9 shows a comparison of the debris dispersal results with and without cavity structures present. As expected from the flow mapping results, the lower threshold for dispersal is not greatly different for the two cases. The estimated slope of the results, however, is somewhat less steep for the cavity with structures causing the upper threshold to occur at approximately 1 MPa higher pressure. This suggests that the structures affect the overall behavior in a somewhat similar manner as the use of a smaller discharge orifice. It is not obvious from the flow map at higher pressure that the observed behavior is the result of a change in the flow pattern. The reduced fraction may be caused by trapping of the liquid drops within the tube structures at the higher gas flow velocities.

II. Phenomelogical Modeling

Construction of codes to predict the consequences of severe accidents involving core debris dispersal is complicated by in-vessel processes such as core melting and slumping, debris bed formation, and failure of the primary system boundary; and by containment phenomena such as radiation heat transfer, aerosol behavior, and hydrogen combustion. Consequently, the models developed to describe HPME and DCH phenomena are by themselves inadequate to describe the reactor accident sequences. The models must be incorporated into larger system-level codes like MELPROG[6] and CONTAIN[7] which include detailed descriptions of these important phenomena. Because CONTAIN is a "lumped parameter" code it does not lend itself well to the implementation of detailed mechanistic models. Consequently, a two-field hydrodynamics code, KIVA,[8] is being modified and used for the purpose of experiment analysis and model development. Developments in the understanding of the direct heating derived from KIVA of direct heating tests are used to improved the parametric models in CONTAIN. Recent advances in these two codes are described Section III.

Phenomelogical model development is currently concentrated in four areas:

1. Improve understanding of the in-vessel processes that lead to HPME such as thermal attack of the lower RPV head, instrument tube failure, and aperture ablation.

2. Modeling of the in-cavity phenomena: debris entrainment, hydrogen generation, and the effect of pre-existing water.

3. Debris behavior and energy transfer in the containment. This involves debris-structure interactions, heat and mass transfer from the debris to the atmosphere and structure, the influence of water in the atmosphere, and the generation and combustion of hydrogen.

4. Aerosol generation and behavior and the release of radionuclides from the core material.

Present accident predictions indicate that in order for direct heating of the containment to occur, a small aperture must form in the lower head of the RPV while the primary system is pressurized. If the opening remains small, the gas mass flux into the cavity will be too low to cause large entrainment of the molten debris. Conversely, too large an opening (i.e. nearly the full diameter of the RPV) may also limit the dispersal because the duration of the blowdown interval is short. It is not known if the current model can be extended to this extreme, but experimental confirmation is required to reduce the uncertainty in the calculations. Current emphasis is on refining the model used to predict the ablation of the head after an instrument tube has failed and been ejected from the vessel. The improvement will also consider the influence on the ablation rate if a refractory crust is on the lower head that may inhibit the steel erosion. Investigation is underway towards understanding the mechanisms involved in the attack and failure of the instrument tube penetrations in the lower head.

All present debris dispersal models use area-averaged gas flow velocity to predict entrainment from the cavity. As seen in the low-pressure debris dispersal experiments, the actual gas flow is much higher near the floor of the cavity than would be obtained from such a simple approach. Most entrainment correlations are derived from annular two-phase flow experiments. The present development is concentrating on methods to calculate the gas flow patterns within the cavity during the blowdown of the primary system. Having a more accurate estimate of the gas velocities in the cavity will permit more certain predictive ability. In addition, the entrainment rate model is being developed from the governing equation for the mass flux of particles out of the cavity. The model is being applied against the water dispersal test results to aid in the development. Extending the model to reactor scale will also be inherently more accurate because the functional dependency of the variables will be established.

Having an accurate model of the debris entrainment rate in the cavity will permit calculating the rate at which the steam blowdown gas reacts with the metallic debris. In addition to the size and number of the particles, the model will consider local depletion of the oxidant and the rate at which the oxygen diffuses into the molten drop. Experiments are planned for the near future to incorporate a steam-driven melt into the scale model of the Surry cavity. By collecting the debris and gas from the cavity in the Surtsey test chamber, the extent of debris oxidation and hydrogen generation can be measured. These data will provide the basis for verifying the accuracy of the models. The high-temperature melt in this test will be generated from the metallothermitic reaction of iron oxide and aluminum powders to form 55-w/o iron and 45-w/o alumina.

Most present models of the direct heating process use a single-droplet formulation to predict the energy transfer to the atmosphere.[9] By specifying a mean particle size, the overall energy transfer is computed from the mass dispersed into the atmosphere. The models consider the gas (oxidant) diffusing to the surface of the particle, chemical reactions and heat transfer at the surface, diffusion of the gas into the particle, circulation within the molten drop, and the outward flow of heat and mass. Limits on the energy transfer are normally specified to be on the gas-side or the liquid-side diffusion rates. Recent DCH experiments have indicated a need to consider another rate limiting step to the heat and mass transfer processes. This has been termed the plume effect. Within the plume of debris and gas, the local oxidant may be depleted even though abundant oxidant is available on a more global basis. Debris oxidation could then be limited by the rate at which oxidant diffuses into the plume. The plume effect also hinders the rate at which energy is exchanged with the atmosphere, because the local gas temperature within the plume is high even though global gas temperatures are lower. Heat transfer becomes limited by the surface area of the plume and not by the combined surface area of all the particles. Advances in modeling the plume effect have been incorporated into the KIVA and CONTAIN codes.

The interaction of the debris with containment structures has been shown to play an important part in DCH. Models for debris freezing on steel structures, splashing, and dripping heve been developed to correlate with the observed test results. Structures can also breakup the debris-laden plume to enhance mixing with the atmosphere. Models that predict the behavior of the particles upon encountering obstructions are being studied. Separate effects experiments are planned tc supplement the existing data base in the regime of interest.

The pressurized ejection of core debris may result in a large and rapid ex-vessel production of hydrogen. Because direct heating of the atmosphere may coincide with the propagation of hydrogen into the containment, the combustion of hydrogen in a high-temperature environment becomes important. It is expected that steam inerting is not effective when the atmospheric temperature is above 200°C.[10] Likewise, the concentration limits for detonation begin to approach those for combustion.[10] Although the current data base is limited, the ZND model (Zeldovich-von Neumann-Doering)[11] is being used to investigate the detonability of H_2/steam mixtures at elevated temperatures.

III. CONTAIN-DCH and KIVA-DCH Modeling and Analyses

Containment-levelmodeling and analysis of DCH at Sandia National Laboratories involves the development and application of two separate computational tools: CONTAIN-DCH and KIVA-DCH. While the DCH models in these two codes are similar in many ways, they are considerably different in scope and overall capabilities. CONTAIN-DCH is a tool for predicting containment response of full-scale reactor plants under DCH accident conditions. KIVA-DCH, on the other hand, is much too specialized and detailed for the analysis of full scale containments. KIVA-DCH is primarily intended for the analysis of well-defined DCH events, such as the Surtsey experiments, but at a highly

detailed level. An overview of Sandia's activities in the areas of DCH modeling and analysis with CONTAIN-DCH and KIVA-DCH is presented in the following sections. These sections focus on the DCH-1 and DCH-3 tests, and comparisons are only shown for the DCH-3 experiment.

A. CONTAIN-DCH

Modeling for Direct Containment Heating has been incorporated into the CONTAIN best-estimate, mechanistic severe accident analysis code; the resultant code has been designated CONTAIN-DCH. The primary objective of CONTAIN-DCH is to provide a computational tool for performing best-estimate containment response predictions for full-scale plants subjected to DCH. An important step toward the fulfillment of this objective has been, and continues to be, the validation of the code through the comparison of pretest and posttest calculations against Surtsey experiment results.

CONTAIN-DCH models DCH phenomena following the HPME phase of the accident scenario. That is, the code relies on user input for the characterization of the HPME, including the rate, composition, and temperature of the ejected debris and blowdown gases. Mechanistic, rate-limiting models for heat transfer and chemical reactions are incorporated into CONTAIN-DCH; however, poorly understood phenomena, such as debris-structure interactions, are modeled more parametrically. For example, the model for heat transfer between debris and the atmosphere is based on a Reynolds correlation for flow over a sphere; however, the interaction of debris with containment structures (a phenomenon often called "trapping") is treated non-mechanistically by removing debris from the atmosphere at a user-specified debris trapping rate, $\underline{ftr}$. A gravitational fall time (GFT) criterion ($\underline{ftr}$ = Vt/H, where Vt is the terminal fall velocity, and H is a characteristic cell height) is often used to specify trapping rates in the analysis of both the Surtsey tests and full scale DCH events. Several papers are available in the literature that describe the CONTAIN-DCH models in more detail.[9,12,13]

The CONTAIN-DCH blind pretest pressure prediction for the DCH-1 test is in excellent agreement with the pressure measured in the experiment (see References 9, 12, and 13). This good agreement is particularly significant from a model validation standpoint, because the processes that are modeled mechanistically in CONTAIN-DCH dominate the chamber response in the DCH-1 experiment.

A CONTAIN-DCH pretest prediction for the DCH-3 experiment was performed using the input same input parameters that were used in the DCH-1 calculation, but with increased debris masses. It is emphasized that the GFT criterion was used to specify the debris trapping rate in both calculations. As seen in Figure 10, the CONTAIN-DCH pressure increase predictions are far in excess of the experimental results. Clearly there are some aspects of the scaling with respect to debris mass that are not captured by the model as it is employed. In particular, the GFT criterion does not adequately describe the rapid rate of debris trapping seen in the DCH-3 experiment. Also, the model does not take into account limited availability of local oxygen and thermal shielding within the debris-gas-aerosol cloud.

A posttest DCH-3 CONTAIN-DCH calculation was performed using a time-to-first-impact (TFI) criterion to specify $\underline{ftr}$. The TFI criterion corresponds to a debris residence time equal to the time required for the ejected to debris to reach the upper head of the vessel (based on an assumed ejection velocity of about 70 m/s). As seen in Figure 10, the pressure prediction in the TFI case agrees more closely with the experimental results than the DCH-3 pretest prediction. Note, however, that the two peak behavior recorded in the experiment is not seen in the pressure histories of either of these simulations.

A second DCH-3 posttest calculation was performed using a three-cell CONTAIN-DCH representation of the Surtsey chamber. Cell 1 is a small cell in the center of the chamber that represents the vicinity of the coherent debris jet. Zero trapping was assumed in this cell during the gas blowdown phase, and GFT trapping thereafter. The TFI trapping ($\underline{ftr}$ = 8 s^{-1}) was assumed in Cell 2, because this cell models the region of the vessel just below the upper head. A negative trapping rate was used in Cell 2 after about two seconds to represent, in an ad-hoc manner, drop formation and dripping. As discussed above, this debris re-entrainment through dripping was believed to occur in the experiment. The GFT criterion was applied to the remainder of the chamber, which was represented by the third and final cell. The gauge pressure history prediction using this model is shown in Figure 10, where improved agreement over both one cell predictions is clearly evident. This is, in part, attributed to the simulation of the complex debris-structure interactions seen in the experiment. The debris cloud effect was also captured in this calculation, to some extent, because debris in Cell 1 was not in thermal contact with gas or structures in Cell 2 and Cell 3. It should not be forgotten, however, that the three cell nodalization, and the trapping parameters specified in the calculation were largely based upon knowledge of the experimental results. This calculation is nevertheless important, because it clearly illustrates the need for refined modeling capabilities in CONTAIN-DCH, particularly in the area of debris-structure interactions. This calculation also provides support for the hypothesis of debris re-entrainment by dripping and the debris cloud effect.

B. KIVA-DCH

A number of ongoing DCH phenomenological modeling and experimental efforts are focused on modeling the extent of debris dispersal from reactor cavities following a HPME. The concerns addressed by these efforts are founded primarily on the premise that for DCH to be important, substantial amounts of reactive debris must enter the upper containment regions, where it can interact with the bulk of the containment atmosphere. CONTAIN-DCH analyses have also suggested the importance of the transport of hydrogen produced in lower compartments to upper containment regions. Consequently, realistic treatment of the transport of both debris and gases through the various containment compartments is viewed as an important part of DCH modeling. However, a control-volume code like CONTAIN-DCH cannot address all aspects of these issues, particularly in the regime of momentum dominated transport. Recent emphasis has therefore been on the development and application of KIVA-DCH to these problems.

KIVA-DCH is an adaptation of the KIVA code, capable of representing with considerable resolution the processes of debris and gas transport for certain well-defined DCH events, such as the Surtsey experiments. Gas motion on a multi-dimensional grid is calculated in KIVA-DCH using a finite-difference solution to the Reynolds-averaged Navier-Stokes equations. Realistic models for turbulence and debris-gas drag are also included. These capabilities provide for a more detailed look at such areas as: gas flow, particle transport, debris-structure interactions, and permit a less uncertain estimate of debris-gas interaction. It is important to understand that KIVA-DCH is not a containment response tool; however, it is capable of predicting pressures and temperatures resulting from DCH in the Surtsey experiments. More details about the models in KIVA-DCH are given in Reference 13.

1. KIVA-DCH Experiment Analysis

The DCH-1 experiment provided an excellent opportunity to validate the DCH modeling in KIVA-DCH. Pretest predictions were not possible, because the DCH-1 test was conducted prior to the development of the first version of KIVA-DCH. Pressure predictions were in excellent agreement with the experiment, as shown in Reference 14.

The DCH-3 pretest pressure predictions using KIVA-DCH are compared against the test results in Figure 11. In this calculation debris particles striking a surface are assumed to be removed from the atmosphere with a 5 percent probability. (The same assumption used in the DCH-1 calculation.) As noted above, large amounts of debris were found adhered to the dome following the test, and debris dripping was seen in the film records of the experiment. The 5-percent probability value used in the KIVA-DCH pretest calculation, together with the overall simplicity of the debris-structure interactions model, are believed to be the primary reasons for the severe pressure over prediction shown in Figure 11.

A posttest KIVA-DCH calculation was performed using an enhanced version of the code to more realistically describe the behavior of the debris-structure interactions in the DCH-3 experiment. In this calculation, debris particles striking the upper head are trapped with a 90-percent probability and retained as a film. Dripping from the dome is treated by introducing 2.5 mm diameter debris particles, as measured from the film on the dome, into the atmosphere after a pre-determined time delay (two seconds was chosen based on experimental observations). This calculation leads to improved agreement with the experiment as shown in Figure 11. The two-peak behavior is also reproduced by this calculation. More DCH-3 calculations, and several DCH-4 KIVA-DCH calculations are given in Reference-15.

2. Recent Progress in KIVA-DCH Model Development

The new model for debris/steam chemical reactions has been incorporated into KIVA-DCH code. The version of KIVA-DCH used in the calculations described above included modeling for only debris/oxygen chemical reactions. Steam chemistry modeling is essential if calculations are to be performed for future Surtsey tests. Such calculations will be useful for providing pretest calculational support as well as posttest analysis and CONTAIN-DCH cross validation.

Modifications were also made to the energy accounting scheme in KIVA-DCH. In addition to including the Fe/H_2O chemical energy term in the existing drop temperature evolution equation, enhancements were made that allow for a more rigorous treatment of the thermal coupling between debris and the atmosphere. An energy balance equation is written for the drops in a parcel and its respective hydrodynamic cell (with drop temperature and gas temperature as the end-of-time-step unknown quantities). These equations include terms for O_2 and H_2O chemical reactions, convection heat transfer, and radiation from the particle to the gas. The energy associated with H_2 (produced in the Fe/H_2O reaction) re-combination is also accounted for in the gas energy balance equation. Finally, a new option was added for direct drop-to-structure radiation modeling. If this option is used, an additional energy exchange term will be accounted for in the drop energy balance equation. The two coupled equations are solved simultaneously for each debris parcel to give end-of-time step drop and gas temperatures.

The capability to specify temperature dependent drop diffusivity was also added to KIVA-DCH. A similar model has been available in CONTAIN-DCH for some time; however, its utility in modeling drop-side reaction rate limits has been somewhat limited due to the single-field assumption employed in CONTAIN-DCH to describe debris in a cell. The temperature dependent model should prove more useful for KIVA-DCH, since it tracks debris in multiple packets, each with its own composition and temperature.

Steam-driven calculations for conceptual Surtsey test cases using the new version of KIVA-DCH are currently being performed. Current KIVA-DCH modeling efforts are focused on the development of the code architectural enhancements that are needed for the incorporation of a deterministic debris-structure interactions model. The major code areas requiring modification have been identified, based on recent progress made in the debris-structure interactions area or research (see Reference 16).

Conclusions

The low-temperature simulant fluid tests being performed at Brookhaven National Laboratory show that debris is readily dispersed from the scale model of the Surry cavity. The data near the lower threshold for dispersal are correlated with a dimensionless grouping related to the Kutateladze number of the gas blowdown. Based upon the experimental results, a preliminary criterion for the low-pressure cutoff for debris dispersal from the Surry cavity has been selected. The criterion is used to estimate the values of the primary system pressure below which negligible melt dispersal will occur, given various sizes of the hole in the reactor pressure vessel. If this trend is also true for the full scale geometry, then efforts to use depressurization as a means to avoid the consequences of DCH may be futile unless the primary system can be completely depressurized.

The low-temperature debris dispersal experiments at Sandia National Laboratories show that the Zion and Surry cavities have nearly equivalent dispersed fractions at similar conditions. The results indicate that the lower threshold for dispersal is at relatively modest pressure levels, on the order of 0.5 MPa for both Zion and Surry. The upper bound for dispersal is

greater than 85% for both cavities, with Zion exhibiting slightly higher total dispersal. The pressure range from lower to upper threshold is narrow, approximately 1.0 MPa. Over this range, slight changes in the driving pressure result in large changes in the fraction of material dispersed.

Flow mapping of the Zion cavity shows that the gas velocities during blowdown are highly stratified, with the largest velocities along the floor of the tunnel region. Weak recirculation back towards the pressure vessel was measured from about the mid-height to the ceiling of the tunnel. The introduction of simulated instrument tubes and their support structures into the cavity did not greatly influence the gas flow patterns. This was correlated by the debris dispersal results under similar conditions with the structures and tubes in place, which were not significantly different than without the devices.

Modelling of the debris dispersal phenomena is underway at Sandia. The objective is to mechanistically calculate the gas flow patterns and magnitudes for any given cavity geometry. This is being combined with an entrainment model to predict debris particle size, velocity, and direction of movement. The model also incorporates a droplet/gas interaction model to calculate hydrogen generation and aerosol production in the cavity region. The output of the code will provide the source input for system-level containment response codes such as CONTAIN.

CONTAIN-DCH calculations have been performed and compared to the experimental results of the Surtsey DCH tests. Excellent agreement with the experimental results using both CONTAIN-DCH and KIVA-DCH is shown for the DCH-1 test, verifying that the well understood processes, such as heat transfer and chemical reactions, are adequately modeled. The need for refinements in the area of debris-structure interactions and cloud plume effects was demonstrated by the DCH-3 calculations. Good agreement was only achieved when the complex debris-structure interactions witnessed in the experiment were incorporated into the models and input parameters of the codes. Both the CONTAIN-DCH and KIVA-DCH codes suffer from the lack of more mechanistic models for debris-structure interactions. Current emphasis is being placed on development in this area. Preliminary investigations indicate that the KIVA-DCH code may be more suitable for the implementation of mechanistic debris-structure interactions models. It is hoped that this can be used to facilitate the selection and implementation of an appropriate model for CONTAIN-DCH.

References

1. Zion Probabilistic Safety Study, Commonwealth Edison Co., Chicago, IL, 1981.

2. Indian Point Probabilistic Safety Study, Power Authority of the State of New York, Consolidated Edison Company of New York, Inc., Buffalo, NY, 1982.

3. W. W. Tarbell. et al., Pressurized Melt Ejection Into Scaled Reactor Cavities, NUREG/CR-4512, SAND86-0153, Sandia National Laboratories, Albuquerque, NM 1986.

4. T. Ginsberg and N.K. Tutu, "Recent Experimental and Analytical Results of BNL Direct Containment Heating Programs," Transactions of the Fourteenth Water Reactor Safety Information Meeting, NUREG/CP-0081, Gaithersburg, Maryland, Oct 27-31, 1986,

5. W.W. Tarbell et al., High-Pressure Melt Streaming (HIPS) Program Plan, NUREG/CR-3025, SAND82-2477, Sandia National Laboratories, Albuquerque, NM 1984

6. W. J. Camp, et al., MELPROG-PWR/MOD0: A Mechanistic Code for Analysis of Reactor Core melt Progression and Vessel Attack Under Severe Accident Conditions, NUREG/CR-4909, SAND85-0237, Sandia National Laboratories, Albuquerque, NM, Apr 1987.

7. K. K. Murata, et al., User's Manual for CONTAIN 1.1, A Computer Code for Severe Nuclear Reactor Accident Containment Analysis (Draft), SAND87-2309, Sandia National Laboratories, Albuquerque, NM 1987.

8. A. Amsden, et al., KIVA: A Computer Program for Two- and Three-Dimensional Fluid Flows with Chemical Reactions and Fuel Sprays, LANL Report LA-10245-MS, Los Alamos, NM 1985.

9. K. D. Bergeron, et al., "Development and Applications of the Interim Direct Heating Model for the CONTAIN Computer Code," Transactions of the Fourteenth Water Reactor Safety Information Meeting, NUREG/CP-0081, Gaithersburg, Maryland, Oct 27-31, 1986.

10. R. K. Kumar, "Flammability Limits of Hydrogen-Oxygen-Diluent Mixtures," Journal of Fire Sciences, V3, 1985.

11. J. E. Shepard, "Chemical Kinetics of Hydrogen-Air-Diluent Detonation," Progress in Astronautics and Aeronautics, Vol. 106, 1985.

12. D. C. Williams, et al., "Impact of Chemical Phenomena in Direct Containment Heating," SAND86-2020C, presented to the Americal Chemical Societry Severe Accident Chemistry Symposium, Anaheim, Ca 1986.

14. K. D. Marx, A Model for the Transport and Chemical Reaction of Molten Debris in Direct Containment Heating Experiments, NUREG/CR-5120, SAND88-8213, Sandia National Laboratories, Livermore, CA, 1988.

15. W. W. Tarbell, et al., "Direct Containment Heating and Aerosol Generation During High Pressure Melt Ejection Experiments," SAND88-1504C, presented at the 1988 Winter ANS Conference, Washinton, DC, Oct 1988.

16. L. Baker Jr., "Droplet Structure Interactions in Direct Containment Heating," presented at the 1988 Winter ANS Conference, Washington, DC, Oct 1988.

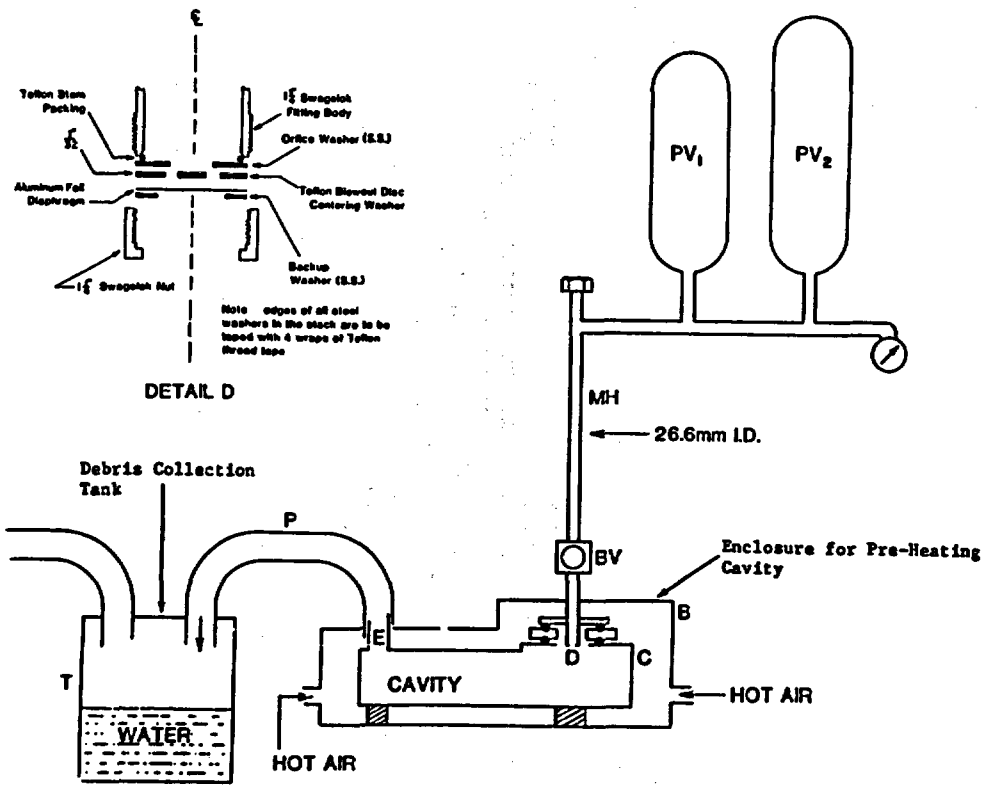


FIGURE 1. SCHEMATIC OF BNL EXPERIMENTAL SETUP (MELT HOLDER, MH, BALL VALVE, BV, AND PRESSURE VESSEL. PV_1 AND PV_2 ARE ALL WRAPPED WITH HEATING TAPES AND INSULATED).

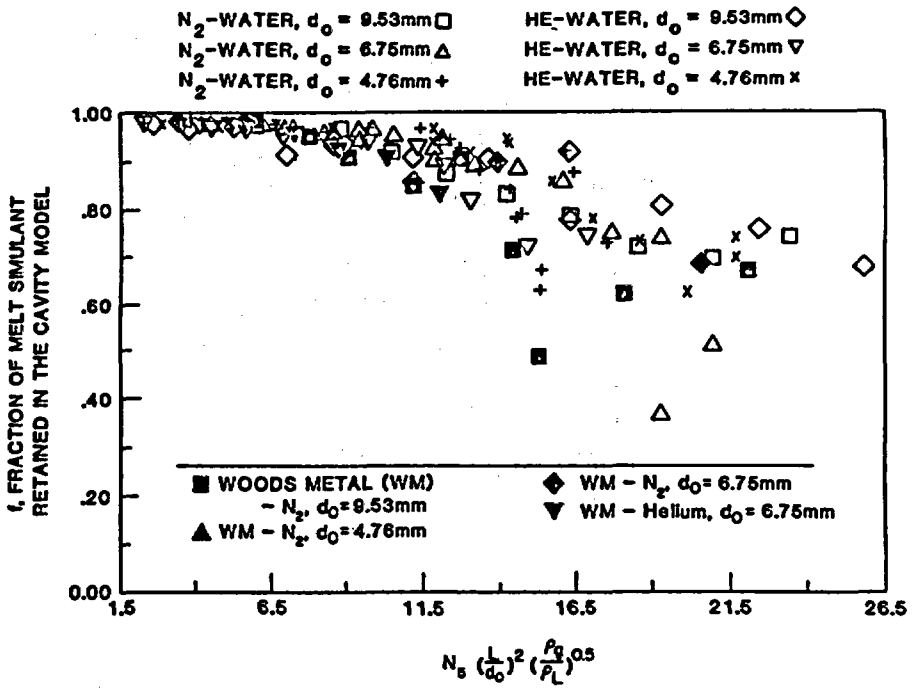


FIGURE 2. CORRELATIONS OF ALL THE BNL DEBRIS DISPERSAL DATA NEAR THE THRESHOLD FOR DEBRIS DISPERSAL. RESULTS FOR SURRY CAVITY MODEL.

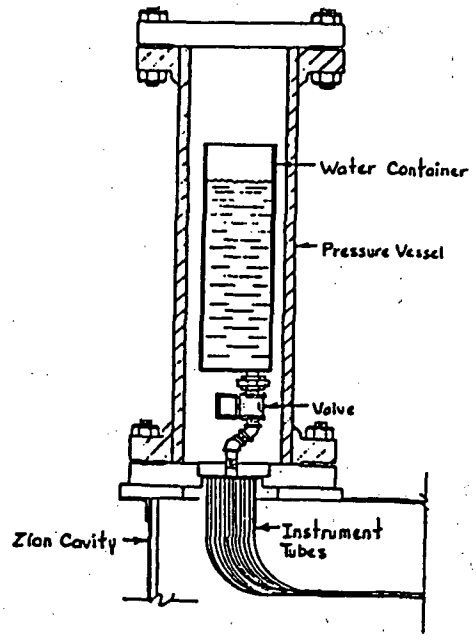


FIGURE 3. SCHEMATIC OF PRESSURE VESSEL AND WATER RESERVES USED IN THE SNL DEBRIS DISPERSAL EXPERIMENTS.

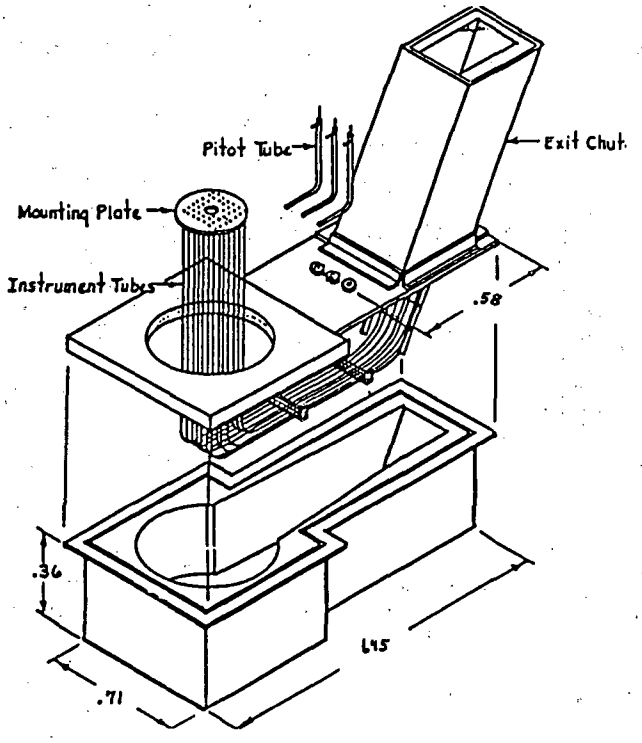


FIGURE 4. EXPLODED SCHEMATIC REPRESENTATION OF SCALE MODEL OF ZION CAVITY. (DIMENSIONS IN METERS)

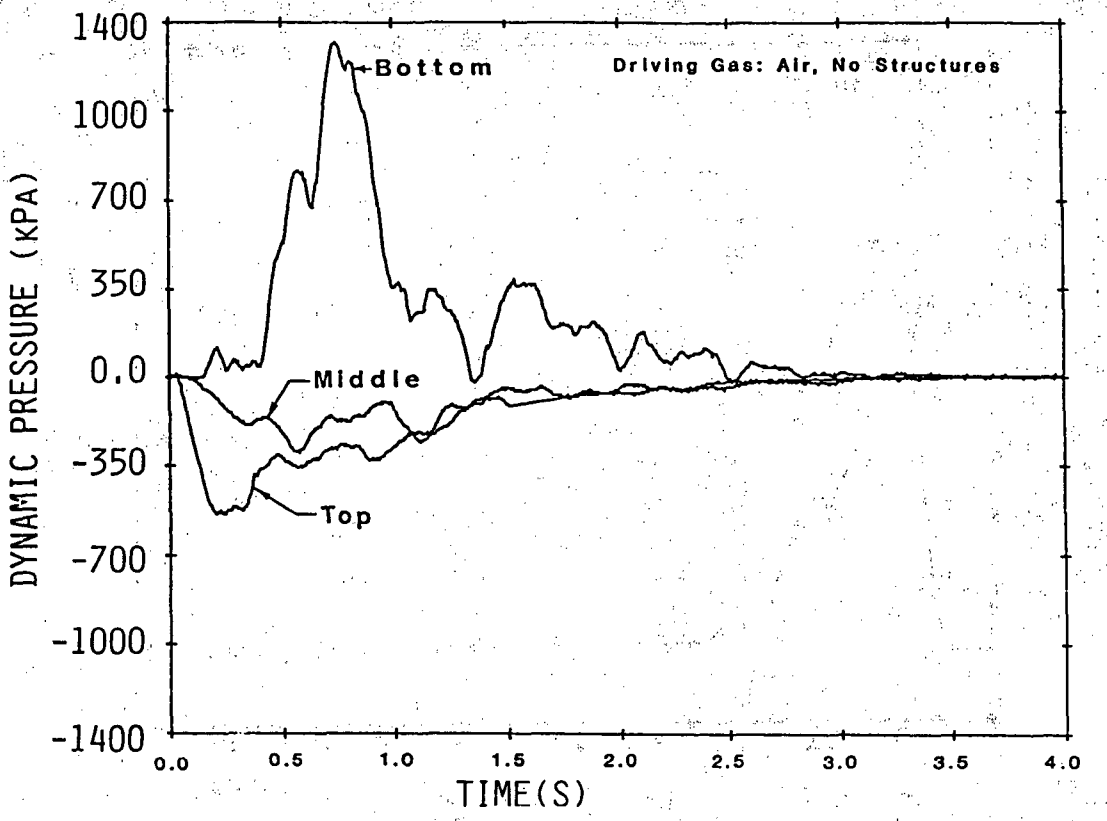
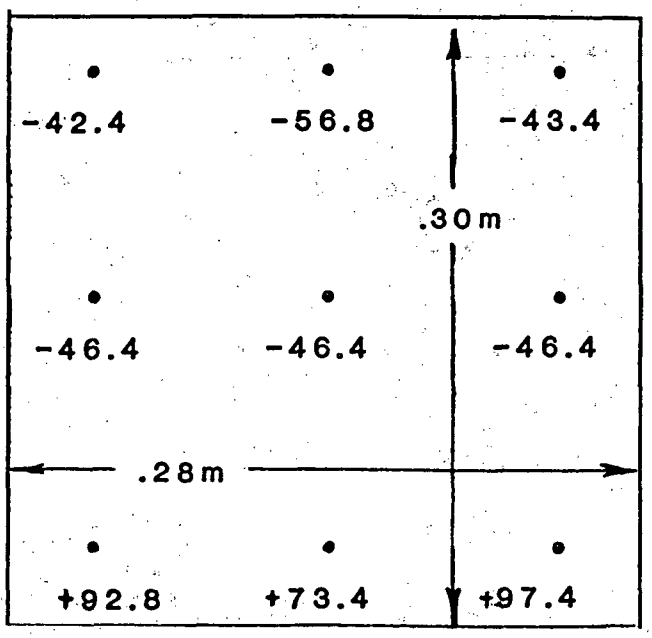


FIGURE 5. DYNAMIC PRESSURE IN THE CAVITY AS A FUNCTION OF TIME FOR THREE PITOT-TUBE POSITIONS IN THE TUNNEL OF THE ZION CAVITY.



(VELOCITY IN M/S)

FIGURE 6. PEAK GAS VELOCITIES FROM PITOT-TUBE MEASUREMENTS IN THE ZION CAVITY (WITHOUT INSTRUMENT TUBES IN-PLACE).

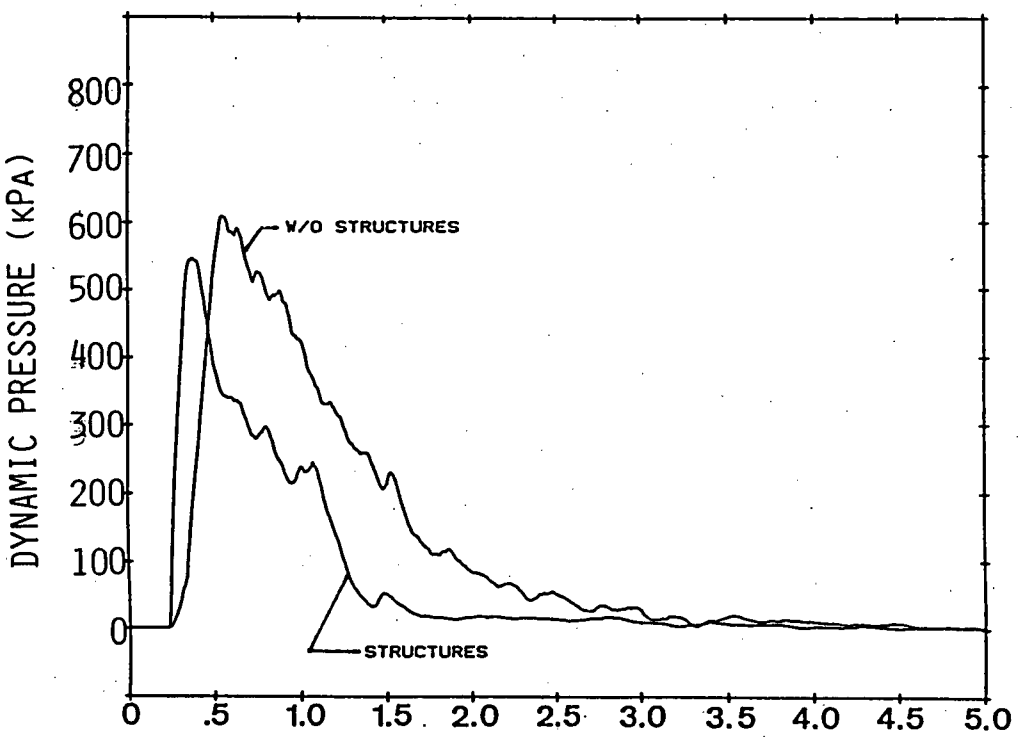


FIGURE 7. COMPARISON OF PITOT-TUBE MEASUREMENTS WITH AND WITHOUT INSTRUMENT TUBE STRUCTURES IN THE ZION CAVITY.

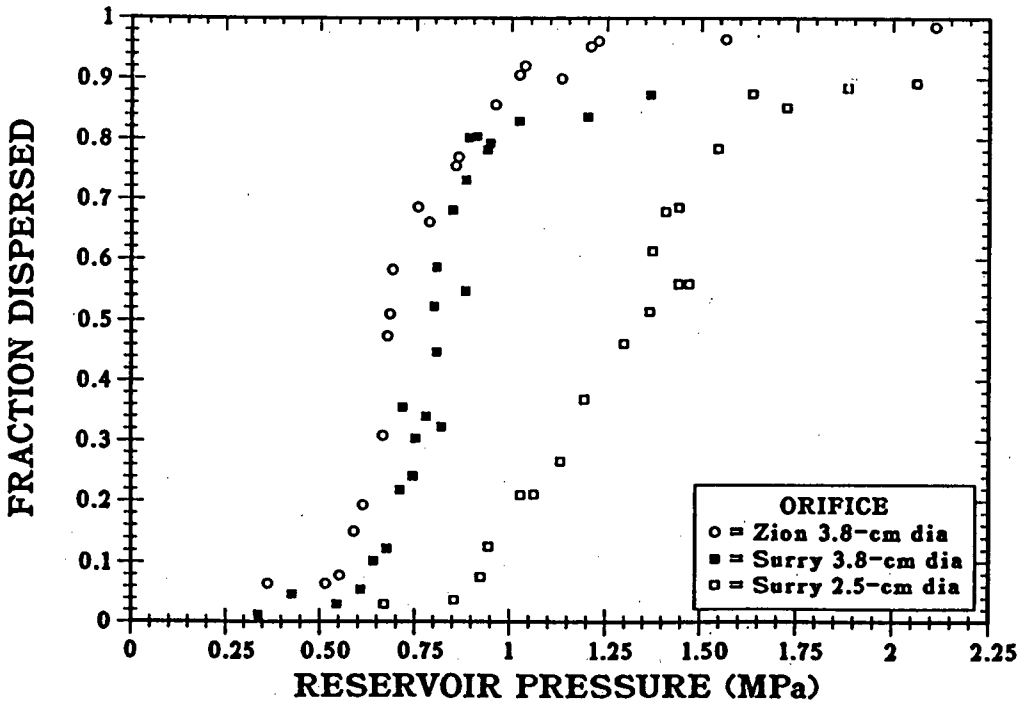


FIGURE 8. DEBRIS DISPERSAL AS A FUNCTION OF DRIVING PRESSURE FOR THE ZION AND SURRY SCALED CAVITIES.

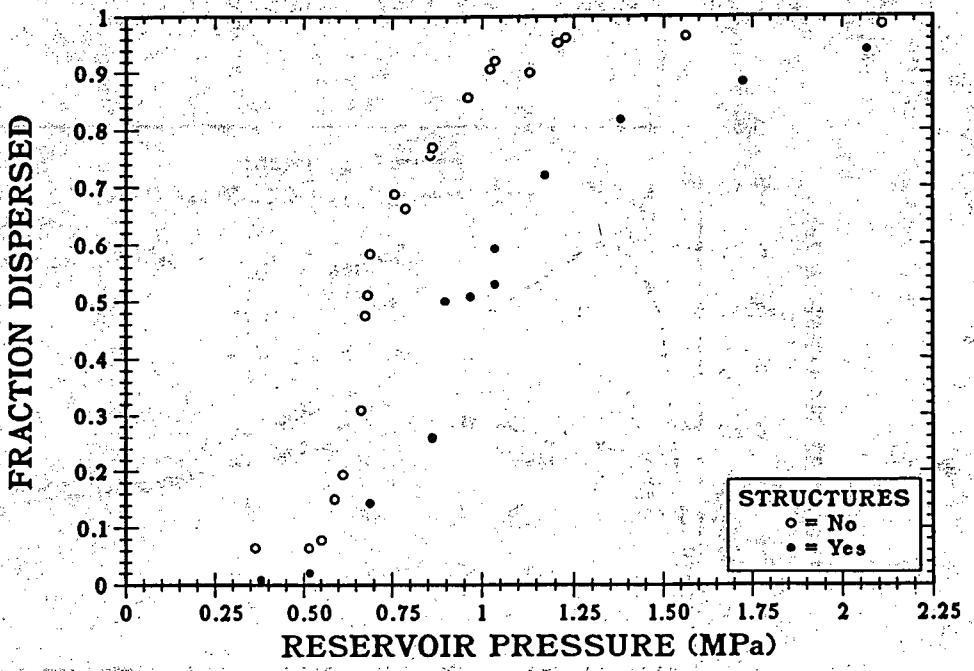


FIGURE 9. DEBRIS DISPERSAL RESULTS FROM THE ZION CAVITY SHOWING THE EFFECT OF INSTRUMENT TUBE STRUCTURES.

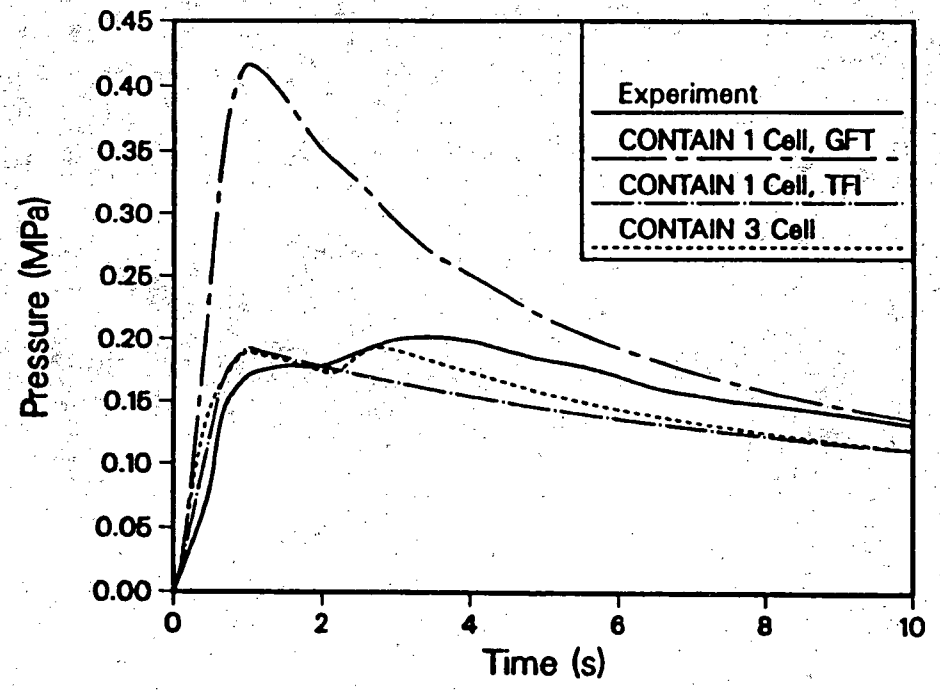


FIGURE 10. COMPARISON OF CONTAIN-DCH CALCULATIONS WITH THE DCH-3 EXPERIMENTAL RESULTS.

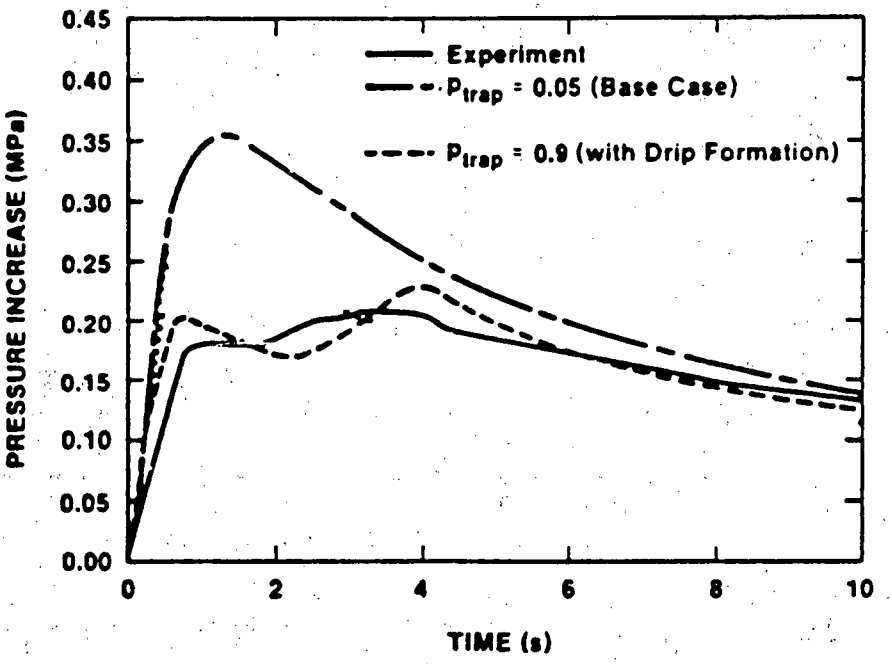


FIGURE 11. COMPARISON OF KIVA-DCH CALCULATIONS WITH THE DCH-3 EXPERIMENTAL RESULTS.

PARTICLE CAPTURE IN AN EXPERIMENTAL ICE CONDENSER AT LOW FLOW RATES

L. D. Kannberg, M. W. Ligotke, B. A. Ross, E. J. Eschbach, and J. M. Bates
Pacific Northwest Laboratory[a]
Richland, Washington 99352

ABSTRACT

Data are reported from engineering-scale tests of particle deposition in a small section of an ice condenser typical of that used in certain pressurized water reactors (PWRs). The data will be used to validate a computer code (ICEDF) that estimates the extent of particle deposition in the ice compartments of PWR ice condenser containment systems. The code was developed to assess the effectiveness of one type of engineered safety feature (ESF). Such assessment is part of a U.S. Nuclear Regulatory Commission effort to reassess and update analytical procedures for estimating accident source terms for nuclear power plants.

The engineering-scale test facility is capable of passing a mixture of steam-air aerosols through a test section containing the equivalent of four full-scale ice basket columns typical of those at PWR plants. Although a range of flow rates from 0.03 to 0.38 m^3/sec is possible at temperatures up to 200°C, early tests have concentrated on flows having low steam content or low bulk flow rates. Aerosols are generated with either dispersion of powders in an energy jet mill or ultrasonic atomization of liquids.

Results of testing conducted to date indicate that aerosol behavior is strongly affected by thermohydraulic conditions in the test facility. A region of strong vertical thermal stratification develops in a diffuser immediately upstream of the test section. Recirculating flow cells are established in the vertical test section as warm gases flow up channels between the ice baskets on one side of the test section and flow down similar flow channels on the other side of the test section. First order analysis indicates that the buoyant forces are on the same order as the inertial forces of the gas flowing into the system for instances when recirculations were observed. The strong thermal stratification was observed in the inlet diffuser regardless of the steam fraction.

A substantial portion of the aerosol particles are often captured in the inlet diffuser and lower turning vanes. It is speculated that this is due to rapid aerosol growth and/or settling. Particles are also retained by the vertical test section when steam and/or ice are present. In contrast, penetration approaches 100% upon

---

(a) Operated for the U.S. Department of Energy by Battelle Memorial Institute under contract DE-AC06-76RLO 1830.

depletion of the ice inventory. Data also indicate that particle growth occurs in the test section under favorable conditions (i.e., condensing environments).

INTRODUCTION

The U.S. Nuclear Regulatory Commission (NRC) is undertaking numerous studies to refine earlier estimates of radioactive emissions from nuclear power plants during severe accidents. This effort to define source terms includes the evaluation of various engineered safety features (ESFs) as a means of reducing the postulated airborne concentrations of radioactive aerosols within a power reactor containment system following a severe reactor core accident.

One ESF in certain pressurized water reactor (PWR) containment buildings is an ice condenser. The primary function of this ESF is to condense steam that would otherwise contribute to a buildup of pressure in the containment shell. A typical ice condenser is illustrated in Figure 1. The ice condenser is composed of 1,944 baskets, each 48-ft (14.6-m) tall and 1-ft (30.5-cm) in diameter. Each basket contains flaked, borated ice. The amount of ice typically present during reactor operation is in excess of 1.1 million kg (2.4 million lb).

Results of an earlier examination of the ice condenser suggest that it could serve as a very effective aerosol trap during severe nuclear accidents (Winegardner, Postma, and Jankowski 1983). A computer program, ICEDF, was developed to estimate the extent of aerosol deposit in the ice condenser (Owczarski, Schreck, and Winegardner 1985). However, the code developers found inadequate data for code validation.

To help validate the ICEDF code, researchers at Pacific Northwest Laboratory (PNL) have initiated a program to obtain data on the deposition of aerosols in a representative section of an ice condenser. In the test section, all pertinent thermohydraulic and aerosol deposition processes anticipated during reactor accidents are represented as closely as feasible.

Before initiating design and construction of the test facility, a review of the available information on severe accident sequences was conducted for PWRs having ice condensers. Information on thermohydraulic and aerosol conditions at the inlet to the ice condenser was used to develop functional design criteria for the test facility and to help design a matrix of conditions at which testing would be conducted. This test matrix is shown in Table 1. The underlined tests have been completed. Those having an asterisk in front of the test number were completed since October 1987.

The program was initiated in 1985. This paper provides an update on information presented a year ago (Kannberg et al. 1987). Discussion focuses on the results of tests conducted at low flow rates (all tests conducted to date) and on special tests conducted to better characterize observed thermohydraulic and aerosol behavior.

This work was supported by the U.S. Nuclear Regulatory Commission under Contract DE-AC06-76RLO 1830, NRC FIN B2444.

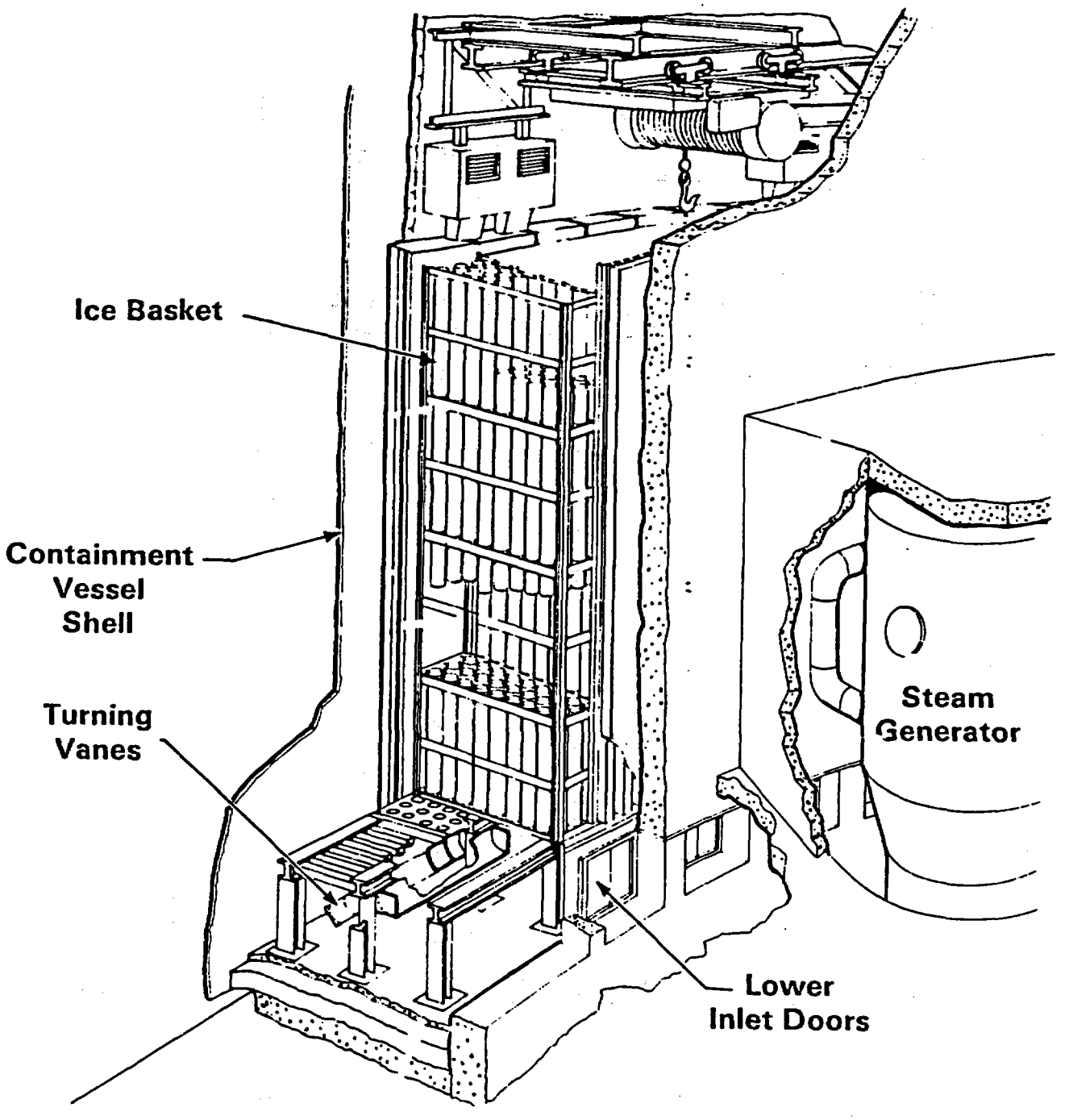


FIGURE 1. Isometric Diagram of Ice Condenser

TABLE 1. Test Matrix

Test No.	Particulate Characteristics: MMAD, m	Density, g/cc	Mass Conc., g/m^3	Material Solubility	Test Section Inlet Stream Parameters: Temperature, °C	Volume Flow Rate, m^3/s	Steam Mole Fraction	Test Section: Ice Fraction
1	12.00	4.5	7.0	1	60	0.15	0.20	1
2	12.00	2.0	0.74	-1	60	0.030	0.04	1
3	0.70	2.0	0.0037	-1	60	0.15	0.04	1
4	12.00	2.0	20.0	-1	105	0.033	0.90	1
5	4.22	2.0	7.0	1	105	0.380	0.90	1
6	12.00	2.0	1.8	1	200	0.030	0.04	1
* 7	4.98	4.5	7.0	-1	200	0.15	0.04	1
8	12.00	2.0	0.74	-1	200	0.380	0.90	1
* 9	1.25	4.5	0.0037	1	200	0.030	0.90	1
10	6.00	2.0	4.0	1	125	0.220	0.42	1
* 11	2.00	4.5	0.025	-1	125	0.220	0.60	1
Replicate								
12 (4)	12.00	2.0	20.0	-1	105	0.033	0.90	1
13 (5)	4.22	2.0	7.0	1	105	0.380	0.90	1
14 (10)	6.00	2.0	4.0	1	125	0.220	0.42	1
No ice								
15 (2)	12.00	2.0	0.74	-1	60	0.030	0.04	0

Notes:
Material solubility: 1 = soluble, -1 = insoluble
Ice fraction: 1 = full ice baskets, 0 = empty ice baskets
AMMD = aerodynamic mass median diameter
Underlined tests completed as of 10/01/88
* = Completed since 10/01/87

FACILITY DESCRIPTION

The purpose of testing conducted in the ICEDF test facility is to measure the retention of airborne particles that would occur under prototypic conditions in a nuclear power plant ice condenser. A number of testing capabilities have been developed:

- generation of uniformly-mixed steady-state streams of heated air, superheated steam, and various aerosols
- introduction of gas/aerosol mixtures into a representative full-height ice condenser test section
- measurement of gas temperature, steam content, and aerosol concentration and size distribution at the entrance, exit, and various locations within the ice condenser test section
- measurement of the test section gas temperatures and rate of liquid draining from the test section.

Construction of the test facility was completed in April 1987. An isometric view of the facility is presented in Figure 2.

The inlet stream to the ice condenser test section is composed of steam and hot air mixed with various aerosols as required for each individual test. A total inlet gas flow rate range of 0.03 to 0.38 m^3/sec corresponds to prototypic plant flow rates of approximately 16 to 200 m^3/sec. Steam is generated for most of the testing in a 150-kW electric boiler and can be superheated to 200°C. Steam for high flow tests (0.38 m^3/sec), scheduled for FY 1989, will be provided by a rented, gas-fired boiler capable of providing 910 kg/hr (2000 lb/hr). Filtered compressed air is used for tests requiring low noncondensible flow rates. Higher noncondensible flow rates are provided by a 45-kW (60-hp) blower. A heater is used to heat the air stream to 200°C.

The test section has a square cross section and contains the equivalent of four full-height [48-ft (14.6-m)] ice baskets. The cross section has one whole basket (graciously provided by Duke Power Co.) and four each of half- and quarter-section baskets. A lattice work of support members matching the plant arrangement is provided every 6 ft of elevation in the test section. Turning vanes are provided in the 90° corner ducts above and below the ice baskets to reduce nonuniform gas flows that may be caused by flow redirection. The test section contains 11 access doors (including one for ice loading), 11 4-in. (10.2-cm) windows, and 12 instrument probe panels. A valved bypass is provided to permit operation of fluid and aerosol streams while maintaining the ice condenser test section in isolation.

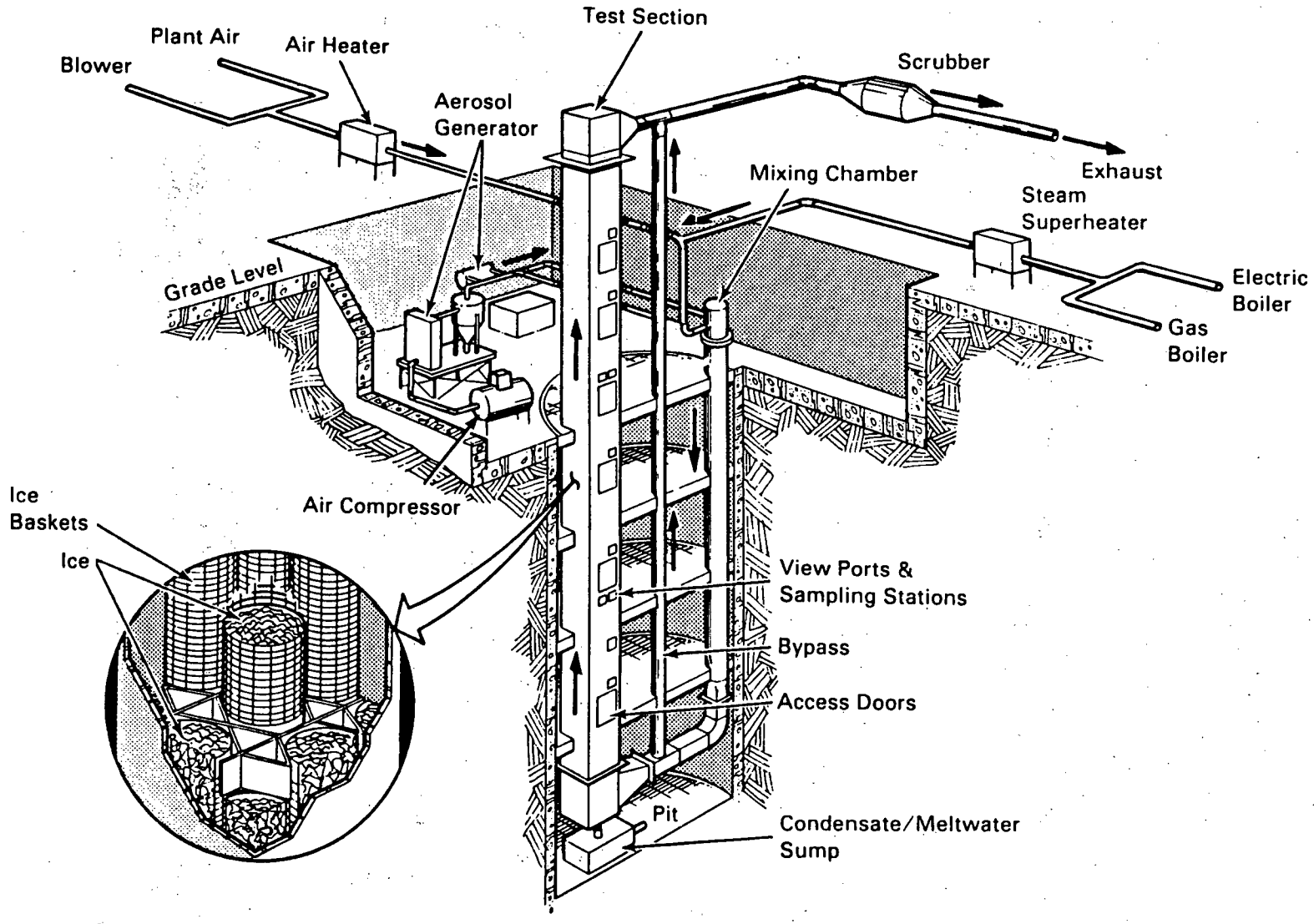


FIGURE 2. Ice Condenser Aerosol Deposition Test Assembly

All fluid streams supplied to the test section inlet are characterized with variable area flowmeters, with the exception of the high flow air supply, which is monitored with a vortex meter. The exit gas flow rate is measured with a pitot-static tube.

Liquid drained from the test section is measured in a sump and periodically pumped to waste. Liquid collected in the sump is sampled periodically during the test to evaluate particulate matter concentration in the meltwater.

Temperatures and pressures of all fluid streams are monitored entering and exiting the test section and at various locations in the test section. The measurements of temperature in the test section are made in the channels between the baskets where the primary gas flows occur when ice is present. During a test, thermohydraulic data are gathered and stored automatically by a computer data acquisition system (DAS). The DAS records output from 80 temperature sensors, 8 pressure transducers, 7 flowmeters, 2 load cells, and a laser transmissometer.

Aerosol mass concentration and particle size distribution characteristics are measured by withdrawing samples from the test system using sharp-edged sampling nozzles. Modifications made during the past year increased the number of available sampling station ports to 21; about 14 are typically used during each test. The active stations and selected other stations also provide information on test section temperatures and steam mole fractions during the tests. Aerosol samples are collected using sampling flow rates compatible with test section conditions and aerosol characteristics to limit sampling-line losses. Aerosol concentration is measured by collecting particles on glass fiber filters. Particle size distribution is measured using calibrated Andersen cascade-style impactors operated at less than nominal sample flow rates. Samplers and sample probes are heated to prevent condensation in the sampling lines or on collection substrates. Critical orifices are used to control sample flow rates. Chilled condensate traps are used to condense water to determine the steam mole fraction in the test section gas periodically during the test.

The range of aerosol conditions required for testing is too broad for any single generation material or method. Consequently, a variety of materials have been identified for use in the tests and two principal generation methods are used. The aerosol materials used in tests to date and planned for remaining tests are provided in Table 2 along with their planned method of aerosol generation. Two aerosol generation methods are used, an energy mill and an atomizing nozzle, depending on the aerosol materials and desired inlet conditions.

THERMOHYDRAULIC RESULTS AND OBSERVATIONS

For the FY 1987 tests, all test section aerosol samples were obtained from a single flow channel. Temperature measurements and limited flow visualization observations with smoke during testing conducted at the close of FY 1987 indicated that large-scale flow recirculation existed within the test section for low flow rates. Detection of this thermal and flow behavior argued strongly that the aerosol sampling locations should be reconfigured to support more

TABLE 2. Aerosol Generation Techniques and Materials for ICEDF Tests

Test No.	Generator	Primary/Backup Material
1	EM	CsI/-
2	EM	SiO_2
3	AN	Fluorescein/SiO_2
4	EM	SiO_2/Fluorescein
5	EM	NaCl/KCl
6	EM	KCl/NaCl/Uranine
7	EM	ZnS
8	EM	SiO_2/Fluorescein
9	AN	CsI/-
10	EM	KCl
11	AN	ZnS

Material	Formula	Material	Formula
Primary		Secondary	
Alumina	Al_2O_3	Calcium carbonate	$CaCO_3$
Cesium iodide	CsI	Cesium hydroxide	CsOH
Potassium chloride	KCl	Magnesium oxide	MgO
Silica	SiO_2	Tellurium dioxide	TeO_2
Sodium chloride	NaCl	Tin	Sn
Titanium dioxide	TiO_2	Zinc chloride	ZnCl
Zinc sulfide	ZnS		
Fluorescein	$C_{20}H_{12}O_5$		

EM = Energy mill
AN = Atomizing nozzle
Underlined tests are those completed to date (note that in Table 1, Test 15 has same inlet aerosol conditions as Test 2)

accurate spatial representations of aerosol mass flow rate. In fact, it appeared that the channel initially selected for sampling experienced downflow at low flow rates. A number of facility modifications were undertaken to add additional aerosol sampling stations. Aerosol sampling stations were added to enable sampling from all four quadrants at two elevations. A sampling location was also added to the test section exhaust. The sampling locations are shown in Figure 3.

The gas temperature and aerosol concentration had been observed to diminish considerably in the diffuser leading to the turning vanes below the ice-column-filled test section. Therefore, additional thermal sampling ports were added to the diffuser to determine if there was significant thermal stratification in the diffuser during low flow rate tests.

The thermohydraulic observations during "matrix" tests conducted after these modifications (Tests 7-5, 11-6, and 9-7) will be discussed in some detail, as will velocity measurements obtained during a special non-aerosol, no-steam test conducted in June, 1988, (THERMO-1). Both velocity measurements and smoke observations were made during this test. Velocity measurements were made for four sets of conditions including low and high flow rates and low and high temperatures. The inlet thermohydraulic and aerosol conditions and observed aerosol characteristics at various locations are summarized in Table 3 for all of the "matrix" tests conducted to date. The tests are listed in order of performance. A discussion of aerosol results from "matrix" and sample probe calibration tests follows this section.

DIFFUSER THERMOHYDRAULICS

Measured temperature profiles at two locations in the inlet diffuser are presented in Figure 4 for Tests 7-5, 11-6, and 9-7. The inlet temperature and steam mole fraction is different for each of the three tests depicted. The data clearly indicates a strong thermal stratification in the diffuser. The temperature profiles indicate a region of cool gas in the bottom of the diffuser. The velocity profile for the special test, THERMO-1, is shown in Figure 5. Because the hot wire anemometer used for this velocity measurement permitted only measurement of the velocity magnitude, the direction of flow has been determined by examination of the shape of the velocity profile, particularly the shear layer, and the requirements of mass continuity. Considering both sets of data, it appears that cold air is flowing upstream along the bottom of the diffuser and mixing in a shear zone with inlet gases. The temperature in the bottom of the diffuser at location T-4 (immediately upstream of the turning vanes) is only a few degrees (C) above the temperature of the water draining from the ice condenser. Clearly, cool air from the zone below the ice baskets, where meltwater collects for drainage to the sump, flows into the bottom of the ice condenser and mixes with the inlet gas.

Mixing in the diffuser has several effects. First, the temperature of the gas entering the bottom of the ice condenser test section is reduced. Second, the steam mole fraction is reduced as a result of cooling and condensation of vapor. A significant reduction in aerosol concentration occurs in the diffuser. Coupled with the steam mole fraction reduction, it is suspected that condensational particle growth leads to enhanced settling of aerosol particles.

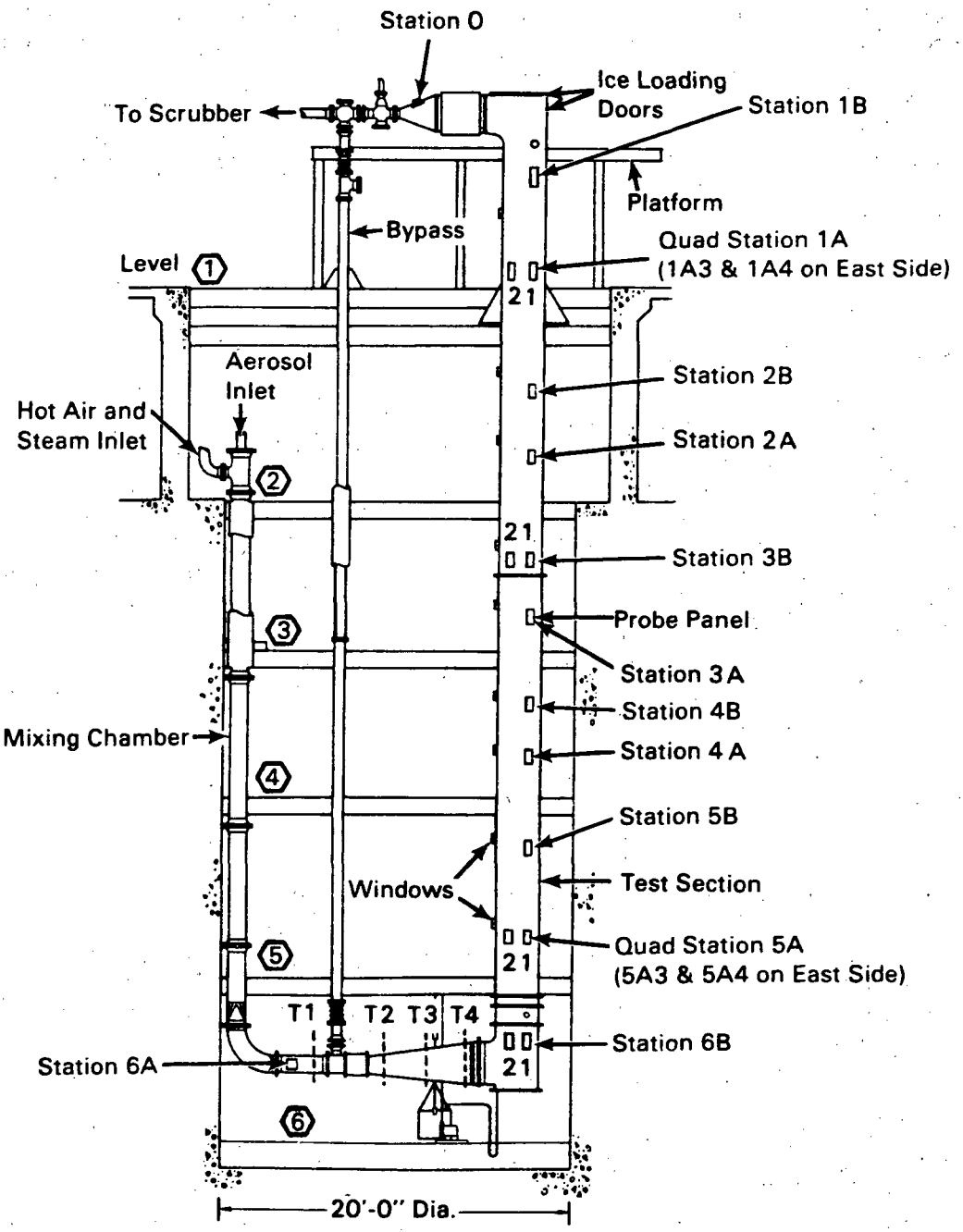


FIGURE 3. Elevation View (West Side) of Test Facility Showing Locations of Aerosol Sampling Stations and Diffuser Thermocouple Rakes (T#)

TABLE 3. Summary of Conditions Measured During Tests

	Thermohydraulic[a]					Aerosol						
						Inlet[a]		Test Section Aerosol Observations				
Test	Initial Ice Fraction	Average Gas Flow Rate, m^3/s	Average Temperature, °C	Average Steam Mole Fraction	Material	Mass Concentration, mg/m^3	PSD MMAD/GSD, μm/-	Sta 5[b] PSD MMAD/GSD, μm/-	Sta 1[b] PSD MMAD/GSD, μm/-	Inlet[c] DF	Test Section[c] DF	System DF
15-2	0	0.031	91	~0	KCl	1150 ± 220	NA[d]	6.1/2.7	6.3/2.6	2.4 ± 0.5	1.0 ± 0.03	~2.5[e]
2-3	0.79	0.031	89	~0	SiO_2	500 ± 30	>15[f]	9.7/3.7	5.2/3.0	4.4 ± 1.0	2.1 ± 0.1	9.3[e]
10-4	0.61	0.217	125	0.40	KCl	1710 ± 330	9.0/3.6	2.4/3.2	9.1/2.4	5.0 → 13.4	3.6 → 1.0	~13 to ~17[e]
7-5	0.72	0.154	104	~0	ZnS	870 ± 120	5.7/3.7	3.0/2.1	4.0/2.1	1.0 ± 0.1	1.2 → 2.4	2.3 ± 0.2
11-6	0.62	0.158	123	0.70	ZnS	52 ± 1	3.6/2.3	3.5/2.0	~9	NA	NA	NA
9-7	0.63	0.058	145	0.64	CsI	1.79 ± 0.35	3.3/2.6	3.7/2.3	1.6/2.3	11.2 ± 0.4	4.1 ± 0.5	38 ± 6

(a) Inlet (Station 6A) conditions

(b) Averaged values. PSD = particle size distribution, MMAD = mass median aerodynamic diameter, GSD = geometric standard deviation.

(c) Averaged values. See Figures 4 and 5 for aerosol mass flow rate at various sampling stations. Listed variance is observed range from average value.

(d) Not yet available

(e) System DF between Station 6A and 1A, sampling station 0 was installed between Tests 10-4 and 7-5.

(f) Measurements do not have sufficient resolution for accurate estimates. Considerable settling occurred in diffuser.

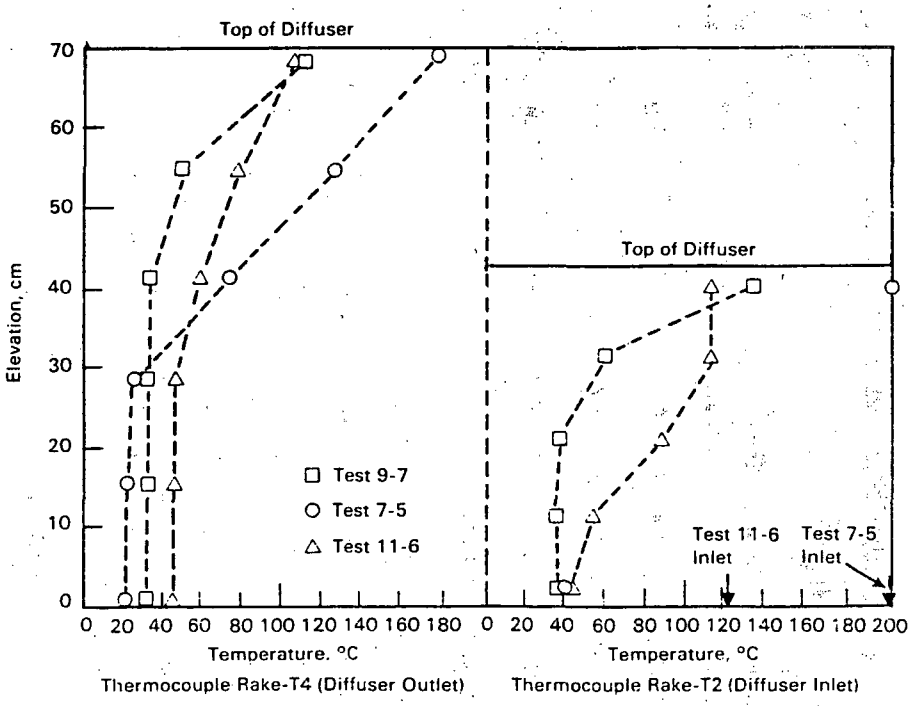


FIGURE 4. Vertical Temperature Profiles at the Centerline of the Diffuser at Two Locations Along its Length

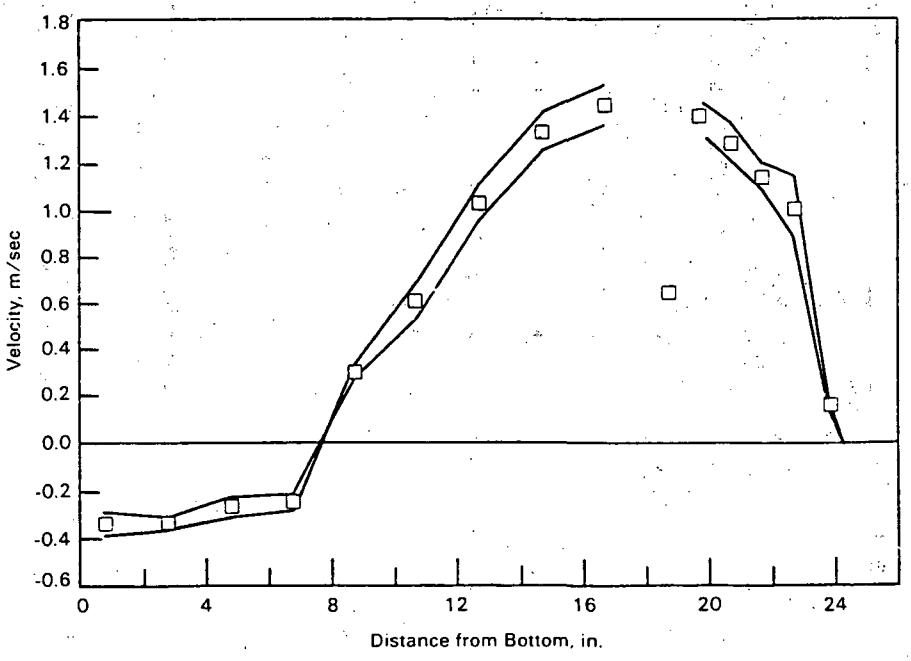


FIGURE 5. Vertical Velocity Profile for THERMO-1 Test at the Downstream End of the Diffuser; 0.14 m^3/sec, Inlet Temperature, 77°C

TEST SECTION THERMOHYDRAULICS

Once the warm inlet gas arrives at the bottom of the ice condenser test section, temperature, flow visualization, and velocity measurements indicate that preferential flow occurs; upward in two or three channels between the baskets and downward in one or two channels.

Vertical temperature profiles in each of the four major flow channels are depicted in Figures 6, 7, and 8 for three tests, Tests 10-4, 7-5, and 11-6 (data was not available for Test 9-7 at the time the paper was written). Several features are discernable from the profiles. First, the northern flow channels are typically warmer than the southern flow channels. This is because the warm gas flowing from the top of the diffuser enters the northern flow channels. Second, temperatures for Test 7-5 are hotter at the bottom and much colder at the top than either Test 10-4 or 11-6. This is probably because no steam was present in the inlet gas (lowering its effective heat capacity because no condensation was possible). Third, the gas temperature for Tests 10-4 and 11-6 decreased only 10 to 15°C from bottom to top; considerably less than that observed for Test 7-5. This, again, may be attributable to the higher steam content of the inlet gas for these tests. Finally, although downflow has been observed in one or both of the south flow channels, the temperatures in both north and south quadrants decrease from bottom to top. This could only occur if there was a reasonable amount of mixing between the flow channels.

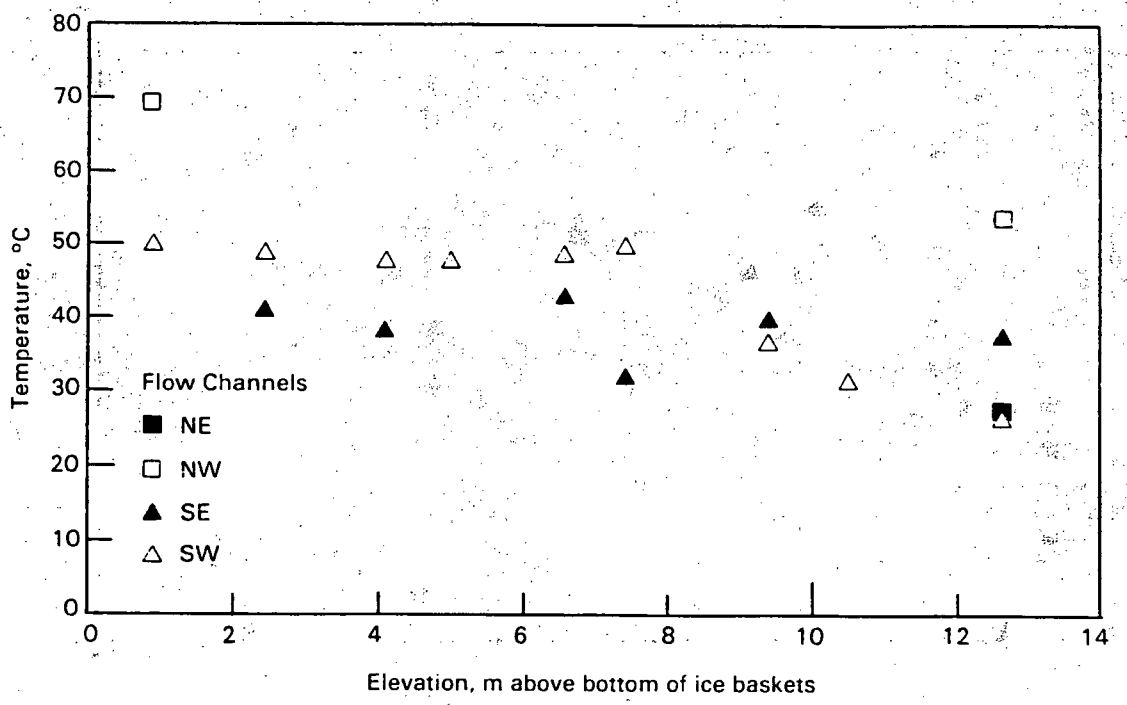


FIGURE 6. Test 10-4 Flow Channel Temperature Profiles

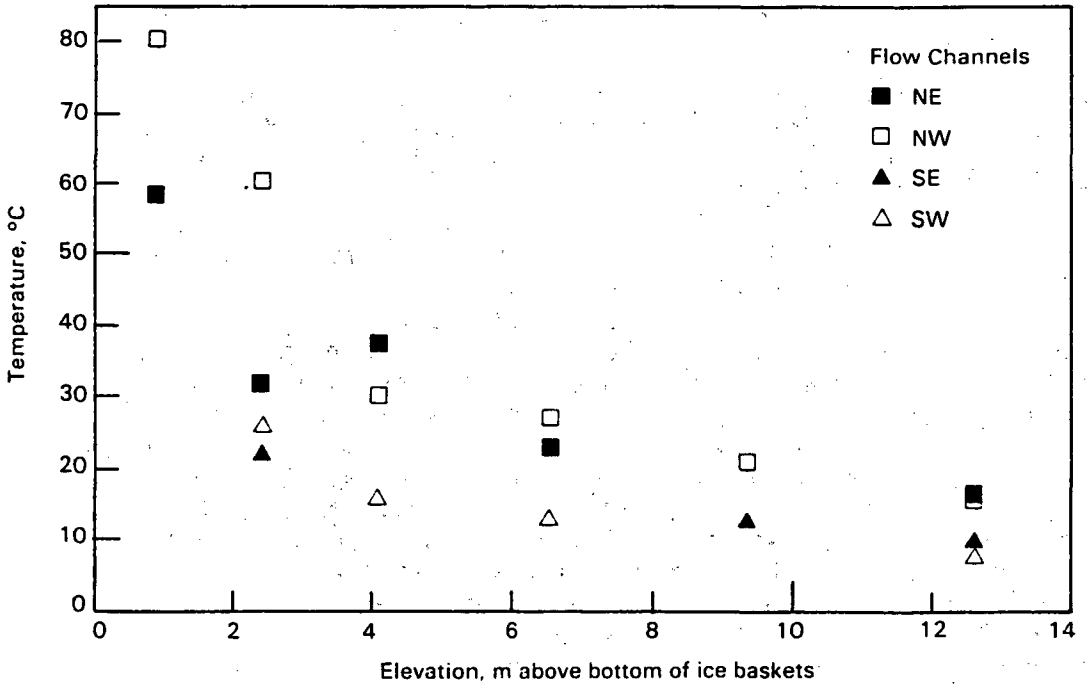


FIGURE 7. Test 7-5 Flow Channel Temperature Profiles

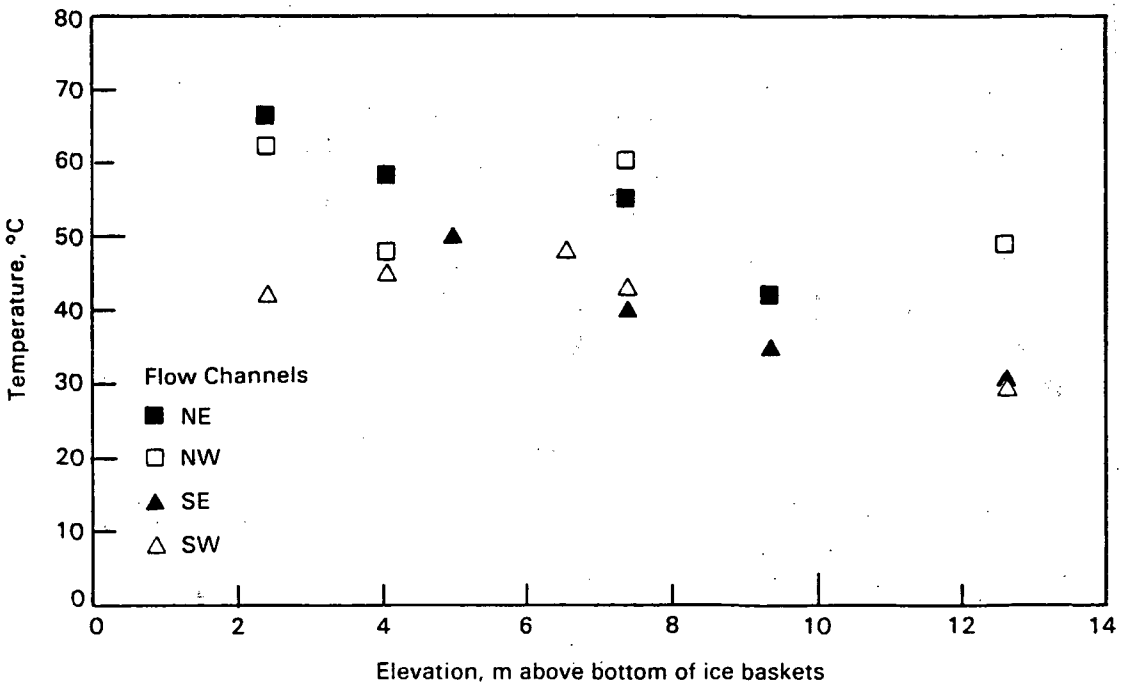


FIGURE 8. Test 11-6 Flow Channel Temperature Profiles

Velocity measurements were made through the centerline of the flow channels along east-west transects at various locations in the test section. Furthermore, visual smoke observations were made at some locations to determine the direction of flow and the qualitative duration of flow in various directions at selected locations.

Velocity profiles obtained from THERMO-1 are shown in Figures 9, 10, and 11. The measured velocity is plotted along with the observed range of velocities observed during a short (15 sec) observation period. The velocity profiles for transects through the north and south flow channels at Level 5 (2.2 m above bottom of ice baskets) are shown in Figure 9 for a low flow rate (0.14 m^3/sec) and low temperature inlet condition (approximately 27°C). Review of Figure 9 will reveal that the flow is upward (positive) in three quadrants but down in the southwest quadrant. Again, the direction of flow was determined from smoke injection. If the velocity in the southwest flow channel had been positive, the profile would have agreed well with the other four quadrants. The observed velocity profiles at Level 1 (12.6 m above bottom of ice baskets) are shown for the same conditions in Figure 10. Although smoke observation was difficult, no downflow was observed in any of the quadrants at this elevation. When, the temperature was increased to 77°C at the inlet (upstream of the diffuser), the velocity profile at Level 5 retained its previous form; however, the velocity profiles at Level 1 (near the top of the test section) changed to the form shown in Figure 11. The velocities in the south flow channels are substantially less than those of the north flow channels. When the flow rate was increased to 0.295 m^3/sec, no downflow was observed in any flow channels at any elevation.

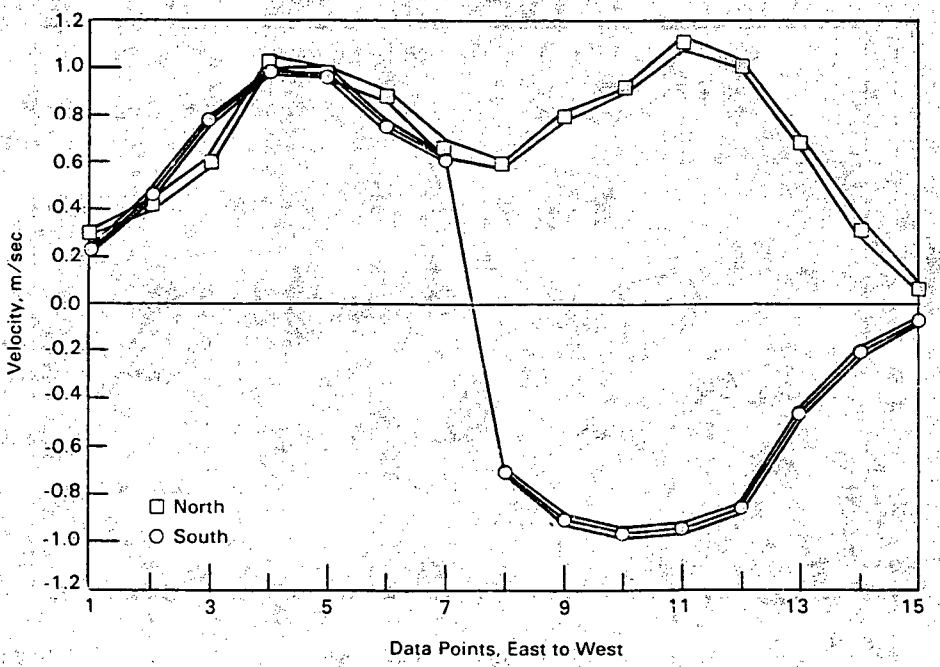


FIGURE 9. Velocity Profiles for THERMO-1 Test Along East-West Transects Through North and South Flow Channel Centerlines at Level 5 for an Inlet Gas Flow Rate of 0.14 m^3/sec and Inlet Temperature of 27°C.

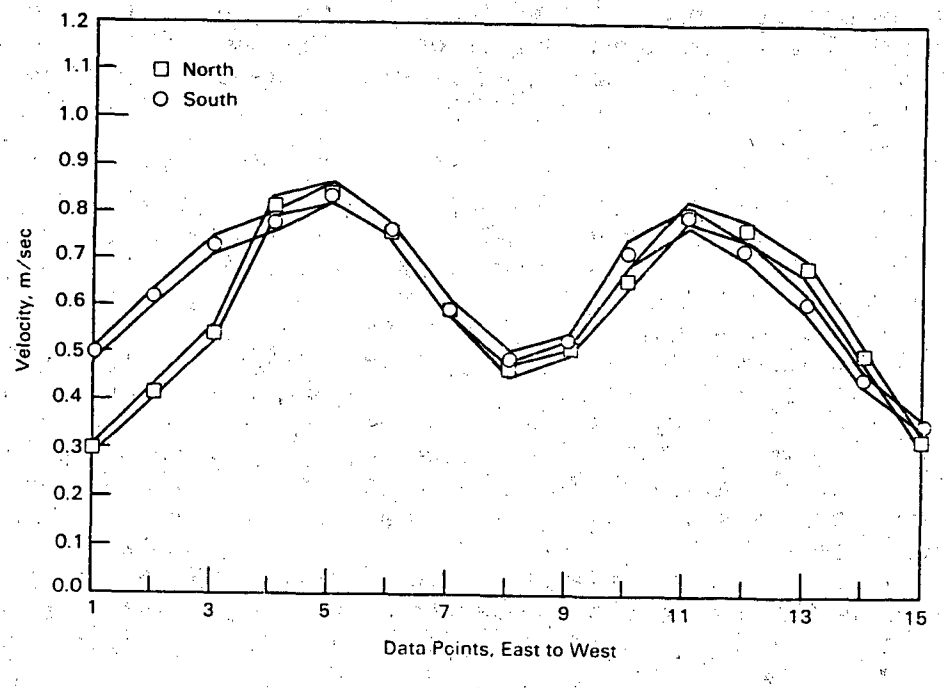


FIGURE 10. Velocity Profiles for THERMO-1 Test Along East-West Transects Through North and South Flow Channel Centerlines at Level 1 for an Inlet Gas Flow Rate of 0.14 m^3/sec and Inlet Temperature of 27°C

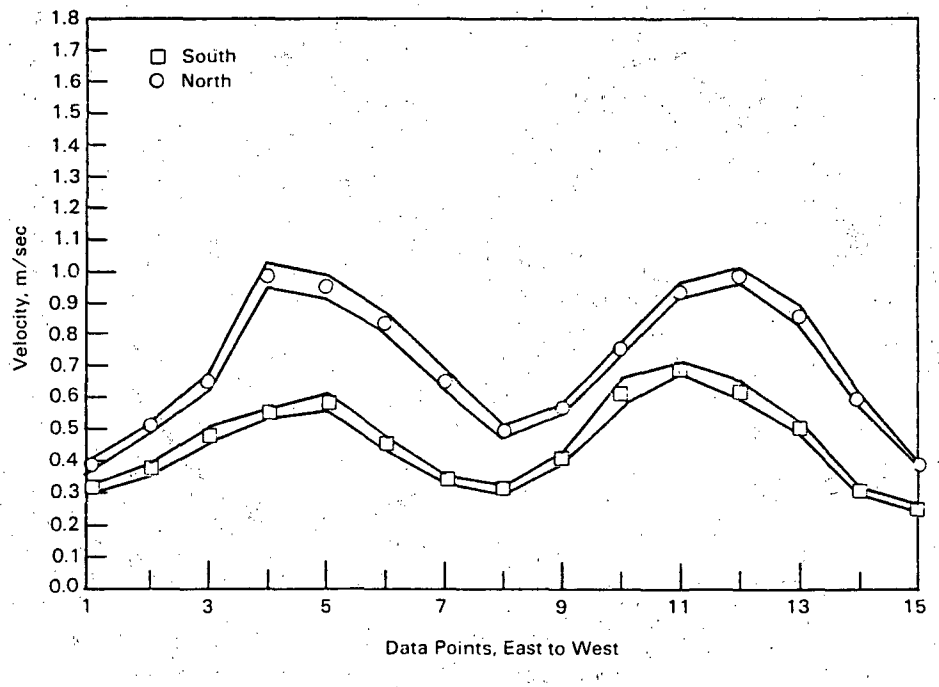


FIGURE 11. Velocity Profiles for THERMO-1 Test Along East-West Transects Through North and South Flow Channel Centerlines at Level 1 for an Inlet Gas Flow Rate of 0.14 m^3/sec and Inlet Temperature of 77°C

Clearly, at low flow rates downflow occurs in at least one of the flow channels in the lower part of the ice condenser (or zone occupied by ice). However, upflow was observed in all flow channels for all conditions at the top of the ice condenser for the conditions of THERMO-1 (flow rate from 0.14 to 0.295 m^3/sec, inlet temperature from 27 to 77°C).

AEROSOL RESULTS AND OBSERVATIONS

The primary purpose of these engineering-scale ice condenser tests is to determine the degree to which the ice condenser contributes to the reduction of aerosol mass present in the gas flowing from the lower to upper compartments. Therefore, the emphasis of aerosol sampling and characterization has been to determine the decontamination factor (DF), the ratio of the aerosol mass flow rate into to that out of the ice condenser test system. Because thermohydraulic influences of the ice condenser extend upstream and downstream of the zone occupied by the ice columns, the overall, or bulk, DF is measured between locations just upstream and just downstream of the lower and upper turning vanes. Additional aerosol data are also obtained within the test system to provide information on aerosol behavior in the various components of the ice condenser; thus potentially enabling subsequent improvement of numerical aerosol deposition models.

Aerosol behavior in the ice condenser is expected to be dependent on thermohydraulic conditions. The measured presence of downflow in one or two of the flow channels under low inlet flow rate conditions, described above, necessitated the installation of additional aerosol sampling stations--particularly the establishment of "quad" sampling stations at Levels 1 and 5 (near the top and near the bottom of the ice columns, respectively). Quad stations differ from the other stations located along the ice condenser because they include four sampling nozzles, one in each open flow channel; other stations have only one sampling nozzle located in the southwest flow channel. In addition to the quad stations, two sampling ports were added to create Station 6B between the lower turning vanes and the bottom of the ice baskets, and Station 0 was installed to allow measurement of outlet aerosol characteristics.

Aerosol test procedures include generation and characterization. Aerosols are generated by dispersing powders in an energy mill or atomizing liquid solutions in an ultrasonic nozzle. Aerosol generation procedures are driven by aerosol solubility, concentration, and particle size distribution requirements. Aerosol characteristics are measured to provide information about test conditions, particle size distribution, and aerosol mass concentration and mass flow rate at the test system inlet, outlet, and within the ice condenser test section. These data provide measurements of bulk and compartment DFs and for post-test material mass balance calculations. The discussion here will primarily concentrate on two of the three tests performed in the past year, Tests 7-5 and 9-7.

Tables 2 and 3 list the aerosol source material and generation method for tests completed and planned. ZnS powder was generated by energy mill during Test 7-5, and CsI was generated from an aqueous solution by ultrasonic nozzle during Test 9-7.

Results of particle size distribution measurements are listed in Table 4. Most samples indicated the aerosol to be log-normally distributed; thus, the measured mass median aerodynamic diameter (MMAD) and geometric standard deviation (GSD) of the aerosols were used to describe the aerosols. Samples were typically obtained twice during tests, at about 25% and 75% test completion periods. Samples were usually obtained at the inlet (Station 6A) and the bottom (Stations 5A or 6B) and the top (Stations 1A or 1B) of the ice columns. With the exception of Test 9-7, tests with steam showed significant particle growth as the aerosol passed up the ice condenser. The flow rate in Test 9-7 was very slow (about 0.06 m^3/sec), particularly after most of the steam had been condensed in the diffuser and the lower test section. The resulting increased residence time of particles in the ice condenser is speculated to have been sufficient to favor deposition of large particles, thus decreasing the MMAD present at the top of the section. Tests without steam provided no indication of particle growth--even during Test 7-5 when the inlet temperature and flow rate provided a maximum dry-gas ice melting condition.

Significant temperature differences, noted in earlier tests, between various flow channels and observations of downflow in the south flow channels near the bottom of the ice condenser for low flow rate cases suggested that aerosol distribution might not be uniform among flow channels. Figure 12 shows aerosol concentrations in each flow channel measured during Test 9-7 at quad stations near the bottom (Station 5A) and the top (Station 1A) of the ice condenser. Greater aerosol concentrations were measured in the north flow channels at Station 5A; however, near the top of the ice condenser (Station 1A), the concentrations were nearly uniform between the four flow channels. This is consistent with earlier observations of gas velocity profiles and orientations (although for somewhat different conditions), and, to a large degree consistent with measured temperature differences.[a] An important result of these data, although perhaps only applicable to tests with low gas flow rates, is that measurements of DF determined between locations of the test section other than the lower region of the ice condenser may be performed using aerosol data from only a single flow channel. Using aerosol mass flow rate data from the lower portion of the ice condenser to calculate DF requires that aerosol mass concentration data include all flow channels and flow profiles be defined.

Aerosol mass flow rate data for Tests 7-5 and 9-7 are provided in Figure 13 and 14 as functions of time and location within the test system. Of importance is the substantial decrease in aerosol mass flow rate that occurred between the inlet and the bottom of the ice columns. The DF at the inlet is speculated to be caused by settling and possibly diffusiophoresis. Substantial particle

---

(a) It is recognized that the existence of flow reversals could conceivably contribute to reduced aerosol sampling effectiveness, especially for large particle sizes and high flow velocities. However, review of fluid and aerosol conditions existing during Test 9-7 indicate that this phenomena is not the primary reason for the large concentration differences shown in Figure 12 for Station 5A.

TABLE 4. Particle Size Distribution for Completed Tests at Inlet, Bottom, and Top of Test Section

Particle Size: MMAD[a] [μm] (GSD)[b]

Test	Ice	Steam	Inlet	Ice Columns: Bottom	Ice Columns: Top
10-1	Yes	Yes	NM[c]	ND[d]	6.0 (2.6)
			NM	3.8 (2.9)	9.0 (2.4)
15-2	No	No	NM	6.2 (2.8)	6.0 (2.7)
			NM	6.1 (2.6)	6.5 (2.6)
2-3	Yes	No	>15 (-)	12.1 (4.5)	5.7 (2.7)
			>15 (-)	7.3 (3.0)	4.8 (3.1)
10-4	Yes	Yes	7.9 (3.4)	2.9 (2.4)	9.3 (2.6)
			11.6 (3.9)	1.9 (4.1)	9.0 (2.2)
7-5	Yes	No	5.4 (3.7)	3.8 (2.1)	ND
			6.8 (4.0)	3.8 (2.2)	4.0 (2.1)
11-6	Yes	Yes	3.3 (2.1)	ND	~9 (-)
			3.9 (2.5)	3.5 (2.8)	ND
9-7	Yes	Yes	3.3 (2.7)	3.8 (2.3)	1.6 (2.3)
			3.3 (2.4)	3.6 (2.3)	ND

(a) MMAD - mass median aerodynamic diameter
(b) GSD - geometric standard deviation
(c) NM - not measured
(d) ND - not determined

growth, enhancing deposition by settling, is suspected due to steam condensation. In addition, the presence of cold reverse flow in these locations provides an unknown degree of mixing and, possibly, increased particle residence time. As no aerosol sampling was performed in the inlet diffuser, specific aerosol behavior can only be speculated based on inlet and outlet conditions, on temperature profile measurements indicating the presence of reverse flow, and on measured decreases in both bulk gas temperature and steam mole fraction.

Aerosol mass flow rate at other locations of the test system are also shown in Figures 13 and 14, including average values measured at Quad Stations 5A and 1A during Test 9-7. Neglecting Station 6B, which is located within (and

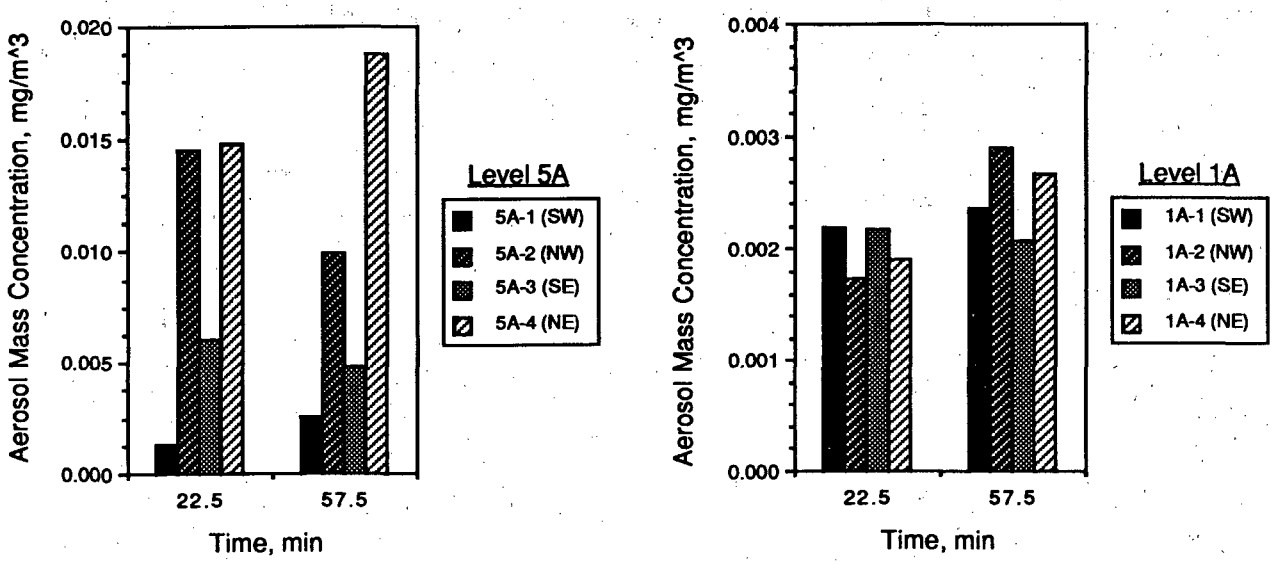


FIGURE 12. Aerosol Concentrations (mg/m^3) in Various Flow Channels for Two Time Intervals at Levels 5A and 1A for Test 9-7

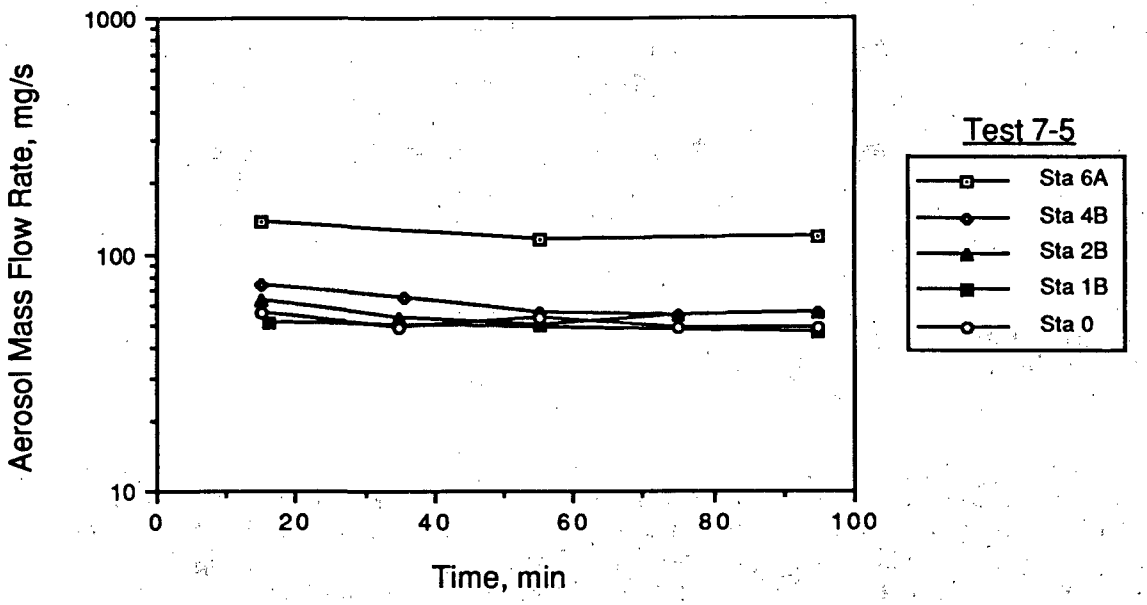


FIGURE 13. Aerosol Mass Flow Rate Through the Test Facility as Measured at Various Sampling Stations During Test 7-5

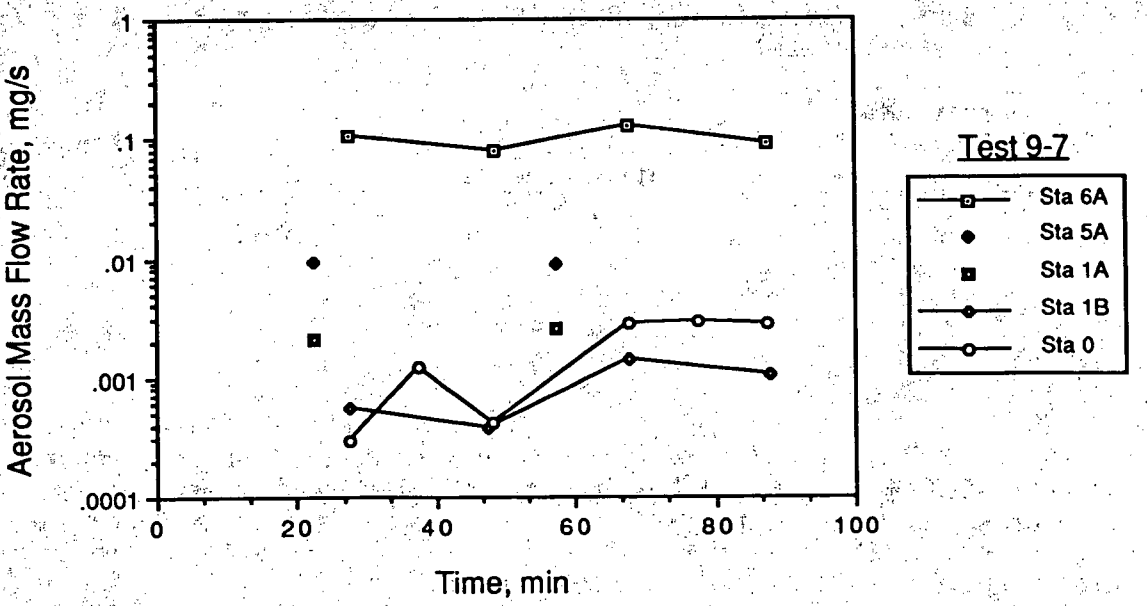


FIGURE 14. Aerosol Mass Flow Rate Through the Test Facility as Measured at Various Sampling Locations during Test 9-7

may have been influenced by) the area of probable flow reversals, a general decrease in aerosol mass flow rate is seen with increasing elevation in the ice condenser during both tests. The cause of a measured increase in aerosol mass flow rate between the top of the ice condenser (Station 1B) and the test system outlet (0) during Test 9-7 is not known; however, no significant DF is thought to have occurred there because of the small particle size, cold temperature, and relatively short residence time between the two locations.

DF values are listed in Table 3 for the inlet section (between Stations 6A and 6B or 5A), the ice condenser (Station 6B or 5A to 1A or 1B), and the overall test system (Stations 6A to 0). DF is substantially increased during tests when steam is a major component of the inlet gas. Furthermore, a large portion of the DF occurs in the inlet diffuser, especially for tests with a large fraction of steam in the inlet gas. In all tests, DF progressed toward 1.0 (greater than 95% penetration) when the ice was completely depleted.

Additional tests were conducted with monodisperse aerosols (to calibrate aerosol sampling instrumentation), in the absence of both ice and steam. Results of these tests are presented in Table 5. In combination with Test 15-2, they indicate that there is very little DF in the ice condenser after ice is depleted.

To establish an independent measure of accuracy for the tests, an aerosol material mass balance was conducted for Test 10-4 and a similar procedure is planned for selected tests. The aerosol masses associated with generation, mixing, deposition in the test section, meltwater and condensed steam (measured

TABLE 5. Summary of DF for Monodisperse Aerosols Over the Length of the Ice Baskets from Station 6B to 1B. (System flow rate = 0.15 m^3/sec, no ice, no steam)

Aerodynamic Particle Size, μm	Number of Measurements	DF	Range of Data, ±DF
4.6	2	1.017	±0.001
11.4	6	1.107	±0.016
15.0	7	1.155	±0.106

together), diffuser, and exhaust scrubber were determined and compared with the estimated DF determined from the aerosol samples. A material mass balance was achieved accounting for 93% + <13% of the material introduced into the test system via the generator. A DF of 14 ± 2 was computed based on the mass balance between the inlet and outlet sampling stations. This is similar to and lends validity to the DF of 13 to 17 (varying with time during the test) determined from the aerosol samples.

CONCLUSIONS

Based upon tests conducted in a unit cell ice condenser test facility, the following observations and conclusions can be stated. As long as ice is present, the following are evident.

- There is considerable energy exchange and aerosol loss in the entrance zone to the ice condenser (diffuser in the test facility) due to counter current flow of cool gas in the lower regions of the flow passage.
- Thermal stratification is present in the diffuser.
- Recirculating flows were observed in the lower portion of the ice condenser for a special test (no steam or aerosol) having an air flow rate of 0.035 m^3/sec/ice basket; however, no downflow was observed near the top of the ice condenser at this flow rate, and no recirculation was observed anywhere in the test section when air flow rate was 0.0738 m^3/sec/ice basket.
- The presence of steam in the inlet gas has the following effects:

  i) temperature gradients are less severe from top to bottom in the ice condenser than when steam is not present;

  ii) substantial amounts of steam are condensed in the entrance zone;

  iii) substantial amounts of aerosols are scrubbed from the inlet gas in the entrance zone;

iv) particle growth is evident for aerosols sampled at increasing elevation in the ice condenser except for very low, noncondensible, gas flow rates;

v) total DF between inlet and outlet is much higher than for cases where steam is not present.

- Aerosol concentration is non-uniformly distributed among flow channels at the bottom of the ice condenser but is essentially uniform at the top of the ice condenser; at least for very low flow rates (Test 9-7).

When ice is absent from the ice condenser the test section DF ranges from 1.017 to 1.155 for particle sizes from 4.6 μm to 15 μm for a gas flow rate of 0.15 m^3/sec (0.0375 m^3/sec/ice basket).

The aerosol material mass balance for Test 10-4 was excellent, as 93% ($\pm$ <13%) of the material entering the aerosol generator was accounted for.

Goals for next year include renting a large-scale steam generator, modifying aerosol sampling procedures, completing scheduled tests, investigating thermohydraulic effects, and compiling summary tables of aerosol and thermohydraulic conditions for subsequent use in validating and improving the numerical aerosol code ICEDF.

REFERENCES

Kannberg, L. D., M. W. Ligotke, E. J. Eschbach, and B. A. Ross. 1987. "Preliminary Results of Aerosol Deposition Experiments in an Engineering-Scale Ice Condenser." PNL-SA-15140, Pacific Northwest Laboratory, Richland, Washington. Presented at the Fifteenth Water Reactor Safety Research Information Meeting, Gaithersburg, Maryland, October 26-30, 1987.

Owczarski, P. C., R. I. Schreck, and W. K. Winegardner. 1985. A Code for Aerosol Particle Capture in Ice Compartments. NUREG/CR-5130, U.S. Nuclear Regulatory Commission, Washington, D.C.

Winegardner, W. K., A. K. Postma, and M. W. Jankowski. 1983. Studies of Fission Product Scrubbing Within Ice Compartments. NUREG/CR-3248, U.S. Nuclear Regulatory Commission, Washington, D.C.

RESULTS OF THE PRELIMINARY HYDROGEN DISTRIBUTION EXPERIMENT AT HDR AND FUTURE EXPERIMENTS FOR PHASE III

L. Wolf* L. Valencia

Kernforschungszentrum Karlsruhe GMbH
Projekt HDR/HT
Postfach 3640
D-7500 Karlsruhe 1, FRG

* Battelle-Institut e.V.
Am Römerhof 35
D-6000 Frankfurt/Main 90, FRG

During Phase II of the HDR Safety Program, a preliminary H_2-distribution experiment, T31.5, was performed in December of 1987 in the aftermath of ISP 23 for the purpose of obtaining a first set of experimental data for long-term gas transport behavior in a large-scale, multi-compartment facility in the presence of steam under natural convection conditions.

This preliminary experiment was needed for reliably planning the major H_2-distribution test series E11.1 through E11.5 to be performed between March and July of 1989 during Phase III of the HDR Safety Program (1988-1991).

At the same time, this experiment constituted an excellent opportunity to evaluate the predictive capabilities of present state-of-the art computer codes for hydrogen distribution analyses by virtue of blind post-test predictions. Therefore, Project HDR called for an international benchmark exercise which was accepted by a variety of different institutions.

The paper presents major experimental results in form of the transient built-up and decay of gas concentration as well as the time evolution of other important quantities influencing the gas transport. The effect of the non-uniform axial temperature profile prior to the gas release will be discussed. The presentation will show the space-time evolution of the major measurement quantities in form of continuous color graphics.

The presentation will close with a brief outlook of the forthcoming main test series for hydrogen distribution their experimental procedures, objectives and time schedule.

1. INTRODUCTION

During severe accidents in light-water reactors, substantial amounts of hydrogen can be generated by the metal-water reaction during core heat-up and by core-uncovery as well as by virtue of core-concrete interactions after vessel lower head failure. This hydrogen is released into the containment. The hydrogen distribution within the multicompartment geometry of the containment, its potential ignition and following combustion under simulated typical accident containment conditions has been and still is the subject of various experimental and analytical investigations of different complexities and scales.

A key issue within this context relates to the global ad local hydrogen distribution and associated mixing phenomena in order to plan for proper mitigation measures.

In the case, that no mitigating measures are provided it has to be demonstrated at least that the containment integrity is not threatened by the combustion of hydrogen including local detonations.

Experimental and theoretical investigations into the hydrogen behavior have been initiated and perforemd to a large extend in the USA following the TMI-accident. In accordance with the requirements of the Severe Accident Rulemaking these continuing activities are devoted mainly to the investigation and development of mitigating measures.

The four known past experiments on hydrogen distribution together with the major characteristics and most important results are listed in Table I.

The experiments performed at the University of Pisa /1/ and at the Karman-Institute /2, 3/ are related to the Design Basis Accident (DBA) as concerns the H_2-release rate. The most important influencing factors "reactor-typical geometry" and "accident- typical thermodynamics in the containment" have either been simulated not at all or in a wrong manner. Therefore these experiments are not representative with respect to the conditions during severe accidents in LWRs.

Accident-typical thermodynamic conditions have been established in the HEDL-experiments /4, 5/. These are, however, of limited value because of their limited objective of demonstrating a homogeneous H_2-distribution in the lower compartment of a PWR with ice-condenser containment and the resulting limitations of an essentially one-compartment geometry; the use of a blower in the upper compartment to homogenize the atmosphere; blower outlet into the test compartment; and a test compartment open to the en-

vironment. Therefore the extrapolation of the HEDL-tests to real containments especially of the European designs, is rather limited.

The two Battelle-test series /6, 7/ assume an in-between position: the atmospheric conditions do not correspond to those anticipated during the course of an accident (with the exception of a negative temperature gradient, which was simulated), but the H_2-release rate applied during the experiments is an order of magnitude greater than is typical for a DBA. The geometry is also closer to typical European designs compared to other experimental facilities. The 6-compartment geometry is of a rather large scale and the arrangement of compartments and flow openings permit the establishment of recirculating flow patterns. The distribution of the released hydrogen, however, is determined by the transport mechanism of density convection and diffusion. This means that the buoyancy - or momentum flux - controlled jet-effects occuring in a severe accident were not simulated in the tests.

Assessing Table I and the informations provided in the references cited with respect to the potential of the experiments to simulate the H_2-distribution in the case of a DBA- or Core Melt Accidents, it has to be recognized, that all of the above mentioned experiments have certain limitations and therefore are of limited value because:

1. The H_2-release rates, the thermodynamic and fluiddynamic initial and boundary conditions as well as the geometry did not correspond to accident-typical conditions.

2. In the experiments with accident-typacil conditions, only a one-compartment geometry was used (HEDL).

3. In the experiments with multi-compartment geometry no accident-typical conditions were simulated (Battelle).

From the above, it is evident that the accident-typical combination of

- sufficiently large scale
- high H_2-release rates
- multi-compartment geometry with sufficiently large dome volume representation
- condensing vapor environment
- multiple steam and H_2-injection phases

has not been experimentally investigated yet with respect to the hydrogen distribution phenomena.

A cross-section of presently available data from past experiments is provided in Fig. 1 where the maximum concentration difference C, observed in various experiments, is given as a function of the hydrogen source term Q_H Q_H is defined as the ratio of the volumetric release rate V_H and the volume of the source compartment, V_{SC}, and is therefore to some extend independent of the geometrical data of the individual experimental facility.

Fig. 1 shows, that

- the maximum concentration differences observed in a one-compartment geometry increase only moderately with an increasing source term Q_H even over three orders of magnitude (dash-dotted line with PA, KM, BF 1, HM 1, HM 2).
- in the multi-compartment geometry (with inverse temperature stratification) the maximum concentration differences increase significantly with only a small increase in the source term Q_H (dashed line with BF 12, BF 18, BF 21, BF 16, BF 20).
- statements concerning the concentration distribution in a multi-compartment geometry, characteristic for a real PWR, can not be made in the range of source terms representative for severe accidents which encompasses more than two orders of magnitude. Thus, the shaded area in Fig. 1 should be the subject of further experimental and analytical investigations.

Despite of the aforementioned shortcomings, noticeably the HEDL- and Battelle experiments produced a first set ot data for the validation and qualification of different computer codes developed by a variety of institutions in different countries.

Most of the computer codes applied for the calculation of hydrogen distribution have been derived from already existing fluid dynamic codes. Table II provides an overview of major characteristics of a cross-section of computer codes applied for hydrogen distribution analyses. Nearly all of the codes listed in Table II have been verified in pre- and post-test calculations of experiments on hydrogen distsribution performed by Batatelle and HEDL. The codes listed in Table II can be subdivided into two groups:

- Lumped parameter (LP) codes: HECTR, MAPHY,RALOC, THETYS, COBRA-NC, WAVCO
- Finite Difference (FD) codes: COBRA-NC (mostly operated in LP-mode), HMS, LIMIT, TEMPEST.

As has been demonstrated by comparison with experimental data, the fundamental strength of the FD-codes lies in their ability to calculate three-dimensional velocity, temperature and concentra-

tion fields including the modeling of momentum controlled jets and turbulent effects.

However, the disadvantage of the FD-codes lies in the substantially increasing expense associated with the modeling of complex containment geometries, which can lead to prohibitive computation times.

On the other hand, the application of the LP-codes requires a large amount of experience in discretizing the containment geometry by the code user. LP-codes can quite readily be extended to system codes, i.e. the determination of the thermodynamic boundary conditions necessary for the calculation of the distribution. Details of jets and boundary driven plumes cannot be modeled.

The codes LIMIT and COBRA-NC assume an in-between position between these two code categories by virtue of their capability to use a mixture of spatial resolutions of different regions of the containment geometry, i.e. lumped,one, two- or even three- dimensional dependent upon the user's requirements for local details. A direct comparison of the predictive qualities of the different codes listed in Table II on the basis of past experiments is still difficult because no consistent Standard Problem or Benchmark case has been performed yet on the basis of an unique experiment. However the review of available comparison between measurements and code predictions reveals the following observations:

1. Qualitative and quantitative discrepancies exist between experiments and code predictions.
2. Momentum driven problems (HEDL) are solved with better predictive quality than long-term buoyancy governed natural current driven experiments (Battelle).
3. The critical question about the spatial resolution, e.g. number of nodes necessary to adequately solve a given hydrogen distribution problem remains unanswered though a tendency towards 20 - 40 nodes can be recognized.

4. Whereas previously it was thought by code developers and users that long-term transients in containments do not pose any problems compared to the blowdown driven phase, it is now recognized that the slow transient at late times (hours, days) impose stringent requirements upon the effectiveness of numerical solution schemes, accuracy, spatial resolution and computational resources.

5. One of the major difficulties evidently concerns the simulation of heat transfer between participating metal and concrete structure and the containment atmosphere. These regions are coupled by the conjugated convective - conductive

process.

6. Not all of the available experimental information has been consistently used for code verification purposes yet. This is especially true for the Battelle multi-compartment experiments /6, 7/.

From the aforementioned overview of past experiments the following types of experiments deem recommendable:

1. H_2-distribution tests for accident typical thermodynamic and fluiddynamic conditions in a large-scale mulit-compartment geometry with realistic surface-to-volume ratio and metal/concrete volume/surface ratios.

2. Experiments to evaluate the interaction between H_2-distribution and combustion for the determination of flame acceleration.

3. Experiments to evaluate in interaction between H_2-distribution and aerosol distribution.

The main objectives of the proposed experiments should be to determine the dependence of the H_2-distribution upon the following major parameters:

** H_2-release rate
** Initial temperature distributions within the overall containment prior to the H_2-release
** Arrangement of multi-compartment geometry (loop, closed end, partly blocked)
** Effect of multiple sequential steam and H_2-releases
** Effect of engineered safety features.

The HDR-facility as shown to scale in Fig. 2 in comparison with the Battelle Model Containment and a German PWR satisfies most of the requirements for hydrogen distribution experiments because with a net free volume of 11 300 m^3 it features a volumetric scaling factor of 5 compared to a prototypical German large-dry containment.

As becomes apparent from Fig. 2, the HDR-facility has a multi-compartment geometry (72 subcompartments) with a large amount of steel structures and a very large dome with a volume of about 5000 m^3. Furthermore the surface-to-volume ratio and the overall height are almost identical to the values of a prototypical plant.

It is evident from Fig. 2 that hydrogen distribution and combustion experiments in the HDR-facility would mean a large step

forward in terms of scale-up and with respect to close to realistic conditions as compared to the previous experiments in much smaller and simpler facilities.

2. OBJECTIVES AND EXPERIMENTAL PROCEDURES FOR THE HYDROGEN TEST SERIES E11 AND E12 DURING THE HDR-SAFETY PROGRAM PHASE III

By recognizing that the emphasis in containment research is shifting from DBA-oriented research towards containment issues related to severe core accidents and mitigation in recent years, experiments in the HDR containment slowly but steadily moved in the same direction. For instance with reference to Fig. 3 already for the experiments V21.1 and V43 of Phase I, the thermohydraulic conditions inside the containment were followed up to 20 hours. These large break (in terms of HDR-piping 350 - 450 mm Ø) water- and steam blowdown scenarios were supplemented by the two small break experiments, T30.4 and T31.6, with different break cross-sectional areas performed during Phase II of the HDR Safety Program. Again, the thermohydraulic containment conditions were measured up to 20 hours into the transients. A detailed account of the various long-term experiments and their difference is provided in /8/. This report also summarizes the comparisons between experimental data and first demonstration computations with the codes CONTAIN and COBR-NC.

Also, from Fig. 3 it becomes apparent that the last experiment performed in Phase II, T31.5, represents a connecting link between the research objectives of Project HDR for Phase II and those of the present Phase III.

Phase III of the HDR Safety Program complies with the special needs existing for experimental data on hydrogen distribution, mixing and combustion in a large-scaled facility with multi-compartment geometry and multiple steam- and H_2-injections. Therefore, the first Test Group, E11, which consists of 5 experiments will examine the phenomena of H_2-distribution under a variety of geometric and thermodynamic conditions. All five experiments will be performed "en bloc" between end of March and the end of July 1989.

Fig. 4 and 5 present some details about two of the five experiments, namely E11.2 and E11.5, respectively. Whereas the former one examines the small break scenario, the latter studies the impact of a large break thermodynamic environment. It is worthmentioning that during experiment E11.2 additional steam will be injected at a lower position in the containment in order to examine potential destabilization of a possibly stratified atmosphere. Furthermore, both external and internal spray systems will be initiated during specific phases of the experiment.

Whereas the original system is used for the internal spray, a new one is being installed in the annular gap between steel shell and secondary concrete containment in order to spray the external top of the former.

As can be seen from Fig. 5, five sequential steam injections,one with combined H_2-injection are planned during the course of this experiment. Furthermore, a large energy source is planned to be installed in order to supply additional energy into the containment atmosphere together with a second H_2-injection phase. In the aftermath it is anticipated to examine the behavior of the boiling sump. E11.5 will be concluded by virtue of a depressurization procedure through filter venting.

It is believed that all five experiments /9/ will generate a broad data base for computer code validation and verification efforts for a number of most interesting thermodynamic and thermal-hydraulic containment conditions.

After finishing and evaluating the mixing experiments as described above, Test Group, E12, consisting of five H_2-deflagration experiments are planned to be performed in October - November of 1990 and May - June of 1991.

Fig. 6 and 7 give an overview of two of the five tests, namely, experiments E12.3 and E12.4. Whereas experiment E12.3 is planned to examine the H_2-deflagration phenomena in the vertical multi-compartment HDR-geometry with multiple H_2-releases and steam injections as well as sequential glow plug ignitions at the top and bottom of containment as well as within the dead-end subcompartment, experiment E12.4 is supposed to examine the H_2-deflagration in a horizontal multi-compartment geometry. For E12.3, four consecutive H_2-release and steam injection phases are planned together with three ignitions. Recombiners will be installed in the ventilation system and the experiment concluded with a depressurization procedure by virtue of filter venting. In case of experiemnt E12.4 no recombiners will be used.

In order to reliably ensure the integrity of the HDR-facility, details for Test Group E12 will be specified upon the outcome of H_2-deflagration and DDT experiments performed by Batatelle in the Batttelle Model Containment over the next year and the associated computer code verification efforts.

3. OBJECTIVES OF THE CONNECTING LINK EXPERIMENT T31.5

The foremost objective of experiment T31.5 was to establish the data base for the International Standard Problem No. 23 (ISP 23) on issues related to DBA-oriented containment research and

associated computer code verification efforts. In this capacity, T31.5, stood at the very end of the typical containment blowdown test series of Phase I and II of the HDR-Safety Program as indicated in Fig. 3. It is hoped that ISP 23 will resolve all issues with respect to thermal-hydraulic short- and mid-term containment behavior which surfaced since containment experiments were performed at the HDR-facility. To reach this goal of issue resolution great efforts were put into the application of advanced instrumentation for this experiments as well as into the improvements of models implemented into the computer code. Beyond the scope of ISP, however, experiment T31.5 had the important mission of providing the important link between past and future containment research activities by the Project HDR.

In this new capacity, the objectives of T31.5 as a preliminary and scoping experiment with respect to hydrogen distribution were to:

1. provide consistant thermodynamic and thermal-hydraulic initial- and boundary conditions throughout the containment atmosphere prior to the injection of steam and hydrogen

2. test the availability and functionability of a HDR-external steam source being supplied by a nearly coal-fired power station

3. test the feasibility of the designed H_2/H_e-injection system under realistic containment atmosphere condition

4. prove the feasibility and functionability of the continuous, on-line hydrogen concentration measurement system

5. provide consistent sets of atmospheric, inside- and outside steel shell temperatures to follow the transient course of the stratification pattern

6. prove the applicability of newly designed steam/air concentration devices for long-term operation

7. prove the applicability of heat transfer blocks and the associated evaluation procedure of the solution of the inverse heat conduction problem for long-term operation

8. obtain a first set of temporal hydrogen concentration profiles along the major HDR-flow paths with a reduced number of sensors

9. provide a first basis of long-term (20 h) thermohydraulic and H_2-concentration data for code validation purposes (PHDR-H_2 Benchmark case)

3.1 HDR-Facility

The HDR-containment (11.300 m^3 volume) consists of a steel shell with a 60 m height and a diameter of 20 m. This steel shell is surrounded by a secondary concrete shell which is separated by the former by an annular gap. Fig. 8 gives two vertical cross-sections through the HDR-Facility. The containment is subdivided into 62 subcomparments of different forms and sizes by concrete partition walls. A horizontal cross-section at + 17.55 m through the facility is shown in Fig. 9 which indicates the rather complex shape and large size of the break subcompartment R 1.704. A vertical cut of that subcompartment in the plane 00 - 180° is depicted on the left side of Fig. 8 with the blowdown pipe for ISP 23 pointing upward.

The break compartment is connected to the rest of the containment by vent flow openings. The primary flow paths connect the break subcompartment with two long vertical flow channels with the upper dome which has a volume of 5000 m^3. The flow channels are termed spiral stair case (270°) and stair case (90°) in what follows and are clearly visible on the right side of Fig. 8.

According to the vent openings and associated flow resistances it has to be expected that the flows will preferentially exit into the spiral stair case.

Altogether, the subcompartments are interconnected by about two hundred vent openings.

With the aim to supply best-estimate input for computer codes - data concerning the geometry of the structural material in the containment as well as the overflow openings - a hitherto unique effort was made to measure and document these data for the HDR containment. These data were organized into a computerized data bank which allows to automatically deduce various kinds of computer models with respect to node numbers. By recognizing the need for additional details further efforts were put into the data bank which now allows the setup of models accounting for all subcompartments with their details. Beyond that, additional efforts were devoted towards the assistance of modeling by finite-difference codes like HMS which need even more local details for their simulations.

The HDR containment test instrumentation consists of about 230 thermal-hydraulic and 80 structural measuring channels for both short-term and long-term measurements. It also includes special measuring systems for heat transfer, steam/air composition and vent mass flow and velocities through the major vents out of the break subcompartment. From the vent measurement system, the diameter of passing liquid droplets can be inferred. Thus, the instrumentation applied in the HDR-facility is one major step forward as compared to that which had been applied previously for the Battelle-Containment experiments.

Recognizing the need for measuring low flow velocities over long periods of time and accounting for the possibility of flow reversals four pairs of special thermocouple devices were applied to deduce flow velocities by correlation analysis of the fluctuating temperature signals. This measurement and evaluation procedure was successfully tested during the previous HDR-experiment T 31.6 (see Fig. 3) and validated against the ITI "wind-mill"-type sensors applied later in the LACE-experiment.

Furthermore, 16 newly designed, much lighter and simpler steam-air concentration measurement devices were applied for the first time during experiment T 31.5, which supplemented those of the older design, the latter being primarily installed in the break subcompartment and its major vents, respectively.

Details of the break subcompartment R 1.704 are shown in Fig. 10 with the top figure depicting the isometry of the blowdown pipe penetrating and pointing upwards into the compartment. The bottom figure shows in a vertical cut through this break subcompartment the arrangement of the piping with diffusor for the additional sequential steam and H_2-/He-mixture injections. As can be seen the diffusor is directly located in the vicinity of the blowdown pipe.

With the major flow paths in the spiral and stair cases emphasis in applying major parts of the instrumentation was put into and along these flow channels and naturally into the upper dome region. Figs. 11 and 12 reflect the density of instrumentation in terms of H_2-concentration sensors and thermocouples measuring the containment atmosphere as well as inside and outside steel shell temperatures, respectively. More details and the other types of instrumentation are listed in the experimental test report /10/.

Details of measurement principles, associated evaluation procedures of other advanced sensors together with results are provided in the supplemental report /11/.

3.2 Experimental Procedure

Once a realistic temperature gradient was established in the containment as initial and boundary condition resulting from the large break LOCA-experiment of ISP 23, it was decided to initiate the steam injection 20 min after blowdown begin for 15 min. Immediately after shut-off of the steam injection, the H_2/He-mixture injection was begun, lasting about 12 min. The mixture used consisted of 85 % He and 15 % H_2. The blowdown, steam and H_2/He-mixture mass flow rates are shown in Figs. 13 and 14, respectively. These curves together with constant or tabulated values for the enthalpies were provided to the code users in order to perform a blind post-test computation.

3.3 Experimental Results

In the following, Figs. 15 through 18, present the experimental results in an unique format. With reference to the dense sensors applications shown in Figs. 11 and 12 continuously bright coloured space-time evolution maps (oral presentation) for temperature and H_2-concentration were produced separately for the two major flow paths, respectively. These figures, unfortunately only reproducible in grey pattern for printing purposes, contain in a very much condensed form all of the major informations and experimental results. The figures at the top present the quantities along the height of the spiral stair case, whereas the bottom figures show the same physical quantity along the stair case. In this way, Fig. 15 summarizes the total temperature histories in both flow paths for the duration of 1000 min.

As can be inferred from Fig. 15, a temperature stratification pattern develops in both flow paths with some differences in local detail. The highest temperatures are concentrated in the spiral stair case more closely to the break subcompartment, whereas in the stair case this region extends over a larger region of the height. Clearly visible are the rather fast temperature decays after the blowdown ends prior to the steam release. Yet, a sizeable temperature gradient of at least 50 °C remains between lower and upper parts of the containment. However, with some local exceptions, the temperatures are rather homogeneous from at least the level of break subcompartment on upwards. It is interesting to note, that the additional steam injection for over 15 min barely disturbs the homogeneity. The gas mixture injection starting at 35 min into the transients leads to a gradual cooling of the containment atmosphere. The stratifications in both flow paths diminish gradually with time with the exception of a localized region in the stair case at the level of +26 m where higher temperatures persist over the total of 20 hours measurement time.

Fig. 16 shows the inside and outside steel shell temperatures along the spiral stair case. Interesting local phenomena are observable in the dome area at early times and and it deams by visual inspection that the outside temperature stays at higher temperature for a longer period of time, especially in the upper containment region.

Changing the time scale, Fig. 17 shows the space-time evolution of the H_2-concentration for spiral and stair case flow channels, respectively. The H_2/He-injection starts at 35 min into the transient. Highest concentrations in both flow channels start to build up with appreciable time delay and reach their maximum at the end of the injection period after 12 min. Also worthmentioning is the fact that lower levels of the containment are affected, although by a lesser degree - obviously by virtue of diffusion. The extent to which lower levels are penetrated by th hydrogen is quite different in both flow paths. Also, the stair case region shows some distinct spatial changes in H_2-concentration with a region of higher concentration persisting

underneath a region of lower concentration. By all accounts, a distinct, large H_2-concentration gradient exists in both flow paths at 60 min.

Fig. 18 presents the H_2-concentration distribution over a period of 1000 min. Some amazing results are observable. First, the highest concentration, persisting in the dome area, remains undiluted for over 300 min. Then, first gradually, somewhat later rather abruptly a substantial concentration decrease starts, obviously transporting hydrogen to lower levels in the containment, resulting in higher concentrations there, than in the upper regions. This holds for the spiral stair case. Although, there is clearly a homogenization throughout that region visible, even at the end of measurement time concentrations are slightly higher at lower than upper regions. This redistribution phenomenon is also clearly observable in the stair case space. Also, starting at 350 min, H_2-concentration decreases rather abruptly in the dome space and the hydrogen is transported primarily into the middle section of the containment where it slowly homogenizes. But differently to the behavior in the spiral stair case space, lower sections stay at lower concentrations. However, at 650 min into the transient a noticeable H_2-enrichment starts at the lowest containment level spreading with time.

Besides of these patterns described above, globally and with ongoing time homogenization of the gas concentration from a clearly stratified situation is the most remarkable result of this preliminary and scoping HDR-experiment T 31.5 in complex, multi-compartment geometry. Several convective and diffusive transport and mixing processes contribute to this global effect.

Finally, it should be pointed out that the results discussed in the foregoing evolve from a typical representative HDR large break LOCA-scenario. Other scenarios, especially those for small break scenario may lead to quite different patterns. This will be the subject of the H_2-distribution test group E 11.1-E 11.5 in the first half of 1989.

Finally, Fig. 19 being a duplicate of Fig. 1 but now with the addition of the point as specified by T 31.5 clearly indicates that this scoping experiment reached all objectives set out as a result of the review of past experiments. This confirms that the forthcoming test series will be of special value and interest, with T 31.5 as a scoping beginning.

3.4 Computer Code Analyses

Blind post-test predictions were performed by a variety of national and international institutions using a broad spectrum of different computer codes for hydrogen distribution analysis. Participating codes were: COBRA-NC, CONTAIN, HECTR, HMS, MELCOR, RALOC and WAVCO covering the whole spectrum of internationally known models for two-phase flow and gas transport in nuclear

reactor containments. Nodalizations ranged from 16 up to 7031 computational cells (lumps) and the problem times covered were 1 hour up to 20 hours.

No computational results will be presented here before the meeting of all of the participants took place. This meeting is scheduled now for the middle of January 1989 putting all participating institutions at the same level of informations and interpreting evaluations. The individual and overall comparisons will be certainly published thereafter and are of special interest because the HDR-constituted a "virgin" facility of large-scale size with respect to H_2-distribution issues. Accordingly, the learning effects from this comparison will certainly benefit the predictive capabilities for the forthcoming HDR test group.

Acknowledgements

This work has been financially fully supported by the German Federal Ministry of Research and Technology (BMFT) within the framework of Phase II of the Safety Program of Project HDR at KfK, Karlsruhe, FRG. The excellent cooperation by the various institutions is greatly appreciated. The dedicated efforts undertaken by the HDR- and PHDR-staffs are highly regarded.

REFERENCES

/1/ Fineschi, F. et al.: Mixing of Hydrogen in a Closed Containment; Instituto di Impianti Nucleari di Pisa, Report RP 296 (77), Pisa, 1977

/2/ Olivari, D.; Thiry, F.: Helium Dispersal in the Model of the Drywell of the Caorso Power Plant - Adiabatic Tests; Report 131, von Karman Institute for Fluid Dynamics Rhode Saint Genese/Belgien, Juni 1977

/3/ Olivari, D.; Thiry, F.: Helium Dispersal in the Model of the Drywell of the Caorso Power Plant - Phase II; Report 142, von Karman Institute for Fluid Dynamics, Rhode Saint Genese/Belgien, April 1978

/4/ Bloom, G.R. et al.: Hydrogen Mixing and Distribution in Containment Atmosphers; Report NP-2669 for the Electric Power Research Institute, Palo Alto, Ca./USA, March 1983

/5/ Bloom, G.R., Postma, A.K.: Hydrogen Mixing in Compartments With a High Velocity Source; Proc. International Meeting on Light Water Reactor Severe Accident Evaluation, Vol 1, Cambridge, MA./USA, September 1983

/6/ Langer, G.; Jenior, R.; Wentlandt, H.G.: Experimentelle Untersuchung der Wasserstoffverteilung im Containment eines LWR nach einem Kühlmittelverlust-Störfall; Bericht des Battelle-Instituts Frankfurt zum Vorhaben 246 des Bundesministeriums für Forschung und Technologie, Mai 1979

/7/ Langer, G.: Experimentelle Untersuchung der Wasserstoffverteilung in einem Modellcontainment - Grundlagenversuche Phase III; Bericht des Battelle-Instituts zum Vorhaben 150.375 des Bundesministeriums für Forschung und Technologie, Juli 1982

/8/ Schall, M.; Wolf, L.; Valencia, L.: Pressurization of a Reactor Containment During and After Blowdown-Longterm Behavior (In German), Quick Look Report, Test Group CON, Experiments V21.1, V43, T30.4, T31.6, Technical Report PHDR 72-87, Sept. 1987

/9/ Katzenmeimer, G.; Wolf, L.: Overview of the HDR Safety Program Phase III (1988 - 1991), PHDR Working Report 05.41/88, June 1988 (available upon request from KfK/PHDR-HT)

/10/ Wenzel, H.-H.; Grimm, R.; Löhr, L.: Experimental Test Report: Blowdown and H_2-Distribution Experiment, Test Group CON, Test T 31.5, (In German), PHDR-Working Report No. 3.520/88, Dec. 1987

/11/ Jansen, Bader, Lenz: Supplement to Experimental Test Report, (In German), PHDR-Working Report No. 3.524/88, Feb. 1988

TABLE I: SUMMARY OF PAST HYDROGEN DISTRIBUTION EXPERIMENTS, MAJOR CHARACTERISTICS AND RESULTS

Institution / Test Data	Università di Pisa Italy	von Karman Institute Belgium	Battelle - Institut Germany	Hanford Engineering Development Lab./USA
Objective	H_2-distribution in a single compartment geometry with DBA-typical H_2-release rates.	H_2-distribution in a model of a BWR-Mark-II drywell with DBA-typical release rates. Efficiacy of mixing fans.	Invesigation of dominant parameters on H_2-distribution in a multi-compartment geometry with H_2-release rates somewhat higher than DBA-typical. Efficiacy of mixing devices.	H_2-distribution in a single-compartment geometry simulating the lower compartment of an Ice-condenser PWR-containment under DCA-typical conditions.
Sponsor	CNEN (Cominato Nazionale per l'Energia Nucleare)	AMN	BMFT (Bundesministerium für Forschung und Technologie).	EPRI (Electric Power Research Institute)
Reference	/1/	/2,3/	/6,7/	/4,5/
Program Terminated	1977	1978	1982	1982
Test facility	cylindr. steel vessel; D = 4,0 m; H = 8 m; V = 100 m^3, insulated, large area H_2-source	conical plexiglass vessel; V = 2 m^3, H = 2 m, small area H_2-source	cylindr. concrete vessel, V = 240 m^3, D = 8 m, H = 6 m, large area H_2-source	cylindr. steel vessel, D = 7,6 m; H = 4,7 m V = 150 m^3, insulated, small area H_2-source
Test conditions and parameters				
- pressure /bar/	0,1	0,1	0,1	0,1
- temperature gradient	isothermal; also positive ($T_{lower} > T_{upper}$)	isothermal; also positive ($T_{lower} > T_{upper}$)	isothermal, also negative ($T_{upper} > T_{lower}$)	quasi-isothermal
- temperature level (°C)	16 - 85	20 - 60	14 - 53	20 - 94
- steam content	no	no	φ max = 90 %	yes (saturation)
- state of atmosphere	calm	calm; also fan	calm; also fan	highly turbulent
- H_2-release rate[a] (1/h)	0,0009	0,004	0,008 - 0,03	up to 2,24
- gas released	H_2	He	H_2, also He	He, also H_2
- exiting velocity of gas (m/s)	0,02	not known	0,01	200
Test results	H_2-distribution homogeneous above the source, minor fluctuations near the source	H_2-distribution homogeneous, little concentration increase near the source	- isothermal tests: H_2-distribution homogen. - negative temp. gradient: ΔC up to 2,6 % Vol. and $\Delta C \sim \nabla_{H_2}$	nearly homogeneous H_2-distribution, ΔC up to 2,4 % Vol. in release compartment; ΔC up to 3,5 % Vol. between upper and lower compartment

a) release rate normalized to volume of source compartment: ∇_{H_2} / V_{SC}

TABLE II: OVERVIEW OF COMPUTER CODES USED FOR HYDROGEN DISTRIBUTION ANALYSIS

		COBRA-NC	HECTR	HMS	LIMIT	MAPHY	RALOC	TEMPEST	THETYS	WAVCO
Developed/ Used by		BPNL; BF[a] (USA/D)	SANDIA (USA)	LANL (USA)	MIT (USA)	Mitsubishi et al. (J)	GRS/SANDIA (D/USA)	BPNL (USA)	CEA (F)	KWU (D)
Type of code		FD/LP[c] multi-dimensional	LP	FD multi-dimensional	FD multi-dimensional	LP	LP	FD multi-dimensional	LP-FD	LP
Tests analyzed		BF (2- and 6-compartm.);HEDL	BF (2- and 6-compartm.);HEDL	BF (2-compartm.) HEDL	BF (2-compart.)	BF (6-compart. isothermal)	BF (2- and 6-compart.)HEDL	BF (2-compart.) HEDL	-	BF (6-compartm.) HEDL
Agreement Experiment/ Analysis		HEDL: good BF (2-comp.): good BF (6-comp.): insufficient	HEDL: good BF (2-comp.): good BF (6-comp.): insufficient	HEDL: good[d] BF: not calcul.	HEDL: not calc. BF (2-comp.): good/fair	HEDL: not calc. BF: only isotherm. tests calculated	HEDL[d]:fair/good BF (2- and 6-comp.):good	HEDL[d]; insufficient BF (2-comp.): good	-	HEDL: good BF (6-compartm.): good/fair
Application on real containments		not known	BWR-Mark-III (Grand Gulf)	BWR-Mark-III (Grand Gulf)	not known	BWR-Mark-III	BWR-Mark III (Grand Gulf) German PWR	not known	French PWR	German PWR
Shear forces		turbulent + molecular mixing length model	no	molecular	turbulent + molecular 1-parameter model	no	no	turbulent 2-parameter model	?	no
Diffusion			no	no		molecular	molecular	turbulent + molecular	?	yes
Compressible		yes	?	no	no	?	?	no	?	?
Buoyancy forces		yes	yes	yes	yes	yes	yes	yes	?	yes
Nodalisation		BF (6-comp.): 15 nodes; HEDL: 250 nodes	BF: 28 nodes HEDL: 37 nodes BWR-Mark-III: 18 nodes	HEDL: 450 nodes BWR-Mark-III: not known	BF: 50 nodes	BF: 7 nodes BWR-Mark-III: 17 nodes	BF: 44 nodes HEDL: 26 nodes German PWR: 26 nodes	BF: 200 nodes HEDL: 1056 nodes	-	BF: 10 nodes German PWR: not known

a) BF = Battelle-Institut Frankfurt
b) FD = Finite Differences
c) LP = Lumped Parameter
d) "Blind" Pre-Test Calculations

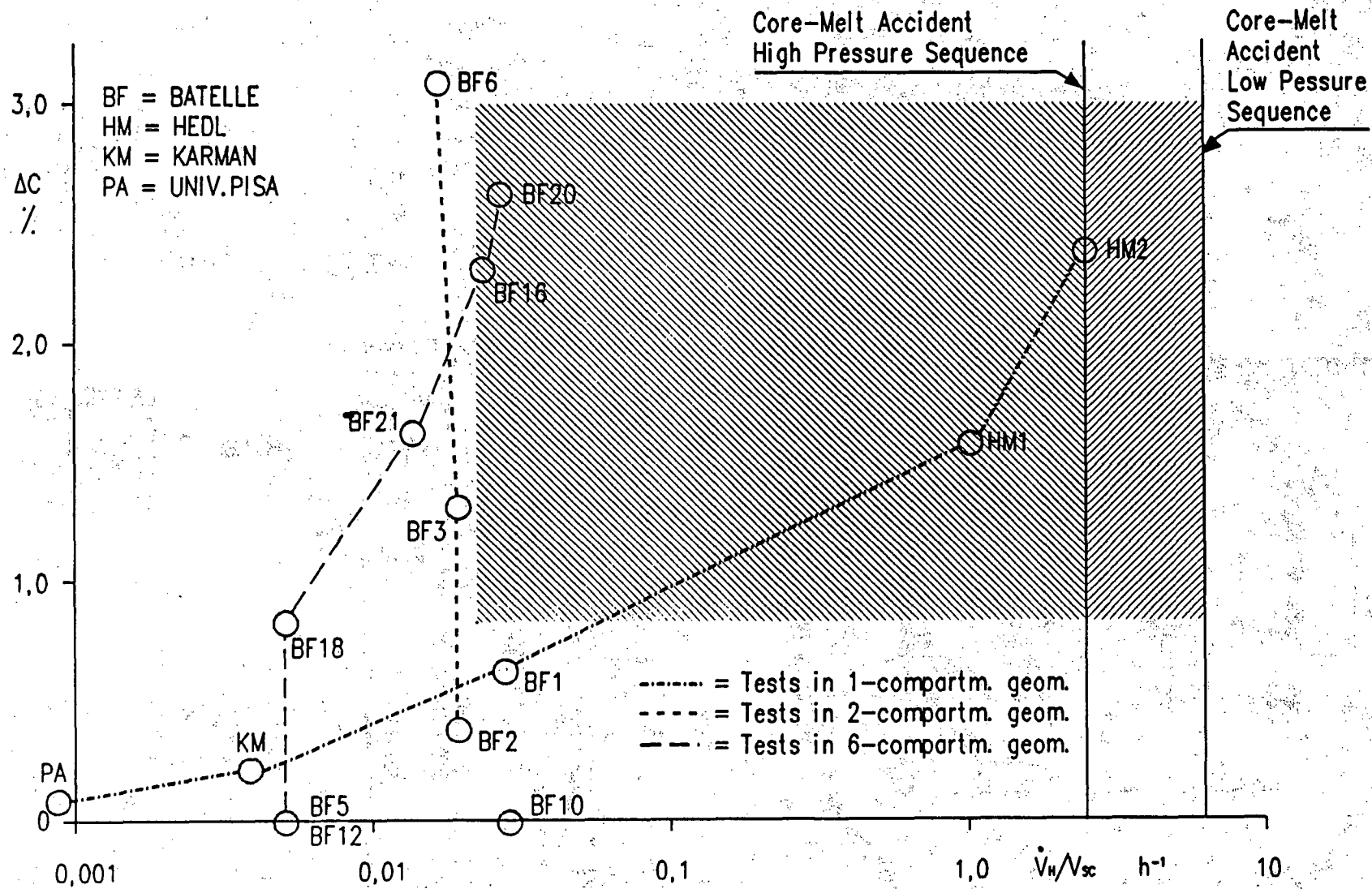
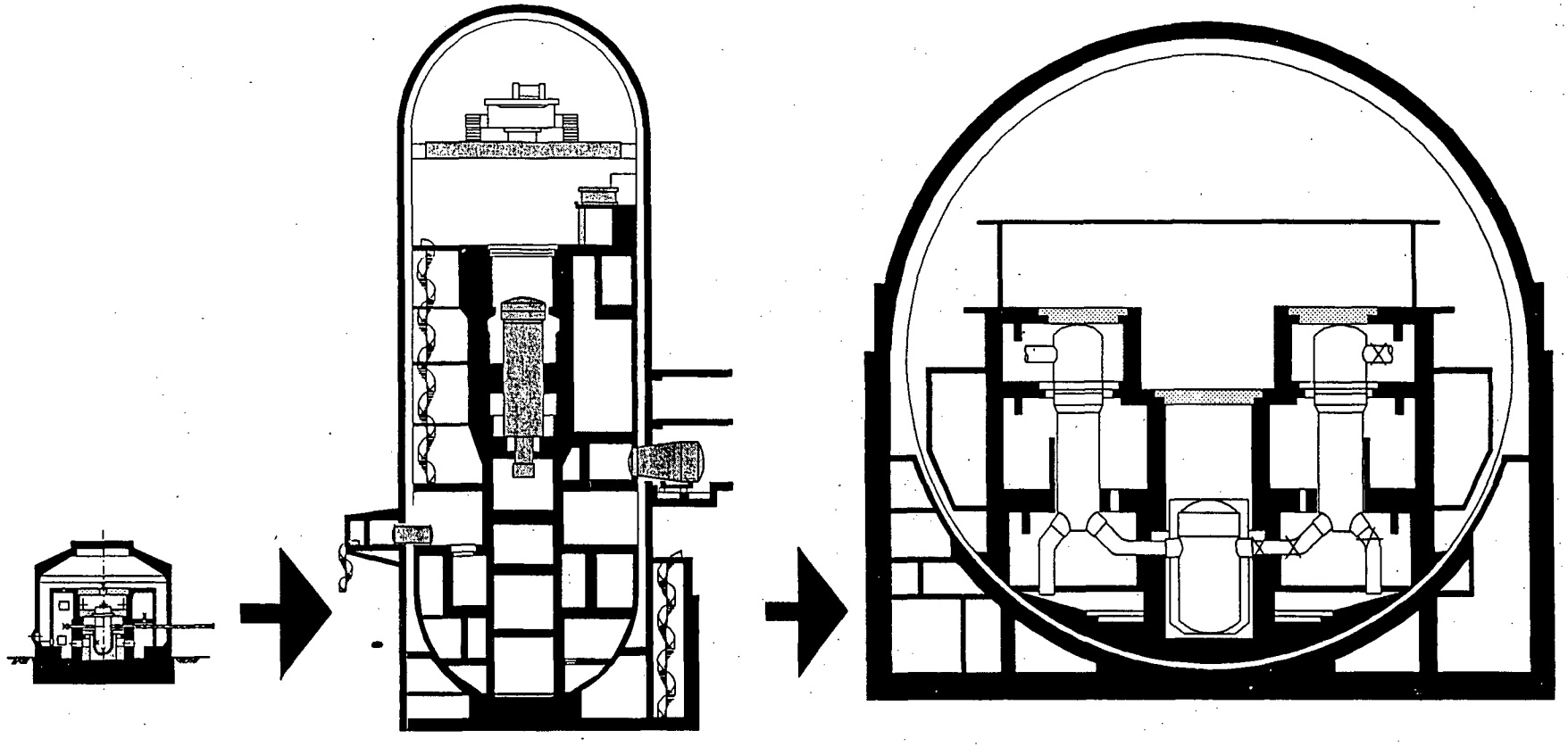


FIG. 1: OBSERVED HYDROGEN CONCENTRATION DIFFERENCES FOR PREVIOUS EXPERIMENTS



Battelle Frankfurt
Model Containment
600 m^3
Tests 1975 – 1979

HDR
facility
11300 m^3
Tests 1982 – 1987

German PWR plant
(KWU 1300 MW)
65000 m^3

FIG. 2: COMPARISON BETWEEN EXPERIMENTAL FACILITIES AND A PWR–PLANT

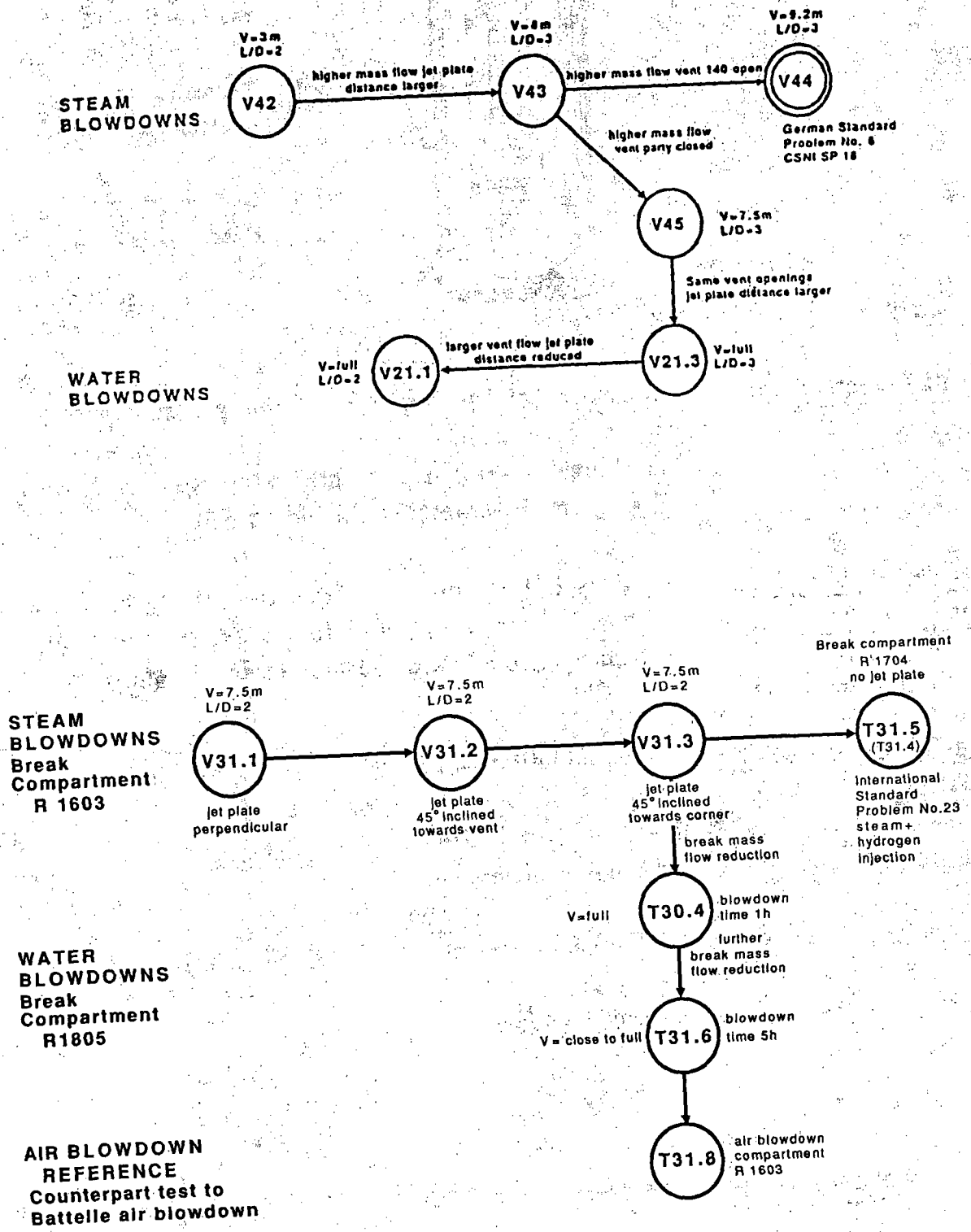
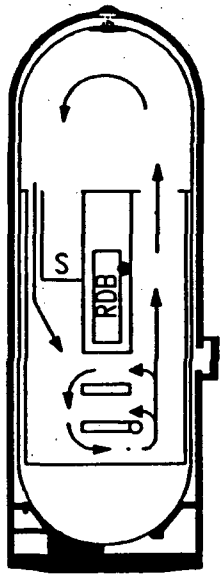


FIG. 3: EVOLUTION OF CONTAINMENT BLOWDOWN EXPERIMENTS AT HDR DURING PHASE I (TOP) AND PHASE II (BOTTOM)



- ● Position of break and injection, BS
- ○ 2. position of injection
- S Dead end room closed at its lower end

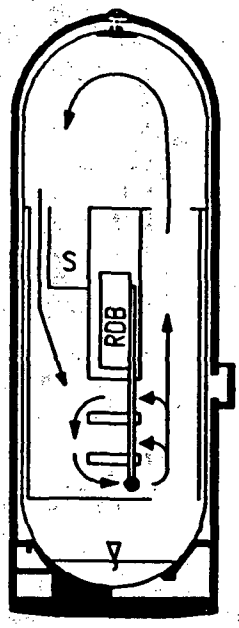
Overall Objective:	Simulation of the beginning of low-pressure path ND* of severe core accident scenarios in loop-geometry Small leak at H = +23 m; steam injection at 2. position, H = ±0 m; H_2-injection; inside spraying
Experimental Objectives (Measurements):	same as E11.1, however examination of effect of using 2. position for steam injection to examine destabilization of stratification, effect of inside spraying

Course of Experimental Procedure:

Steam injection at BS	4.5 h
steam + H_2-injection at break position	1.5 h
add. steam injection	(2. position), 3 h
natural cooldown	
inside spray	till cooldown and depressurization

KfK

FIG. 4: OBJECTIVES AND EXPERIMENTAL PROCEDURE FOR H_2-DISTRIBUTION TEST E 11.2



- Break and injection positions, BS

S Dead end compartment, closed at lower end, 1802

Overall Objective:

- Simulation of low-pressure path ND of severe core accident scenarios in loop geometry
- Large break at H = ±0 m; H_2-injections at break position, all steam injections at break position; addition of dry energy, heated sump, filter-venting

Experimental Objectives (Measurement):

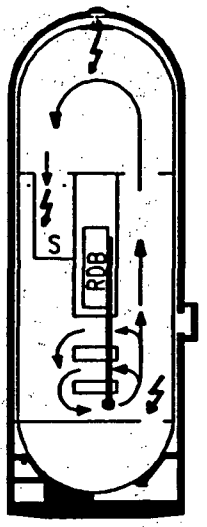
- Steam/Air distribution after large break (comparison with Test E11.4)
- Steam/Air/H_2-distributions and atmospheric saturation in long term under different conditions (comparison to E11.4)
- Saturation conditions
- Effects of mitigative filter-venting (higher initial pressure than E11.4j)

Course of Experimental Procedure:

- Blowdown	1 min
- steam injection at BS	0.3 h
- natural cooldown	1.5 h
- steam + H_2-inject. at BS	1.5 h (at break position)
- steam injection at BS	1 h
- add. dry energy + H_2 + superh. steam	7 h
- steam injection at BS	1 h
- boiling sump	1.5 h
- steam injection at BS	2 h
- filter-venting	till complete depressurization

KfK

FIG. 5: OBJECTIVES AND EXPERIMENTAL PROCEDURE FOR H_2-DISTRIBUTION TEST E 11.5



● Position of break

S Dead-end subcompartment, closed at lower end

Positions of glow plug ignition

Overall Objective:

H_2-deflagration in vertical multi-compartment geometry (no loop) with dead-end subcompartment; small leak at H = ±0 m, multiple H_2-releases and steam-injections; glow plug ignitions at top of containment dome, bottom and in dead-end-subcompartment; recombiners in ventilation system; filter-venting (with low H_2)

Experimental Objectives (Measurement):

H_2-distribution in multi-compartment geometry, pressure-temperature for deflagration (burn, flame front propagation from dead-end subcompartment (higher H_2-concentration) into containment dome (top ignition) effects of mitigative measures such as glow plug ignition, recombiners, filter-venting

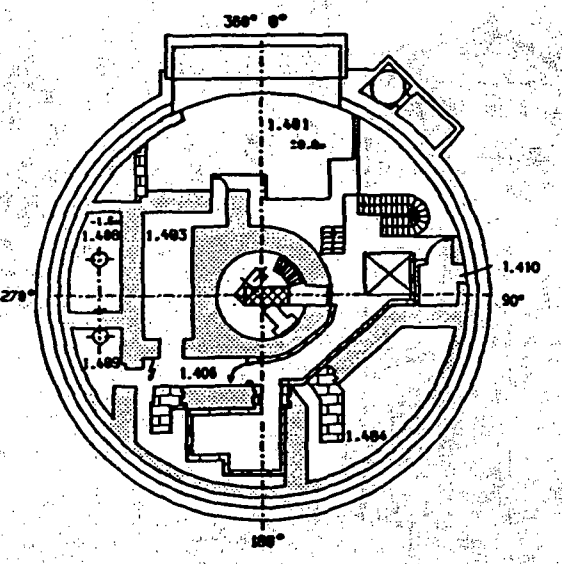
Course of Experimental Procedure:

- Blowdown/or steam injection
- 1. H_2-release with steam injection
- steam injection
- glow plug ignition (⚡)
- 2. H_2-release with steam injection
- steam injection
- glow plug ignition (⚡)
- O_2- and steam injection
- 3. H_2-release
- glow plug ignition (⚡)
- 4. H_2-release with steam injection
- recombiners in ventilation system
- filter-venting

4 h
↓
2 h
↓
2 h
↓
dead-end subcompartm.
↓
2 h
↓
2 h
↓
top of dome
↓
1 h
↓
2 h
↓
bottom
↓
2 h
↓
2 h (much H_2)
↓
till depressurization (low H_2)

KfK

FIG. 6: OBJECTIVES AND EXPERIMENTAL PROCEDURE FOR H_2-DEFLAGRATION TEST E 12.3



Overall Objectives:

H_2-deflagration in horizontal multi-compartment geometry, small leak at H = ±0; multiple K_2-and steam injections, glow plug ignition in room 1.403; filter-venting (with much H_2)

Experimental Objectives:

- Pressure- and temperature histories for H_2-deflagration
- Flame front propagation in horizontal room chain
- Effects of mitigative measures (glow plug ignition, filter-venting)

Course of Experimental Procedure:

Blowdown/or steam injection

4 h

1. H_2-release with steam injection

2 h

glow plug ignition (⚡)

bottom

2. H_2-release with steam injection

2 h

filter venting

till depressurization (much H_2)

KfK

FIG. 7: OBJECTIVES AND EXPERIMENTAL PROCEDURE FOR H_2-DEFLAGRATION TEST E 12.4

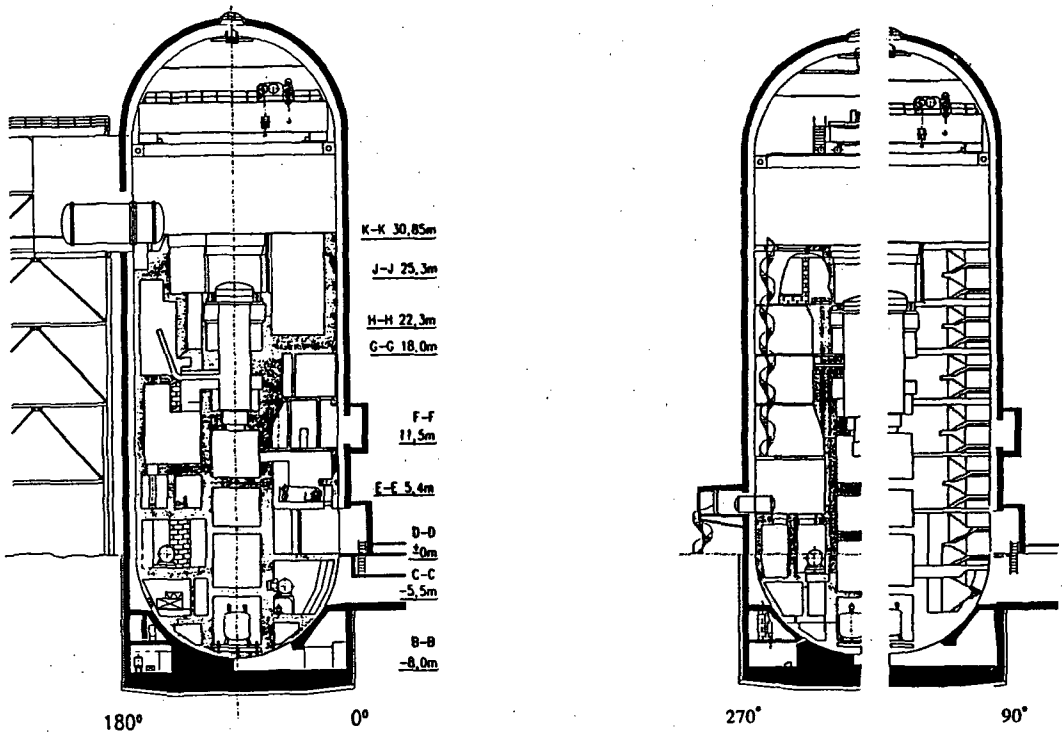


FIG. 8: VERTICAL CROSS–SECTIONS THROUGH THE HDR–FACILITY

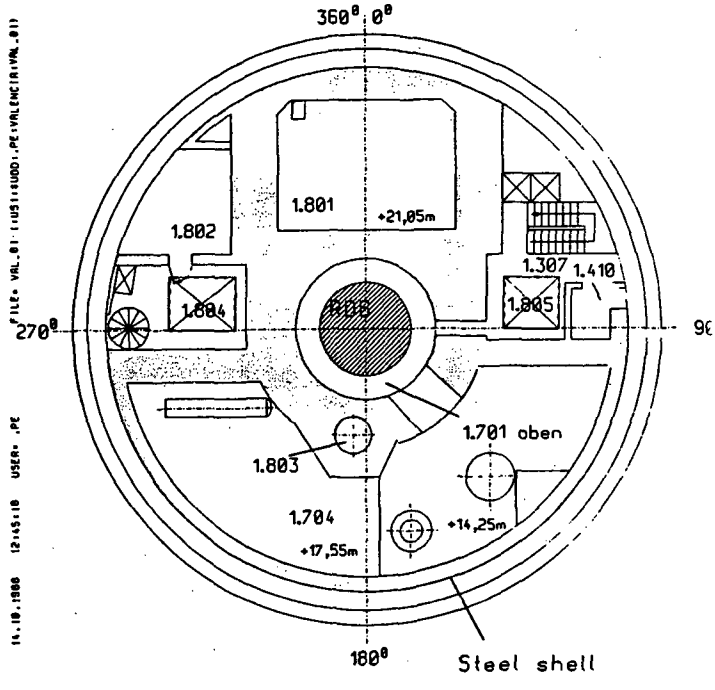


FIG. 9: HORIZONTAL CROSS–SECTION THROUGH THE HDR–FACILITY AT + 17,55 m

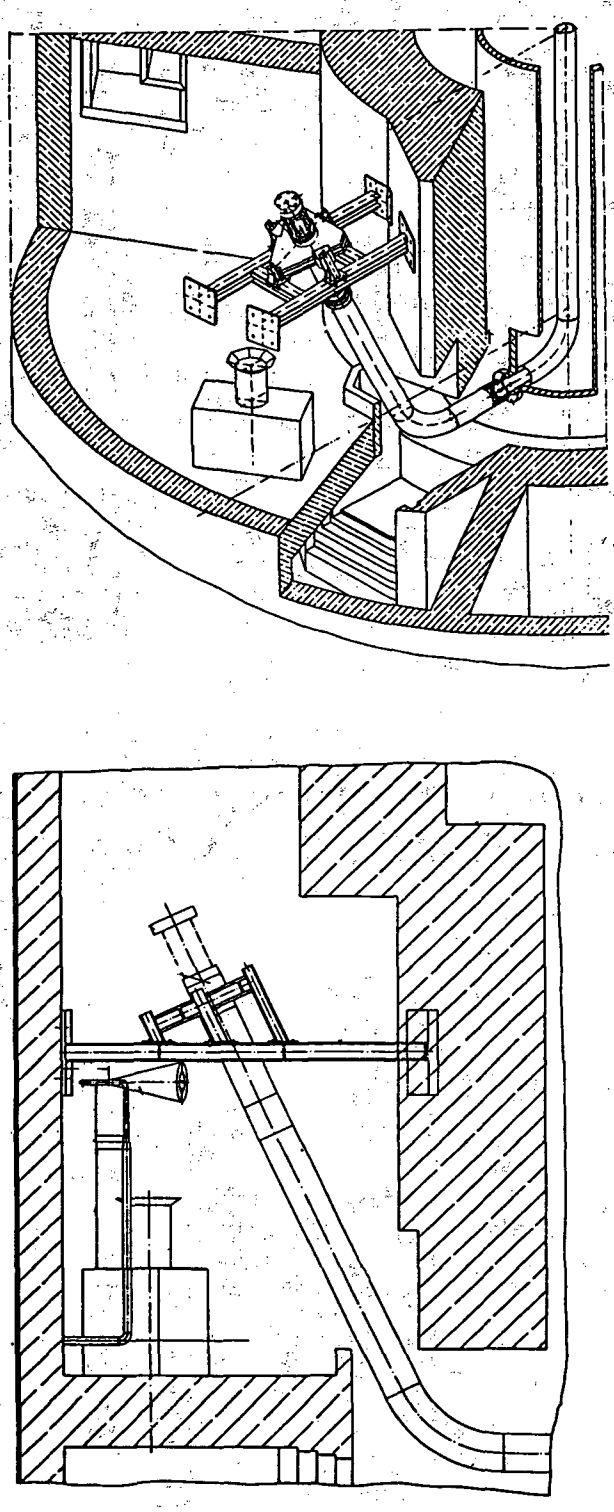


FIG. 10: ISOMETRY (TOP) AND BLOWDOWN PIPE–H_2/He–DIFFUSOR (BOTTOM) IN R 1.704

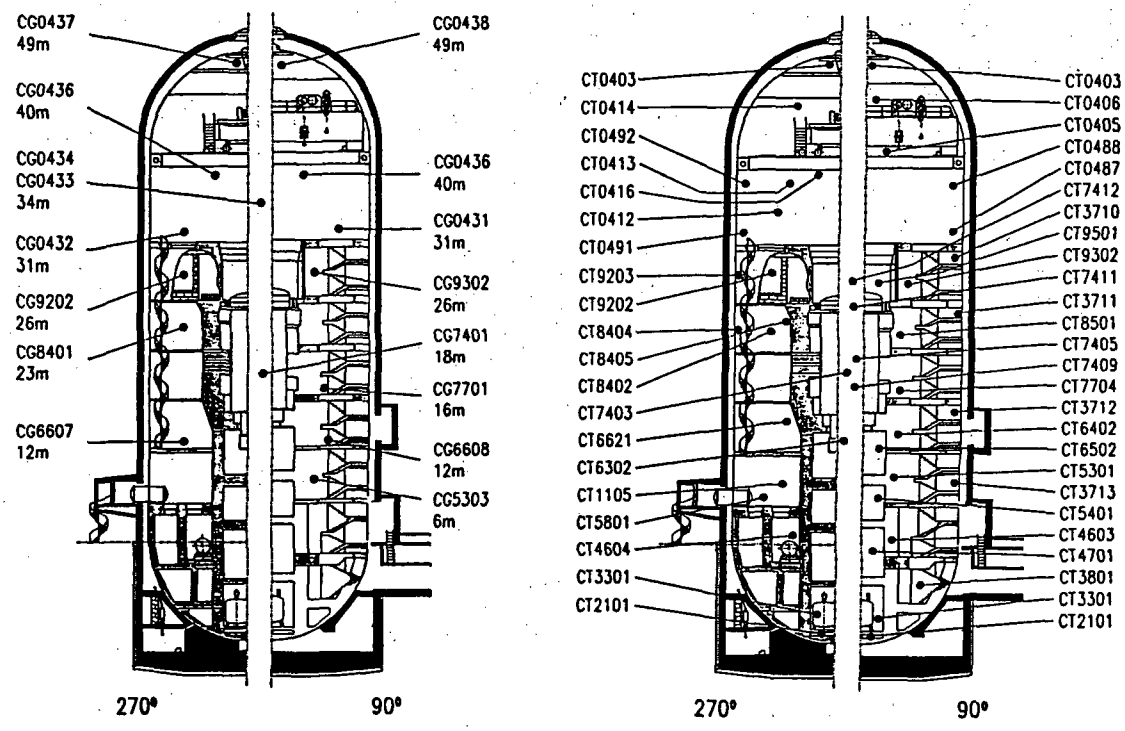


FIG. 11: POSITIONS OF H_2–SENSORS (LEFT) AND TEMPERATURE SENSORS (RIGHT) ALONG MAJOR FLOW PATHS

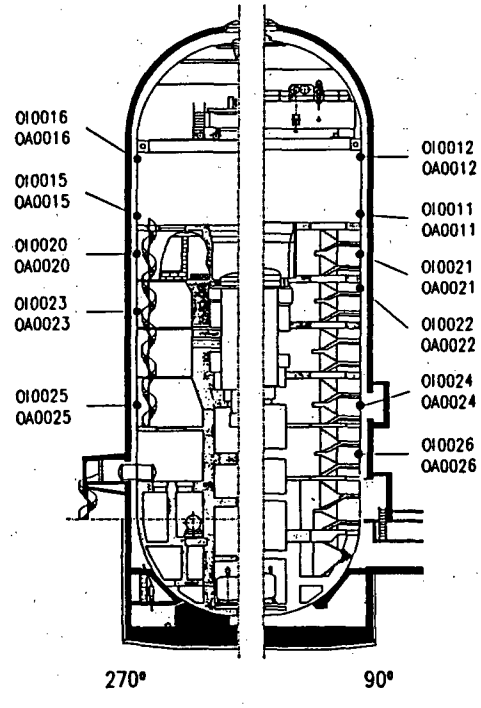


FIG. 12: POSITIONS OF INSIDE (OI) AND OUTSIDE (OA) STEEL SHELL SURFACE TEMPERATURE SENSORS

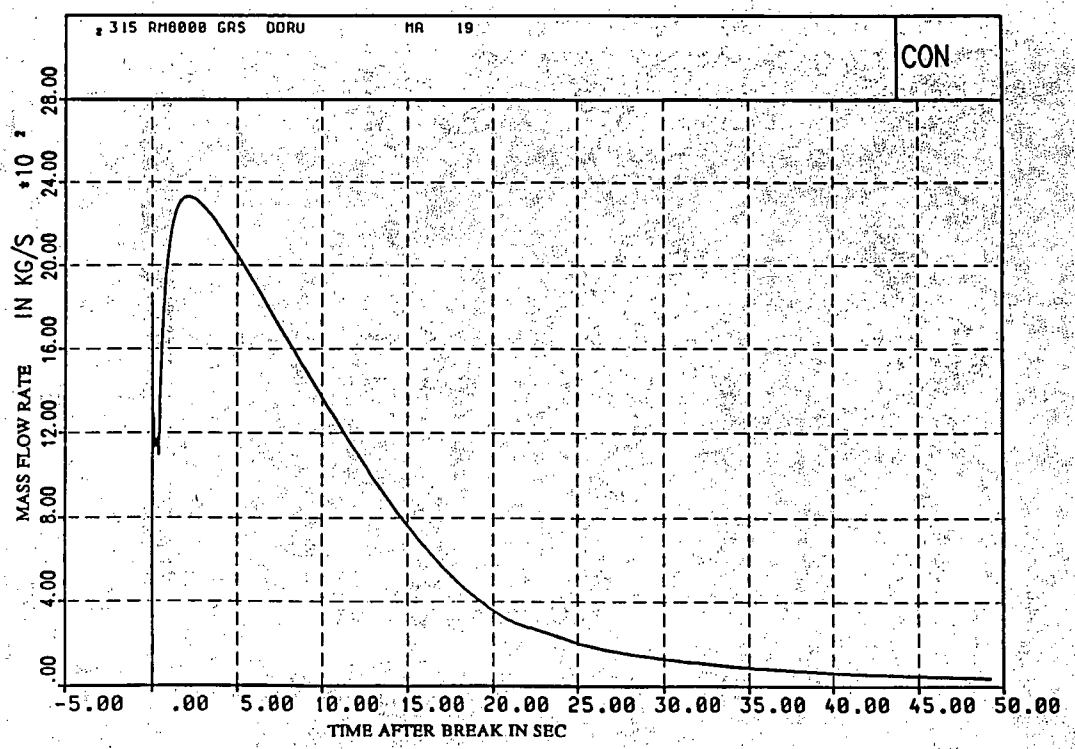


FIG. 13: BLOWDOWN MASS FLOW RATE INTO THE CONTAINMENT

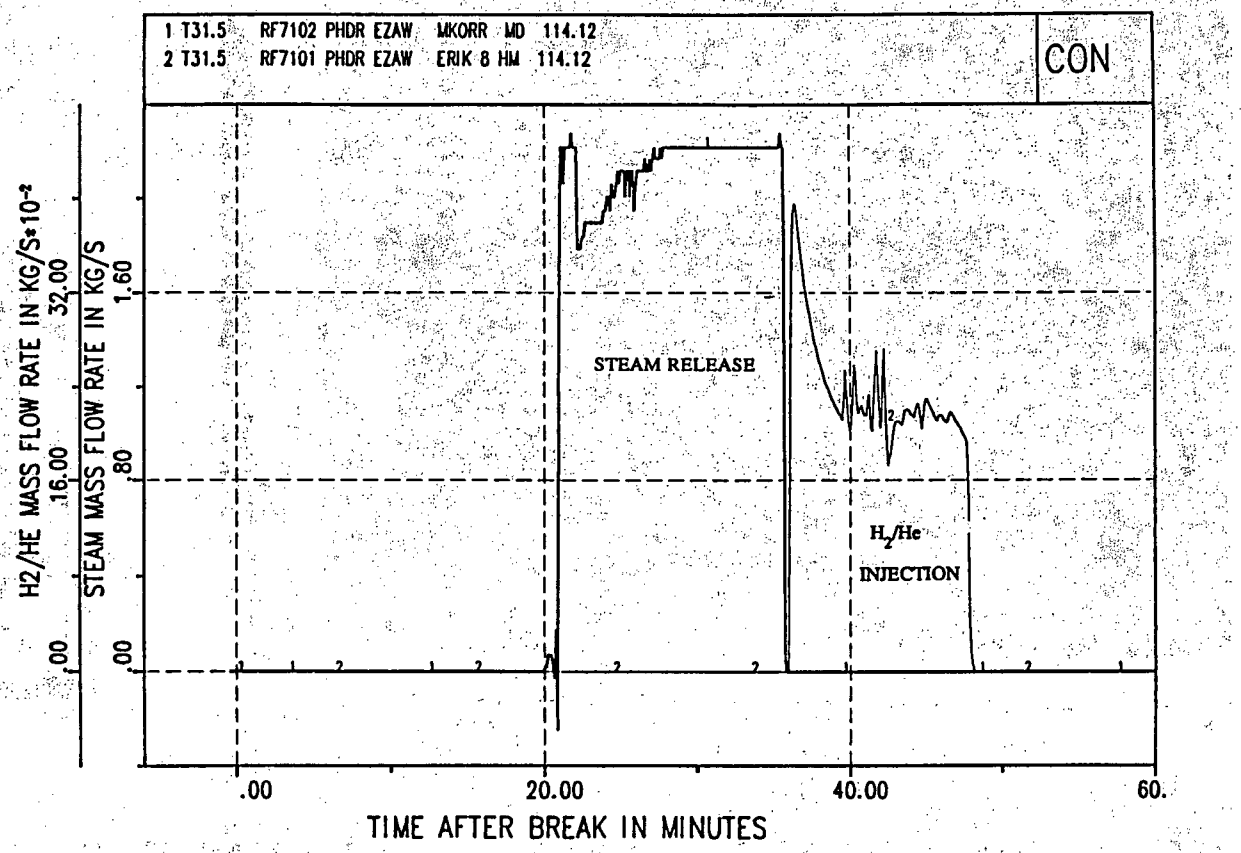
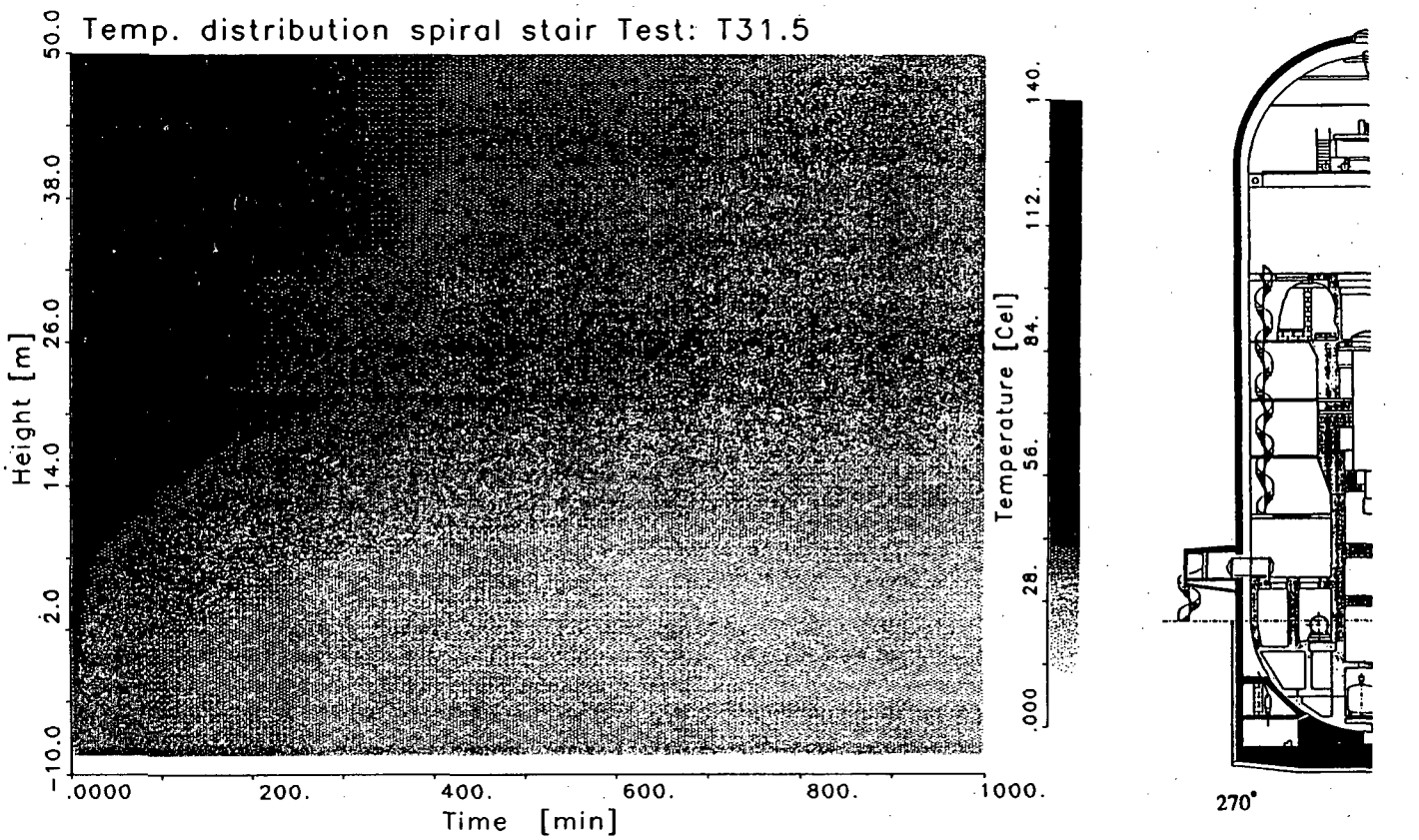


FIG. 14: SEQUENTIAL STEAM– AND H_2/He MASS FLOW RATES INTO THE CONTAINMENT



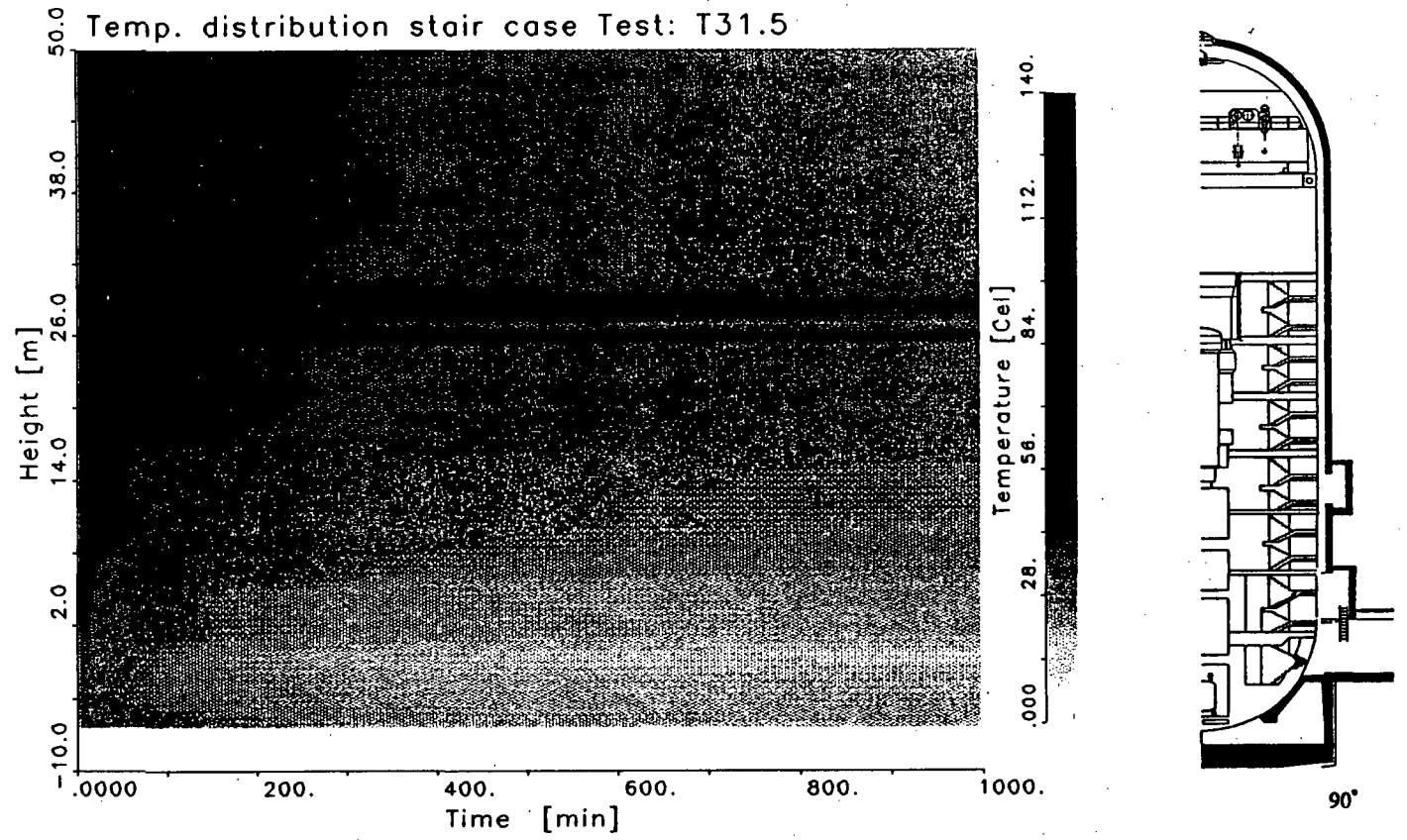


FIG. 15: SPACE–TIME EVOLUTION OF CONTAINMENT ATMOSPHERE TEMPERATURES IN SPIRAL (TOP) AND STAIR CASE (BOTTOM)

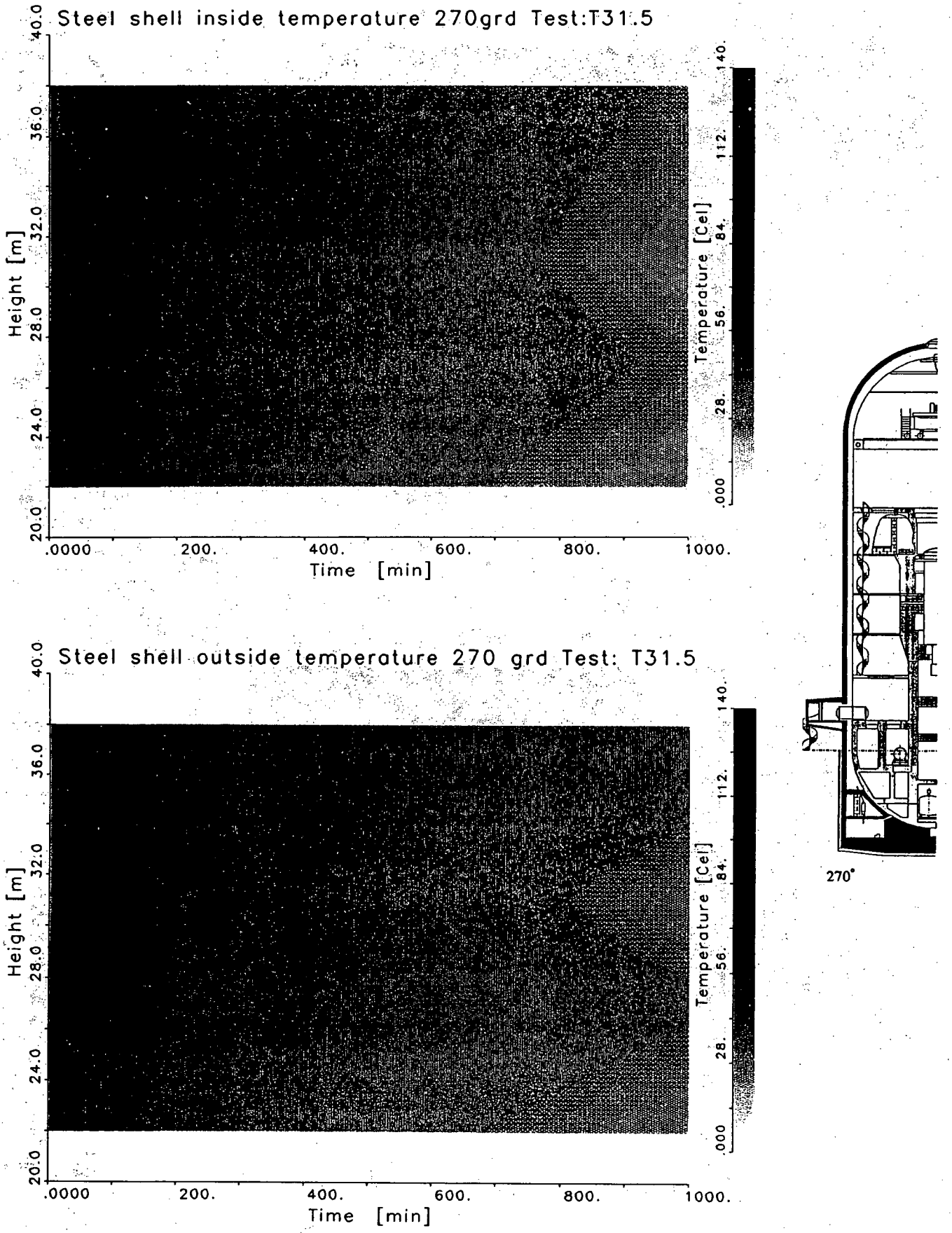


FIG. 16: SPACE–TIME EVOLUTION OF STEEL SHELL INSIDE (TOP) AND OUTSIDE (BOTTOM) SURFACE TEMPERATURES AT SPIRAL STAIR CASE (270°)

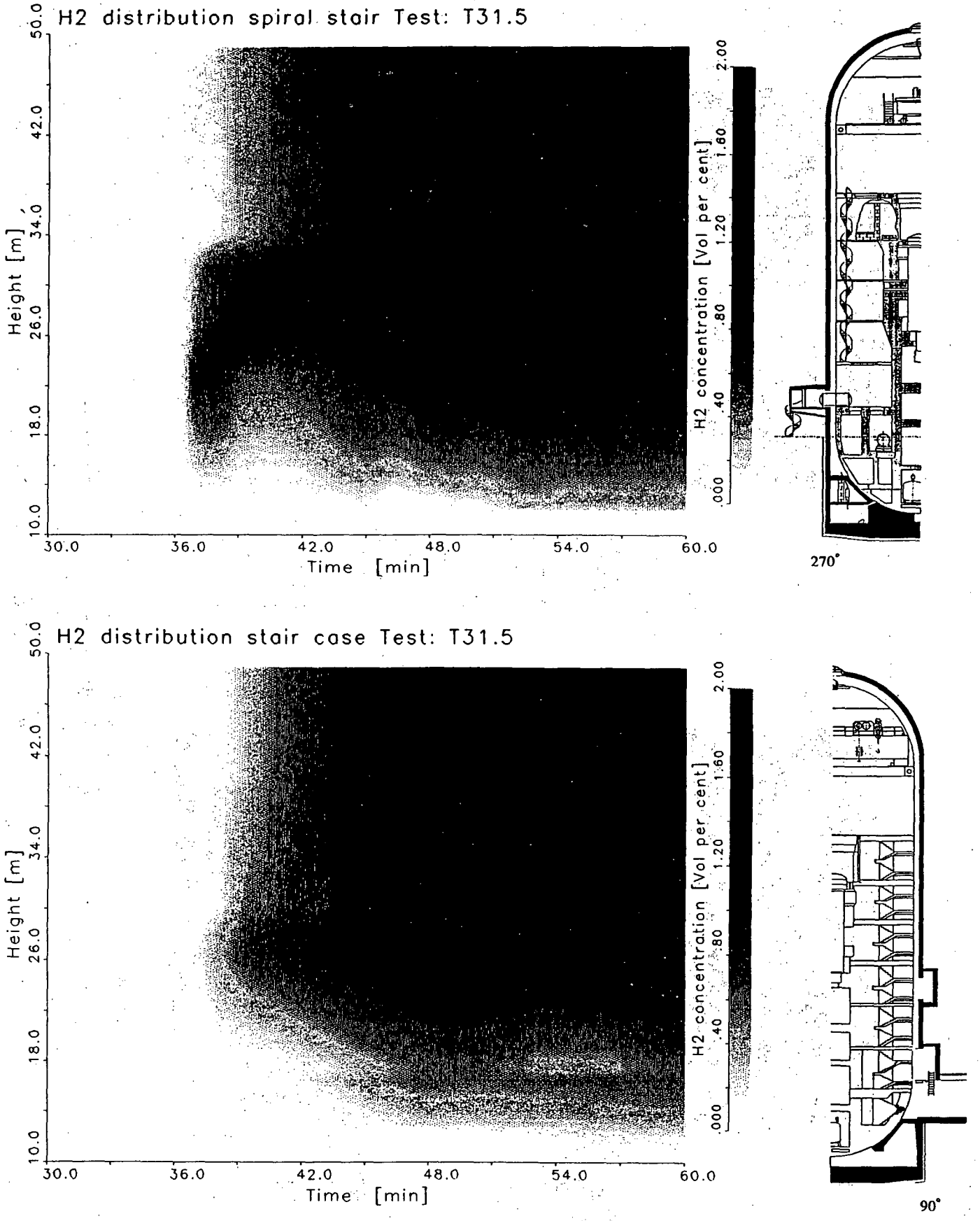


FIG. 17: EARLY SPACE–TIME EVOLUTION OF H_2–CONCENTRATION IN SPIRAL (TOP) AND STAIR CASE (BOTTOM)

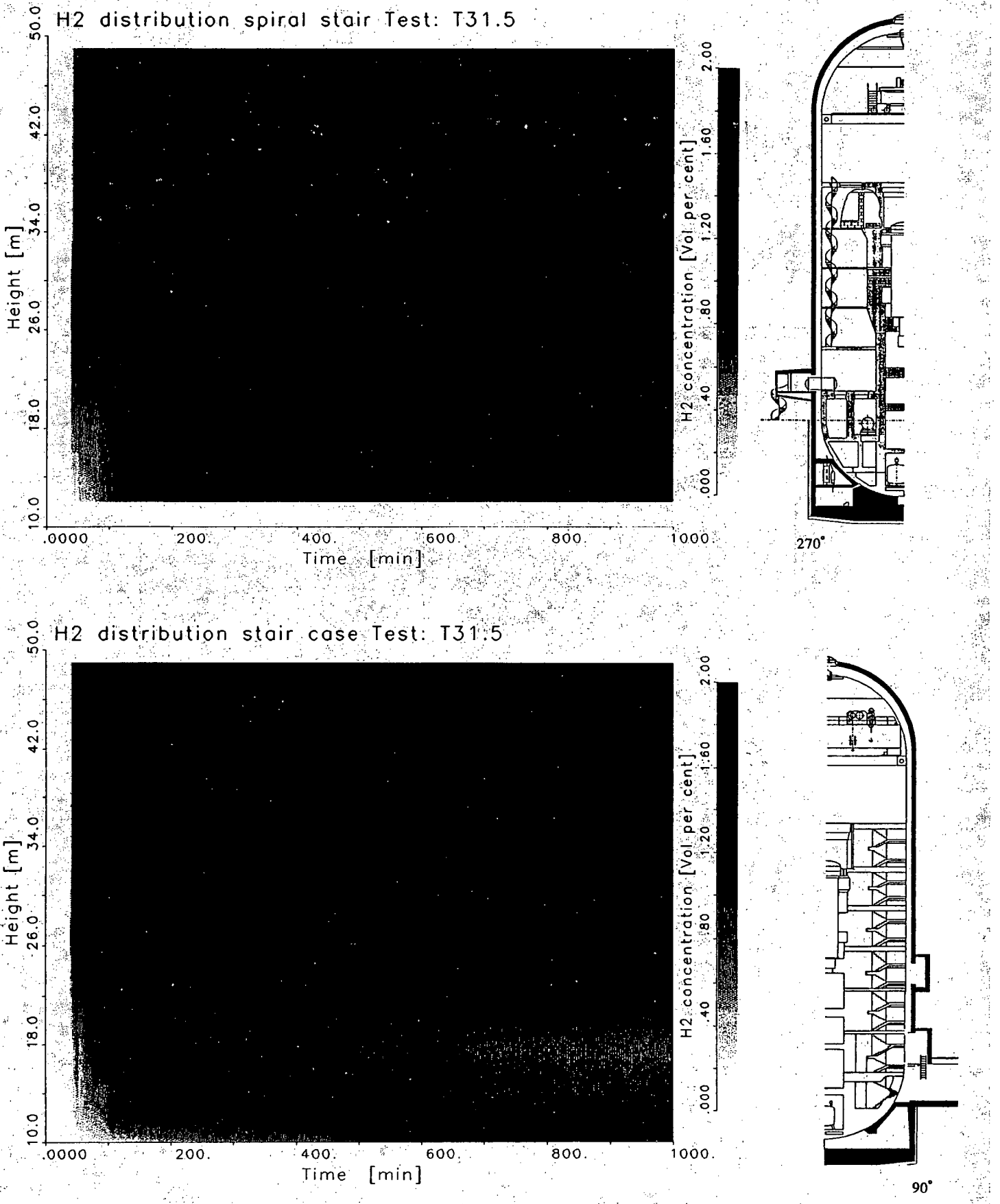


FIG. 18: LONG–TERM SPACE–TIME EVOLUTION OF H_2–CONCENTRATION IN SPIRAL (TOP) AND STAIR CASE (BOTTOM)

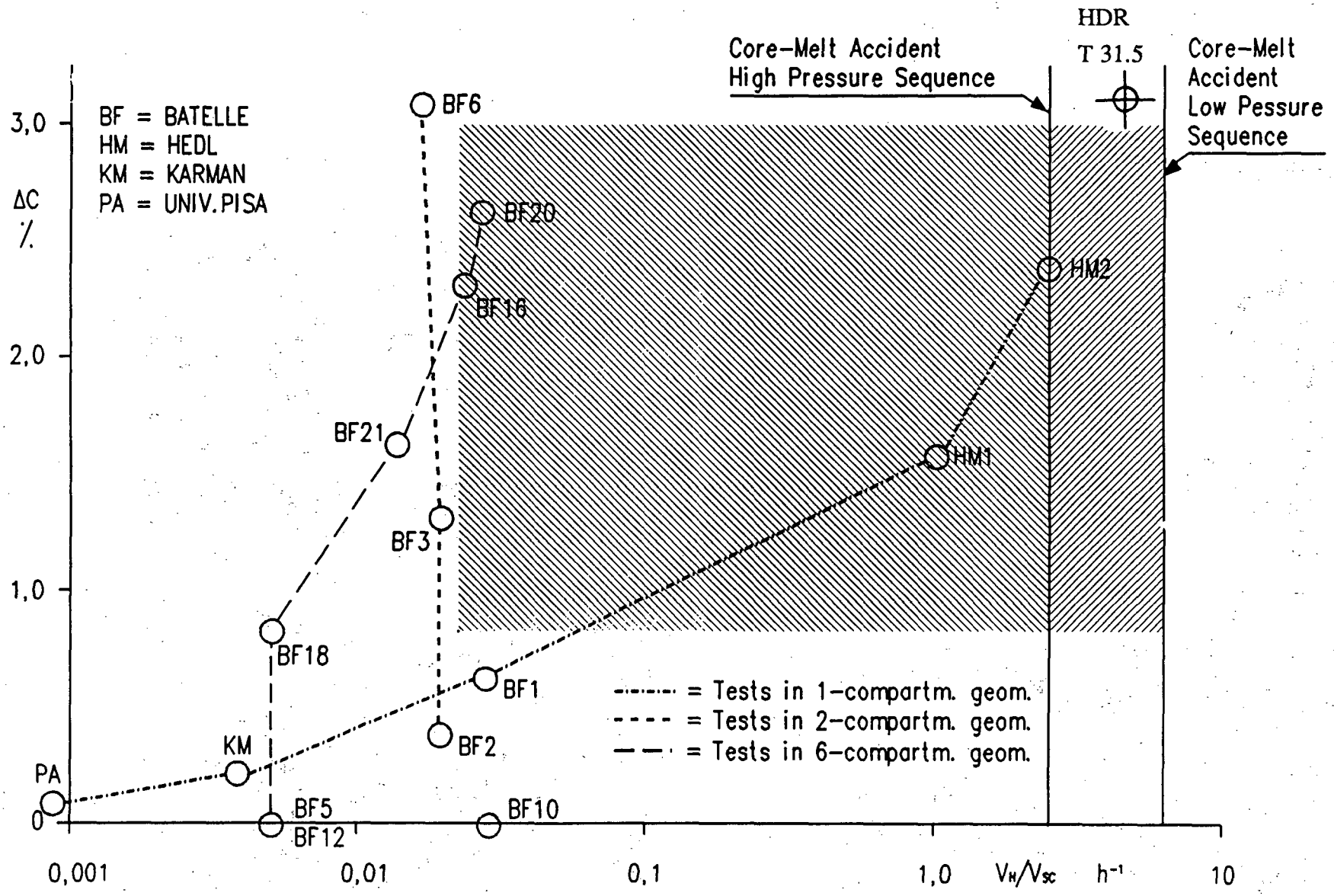


FIG. 19: OBSERVED HYDROGEN CONCENTRATION DIFFERENCES FOR PREVIOUS EXPERIMENTS AND HDR T 31.5

HMS HYDROGEN DISTRIBUTION RESULTS FOR THE PHDR HYDROGEN BENCHMARK EXPERIMENT

J. R. Travis

Safety Assessment Group
Nuclear Technology and Engineering Division
Los Alamos National Laboratory
Los Alamos, New Mexico 87545

ABSTRACT

A blind prediction and a post-test analysis have been performed with the HMS computer code for the HDR T31.5 hydrogen distribution benchmark experiment. Comparisons between the predictions and the experimental data were generally good; however, it was found that some essential physics was not represented in the HMS energy equation. A demonstration calculation also showed the importance of physically locating the internal steel structures in a representative manner.

---

1. INTRODUCTION

The HMS (Hydrogen Mixing Studies) computer code[1-5] is the US Nuclear Regulatory Commission's (NRC's) best-estimate code for predicting the transport, mixing, and combustion of hydrogen inside a reactor containment building during a severe accident. The code models the time-dependent, three-dimensional, single-phase, multispecie behavior of mixing gases in small- and large-scale complex geometries. Convection and condensation heat-transfer phenomena involving walls and internal structures are calculated using a Reynolds analogy formulation. Solutions are obtained using a modified Los Alamos Arbitrary Lagrangian Eulerian (ALE) semi-implicit, finite-difference numerical algorithm that allows flows from low Mach numbers to sonic velocities without computational time-step limitations based on the local sound speeds. We have used this code to calculate blind predictions for HDR hydrogen distribution experiment T31.5.

II. CONTAINMENT REPRESENTATION

A. Computational Mesh

The HDR containment is represented by a three-dimensional computational mesh consisting of 9 radial cells, 30 axial cells, and 22 azimuthal cells (a total of 5940 computational cells). Using this representation, we present a vertical section of the containment at an azimuthal angle of 90° (actual and modelled) in Fig. 1 and a horizontal cross section at a height of 16 m in Fig. 2. We can represent all the major walls and floors using internal obstacles (the shaded regions actually blocking out computational cells) or inertial barriers (the simple lines positioned on computational cell edges). Even though the inertial barriers have zero thickness in the computational mesh, condensation heat-transfer calculations are based on an average wall or floor thickness of 1 m. In this modelling procedure, we physically represent all compartments; however, because of the constraints inherent in an orthogonal, three-dimensional, cylindrical geometry computing mesh, we are not able to represent the exact flow areas (doors, connections, and other openings) between compartments.

We use a variable mesh spacing capability to represent the physical dimensions as accurately as possible. In HDR containment coordinates, the vertical edge (the radial position) of the mesh is given in meters at

0.0	1.5	2.3	3.5	5.0	
	6.5	8.0	9.5	10.0	10.6

for a total of nine active radial computational cells. Note that the innermost computational cells have a radial width of 1.5 m (1.5-0.0) and the ninth, or outermost, cells have radial width of 0.6 m (10.6-10.0). The horizontal edge (the axial position) is given in meters at

-8.0	-6.8	-5.8	-4.0	-3.0
-2.0	-1.0	1.8	2.8	3.8
4.8	6.4	7.4	9.0	10.0
12.5	13.75	14.75	16.55	17.55
19.25	21.0	22.5	25.0	27.5
29.5	30.85	34.0	40.0	47.0
48.0				

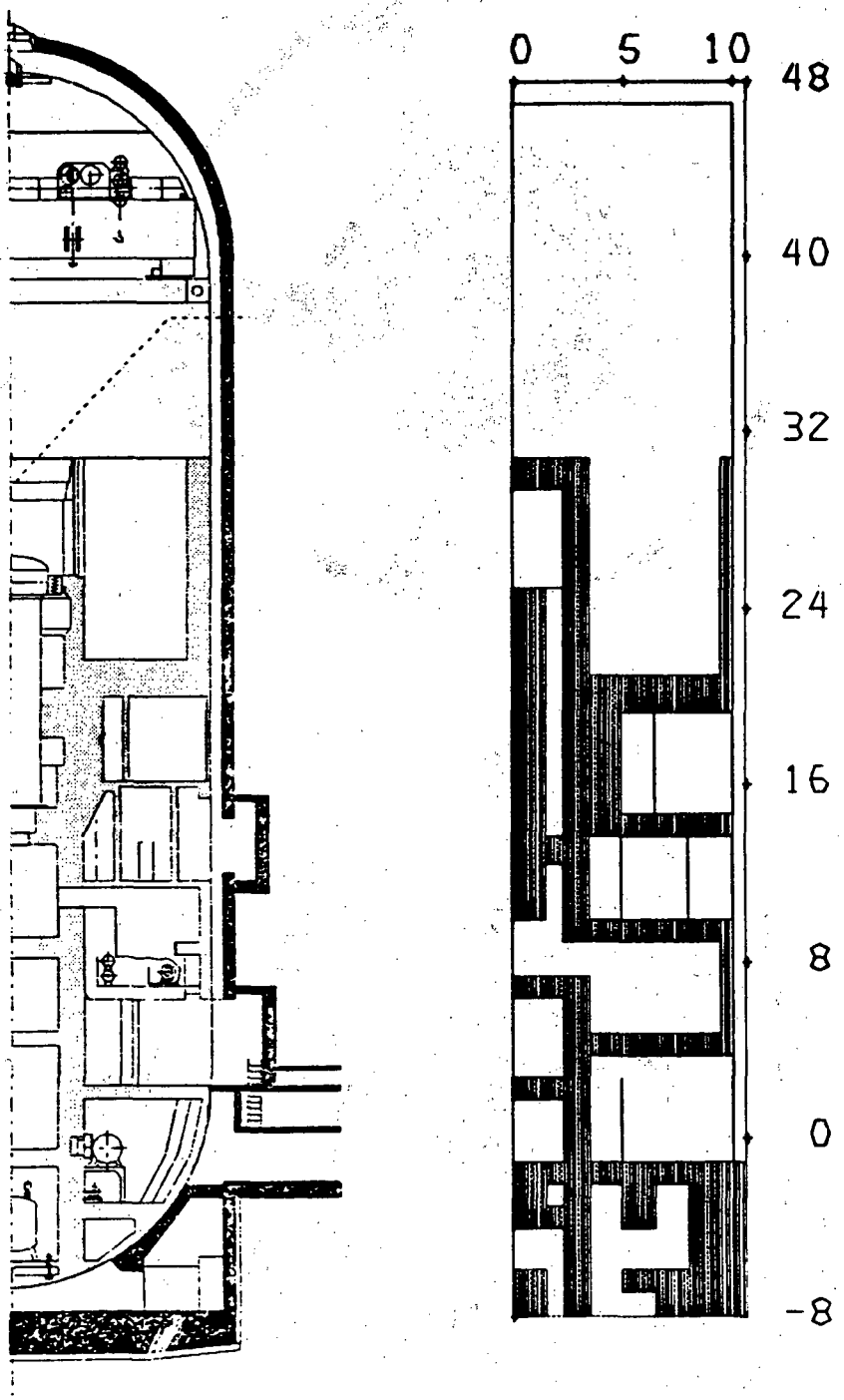


Fig. 1.
HDR vertical cross section at 90°. The physical model is on the left side, and the HMS model is on the right side.

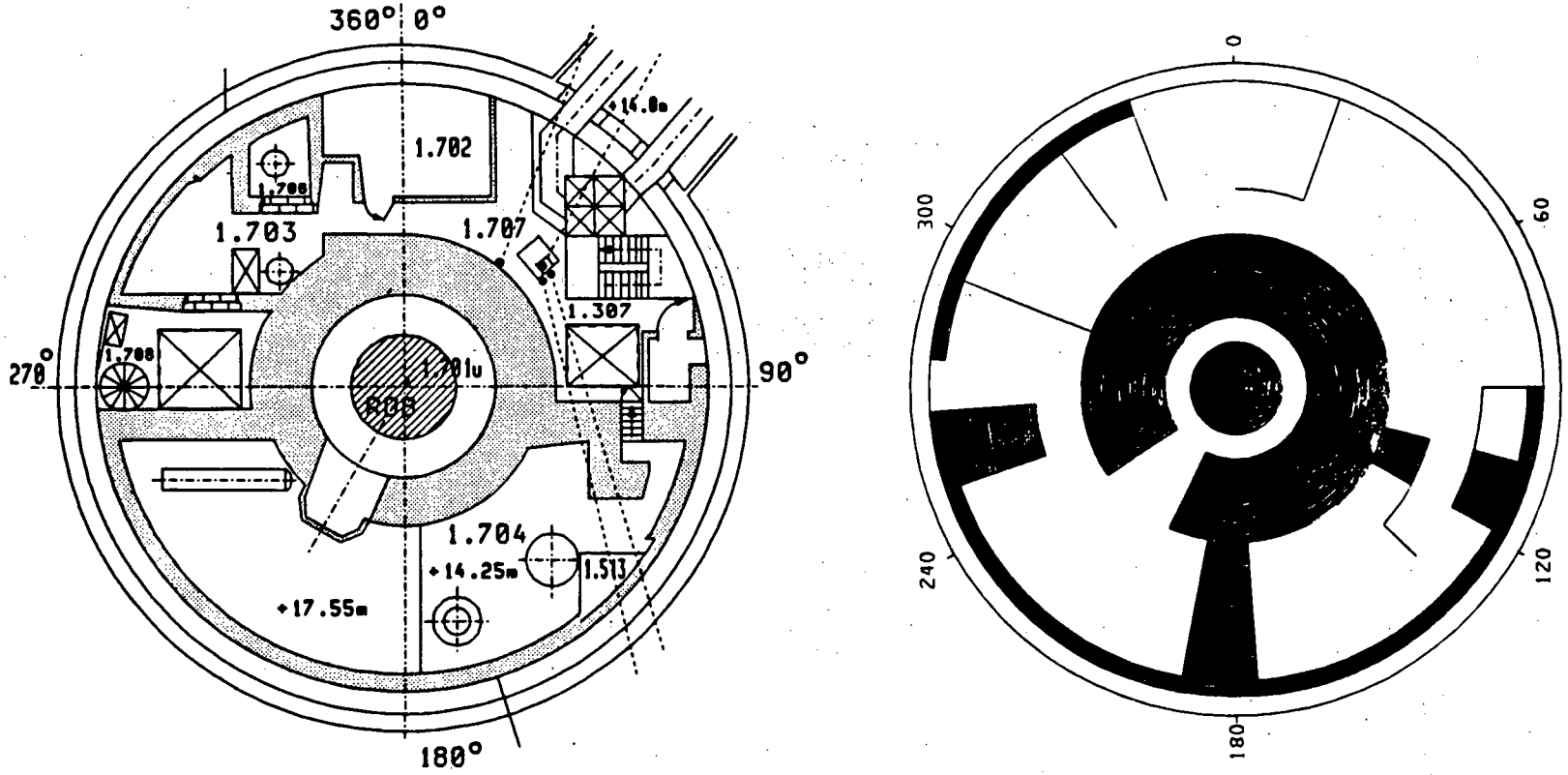


Fig 2.
HDR horizontal cross section at 16 m. The physical model is on the left side, and the HMS model is on the right side.

for a total of 30 active axial computational cells. The azimuthal edge (the angular position) is given in degrees at

20	38	55	71	90
105	119	133	147	163
176	191	206	221	236
251	266	276	292	308
324	340	360 ,		

for a total of 22 active azimuthal computational cells.

B. Internal Structures

We have modelled the containment's internal heat sinks by specifying the total heat sink surface area divided by the free volume for a particular containment region. We also specify ½ the average thickness for these internal heat sinks. By knowing the free volume for a particular region in the computational mesh and the average heat sink density, we can compute the heat sink mass. Conversely, to compute the average thickness and the surface area per unit volume, we must know the region's free volume, the total surface area, and the heat sink mass. We have chosen to subdivide the HDR containment into horizontal disks extending radially from the centerline to the steel shell and axially between the edges of each vertical computational cell. Table I specifies the ½-thickness, surface area, and free volume for each horizontal disk region.

III. SOURCE DATA

PHDR hydrogen benchmark experiment T31.5[6] involves a large-break blowdown of the HDR pressure vessel (30 Mg water-steam mixture in 50 s) followed by a super-heated steam release (2.2 kg/s between roughly 21 min and 36 min after the beginning of the blowdown) and then a "light-gas" (15% hydrogen and 85% helium on a volume basis) release (0.24 kg/s between 36 min and 58 min after the beginning of the blowdown). These releases were at about the 22-m height level. Because HMS is a single-phase compressible fluid flow code and therefore is unable to model the two-phase critical flow mixture entering the containment, we must develop a blowdown jet expansion model to extract the correct mass flow rate and temperature for the steam source. The liquid

TABLE I

INTERNAL HEAT SINK SPECIFICATIONS

Disk Height (m)	½-thickness (cm)[a]	Surface Area (cm^2)/ Free Volume (cm^3)	Free Volume (m^3)
-8.0 < Z < -6.8	0.47	0.0142	126.67
-6.8 < Z < -5.8	0.0	0.0	16.74
-5.8 < Z < -4.0	0.32	0.0185	329.11
-4.0 < Z < -3.0	0.30	0.0171	156.98
-3.0 < Z < -2.0	0.30	0.0176	171.41
-2.0 < Z < -1.0	0.29	0.0090	35.85
-1.0 < Z < 1.8	0.37	0.0182	759.97
1.8 < Z < 2.8	0.37	0.0131	251.56
2.8 < Z < 3.8	0.38	0.0128	267.10
3.8 < Z < 4.8	0.36	0.0052	54.90
4.8 < Z < 6.4	0.36	0.0179	381.95
6.4 < Z < 7.4	0.28	0.0226	224.05
7.4 < Z < 9.0	0.28	0.0131	328.65
9.0 < Z < 10.0	0.64	0.0216	93.19
10.0 < Z < 12.5	0.44	0.0137	611.91
12.5 < Z < 13.75	0.44	0.0247	303.75
13.75 < Z < 14.75	1.13	0.0291	72.99
14.75 < Z < 16.55	0.52	0.0172	377.59
16.55 < Z < 17.55	0.52	0.0373	166.21
17.55 < Z < 19.25	0.39	0.0174	339.81
19.25 < Z < 21.0	0.42	0.0176	217.61
21.0 < Z < 22.5	0.52	0.0301	284.21
22.5 < Z < 25.0	0.59	0.0152	361.45
25.0 < Z < 27.5	0.71	0.0128	504.90
27.5 < Z < 29.5	0.92	0.0098	399.89
29.5 < Z < 30.85	0.0	0.0	91.19
30.85 < Z < 34.0	0.72	0.0198	901.07
34.0 < Z < 40.0	0.72	0.0109	1784.93
40.0 < Z < 47.0	0.0	0.0	2199.11
			11814.78

[a]We use the ½-thickness specification for ease in developing a one-dimensional transient heat-transfer calculation with an insulated centerline.

component of the blowdown and any condensate are assumed to drain into the containment sump and effectively are removed from the containment mass inventory. Time-dependent mixture pressures, temperatures, qualities, and mass flow rates are specified immediately upstream of the blowdown pipe exit. A blowdown model, which appears quite realistic, assumes the mixture to be in equilibrium at the pipe exit and after the expansion to the containment pressure. Assuming a reversible adiabatic expansion from the pipe exit pressure and quality to the containment pressure, we compute the quality and temperature of the expanded blowdown jet.

We show the blowdown pipe pressure (labeled P) and the containment pressure (labeled C) for two time intervals, 0 to 5 s and 0 to 50 s, for the large-break blowdown in Fig. 3. By assuming thermal equilibrium, the water vapor, liquid, and saturation temperatures are all equal. The blowdown temperatures in the pipe and after the expansion into the containment are represented in Fig. 4 for the two time intervals. Comparisons of the pipe temperatures shown in Fig. 4 and the vapor and liquid temperatures provided by the T31.5 test specifications indicate that they are all less than 1% of each other. Assuming an adiabatic expansion of the blowdown jet from the pipe conditions (pressure in Fig. 3, temperatures in Fig. 4, and quality in Fig. 5) to the containment conditions (pressure in Fig. 3 and temperature in Fig. 4), we can calculate the amount that the blowdown jet flashes or condenses in the containment. For example, from Fig. 5, for a time less than roughly 0.5 s, the jet actually condenses because the containment quality is less than the pipe quality. Also, for a time greater than about 17 s, the jet is condensing some because of the higher pipe quality. Between times of 0.5 s to 17 s, the jet is flashing, as demonstrated by the higher containment quality shown in Fig. 5 for this time interval.

The efficiency of this blowdown process is depicted in Figs. 6 and 7. We show the total blowdown mass flow rate in both figures (the upper unlabeled curve in all plots), whereas the steam mass flow rates for the pipe and containment are shown in Fig. 6, and the liquid mass flow rates for the pipe and containment are drawn in Fig. 7. The liquid component mass flow rate appears larger than the steam component during most of the blowdown into the containment. This is more obvious after the mass flow rate curves in Figs. 6 and 7 are integrated, and the results are presented in Figs. 8 and 9. The unlabeled

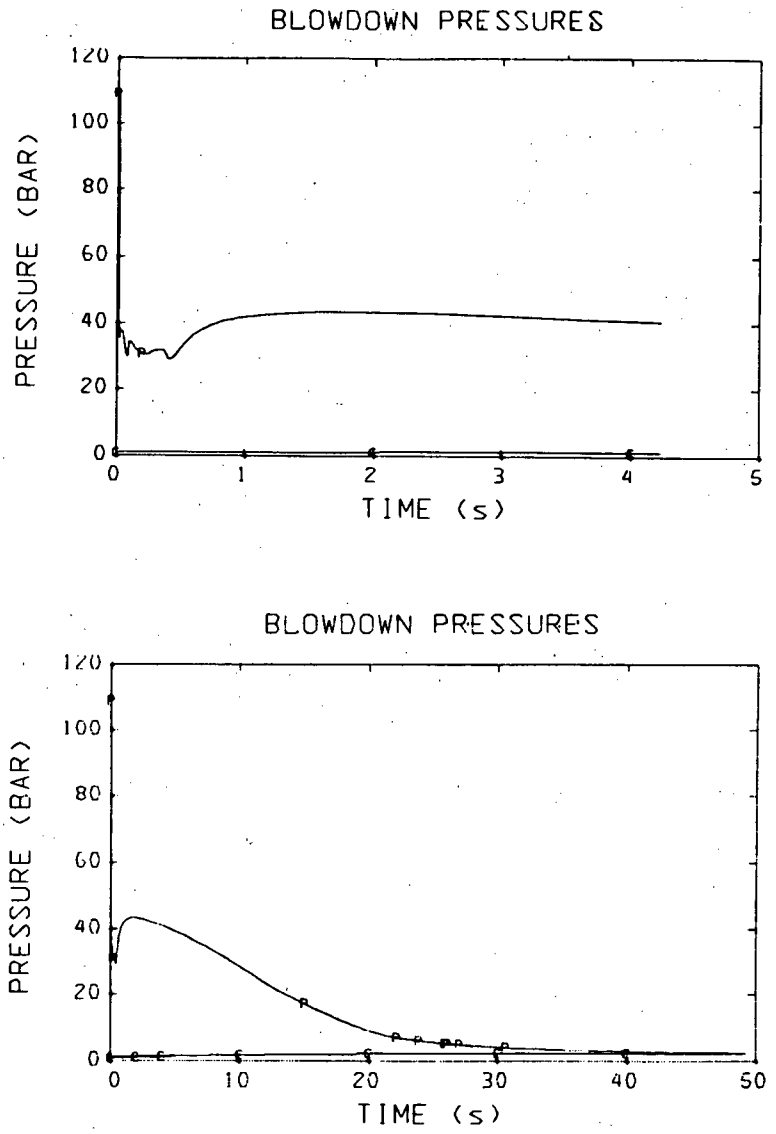


Fig. 3.
Pressure in the blowdown pipe (p) and pressure in the containment (c) for two time intervals.

top curve in Figs. 8 and 9 is the total mass of liquid and steam jetting into the containment, whereas the steam mass in the pipe and containment after jet expansion is shown in Fig. 8 and the liquid mass in the pipe and containment is shown in Fig. 9. These figures show that at about 50 s after the blowdown began, 14 Mg of steam and 16 Mg of liquid had entered the containment by the adiabatic expansion. This can be compared with the 12 Mg of steam and 18 Mg of liquid in the blowdown pipe. Because HMS is not a two-phase code, the liquid

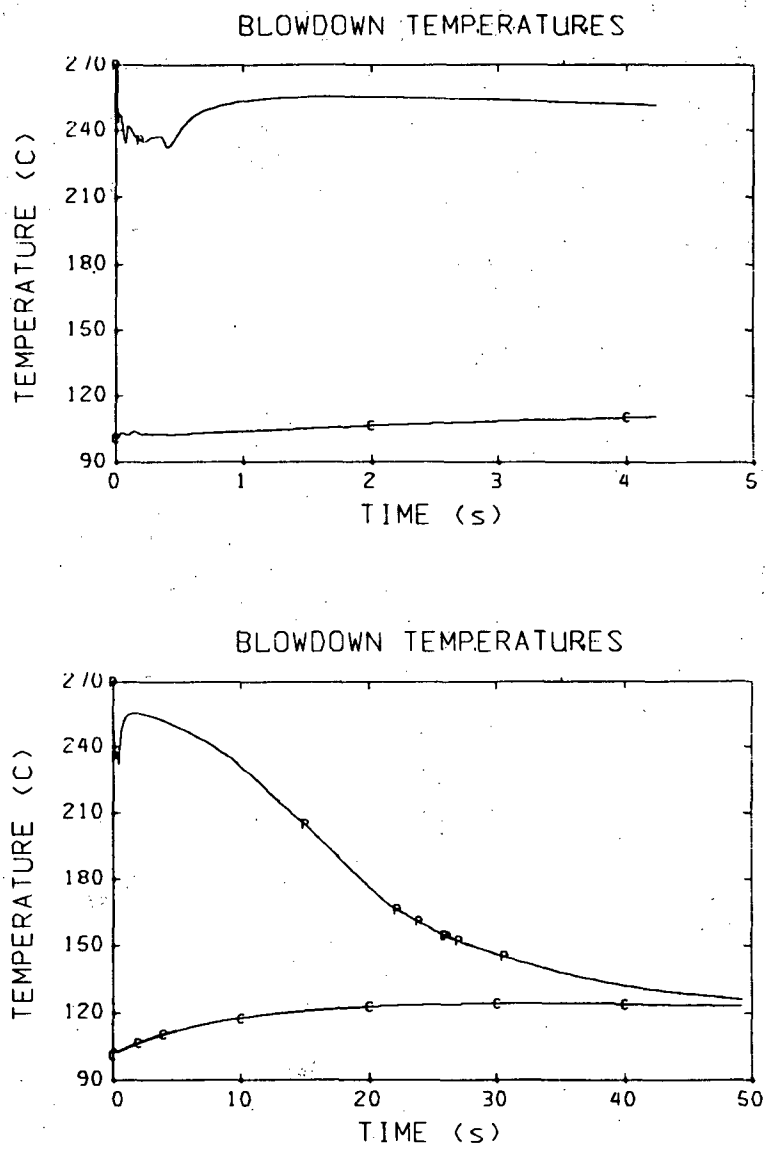


Fig. 4.
Temperature in the blowdown pipe (P) and temperature in the containment (C) after the expansion of the blowdown jet for two time intervals.

inventory is not calculated; therefore, the liquid immediately disappears from the calculation. Any steam that condenses on walls, floors, and/or internal heat sinks also is assumed to disappear from the calculation. The amount of steam in the containment at any time is plotted in Fig. 10. Here, the upper curve is the total steam mass source, and the lower curve is the total steam mass in the containment. At roughly 50 s, there is about 6.5 Mg of steam in

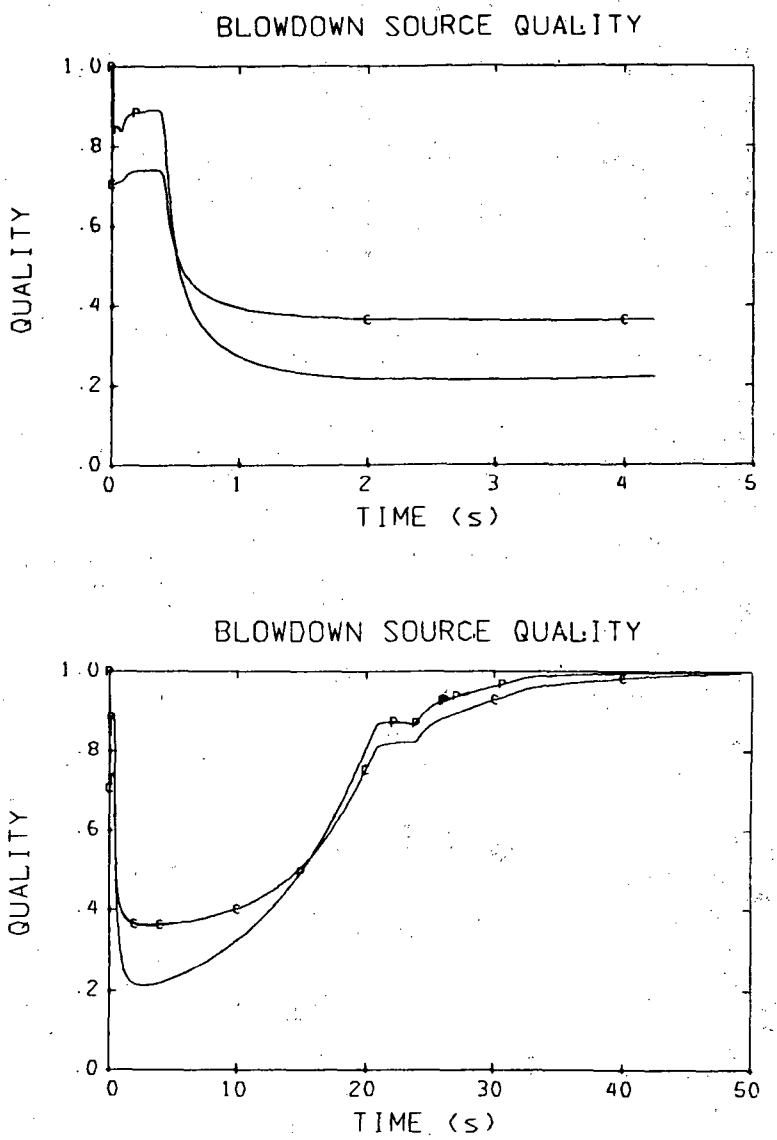


Fig. 5.
Quality in the blowdown pipe (P) and quality n the containment (C) after the expansion of the blowdown jet for two time intervals.

the containment as compared with the total source of 14 Mg, meaning that 7.5 Mg of steam have condensed on surfaces within the containment.

Figure 11 shows pipe and containment pressure, temperatures, and mass flow rates for the steam and light-gas release, phase. Note that during the light-gas release, the flow rate is small and the expansion effects are minimal so the pressures and temperatures in the pipe and expansion values are nearly equal.

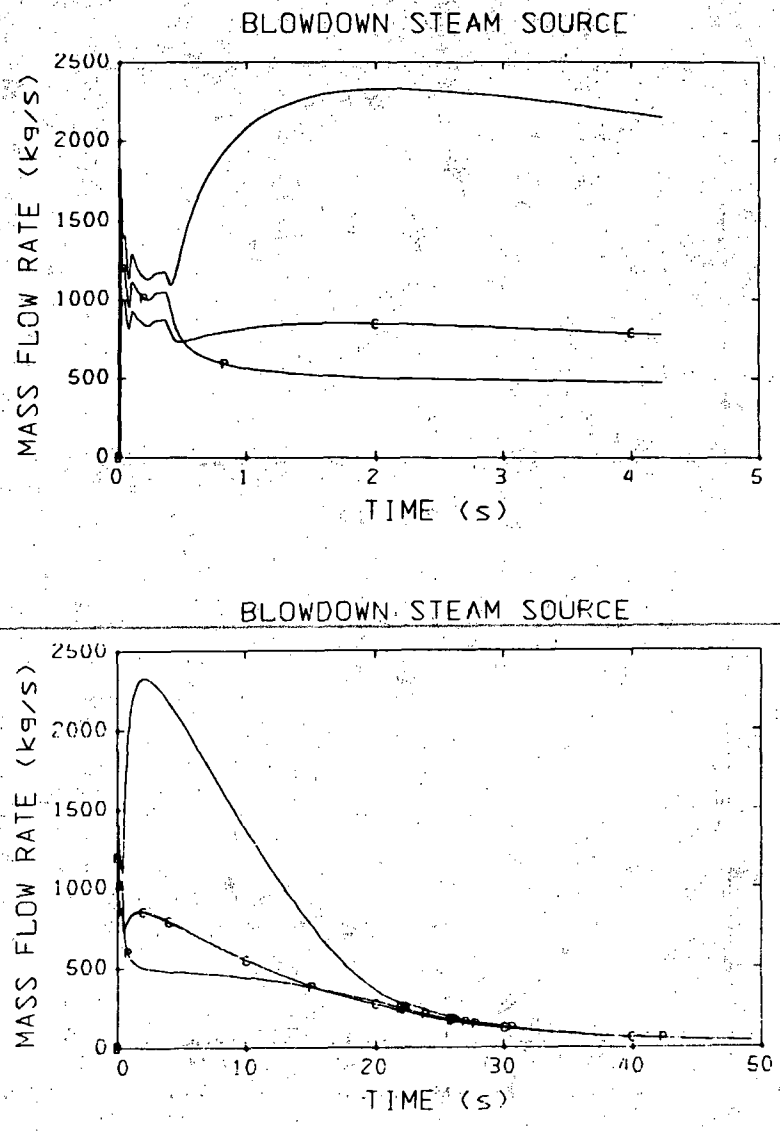


Fig. 6.
Blowdown mass flow rates for two time intervals. The total mass flow rate is given by the upper (unlabeled) curve. The steam mass flow rate in the pipe (P) and the steam mass flow rate after the jet expansion into the containment (C) are shown in the lower two curves.

There is some condensation of the steam jet as the mass flow rate plot shows a smaller value in the containment than in the pipe. The steam mass after expansion is used as the steam source in the code, and we have referred to it as the modified source mass. In Fig. 12, the modified steam source mass and the actual steam inventory in the containment are shown in the upper and lower plots,

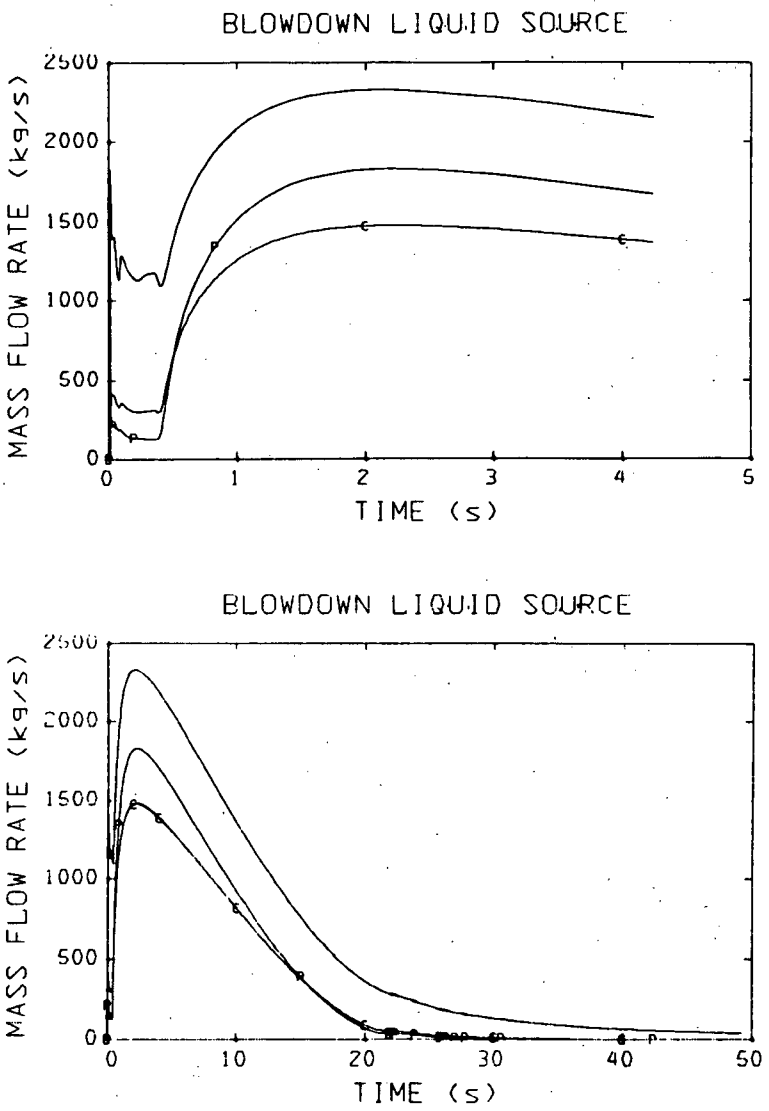


Fig. 7.
Blowdown mass flow rates for two time intervals. The total mass flow rate is given by the upper (unlabeled) curve. The liquid mass flow rate in the pipe (P) and the liquid mass flow rate after the jet expansion into the containment (C) are shown in the lower two curves.

respectively. Note that the total steam source mass is roughly 16.2 Mg, and at 1 h there is only about 1 Mg, steam in the containment. More than 90% of the steam released into the containment has condensed on floors, walls, ceilings, and internal structures during the first hour. The total amount of light gas released is approximately 168 kg.

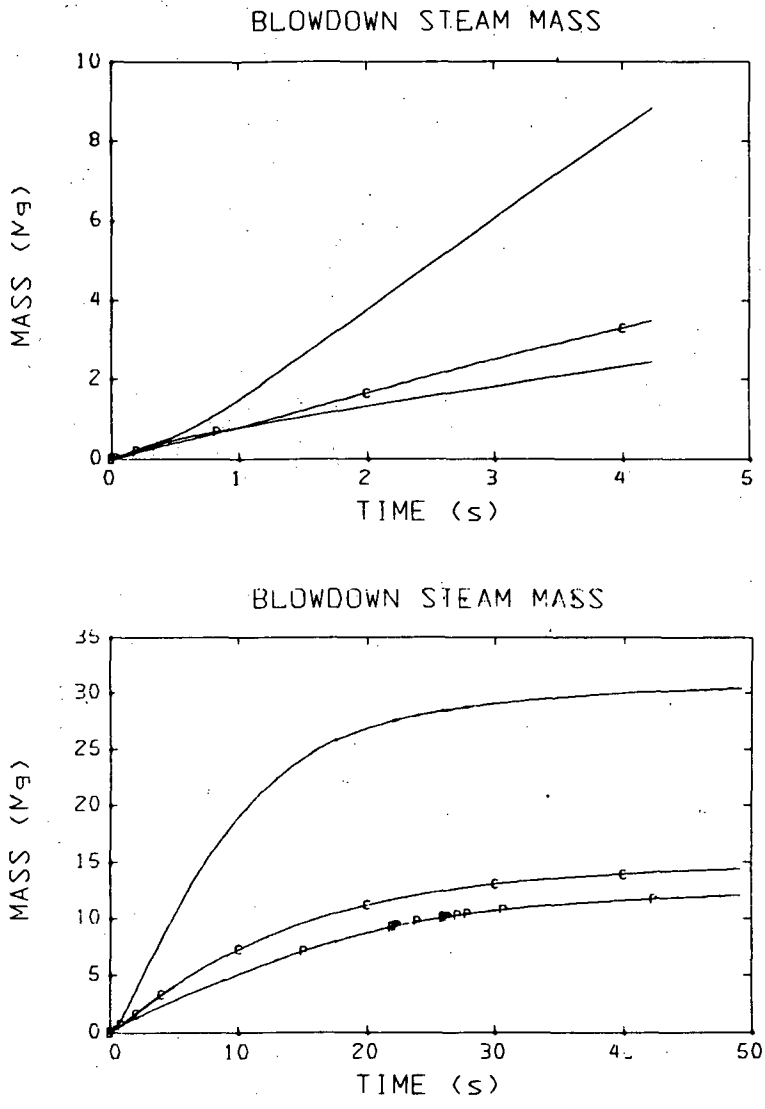


Fig. 8.
Blowdown masses for two time intervals. The total blowdown mass is given by the upper (unlabeled) curve. The steam mass in the pipe (P) and the steam mass after the blowdown jet expansion into into the containment (C) are shown in the lower two curves.

IV. COMPARISON OF BLIND PREDICTIONS WITH EXPERIMENTAL RESULTS

We have compared the HMS blind predictions with HDR experiment blowdown and hydrogen distribution test T31.5 up to the problem specification time of 1 h. Figure 13 shows a comparison of the experimental reference pressure (1) and the calculated value (2). Temperatures in the dome, mid-plane, and basement are compared between the experiment and the calculation in Fig. 14. Note

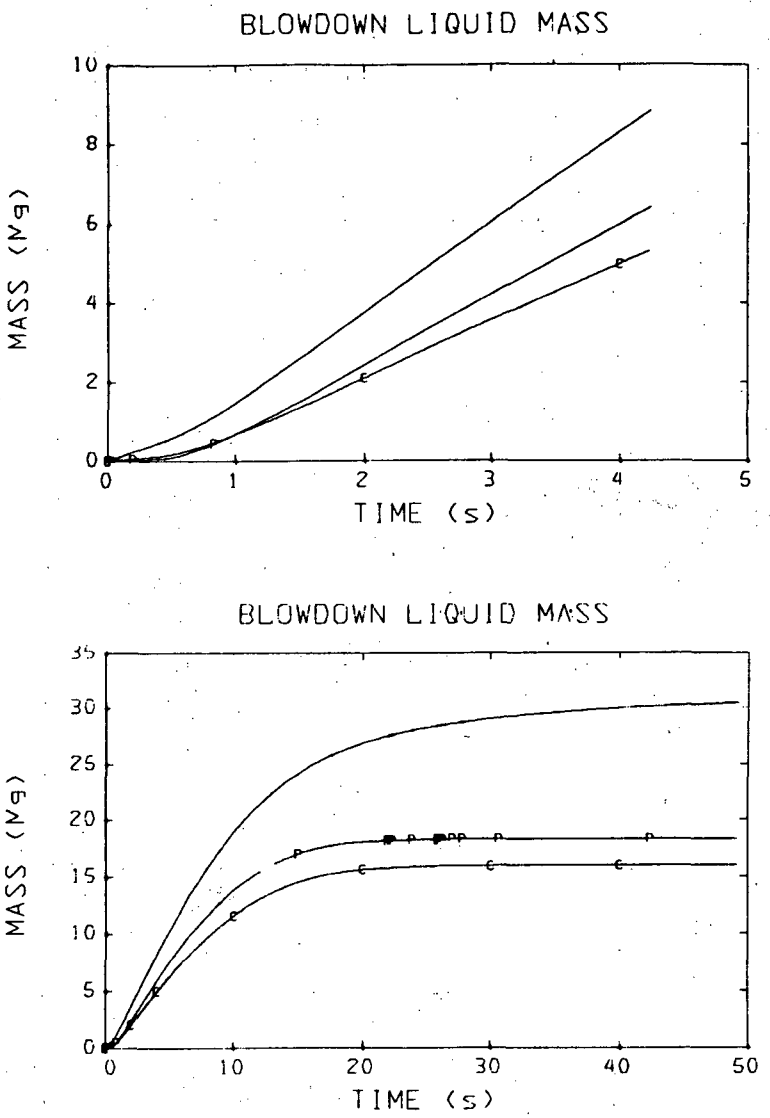


Fig. 9.
Blowdown masses for two time intervals. The total blowdown mass is given by the upper (unlabeled) curve. The liquid mass in the pipe (P) and the liquid mass after the blowdown jet expansion into the containment (C) are shown in the lower two curves.

that there are generally higher predictions during the large-break blowdown (0-50 s) and at later times the calculated values are higher than the experiment values. We have performed a post-test analysis, and this discrepancy will be addressed in the next section. Hydrogen concentrations in the dome, at roughly the mid-plane, and in the basement are compared in Fig. 15. The calculated values are a little high in the dome and low in the basement. This indicates a lack of mixing that could identify the turbulence model for examination.

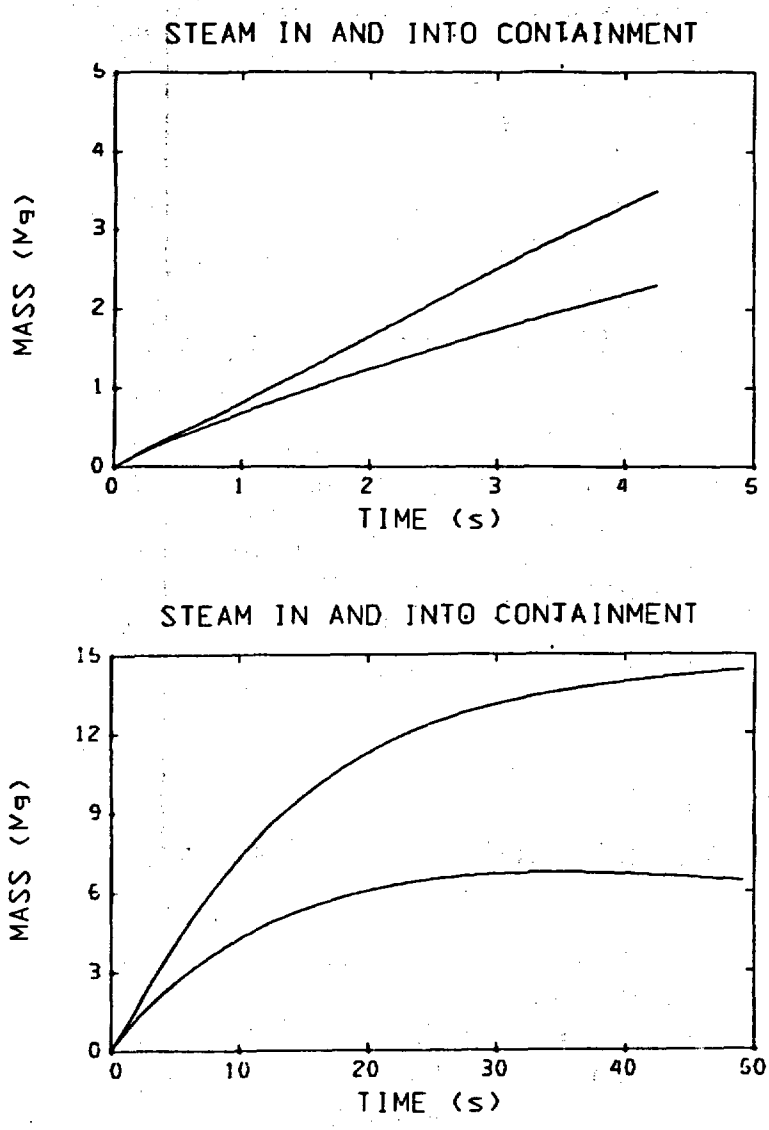


Fig. 10.
The upper curve shows the amount of steam jetting into the containment. The lower curve gives the actual amount of steam in the containment. The difference between the two curves is the amount of steam that has condensed on all surfaces.

Concentrations of three gaseous components, air, steam, and 15% of the light gas (hydrogen) are shown in Fig. 16. Note that steam component seldom gets larger than 20% and the air component seldom gets smaller than 80%.

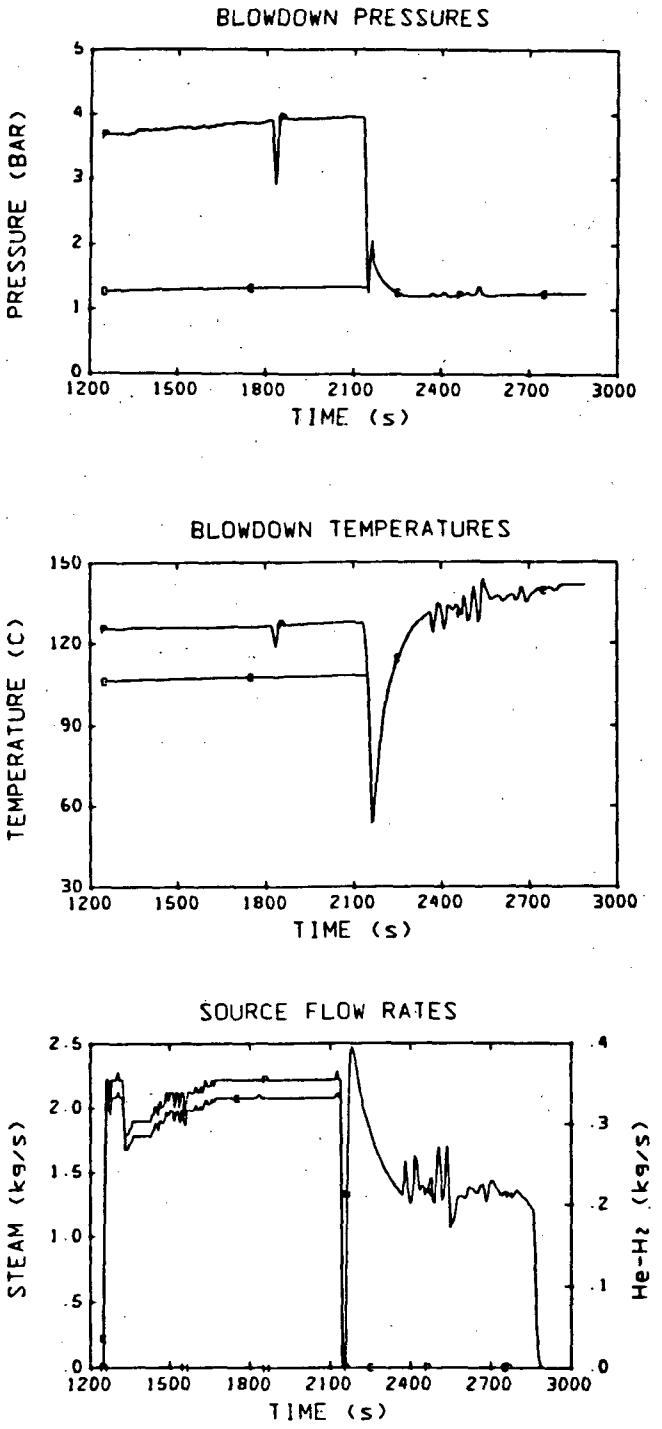


Fig. 11.
Pressures, temperatures, and mass flow rates for the steam and light-gas release phases. Note the two curves on the mass flow rate plot during the steam release phase. Curve (P) is the steam in the pipe and curve (C) is the steam source in the containment after the isentropic expansion process.

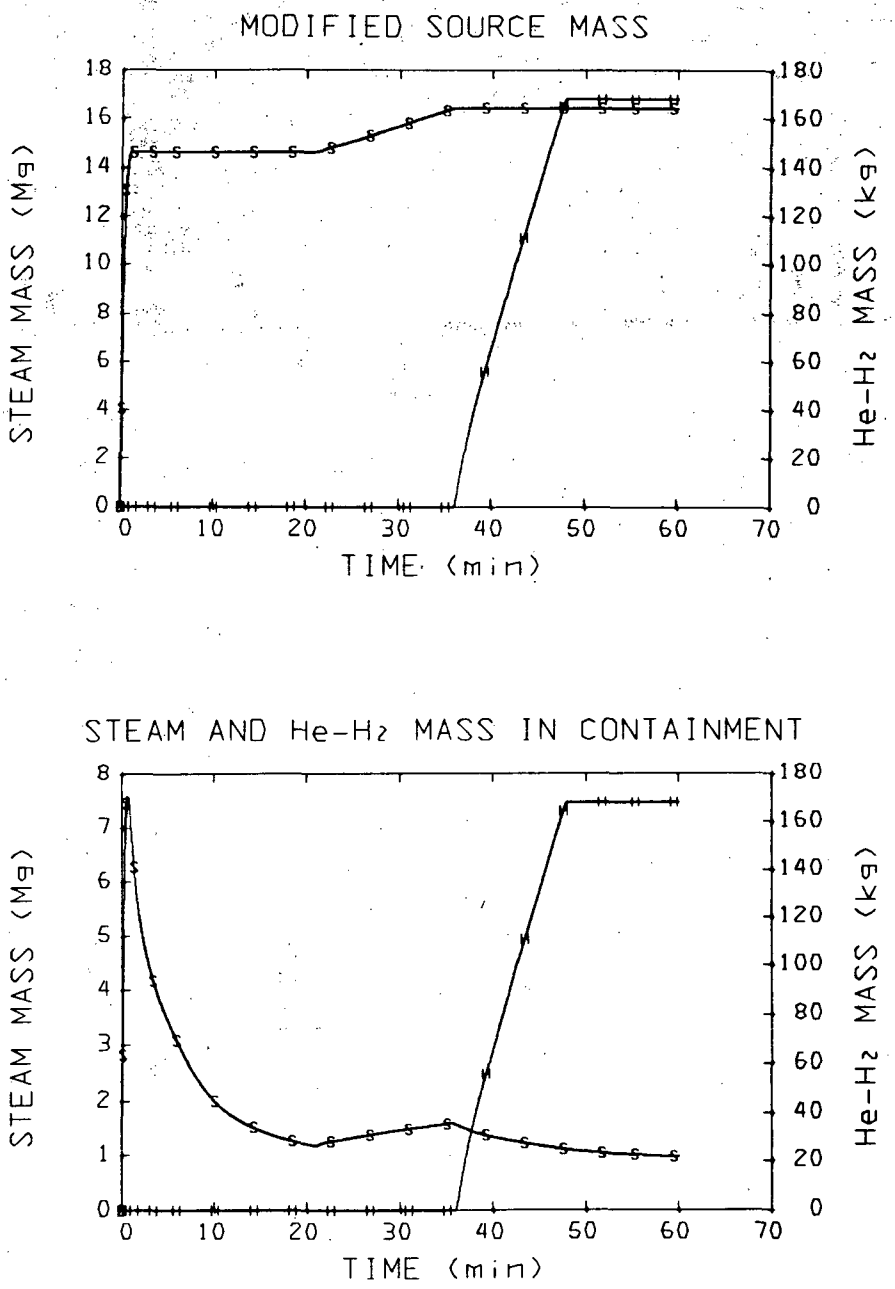


Fig. 12.
Modified steam source (integrated steam flow rate after expansion from the pipe to containment) and light-gas mass in upper-plot. Actual steam and light gas in the containment in the lower plot.

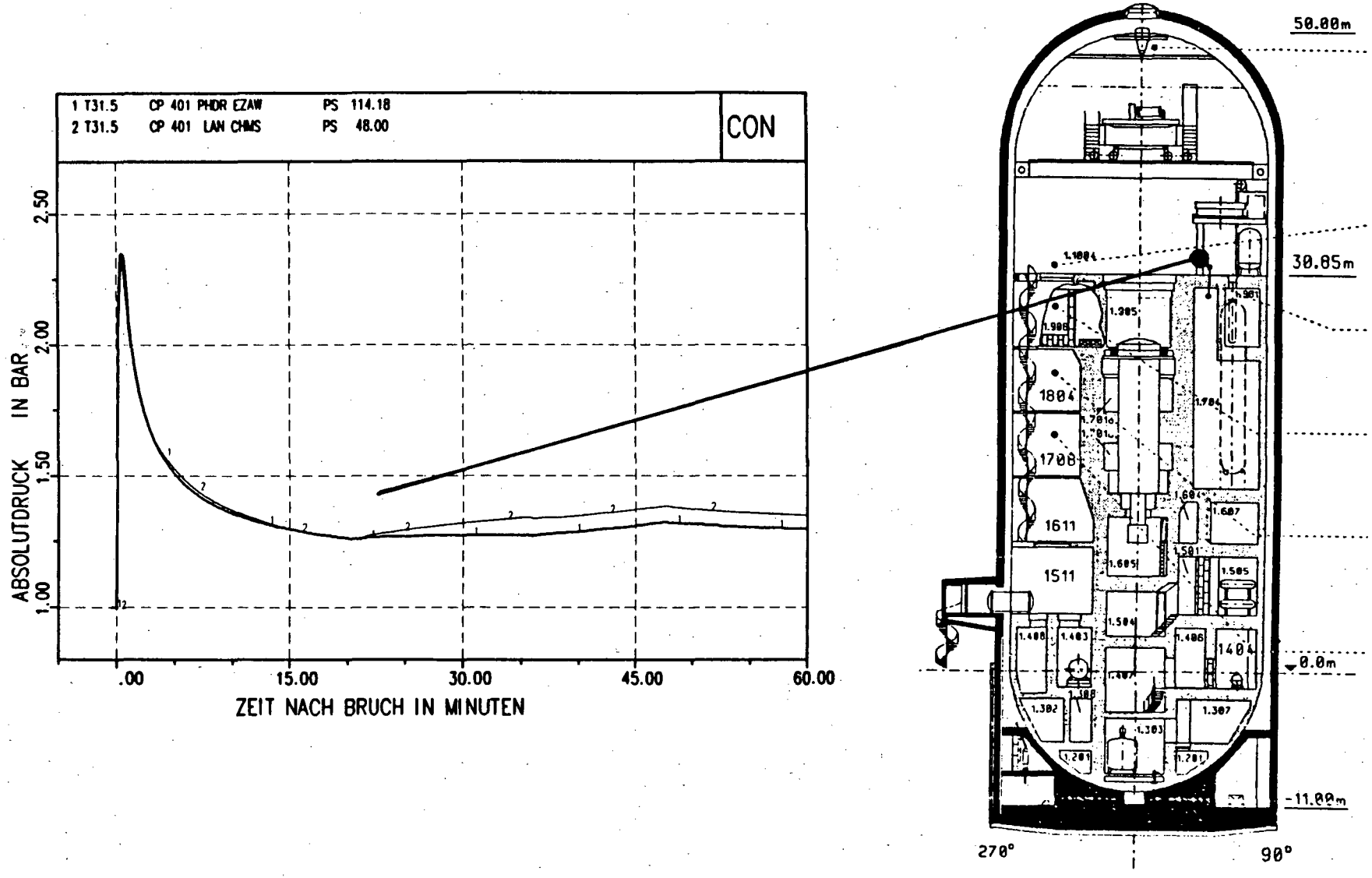


Fig.13.
Reference pressure for HDR T31.5 (1) compared with the HMS calculation (2).

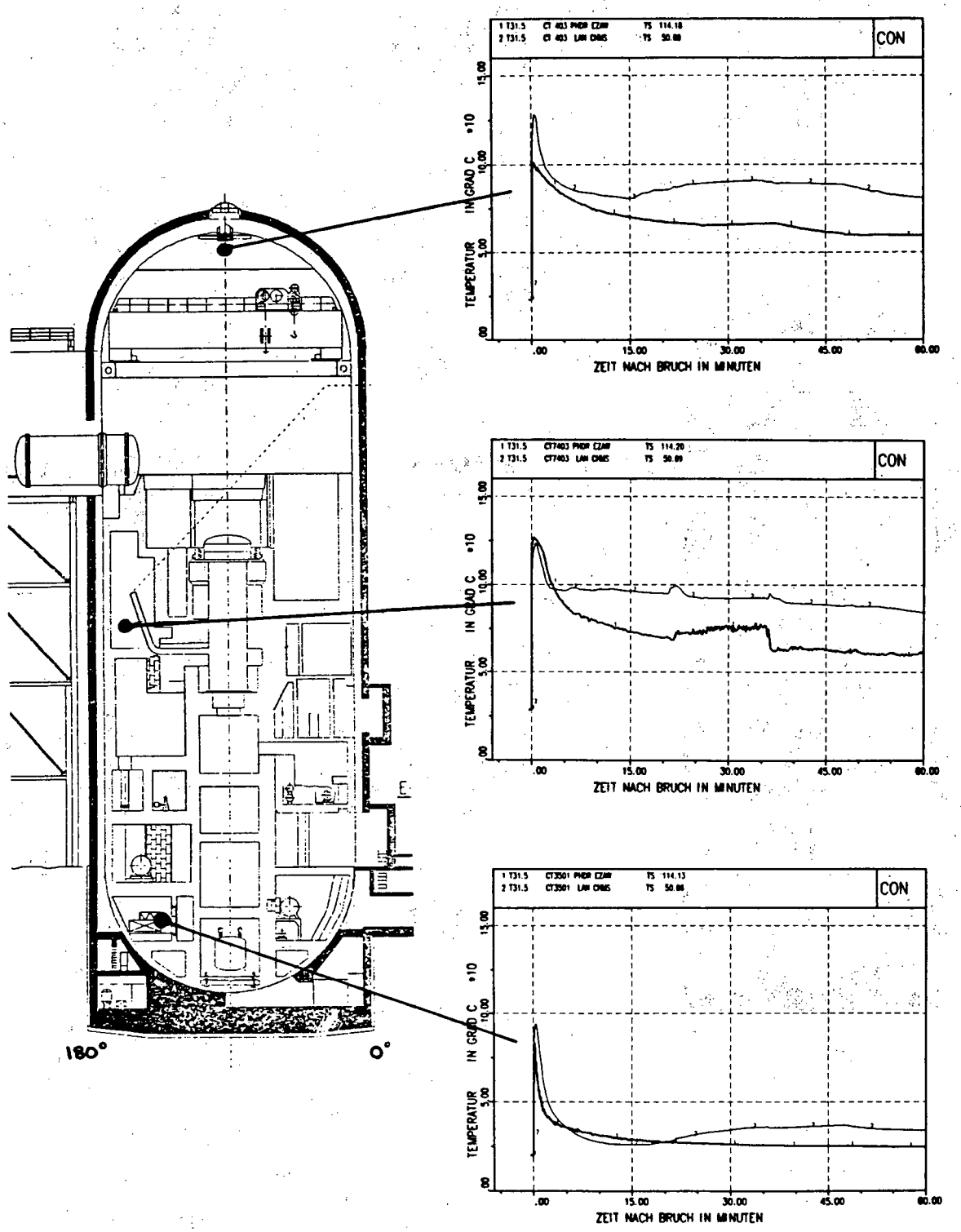


Fig. 14.
Comparison of temperatures from the HDR T31.5 test (1) and the HMS code (2).

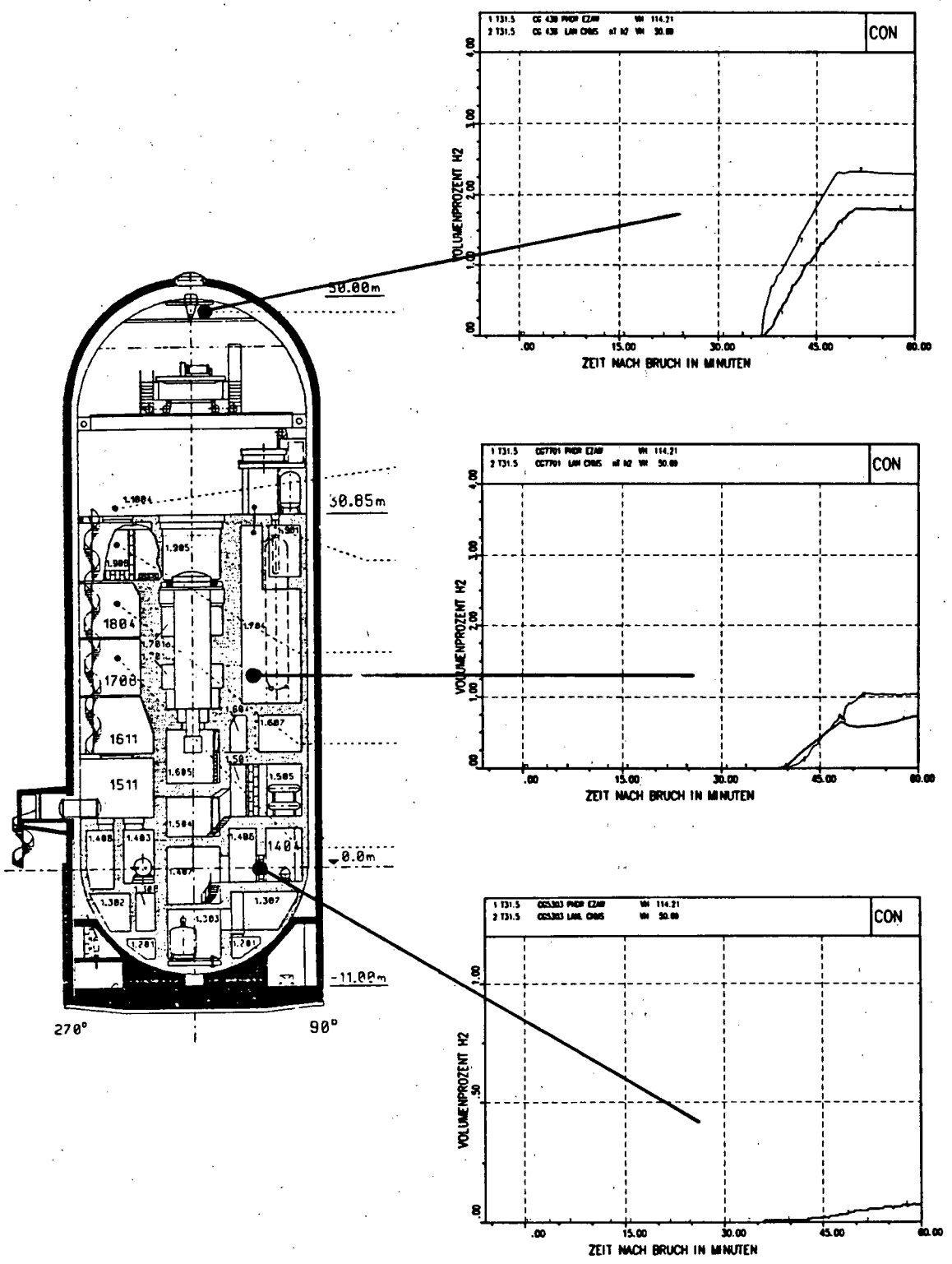


Fig. 15.
Comparison of hydrogen concentrations from the HDR T31.5 test (1) and the HMS code (2).

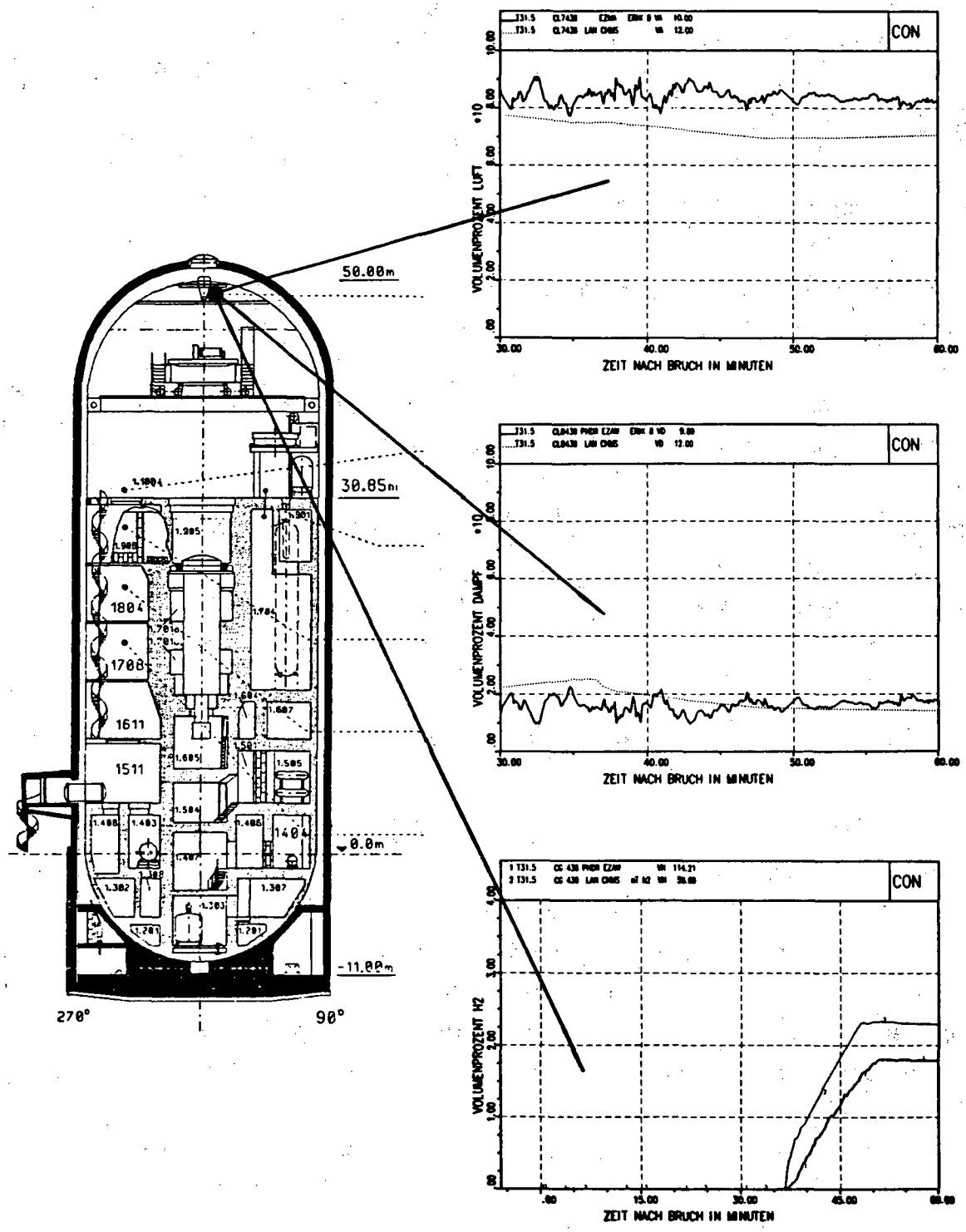


Fig. 16.
Comparison of air, steam, and hydrogen concentrations at the top of the dome from HDR T31.5 (heavy line) and the HMS code (light line).

V. POST-TEST ANALYSIS

We noted during discussions of temperature comparisons (Fig. 14), that the calculated values are often nonphysically high during the large-break blowdown. The HMS energy equation is

$$\frac{\partial(\rho I)}{\partial t} + \underline{\nabla}\cdot(\rho \underline{u} I) = -p\underline{\nabla}\cdot\underline{u} + \underline{\nabla}\cdot\underline{q} + Q \quad , \tag{1}$$

where ρ is the fluid density, I is the specific internal energy, $\underline{u}$ is the fluid velocity vector, p is the pressure, Q is the source term for heat transfer and condensation, and $\underline{q}$ is the energy flux vector. In this equation, there is no representation for the physical process of gas expansion into the change of volume when steam condenses on walls, floors, and ceilings that bound a computational cell or on internal structures within a computational cell. In other words, when condensation occurs, there is a change of gas volume of about a factor of 1000 when steam condenses to liquid water. The remaining gas expands into this vacated volume, which has a cooling effect. The HMS energy equation has been modified to reflect this effect by rewriting it as

$$\frac{\partial(\rho I)}{\partial t} + \underline{\nabla}\cdot(\rho \underline{u} I) = -p\left(\frac{1}{V}\frac{\partial V}{\partial t} + \underline{\nabla}\cdot\underline{u}\right) + \underline{\nabla}\cdot\underline{q} + Q \quad . \tag{2}$$

The change of volume is calculated from a knowledge of the amount of condensate associated with each computational cell for every time step. In Fig. 17, this cooling effect is shown in comparison with the data (curve 1), the blind prediction (curve 2), and the post-test calculation (curve 3). For the short term (up to about 12 min), there is excellent agreement between the data and the post-test analysis using Eq. (2). This period is when heat-transfer sinks are heating up, and with copious amounts of steam available, condensation is the dominant heat transfer mechanism.

After the 12-min periods, there is yet another nonphysical behavior in the calculated temperature when it begins to increase. This is thought to occur because of the crude homogeneous smearing of the internal steel structures (heat sinks) throughout the horizontal disk regions, which are discussed in Sec. IIb and tabulated in Table I. The internal steel structures are usually

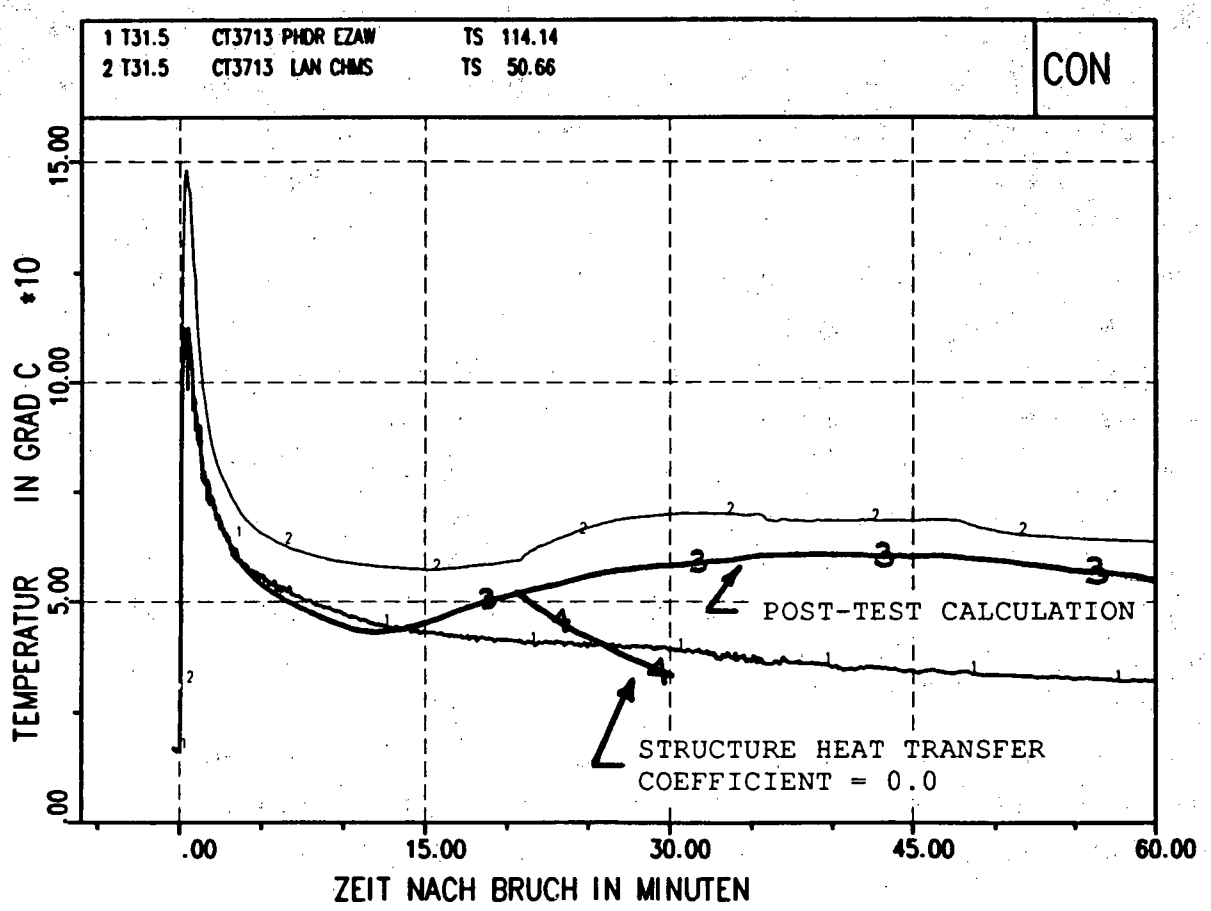


Fig. 17.
Temperature comparisons between the experiment (1), the blind calculation (2), the post-test calculation (3), and the partial the post-test calculation with the structure heat-transfer coefficient = 0.0.

thin (less than 1 cm), and they follow the gas temperature relatively well. When the gas temperature decreases, the internal steel structures give their energy back to the gas. Because of the nonphysical smearing to computational cells that actually do not contain any structure, these cells exhibit a temperature increase that is opposite to the decrease seen in the experimental data. This effect is shown very well in Fig. 17, which results from restarting the post-test calculation at roughly 20 min with the internal structure heat-transfer coefficient set equal to zero for all computational cells. The curve labeled (4) in Fig. 17 shows the result. It is clear that stored energy is transferred back to the gas from the internal structure because the gas temperature decreases to quickly when this physical process is neglected.

VI. CONCLUSIONS

We have learned that the resolution of the internal steel structures must be commensurate with the spatial resolution given by the computational mesh. It is not wise to lump all internal structures and then smear their mass and surface area homogeneously throughout the computational volume. In the case for the HDR containment, three thicknesses were characterized for each room. When mapping the internal structures into a three-dimensional finite-difference mesh, one must be careful to distribute them as they are actually located and not homogeneously smear them over arbitrary volumes.

The apparent lack of mixing as shown in Fig. 15 may point to the need of a more sophisticated turbulence model. The current analyses have used an algebraic mixing length model, which relates the turbulent viscosity to an estimate of the turbulent kinetic energy and a length scale. A closer examination of this approach should be made.

In the overall, the blind predictions of the HDR T31.5 hydrogen distribution test provided an adequate representation of the data. The trends, if not the absolutes, of this complex experiment in an extremely complicated containment geometry were well represented.

REFERENCES

1. J. R. Travis, "HMS: A Model for Hydrogen Migration Studies in LWR Containments," Second International Workshop on the Impact of Hydrogen on Water Reactor Safety, October 3-7, 1982, Albuquerque, New Mexico.

2. J. R. Travis, "Hydrogen Diffusion Flames in a MARK III Containment," Joint ANS/ASME Conference on Design, Construction, and Operation of Nuclear Power Plants, August 5-8, 1984, Portland, Oregon.

3. J. R. Travis, "HMS: A Computer Program for Transient, 3-D Mixing Gases," Los Alamos National Laboratory report LA-10267-MS, NUREG/CR-4020 (1985).

4. J. R. Travis, "A Heat, Mass, and Momentum Transport Model for Hydrogen Diffusion Flames in Nuclear Reactor Containments," Nuclear Engr. and Design 101, 149-166 (1987).

5. J. R. Travis and T. G. Theofanous, "Some Examples of Hydrogen Transport and Mixing," 1987 National Heat Transfer Conference, August 9-12, 1987, Pittsburgh, Pennsylvania.

6. L. Wolf and L. Valencia, "Results of the Preliminary Hydrogen Distribution Experiment at HDR and Future Experiments for Phase III," 16th Water Reactor Safety Information Meeting, Gaithersburg, Maryland, October 24-27, 1988.

Severe Accident Natural Circulation Studies Using SCDAP/RELAP5[a]

Paul D. Bayless

Idaho National Engineering Laboratory
EG&G Idaho, Inc.

ABSTRACT

Sensitivity calculations have been performed to investigate the effects of natural circulation modeling uncertainties on the response of the Surry plant during the heatup and core damage phase of a station blackout transient. Creep rupture failure of the pressurizer surge line was predicted to occur in all of the calculations except one, in which the hot leg failed shortly before the surge line. The failure time was fairly insensitive to the parameters varied, and occurred near the time that fuel rod relocation began. A calculation was also performed in which creep rupture failure of the surge line was modeled. The subsequent blowdown led to rapid accumulator injection and quenching of the entire core.

INTRODUCTION

Natural circulation in the reactor coolant system is one of the major severe accident uncertainties identified in NUREG-0956.[1] Multidimensional natural circulation flows in the reactor vessel and hot legs have been investigated using the SCDAP/RELAP5 computer code.[2] Analyses of a station blackout transient (TMLB′ sequence) for the Surry nuclear power plant have been performed to determine the effects of these flows on the plant damage progression.

Previous work investigated the overall system effects of the in-vessel and hot leg natural circulation flows, and indicated that the surge line is likely to fail prior to lower head melt-through in a TMLB′ transient.[3] The current work[4] focused on sensitivity studies that investigated how uncertainties in some of the key phenomena and modeling assumptions may affect the failure timing and location. Parameters included in the sensitivity studies were the axial power profile, the amount of mixing in the steam generator inlet plena, heat loss through the hot leg and surge line piping, and the crossflow (radial) resistance in the reactor vessel. An analysis of the depressurization following failure of the surge line was also performed. The potential for creep rupture failure of the hot leg, pressurizer surge line, and steam generator tubes was monitored throughout the calculations.

[a] Work supported by the U. S. Nuclear Regulatory Commission, Office of Nuclear Regulatory Research under DOE Contract No. DE-AC07-76ID01570.

ANALYSIS RESULTS

The base case calculation assumed best-estimate values for the sensitivity parameters. The calculation started when the core uncovering and heatup began, at 160 min. As the core uncovered, a natural circulation flow was established between the core and upper plenum. The presence of superheated steam in the upper plenum also resulted in a countercurrent flow being established in the hot legs, with hotter vapor flowing along the top of the hot legs to the U-tube steam generators and cooler vapor returning along the bottom of the hot legs to the reactor vessel. About 75% of the core heat was removed by the coolant during the heatup, with 30% of this energy being deposited in the coolant loops. While the hot leg countercurrent flow caused the hot leg piping and steam generator tubes to heat up, the power-operated relief valve cycling led to heatup of the surge line pipe by drawing hot vapor into the surge line. Figure 1 shows the hottest piping temperatures in the hot leg, surge line, and steam generators. Creep rupture failure of the surge line was predicted to occur at 246 min, at a temperature of 1219 K. Fuel rod relocation did not begin until 248 min, shortly after the surge line failure.

A chopped cosine axial power profile was used in the next calculation. This represented a profile more representative of the beginning of a fuel cycle, rather than the flatter end-of-life profile used in the base case. There was little difference in the plant response from the base case. Creep rupture failure of the surge line occurred at 245 min, virtually the same time as in the base case, but at a slightly higher temperature, 1238 K.

The natural circulation flow in the hot legs and steam generators is controlled by the mixing in the steam generator inlet plena. This mixing between the hot and cold vapor determines the density difference that drives the hot leg countercurrent flow. Large changes in the amount of mixing were modeled in two sensitivity calculations, because the uncertainty in the hot leg flow rates are relatively large. In the first calculation, the mixing was reduced so that the hot leg flow rate at any given (hot leg) inlet vapor temperature increased by 25% over the base case. The higher flow rates changed the energy distribution compared to the base case. About 6% more of the core decay energy was removed, and more of the energy removed from the core was deposited in the loops, particularly in the steam generators; the fraction of the energy removed from the core that was transferred to the steam generators increased by 30%. Higher energy removal from the core slowed the core heatup, extending the time to fuel rod relocation and to the surge line failure. The slower core heatup caused complete oxidation of much of the fuel rod cladding before Zircaloy melting temperatures were reached. Relocation began near 254 min, less than 1 min before the surge line failed at a temperature of 1256 K.

In the second calculation, there was no mixing in the steam generator inlet plena. This limiting condition resulted in a 50-60% increase in the hot leg countercurrent flow rate at any given hot leg inlet vapor temperature compared to the base case. The higher flow rate resulted in the

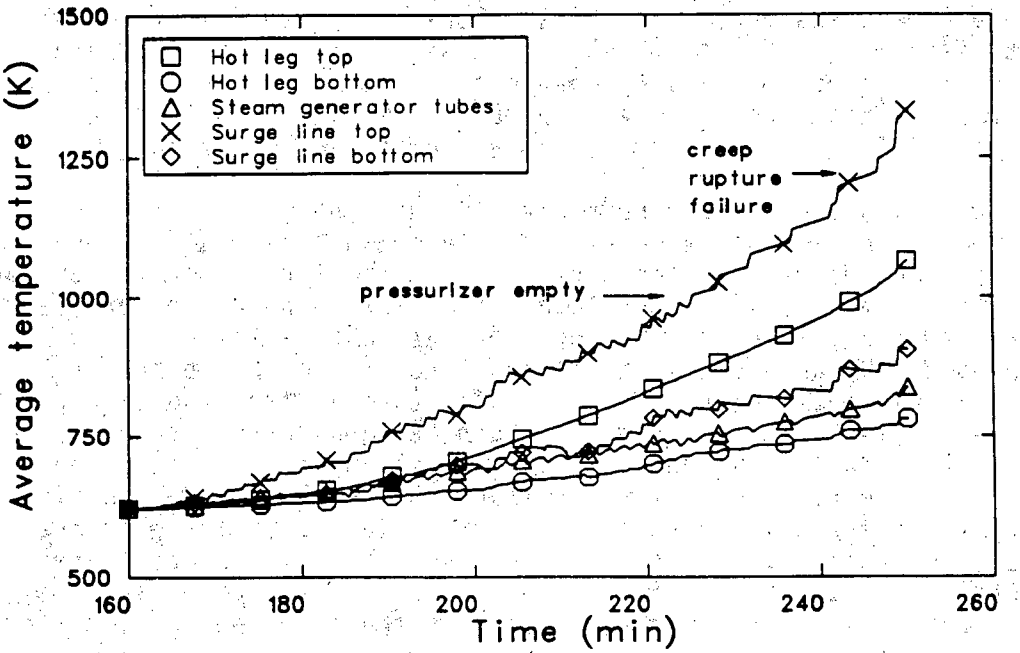


Figure 1. Volume-average temperatures of the hottest Loop C hot leg, surge line, and steam generator tubes for sensitivity Case 1.

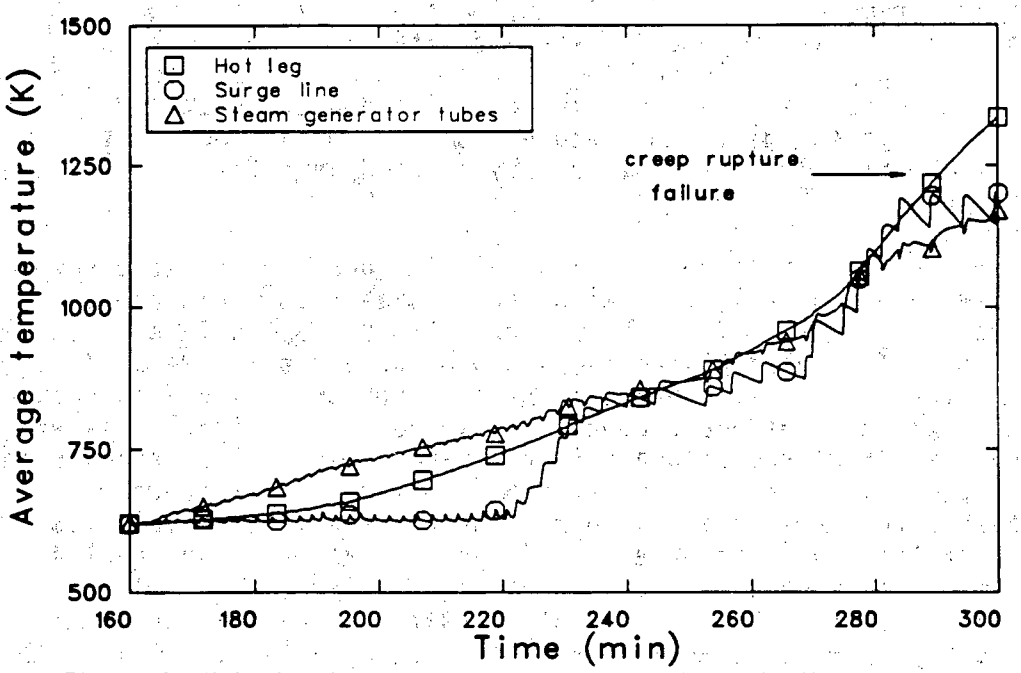


Figure 2. Highest volume-average pipe temperatures in the Loop C hot leg, surge line, and steam generator tubes for sensitivity Case 4.

loop structure temperatures being closer together. Figure 2 shows the highest hot leg, surge line, and steam generator tube temperatures during this calculation (Case 4). Higher energy removal from the core again extended the transient. The reactor coolant system failure location was the pressurizer loop hot leg, which failed at 291 min at a temperature of 1233 K. Fuel rod relocation began near 275 min. The slow core heatup resulted in oxidation of more than 60% of the fuel rod cladding, generating more than 440 kg of hydrogen by the end of the calculation.

Two calculations were performed in which heat loss through the hot leg and surge line piping was modeled; in the base case, these pipes were modeled with adiabatic outer surfaces. In the first case, a constant convective heat transfer coefficient and sink temperature were used. About 4% of the energy removed from the core was lost to the containment through the piping. Because of the heat loss through the hot legs, the vapor entering the steam generators was cooler than in the base case. This resulted in less heat transfer in the steam generators, so that the tubes were cooler than in the base case. The cooling of the piping also delayed the surge line failure by 7 min compared to the base case. Differences in the core temperatures were not as great as in the loops, with fuel rod relocation beginning less than 2 min later than in the base case. This indicates that the heat loss through the piping was compensated by less heat transfer to the steam generators, so that the total energy transfer to the coolant loops was nearly the same as in the base case. In the second heat loss case, a radiative heat transfer coefficient was added to the convective coefficient. This increased the heat loss through the piping to about 5% of the energy removed from the core during the transient. Again, less heat transfer in the steam generators compensated for the additional heat loss through the piping. The cooling of the surge line delayed its failure by an additional 6 min, to 259 min. In both of these calculations, the hot leg flow at any given inlet temperature was the same as that in the base case because the heat loss was balanced by reduced heat transfer in the steam generators.

The fourth set of sensitivity calculations investigated how the in-vessel behavior was affected by the radial flow resistance. Decreasing the upper plenum resistance by a factor of 10 had little effect on the transient. The upper plenum temperatures were a bit more uniform radially than in the base case, causing a small reduction in the flow recirculating between the core and upper plenum. This led to a slightly faster core heatup, with fuel rod relocation beginning 3 min earlier than in the base case. Surge line failure occurred at 245 min, at a temperature of 1258 K. Decreasing the core radial flow resistance by a factor of 10 also had little effect on the plant response. Fuel rod relocation began about 4 min earlier than in the base case, and the surge line failed 2 min earlier, at a temperature of 1252 K. In the last sensitivity calculation, both the core and upper plenum resistances were increased by a factor of 10. The increased radial flow resistances tended to make the flow more one-dimensional in the core and upper plenum. In this calculation, ballooning of the fuel rod cladding had a significant impact on the course of the transient. Before ballooning occurred, the results were close to

those of the base case. When ballooning occurred, the flow pattern in the core changed, as did the heatup rate. Figure 3 presents the peak cladding temperatures from this calculation (Case 9) and the base case (Case 1). The heatup rate increased because the cladding ballooned and ruptured. Failure of the cladding exposed the inner surface of the ballooned cladding to steam, allowing it to oxidize. The exothermic oxidation reaction increased the heatup rate of the fuel rods. Higher cladding temperatures resulted in higher vapor temperatures, which in turn led to higher temperatures in the loops. The surge line failed at 234 min, at a temperature of 1252 K.

In all of the calculations, cladding failure was based on strain or temperature. If the temperature reached 1470 K, the cladding failed, simulating the interaction of the Zircaloy cladding with Inconel grid spacers.[5,6] This last sensitivity calculation was the only one in which ballooning noticeably altered the transient progression. Ballooning occurred in some of the other calculations, changing the magnitude of the flows but not the flow patterns.

A final calculation was performed in which the base case calculation was continued with a 15-cm diameter hole in the side of the surge line modeled at 246 min. The pressure decreased rapidly, from 16.2 to 1.7 MPa in 1.25 min. Steam cooling driven by the depressurization prevented the core from heating up further. Water from the accumulators then entered the reactor vessel and core. A complete quench of the core ensued. While the embrittled fuel rods would be expected to shatter and form a rubble bed during the quench, a rodlike geometry was assumed to be maintained in the calculation. At the end of the calculation, near 267 min, the accumulators were empty, the reactor coolant system pressure was below 1 MPa, and the two-phase liquid level was just above the top of the core.

SUMMARY AND CONCLUSIONS

The hot leg flow was affected only by the inlet vapor temperature and the steam generator inlet plenum mixing. With decreased inlet plenum mixing, the flow increased, increasing the heat transfer in the loops and moving more of the energy to the steam generator tubes. Any changes in the upper plenum conditions affected the hot leg flow only by altering the hot leg inlet vapor temperature.

Heat loss through the hot leg pipe also affected only the loop energy distribution, and not the hot leg flow. The heat loss through the pipe reduced the temperature of the vapor entering the steam generators. With lower temperatures, the steam generators removed less energy, and the tube temperatures were reduced. The heat loss delayed the surge line failure by 6-13 min.

With a simple model in SCDAP/RELAP5 simulating the effects of cladding/grid spacer material interactions, ballooning did not occur as frequently as in past calculations. In most of the sensitivity calculations, the fuel rod cladding failed when the calculated temperature reached 1470 K, a value input to simulate the effects of eutectic formation

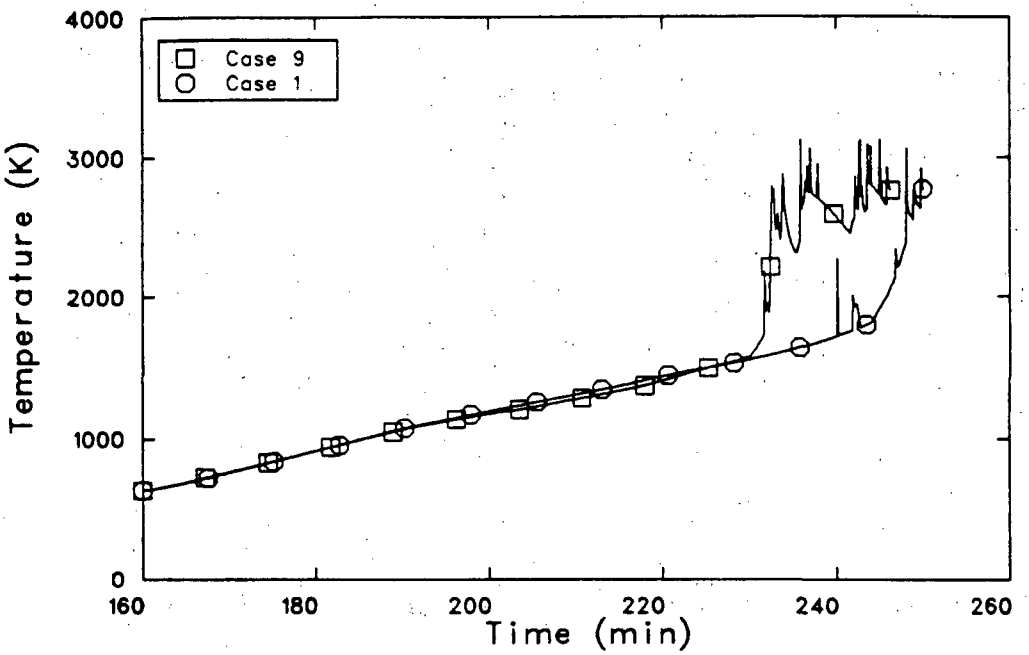


Figure 3. Peak cladding temperatures for sensitivity Cases 9 and 1.

between the Zircaloy and iron or nickel, rather than failing because of excessive strain following ballooning. The ballooning that did occur generally had only a small effect on the core flows and early heatup behavior. Only in the sensitivity calculation with increased reactor vessel radial flow resistances did the ballooning have a significant effect on the core flow pattern and heatup rate.

The pressure boundary failure in all the cases occurred very close to the time that fuel rod relocation began. The largest differences in the timing of these two events were 7.4 min in the second heat loss sensitivity calculation and 15.2 min in the calculation with no mixing in the steam generator inlet plena; the initial fuel rod relocation and surge line failure occurred within 3.1 min of each other in all the other calculations. The significance of that is its relation to the timing of the reactor vessel lower head melt-through. The results of a MELPROG calculation[7] showed that the melt-through occurred nearly 100 min after the initial fuel rod relocation. Since the reactor coolant system failure occurred no more than 15.2 min later than the initial fuel rod relocation in the sensitivity calculations, it should occur at least an hour before the vessel failure. This allows a long time for the system to depressurize.

With a 15-cm diameter failure, this would be more than enough time to depressurize the primary system to nearly the containment pressure. In the surge line failure calculation, the pressure decreased from 16.2 to less than 1.0 MPa within 16 min.

The reactor coolant system failure time and location were fairly insensitive to the parameters varied in the sensitivity calculations. The surge line was predicted to fail in all of the calculations except in the calculation with no inlet plenum mixing, where the hot leg failed shortly before the surge line. However, even in that case, the calculated surge line behavior may have resulted in lower surge line temperatures than one might expect. Failure of the surge line occurred within 13 min of the base case time of 246 min in all of the cases, again with the exception of the calculation with no steam generator inlet plenum mixing, where the hot leg failed 44 min later. It must be remembered that this latter case was a bounding calculation that maximized the hot leg countercurrent flow, so a longer delay was expected.

REFERENCES

1. M. Silberberg, J. A. Mitchell, R. O. Meyer, and C. P. Ryder, Reassessment of the Technical Bases for Estimating Source Terms, NUREG-0956, July 1986.

2. T. C. Cheng et al., "RELAP5/SCDAP - An Integrated Code for Severe Accident Analysis," Proceedings of the Thirteenth Water Reactor Safety Research Information Meeting, Gaithersburg, MD, October 22-25, 1985, NUREG/CP-0072, pp. 347-355.

3. P. D. Bayless, "SCDAP/RELAP5 Applications to RCS Natural Circulation," Fifteenth Water Reactor Safety Research Information Meeting, Gaithersburg, MD, October 26-29, 1987.

4. P. D. Bayless, Analyses of Natural Circulation During a Surry Station Blackout Using SCDAP/RELAP5, NUREG/CR-5214, EGG-2547, to be published (manuscript completed September 1988).

5. S. Hagen and P. Hoffmann, Physical and Chemical Behavior of LWR Fuel Elements up to Very High Temperatures, KfK4104, June 1987.

6. S. Hagen, L. Sepold, P. Hoffmann, and G. Schanz, "Out-of-Pile Experiments on Severe Fuel Damage Behavior of LWR Fuel Elements (CORA Program)," IAEA International Symposium on Severe Accidents in Nuclear Power Plants, Sorrento, Italy, March 21-25, 1988.

7. J. E. Kelly, R. J. Henninger, and J. F. Dearing, MELPROG-PWR/MOD1 Analysis of a TMLB' Accident Sequence, NUREG/CR-4742, SAND86-2175, January 1987.

SUMMARY OF TMI-2 CORE SAMPLE EXAMINATIONS[a]

Richard K. McCardell
Malcolm L. Russell
Douglas W. Akers
Charles S. Olsen

Idaho National Engineering Laboratory
EG&G Idaho, Inc.
Idaho Falls, ID 83415

ABSTRACT

Core debris samples were obtained from the upper plenum debris, the central consolidated region, standing fuel rod assemblies, and the lower plenum debris to determine the temperatures that were reached during the TMI-2 accident. The materials interactions that occurred, bulk composition of the materials, oxidation of the materials, and retention of fission products in the core materials were also determined. The results of the metallurgical examinations and the bulk compositions are described in this paper.

INTRODUCTION

The TMI-2 Sample Acquisition and Examination is being conducted by the Department of Energy and the Nuclear Regulatory Commission to provide information to complete the understanding of the TMI-2 accident, and to help resolve severe accident and source term technical issues. Following the accident, the TMI-2 core region consisted of an upper void region almost entirely surrounded by damaged, but standing, peripheral fuel assemblies. Directly below the void region was a region of loose debris resting on a hard crust. The crust completely surrounded a centrally located, consolidated region that was previously molten. A region of intact standing fuel rods extended upwards from the bottom of the core to the bottom of the crust surrounding the previously molten region. About 19,100 kg of molten core material relocated to the lower plenum region of the reactor vessel. Samples have been obtained from the upper debris bed; the standing fuel assemblies surrounding the upper void region; the

---

a. Work supported by the U. S. Department of Energy, Assistant Secretary for Nuclear Energy, Office of LWR Safety and Technology, under DOE Contract No. DE-AC07-76ID01570.

centrally located, previously molten region and surrounding crust; the standing fuel assemblies supporting the lower crust of the previously molten region; and, the previously molten debris that relocated to the lower plenum region. These samples have been subjected to extensive metallurgical and radiochemical examinations to determine elemental composition, oxidation state, materials interactions, peak temperatures, and fission product retention. Selected results of these examinations are the subject of this paper.

UPPER CORE FUEL ASSEMBLIES AND DISTINCT COMPONENTS

The upper void region, illustrated in Figure 1, was approximately 1.5 m deep with an overall volume of 9.3 m^3. Forty-two of the original 177 fuel assemblies were standing at the periphery of the core void. Only two of these fuel assemblies contained more than 90 percent of their full-length cross sections with the majority of the fuel rods intact. Non-destructive exams were performed for fuel assembly and control rod and burnable poison rod assembly upper end fittings from this region. Both non-destructive and destructive examinations were performed on fuel and control rod upper ends. The examinations that were performed are listed in Table 1[1]. Results of the examinations of these components indicated large radial and axial temperature gradients, and differences in cooling behavior of control material existing over short distances. Peak temperatures of the upper spacer grids were 1500 to 1700 K. Previously molten control material had flowed upwards into the plenum spring region of control rods. Also, in the upper end of a fuel rod that had broken off, a previously molten mixture of fuel, cladding, and control and structural material had migrated upwards into the fuel cladding gap for several centimeters. This indicates that at some time during the accident the lower ends of the upper core region were immersed in liquid core materials.

TABLE 1. TMI-2 DISTINCT CORE COMPONENT EXAMINATION PROGRAM

	Non Destructive exams				Destructive exams		
Component	insitu CCTV	photo graph	neutr radio	gamma scan	metal ograph	chem comp	radio chem
Fuel Assembly Upper End Fittings	X	X					
Control and Burnable Poison Rod Assembly Upper End Fittings	X	X					
Fuel Rod Upper Ends	X	X	X	X	X	X	X
Control Rod Upper Ends	X	X	X	X	X	X	X

UPPER PLENUM DEBRIS

The loose debris bed below the core void that was resting on a crust ranged in depth from 0.6 to 1 m, and consisted of whole and fractured fuel pellets, control rod spiders, end fittings and resolidified material[2] totaling about 26,600 kg. Samples obtained from the upper debris bed for examination are shown in Figure 2. The debris bed was heterogeneous, exhibiting a broad range of oxidation and material interactions, but was well mixed. Ninety percent of the sample particles were between 1 and 5 mm in their maximum dimension. Most of the debris bed consisted of shattered and resolidified material that contained regions of previously molten $(U,Zr)O_2$, indicating temperatures greater than 2700 K. There were also a few samples of previously molten material that were almost pure UO_2, indicating temperatures up to 3100 K. Metallographic examinations of individual particles indicated that most of the debris bed had remained at temperatures below 2000 K, or was exposed to high temperatures for only a short time. The bulk composition of the loose debris bed was primarily uranium, zirconium and oxygen with significant depletion of silver, indium, and cadmium control material, Zircaloy cladding, and structural material. Thus, the materials that are the first to melt and/or form eutectics and relocate are depleted from the upper debris bed. The upper debris bed consists of the remnants of highly oxidized fuel rods that shattered when they were cooled, and that were depleted of control, structural and cladding material before cooling.

Figure 3 displays the major melting and interaction points of core materials versus a temperature scale. The determination of whether these phenomena have occurred make it possible to bound peak temperatures. The silver, indium, cadmium control material melting range is between 1073 and 1100 K. Zircaloy transforms from the alpha to the beta phase between 1105 and 1245 K. Zirconium (from the cladding) forms eutectics with iron and nickel (from stainless steel control rod cladding or Inconel grid spacers) at 1200 K but the solid diffusion rate is too slow to be of concern until the temperature reaches 1500 K. Inconel, stainless steel and Zircaloy melt at 1660, 1720, and 2030 K, respectively. The dissolution of UO_2 by zirconium begins at 2030 K.

CENTRAL PREVIOUSLY MOLTEN REGION

The large, crust-enclosed previously molten, consolidated region below the loose debris was approximately 3 m in diameter, 1.5 m thick at its center, and 0.25 m thick at its periphery, and was comprised of about 32,700 kg of material. The previously molten region inside the crust consisted of a mixture of structural, control, and fuel material that reached temperatures of 2700 K, and possibly as high as 3100 K during the accident[3]. The bulk of the previously molten region was determined to be a mixture of both ceramic and metallic phases; however, examples of entirely ceramic and metallic particles were also

present. An example of an entirely ceramic particle from the central region is shown in Figure 4 which is a back scattered electron (BSE) image. The BSE image represents a composite average of the atomic number of the elements in a particular phase where the degree of brightness is proportional to the atomic number of the element (e.g., the high atomic number uranium is brighter than the lower atomic number iron). Examination of this ceramic particle indicated that the light regions were uranium and zirconium oxides, and the dark regions were mixtures of iron, chromium, and aluminum oxides. An entirely metallic particle from the central, previously molten region is shown in Figure 5. The metallic matrix of this sample consisted of a nearly dendritic structure of iron-nickel-chromium with circular inclusions containing silver-indium-tin. Although some of the Ag-In-Sn inclusions contained voids, many contained a spherical particle of chromium oxide (Cr_2O_3).

An example of a particle from the central, previously molten region that contained both metallic and ceramic phases is shown in Figure 6. The ceramic phase is primarily oxides of zirconium and uranium with small amounts of iron and nickel oxides, and is similar to the entirely ceramic particles found both in the central region and in the upper debris bed. The bulk composition of the metallic phases in the central region (which comprised about 15% of the central region) consisted principally of Fe-Ni and Ag-In phases. Thus, the central region contained much more metal than the upper debris bed where no pure metallics were found. Metals from the stainless steel cladding of the control rods, the silver, indium, cadmium control materials, and the Inconel spacer grids (only the Inconel contains molybdenum), existed in abundance in the central, previously molten region.

UPPER CRUST

The upper crust consisted of two phases, a ceramic phase containing mostly fuel material components, and a metallic phase (which comprised about 25% of the upper crust) containing mostly structural and control rod material components. No intact fuel material was present. The peak temperature of the upper crust was at least 2700 K. A representative sample of the upper crust from core position K9 is shown in Figure 7. In this figure, the lighter colored phases are the metallic and the darker phases are the ceramic. The ceramic material in the upper crust was similar to the ceramic material in the central region and the ceramic material in the upper debris bed. However, the bulk composition of the metallic in the upper crust differed from the metallic in the central region. The metallic composition of the upper crust consisted primarily of three phases, namely Fe-Ni, Ag-In-U, and Ni-Sn. The upper crust contained considerably more metallic uranium than the central region and considerably less cadmium.

PERIPHERAL CRUST

The peripheral crust was similar to the upper crust except that there were remnants of intact fuel pellets that may have fallen into the peripheral crust from the upper debris bed, and the metallic phases in the crust were rich in zirconium as compared with the upper crust and the central region. The bulk composition of the metallics in the peripheral crust was similar to the lower crust, except the principal element in the peripheral crust was zirconium. Three phases existed in the metallic portion of the peripheral crust; namely Fe-Zr-Ni-Cr, Ag-In, and Zr-Ni-In. As is the case for the metallics in the upper crust and the previously molten central region, the constituents of the metallic region, with the exception of uranium, zirconium and cadmium, are all several times the core average. The high percentage of zirconium in the peripheral crust implies that this crust was formed at a time in the accident when the molten zirconium and control and structural material was flowing downward and freezing.

LOWER CRUST

The lower crust consisted of vertical fuel pellet stack columns surrounded by previously molten material as illustrated in Figure 8. Apparently during the early part of the accident, structural and control rod material flowed down the coolant channels, dissolved the Zircaloy cladding and flowed into the pellet/pellet interfaces and cracks in the pellets and froze forming the lower crust. The molten material was composed of a mixture of metallic structural and control rod components with relatively small (100 to 200 micron) UO_2 inclusions. It is clear that the eutectic between zirconium and iron and zirconium and nickel formed, and therefore, the previously molten metallic in the lower plenum reached at least 1400 K. Also, rounded edges of ceramic UO_2 particles that were carried downward in the melt indicate the onset of dissolution requiring that temperatures in the melt approach 2200 K. The metallic material in the lower crust contained an even higher percentage of zirconium than the peripheral crust. The composition of the three phases of the metallic material in the lower crust were Zr-Fe-Ni-Cr, Ag-In, and Zr-Ni-In.

STANDING FUEL ASSEMBLY STUBS

The standing fuel assembly stubs below the previously molten region varied in length from about 0.2 to 1.5 m, with the longer fuel assembly stubs located at the core periphery. Metallographic examinations indicate that the fuel rod stubs reached relatively low temperatures (below 1100 K) during the accident. The standing fuel assembly stubs supporting the previously molten region taken together with the intact peripheral fuel assemblies surrounding the upper void region comprised 44,500 kg.

Although no significant damage occurred to the fuel rod stubs, zirconium rich metallic material, similar to that in the lower crust, flowed downward inside of an empty instrument tube in Assembly G8. Thus, empty instrument guide tubes provide an escape path for the relocating molten metallic material and some of this material may have reached the lower plenum by this means.

LOWER PLENUM DEBRIS

The debris resting on the lower head accumulated to a depth of 0.75 to 1 m above the lowest head elevation, and to a diameter of 4 m. The spatial distribution of the lower plenum debris was neither uniform nor symmetric, which may be the result of debris redistribution caused by hydraulic forces during operation of the A-loop reactor coolant pump after relocation of the debris to the lower plenum. Particle sizes varied from large "rock" (up to 0.2 m) to granular particles (less than 0.1 mm). The particles were previously molten ceramic, $(U,Zr)O_2$, homogeneous and very porous[4]. A lower plenum ceramic particle is shown in Figure 9. These ceramic particles were similar in composition to the ceramic particles in the upper debris bed and the previously molten central region and to the ceramics in the upper and peripheral crusts. The peak temperature of the lower plenum debris varied between 2700 and 3100 K. Additional large volume samples from the lower plenum region are to be analyzed to confirm the results of radiological measurements that indicate that iodine, ruthenium and antimony exist in much lower concentrations in the lower plenum debris than in the upper debris bed.

CONCLUSIONS

Based on the metallurgical examination of TMI-2 core samples, the temperatures reached in the upper debris bed, the upper crust, the peripheral crust, the central previously molten region and the lower debris bed were all between 2700 and 3100 K. The ceramic material in these regions was similar, and consisted primarily of oxidized uranium and zirconium with lesser amounts of iron and nickel oxides precipitated on the grain boundaries of the U-Zr-O matrix. The temperature of the lower crust was greater than 1400 K and probably close to 2200 K.

The metallic material in the various parts of the central consolidated region varied depending on the region. The lower and peripheral crusts contained zirconium rich metallics that were principally zirconium, iron, nickel, and uranium with lesser amounts of silver, chromium, tin, indium, molybdenum and cadmium. Metallics in the central, previously molten region were primarily iron and nickel, with lesser amounts of silver, tin, chromium, molybdenum, indium and cadmium. Metallics in the upper debris bed contained a large fraction of uranium and were composed principaly of iron,

uranium, nickel and zirconium with lesser amounts of silver, chromium, tin, indium, molybdenum, and cadmium. Only trace amounts of oxidized metallics were found in the upper and lower debris beds. These two regions were significantly depleted of both control and structural materials.

The temperatures and compositions of the various regions of the core are consistent with the following materials interactions that have been determined from both in- and out-of pile experiments[5-7]. As the temperature increases the silver, indium and cadmium control material melt at about 1100 K but are contained within the stainless steel cladding. The first melt to form that is free to flow downward results from the eutectic interaction between the Inconel spacer grids and the Zircaloy fuel rod cladding and Zircaloy guide tubes and stainless steel cladding of the control rods at about 1500 K. Once this first liquid is formed, additional eutectic (such as between the Inconel and Zircaloy reaction products and the stainless steel control rod cladding which would allow the already molten silver, indium and cadmium to join in the eutectic formation sequence) forms more rapidly due to enhanced atomic mobilities in the liquid as opposed to the solid state. The combination of liquid cladding, structural and control materials is then capable of flowing downwards. The temperature increases at a much faster rate when the oxidation of the zirconium in the cladding accelerates at around 1700 K and at about 2200 K dissolution of the UO_2 in the fuel rods begins. At about this same temperature, the stainless steel control rod cladding melting point is reached allowing control rods to fail at locations other than at spacer grids, releasing much more molten silver, indium and cadmium which interacts with the Zircaloy control rod guide tube as does the molten stainless steel. The complex mixture of liquid uranium, zirconium and tin from the fuel rods and the structural and control materials then flows downward apparently carrying UO_2 particles with the melt. When this complex mixture reaches the lower part of the core that is covered with water, it freezes forming a lower crust which grows to the periphery of the core and supports the upper part of the core which continues to increase in temperature. These interactions are consistent with the formation of the lower crust in the TMI-2 core, the depletion of control and structural materials in the upper plenum debris, the formation of the central molten region in the core, and the bulk compositions that were found in the various ceramic and metallic regions of the core. The absence of control and structural materials in the lower plenum debris samples is consistent with relocation of ceramic material from the central molten region of the core.

It is clear that the integrity of the lower head of the reactor pressure vessel was challenged by the relocation of 19,200 kg of molten core material to this region. The U. S. Nuclear Regulatory Commission, in parterniship with the Organization for Economic Co-Operation and Development, has initiated a program to obtain and examine samples from the TMI-2 lower reactor pressure vessel head and from debris located adjacent to the lower head.

REFERENCES

1. S. M. Jensen, et. al., Examination of the TMI-2 Core Distinct Components, GEND-INF-082, September 1987.

2. D. W. Akers, et. al., TMI-2 Core Debris Grab Samples--Examination and Analysis, GEND-INF-075, September 1986.

3. D. W. Akers, et.al., The TMI-2 Lower Core Region: Examination and Analysis (Draft), GEND-INF-092, September 1988.

4. C. S. Olsen, et. al., Examination of Debris from the Lower Head of the TMI-2 Reactor, GEND-INF-084, January 1988.

5. S. Hagen et. al., "Out-of-Pile Experiments on Severe Fuel Damage Behavior of LWR Fuel Elements (CORA-Program)", IAEA International Symposium of Severe Accidents in Nuclear Power Plants, Sorrento, Italy, March 21-25, 1988.

6. D. J. Osetek, "Results of the Four PBF Severe Fuel Damage Tests", Proceedings of the Fifteenth Water Reactor Safety Information Meeting, NUREG/CP-0090, October 1987.

7. R. R. Hobbins et. al., "Molten Material Behavior in the TMI-2 Accident", AM. NUCL.SOC. TMI-2 Topical Meeting, Washington, D.C., October 31-November 4, 1988.

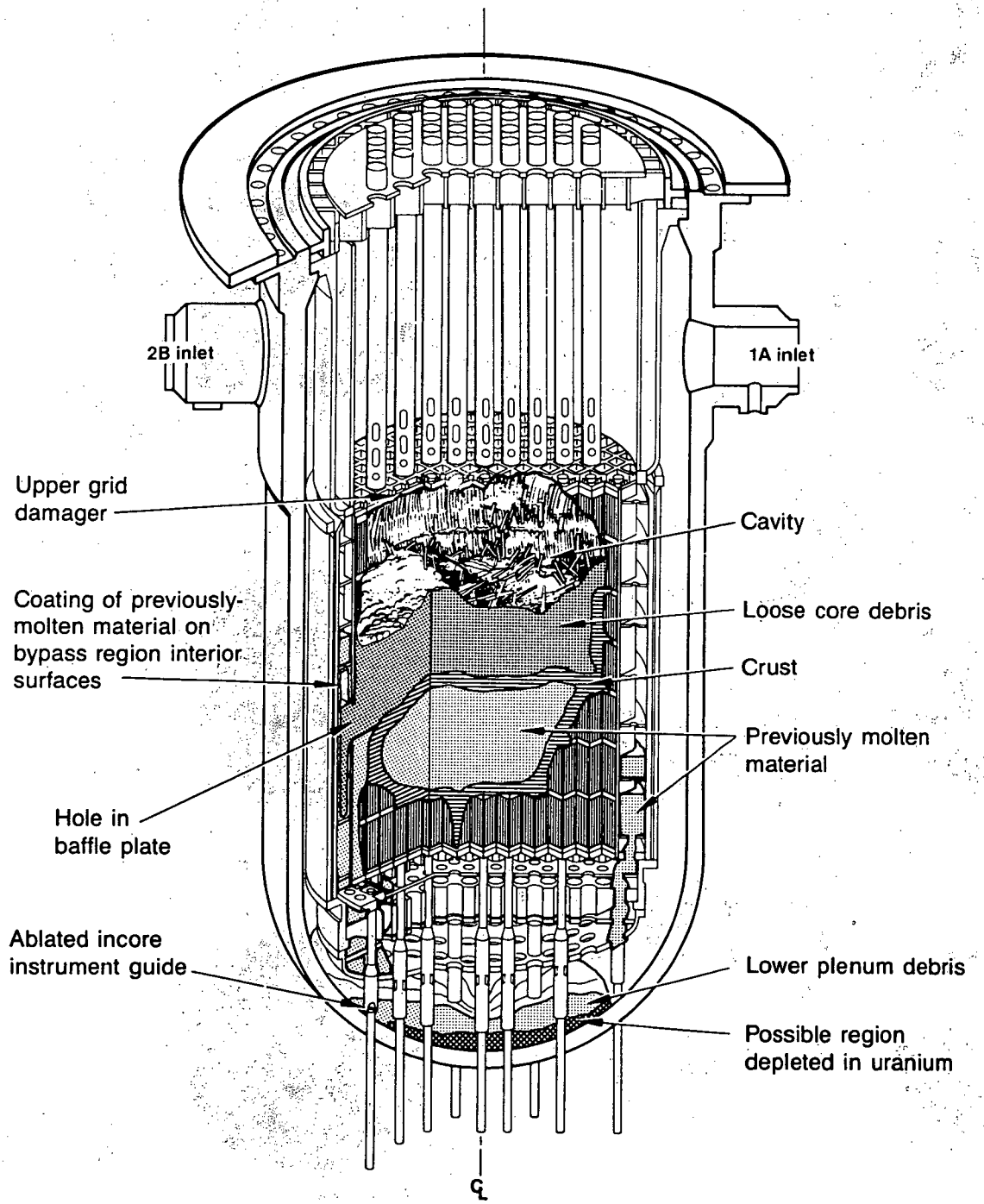


Figure 1. TMI-2 end state core condition. 8-9078

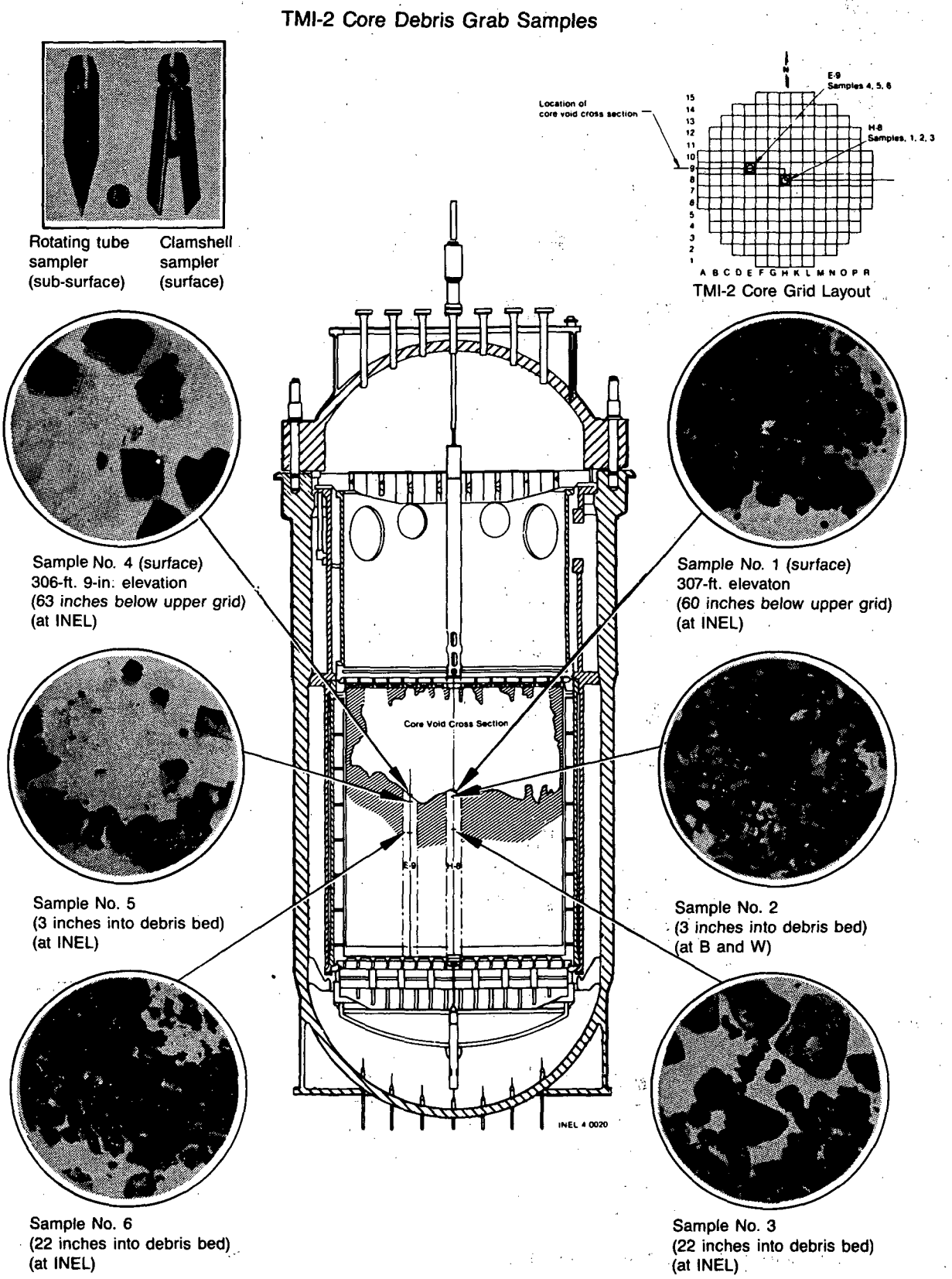


Figure 2. TMI-2 core debris grab samples.

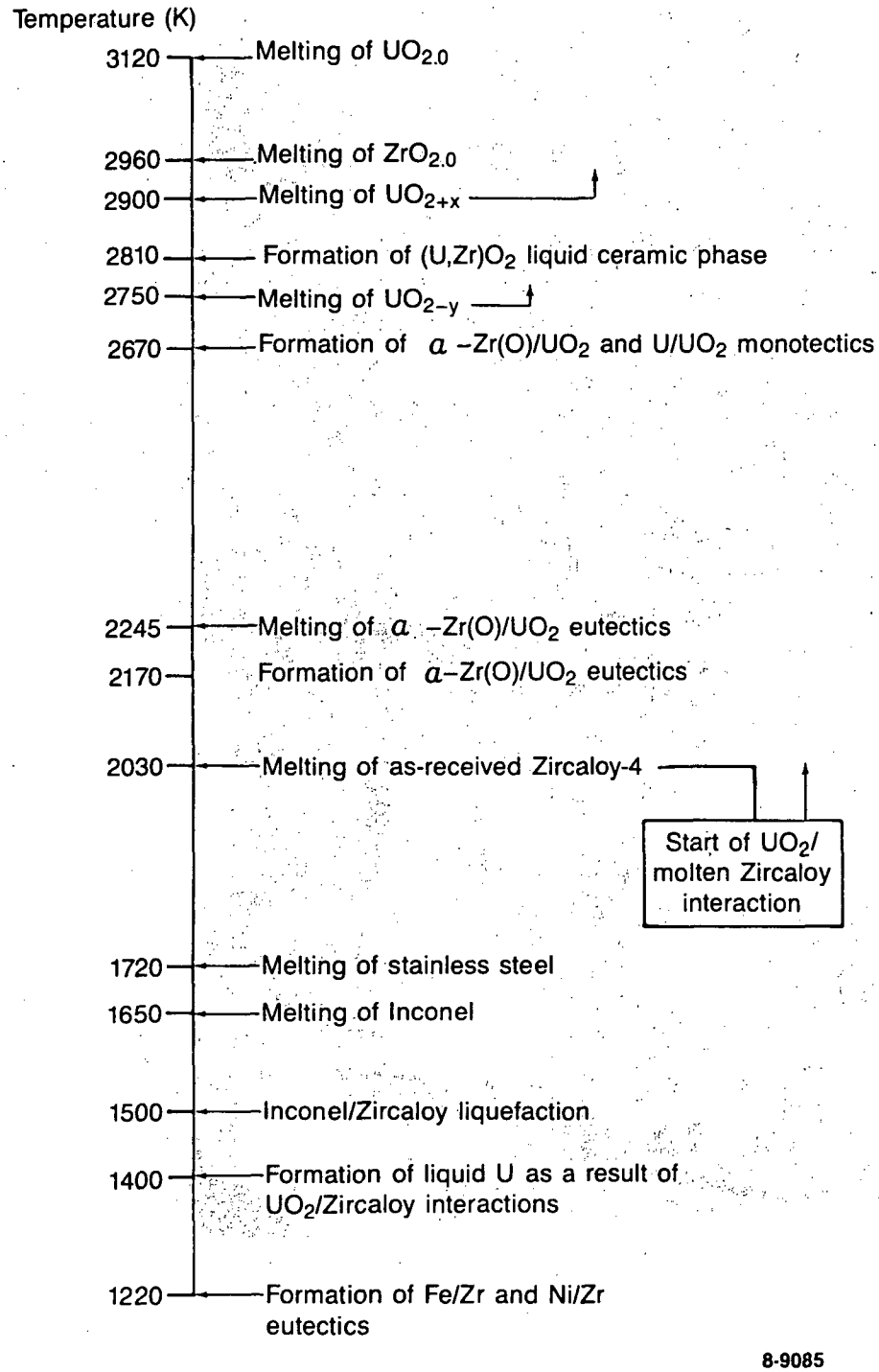


Figure 3. Temperature indicators for nuclear core materials.

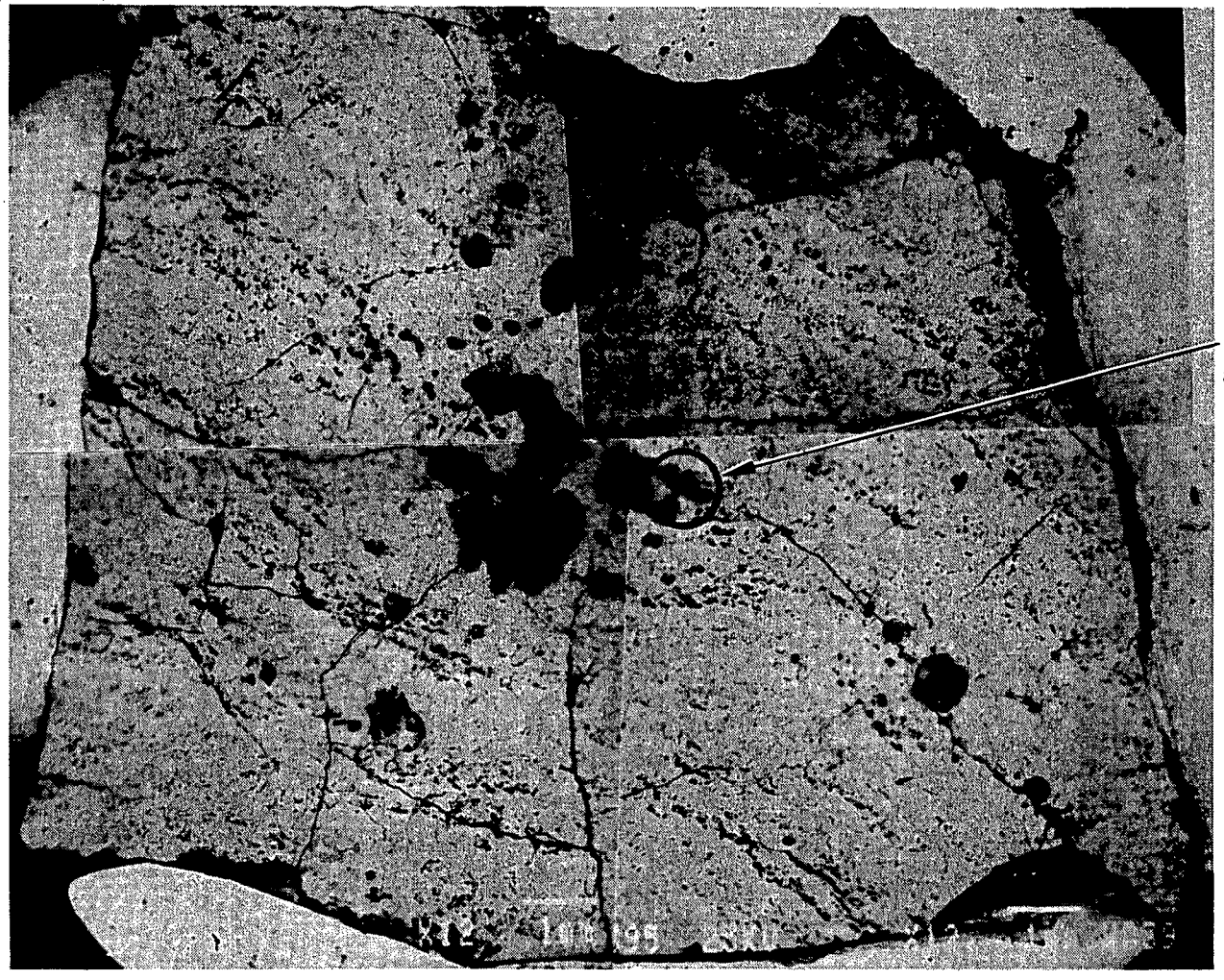


Figure 4. Core location K9 — ceramic particle (BSE image).

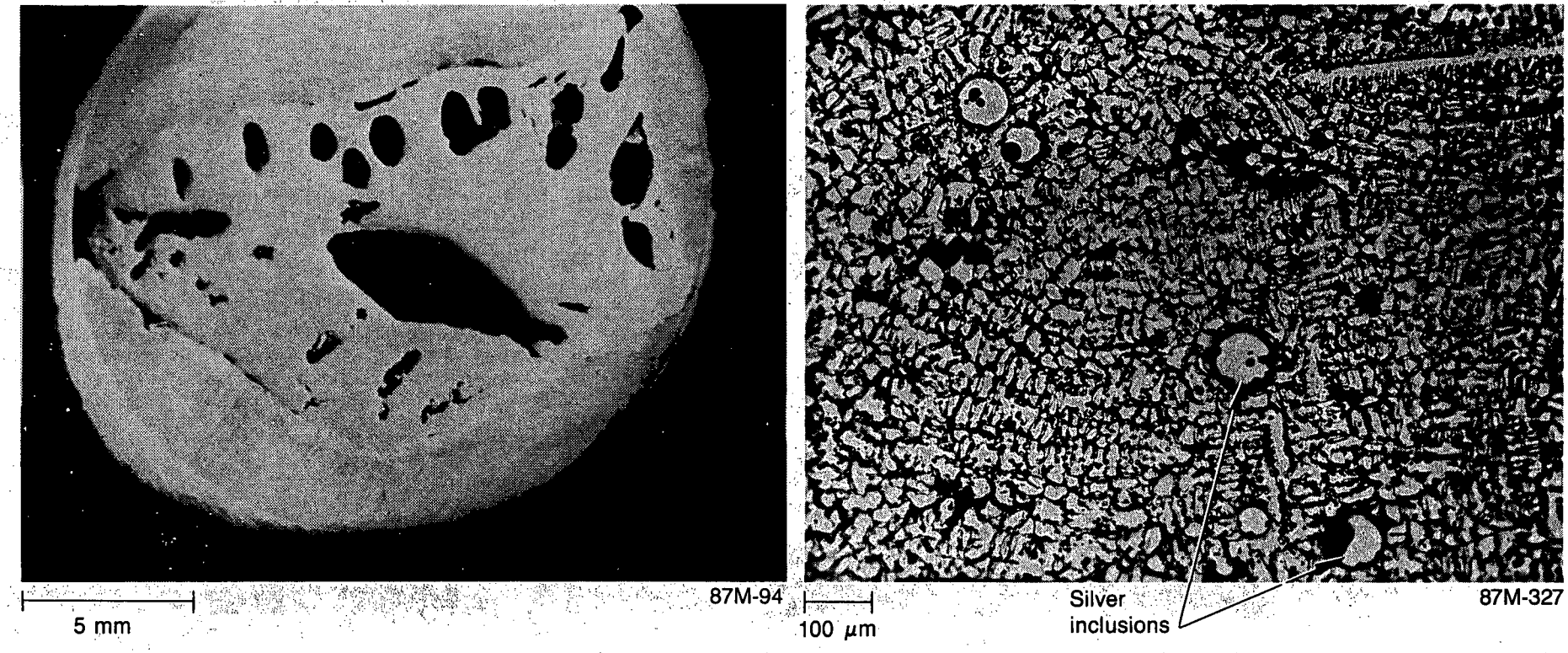


Figure 5. Core location 09 — metallic particle.

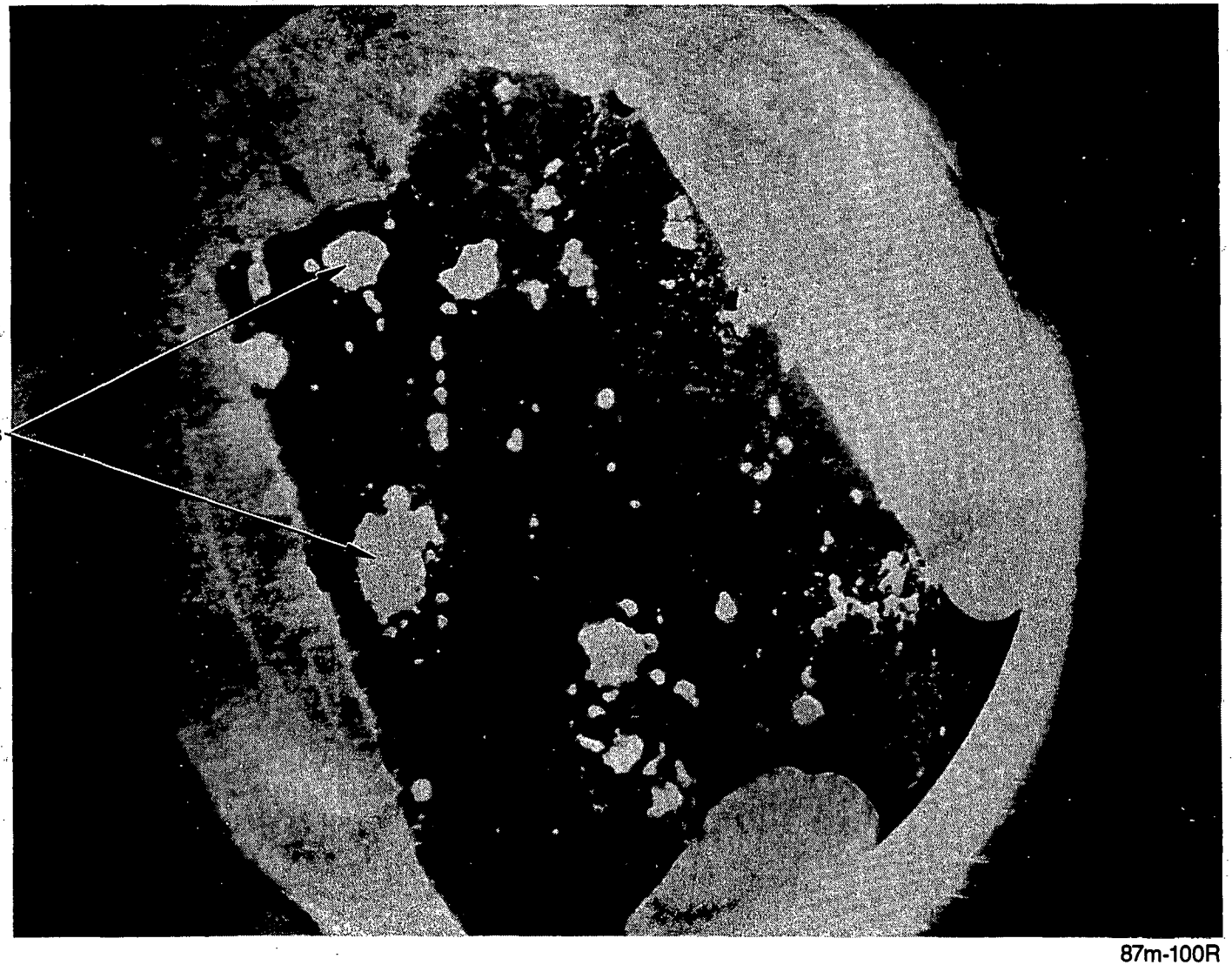
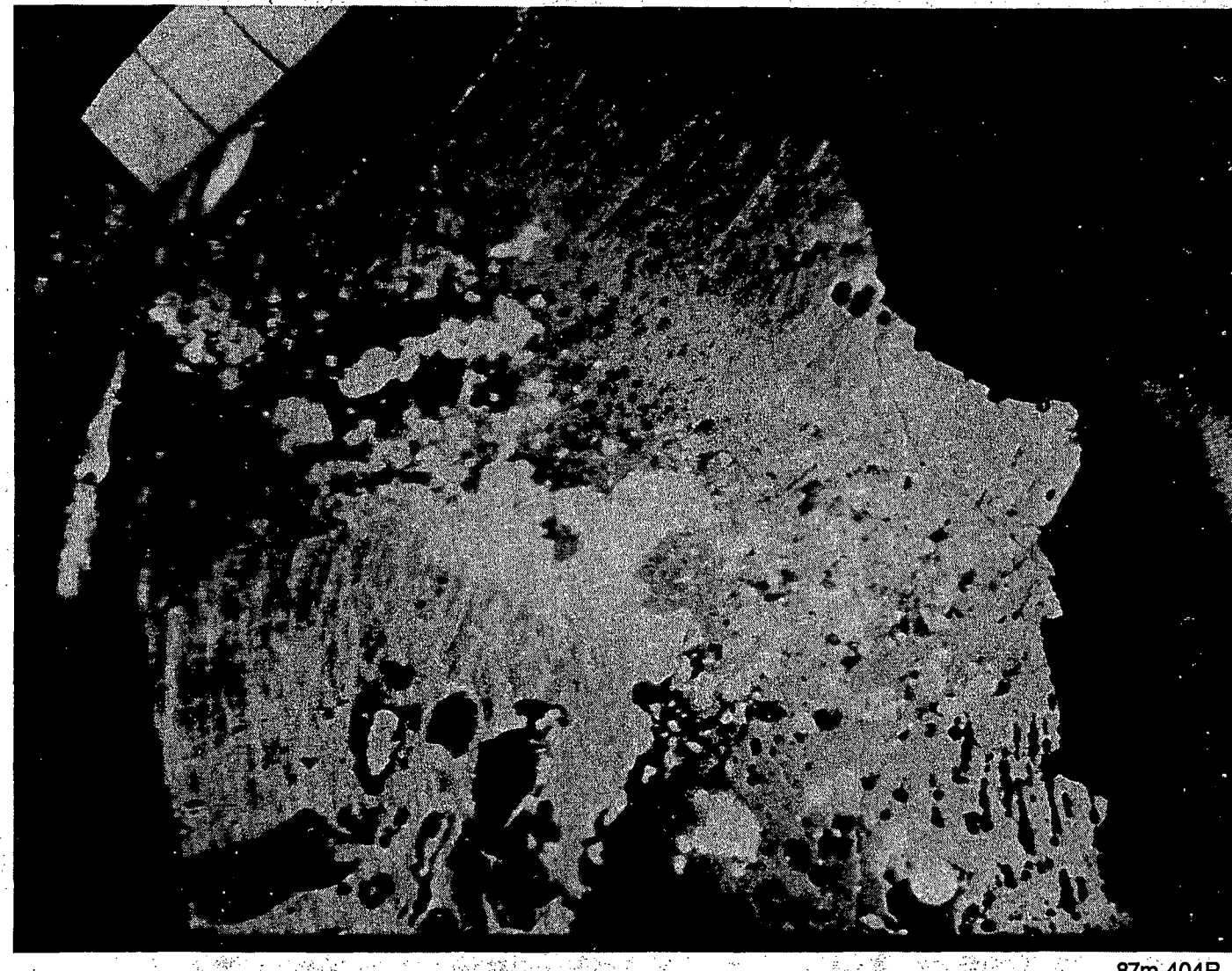


Figure 6. Ceramic particle with metallic inclusions (core location G12)



87m-404R

Figure 7. Core location K9 — upper crust.

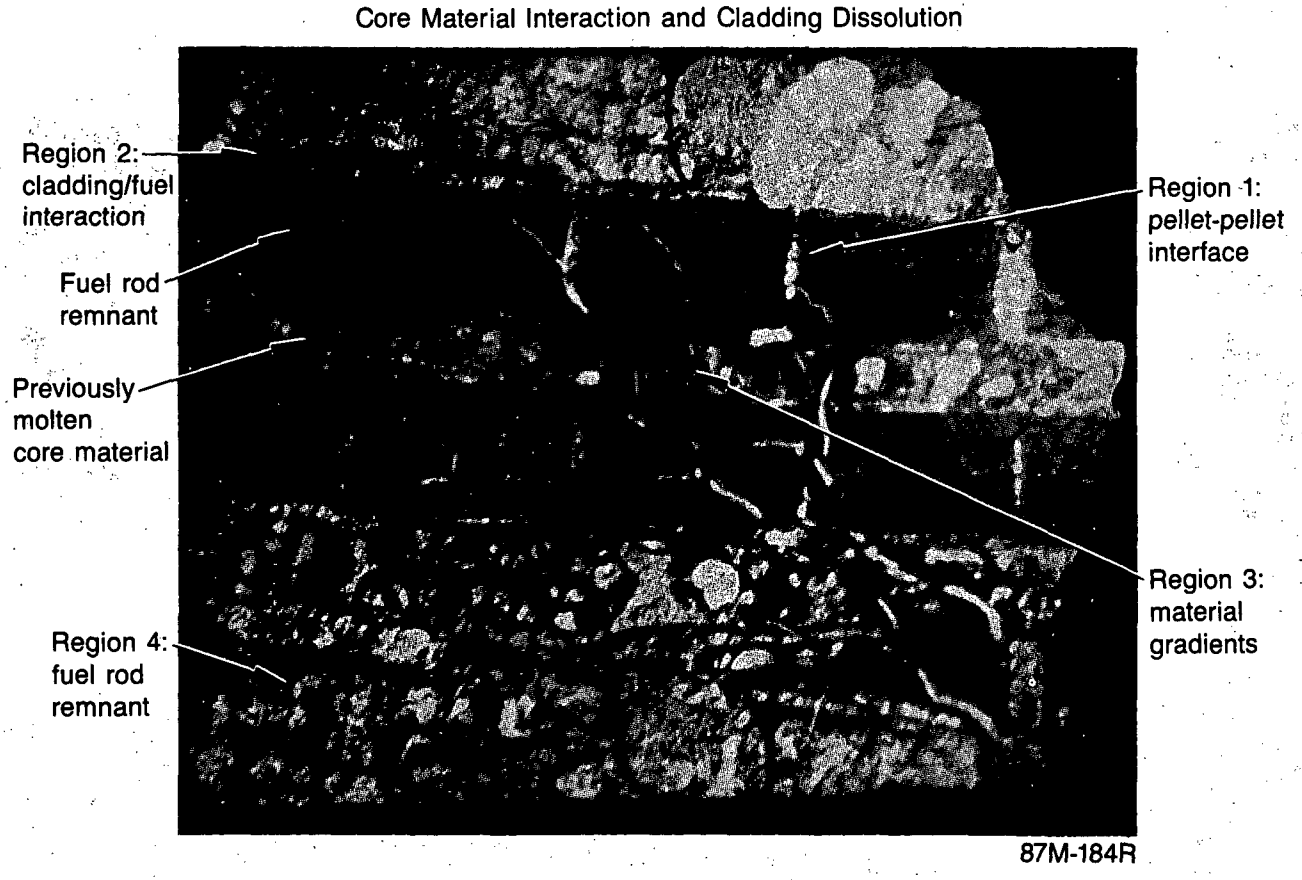
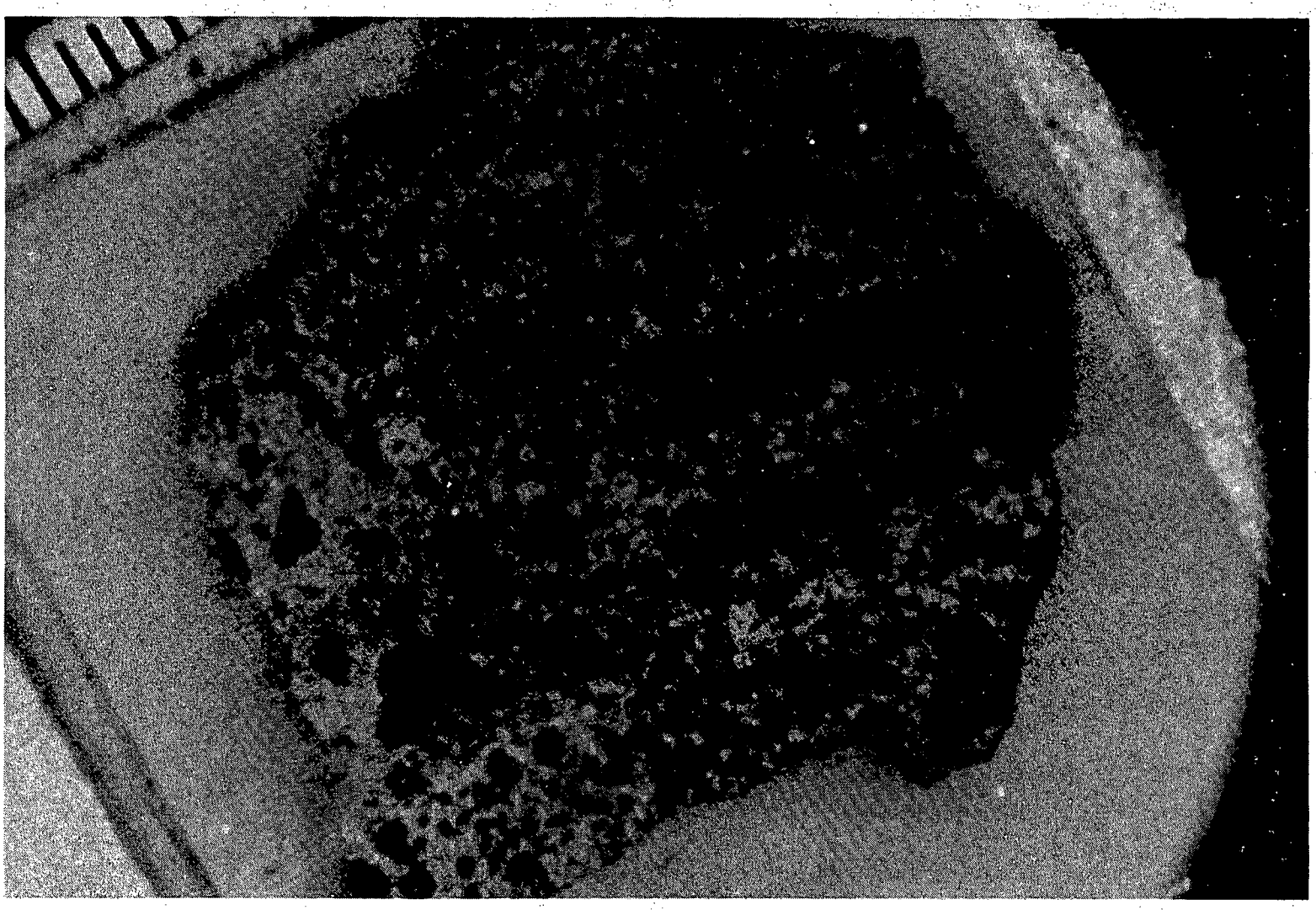


Figure 8. Lower crust from core position K9 illustrating previously molten metallic material frozen around fuel rods.



11-5-C Sampling Locations

Figure 9. Cross-section of lower plenum particle 11-5.

TMI-2 CORE MATERIALS AND FISSION PRODUCT INVENTORY[a]

Douglas W. Akers
Richard K. McCardell
Malcolm L. Russell
Getachew Worku*

Idaho National Engineering Laboratory
EG&G Idaho, Inc.
Idaho Falls, ID 83415
*Grove Engineering Inc.
Rockville, Maryland

ABSTRACT

Examinations have been performed to characterize the distribution of core materials and fission products at the damaged Three Mile Island Unit 2 (TMI-2) reactor. The purpose of this paper is to summarize the current status of the core materials and fission product inventory evaluations at TMI-2 and to present results that may affect reactor source term issues. Principal subjects include the relocation of core materials outside the reactor vessel, the formation of complex, core material interaction products, cesium retention in prior molten material, and the retention of tellurium, antimony, and ruthenium in association with core materials. Material examinations have now been performed on samples from throughout the reactor building and vessel. These examinations have helped define the end state core configuration and materials behavior. The examination results have been used to estimate the redistribution and inventories of core materials and fission products in the damaged reactor core for comparison with expected materials behavior, particularly for fission products.

INTRODUCTION

The Three Mile Island Unit 2 (TMI-2) pressurized water reactor underwent a prolonged loss of coolant accident on March 28, 1979, resulting in severe damage to the reactor core. As a consequence of the TMI-2 accident, numerous aspects of light water reactor (LWR) safety have been questioned, and the U. S. Nuclear Regulatory Commission (NRC) has embarked on a thorough review of reactor safety issues, particularly the causes and effects of severe core damage accidents. The nuclear community acknowledges the importance of examining TMI-2 in order to understand the nature of the core damage. Immediately after the accident, four organizations with interests in both plant recovery and acquisition of

---

a. Work supported by the U. S. Department of Energy, Assistant Secretary for Nuclear Energy, Office of LWR Safety and Technology under DOE Contract No. DE-AC07-76ID01570.

accident data formally agreed to cooperate in these areas. These organizations [General Public Utilities Nuclear Corporation (GPU Nuclear--owner/operator of TMI), Electric Power Research Institute (EPRI), the NRC, and the U. S. Department of Energy, collectively known as GEND] are presently involved in postaccident evaluations of TMI-2. The DOE is providing a portion of the funds for reactor recovery in those areas where accident recovery knowledge will be beneficial to the U. S. LWR industry. In addition, DOE is providing funds to acquire and examine samples obtained from the damaged reactor core.

The examinations of the TMI-2 reactor core began shortly after the accident with the evaluation of plant monitoring instruments[1], and sampling and analysis of the reactor coolant[2]. This was followed by examinations of samples of highly contaminated water, and sediment from the auxiliary and reactor buildings[3,4]. Much of this data has been analyzed and provides sufficient information to characterize the distribution of core materials outside the reactor core[5].

The end-state configuration of the TMI-2 core just after the accident as determined by closed circuit television (CCTV),[6,7] mechanical probing, and core boring operations[8] is illustrated in Figure 1. The initial examinations for core materials were performed on sections of control rod drive leadscrews, which extended from the upper plenum through to the beginning of the core proper[9,10]. Visual observations through the leadscrew guide tubes indicated the presence of a void region above a region of loose fuel debris (up to 94 cm deep) which was first sampled in October 1983[11,12]. As part of these examinations, it was determined that a crust layer was present below the debris bed. This crust layer was finally sampled using specialized core boring equipment adapted from the mining industry.

The visual examinations of the lower region of the reactor core (reference 8) indicated the presence of a central prior molten region contained by partly or fully metallic crust layers. Destructive examination of the core bores[13] obtained from the lower core indicate that the crust layers were composed principally of metallic constituents of the core that had not oxidized during the accident. Video examinations of the region below the reactor core were also performed, which indicated that prior molten material had relocated to the lower head of the reactor. Samples of this debris were obtained through the annulus between the thermal shield and the reactor vessel. Examination of this debris[14] indicated that it was a mixture of prior molten fuel, cladding, and structural materials which had oxidized and flowed down onto the lower head of the reactor. These examinations provide the bulk of the data on the distribution of core materials in the damaged reactor core.

The following sections discuss the distribution of the bulk debris in the reactor vessel, the segregation and redistribution of the elemental constituents of the various core components, and finally, a discussion of the redistribution of fission products and the possible effects on source term issues.

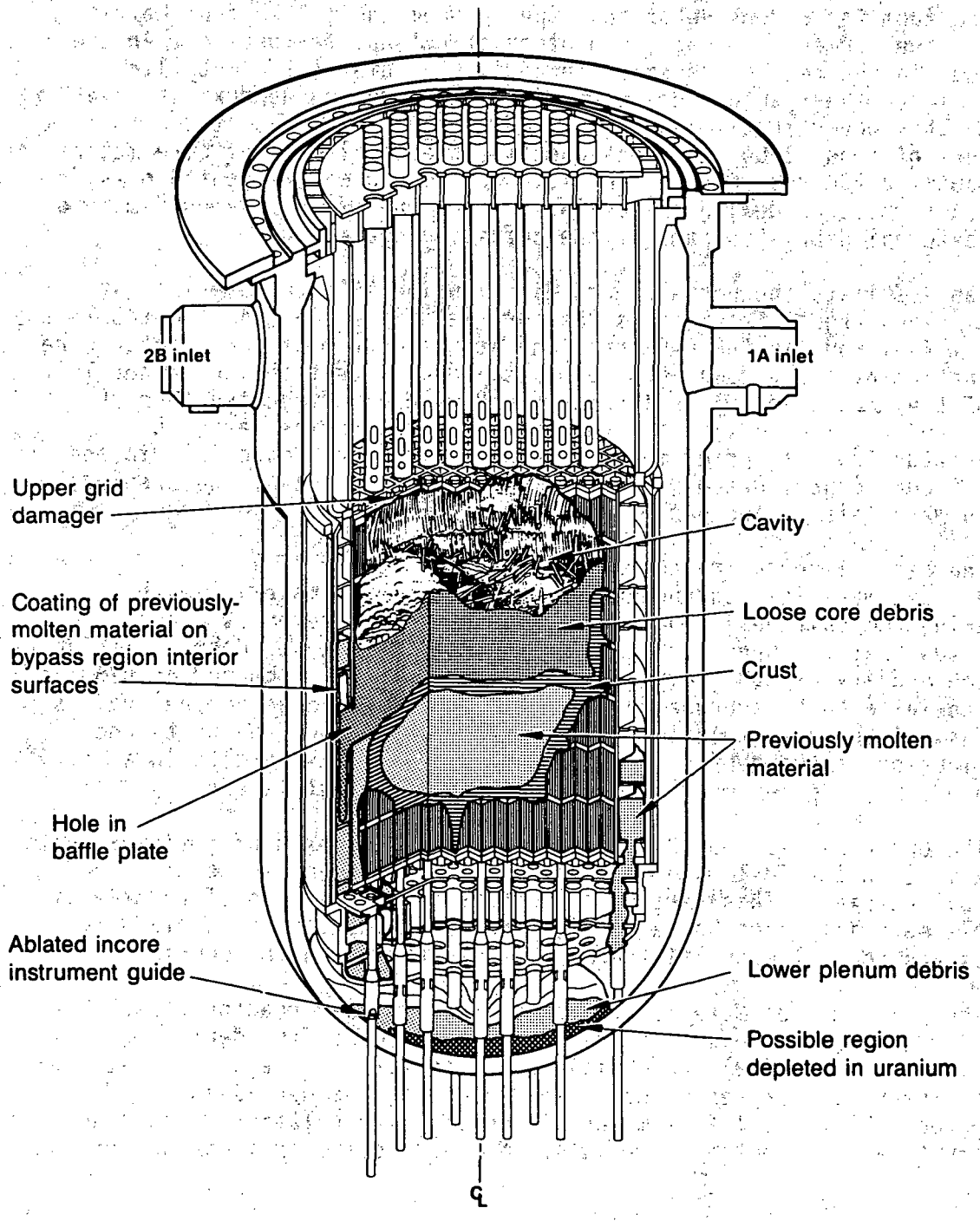


Figure 1. TMI-2 end state core condition. 8-9078

CORE MATERIALS INVENTORY

The original core materials inventory included approximately 94,000 kg of UO_2 fuel and 35,500 kg of cladding, structural, and control materials[15,16]. As a consequence of the accident, some material has been added to this inventory due to ablation of other reactor vessel materials and oxidation of some of the metallic structural components. Approximately 229 kg of structural steel was estimated to have been ablated from the underside of the upper plenum and 182 kg from baffle plates, the former core wall, and other structural features not in the core but in the reactor vessel. In addition, some of the metallic materials in the reactor core were oxidized producing approximately 459 kg H_2[17]. This would result in a total addition of oxygen as oxides to the core of about 3300 kg. Consequently, the total mass of core materials is about 133,250 kg. Of this total, about 100 kg was relocated outside the reactor vessel during the accident. GPU Nuclear has removed much of this external debris as part of the defueling operation.

Table 1 lists the postaccident distribution of core materials at TMI-2. The largest fraction of the core materials (33%) is located in the partial fuel rods in the periphery and at the bottom of the reactor core. Examination of these damaged assemblies indicate that they have not lost any of their core materials inventory and were not subjected to high temperatures. The remaining core material repositories range in composition from the prior molten fuel and structural materials in the central core consolidated region to the mixture of intact and previously molten materials in the upper core debris bed.

The central consolidated mass region is composed of a core of prior molten fuel materials surrounded by layers of crust material with differing compositions. Analysis of the data in references 8 and 13 indicates that the upper crust is composed of 2450 kg of debris with an average density of 8.3 g/cm^3, and the lower crust is composed of 8760 kg of material with an average density of 7.3 g/cm^3. These nominal values have associated uncertainties of 30-40% due to the heterogeneity and distribution of the debris in the crust layers. This results in a total of 25,990 kg of prior molten debris between the crust layers.

The upper debris bed (20% of core mass) is composed of a mixture of relatively intact fuel materials and prior molten fuel structural and control material. This part of the debris bed is made up of relatively friable material which has a density from 3-5 g/cm^3. Intact cladding shards and control material fragments were present in the debris.

The prior molten material relocated to the lower reactor vessel head (19,100 kg) has been examined only at the surface of the debris bed. This material (reference 19), which may not be representative of all material on the lower reactor vessel head, indicate that the debris is a homogeneous mixture of fuel materials (U,Zr) with relatively small amounts of structural and control materials. Nondestructive examinations of the

TABLE 1. ESTIMATED POSTACCIDENT CORE MATERIALS DISTRIBUTION

Core region	Estimated quantity(kg)	Uncertainty[a] (%)	Percent of Total core(%)
Intact fuel assemblies (Partially or fully intact)	44,500	5	33.4
Central core region resolidified mass	32,700	5	24.5
Upper core debris bed	26,600	5	19.9
Prior molten material on the Lower reactor vessel head	19,100	20	14.3
Lower core support assembly[b]	5,800	40	4.3
Upper core support assembly[b]	4,200	40	3.2
Outside the reactor vessel	100	-[c]	0.3

a. The uncertainty estimates are based on defueling. Those areas which have been defueled at this time have relatively low uncertainties[,] whereas those which have not have relatively high uncertainties.

b. The lower core support assembly is that portion of the reactor vessel below the core which includes the lower grid assembly and five flow distributor plates. The upper core support assembly is a coolant flow region outside the vertical baffle plates[,] which make up the peripheral boundary of the core.

c. Estimates of the amount of fuel material outside the reactor vessel are based on nondestructive evaluations of reactor components in the reactor and auxiliary buildings. They range from 60 to about 430 kg.

lower head suggest that structural materials may have relocated to this area of the reactor vessel[18], and examinations are in progress to better define the composition of this debris.

The remaining repositories in the reactor vessel (10,000 kg) have not been characterized, but are expected to be similar in composition to the material found on the surface of the debris bed on the lower reactor vessel head.

CORE MATERIAL DISTRIBUTION

Three principal types of core materials are present in the TMI-2 reactor core: the fuel rod constituents (uranium, zirconium, and tin), the control rod materials (silver, indium, and cadmium), and the structural materials (stainless steel and Inconel). Examinations by GPU Nuclear indicated that only about 100 kg of core material have relocated outside the reactor vessel, as previously discussed, and that the bulk of this material, a mixture of prior molten and intact fuel and structural materials, is located in the reactor coolant system in the steam generators and in the pressurizer. All other core materials remained in the reactor vessel.

Fuel Rod Constituents

Before the accident, the TMI-2 fuel rods consisted of 94,000 kg of UO_2, 24,000 kg of zirconium present mostly in the form of metallic Zircaloy, and approximately 370 kg of tin as a component of the Zircaloy. The UO_2, present as the oxide fuel, may be dissolved by the zirconium, which can be oxidized by steam as part of the high temperature melting process. During the accident at TMI-2, a significant fraction of the metallic zirconium was oxidized to ZrO_2 as indicated by the production of hydrogen. Approximately 43% of the Zr was oxidized during the accident; this estimate is based on the amount of H_2 (459 kg) produced by oxidation. However, some of the oxygen produced would have been used to oxidize structural metallic material (e.g., Fe, Cr). Consequently, the estimated 43% oxidation of Zr is conservatively high. Tin is expected to remain metallic in the conditions present during the accident at TMI-2[19], and its behavior during the accident would be expected to be different from the oxidized zirconium.

Analyses were performed on samples obtained from throughout the reactor core, which provided information on the redistribution of uranium in the reactor system. Table 2 lists the distribution of the principal fuel rod constituents in the various regions of the damaged reactor core. As indicated in the table, this distribution accounts for approximately 97% of the total uranium inventory. The principal repositories for uranium are the partial fuel assemblies, the upper core debris bed, debris relocated to the lower reactor vessel head, and the debris in the central consolidated region. The partial fuel assemblies around the periphery of the core (22.7%), and the partial assemblies below the central consolidated region (10.7%) make up the largest repository of core

TABLE 2. FUEL MATERIAL DISTRIBUTION IN THE REACTOR VESSEL

Core Material Repository	Core material distribution Percent of Inventory [a] Uranium	Zirconium	Tin
Upper reactor plenum	-b-	-b-	-b-
Upper core debris	24	13	-c-
Upper crust region			
- ceramic	1.3	1.2	2.3
metallic	--	0.3	6.1
Consolidated region			
ceramic	12	18	--
metallic	--	0.2	5.8
Lower crust region			
ceramic	3.6	2.8	9.3
metallic	--	5.6	26
Intact fuel rods	33	33	33
Lower reactor vessel head	15	11	-c-
Lower core support assembly	4.6	3.3	-c-
Upper core support assembly	3.3	2.4	-c-
Total	97	91	82

a. Percentage of the total amount of the element originally present in the core.
b. Insignificant amount (<0.1 wt%) based on the upper plenum measurements.
c. Elemental constituent not detected based on detection limits of approximately 0.1 wt%.

materials following the accident. Examinations indicate that the intact portion of these fuel rods show no evidence of accident damage.

The next largest repository for uranium at TMI-2 is the loose debris in the upper part of the reactor core. This material is particulate debris from 1 to 5 mm in diameter and is composed of prior molten fuel materials mixed with partial fuel pellets, cladding, and structural material pieces. This debris averages 75 wt% uranium which is higher than the core average concentration of about 66 wt%. The high uranium concentration is due to the melting and downward relocation of zirconium to the central part of the reactor core which is discussed in a following paragraph.

Approximately 15% of the core inventory of uranium was relocated to the lower reactor vessel head. Examinations performed on debris from the surface of the debris bed suggest that this material is a relatively homogeneous mixture of uranium and zirconium, with the uranium concentration (65 wt%) near the core average.

The consolidated core region, composed of the upper and lower crusts and the central core region, makes up the bulk of the remaining core inventory (17%). The uranium content is quite variable due to the high degree of heterogeneity of the materials in this part of the core. The average concentrations for uranium are: upper crust (49 wt%), central region (54 wt%), and lower crust (34 wt%), with a significant range of concentrations at all locations due to the heterogeneity of the debris. The lower crust contains only about half the expected amount of uranium as compared to the core average, indicating the presence of significantly more structural components in this part of the core. In general, these data suggest a very distinct segregation between the U-Zr-O and the metallic or oxidized structural materials. This is consistent with the expected behavior of uranium, in that it is expected to interact significantly only with the zirconium in the system. Structural materials are present as contaminants [and are] located in inclusions or at grain boundaries in the U-Zr-O matrix.

The zirconium data in Table 2 show a similar distribution to that indicated for uranium, except that the percentages of inventory are less, reflecting differences between the chemical behavior of the ceramic UO_2 and the metallic zirconium. The data indicate that almost half the zirconium originally present in the upper core (i.e., the upper debris bed) has relocated to lower regions of the reactor core. The data from the crust layers and the central core region indicate that the relocated zirconium contributed to the formation of the crust layers and was retained in the central core region as metallic inclusions. The high zirconium concentrations are present only in the metallic phase, and the data indicate that the zirconium forming these layers did not participate in the zirconium-water oxidation reaction and was transported as metallic zirconium or Zircaloy (melting point 2030 K) to form the layers in the central region of the core. This behavior suggests a core damage progression where the upper core region was not heated to high temperatures (>2200 K) until after the upper crust had formed.

The data for the debris relocated to the lower reactor vessel head indicate a lesser percentage of zirconium (about 4% of core inventory) for the quantity of uranium present. These data suggest that some zirconium did not remain with the uranium relocated to the lower reactor vessel head, but contributed to the formation of the lower crust. The summed data for the various repositories indicate that about 9% of the core inventory of zirconium has not been accounted for. Although there is a relatively large uncertainty due to the few number of samples examined relative to the mass of the reactor core, these data suggest the presence of additional Zr repositories.

The tin distribution in the reactor vessel is significantly different than that observed for the Zr. The core materials distribution data in Table 2 indicate that no significant amounts of Sn were found in the upper reactor plenum, the upper core debris bed, the debris on the lower reactor vessel head, and by inference from the lower reactor vessel debris data, in the lower and upper core support assemblies. The data indicate the presence of significant amounts (factors of 4 to 6 times greater than the core average concentration - 0.3 wt%) in the upper and lower crusts and the central core region. The data for the metallic region data indicate concentrations from 7 to 20 times the core average with higher concentrations in metallic inclusions in the central core region. The significant concentrations of Sn in the metallic region might be expected from the chemical behavior of Sn (i.e., a high free energy requirement for oxidation).

In the lower crust of the central consolidated region, there is evidence of accumulations of Sn in the metallic samples; however, in contrast to the upper crust there are also accumulations of Sn in the ceramic samples relative to Zr. These data suggest a scenario where much of the Sn in the upper part of the core flowed down and was either trapped as metallic inclusions in the ceramic melt or contributed to formation of the metallic lower crust.

The inventory data for tin in Table 2 suggest that approximately one third of the structural tin originally present in the core is now located in the lower crust and that almost half is present in the central core region.

Control materials

The TMI-2 reactor core contained 2200 kg of silver, 412 kg of indium, and 137 kg of cadmium control materials. These control materials were originally present in controls rods with 80% silver, 15% indium, and 5% cadmium. During the accident at TMI-2, a significant fraction of this material was expected to melt and possibly volatilize due to the relatively low melting point of the alloy (1072 K - 1123 K), and the low boiling points of the individual constituents. Analyses indicate that at TMI-2, control materials melted, and due to the pressure, did not produce a forcible ejection upon failure of the control rod cladding[20].

Table 3 lists the distribution of control material in the reactor vessel. The data indicate the presence of no measurable amounts of silver, the least volatile control material, on the lower reactor vessel

head, and by inference, in the upper and lower core support assembly regions. The data also indicate that a small amount of silver (10%) was deposited on the upper plenum surfaces. The bulk of this material was deposited with other fuel and structural materials as loose debris, which, based on particle size, could have been transported to the upper plenum as either a hydrosol or an aerosol. Examinations of samples from outside the core indicate that only small amounts of the control materials were released from the core, substantiating the analytical conclusion that a forcible ejection of the control materials probably did not occur.

Below the upper plenum structure is a void and the loose debris bed, which accounts for approximately 20% of the core mass. Based on the analytical results, only 1.8% of the core inventory of silver is contained in this mass. These data suggest that much of the silver (22%) melted and flowed down to form the crust layers and some was retained as inclusions in the central core region.

The silver data in Table 3 indicate that only about 47% of the core inventory of silver can be accounted for. Although the uncertainties associated with these data are relatively large due to the small percentage of the whole core examined, the data suggest additional repositories where a significant fraction of the silver inventory is located. The high density of metallic silver (10.5 g/cm^3--near the highest of the core materials) would suggest that it is deposited near the bottom of the core or possibly on the lower head of the reactor vessel. This is consistent with the lower crust data where the silver concentration (4.5 wt%) is the highest of any of the core regions examined.

Table 3 indicates that indium is concentrated in the central core region at higher relative concentrations than was the silver. The highest concentrations are in the lower crust at 1.1 wt%, which is 3-4 times the core average. This element is present in the metallic phases similar to silver. However, a significant amount is also present in the ceramic parts at concentrations 2-3 times the core average. If extrapolated to the mass of the various regions of the lower core, approximately 81% of the core inventory of indium is present in the lower core region. Although this estimate has a relatively large uncertainty, the data indicate that approximately 30% more indium than silver is located in the lower core, which suggests a different distribution of indium than silver and indicates that a significant fraction of the silver behaved differently than the indium and is located in another part of the reactor vessel[21].

The cadmium data indicate concentrations for the lower core that are similar or less than the core average concentration of 0.1 wt%. The data indicate lesser concentrations in the ceramic regions than the metallic regions, which might be expected as cadmium is not expected to oxidize. Much of the relatively volatile Cd was not released from the core but was retained in the central molten part of the core as a gas during the early part of the accident, probably as inclusions in the molten metallic material.

TABLE 3. CONTROL ROD MATERIALS DISTRIBUTION IN THE REACTOR VESSEL

Core material Repository	Core material distribution Percent of Inventory[a] Silver	Indium	Cadmium
Upper reactor plenum	1.0	-b-	-b-
Upper core debris	1.8	-c-	-c-
Upper crust region			
ceramic	1.2	3.6	0.65
metallic	2.4	3.3	0.39
Consolidated region			
ceramic	10	27	6.1
metallic	1.6	2.1	1.1
Lower crust region			
ceramic	7.3	7.2	1.4
metallic	11	16	2.9
Intact fuel rods[d]	11	11	11
Lower reactor vessel head	-c-	-c-	-c-
Lower core support assembly	-c-	-c-	-c-
Upper core support assembly	-c-	-c-	-c-
Total	47	70	23

a. Percentage of the total amount of the element originally present in the core.
b. Insignificant amount (<0.1 wt%) based on the upper plenum measurements.
c. Elemental constituent not detected based on detection limits of approximately 0.1 wt%.
d. Only 10.7% of the partially intact fuel assemblies contain control material as the balance (22.7%) are peripheral assemblies which do not contain control materials.

Structural materials

The distribution of structural materials in the various parts of the lower core region is discussed in detail in reference 22. The extrapolated data for the four elements considered (iron, nickel, chromium, and molybdenum) indicate extrapolated inventories up to 3 times the core inventory (only for molybdenum). The principal source of this bias is the central core region which has a non-representative sample distribution due to the core boring technique used to obtain the samples. If the central core region data are excluded, the inventories are below 100%.

The iron data for the reactor core indicate that the upper core debris bed is depleted in iron content relative to the percentage of core mass (i.e., 20%), but that there are significant concentrations of iron in the lower crust and the central, consolidated region. Iron makes up large percentages of the metallic phases in all regions of the lower core with the highest percentage in central region inclusions. Metallurgical data indicate that the iron is mostly (80%) not oxidized and is found alloyed with nickel and lesser amounts of chromium.

The bulk of the core inventory of chromium (>50%) is found in the lower core region at concentrations ranging from 1.4-1.7 wt% and that the bulk of this element is located in the metallic region. Metallurgical examinations of prior molten debris indicate similar concentrations to those found in the lower core, and that a fraction of the chromium is oxidized and retained in the grain boundaries of the prior molten fuel material.

Almost 50% of the core inventory of nickel is located in the lower crust. The data range from 2-6 times the core average concentration. The concentrations of Ni in the upper and lower crusts and the central consolidated region are similar and significantly higher than other portions of the reactor vessel. The Ni, as might be expected due to its high free energy requirement for oxidation, is located mostly in the metallic phases, with only a few percent located in the ceramic samples. The inventory data (i.e., 116% of core inventory) again indicate that the samples of the central core region are not representative of all the material in the central core, and are probably representative only of the fraction of the central core region that has a significant amount of metallic inclusions.

The molybdenum data indicate the bulk of the molybdenum is located in the metallic phases. As molybdenum is not a constituent of stainless steel, ratio comparisons were performed to evaluate the contribution of the Inconel core components (i.e., grid spacers, etc.) to the formation of the crust layers. The ratio data suggest that much of the metallic material that formed the upper and lower crust layers was relocated Inconel grid spacers. These data suggest that the formation of the crust layers in the core was controlled by the melt behavior of the grid spacers, and that other structural components contributed to a lesser extent to the formation of the crusts.

FISSION PRODUCT INVENTORY

The following sections discuss the distribution of fission products in the TMI-2 reactor system. This distribution is based on representative examples of each group of fission products that were measurable at the time the fission product measurements were made (4-7 years after the accident). The low volatility fission products include elements from the noble metals, some rare earths and actinides, tetravalents, and early transition elements. Generally, the oxides of these elements have low volatilities; however, some (e.g., LaO or CeO) have higher volatilities than do the elements. The only radionuclides from this group which were measurable during the lower vessel debris examination program were Cerium/Praseodymium-144, Europium-154, and Europium-155. The Ce-144 is produced principally by direct beta decay from fission, whereas the europium radionuclides are produced by neutron activation of fission produced species. The radionuclides produced by neutron activation have greater associated uncertainties with their data due to the neutron activation as it makes their production more dependant on neutron flux and consequently on the core location of the fuel material. The medium volatile species are Sr-90, Sb-125, and Ru-106. The strontium is expected to be an oxide whereas the antimony and ruthenium are expected to remain as metallics. The high volatiles are the noble gases, cesium, and iodine, which are released to a large extent at the temperatures found during a severe reactor accident.

Low Volatiles

Table 4 lists the fission product retention and distribution in the TMI-2 reactor system for the three low volatile fission products measured (i.e., Ce-144, Eu-154, and Eu-155). The low volatiles were not transported out of the reactor core and only a little fuel material was physically transported to the reactor coolant system. In the reactor vessel, the fuel material distribution is similar to the mass distribution. The Eu-154 and Eu-155 data is similar to that seen for the Ce-144, except for variations in the measured retention values. The relatively large uncertainty associated with the inventories of radionuclides (Eu-154) is due to the fact that this isotope is produced by neutron capture by another radionuclide. In this instance, Eu-155 is produced by neutron capture by Sm-154, a stable fission product. The data indicate that all low volatile fission products are retained in the reactor vessel.

Medium Volatiles

Table 5 lists the fission product distribution data for the medium volatiles. The data for Sr-90, the radionuclide in this category which exhibited the least mobility, indicates that only a small amount (<3.5 %) was released from the reactor vessel. The distribution is again similar to the fuel material distribution, which suggests that the bulk of the activity was retained in the prior molten fuel material. While the examination data indicate that the bulk of the Sr-90 is located in the ceramic parts of the samples, there has been some transport of the Sr-90 to the metallic region samples. Almost complete accountability is indicated for the Sr-90.

The Sb-125 data in Table 5 indicate high concentrations in the metallic portions of the lower reactor core. The metallic sample concentrations are 6-20 times those found in intact fuel. These data suggest that the Sb-125 remained in a metallic state. The percent of core inventory data indicate that 62% of the core inventory of Sb-125 was contained in the lower core.

The Ru-106 data listed in Table 5 follow a similar distribution to that observed for Sb-125, and indicate that much of the Ru-106 is found in association with metallic samples at concentrations 4-12 times those found in intact fuel. Of particular importance to the accident scenario is the timing of the transport of the metallic material to form the crusts and the metallic inclusions in the consolidated region. The metallic materials had to have been transported to form the upper regions of the core after the Ru-106 (boiling point 4423 K) and Sb-125 (boiling point 1653) were released from the fuel matrix.

High volatiles

Table 6 lists the distribution of the high volatiles (Kr-85, I-129 and Cs-137). These radionuclides were significantly relocated and transported to the reactor coolant, and consequently to the reactor building basement. The data for Kr-85 is accurate to within 5-10% as the quantity of intact fuel is known from defueling, and the measurement of this radionuclide in a known gas space (i.e., the reactor building) is also quite accurate. In addition to the approximately 85% accounted for in these measurements, it is expected that some fraction of the core inventory was also retained in the upper core debris bed.

The uncertainties associated with the I-129 data are significantly greater than the noble gases because I-129 is highly reactive and may plateout on surfaces, making accurate assessments difficult. Measurements of radioiodine concentrations in the reactor building basement indicate a wide range of concentrations in the particulate debris. Extrapolation of these concentrations to the quantity of debris present in the basement indicates that much of the core inventory of radioiodine remained in the reactor building basement. Table 6 shows the same retentions for iodine and cesium in the basement, as transport of the two radionuclides to the reactor building would be expected to be similar. However, a lesser fraction of the Cs-137 would be expected to plateout on surfaces; therefore much of the Cs-137 remained in solution in contrast to the iodine.

The Cs-137 data indicate almost complete retention of the cesium in the reactor building with only 5% released to the auxiliary building. This activity is located principally in the reactor coolant bleed tanks and the letdown demineralizers.

TABLE 4. LOW VOLATILE FISSION PRODUCT DISTRIBUTION IN THE REACTOR SYSTEM

Fission product Repositories	Fission product distribution Percent of Inventory [a]		
	Ce-144	Eu-154	Eu-155
Ex-vessel			
Containment atmosphere, basement, and tanks	.01	-b-	-b-
Reactor coolant system	-b-	-b-	-b-
Auxiliary building	-b-	-b-	-b-
In-vessel			
Upper reactor plenum	-b-	-b-	-b-
Upper core debris-A	26	30	24
-B[c]	20	19	19
Upper crust region	1.4	2.0	1.6
Consolidated region	24	32	22
Lower crust	5.9	7.9	5.1
Intact fuel rods	30	30	30
Upper core support assembly	3.4	4.5	-d-
Lower core support assembly	4.7	6.3	-d-
Lower head-reactor vessel	16	21	-d-
Total	105	122	110[d]

a. Percentage of the total amount of the fission product inventory calculated from comparisons with ORIGEN2.
b. Insignificant amount (<0.1 wt%) based on the measurement data.
c. Two sets of bulk sample measurements were performed on the upper debris bed. The A series was performed on samples from near the center of the core at a variety of depths whereas the B series were bulk samples from near the bottom of the debris bed. For the totals, the B series data were used.
d. Measurements not performed for this radionuclide at this core location. The total shown value in parenthesis is a total which assumes the same distribution as Eu-154 for the repositories where measurements were not performed.

TABLE 5. MEDIUM VOLATILE FISSION PRODUCT DISTRIBUTION IN THE REACTOR SYSTEM

Fission product Repositories	Fission product distribution Percent of Inventory [a]		
	Sr-90	Ru-106	Sb-125
Ex-vessel			
Containment atmosphere, basement, and tanks	2.1	0.5	0.7
Reactor coolant system	1	-b-	0.2
Auxiliary building	0.1	-b-	0.7
In-vessel			
Upper reactor plenum	-b-	-b-	-b-
Upper core debris-A	23	14	13
-B[c]	19	16	24
Upper crust region			
ceramic	0.73	0.8	0.5
metallic	-b-	3.8	7.8
Consolidated region			
ceramic	8.3	2.2	3.1
metallic	-b-	9.0	6.9
Lower crust			
ceramic	4.5	5.7	7.4
metallic	-b-	24	36
Intact fuel rods	30	30	30
Upper core support assembly	3.9	0.23	0.22
Lower core support assembly	5.3	0.32	0.30
Lower head-reactor vessel	18	1.1	1.0
Total	93	94	119

a. Percentage of the total amount of the fission product originally present calculated from comparisons with ORIGEN2.
b. Insignificant amount (<0.1 wt%) based on the upper plenum measurements.
c. Two sets of bulk sample measurements were performed on the upper debris bed. The A series was performed on 16 cm^3 samples from near the center of the core at a variety of depths whereas the B series were bulk samples from near the bottom of the debris bed. The data provide a range. For the totals, the B series data were used.

TABLE 6. HIGH VOLATILE FISSION PRODUCT DISTRIBUTION IN THE REACTOR SYSTEM

Fission product Repositories	Fission product distribution Percent of Inventory [a]		
	Cs-137	I-129	Kr-85
Ex-vessel			
Containment atmosphere,	-b-	-b-	54
basement water	47	(47)[c]	-b-
Reactor coolant system	3	1	-b-
Auxiliary building	5	7	-b-
In-vessel			
Upper reactor plenum	-b-	-b-	-b-
Upper core debris-A	5.3	5.9	-b-
-B[d]	4.3	5.3	-b-
Upper crust region	0.41	0.27	-b-
Consolidated region	0.77	2.1	-b-
Lower crust	1.4	3.5	-b-
Intact fuel rods	30	30	30
Upper core support assembly	0.46	0.12	-b-
Lower core support assembly	0.63	0.16	-b-
Lower head-reactor vessel	2.1	0.54	-b-
Total	95	103	85

a. Percentage of the total amount of the fission product originally present calculated from comparisons with ORIGEN2.
b. Insignificant amount (<0.1 wt%) based on the measurement data.
c. Wide range of concentrations and quantity of debris would indicate percentage of total inventory that could be greater than the core inventory. Consequently, the Cs-137 inventory is considered representative of the quantity of iodine deposited in the reactor building.
d. Two sets of bulk sample measurements were performed on the upper debris bed. The A series was performed on 16 cm^3 samples from near the center of the core at a variety of depths whereas the B series were bulk samples from near the bottom of the debris bed. The data provide a range. For the totals, the B series data were used.

In the reactor vessel, the data indicate similar distributions for both the Cs-137 and I-129. The data for the upper core debris indicates that about 20% of the original inventories of both Cs-137 and I-129 were retained in the debris. In the lower parts of the core, evidence suggests that some of the I-129 is associated with the metallic regions of the core. These data suggest that there are reaction mechanisms which cause accumulation of I-129 in the metallic sections, and indicate the probable chemical form of the I-129. The fraction of core inventory found in association with the lower core region prior molten material indicates the presence of only 2.4% of the core inventory.

The Cs-137 data in Table 6 indicate retentions ranging from 2.7 to 13% of the original content in the fuel material. Again, some of the activity is found in association with metallic regions, which provides information on the possible chemical form of the Cs-137, and indicates the presence of reaction mechanisms which define the behavior of Cs-137. The total inventory of Cs-137 present in the lower core is quite low at about 2.6% and indicates significant release and transport of Cs-137 from this part of the reactor core.

CONCLUSIONS

This section summarizes the results of the core material and fission product inventory analysis. The results are based on the examination of a relatively small number of samples obtained from the the TMI-2 reactor vessel. This analysis provides a reasonable accountability for greater than 95% of the core materials and greater than 90% of all fission products. Listed below are some of the specific observations or conclusions of this analysis:

- The distribution of the principal fuel rod constituents accounts for approximately 97% of the total uranium inventory and suggests that this distribution is relatively accurate
- Principal repositories for uranium are the partial fuel assemblies, the upper core debris bed, debris relocated to the lower reactor vessel head, and the debris in the central consolidated region
- Metallurgical data indicate a very distinct segregation between the uranium ceramic and the metallic or oxidized structural materials which is consistent with the expected behavior of uranium in that it interacts significantly only with the zirconium in the system
- Almost half the zirconium originally present in the upper core (i.e., the upper debris bed) has relocated to lower regions of the reactor core
- Relocated zirconium contributed to the formation of the crust layers and was retained in the central core region

- High zirconium concentrations are present only in the metallic phase and the data indicate that the zirconium forming these layers did not participate in the zirconium-water oxidation reaction and was transported as metallic zirconium to form the metallic layers in the central part of the core

- Much of the Sn in the upper part of the core flowed down and was either trapped as metallic inclusions in the ceramic melt or formed the lower crust

- The high density of metallic silver (10.5 g/cm^3--near the highest of the core materials) is consistent with the lower crust data, where the silver concentration (4.5 wt%) is the highest of any of the core regions examined

- The cadmium data suggest that much of this relatively volatile element was not released from the core but was retained in the central molten part of the core as a gas, and was deposited with other, probably liquid metallic constituents as inclusions in the cooling metallic material

- Only a small fraction of low volatile radionuclides and fuel material were physically transported to the reactor coolant system

- In the reactor vessel the fuel material distribution is similar to the mass distribution

- The distribution of Sr-90 is similar to the fuel material distribution[,] which suggests that the bulk of the activity was retained in the prior molten fuel material

- The percent of core inventory data indicate that much of the core inventory of Sb-125 could be contained in the lower core with the bulk of the inventory located in the central core region

- The Ru-106 data listed in Table 5 follow a similar distribution to that observed for the Sb-125 data[,] and indicates that much of the Ru-106 is found in association with metallic samples at concentrations 4-12 times those found in intact fuel

- The Kr-85 data indicate accountability of 85% of the core inventory with other probable repositories in the reactor core

- The Cs-137 data indicate almost complete retention of the cesium in the reactor building with only 5% released to the auxiliary building. This activity is located principally in the reactor coolant bleed tanks and the letdown demineralizers.

REFERENCES

1. H. Lawrowski, A Report on Transport of Radioactivity from the TMI-2 Core to the Environs, Report to the President's Commission on the Accident at Three Mile Island, August 29, 1979.

2. S. Langer et. al., "Fission Product Release Pathways in TMI-2," Proceedings of the ANS TMI-2 Topical Meeting on the TMI-2 Accident, October 31 - November 4, 1988.

3. C. A. Pelletier et. al., Preliminary Radioiodine Source Term and Inventory Assessment for TMI-2, GEND-028, March 1983.

4. C. V. McIsaac and D. G. Keefer, TMI-2 Reactor Building Source Term Measurements: Surfaces and Basement Water and Sediment, GEND-042, October 1984.

5. S. Langer et. al., TMI-2 Fission Product Inventory Program, FY-85 Status Report, GEND-057, November 1986.

6. Quick Look Inspection: Report on the Insertion of a Camera into the TMI-2 Reactor Vessel Through a Leadscrew Opening, GEND-030, Vol. 1, March 1983.

7. J. Adams and R. Smith, Lower Plenum Video Data Survey, EGG-TMI-7429, July 1987.

8. E. L. Tolman et. al., TMI-2 Core Bore Acquisition Summary Report, EGG-TMI-7385 Rev. 1, February 1987.

9. K Vinjamuri et. al., Examination of H8 and B8 Leadscrews from Three Mile Island Unit 2, GEND-INF 052, September 1985.

10. G. M. Bain and G. O. Hayner, Initial Examination of the Surface Layer of a 9-Inch Leadscrew Section Removed from Three Mile Island-2, EPRI NP-3407, January 1984.

11. D. W. Akers et. al., TMI-2 Core Debris Grab Samples--Examination and Analysis, GEND-INF-075, September 1986.

12. G. O. Hayner, TMI-2 H8A Core Debris Sample Examination, GEND-INF-060 Vol 2, May 1985.

13. D. W. Akers et. al., The TMI-2 Lower Core Region: Examination and Analysis, GEND-INF-092, November 1988.

14. C. S. Olsen et. al., Examination of Debris from the Lower Head of the TMI-2 Reactor, GEND-INF-084, January 1988.

15. G. R. Eidam et. al., "TMI-2 Defueling Conditions and Summary of Research Findings," IAEA/NEA International Symposium on Severe Accidents in Nuclear Power Plants, Sorrento Italy, March 21-25, 1988.

16. TMI-2 Accident Core Heat-Up Analysis - A Supplement, NSAC-25, June 1981.

17. J. O. Henrie and A. K. Postma, Analysis of the TMI Unit 2 Hydrogen Burn, GEND-INF-023, Vol IV, Rockwell International, March 1983.

18. Analysis of Gamma Scanning of In-Core Detector #18 (L-11) in Lower Reactor Vessel Head, GPU Nuclear Corporation TPO/TMI-175, June 1985.

19. D. Cubicciotti and B. R. Singh, "Vaporization of Core Materials in Postulated Severe Light Water Reactor Accidents," Nuclear Technology, Vol. 67, November 1984.

20. D. A. Petti, Silver-Indium-Cadmium Control Rod Behavior and Aerosol Formation in Severe Reactor Accidents, NUREG/CR-4876, April 1987.

21. M. Hansen, Constitution of Binary Alloys, New York: McGraw-Hill Book Company, 1958.

22. D. W. Akers and R. K. McCardell, "Core Materials Relocation and Behavior in the TMI-2 Reactor Vessel," Proceedings of the ANS Topical meeting on the TMI-2 Accident, October 31 -November 4, 1988.

EVALUATION OF SELECTED SAMPLES FROM THE TMI-2 CORE

by

Y. Y. Liu, L. A. Neimark, and W. D. Jackson
Materials and Components Technology Division
ARGONNE NATIONAL LABORATORY
Argonne, Illinois 60439

ABSTRACT

Core-bore samples from the K9 and N12 locations in the TMI-2 core were examined for microstructural and microchemical features. The purpose of the examinations was twofold; first to determine core temperatures at known elevations in the core, and second to obtain insight into materials interactions that lead to core degradation. The temperature at the ~50-cm elevation in the N12 location, a control rod position, was estimated to have been ~960°C and dropping sharply to less than 800°C a few centimeters below. These temperature estimates were based on the eutectic reaction between a control rod's Zircaloy guide tube and its stainless steel cladding, the β-phase transformation temperature in Zircaloy, and the melting temperature of the Ag-In-Cd control material. In the K9 location, local transient temperatures to ~900°C at the 37-cm elevation were estimated from the β-phase transformation in the Zircaloy cladding. Interactions of note were the guide tube/cladding eutectic interaction in the control rod, the apparent degradation of Zircaloy cladding by molten Cd and In, and the attack of stainless steel by Sn in a melt of Ag-In-Cd.

INTRODUCTION

Over the past five years, Argonne National Laboratory has been involved in the examination of core debris from a number of locations in the TMI-2 reactor. The principal purpose of these examinations has been to add to the body of knowledge being accumulated by a large number of laboratories in this country and abroad to understand the sequence of events that destroyed the reactor core. Understanding the accident sequence will help to validate core and material behavior codes for accident analysis as well as provide unique data to modify the code models if necessary. Such models are based on known materials' properties and interactions, the latter usually established in controlled-environment separate-effects tests in which specific interactions can be studied. These tests also provide the "known" background

The submitted manuscript has been authored by a contractor of the U. S. Government under contract No. W-31-109-ENG-38. Accordingly, the U. S. Government retains a nonexclusive, royalty-free license to publish or reproduce the published form of this contribution, or allow others to do so, for U. S. Government purposes.

against which the TMI-2 specimen "unknowns" can be compared for the estimation of temperatures at a given core location.

This process is complicated, however, by the sheer extent of the accident and the multitude of materials interactions that occurred with a wide variety of core materials. Nevertheless, information on core temperatures during the accident can be gleaned to a first approximation by careful examination of the microstructure and microchemistry of core samples.

In this paper we will describe the examination of selected specimens taken from the TMI-2 core as "core bores" in a sample acquisition program conducted by the Idaho National Engineering Laboratory (INEL) [1]. A large number of core bore samples from this program are being examined by INEL and a lesser number by Argonne and the other participating laboratories. The twenty-odd core bore samples received at Argonne were classified variously as rod segments (from fuel, control, and poison rods), ceramic "rocks," and "agglomerates" of ceramic and metallic phases, all from seven different core radial locations. The rod segments came from the lower core elevations, the rocks from the molten region, and the agglomerates from the transition region below the molten region and from the crust above it. Because the rocks and the agglomerates generally tended to be rather similar within their grouping, after a general screening we chose to study in detail only those samples that contained striking features that either provided insight into the local temperatures or indicated the range of temperature or type of core damage over a larger axial distance. Our results, therefore, cannot be easily extrapolated to other core regions. Rather, this generalization can only be accomplished by combining our limited results with those of the other laboratories.

SAMPLE DESCRIPTION

In a previous paper [2], an overview was given of the Argonne examinations of some of our core bore samples. Since then more in-depth examinations have been done on (1) the Ag-In-Cd control rod segments from core position N12 and (2) the range of available samples from position K9. This range consists of fuel rod segments from near the bottom of the core and agglomerate samples from the transition region and the upper crust region.

The N12 control rod segment came from the 5-52 cm elevation. The top few centimeters of this segment was unique in that it provided insight into the reaction between the stainless steel cladding and the Zircaloy guide tube in the presence of essentially molten Ag-In-Cd.

The fuel rod segments from K9 came from between the 13- and 36-cm elevations. The transition agglomerate sample came from the

56-66 cm elevation, and the upper-crust agglomerate came from the 183-190 cm elevation.

Optical metallography, scanning electron microscopy, and energy-dispersive X-ray spectroscopy (EDX) were the analytical tools used to examine specimens from these larger samples.

RESULTS AND DISCUSSION

Control Rod Segment

The portion of the control rod segment of greatest interest was the molten tip at the 52 cm elevation and the portion of the rod just below the tip. This end of the rod segment is shown in Figure 1. The bent stainless-steel-clad rod is shown extending from the remnant of the Zircaloy guide tube. Over most of the length shown, the surface of the stainless steel cladding had apparently reacted with the missing section of the guide tube. Just below the semi-rounded top, shown in Figure 2, the stainless steel cladding was almost totally consumed in a eutectic reaction with the Zircaloy. The microstructure consists of a matrix of once-molten Ag-In-Cd, a stick-like phase apparently consisting of Zr_3Sn_2, (as determined from atomic ratios obtained by EDX analysis), and other Zr-rich particles. A single remnant of stainless steel cladding can be seen at 1 o'clock in the figure. This remnant was surrounded locally by a Zr-Fe-Cr-Ni matrix that contained Ag-In-Cd islands. It appears that the stainless steel is dissolving in a Zr-rich matrix and not into the molten Ag-In-Cd. This lack of interaction between the stainless steel and the Ag-In-Cd is consistent with the binary phase diagrams for Ag-Fe, Ag-Cr, and Ag-Ni, which show very limited mutual solubilities for these elements. The mutual solubilities of Ag and Zr are also negligibly small [3], explaining the existence of the Ag-In-Cd islands in a matrix of Zr-Fe-Cr-Ni.

The molten reaction product between the stainless steel and the Zircaloy apparently flowed downward on the outer surface of the rod, candling fashion, reacting with the surface as it went. Figure 3 shows this candling in a longitudinal section just below the transverse section shown in Figure 2. This section captured the upper extent of unreacted cladding on the inner surface while the outer surface was reacting with the candling material from above. The sharp change in the microstructure of the Ag-In-Cd from equiaxed to very elongated grains suggests a sharp temperature boundary where the elongated grains were apparently above the solidus temperature of ~800°C. Particles of the Zr_3Sn_2 phase were present in some of the long grains.

The termination of the candling, ~3.5 cm from the tip of the segment, is shown in Figure 4. Because of the thin reaction layer in this region, it was necessary to use scanning electron

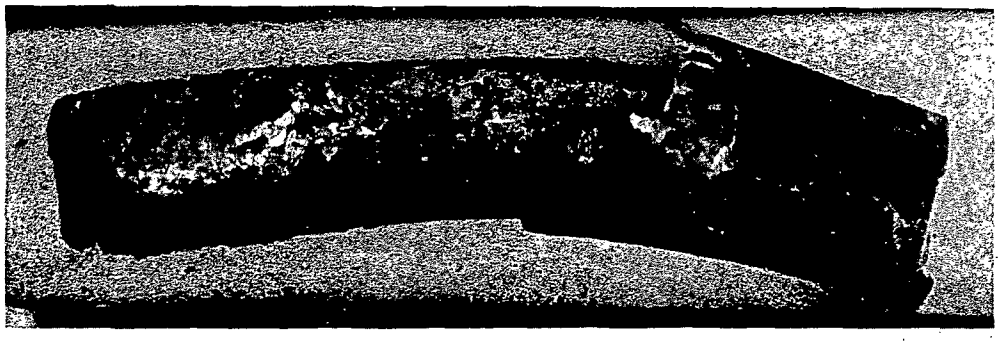
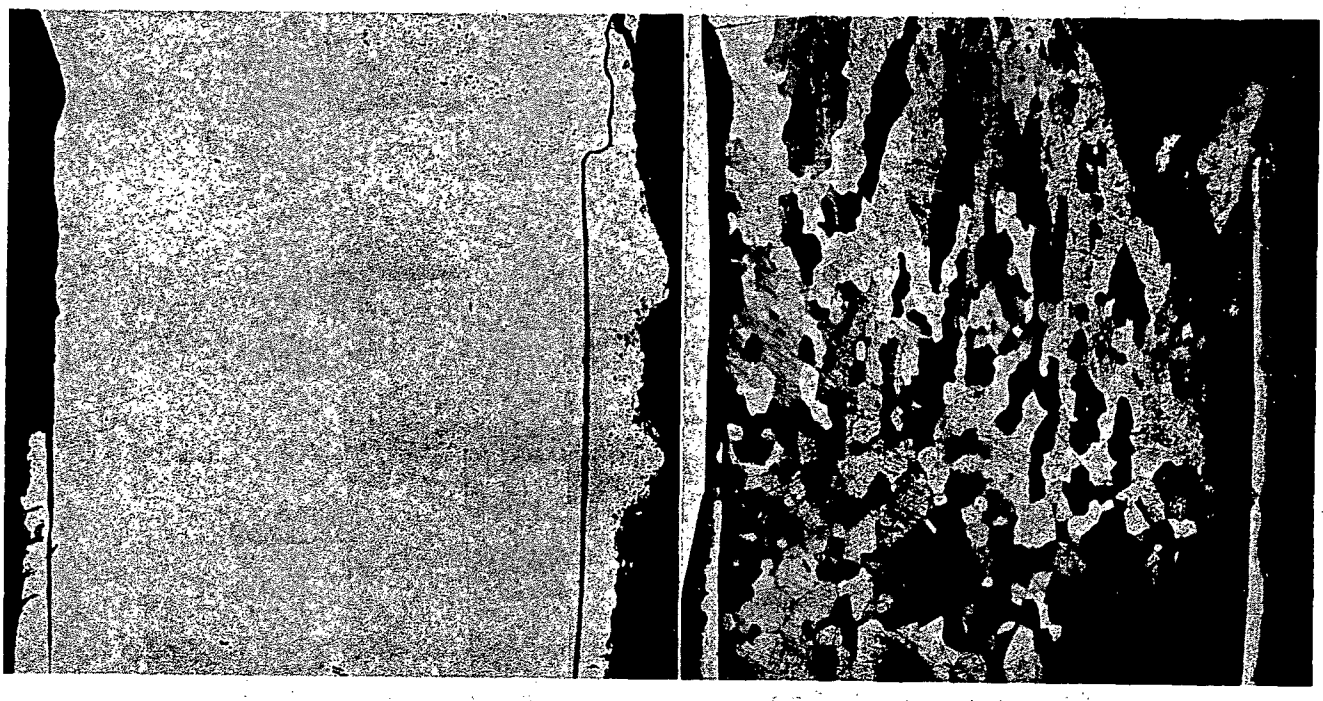


Figure 1. Segment of Ag-In-Cd control rod in guide tube remnant position N12, at the 47-52 cm elevation. Top is to the left where tip had melted.
MCT No. 243745 2X

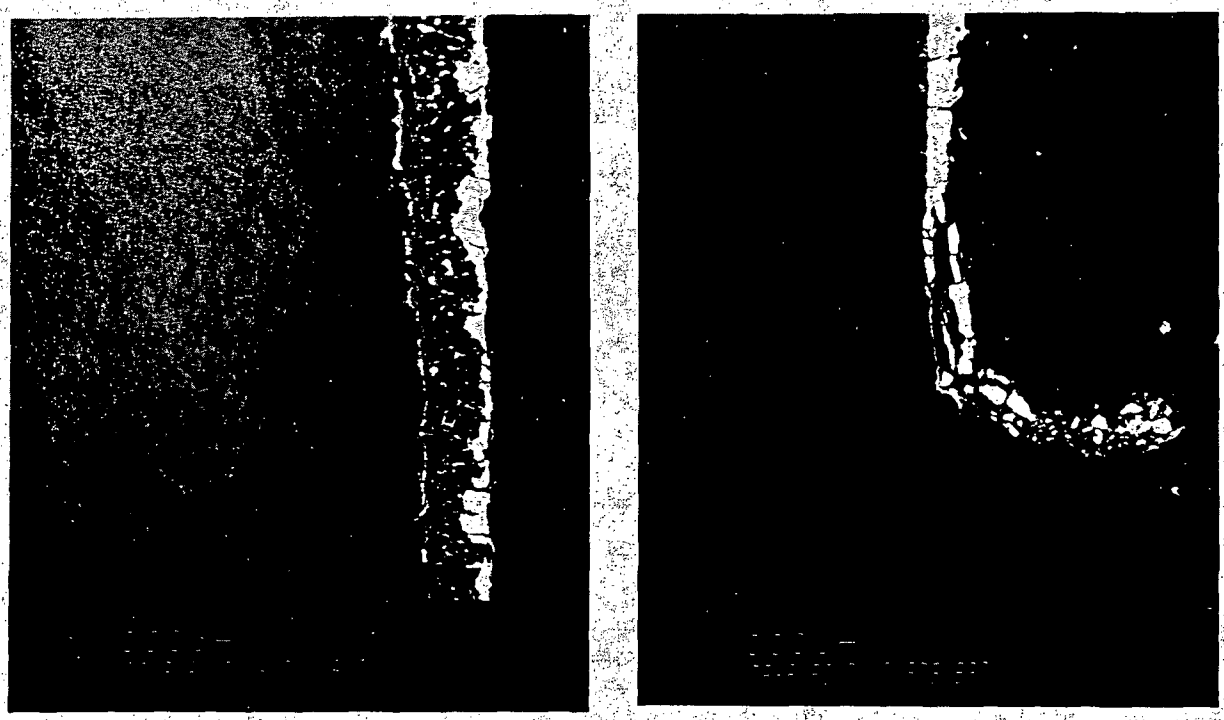


Figure 2. Transverse section just below tip of control rod segment showing a single remnant of cladding (arrow) in a matrix of molten Zr-Fe-Ni-Cr. Particles in molten Ag-In-Cd are Zr_3Sn_2.
MCT No. 245294 25X Original



(a) (b)

Figure 3. Longitudinal section of control rod 1.9 cm from tip, showing candling of reaction product. As-polished structure, (a), shows upper extent of cladding, while etched structure, (b), shows abrupt change in structure of Ag-In-Cd.
MCT No. 245297A and 246762A 25X Original



(a) (b)

Figure 4. SEM backscatter images showing duplex structure of candling reaction product, (a), and its termination ~3.5 cm from the tip end, (b).

microscopy to define the termination of the inner-layer part of the reaction. The inner layer is steel-rich, while the outer layer is Zr-rich. This structure is, in miniature, essentially the same structure found in a transverse section 1.9 cm from the tip [2].

The eutectic temperatures of the binary alloys Zr-Fe, Zr-Ni, and Zr-Ce are 934°C, 961°C, and 1300°C, respectively [4], which are considerably lower than the melting point (1450°C) of Type 304 stainless steel. That the reaction between the cladding and Zr-containing phase occurred adjacent to solid Ag-In-Cd (solidus temperature of ~800°C) suggests that temperatures were not significantly above the eutectic temperatures, and then for only a short period of time. Indeed, the lack of cladding on the left side of the rod adjacent to a free-standing structure of what is believed to have been molten Ag-In-Cd suggests that the events in this region took place very rapidly.

Below the 48.5-cm elevation where the eutectic reaction terminated, the control rod was intact with no obvious reactions between any of the components. The microstructure of the Zircaloy guide tube was fully transformed β-phase, indicating a temperature of greater than 900°C. At the 30-cm elevation, the microstructure of the Ag-In-Cd, shown in Figure 5, was recrystallized in an inner band. This pattern of recrystallization suggests that a second phase or additional element in the periphery of the rod is inhibiting recrystallization there. The identity of such a phase or element was not pursued, however. The Zircaloy guide tube at this elevation was only α-phase.

K9 Microstructures

Only the finding of some areas of transformation in the Zircaloy cladding of the fuel rod segments provided information on the temperature of these segments. Cladding structures at the 15-cm elevation showed no signs of elevated temperature. Only a few circumferentially oriented hydrides were present in the cladding. At the 37-cm elevation, there were occasional "sunburst" patterns of β-phase transformation from the outer surface inward. These areas penetrated about half the cladding thickness, as shown in Figure 6. The local character of these transformed areas suggests a very localized, transient thermal impact.

A specimen from an agglomerate sample taken at a lower transition region (56-66 cm elevation) captured two fuel rods in the process of disintegration, as shown in Figure 7. The composition of the various identified areas is given in Table 1. The matrix material between the two rods is predominantly Zr and Ag with lesser amounts of the other core constituents. Even what appear to be the "ghosts" of the cladding contain significant amounts of Ag. The area at "H," the thin grey line outlining the

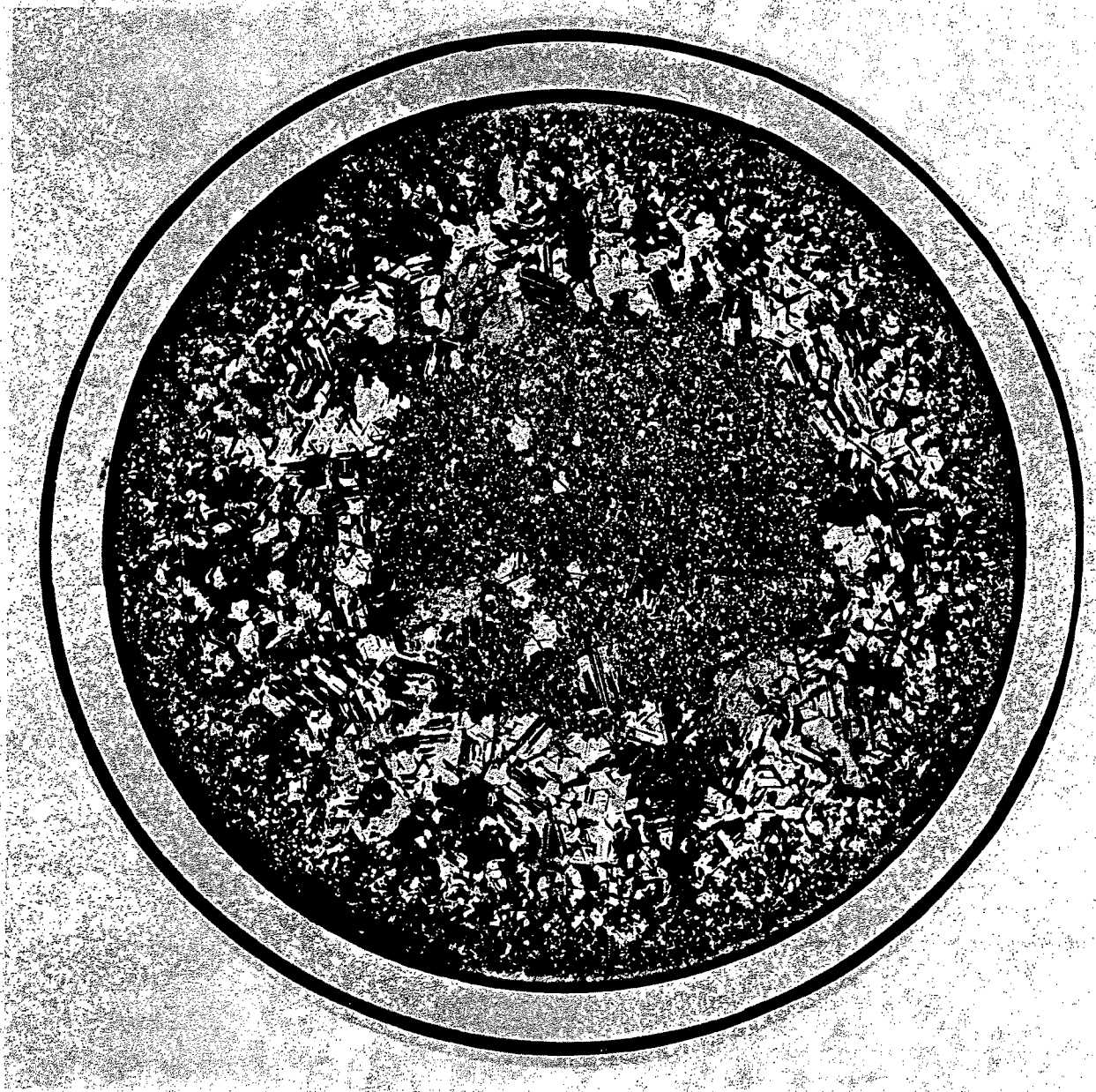


Figure 5. Recrystallized Ag-In-Cd at the 30-cm elevation in position N12.
MCT No. 243760 25X Original

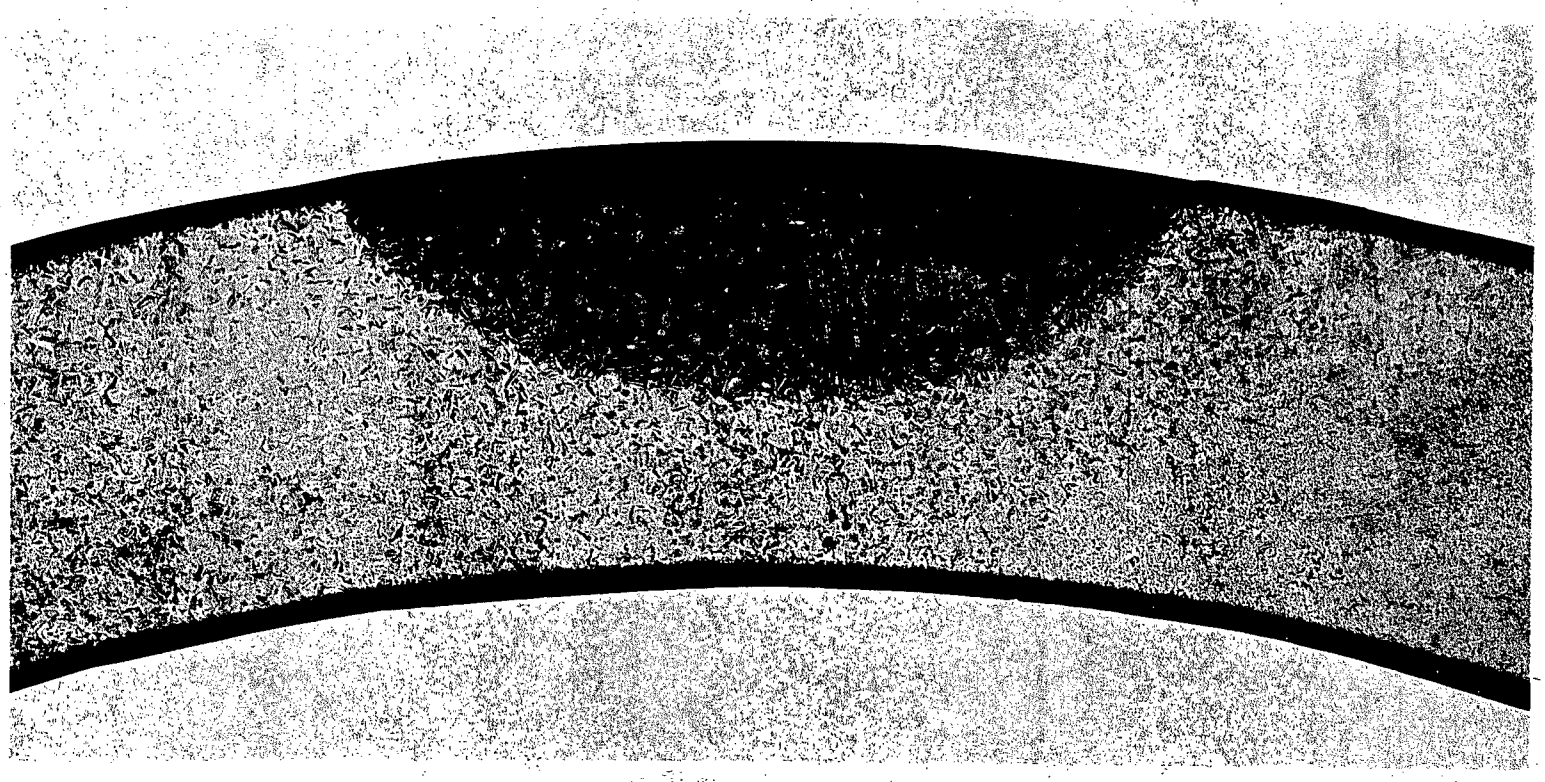


Figure 6. Local β-phase transformation of Zircaloy cladding at 37 cm in position K9.
MCT No. 243802

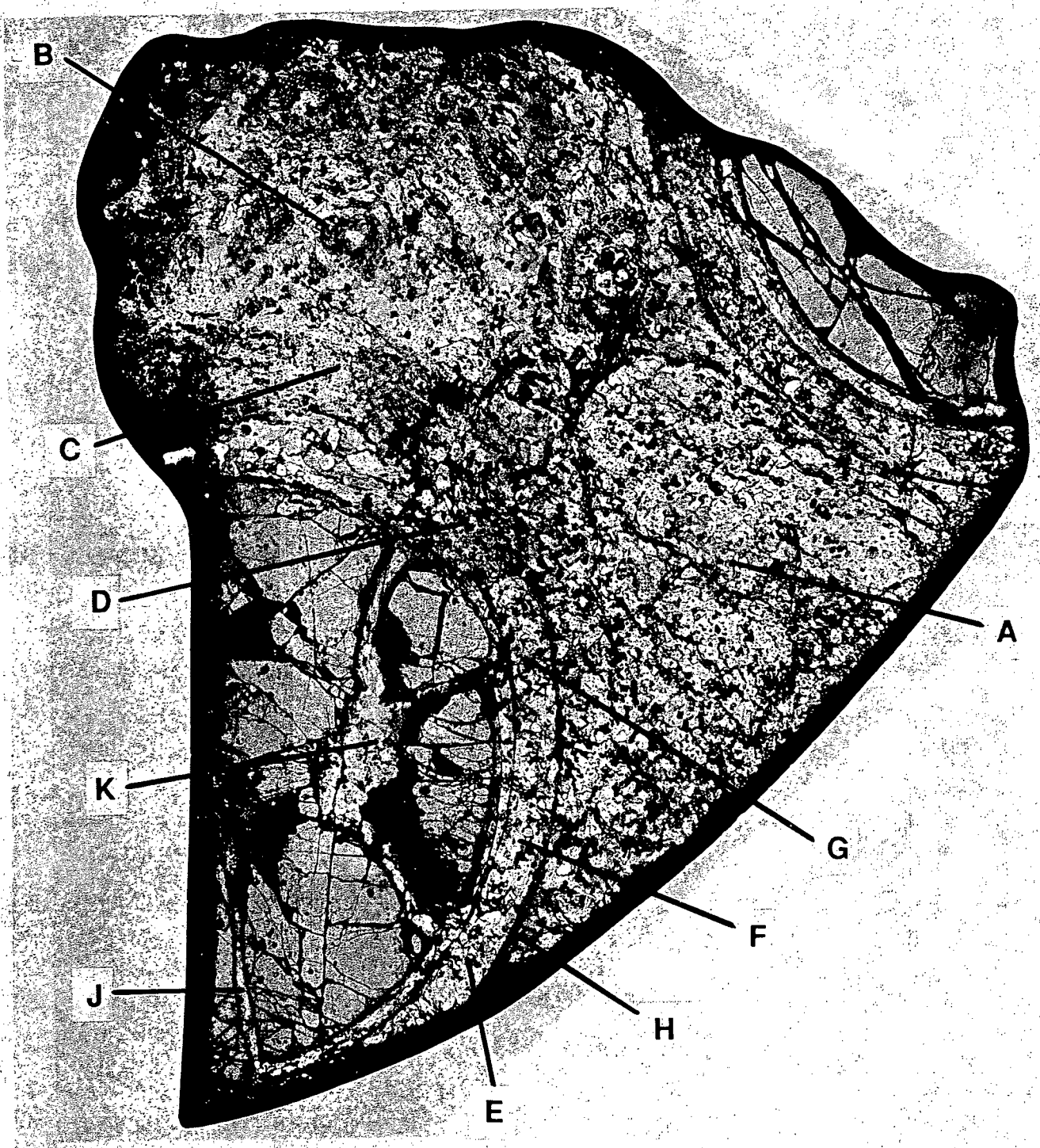


Figure 7. Transition region agglomerate from position K9 showing sections of two fuel rods being degraded.
MCT No. 246387 25X Original

Table 1. EDX Composition Analysis (in wt.%) of Transition Region Agglomerate

	Matrix				"Cladding"				Dikes	
Element	A	B	C	D	E	F	G	H	J	K
Cr	0.9	0.6	0.3	0.2	0.8	1.3	0.9	--	1.5	1.4
Fe	5.2	3.5	2.2	2.1	5.3	5.8	4.8	--	7.4	6.4
Ni	2.8	2.2	2.0	2.0	2.4	2.6	2.1	--	3.8	3.5
Zr	59.3	68.5	75.5	62.9	64.3	58.3	57.9	83.3	67.1	64.5
Ag	21.5	15.5	13.1	22.7	18.5	24.7	24.7	--	*	18.0
Cd	1.5	2.3	0.0	1.5	0.0	1.3	1.0	8.9	*	0.0
In	3.0	3.0	3.0	3.5	0.0	2.6	2.4	7.9	*	0.8
U	5.8	4.4	4.0	5.2	3.5	3.4	2.5	0.0	20.2	5.5

*Not included to avoid biasing results in small sample volume.

"cladding," contained only Zr, Cd, and In as major constituents. This observation could suggest that molten Cd and In were the initiators in degrading the cladding. The cladding at "D" appears to have beem breached, allowing the matrix materials to form dikes in the cracked fuel. The reason for the high U composition of the dike at "J" is apparent from Figure 8, which shows particles of fuel from the walls of the crack being absorbed into the matrix of the dike. In general, this specimen shows a multiphase matrix material, heterogeneous in its appearance of flow zones, but homogeneous in overall composition.

The upper-crust agglomerate as it was received is shown in Figure 9 in a manner that highlights the contrast between the metallic (light) and ceramic (gray) phases. The metallic phase proved to be stainless steel with imbedded large particles of Ag-In-Cd. The ceramic matrix proved to be a generally homogeneous mixture of essentially pure U (presumed to be an oxide) and Zr-rich phases. The Zr-rich phase contained ~14 w/o Cd and 14 w/o In with the balance Zr. Interestingly, this same combination of elements made up the gray rim on the cladding ghosts in Figure 7.

Of note on the surface of the large stainless steel "masses" was a thin reaction zone. This zone, shown in Figure 10, was analyzed and was found to contain Ag, In, Cd, and fingers of stainless steel intimately involved with a Sn phase at the very surface. In areas where Sn was absent, the Ag-In-Cd was compatible with the stainless steel. It appears that the Sn promotes a dissolution of the stainless steel in the molten Ag-In-Cd.

SUMMARY AND CONCLUSIONS

Selected specimens from TMI-2 core bores were examined with the objective of establishing temperatures that likely existed during the accident at known elevations in the core. Given that only a relatively few specimens could be examined in any detail in this program, the results are limited in interpretation to very limited core locations. The examination of these specimens also indicated some materials interactions of note that provide some insight into the degradation mechanisms of the core materials involved.

Probable core temperatures deduced from the examination of fuel and control rod segments from positions K9 and N12, respectively, are as follows:

1) Incipient β-phase transformation in the Zircaloy cladding indicates at least transient temperatures to 900°C at the 37-cm elevation in K9.



Figure 8. SEM secondary electron image of dike of matrix material in UO_2 pellet of transition region agglomerate, showing dissolution of UO_2 along interfaces.



Figure 9. As-received section through upper crust agglomerate from position K9, highlighting metallic phase (bright) in a ceramic matrix of U-Zr-O and Cd-In.
MCT No. 243653

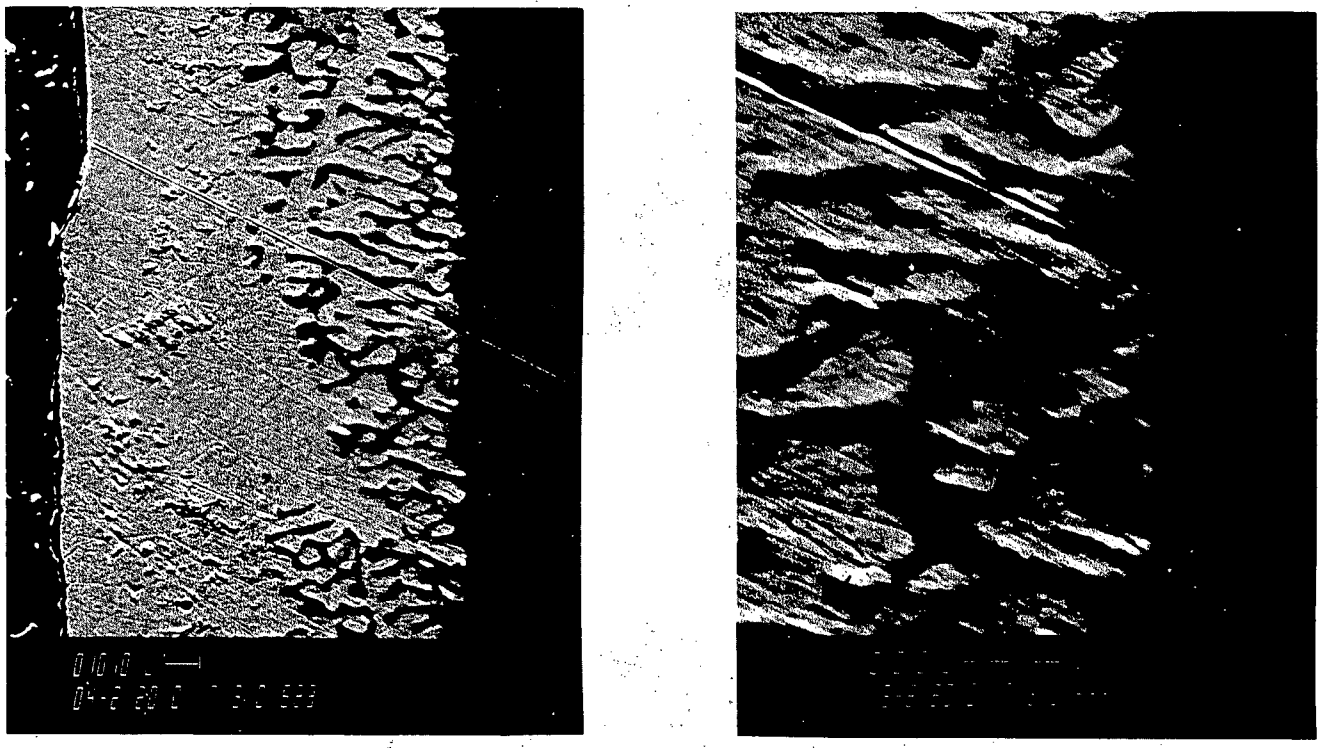


Figure 10. Surface dissolution of upper-crust stainless steel particle (dark gray) by Sn-containing phase (medium gray) in a Ag-In-Cd molten phase (light phase).

2) Complete β-phase transformation in the Zircaloy guide tube at the 48-cm elevation in N12 indicates temperatures >900°C.

3) Zircaloy/stainless steel eutectic reactions at the 52-cm elevation in N12 indicate temperatures in the 935-960°C range.

4) Lack of any β-phase transformation in the Zircaloy guide tube in N12 at the 30-cm elevation indicates temperatures <900°C.

Notable materials interactions were as follows:

1) Zircaloy guide tube/stainless steel cladding interaction at 935-960°C.

2) Molten Sn interaction with stainless steel in the presence of molten Ag-In-Cd, but compatibility between stainless steel and Ag-In-Cd where Sn was absent.

3) Possible degradation of Zircaloy by molten Cd and perhaps In.

ACKNOWLEDGMENTS

This paper was made possible by the diligent efforts of D. Donahue, F. Pausche, W. Kremsner, and H. Lautermilch at Argonne's Alpha-Gamma Hot Cell Facility. The work was supported by the U.S. Nuclear Regulatory Commission.

REFERENCES

1. C. S. Olsen, D. W. Akers, and R. McArdell, "TMI-2 Core Bore Examination Results," *Proceedings of the U.S. Nuclear Regulatory Commission 15th Water Reactor Safety Information Meeting, Gaithersburg, MD, October 26-30, 1987*, NUREG/CP-0091, Vol. 6 (February 1988), pp. 175-198.

2. L. A. Neimark, R. V. Strain, and J. E. Sanecki, "The Microstructural and Microchemical Characterization of Samples from the TMI-2 Core," *Proceedings of the U.S. Nuclear Regulatory Commission 15th Water Reactor Safety Information Meeting, Gaithersburg, MD, October 26-30, 1987*, NUREG/CP-0091, Vol. 6 (February 1988), pp. 199-209.

3. M. Hansen, *Constitution of Binary Alloys*, 2nd Ed., McGraw-Hill, New York, 1958, pp. 17, 20, and 36 for Ag-Cr, -Fe, and -Ni, respectively; p. 66 for Ag-Zr.

4. Ibid, pp. 573, 742, and 1062 for Zr-Cr, -Fe, and -Ni, respectively.

STATUS OF DISASSEMBLY OF THE DAMAGED TMI-2 REACTOR CORE

GREG R. EIDAM
BECHTEL NATIONAL, INC.

The March 1979 accident of the Three Mile Island Unit 2 (TMI-2) pressurized water reactor was the most severe accident to occur in a commercial operating power reactor in the United States. The progression of the TMI-2 accident was finally mitigated by the presence or injection of coolant water. The integrity of the reactor vessel was challenged, but remained intact. During the past 9 years, the TMI-2 accident has been a unique and invaluable source of information for improving and expanding the present knowledge of severe accidents of core melt progression, and of mitigating severe accidents before the reactor vessel and containment are threatened.

The post-accident condition of the plant presented an extremely difficult and complex plant cleanup challenge. The first major step in defueling the TMI-2 core was the removal of the reactor vessel (RV) head in July of 1984. With the head removed from the reactor vessel, it was then possible to lower cameras into the lower plenum region to allow engineers and scientists to see for the first time that 10,000 to 20,000 kg of core material, which appeared to have been molten at one time, was resting on the reactor vessel lower head. This examination, along with metallographic examinations of particles taken from the upper debris bed, indicated that the damage to the core was more extensive and severe than first thought. The upper plenum assembly was removed in May of 1985, and the final preparations to commence defueling operations were completed. On October 30, 1985, defueling began with the first core alterations.

The task of defueling the RV and accounting for all fissile materials has been difficult due to the extensive damage to the core and some of the core support structures, and because of the radiation fields in the Reactor Building. Fuel removal and handling have been challenging. Continuing development and application of unique tools and methods are relied upon to defuel the reactor.

An accurate determination of the post-accident state of the plant has been required to understand not only the accident progression and fission product transport and deposition, but to understand as well the properties of post-accident core material in order to defuel the reactor. This information has been developed from several sources: visual inspections of the reactor vessel internals, metallurigcal-radiochemical examinations of samples during the course of defueling, and readings from on-line instrumentation and experimental data developed from smaller scale tests conducted at various facilities.

Extensive damage to the TMI-2 core has presented unique problems. After the plenum was removed, a shielded rotatable work platform was mounted on top of the RV to provide access to the core through a 45 cm slot. Special long-handled tools, for use with underwater and shielded remote canister handling equipment, were developed to remove the core materials and place them

in specially designed shipping canisters for transport to the Idaho National Engineering Laboratory (INEL). Removal of core material progressed in stages, with each of the different regions of core material being removed individually.

The end state configuration of the original core included a core void or cavity which was approximately 1.5 m deep with an overall volume of approximately 9.3 m^3. Forty-two of the original 177 fuel assemblies standing at the periphery of this void surrounded this cavity. Only two of these fuel assemblies contain more than 90% of their full-length cross section with the majority of the fuel rods intact. The first step in defueling of the core region was to reduce these fuel assemblies and fuel rods into manageable lengths to provide clearance for the rotatable work platform and canister handling equipment beneath the platform. This reduction was accomplished by hydraulic cutters. Beneath this void, a loose debris bed varying in depth from 0.6 to 1 m existed consisting of whole and fractured fuel pellets, control rod spiders, end fittings, and resolidified debris totaling approximately 26,400 kg. This material was picked up with long-handled, pick-and-place tools and loaded into defueling canisters.

Beneath the loose debris bed was a large resolidified mass which was approximately 3 m in diameter, 1.5 m thick at its center, and 0.25 m thick at its periphery and containing approximately 32,700 kg of core debris. A special drilling machine was mounted on the work platform to break up this consolidated mass. The resulting fragmented debris was then placed in defueling canisters by using the pick-and-place tools. Some large pieces, composed of previously molten metallics and ceramics which were too large to be placed directly into the defueling canisters, were broken apart with the use of a hydraulic underwater jackhammer. Beneath this large resolidified mass stood undamaged fuel assembly stubs extending upward from the lower grid plate to the bottom surface of this resolidified region. These stubs varied in lengths of approximately 0.2 m to 1.5 m. Longer, partial fuel assemblies stood at the periphery and the resolidified mass. These fuel assembly stubs were removed with a specially designed fuel assembly puller tool that lifted each assembly and loaded them into defueling canisters. On the east side of the core, four adjacent fuel assemblies were almost completely replaced with previously molten core material; this has indicated a possible relocation path of molten material into the lower core support assembly (LCSA) and core bypass region. During December of 1987, all fuel assembly stubs, with the exception of one, were removed. The remaining assembly (R-6) consisted of a partial end fitting frame with resolidified material filling the space where the assembly would have been. This mass continues into the bypass region. During March of 1988, a hole was drilled into this one remaining stub assembly with a junk mill bit attached to the special drilling machine which was remounted on the work platform. After the drilling, portions of the end fitting and resolidified mass still remained. The standing fuel assembly stubs and peripheral assemblies constituted approximately 44,500 kg of core debris.

The LCSA region consists of 5 stainless steel structures: four plates and a lower grid assembly. The structures vary in thickness from 0.025 m to 0.33 m, with 0.080 m or 0.15 m diameter flow holes. During the accident, molten material flowed through the periphery of these structures and came to rest on the lower head of the RV. There is resolidified material at various locations

on the circumference of the structures. In several places, resolidified material completely fills the flow holes, and columns of once molten material are observed between the plates. The largest accumulation of resolidified material appears to have flowed into the LCSA from the east side of the core. Although most of this material was seen on the southeast side, many columns of resolidified material have been seen all the way around the core beneath the core bypass region.

The special drilling machine was again mounted on the defueling platform to begin disassembly of the LCSA during January 1988. This machine was used to section the LCSA grid plate which was removed from the reactor vessel and transferred to a core flood tank for storage during April. During May, an automated cutting equipment system (ACES), which includes a manipulator arm and an X-Y bridge and trolley system, was installed in the reactor vessel to cut the remaining stainless steel structures. The ACES has completed cutting two of these structures and is currently in the process of cutting the remaining two. During the early part of 1989, the last of these remaining structures will have been removed to provide access to the lower head region. Inspections have revealed that a large quantity of previously molten core material rests on the lower head. The post-accident debris in the lower head region accumulated to a depth of 0.75 m to 1 m above the lower head elevation, and to a diameter of 4 m. Particle sizes varied from granular particles (less than 0.010 m) to large rocks (up to 0.20 m). Visual inspections have indicated that larger rocks, especially in the northeast and southwest areas, were located towards the periphery and the debris pile was lower at the vessel center than at the periphery. A large cliff-like structure formed of previously molten core material exists in the northern region. The cliff base was approximately 0.38 m high and 1.25 m wide. It has been estimated that 19,200 kg of core material was in the lower head region as a result of the accident. The only significant structural damage observed to date in the lower head region was the melting of an incore instrument guide tube.

As a result of defueling the core region, additional material from the core region has been relocated to the LCSA and lower head regions. Therefore, over 28,000 kg of material must be removed from the lower head region. When this region is defueled, additional damage may be identified.

The final stage of defueling will be to disassemble the core baffle plates and remove the previously molten material from the core bypass regions. This core bypass region consists of vertical core baffle plates that form the peripheral boundary of the core, horizontal core former plates to which the baffle plates are bolted, the core barrel, and thermal shield. There are a number of flow holes in the baffle core former plates to which coolant flowed during normal reactor operations.

A large hole approximately 0.6 m wide and 1.5 m high exists, extending across the lower portion of 3 baffle plates. The 0.019 m thick baffle plates and sections of 3 horizontal core former plates (approximately 0.032 m thick), were melted in this region. Molten core material from the core region appears to have flowed through this hole into the upper CSA. The area behind the baffle plates contains loose debris all the way around the core region. The depth of this debris within the upper CSA is approximately 1.5 m on the

northside and a few millimeters thick on the southwest side. There appears to be a resolidified crust on the upper horizontal surfaces of the 3 bottom core former plates. The molten material moved down into the lower CSA through the flow holes in the core former plates. It is estimated that 4,200 kg of core debris is retained in this region. The annulus between the core barrel and the thermal shield was visually inspected and only fine particulate was observed. No major damage to any of the components in the upper CSA have been seen beyond what has been described here.

Defueling will be completed when these operations are concluded. Visual examinations and sampling, which will be conducted during later defueling operations, will give additional insight into the margin-of-failure of the reactor vessel, the core damage progression scenario, and the fission product inventory.

EXPERIMENTS RELATING TO DRYWELL SHELL-CORE DEBRIS INTERACTIONS

Robert E. Henry, Robert J. Hammersley, Boro Malinovic
Fauske & Associates, Inc.
16W070 West 83rd Street
Burr Ridge, Illinois 60521

Raj Sehgal and Edward L. Fuller
Electric Power Research Institute
3412 Hillview Avenue
Palo Alto, California 94303

1.0 INTRODUCTION

The response of BWR Mark I containments under severe accident conditions has recently focused on the potential for liner attack by high temperature molten debris discharged from the reactor vessel. This can be divided into issues related to early attack on the drywell shell immediately following reactor vessel failure and longer term concerns as debris would continue to accumulate on the containment floor. The IDCOR approach for the early transient behavior evaluated the influence of debris, at its melting temperature, coming into direct contact with the containment wall and this was found to result in thermal transients which would not threaten the containment wall integrity. For longer term debris accumulations, the IDCOR analyses demonstrated that water would be necessary to cool the debris long term and thereby to protect the containment integrity.

Debris melting temperatures were used in the IDCOR analysis since it was believed that material would be released from the reactor vessel at about its melting temperature and that cooling of the debris would occur as a result of (1) dynamic interactions between the debris and accumulated water within the pedestal and drywell regions and (2) heat transfer with the extensive structures in the two regions. Hence, the element of major interest is the influence of water on the debris immediately after its release from the RPV. Since experiments directly relating to discharge into a pedestal region and material transport across the drywell floor were not

available, and since this was considered to be a major aspect of the Mark I containment response under accident conditions, experiments were conducted to address this behavior.

2.0 EXPERIMENTAL APPARATUS

The experiments used iron thermite (reaction products are molten iron and molten aluminum oxide) to simulate the molten core debris with 20 Kg being used in two experiments and 11.4 Kg in the remaining two tests. The apparatus simulated the pedestal and drywell regions, including the concrete basemat (both basalt and limestone concrete were used) and a 1/10 linear scale was simulated for the flow path between the pedestal and drywell wall. (Since the principal objective was to measure heat transfer from the molten debris to the water, no attempt was made to use a 1/10th linear scale for the drywell or pedestal volumes.) Included in the experimental apparatus was a recirculating spray flow system, the pressure suppression quench tank, an inerted atmosphere and painted walls as would be the case in a Mark I containment. A sche[illegible]c of the experimental configurations is illustrated in Figure 1, which shows the location of (1) pressure measurements in the crucible, test box and quench vessel; and (2) temperature measurements in the pedestal region (tungsten-rhenium high-temperature thermocouple), the simulated drywell wall, the quench vessel and the recirculation vessel. The test box was fabricated from 0.019 cm (3/4 inch) carbon steel and had inside dimensions of 1 m long, 0.15 m wide and 0.3 m between the upper surface of the concrete basemat and the top of the test box.

Figure 2 illustrates the test box end plate which simulated the drywell wall and also shows the channeled form of the concrete basemat which promoted flow toward the wall and also forced the debris depth to be somewhat deeper (~ 5 cm). This channel configuration helped to represent some of the local debris depth increase that could be observed by two-dimensional flow phenomena as the debris would flow out of the pedestal region. The thermocouple pattern used in the experiments to date (the lower set of four thermocouple holes) are also illustrated in the figure and the enlarged side view shows that the thermocouple wells are drilled to within 0.085 inches

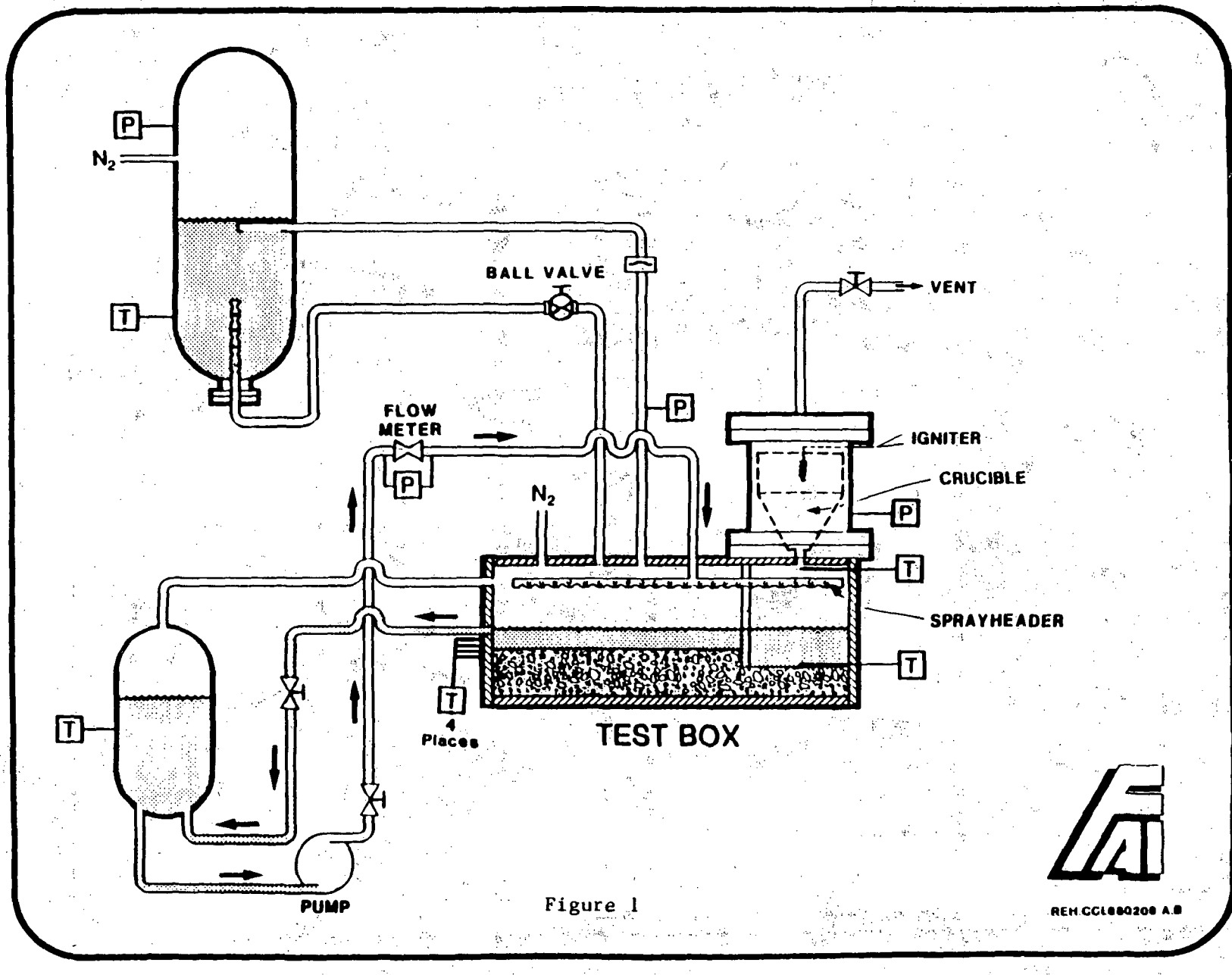

P
N_2
T
BALL VALVE
VENT
FLOW METER
P
P
N_2
IGNITER
CRUCIBLE
P
T
SPRAYHEADER
T
T
T
4 Places
TEST BOX
T
PUMP
REH:CCL880208 A.B

Figure 1

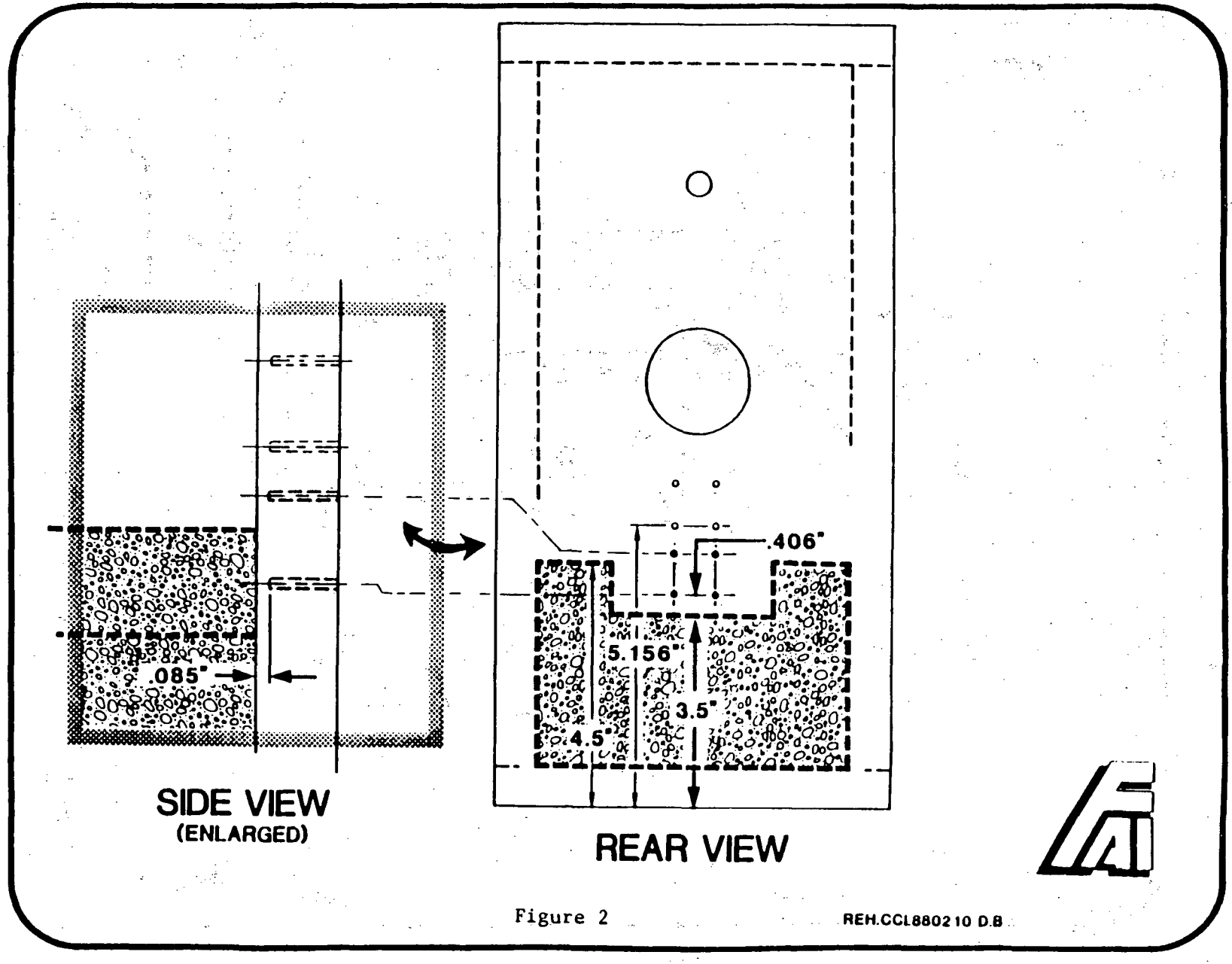


Figure 2

REH.CCL880210 D.8

(2.2 mm) of the inner surface to enhance the dynamic response of the measurement.

Beginning with Test 6, gas samples were taken in the quench tank before and after the tests. This provides information on the masses of hydrogen, carbon monoxide and carbon dioxide generated during the quenching process. These later tests also included thermocouples on the upper regions of the test box walls, which enabled the heat transfer (by steam condensation) to these walls to be measured. This can be coupled with the quench tank and spray flow rate measurements to provide an integral assessment of the heat removed from the debris by steam generation.

3.0 TEST CONDITIONS

The test conditions run to date are shown in Table 1 and include a Test 0 in which the thermite remained in the crucible and the stratified configuration of the debris was observed, which illustrated that the high temperature molten iron would be the first material released followed by the molten aluminum oxide. With the single exception of Test 3, the drywell sprays were operating before the thermite was reacted. The spray system produced an accumulation of water in the test box sufficient to spill over into the recirculation sump which is a level of about 8 cm such that the debris was released into a water pool on the pedestal floor. Tests 1 and 2 were similar except for the melt mass and the rupture disc-relief valve configuration to the quench tank was removed in Test 2 and the quench tank was operated at the same initial pressure as the test box, which more closely simulates the containment conditions. Test No. 3 was similar to Test No. 1 with the exception that the test box was initially dry and water was added 30 seconds after release of the debris. Test No. 4 was 20 Kg of melt with a limestone basemat and sprays operating in a steady-state manner before ignition of the thermite mixture.

Following the first four runs, additional experiments were conducted to verify the reproducibility of the measured heat removal to the water and the influence of pressures on the quenching process. Two special purpose

Table 1

TEST CONDITIONS

Run	Thermite Mass	Concrete	Test Box Pressure	Quench Tank Pressure	Initial Crucible Pressure
0	11.4 Kg	N/A	N/A	N/A	N/A
1	11.4 Kg	Basalt	0.45 MPa	0.1 MPa[1]	0.52 MPa
2	20 Kg	Basalt	0.45 MPA	0.45 MPa	0.55 MPa
3	11.4 Kg	Basalt[2]	0.44 MPa	0.44 MPa	0.52 MPa
4	20 Kg	Limestone	0.48 MPa	0.48 MPa	0.52 MPa
5	20 Kg	Basalt	0.14 MPa	0.14 MPa[3]	0.23 MPa
6	20 Kg	Limestone	0.14 MPa	0.14 MPa[3]	0.21 MPa
7	20 Kg	Basalt	0.45 MPa	0.45 MPa[3]	0.51 MPa
8	20 Kg	Limestone	0.21 MPa	0.21 MPa[3]	0.29 MPa
9	20 Kg	Basalt	0.20 MPa	0.20 MPa[3]	0.29 MPa
10	20 Kg	Limestone[4]	0.20 MPa	0.20 MPa[3]	0.24 MPa
11	20 Kg	Limestone[5]	0.21 MPa	0.21 MPa[3]	0.23 MPa

[1]Used a relief valve - rupture disc configuration.
[2]B - Turned on 30 seconds after melt release.
[3]Used the Phase III configuration with vacuum breaker simulation.
[4]Zircaloy cladding imbedded in surface of concrete.
[5]No channel in basemat to the drywell wall.

tests were performed to evaluate (1) the influence of Zircaloy in the debris-concrete interaction process (Test 10), and (2) the influence of a configuration in which the debris is held within a sump in the pedestal region (Test 11) such that a deeper debris bed is created in the pedestal as would generally be the case in a reactor configuration. For Test 10, the upper surface of the concrete basemat and the sides of the drywell channel were lined with zirconium spacer grids with approximately 2 Kg of Zircaloy being cast into the concrete surface with appropriate anchors. This experiment was designed to promote Zircaloy oxidation and determine if the additional chemical energy source was significant and the influence that this would have on quenching of the debris. Test 11 was performed by eliminating the channel in the drywell region such that the debris accumulated below the reactor vessel in the pedestal sump and then flowed onto the drywell floor.

4.0 EXPERIMENTAL RESULTS

Test No. 1 resulted in test box and crucible pressure histories as illustrated in Figure 3 with the test box pressurization being substantial due to the dynamic interaction of the debris with the accumulated water on the pedestal floor. This pressurization was ~ 2 atm and lasted for about 2 seconds and was due to the rapid generation of steam by the dynamic interaction between the melt and water. Temperature measurements in the quench tank verified that the steam was condensed in the suppression pool and the energy transported was approximately that required to freeze the molten material. Figure 3 also illustrates that the test box blew down to the quench tank pressure following the experiment as a result of the relief valve-low pressure rupture disk configuration used in this experiment in which the rupture disk was broken by the test box pressurization and created the blowdown path to the quench tank (atmospheric pressure). Figure 4 illustrates the measured pedestal temperature behavior and the temperatures in the drywell wall and demonstrate that the temperatures at the wall are only those observed by the recirculating water. Disassembly of the test section demonstrated that neither the molten iron nor the oxide was transported to the test box wall. The iron stopped about 1 cm short of the

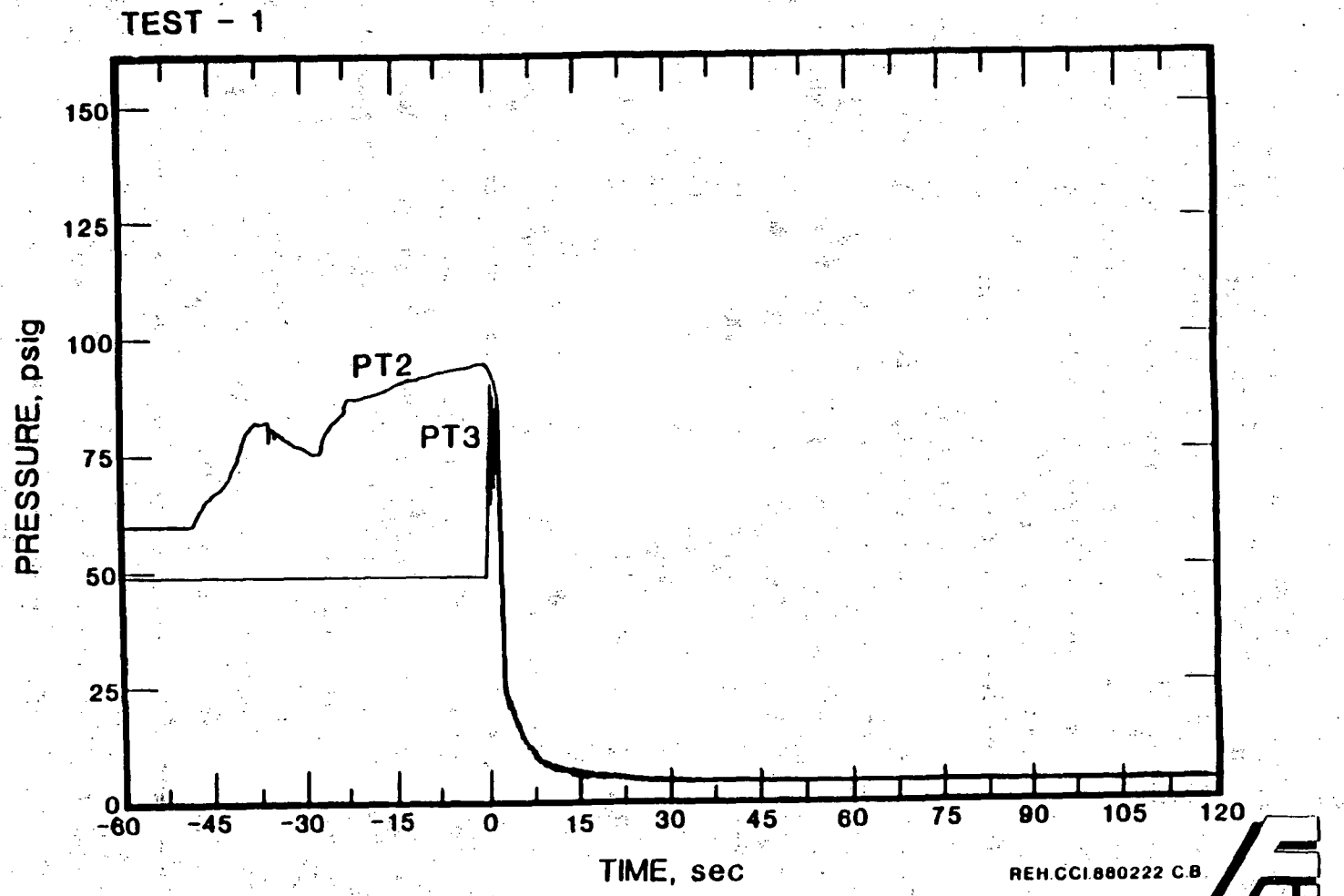
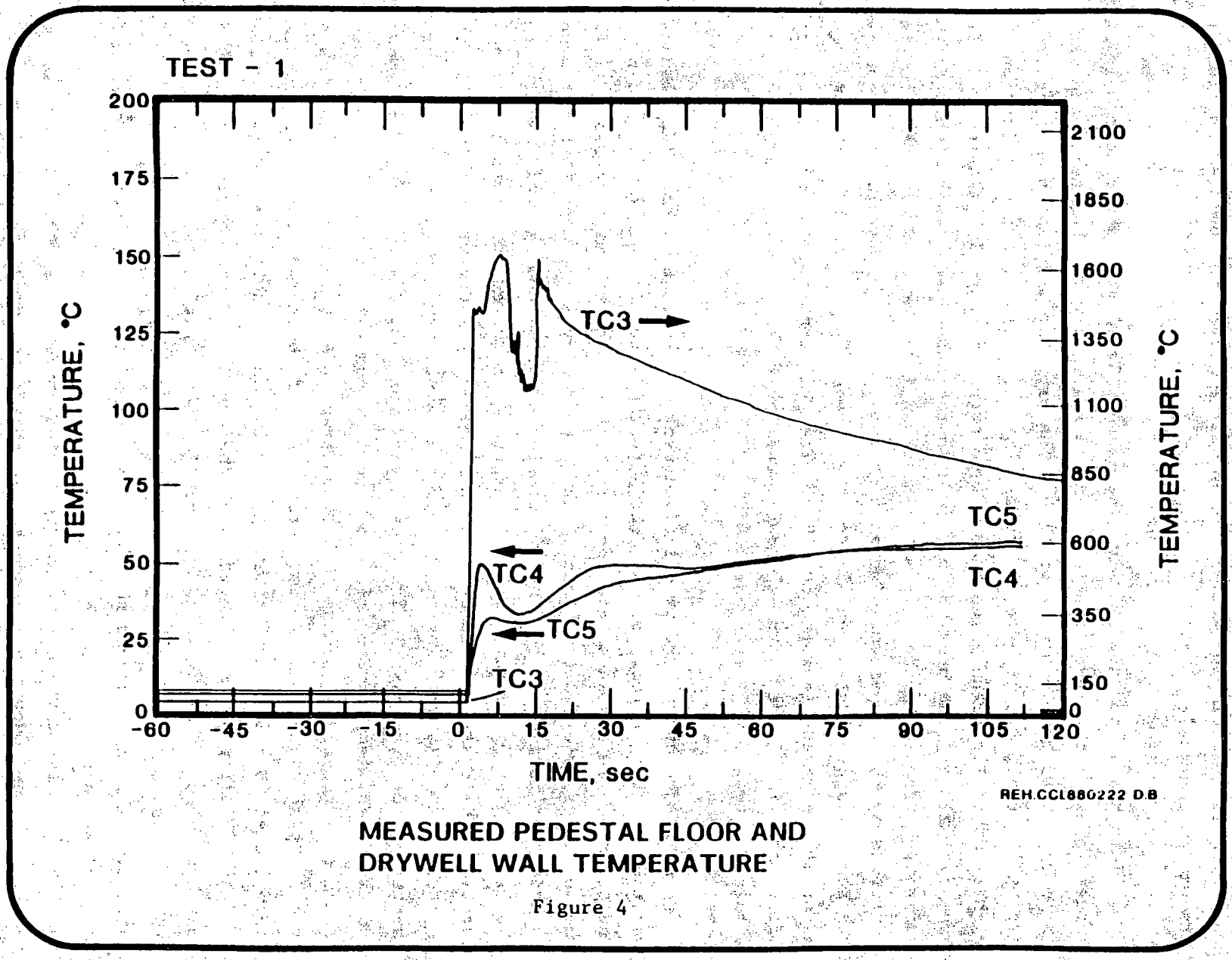


Figure 3 Measured crucible (PT2) and test box (PT3) pressures.



MEASURED PEDESTAL FLOOR AND DRYWELL WALL TEMPERATURE

Figure 4

wall as a solidified pool and the oxide was quenched well before the iron on its way to the wall.

Test No. 2 used almost twice the mass of Test No. 1 and resulted in a larger pressurization of the test box and a longer duration, hence indicating more substantial steam generation. The crucible and test box pressures are illustrated in Figure 5 and as shown, the test box pressurization is higher and of longer duration than was observed in Test 1. These results are typical of the behavior observed in the subsequent tests. This pressurization transports steam from the test box into the quench tank and is confirmed by the temperature increase in the quench tank water. This energy transfer is approximately equal to that required to freeze the molten material released from the crucible. The wall temperatures for Test 2 are illustrated in Figure 6 and as shown, the peak wall temperature on the simulated drywell wall is about 500°C.

As stated above, the principal element addressed by these experiments was the energy transfer from the debris to the water in this dynamic quenching process. To evaluate this energy transfer rate, one must assess: (1) the energy transfer to the quench tank (measured by the temperature increase in the water pool), (2) the energy transfer to the incoming cold water in the recirculating spray, and (3) the energy required to saturate the comparatively cold steel structures as indicated by temperature measurements in the test box walls well above the debris accumulation. Figure 7 illustrates the temperature increase in the quench tank for Test 8 and Figure 8 shows the measured temperature rise of the test box walls after the debris has been discharged and quenching is well underway. A typical spray flow rate is .2 Kg/sec and with a temperature rise of about 100°C, this represents approximately $8 \cdot 10^4$ watts of energy absorption capabilities. Saturation of the incoming water is verified by the continued temperature rise of the test box walls to values which approach local saturation at the test box final pressure. By examining the thermocouple response in the quench tank, which typically occurs over the first few seconds of the interaction, and the temperature increase of the 1.9 cm thick steel side walls of the test box, one can assess the net steam generation rate from the debris as a result of the quenching process. It should be noted that the debris can

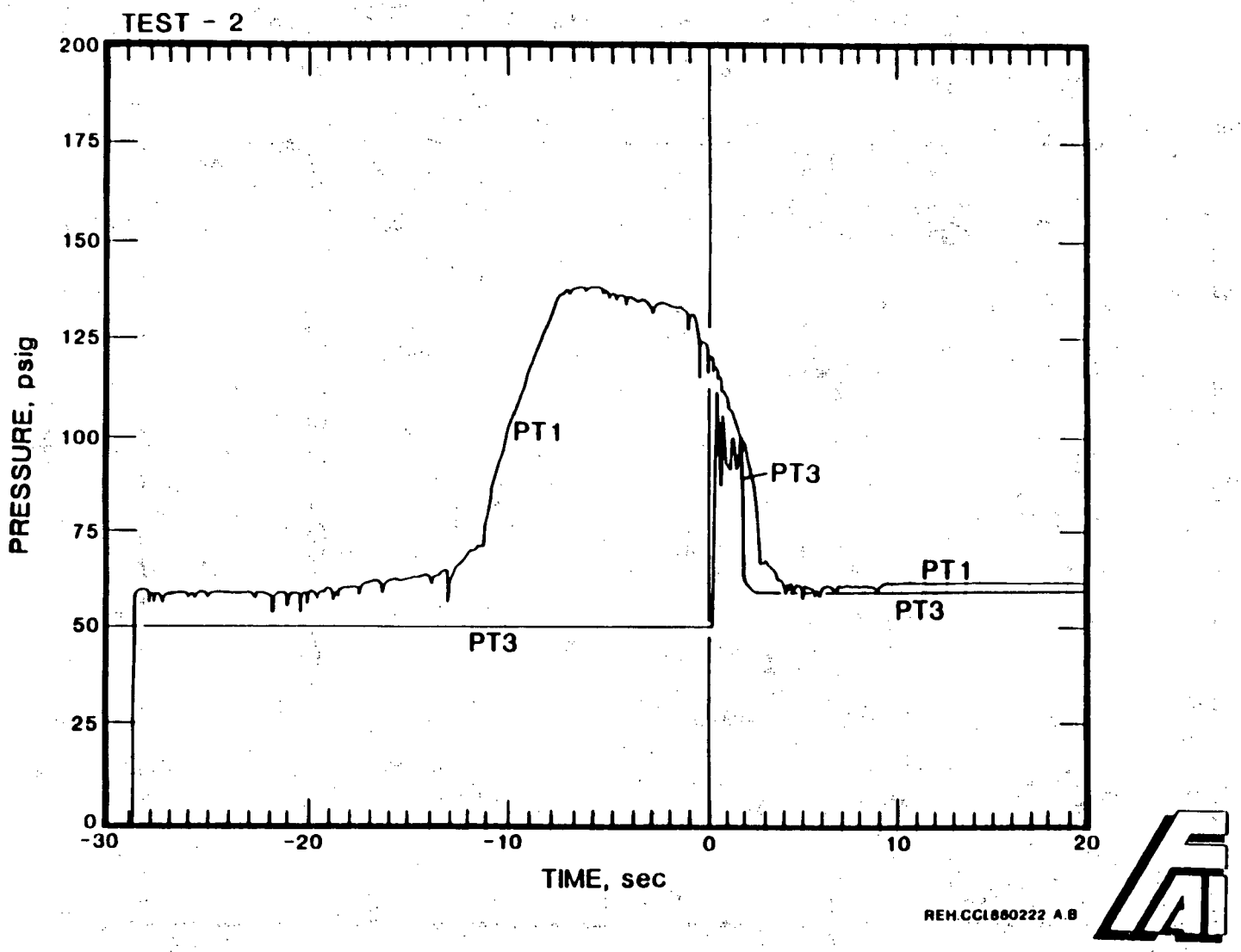
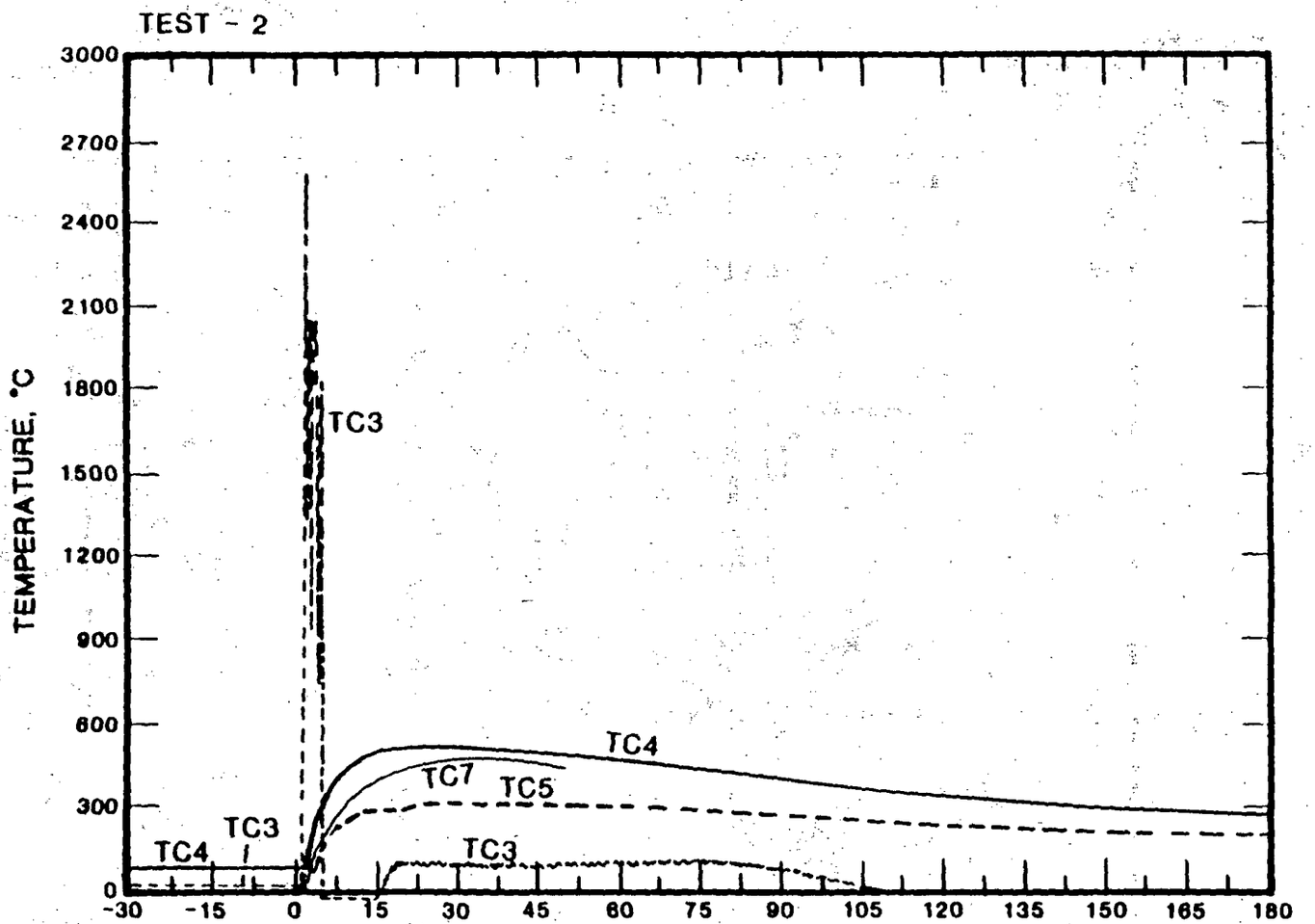


Figure 5 Measured crucible (PT1) and test box (PT3) pressures.



MEASURED PEDESTAL FLOOR AND DRYWELL WALL TEMPERATURES

Figure 6

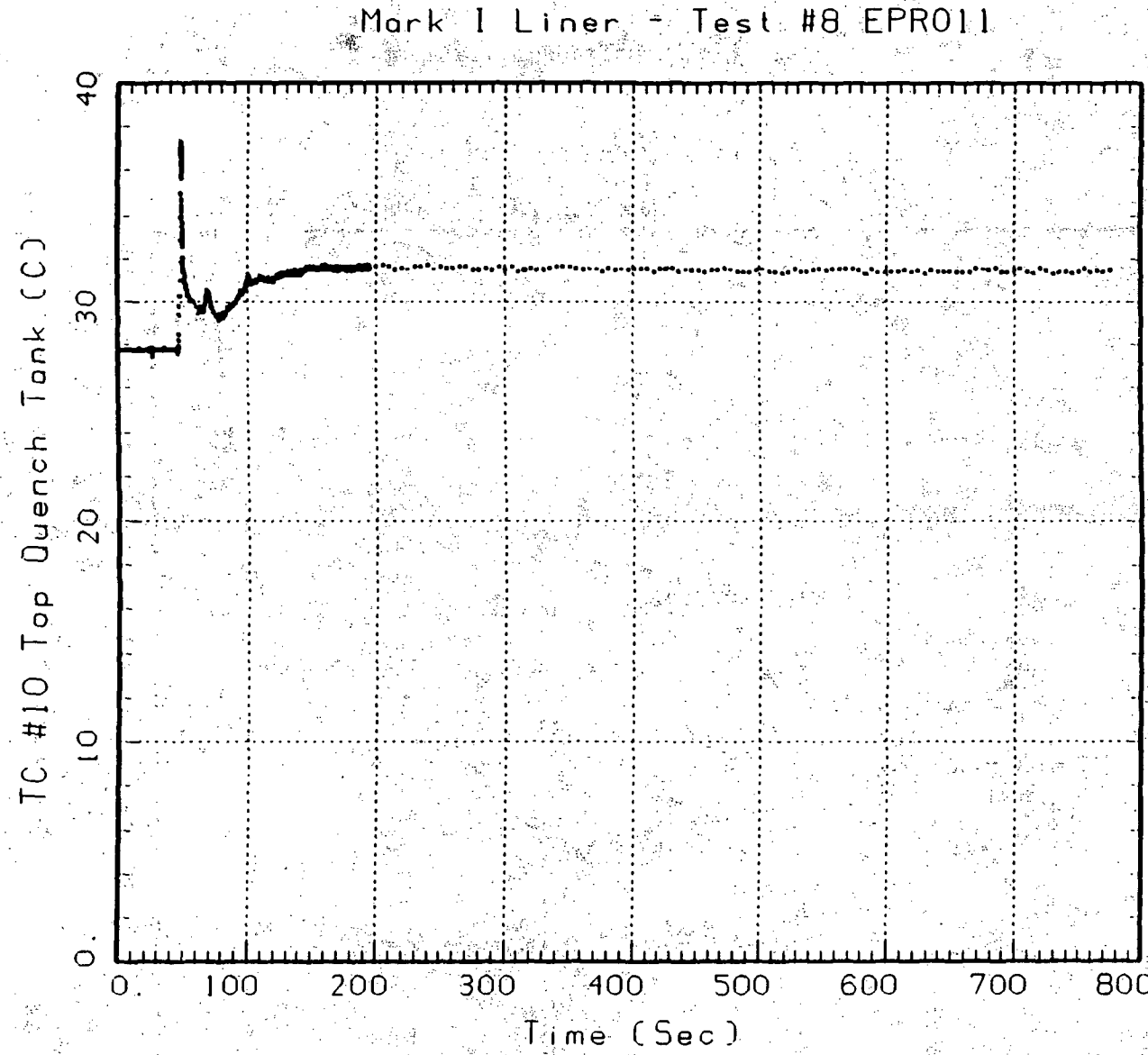


Figure 7 Upper quench tank water temperature.

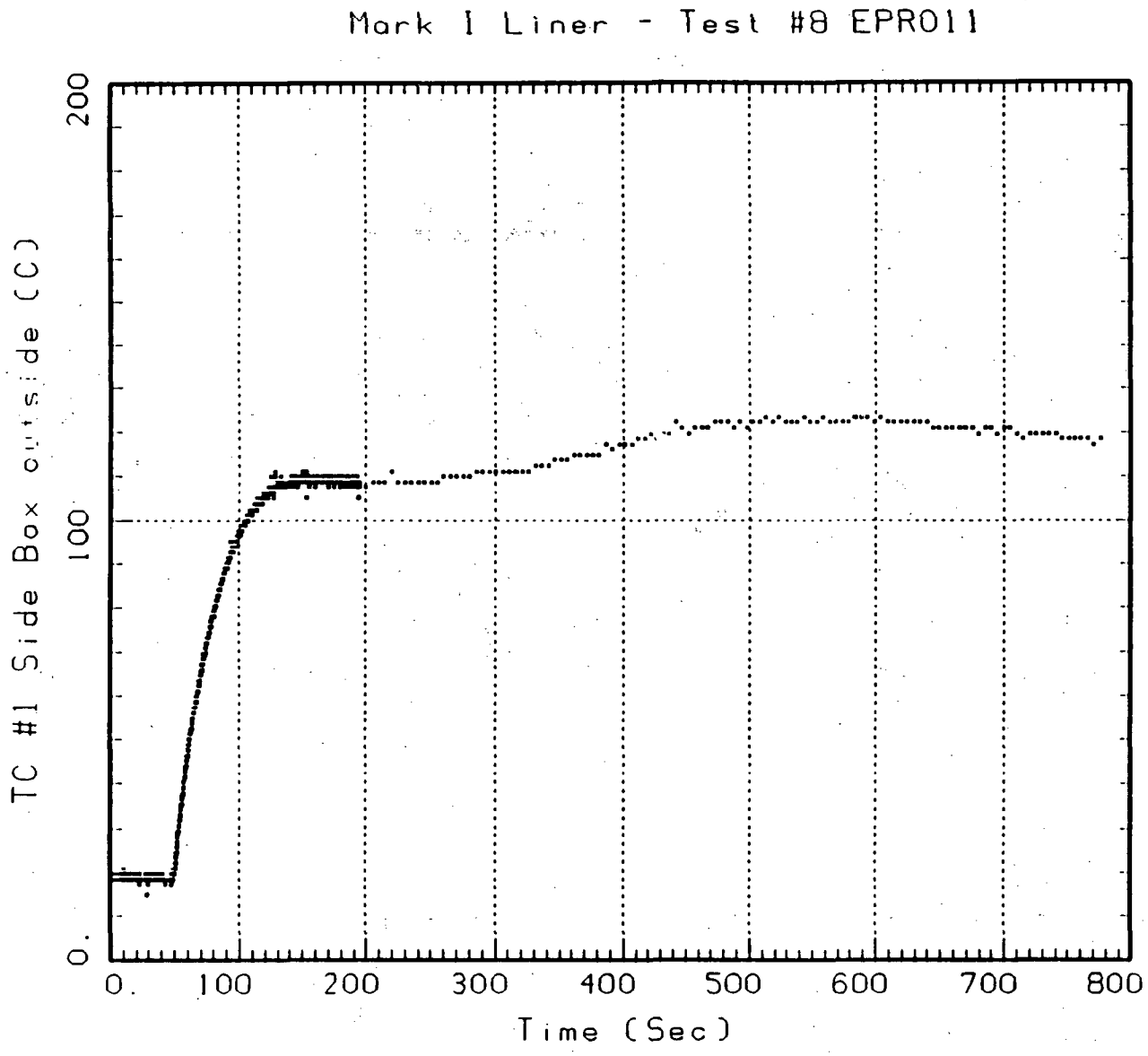


Figure 8 Upper test box temperature.

lose energy to other structures which is not accounted for by this analysis. This calculation focuses on the energy lost from the debris via steam generation. Results for the experiments are shown by the data for Test 8 in Figure 9. These results are represented as a heat flux off the upper surface of the debris which is given the projected area of the test bcx floor (0.15 m^2). As observed, the initial energy removal rate from the debris is much greater than a value typical of the critical heat flux, which likely indicates the dynamic nature of the initial debris interaction with the water and the influence of area amplification. After the debris has distributed over the bottom of the test apparatus, the heat flux decays to levels which are in reasonable agreement with a CHF value. The heat removal from the debris can be compared to the prediction for a semi-infinite slab of aluminum oxide at an initial temperature of 2400K and a surface temperature equal to water saturation. This is shown in Figure 9 which shows the measured heat flux is substantially greater than that which assumes the only limitation is within the quenching debris. Figures 10 and 11 show the measured heat flux data for Tests 9 and 10 and these are consistent with the observations of Test 8. The integral of the steam heat removal rate is shown in Figure 12 which shows that about 75% of the energy is removed in the first 100 seconds.

5.0 IMPORTANCE FOR REACTOR SYSTEMS

The influence of water quenching on debris released from the reactor vessel is shown in Tables 2 and 3 which summarize two different MAAP calculations for Peach Bottom under Station Blackout conditions. Table 2 lists the drywell gas and core debris temperature immediately following vessel failure and over the long term. As shown, the debris is calculated to be quenched in about ten minutes. Thereafter, the debris remains cool even though long term pressurization of the containment would occur without containment heat removal. Table 3 represents the behavior for a similar set of accident conditions without drywell sprays being available. This shows the debris to be quenched by water released from the primary system at vessel failure. However, after this water is vaporized, the dry debris reheats in the pedestal and drywell and also markedly increases the drywell

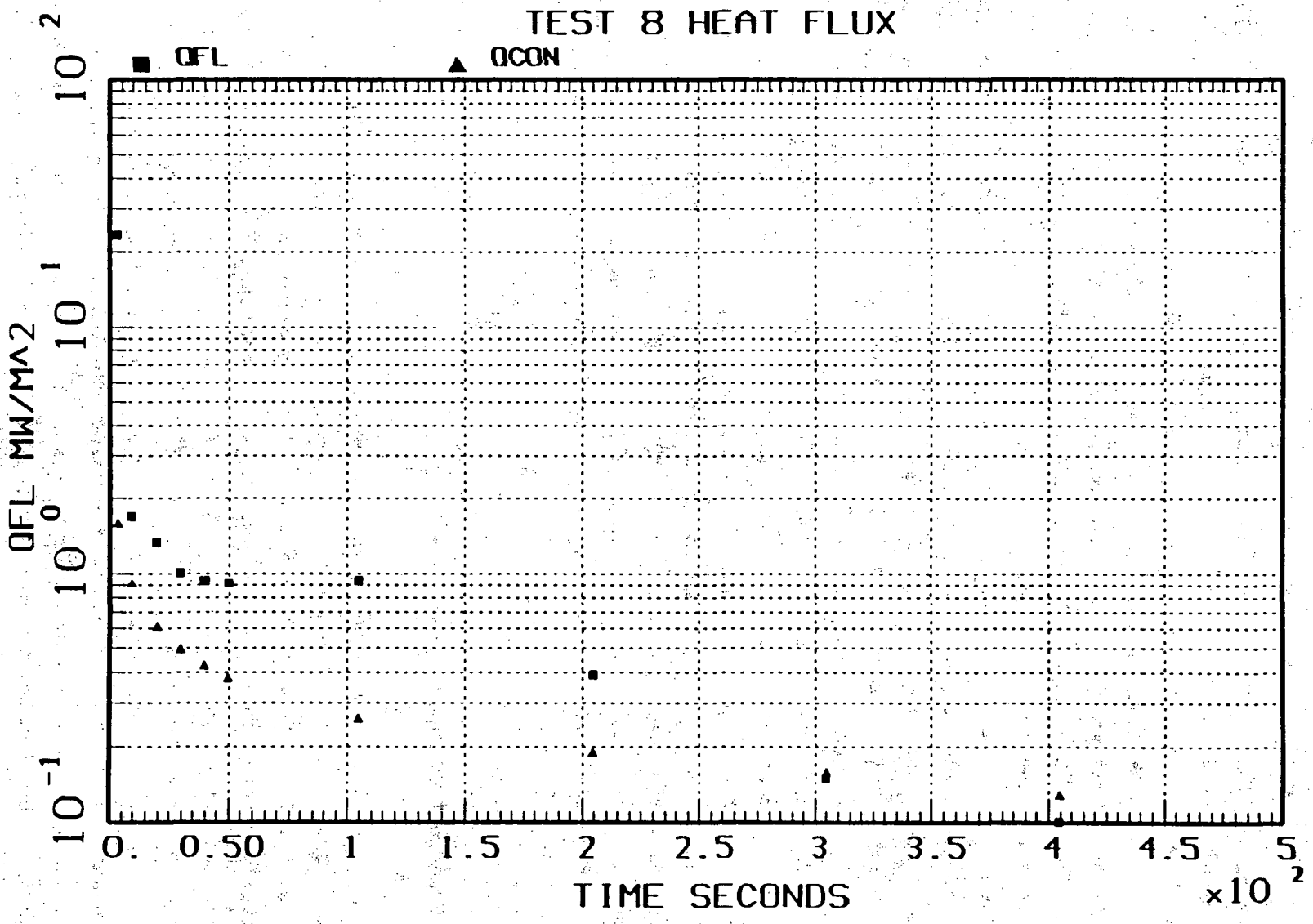

TEST 8 HEAT FLUX
QFL
QCON
QFL MW/M^2
10^{2}
10^{1}
10^{0}
10^{-1}
0.
0.50
1
1.5
2
2.5
3
3.5
4
4.5
5
TIME SECONDS
$\times 10^{2}$

Figure 9

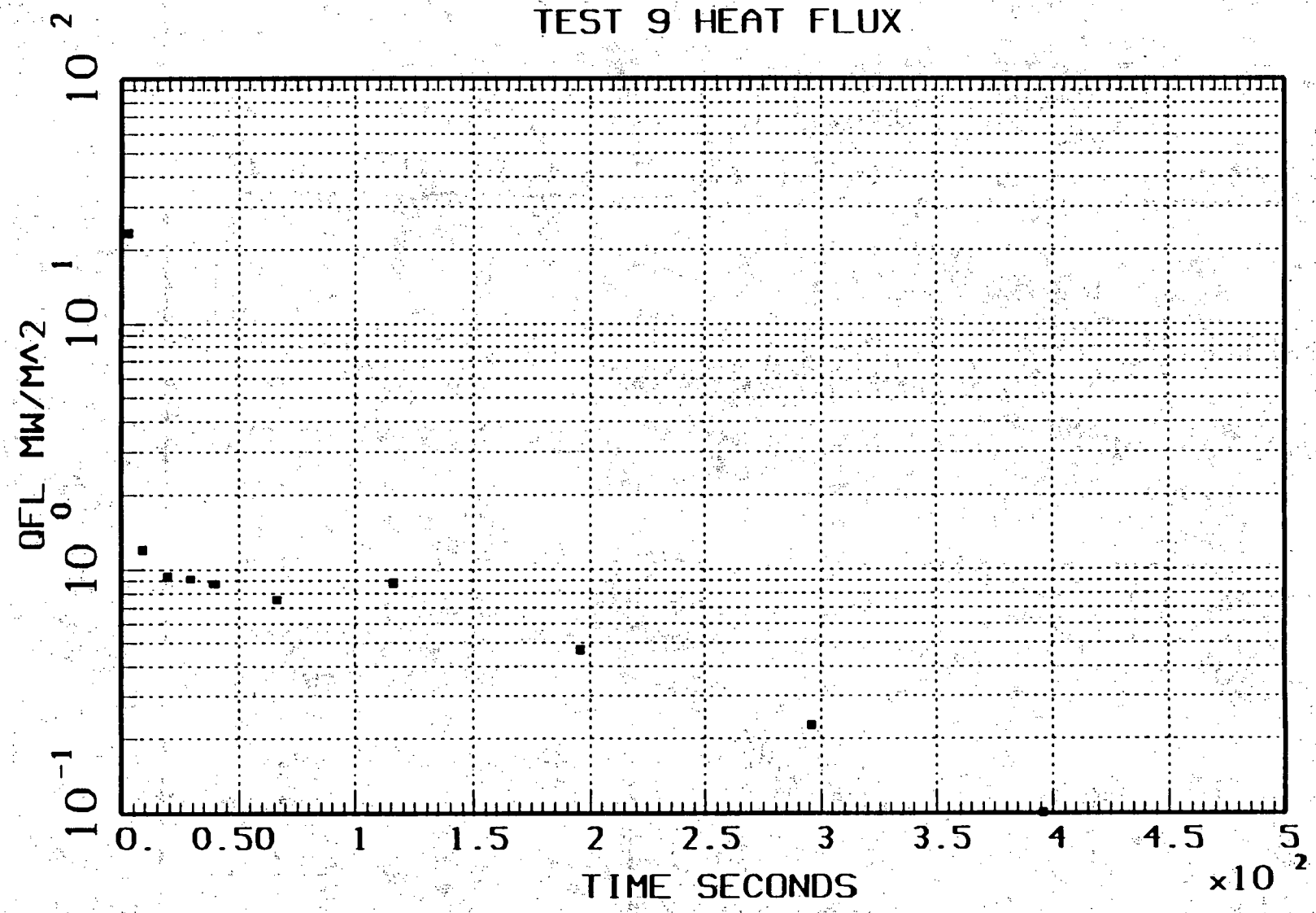

TEST 9 HEAT FLUX
QFL MW/M^2
10^2
10^1
10^0
10^-1
0.
0.50
1
1.5
2
2.5
3
3.5
4
4.5
5
TIME SECONDS
x10^2

Figure 10

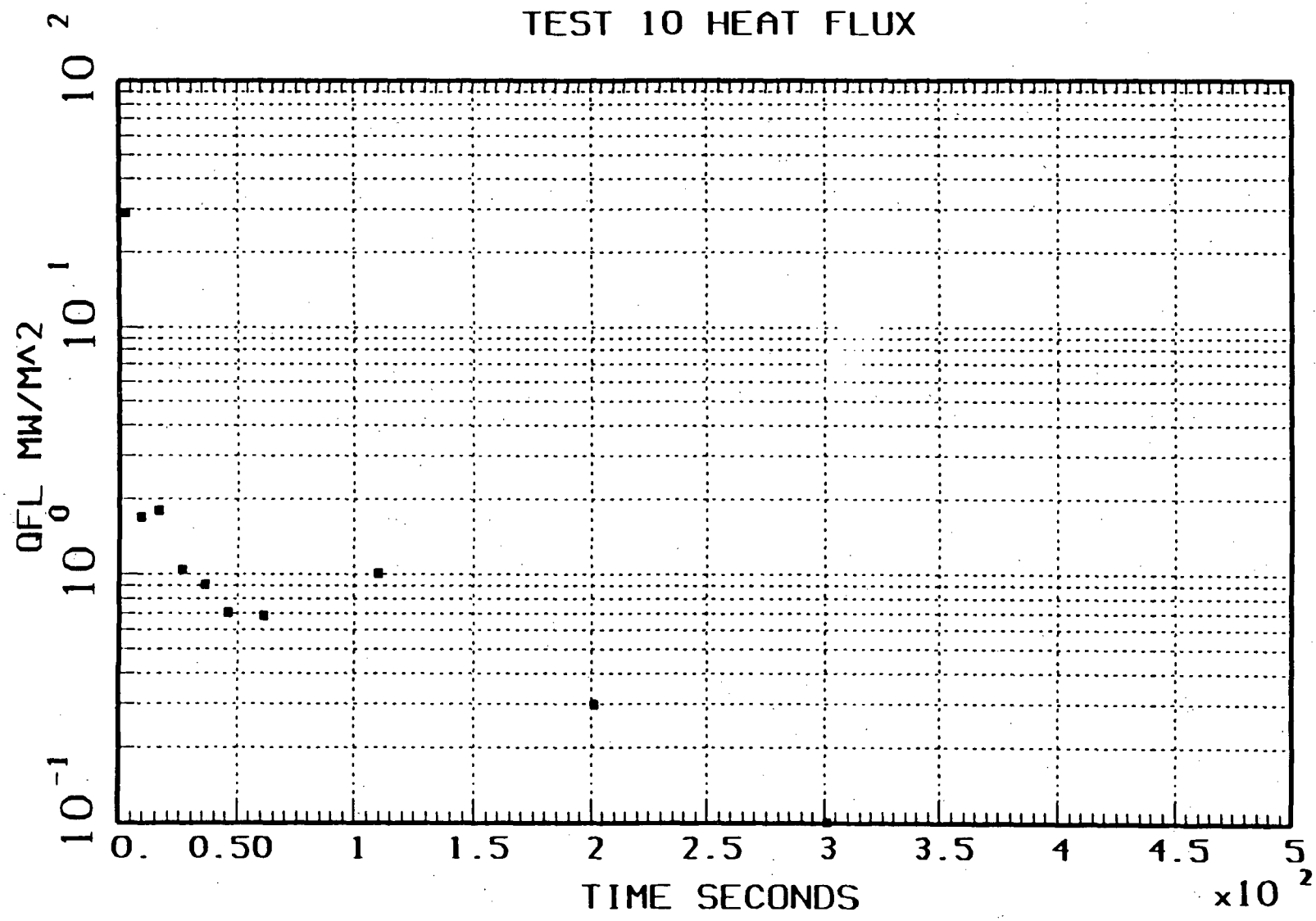

TEST 10 HEAT FLUX
QFL MW/M^2
10^{2}
10^{1}
10^{0}
10^{-1}
0.
0.50
1
1.5
2
2.5
3
3.5
4
4.5
5
TIME SECONDS
x10^{2}

Figure 11

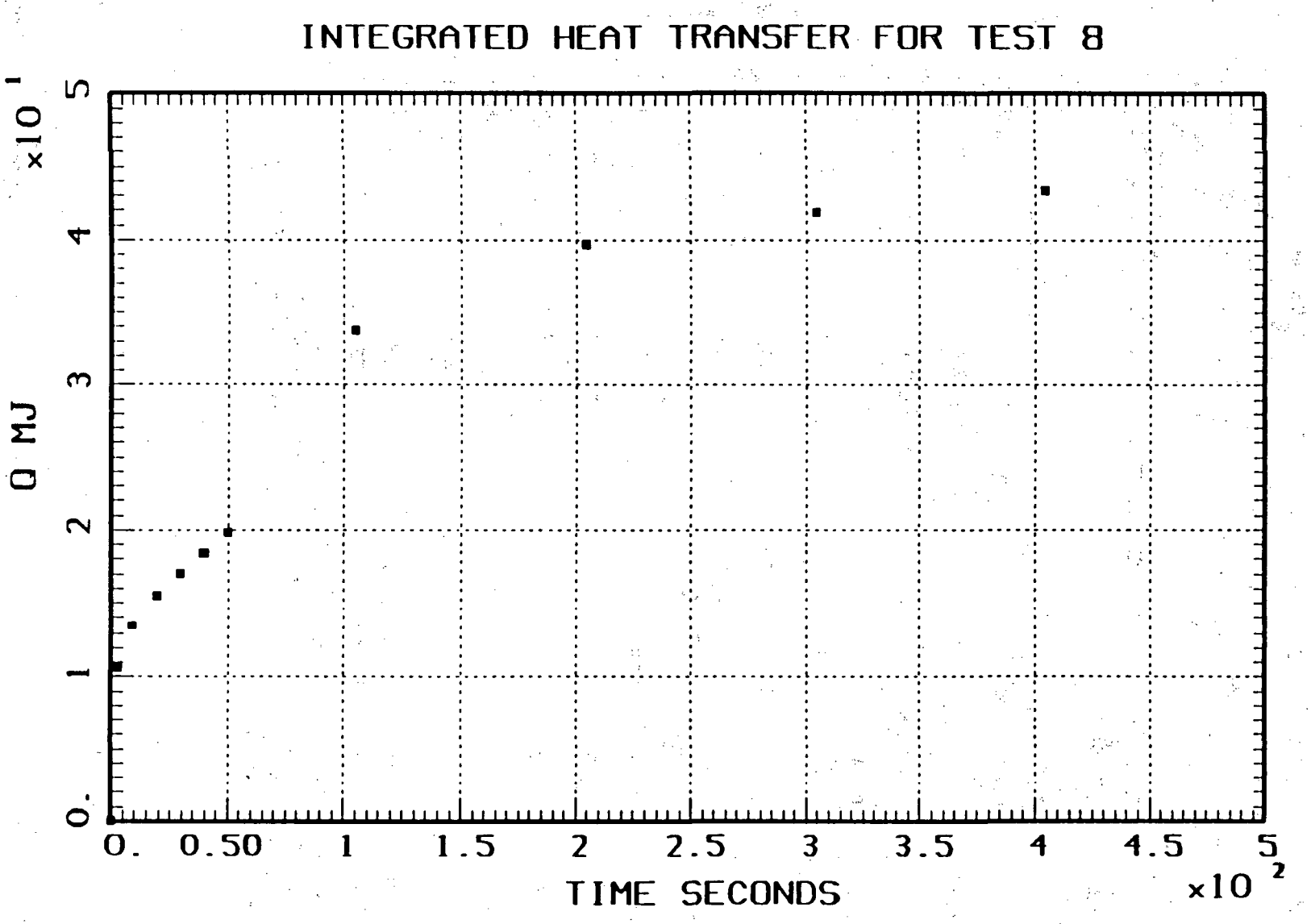

INTEGRATED HEAT TRANSFER FOR TEST 8
Q MJ
x10 1
0.
1
2
3
4
5
0.
0.50
1
1.5
2
2.5
3
3.5
4
4.5
5
TIME SECONDS
x10 2

Figure 12

Table 2

PEACH BOTTOM STATION BLACKOUT DRYWELL SPRAYS ON AT 8 HR

Time Hour	Pressure MPa	Drywell Gas Temperature K	Corium Temperature in Drywell K	Water Mass in Drywell Kg
Short-Term Quench				
11.17^-	0.176	321	N/A	58,900
11.17^+	0.645	433	1759	75,100
11.18	0.730	454	1473	29,900
11.20	0.690	433	1042	33,800
11.21	0.675	432	662	36,000
11.22	0.667	431	446	37,400
11.23	0.613	427	438	40,300
11.24	0.585	424	433	43,000
Longer-Term Overpressure				
11.66	0.440	401	419	45,900
12.00	0.538	422	427	44,400
14.00	0.750	446	441	43,600
16.00	0.850	457	446	43,300
18.00	0.908	468	468	43,200

NOTES: 1. Vessel breach at 11.17 hour.
2. Drywell failure at 18.0 hour at 0.908 MPa.
3. UO_2 mass in drywell remains constant at 43,300 Kg.

Table 3

PEACH BOTTOM STATION BLACKOUT NO OPERATOR ACTIONS

Time Hour	Pressure MPa	Drywell Gas Temperature K	Corium Temperature in Drywell K	Water Mass in Drywell Kg	UO_2 Mass in Drywell Kg
Initial Quench					
10.66	0.188	383	N/A	0	0
10.68	0.555	495	3178	46,600	14,100
10.69	0.555	486	2766	34,300	14,300
10.71	0.520	447	1743	31,400	14,400
10.74	0.532	430	453	25,300	16,600
10.76	0.499	424	471	26,100	16,600
10.78	0.494	424	472	26,000	17,000
Longer-Term Overtemperature and Overpressure					
12.00	0.561	453	429	3200	18,500
12.32	0.592	461	1142	900	42,600
14.00	0.572	536	1313	0	54,400
16.00	0.584	640	1743	0	52,400
16.08	0.585	645	1743	0	52,300

NOTES:
1. Vessel breach at 10.66 hour.
2. Drywell failure at 16.08 hour at 645K (700°F) gas temperature.
3. A large flow of corium from the pedestal to the drywell occurred from 12.0 to 12.3 hour.

gas temperature. While the pressurization rate is lower in this calculated behavior the core debris is not stabilized as it was with water addition.

6.0 CONCLUSIONS

Table 4 summarizes the test results for the experiments to date for the maximum test box pressure, the duration of the pressurization, the peak wall temperature and the time to this peak temperature. The most important part of the experiments is the energy removal rate provided by water. In all of the experiments, the quenching rate far exceeded that which could be supplied to the debris surface by internal conduction and early in the transient far exceeded the critical heat flux value.

Table 4

SUMMARY OF TEST RESULTS

Run	Maximum Test Box Pressure (MPa)	Duration of Pressurization (sec)	Peak Wall Temperature (°C)	Time to Peak Wall Temperature (sec)
0	N/A	N/A	N/A	N/A
1	0.71	- 2	55	90
2	0.84	- 3	507	25
3	0.62	- 1	288	55
4	1.21	- 3	580	45
5	0.17	3	860	12
6	0.38	3.5	1200	10
7	0.93	3	800	20
8	0.62	3	550	10
9	0.50	3	1300	8
10	0.72	3	425	50
11	0.47	3	440	20

Experimental Studies on Melt Spreading, Bubbling Heat Transfer, and Coolant Layer Boiling

G. A. Greene, C. Finfrock, J. Klages and C.E. Schwarz
Brookhaven National Laboratory
Upton, New York 11973

and

S. B. Burson
U.S. Nuclear Regulatory Commission
Washington, DC 20555

Abstract

Melt spreading studies have been undertaken to investigate the extent to which molten core debris may be expected to spread under gravity forces in a BWR drywell geometry. The objectives are to determine the extent of melt spreading as a function of melt mass, melt superheat, and water depth. These studies will enable an objective determination of whether or not core debris can spread up to and contact containment structures or boundaries upon vessel failure. Results indicate that the most important variables are the melt superheat and the water depth. Studies have revealed five distinct regimes of melt spreading ranging from hydrodynamically-limited to heat transfer-limited. A single parameter dimensionless correlation is presented which identifies the spreading regime and allows for mechanistic calculation of the average thickness to which the melt will spread.

Experiments concerning bubbling heat transfer from a pool to a vertical boundary have been undertaken to characterize the magnitude of the lateral heat flux from a bubbling pool of core debris interacting with concrete to a vertical structural boundary. Of particular interest is the dependence of the interfacial heat transfer coefficient upon the superficial gas velocity and the fluid Prandtl number. These studies will enable determination of the boundary convective heat flux for cases in which the core debris may come in contact with containment structures or boundaries. Results indicate that the bubbling heat transfer coefficient is an increasing function of the superficial gas velocity; the heat transfer coefficient varies from 2000-5000 W/m^2K for superficial gas velocity in the range 0.2-2.4 cm/s. A generalized dimensionless correlation is presented which enables mechanistic determination of the bubbling heat flux boundary condition.

Studies have been conducted to examine the mode and magnitude of liquid-liquid boiling at high superheats with a non-condensable gas flux through the boiling interface. These studies simulate the effect of water boiling over a core melt engaged in a core-concrete interaction. Of particular interest is whether the film boiling regime is the applicable mode of coolant boiling and the magnitude of boiling enhancement by the simulated MCCI gas flux. Results indicate that the film boiling regime is preserved for boiling over molten metal pools at superheats exceeding the minimum film boiling point, even in the presence of a non-condensable gas flux through the boiling interface. The gas flux enhances the boiling heat flux above the classical flat plate limit, and does not suppress stratified steam explosion events. A correlation for the gas flux enhancement to liquid-liquid film boiling is presented.

1. Background

Recent assessments of risk due to severe accidents in light water reactors have indicated that the consequences of molten core-concrete interactions (MCCI) may dominate the considerations of containment loads and performance, as well as the release of non-volatile fission product aerosols to the containment building [1,2]. In recognition of the magnitude of this potential threat, the USNRC has supported an aggressive research program of integral and separate-effect experimental investigations into MCCI phenomenology, as well as development of the severe accident source term codes for MCCI analyses, CORCON [3] and VANESA [4].

The separate-effect experimental studies to be described in this paper have been initiated to support the quantification and modeling of several of the most important phenomena that can occur during a MCCI. These include transient spreading of metallic corium simulants on horizontal, flooded surfaces, bubbling heat transfer from simulant corium pools to structural boundaries, and boiling and explosive interactions between bubbling corium simulant pools and an overlying water pool. These three areas of current research will be discussed in greater detail in the sections to follow.

2. Transient Spreading of Metallic, Corium Simulants on Horizontal, Flooded Surfaces

The distribution of molten core debris in the drywell of a BWR during an unterminated core melt accident is of particular interest in assessing containment loads and fission product source term. Also dependent upon such a mechanistic treatment of melt spreading are potential mitigating actions; among these are construction of barriers to limit spreading and the modification of drywell sprays to retain airborne fission products. Prior to implementation of backfits, it would be useful to know the distribution of the debris in the drywell. If, for instance, it could be shown that debris would be expected to contact the Mark I containment shell soon after vessel failure, it may be reasonable to

require a barrier to interdict the debris and prevent contact. In a like fashion, if fission product release would be concentrated inside the pedestal, it would be reasonable to position sprays in that location instead of spreading them out all over the drywell. In that fashion, the greatest benefit from fission product retention may be realized. In order to make these decisions, and similar decisions in a rational framework, it is necessary to have the capability to model and predict melt spreading.

An experimental investigation of the spreading of molten metallic melts upon horizontal surfaces was initiated. The experimental apparatus consists of the following components: a rotating oven in which to heat a prescribed mass to a desired initial superheat, temperature controllers and indicators to monitor the initial conditions, and a target horizontal surface which can be flooded with water to which the melt is delivered. A schematic of the apparatus for the melt spreading studies is presented in Figure 1.

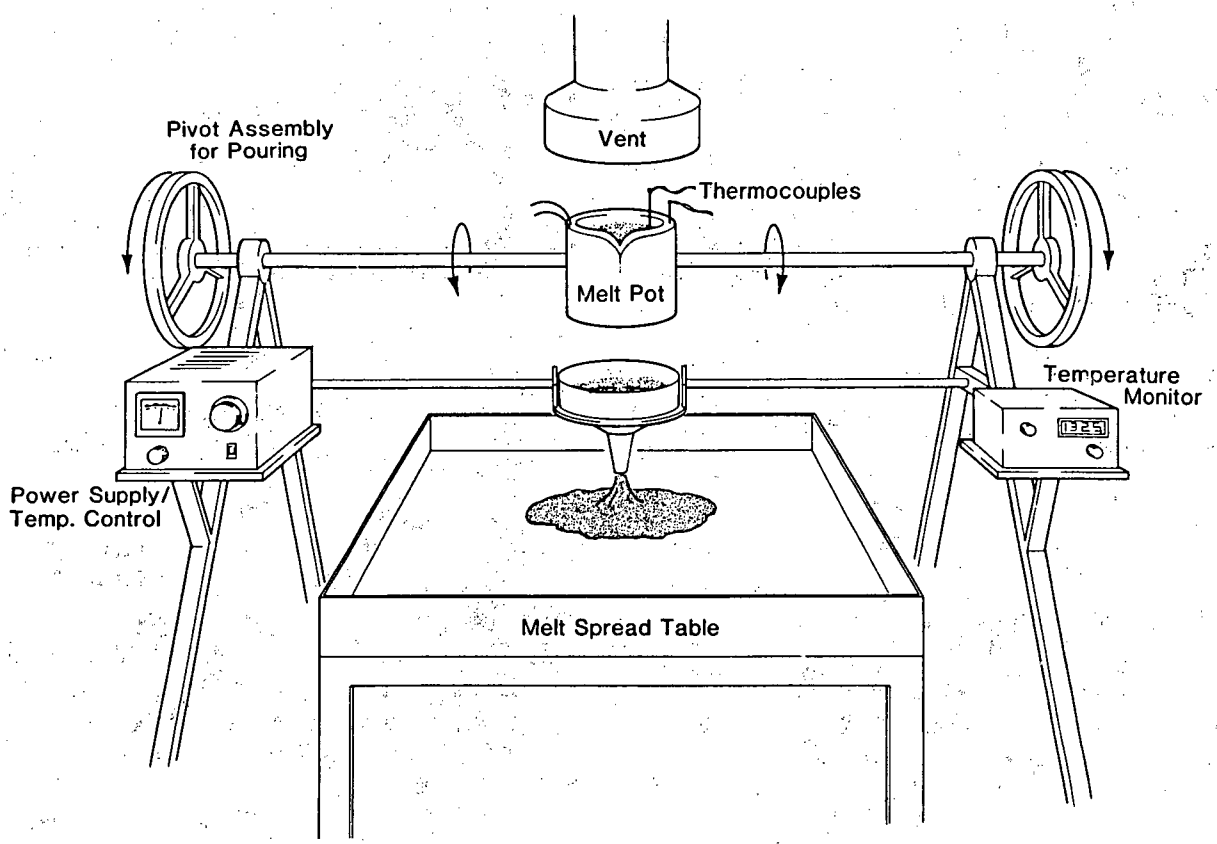


Figure 1 Schematic of Transient Melt Spreading Apparatus

Once the lead melt is heated to the desired superheat, the cylindrical oven is rotated and its contents are poured into a funnel which is mounted off the deck over the spreading surface. The intent is to deliver the melt in such a manner that the melt inertia is minimized and can be neglected. Tests were conducted with molten lead poured onto horizontal wood, steel and marble surfaces. Nominal melt masses employed were 4, 6, 8, and 10 kg. Melt superheats employed were 10, 50, 100, 150, and 200K. Water pool depths employed were zero, 5, 10, 20, 40, and 60 mm deep. The total test matrix consisted of 156 runs. It was readily observed that the geometry of the melt spread could fall into one of five regimes depending upon the melt mass, melt temperature, and water depth. These five regimes are shown schematically in Figure 2. The average melt thickness after spreading was found to be most sensitive to two of the independent variables, melt superheat and water depth. Sensitivity to melt mass was found to be of secondary importance. The measured average (or superficial) melt thickness for all tests which used a wooden surface is shown as a function of water depth and melt superheat in Figure 3. Each point shown is the average of all runs at a prescribed superheat and water depth regardless of delivered mass. Notice that as melt superheat increases, the thickness decreases. Also as the water depth increases, the thickness increases. As previously stated, the thickness was not very sensitive to melt mass.

An empirical approach was undertaken to characterize the spread regimes on the basis of these observations. A dimensionless thickness, t^*, was defined as

$$t^* \equiv \bar{t}/(M/\rho)^{1/3} \equiv (M/\rho)^{2/3}/A_{sp}$$

where $\bar{t}$ is the area-averaged melt thickness (volume/area), M is the melt mass, A_{sp} is the area of spread, and ρ is the melt density. A dimensionless spreading parameter, N_{sp}, was defined which incorporates the effects of melt temperature, mass, and water depth as,

$$N_{sp} = \frac{(M/\rho)^{1/3} h^*_{fs}}{H \; h^*_{fg}}$$

where H is the water depth, h^*_{fs} is the effective latent heat of solidification of the melt $(\equiv h_{fs} + c_p \Delta T_{superheat})$, where $\Delta T_{superheat}$ is the melt superheat and h^*_{fg} is the effective latent heat of vaporization of the water $(\equiv h_{fg} + c_p \Delta T_{subcool})$, where $\Delta T_{subcool}$ is the water subcooling. The data were plotted in this fashion and approximate boundaries in N_{sp} space were determined for each of the five geometric regimes that were observed. These are listed on Figure 2 for each of the regimes specified. The dimensionless presentation of the data for Runs 1-112 is shown in Figure 4.

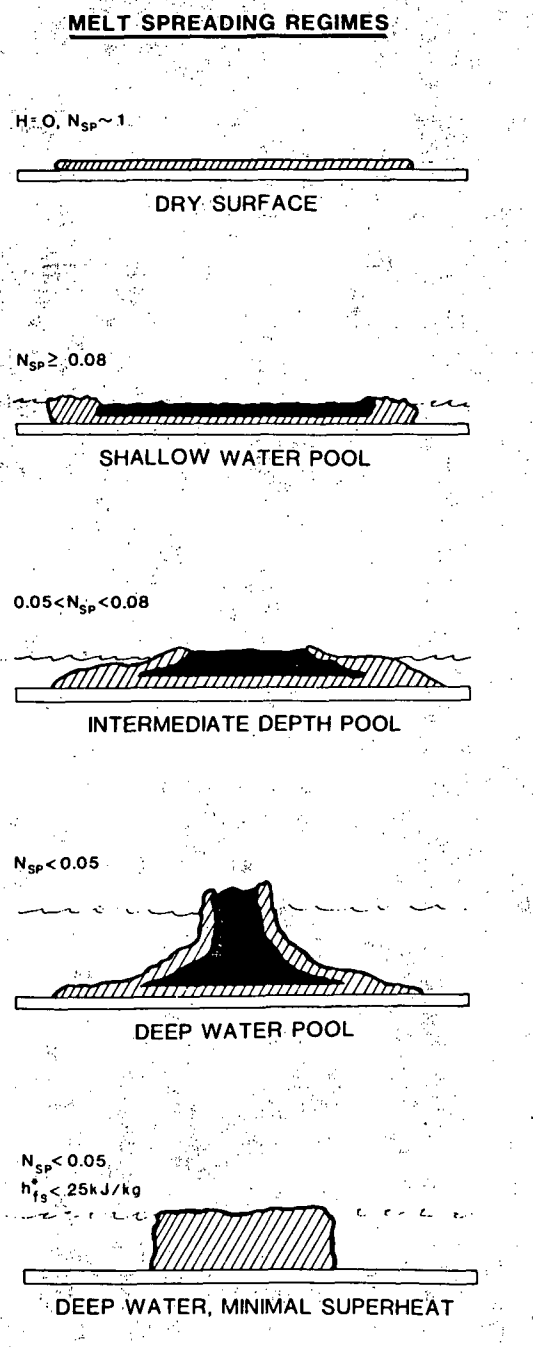


Figure 2 Observed Melt Spreading Flow Regimes

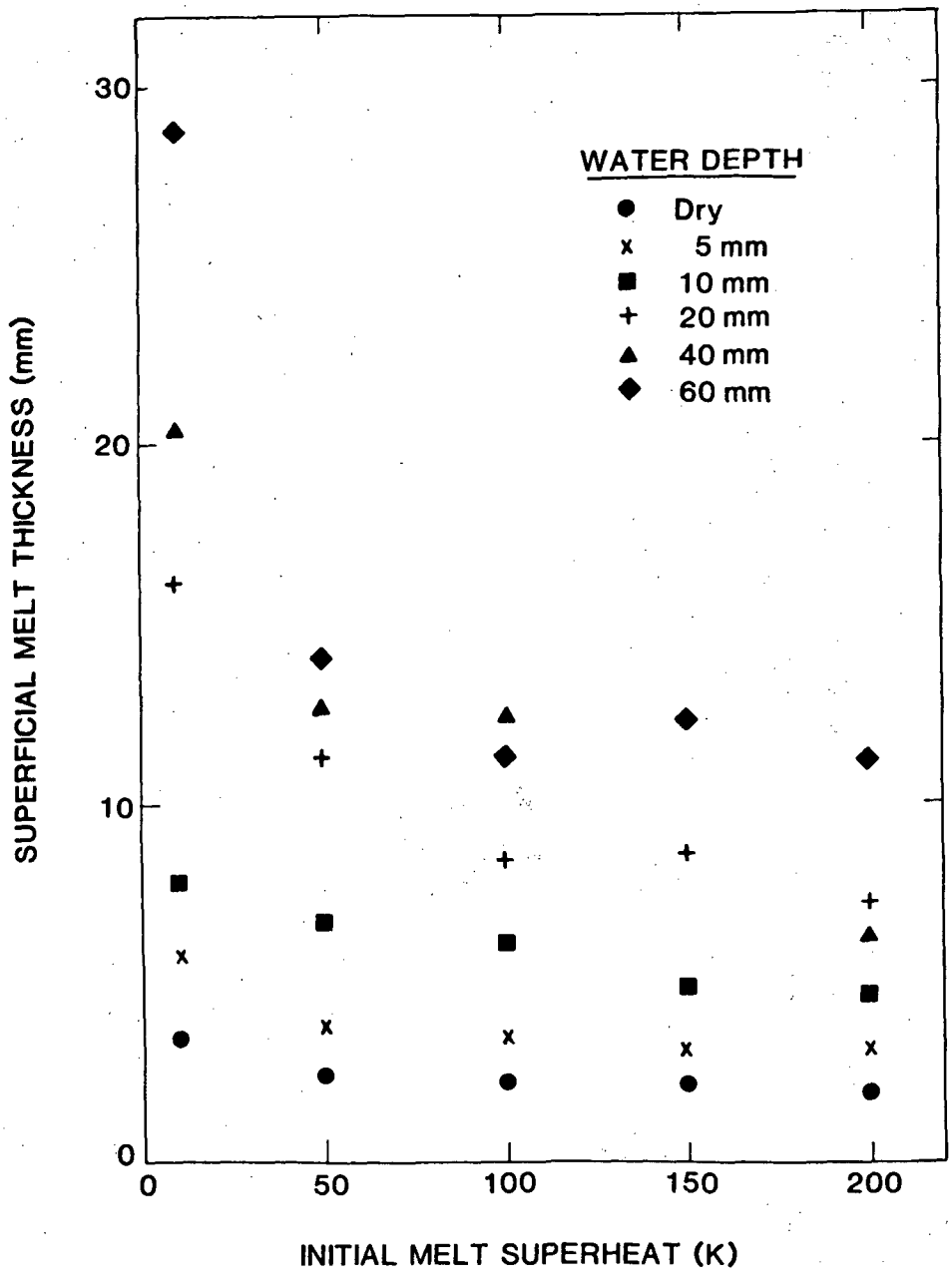


Figure 3 Average Measured Melt Thickness After Spreading vs. Water Depth and Initial Melt Superheat

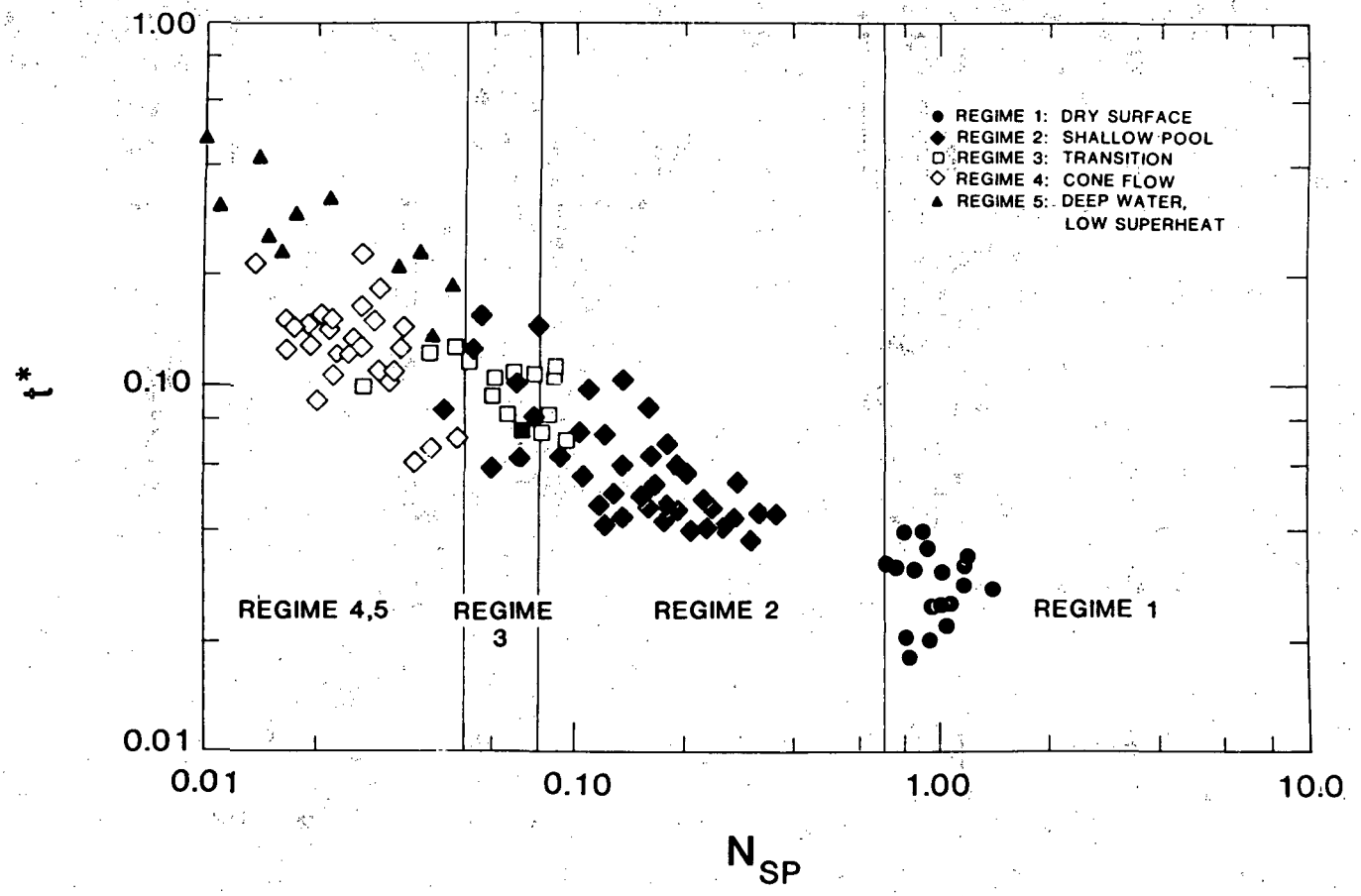


Figure 4 Dimensionless Melt Thickness, t*, vs. Spreading Parameter, N_{SP}

An empirical correlation of t^* vs. N_{sp} was developed on the basis of all 156 runs and is as follows:

$$t^* = 0.03\ N_{sp}^{1/2}$$

Further experiments and modeling are under way to refine this spreading correlation and to develop a model for each of the regimes shown in Figure 2.

3. Heat Transfer from Bubbling Pools to Structural Boundaries

In the assessments of the vulnerability of the Mark I BWR steel shell to contact with molten core debris in the drywell, it has become apparent that the reliability of these assessments is strongly dependent upon the accuracy of several key parameters, models, and boundary conditions. Among these is included the phenomenon of heat transfer from a bubbling corium pool to an adjacent structural boundary. Of particular interest is the dependence of the interfacial heat transfer coefficient upon the superficial gas velocity and the fluid Prandtl number.

In order to investigate this bubbling heat transfer phenomenon, the experimental apparatus portrayed in Figures 5-6 was constructed. Figure 5 shows an overall schematic of the experimental test facility. Highlighted are the gas and water flow control, pool heater control, instrumentation, and test

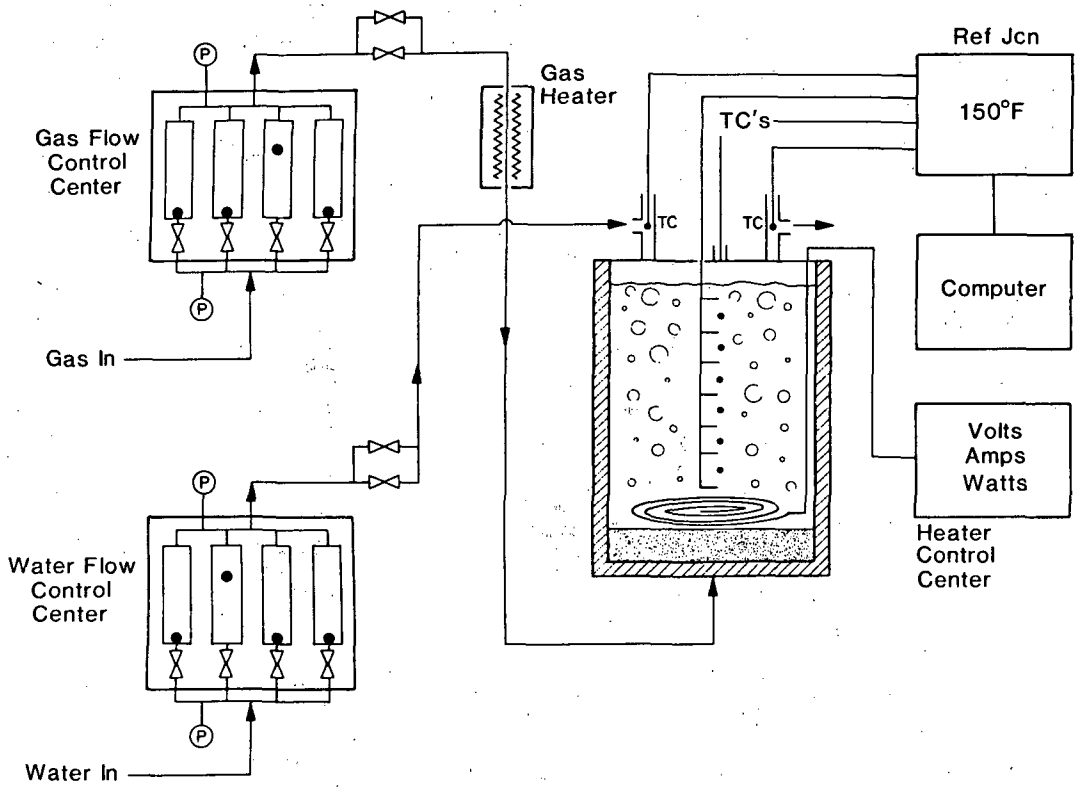


Figure 5 Schematic of Bubbling Heat Transfer Apparatus

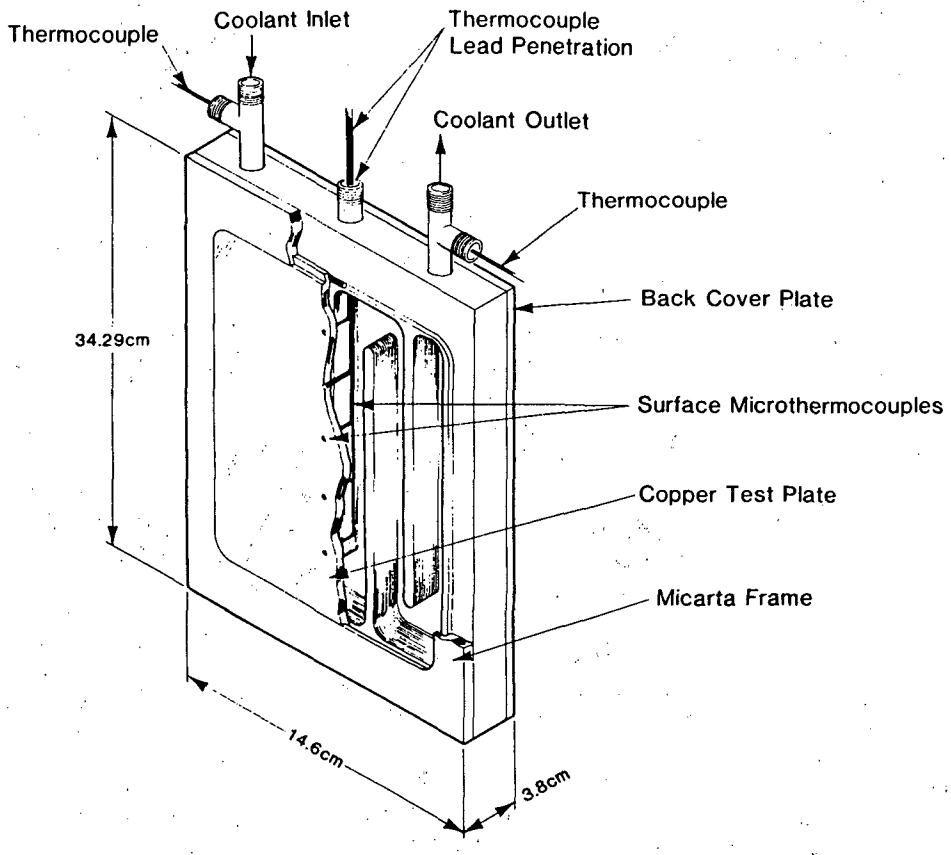


Figure 6 Schematic of Instrumented Test Wall

pool. Also shown are the details of the bubbling test pool. Highlighted are the plexiglass tank, porous frit, thermocouple rake, and coiled heating element. The submerged test wall is highlighted in Figure 6. The important features shown are the micarta window frame construction, copper test plate, serpentine coolant passage, and the surface microthermocouples that are installed in the test plate surface.

A series of experiments was performed to investigate the magnitude of the bubbling heat transfer coefficient from a pool of water to a vertical boundary. The water pool depth was set to 30 cm to avoid shallow pool effects. The boundary heat transfer coefficient was measured as a function of the bubbling superficial gas velocity over the range 0.1-2.5 cm/s. The resulting heat transfer data are shown in Figure 7. The magnitude of the measured heat transfer coefficient varied from a low of 2000 W/m^2K to a high of approximately 5000 W/m^2K over the range of superficial gas velocity that was covered.

These data suggest that bubbling heat transfer boundary conditions for the Mark I steel shell assessments should be in this range in order to reliably represent the actual heat load to the shell. Although the prototypic bubbling melt would be molten metal, it is clear that heat transfer coefficients in the range 10-1000 W/m^2K are too low to be realistic. In order to improve the data base just presented, additional tests with molten metal pools will be executed. In addition, the LINER-QT and WITCH-LINER test data from SNL will be adopted for the development of a final correlation.

In the interim, these data and the correlations developed by Konsetov [5] and Blottner [6] for bubbling heat transfer to a vertical wall were nondimensionalized and compared to assess the current capability of the CORCON-MOD2 computer code to calculate lateral heat loads from a MCCI. A Nusselt number was defined as $Nu = hr_b/k$, where h is the heat transfer coefficient, r_b is the equivalent spherical bubble radius, and k is the fluid thermal conductivity; and a Grashof number was defined as $Gr = g\alpha r_b^3/\nu^2$, where g is the gravitational constant, α is the pool average void fraction, and ν is the fluid kinematic viscosity. Both the models just specified as well as the present heat transfer data were cast in dimensionless form, and are presented in Figure 8. Surprisingly good agreement was found between the Blottner and Konsetov correlations and the present data; in fact the two models bounded all the experimental data points. The best dimensionless correlation to the present data, embodying the modeling approach of Blottner and Konsetov, was found to be as follows:

$$Nu = 0.33\ (Gr \cdot Pr)^{0.33}$$

4. Boiling and Explosive Interactions Between Bubbling Corium Simulant Pools and an Overlying Water Pool

Under a wide spectrum of reactor designs and accident sequences, it is possible, maybe even desirable, for water to come in contact with the molten core debris and form a coolant pool overlying the core debris attacking the concrete. The benefits include but may not be limited to enhancement of the heat flux from the molten core debris as well as decontamination of aerosols which would be released from the core debris and rise through the water in the

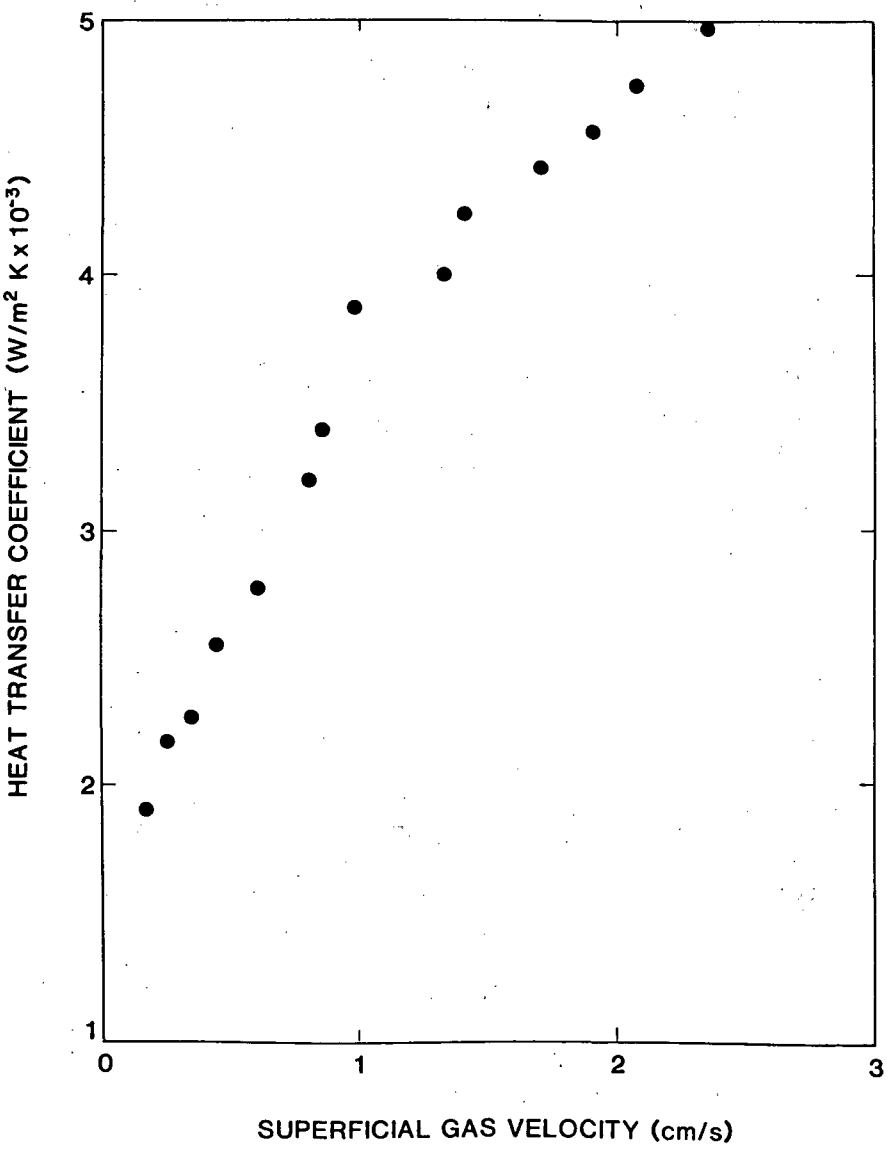


Figure 7 Bubbling Heat Transfer Coefficient vs. Superficial Gas Velocity for a Water Pool Adjacent to a Vertical Surface

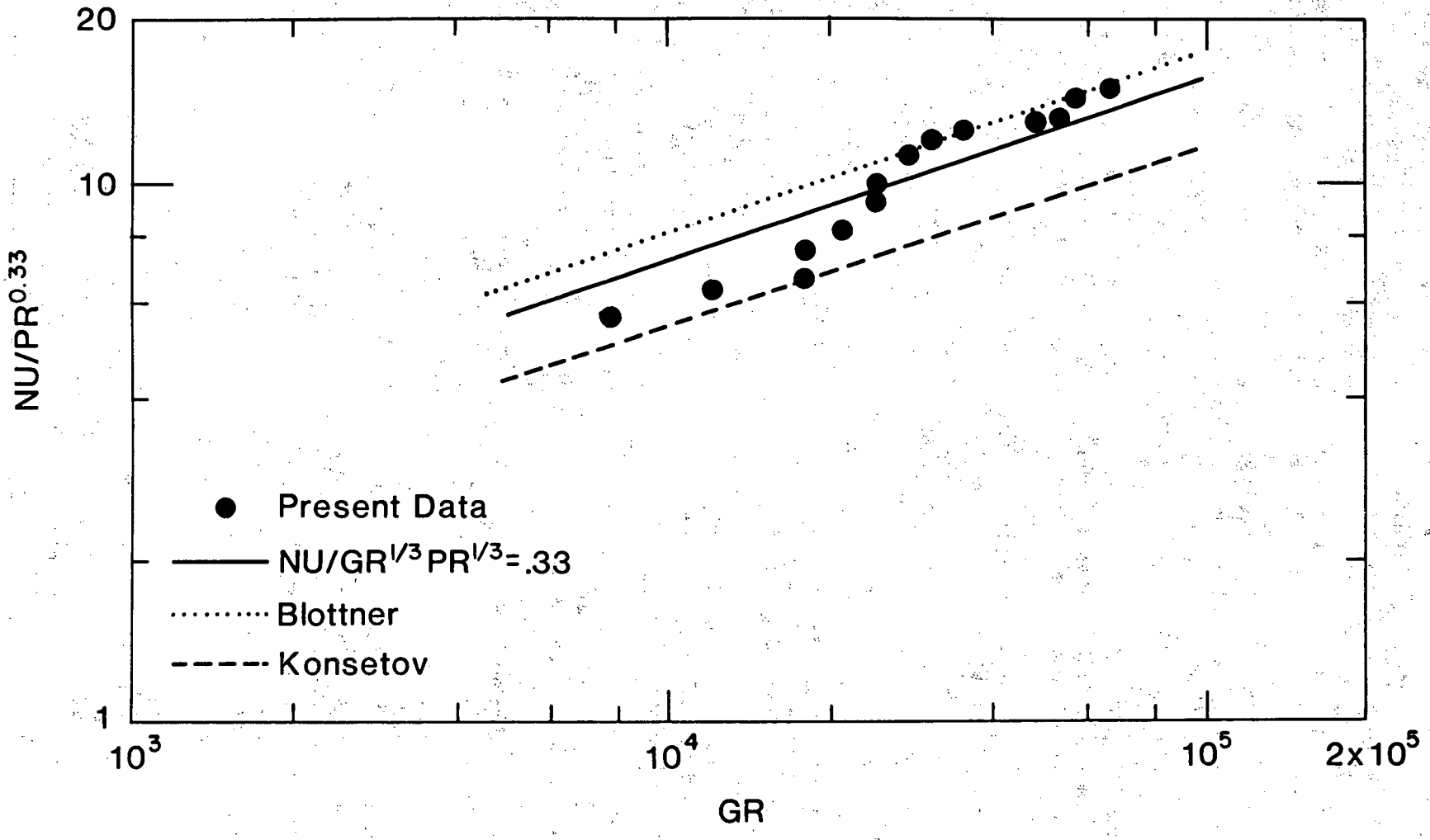


Figure 8 Dimensionless Correlation of Bubbling Heat Transfer Data

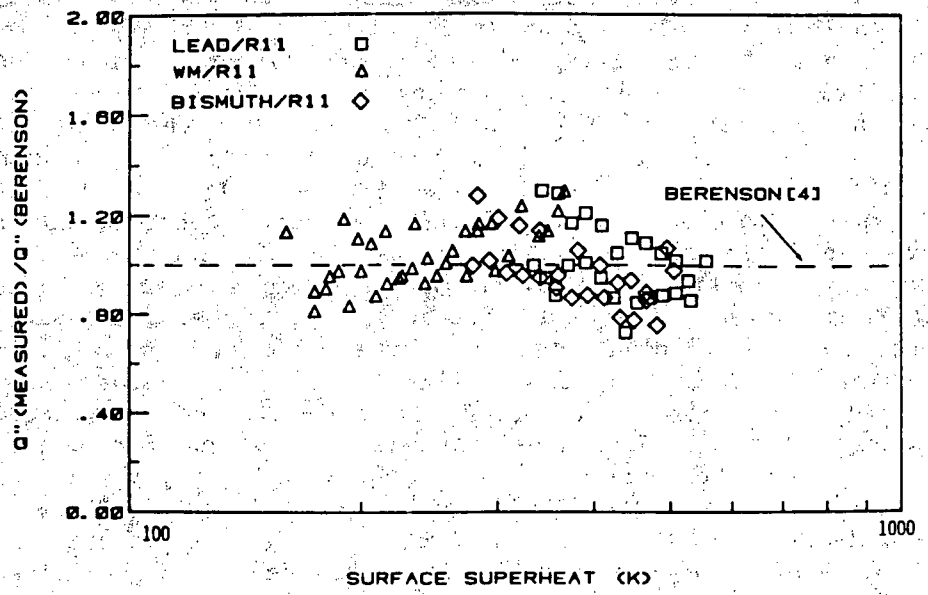
gas stream from the concrete decomposition gases. The investigations into this class of phenomena were intended to quantify the magnitude of the boiling heat flux from bubbling high-temperature melt simulant pools, and to investigate the occurrance of explosive boiling interactions from this stably stratified geometry and the size of the debris so resulting. The experimental procedure and quantitative results will be described in the ensuing discussion.

To perform the investigations into liquid-liquid boiling phenomena [7], the experimental apparatus about to be described was constructed. It consisted of a six-inch steel container in which to hold the melt simulant (liquid metal in this case), coolant reservoirs, heaters, controllers, and temperature instrumentation. The test section was open at the top and all tests were performed at ambient pressure. The test vessel was mounted above a track along which a thermostatically controlled heater was installed. The heater could be slid away and an insulating base moved into place just prior to initiation of the experiment. The entire apparatus was insulated to minimize heat losses; an overall system energy balance was performed to verify each quantitative measure of boiling heat flux from the melt (lead, bismuth, or Wood's metal) to the coolant layer (water or R11 refrigerant).

An assembly of eight thermocouples was installed vertically in the melt pool along the centerline axis of the test section. Seven of the thermocouples were immersed in the 8-cm-deep liquid metal pool, one in the boiling coolant, and numerous along the test section wall (to perform the energy balance). The experiments were begun by first heating the liquid metal pool to a desired temperature while under an argon cover gas, then insulating the base and waiting until quasi-steady conditions were established in the pool. On command, a solenoid valve would discharge two liters of coolant into the vessel to form the initial coolant layer; make-up of the vaporized coolant was managed by monitoring a liquid level indicator in the vessel. The tests were conducted as transients, no heat was applied to the vessel during the test. Both baseline boiling tests with no gas injection and gas flux enhanced boiling tests were performed with R11 and water. The tests to examine the spontaneous explosive boiling behavior were only conducted with water. No tests with R11 experienced explosive interactions. The quantitative boiling heat flux data were determined by an energy balance on the melt, corrected for wall heat losses.

Experiments were performed to examine the film boiling heat flux for both R11 and water over molten metal surfaces, to examine the influence of the mobile heating surface. The molten pools included bismuth, lead, and Wood's metal. Good agreement was found between the measured heat fluxes without gas injection and the prediction of the Berenson film boiling model when corrected for thermal radiation. These data are shown in Figure 9. The composition of liquid metal pool had no influence on the magnitude of the boiling heat transfer. The pool composition only had an influence on the onset of explosive interactions when water was the boiling fluid.

Following these tests, several series of experiments were conducted with R11 and water over the same high temperature liquid metal melts, this time with a non-condensable gas injected from below, to examine the influence of simulated MCCI gases on film boiling over hot, molten pools. The data resulting from both the water boiling tests and the R11 boiling tests are shown in



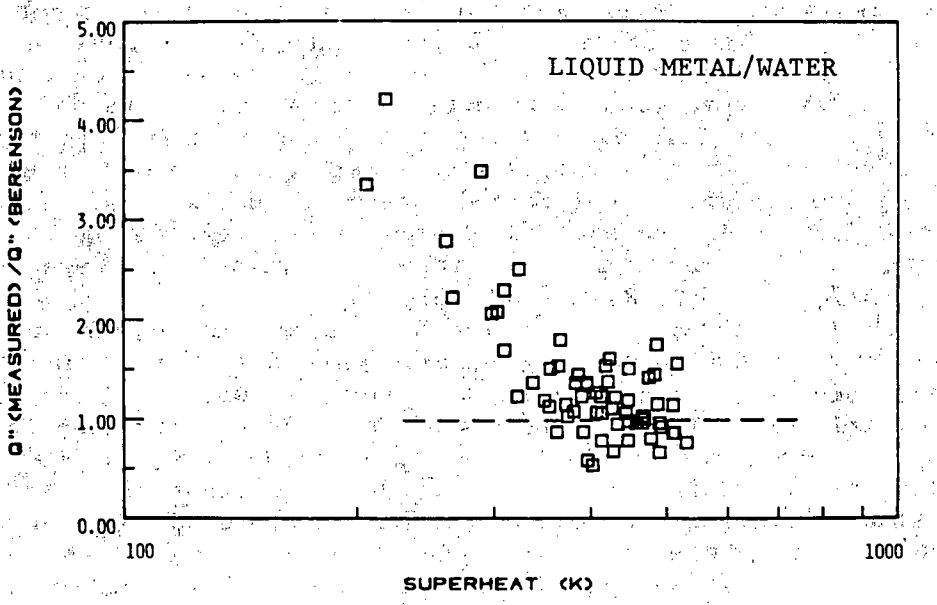
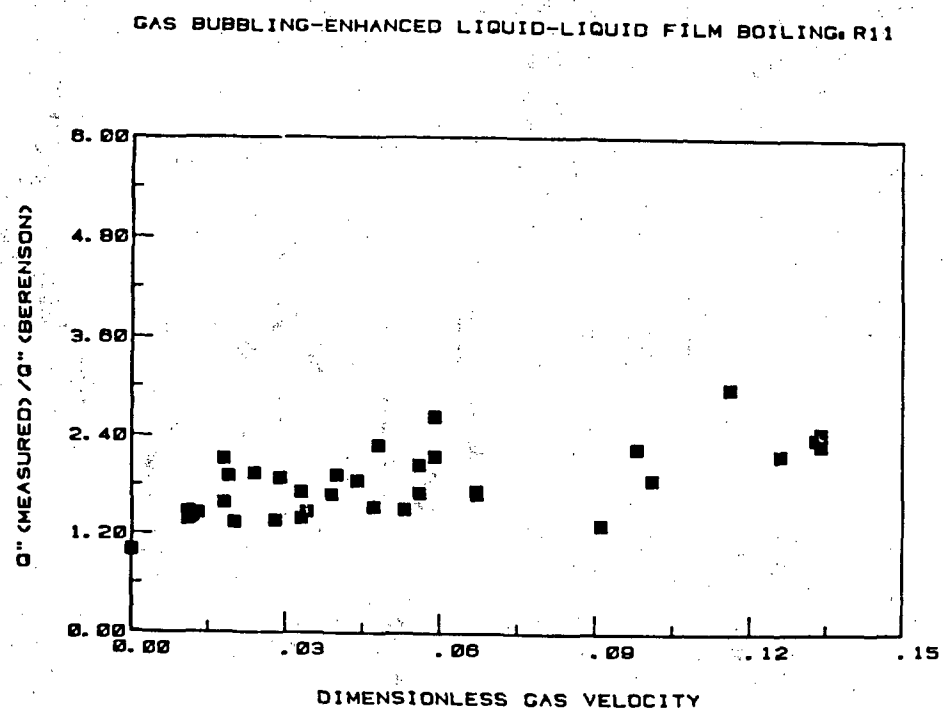


Figure 9 Liquid-Liquid Film Boiling Over Molten Metal Pools ($J_G = 0$)

Figure 10. It was found that the boiling heat flux was a monotonically increasing function of the gas injection superficial velocity. The boiling heat flux is shown normalized to the Berenson prediction, corrected for thermal radiation; the superficial gas velocity has been normalized to the calculated bubble rise velocity (in this case, u_∞ = 22 cm/s). For the case of gas flux-enhanced film boiling of water, the data were shown to exceed the Berenson flat plate film boiling limit by as much as a factor of 5-6 at a superficial gas velocity of less than 3 cm/s. For the case of gas flux-enhanced film boiling of R11, the data were shown to exceed the same limit by as much as a factor of three at the same gas velocity. At the temperatures that these experiments were conducted, the radiation contribution to the calculated Berenson limit was small, approximately 5%; therefore it is assumed that the radiation contribution in the experiments was small as well. This enhancement thus represents an enhancement to the convective component of the film boiling heat flux, not to the radiative component as well. It appears that an asymptotic limit to the boiling heat flux enhancement is being approached. It is expected that this limit would be reached as the gas injection approaches the churn-turbulent transition, which for bottom-injection pools has been found to occur in the vicinity of J_G equal to approximately one-fourth the bubble rise velocity. The enhancement to the radiative component of the film boiling heat flux would be a function of the surface area enhancement by the bubbles and may be small compared to the enhancement of the convective component.

It was found that water boiling over liquid metal melts at superheats in the film boiling range was an unstable system, frequently resulting in explosive interactions. This was found to be the case both with and without noncondensable gas injection. The boiling tests with R11, on the other hand, were always resistant to explosive interactions with and without gas injection. The observations concerning explosive interactions have been discussed previously [7] and will not be reproduced here. However, recent progress has been made in analyzing the debris resulting from these events and this will be discussed. The debris size distributions were characterized in two series of tests, the 500-series which involved water over molten lead without gas injection, and the 400-series which involved water over molten lead with gas injection. The 400-series is the same as shown in Figure 10 (for water only). For the 400-series, the superficial gas injection velocities were as follows: 0.66 cm/s (#417, 418), 0.88 cm/s (#420), 1.1 cm/s (#421), 1.8 cm/s (#423, 424), 2.4 cm/s (#425), and 2.6 cm/s (#415). The cumulative debris size distributions for both the 500- and 400-series are shown in Figures 11 and 12, respectively, plotted on log-probability paper. It was found that the cumulative size distributions for both series of runs were nearly identical, differing only in the magnitude of the spread at a particular particle size. Both distributions are representative of an upper limit lognormal distribution. It was surprising to observe that the gas injection appeared to yield no significant influence over the debris size other than to increase the magnitude of the uncertainty. In a way this is a comforting result, suggesting that the debris size distribution resulting from explosive interactions during a MCCI is not sensitive to the MCCI gas flux, and that inferences concerning the coolability of such debris formation may be assessed without reference to the details of the MCCI.



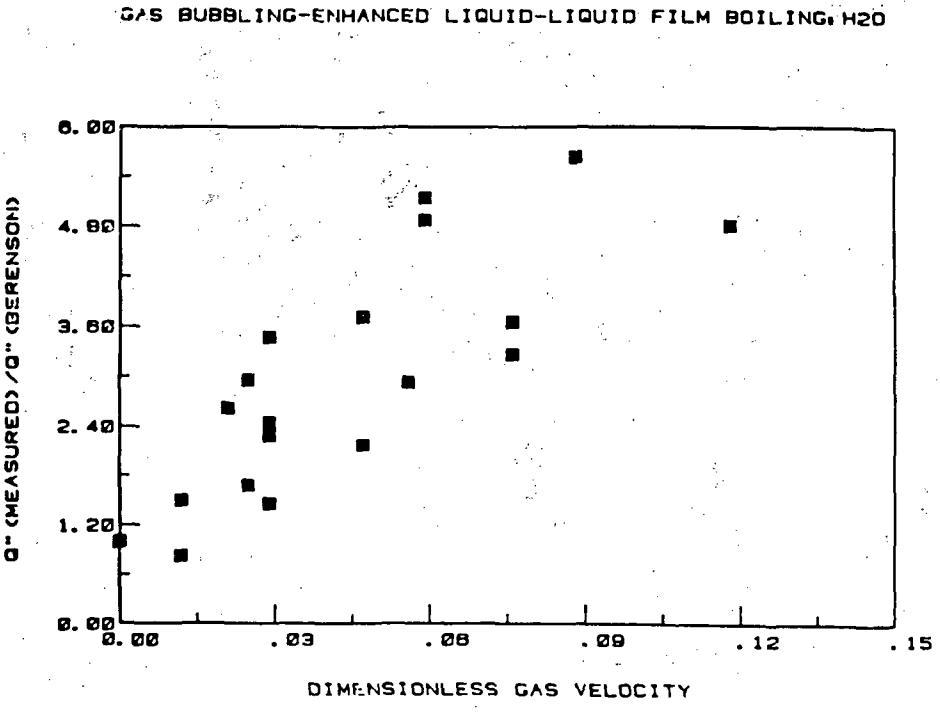


Figure 10 Enhanced Liquid-Liquid Film Boiling Due to Gas Injection From Below

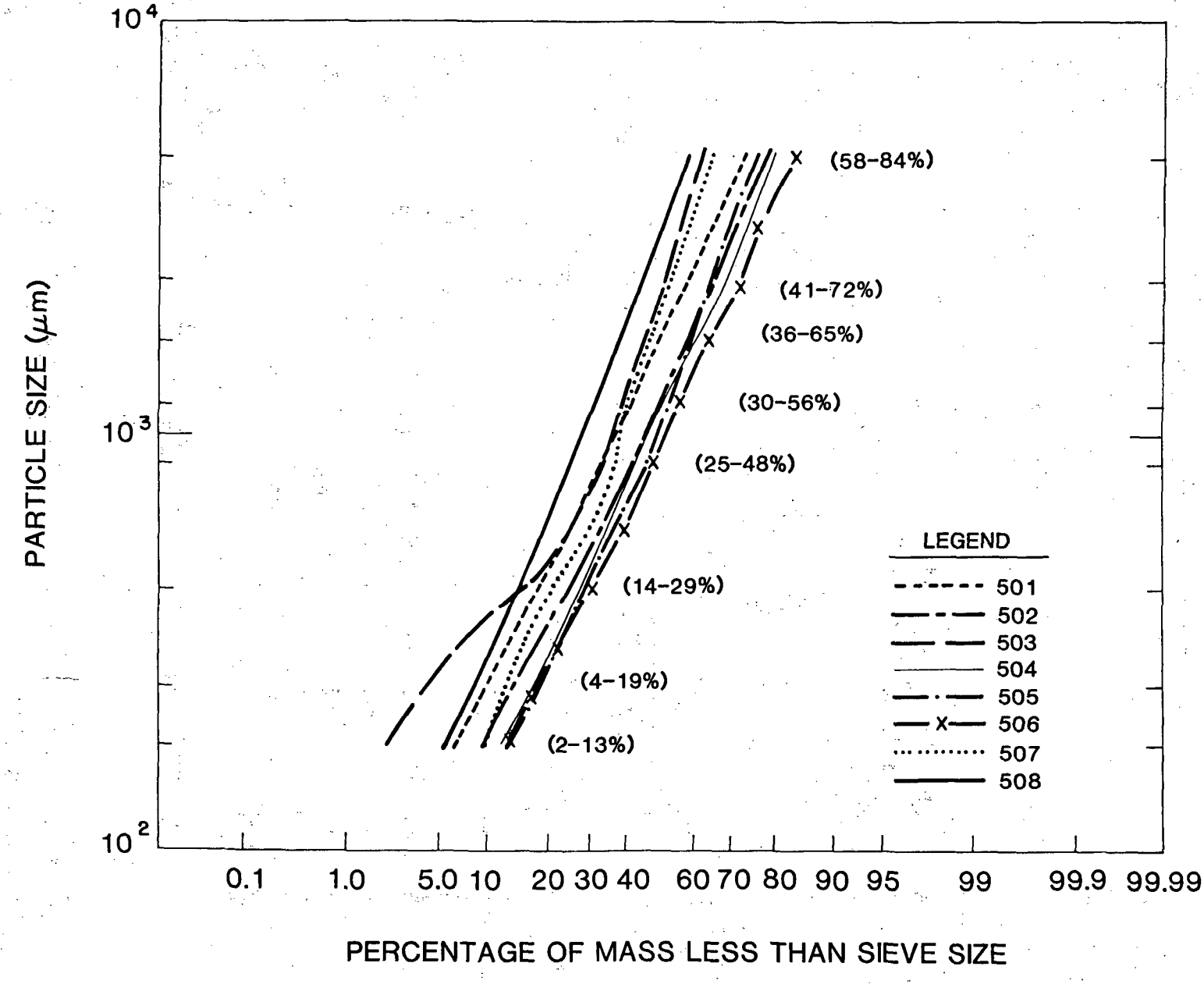


Figure 11 Cumulative Particle Size Distributions From Stratified Explosive Interations; Series 500, Water Over Molten Lead; $J_G = 0$

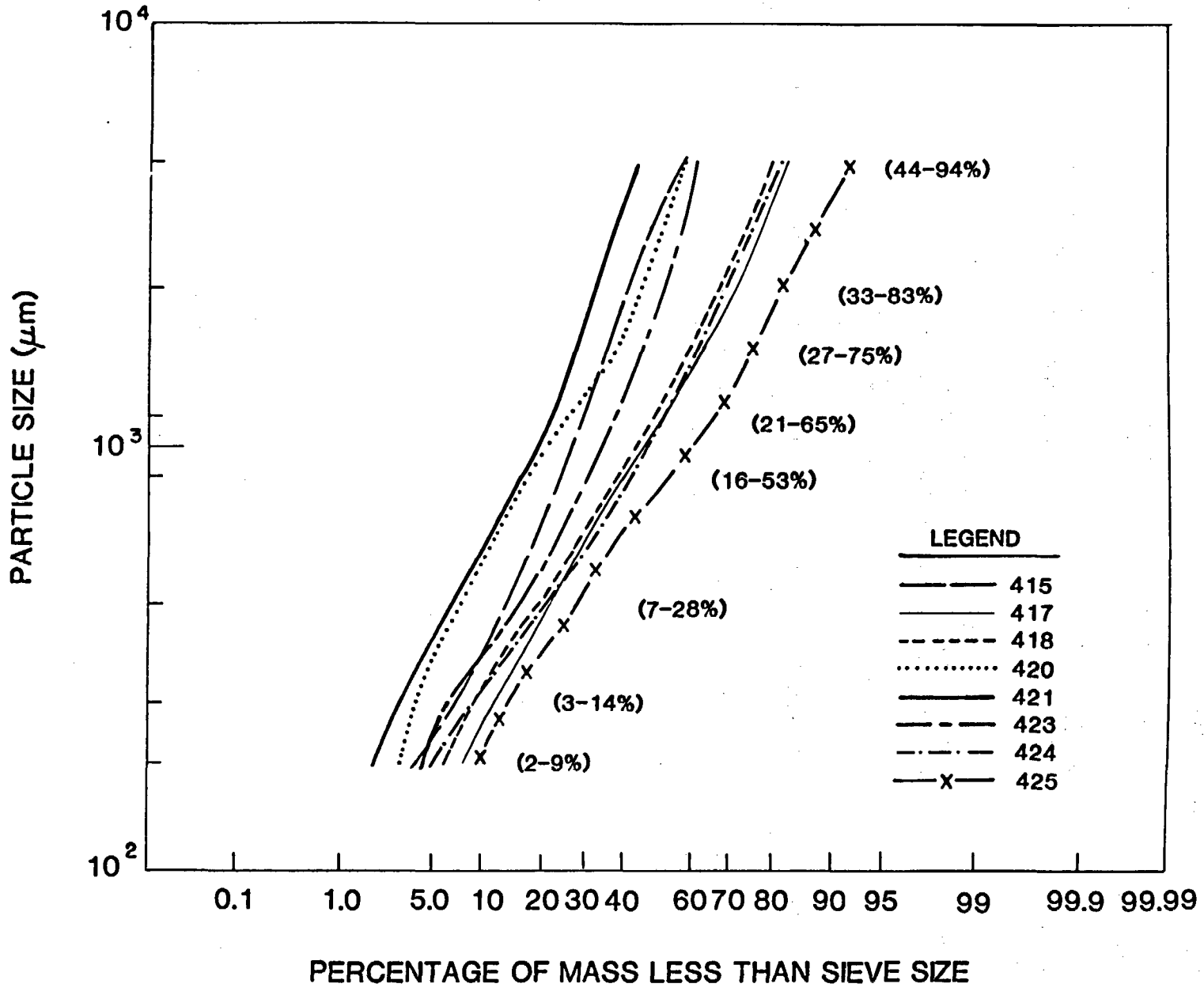


Figure 12 Cumulative Particle Size Distributions From Stratified Explosive Interactions; Series 400, Water Over Molten Lead, $J_G > 0$

References

1. "Reassessment of the Technical Bases for Estimating Source Terms," NUREG-0956 (July 1986).

2. "Estimates of Early Containment Loads from Core Melt Accidents," NUREG-1079 (December 1985).

3. R.K. Cole, D.P. Kelly, and M.A. Ellis, "CORCON-MOD2: A Computer Program for Analysis of Molten Core-Concrete Interactions," NUREG/CR-3920 (August 1984).

4. D.A. Powers, J.E. Brockmann, and A.W. Schiver, "VANESA: A Mechanistic Model of Radionuclide Release and Aerosol Generation During Core Debris Interactions with Concrete," NUREG/CR-4308 (July 1986).

5. V.V. Konsetov, "Heat Transfer During Bubbling of Gas Through Liquid," Int. J. Heat Mass Transfer, 9, pp. 1103-1108 (September 1966).

6. F.G. Blottner, "Hydrodynamics and Heat Transfer Characteristics of Liquid Pools with Bubble Agitation," NUREG/CR-0944 (November 1979).

7. G.A. Greene, C. Finfrock, and S.B. Burson, "Phenomenological Studies on Molten Core-Concrete Interactions," Nucl. Eng. Design, 108, pp. 167-177 (1988).

Feedwater Coast Down Measurement of a BWR

C. A. Kukielka, S. Seyedhosseini, and M. P. Carr
Pennsylvania Power & Light Company

This paper presents feedwater coast down data and shows its influence on the timing of events during severe accident calculations. Susquehanna Steam Electric Station uses steam turbine driven feedwater pumps. A large amount of inertia is associated with the pump turbines. If the steam supply to the turbines is lost, the pump and turbine coast down, pumping a large volume of water into the reactor. We determined this amount of water by investigating a Main Steam Isolation Valve (MSIV) closure event at our Susquehanna plant. These data are presented first followed by a discussion of two transient calculations performed with and without the additional coast down water mass.

We obtained these data from an MSIV closure from 100% power. The following plots were made from data collected by the plant transient recorder: total feedwater and main steam flow, reactor pressure, and reactor water level. These data appear in Figures 1 through 3. Integrating the total feedwater flow with respect to time yields a total of 8.7×10^4 lbm of water injected into the reactor vessel as a result of the feedwater pump coast down.

This additional water mass extends the time needed for significant events to occur in a transient. Table 1 lists times associated with these events for an MSIV closure without injection. The events of particular interest are the time for the water level to reach the jet pump throat and the time of bottom head dryout. These events represent points in time in which sufficient vessel injections assures core and vessel bottom head integrity.

This transient was run with and without the additional water mass from the feedwater pump coast down. We used the plant transient data to describe the initial conditions in the feedwater coast down case. The 8.7×10^4 lbm of water was deducted for the non-feedwater coast down case. This resulted in an initial water level of 561.3 inches and 511.5 inch respectively. All other initial conditions were the same. As shown in Table 1, the mass injection by the feedwater pumps extends the time required to reach these critical events by 20 to 30 minutes. This additional time is often enough to allow for successful execution of many inplant operations. These operations include manual valve alignment, breaker operations, logic circuit bypasses, or AC power recovery.

In the second MSIV closure event examined, vessel injection was provided by two CRD pumps. Core damage is avoided in both cases. However, the additional water from the feedwater pump coast down adds margin. The maximum rod temperature with feedwater coast down is about $1200^{\circ}F$, $325^{\circ}F$ less than the case without coast down. This difference translates into about 2.7 lbm of H_2 generated for the with coast down case versus 19.9 lbm for the non-coast down case. Plots of the collapsed water level as a function of time appear in Figures 4 and 5. Figure 4 shows that, by accounting for the coast down water mass, the water level never drops below the jet pump throat. However, when neglecting the coast down water mass, as shown in Figure 5, the water level drops below the jet pump throat and remains there for almost 3 hours.

We used plant measurements to estimate the maximum CRD flow of 187 gpm. Plant operators must fully open the CRD flow control valve and close the minimum flow bypass lines.

Through this paper we have demonstrated that the consideration of subtleties in the design and operation of nuclear power plants can have a significant effect on the results of transient analysis. This is especially true when these results are being used to address procedural guidance. It is therefore imperative that realistic plant design and operational data be incorporated into severe accident analysis studies if one wishes to draw meaningful conclusions from the analysis.

Table I

The Effect of Feedwater Pump Coast Down on
Event Timing for an MSIV closure without Injection

	Time (minutes)	
	With Coast Down	Without Coast Down
Core Uncovery	52.8	35.2
Water Level Hits The Jet Pump Throat	58.9	40.9
Channel Box Melt Starts	109.2	86.6
Core Plate Dryout	148.2	129.4
Core Plate Fails	171.4	146.0
Bottom Head Dryout	329.2	293.8
Control Rod Guide Tube Fails	362.6	332.8

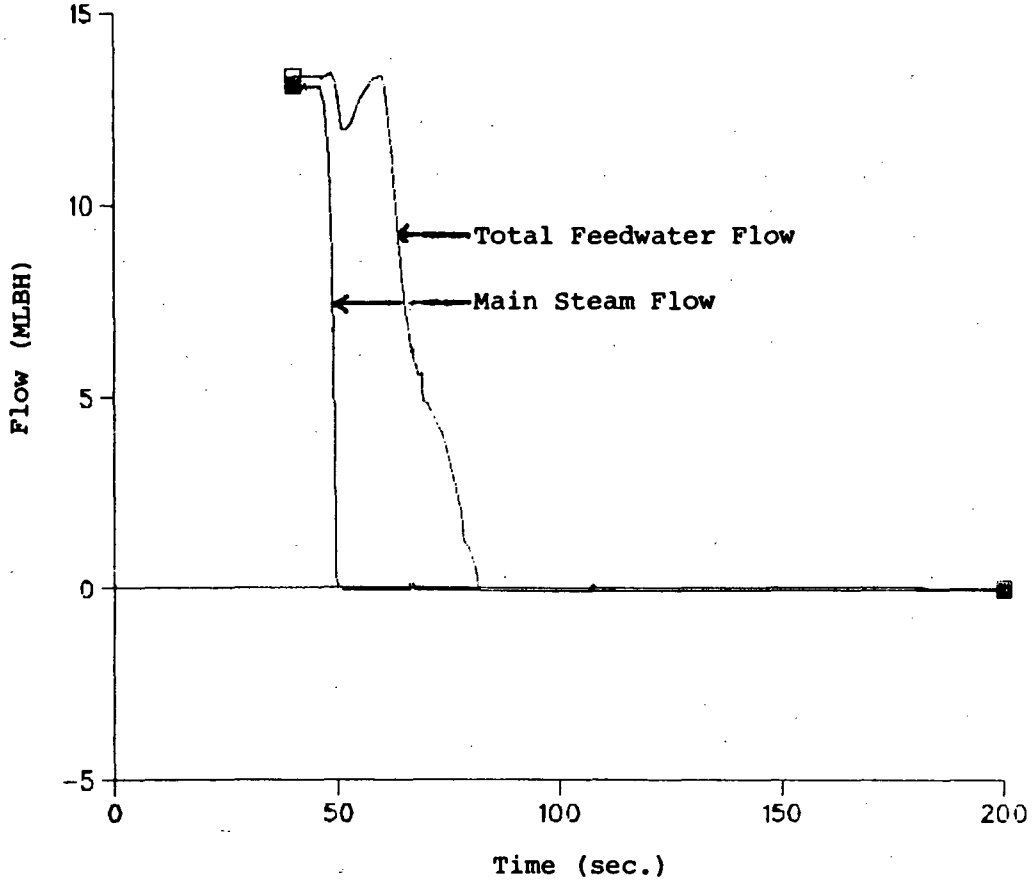


Figure 1 Total Feedwater and Main Steam Flow

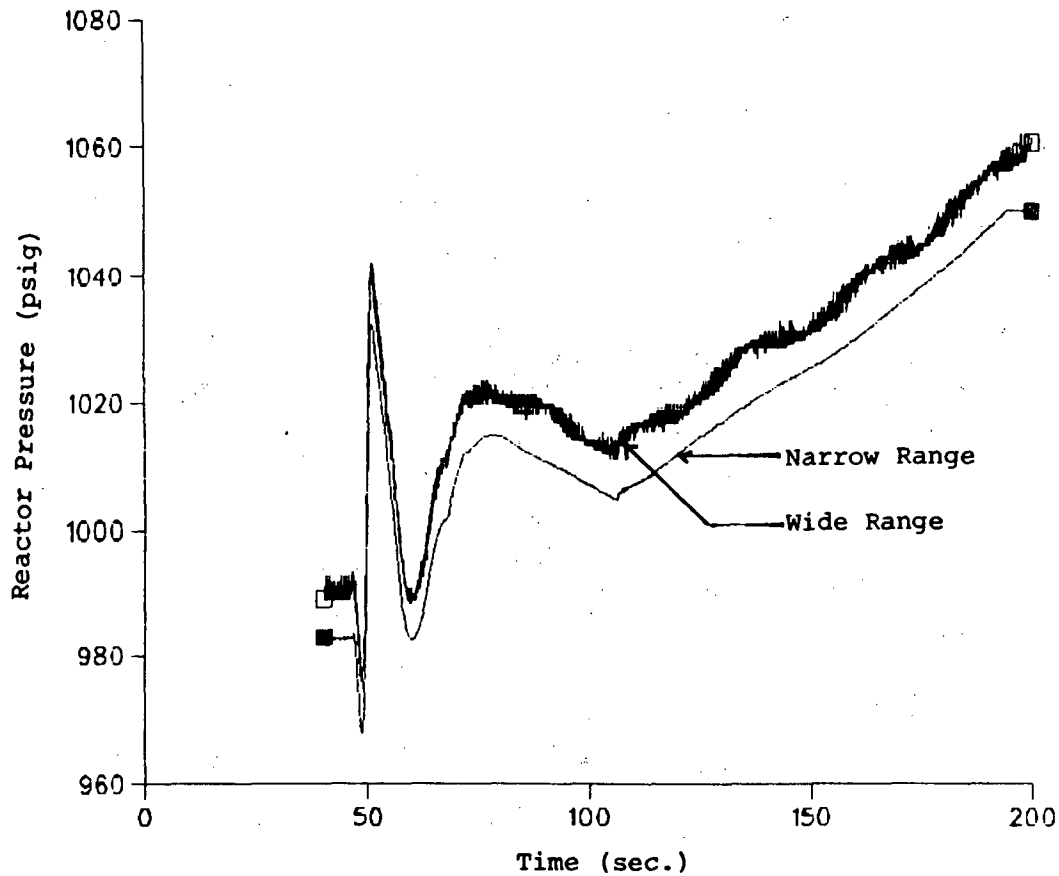


Figure 2 Reactor Pressure

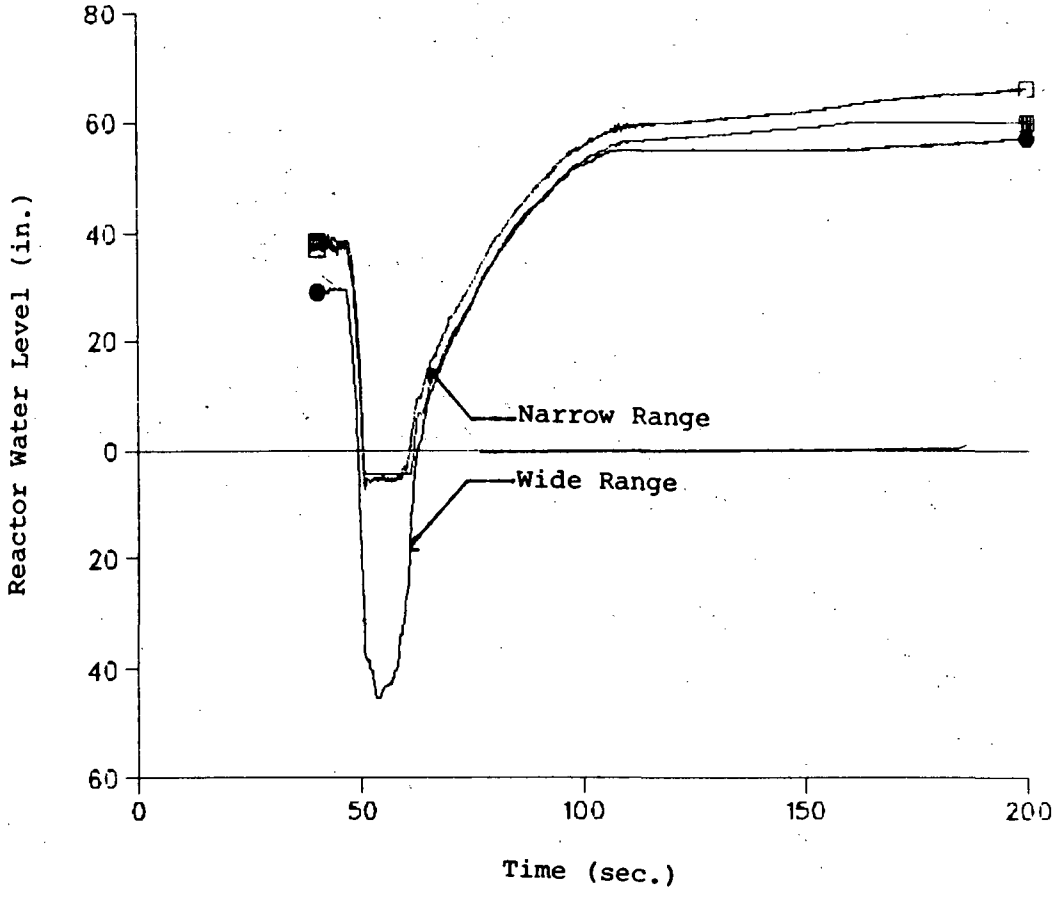


Figure 3 Reactor Water Level

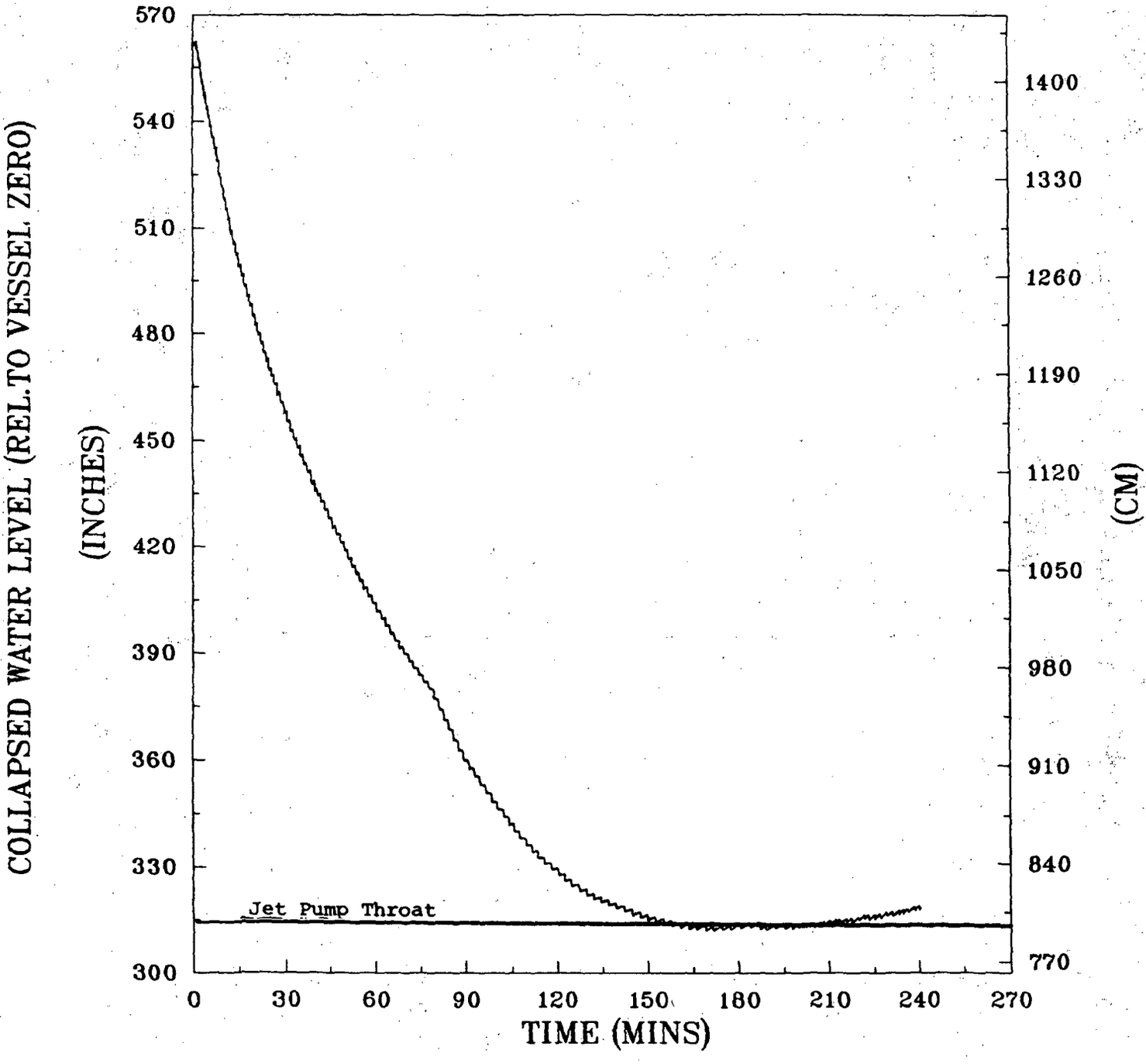


Figure 4 Collapsed Water Level for CRD Injection With Feedwater Coast-Down

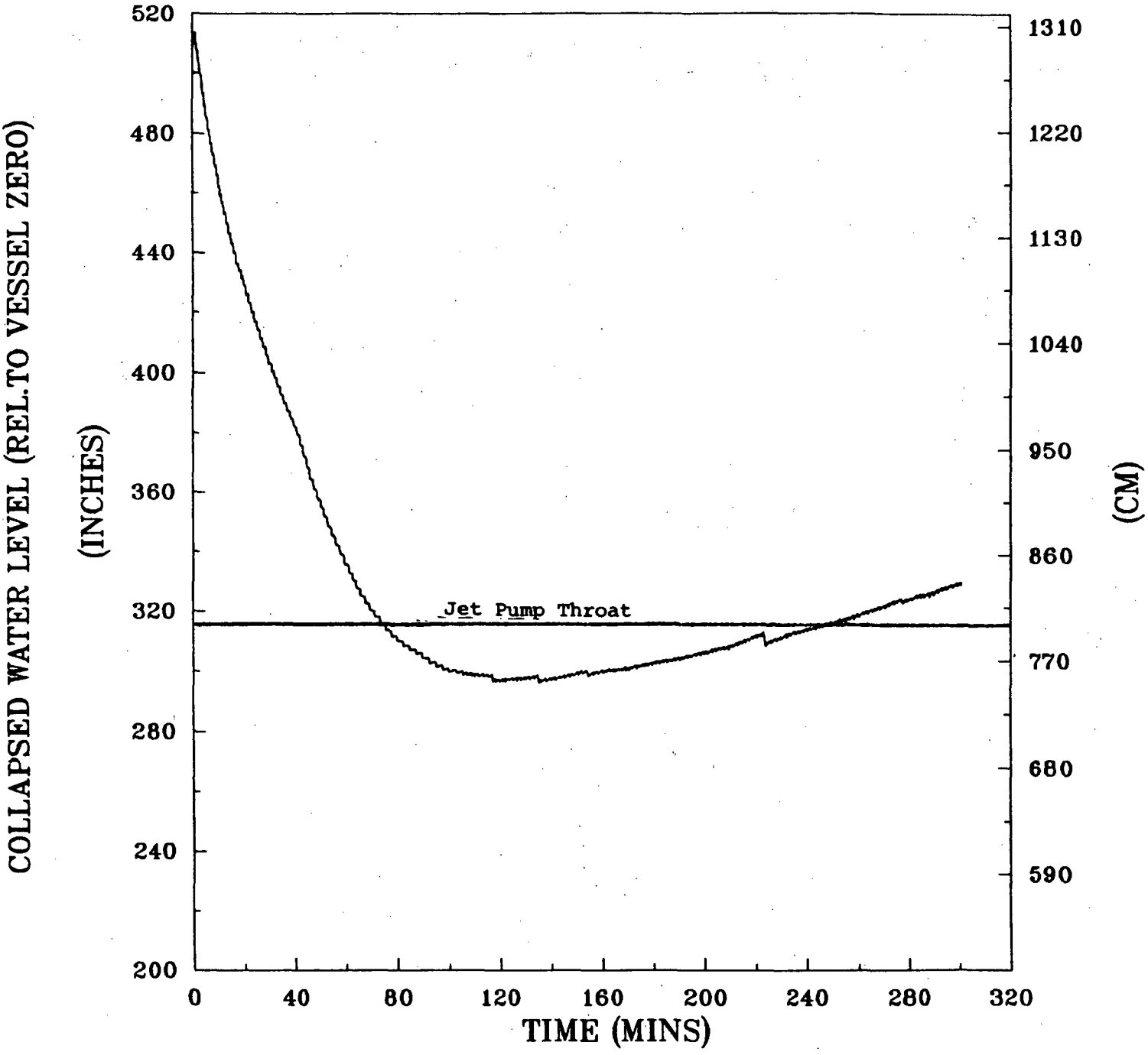


Figure 5 Collapsed Water Level for CRD Injection Without Feedwater Coast-Down

SMALL SCALE BWR CORE DEBRIS EUTECTICS FORMATION AND MELTING EXPERIMENT

G. W. Parker L. J. Ott
S. A. Hodge

Oak Ridge National Laboratory
Oak Ridge, Tennessee 37830

ABSTRACT

A small scale experiment has recently been performed at Oak Ridge under the auspices of the Boiling Water Reactor Severe Accident Technology (BWRSAT) program to provide information concerning the formation of mixtures during heatup of representative BWR reactor vessel bottom head debris and to determine the composition and melting temperatures of these mixtures. The initial structure of the bottom head debris layers modeled in the experiment was taken from the results of recent Boiling Water Reactor Severe Accident Response (BWRSAR) code predictions for the short-term station blackout accident sequence.

The experimental results provide useful information concerning the mixtures formed and their proportions and properties. The observed run-off of a stainless steel-zirconium eutectic alloy supports the contention that the initial pour from a BWR reactor vessel would consist of molten metals at relatively low temperatures.

I. INTRODUCTION

A small scale experiment was performed at Oak Ridge during December 1987 under the auspices of the Boiling Water Reactor Severe Accident Technology (BWRSAT) program to provide information concerning the formation of eutectic mixtures in the BWR reactor vessel bottom head debris and to determine the composition and melting temperatures of these mixtures. The initial structure of the bottom head debris layers modeled in the experiment was taken from the results of recent Boiling Water Reactor Severe Accident Response (BWRSAR) code predictions for the short-term station blackout accident sequence.

The BWR invessel severe accident sequence of events as modeled by the BWRSAR code for the period after the beginning of core degradation is described in Table 1. It should be noted that the first material relocated into the lower plenum is primarily stainless steel from control blades and zirconium metal from channel boxes. Later, UO_2 and ZrO_2 enter the lower plenum by means of collapse of the fuel pellet stacks. These first and second material relocations are quenched by the large

"The submitted manuscript has been authored by a contractor of the U.S. Government under contract No. DE-AC05-84OR21400. Accordingly, the U.S. Government retains a nonexclusive, royalty-free license to publish or reproduce the published form of this contribution, or allow others to do so, for U.S. Government purposes."

volume of water in the bottom head but, eventually, bottom head dryout occurs and the debris begins to reheat. The third and final large relocation of core debris into the lower plenum is predicted to occur when the control rod guide tubes in the lower plenum are sufficiently weakened by overtemperature so that they can no longer support the remaining standing portions of the outer core, which are relatively undamaged. Thus, the BWRSAR code predicts the formation of three layers of debris in the BWR bottom head. It is the purpose of the small scale experiment described here to examine the eutectic mixtures formed as the quenched bottom head debris layers reheat.

II. THE EXPERIMENTAL SETUP

Based upon the BWRSAR code predictions, the experimental approach utilizes a model of layered strata consisting of the appropriate ratios of SS, UO_2, Zr, ZrO_2, and B_4C powder for each of three distinct zones. These three layers are simulated on a one-Kg scale and are subjected to controlled melting in the specially designed two-compartment ZrO_2 crucible shown in Fig. 1. The lower compartment consists of an inverted crucible with a number of drilled perforations that allow the molten phases to relocate below the high temperature induction-heated core mass and quench within the water-cooled cavity.

Two temperature sensing systems are provided for the experimental apparatus. The bottom entry thermocouples are doubly protected with a tantalum metal shield inside an aluminum oxide thimble. An argon-hydrogen gas shield is also provided to exclude air from the single tantalum clad tungsten-rhenium thermocouple, which is inserted near the highest temperature zone. Two platinum-rhenium thermocouples are lower in the thimble near the melt-through zone to record essentially alloy melting temperatures, expected to be below 1700°C (3092°F).

From the top of the crucible, through the quartz envelop, a two-color optical pyrometer is initially focused on the top layer of metal; however, as the core debris melts and relocates, this layer will move downward out of focus of the pyrometer; therefore, a simple following movement of the pyrometer is provided by which a peak temperature can be maintained assuring a continually valid temperature measurement.

The cavity space, sufficient for complete metal run-off, is available below the actively heated region with one thermocouple reserved for this space to detect arrival of the relocated metal phase.

The loading configuration for the test bundle was a neatly ordered layer arrangement as described in Tables 2 and 3. Most of the UO_2 pellets were clad in open-ended sections of zircaloy. However, some of the UO_2 pellets were left unclad in order to attain the proper proportion of zircaloy in the upper two layers. The stainless steel was provided primarily in disc form - alternating where possible with zircaloy either as pellet cladding or in disc form. The B_4C powder was provided in short sections of 4 mm stainless steel tubing crimped at the ends and layered between the discs.

III. INITIAL RESULTS OF THE TEST DEBRIS HEATUP

The surrogate BWR reactor vessel bottom head layered core debris configuration was successfully melted on December 18, 1987. Heating was conducted in two steps with a short interruption at midpoint to correct some instrument malfunctions. Power was on for about 12 minutes; the interruption lasted about 5 minutes. Debris melting was visually detected when the melt penetrated the Al_2O_3 thermocouple thimble at the bottom of the cavity, just below the copper water-cooled furnace.

As discussed in Section II, it was intended that temperature measurements be recorded by three bottom-entry thermocouples at varying height positions and by a two-color optical pyrometer positioned over an optical window, which views the interior of the crucible from above. However, in this initial test of the system, the pyrometer did not respond to the heatup. One Pt-Rh thermocouple in the lowest part of the cavity malfunctioned also from the start. The other Pt-Rh thermocouple remained operational throughout and recorded a maximum temperature above 1773 K (2723°F) for a short while just as the incandescent melt was detected visually.

The single tungsten-rhenium thermocouple, which was located near the center of the bottom layer, indicated a maximum temperature of 1573-1673 K (2372-2552°F) at the end of the first heatup. Sometime during the second heatup, this thermocouple stopped advancing although the temperature was obviously increasing. A blown fuse was responsible, but was not detected until later in the cooldown period. The thermocouple was still operational, however.

Examination of the melt residue by breaking away the ZrO_2 crucible showed that an almost complete meltdown had occurred. Reproductions of post-experiment photographs are provided in Figs. 2 and 3.

Upon initial inspection, the cavity volume, about 87 cm^3 (5.3 $in.^3$), was found to be almost completely filled by three distinct layers of metallic and oxidic melts. The bottom layer appeared to have formed during the first heating cycle and is almost completely metallic. Its volume suggests a mass of about 235 g of the 498 g of SS and Zr metal initially loaded. The middle layer, which also appeared to be largely metallic, contains another 200 g (assuming a specific gravity of 8.0) leaving only about 100 g of metal to be accounted for. The third, or upper layer of the melt, most of which is in the cavity volume, is obviously an oxidic eutectic of $Zr-ZrO_2-UO_2$, which has a reference melting temperature of 2573 K (4172°F). The relative volume of this phase suggests a mass of about 300 g, of which a fair proportion was obviously formed by melting of part of the crucible ZrO_2.

About 50 of the initially loaded 66 UO_2 pellets were identified as remaining up in the crucible. These pellets are almost completely wetted with metallic zirconium and are solidified into three pellet clumps.

IV. RESULTS OF POST-TEST ANALYSES

In the cavity formed by the perforated inverted ZrO_2 (with 5% CaO stabilizer) crucible, two distinct metallic layers were obvious when the exposed residue was photographed. This was confirmed by sectioning into halves, after which an oxide layer was found above the metal, in which the UO_2 and ZrO_2 formed a semi-liquid solution at the highest temperature achieved during the experiment, approximately 2573 K (4172°F). Upon further sectioning, one quarter revealed a third metallic layer, smaller than the first two, about midway into the oxide layer. It is postulated that this upper metallic layer was formed by late extension of the high temperature zone toward the top of the crucible where the UO_2 had been found to be extensively wetted by molten Zr.

Two methods of characterization of the constituents of the debris layers have been pursued. First, a rough melting temperature was determined for each of the three metallic layers by means of micro (milligram) samples taken from each region with a Carbaloy twist drill. The values observed were 1723, 1773, and 1873 K (2642, 2732, and 2912°F) from bottom to top. Matching these with a standard Fe-Zr phase diagram suggests compositions of 17, 22, and 33 atom percent (25, 32, and 45 weight percent) zirconium. For the second characterization, corresponding SEM, EDAX fluorescence analyses on the lower two layers gave tentative values of 22 and 25% Zr, which are in reasonable agreement.

The accumulated data regarding the compositions of the residues of this experiment give a nearly complete description of the eutectics formed and their proportions and properties. By comparing the compositions with the original inventory, some added confidence is assured, even though the non-destructive procedures with SEM-EDAX ratios do not provide quite the quantitative data that would be possible with wet chemical analysis. In reassessing the total metal in the three residual layers of metallic debris, and relating this to the inventory of starting metal, the material balance is close to 100% and the metallic phase average composition is close to 30 wt % zircaloy. The melting points determined by the tungsten filament micro-method are consistent with the published phase diagrams for the Zr-Fe compositions and for the mixed UO_2-ZrO_2 formed with the ZrO_2 in the crucible. Nevertheless, one or two anomalies required a continuing analytical effort: (1) the location and form of the added B_4C was uncertain, and (2) the incongruent melting point of the small third metallic phase was not readily explained. In order to help resolve these questions, some further analyses were requested by the spark-spectrographic method and a series of x-ray microprobe analyses were proposed to locate both the boron and the carbon.

For confirmation of the melting temperature, the third metallic layer, which was found within the oxide layer, was twice again sampled and subjected to the micro-melting test with results similar to those of the initial test. Finally, a tungsten filament with the unmelted residue adhering was subjected to EDAX analysis which suggested that the

solid residue had a high Zr content as well as a high Fe content corresponding possibly to a compound such as $Zr-Fe_2$. One further attempt was made to evaluate the extent of the Zr molten reaction on UO_2 as seen in the upper crucible where about 50 pellets were found coated and/or reacted with bright metallic Zr or Zircaloy. By weight gain, the Zr represents only about 15% of the total weight. For some insight into the Zr reaction, a specimen was requested for metallographic section and EDAX analysis of the U content in the molten phase.

Besides spark source mass spectrometric analyses of the metallic debris to determine the level of boron and uranium, comparative x-ray maps have been made for a cluster of zirconium-coated UO_2 pellets that appeared to have an attached once-molten droplet of a U-Zr reduction alloy. This was clearly confirmed by the x-ray density maps with a sharp line at the UO_2 pellet interface with a complete cutoff of the zirconium where the droplet was attached. More accurate U-Zr ratios in this metallic alloy as well as a direct melting point determination would be expected to confirm the probable composition when compared to the U-Zr phase diagram.

A new detection effort, using the advanced electron microprobe density mapping technique finally identified boron within the oxide debris layer in well-defined 1-5 micron diameter needle form; the boron exists within these needles in conjunction with nearly equal amounts of zirconium and oxygen. The complete absence of Fe, Ni, Cr, and U in the needles is striking. The search for carbon is partly obscured by the epoxy mounting material which penetrates open porosity but one occurrence of carbon in an isolated zone is suggestive of having originated with the boron carbide. Chromium was found in a few places in the complete absence of nickel.

No boron has been found in the metallic phases, which contain up to 10 percent uranium in the third layer.

V. FUTURE TESTS

It is intended to repeat the test described above with similar initial debris layers, with all thermocouple and pyrometer instruments functional, and employing a much slower heatup rate. The slower heatup rate is intended to more closely simulate the slow heatup of BWR bottom head debris under the impetus of decay heat after bottom head dryout.

It is anticipated that follow-on tests can be carried out through higher temperatures by replacing the ZrO_2 crucibles used in the first two tests with ThO_2 or HfO_2 crucibles when they become available.

Table 1. BWRSAT Program Calculational Methodology Employed to Represent Events Between Onset of Core Degradation and Reactor Vessel Failure for BWRs

1. As canister and control blade material becomes molten, it is relocated onto the core plate. This causes:

   a. a temporarily increased steaming rate
   b. core plate dryout and cessation of steaming
   c. buildup of mass on the core plate and core plate heatup.

2. Each radial region of the core plate fails due to loss of strength when its calculated temperature reaches a user-specified value. Each core plate region and its accumulated debris falls into the lower plenum, producing a burst of steam and lowering the water level there as the fallen material is quenched.

3. Molten Zr metal flows downward over the lower core fuel rod nodes, leaving the UO_2 fuel pellets encased in thin ZrO_2 sheaths. Steam rising from the lower plenum cools the core nodes from which all unoxidized Zr has been removed. On the other hand, the rising steam causes energy release in the core peripheral nodes where Zr metal at elevated temperature still remains.

4. The standing portions of the core fall into the lower plenum by radial column. Each core column collapses when its average clad temperature reaches a user-input value, at which time very little of the UO_2 mass in the region has become molten. (The actual failure mechanism is weakening, by overtemperature, of the ZrO_2 sheaths surrounding the UO_2 fuel pellets.) The falling mass is quenched by the water in the lower plenum until the time of bottom head dryout. After bottom head dryout, the debris begins to reheat.

5. The structure of the control rod guide tubes in the lower plenum is heated by the surrounding core debris and is weakened to the point of failure when its temperature reaches a user-specified value. Failure of the control rod guide tubes causes all remaining standing portions of the core to immediately collapse. The control rod guide tube mass is added to the bottom head debris.

6. Bottom head penetrations fail by a simulated creep-rupture mechanism as the debris mass in their vicinity is reheated to about 1800°F (1255 K). The reactor vessel depressurizes and equalizes with drywell pressure.

7. The individual components of the debris mass leave the vessel only after they have reheated to their melting points and thereby become liquid.

Table 2. Composition of first test crucible loading

Layer	Thickness (cm)	Wt. in grams by layer					
		Total Layer	Zry-2	SS	UO_2	ZrO_2	B_4C
Top	2.2	503	28.5	186.1	269.4	18.9	0.6
Middle	1.7	390	66.9	86.7	213.2	22.4	1.4
Bottom	0.7	139	47.3	83.0	4.0	4.0	1.2
Totals	4.6	1032	142.7	355.8	486.6	45.3	3.2

Table 3. Configuration of first test layer assemblies

Top layer:	2, 3 mm SS plates
	2, 1 cm stacks of UO_2 pellets Zry-clad
	1, 3 mm SS plate + 1, 1 mm SS plate
	1, 4 mm x 5 cm SS tube of B_4C powder
	18 g, ZrO_2 powder (loose)
Middle layer:	1, 3 mm SS plate
	2, 1 cm stacks of UO_2 pellets Zry-clad
	2, 1 mm SS plates
	2, 4 mm x 5 cm SS tubes of B_4C powder
	22 g, ZrO_2 powder (loose)
Bottom layer:	2, 1.5 mm Zr plates
	2, 1 mm SS plates
	2, 4 mm x 5 cm SS tubes of B_4C powder
	4 g, ZrO_2 powder (loose)
	1, 3 mm SS plate

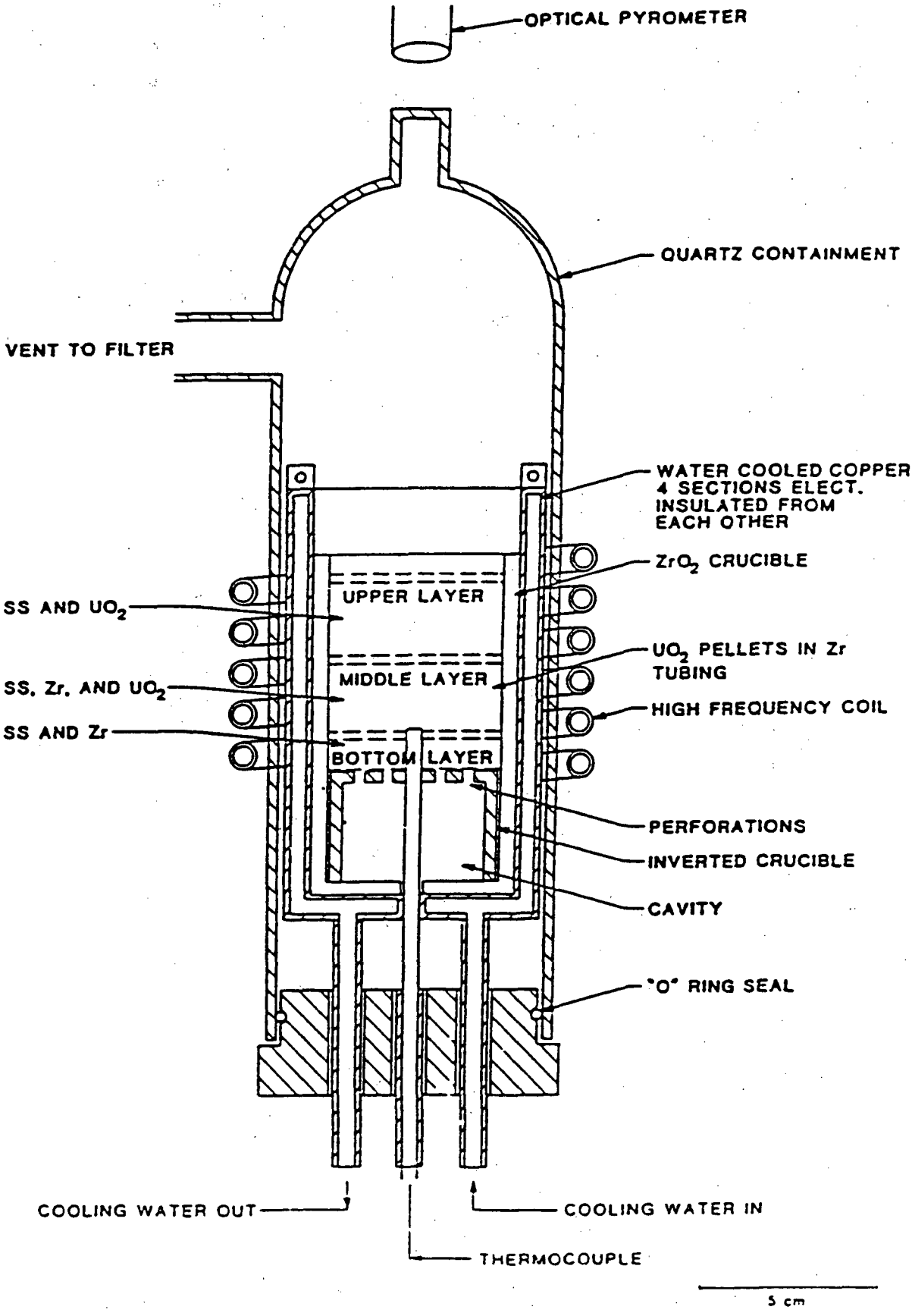


Fig. 1. One-Kg induction furnace with schematic of the three layers of BWR core debris modeled in the eutectic formation and melting experiment.

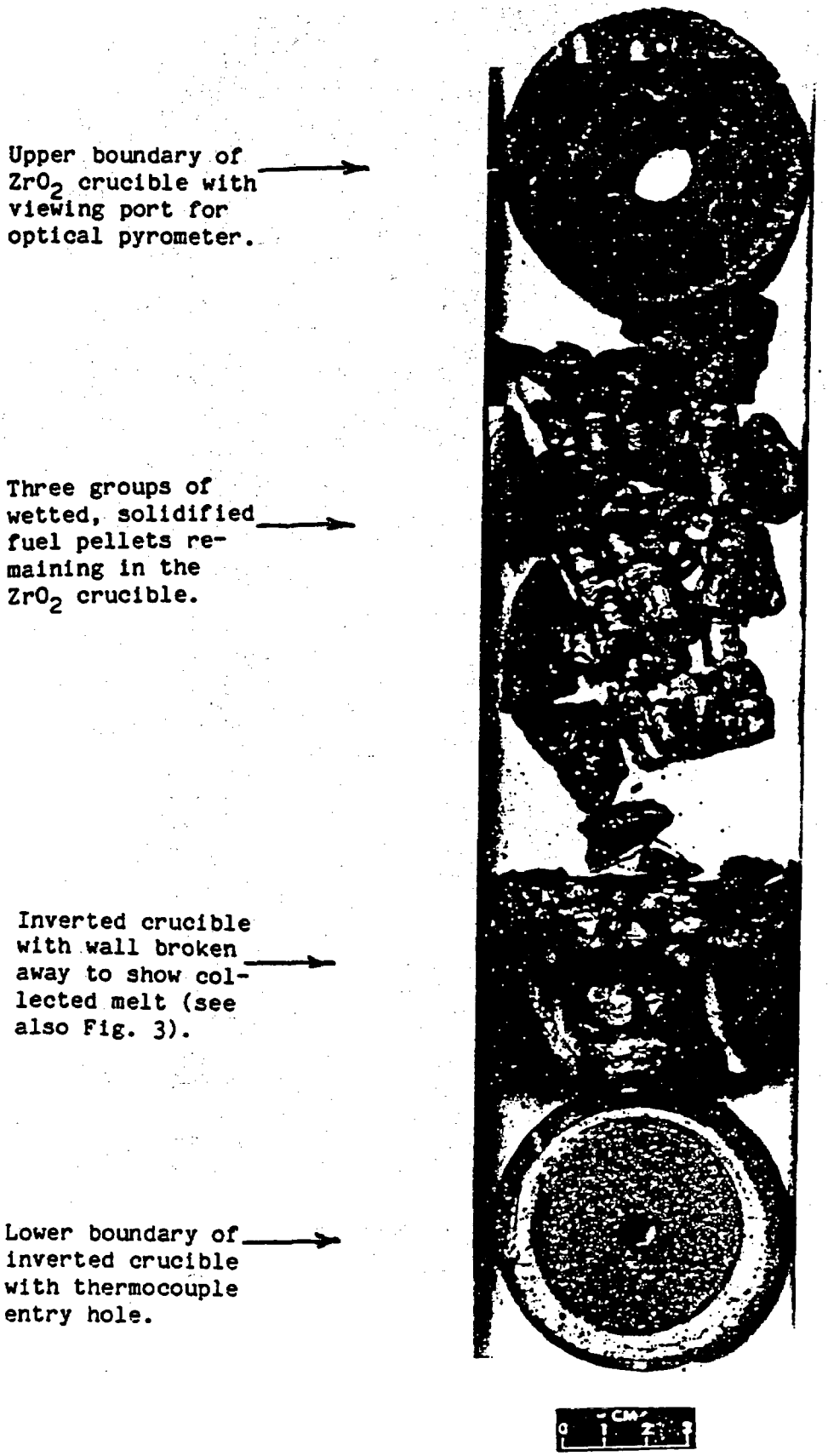


Fig. 2. Post-experiment fuel pellet residue remaining in the ZrO_2 crucible and the layers of frozen metallic and oxidic melt that collected in the inverted crucible after passing through the perforated plate separating the two crucibles

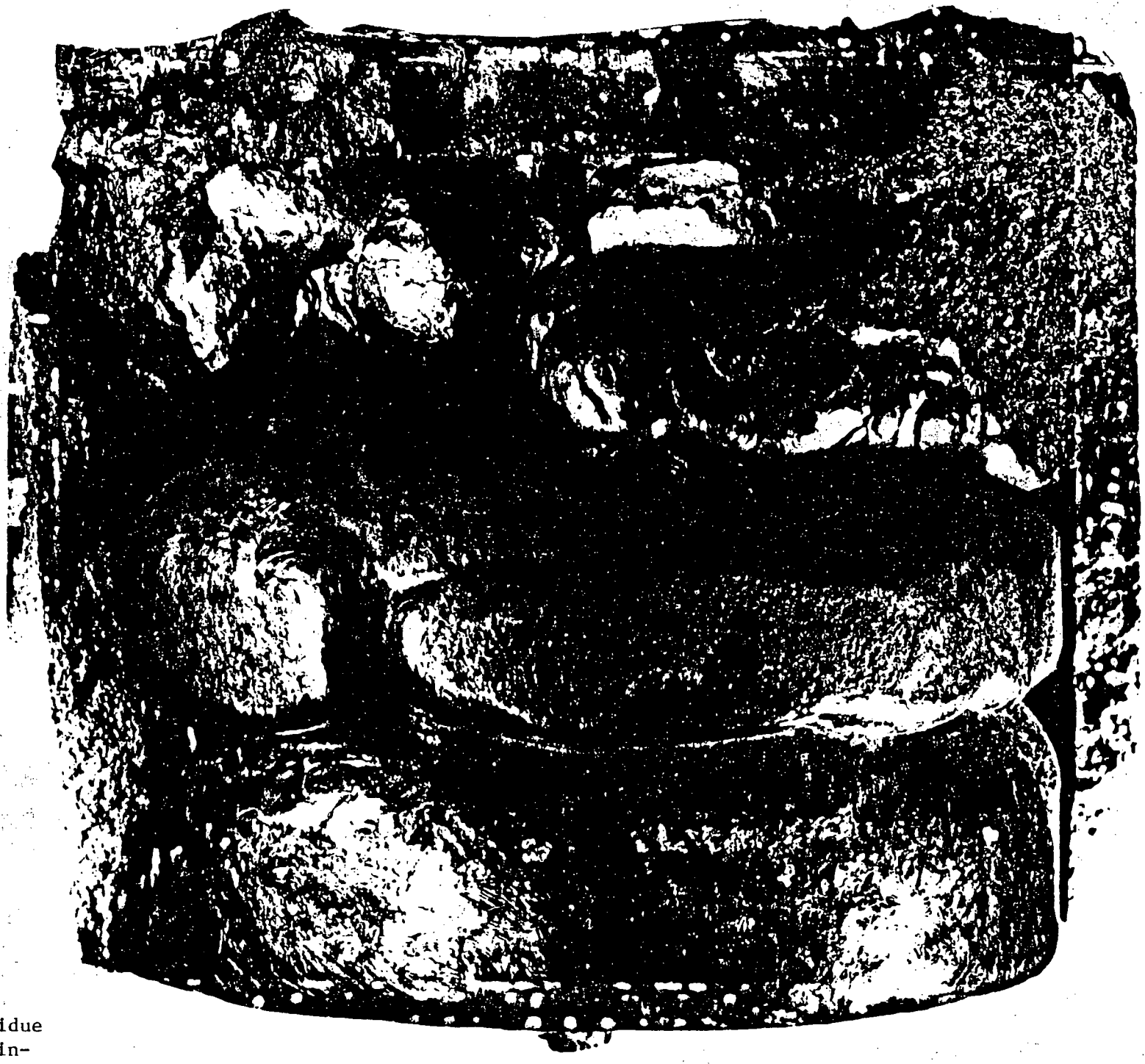


Fig. 3. Residue collected in the inverted crucible.

BWRSAR CALCULATIONS OF REACTOR VESSEL DEBRIS POURS FOR PEACH BOTTOM SHORT-TERM STATION BLACKOUT

S. A. Hodge L. J. Ott

Oak Ridge National Laboratory
Oak Ridge, Tennessee 37831

ABSTRACT

This paper describes recent analyses performed by the BWR Severe Accident Technology (BWRSAT) Program at Oak Ridge National Laboratory to estimate the release of debris from the reactor vessel for the unmitigated short-term station blackout accident sequence. Calculations were performed with the BWR Severe Accident Response (BWRSAR) code and are based upon consideration of the Peach Bottom Atomic Power Station. The modeling strategies employed within BWRSAR for debris relocation within the reactor vessel are briefly discussed and the calculated events of the accident sequence, including details of the calculated debris pours, are presented.

I. Introduction

Boiling Water Reactors (BWRs) and their primary containments have unique features for which special models must be provided if best-estimate severe accident calculations are to be performed. The Boiling Water Reactor Severe Accident Technology (BWRSAT) Program at Oak Ridge National Laboratory (ORNL) has developed and incorporated into its Boiling Water Reactor Severe Accident Response (BWRSAR) code several advanced response models for application to BWR severe accident analyses. Major features of these advanced in-vessel models include representation of (1) heat transfer to all in-core structures including channel boxes and control blades, (2) the effect of safety/relief valve (SRV) actuations, (3) structural/steam reaction chemistry effects, (4) progressive relocation of core structures including candling of the fuel rod cladding, (5) failure of the core plate and formation of a debris bed in the reactor vessel bottom head, (6) bottom head dryout and reheating of the quenched debris, (7) failure of the bottom head penetrations, and (8) the time-dependent egress of molten core debris from the reactor vessel. These models have been discussed in the paper "Advanced Severe Accident Response Models for BWR Application," given at the Fifteenth Water Reactor Safety Information Meeting in October 1987 and to be published in a forthcoming topical issue of Nuclear Engineering and Design. Nevertheless, because of the important effects that the method of modeling of core plate failure, bottom head debris bed formation and melting, bottom head penetration failure, and the release of molten

"The submitted manuscript has been authored by a contractor of the U.S. Government under contract No. DE-AC05-84OR21400. Accordingly, the U.S. Government retains a nonexclusive, royalty-free license to publish or reproduce the published form of this contribution, or allow others to do so, for U.S. Government purposes."

materials from the reactor vessel has upon subsequent conclusions regarding the characteristics and the timing of contact of the released core debris with the Mark I drywell shell, these models for events occurring in the bottom head are here discussed in greater detail than in the previous paper.

This paper also provides a discussion of the results of recent analyses performed by the BWRSAT Program to estimate the debris pours from the reactor vessel during an unmitigated short-term station blackout severe accident sequence. This work was performed at the request of Dr. Thomas J. Walker, Leader of the Task Group on the BWR Mark I Shell Melt-Through Issue established by the Accident Evaluation Branch of the Nuclear Regulatory Commission (NRC) Office of Nuclear Regulatory Research. The Task Group was formed in support of an ongoing effort to determine the response of the drywell shell in the unlikely event that a severe accident were to proceed to the point of release of molten core debris from the reactor vessel.

The specific calculations performed in this work are based upon the short-term station blackout accident sequence at the Peach Bottom Atomic Power Station, which has been determined by the Accident Sequences Evaluation Program (ASEP) to provide about 20% of the total risk of core melt at this facility.[1] The specific case analyzed is based upon the existing plant configuration, where it is assumed that the Automatic Depressurization System (ADS) is actuated in accordance with the BWR Owners Group Emergency Procedure Guidelines. It was assumed for these calculations that the core debris in the reactor vessel bottom head forms two separate mixtures during heatup after bottom head dryout: a single metallic eutectic with a melting temperature of 2750°F (1783 K) and a single oxidic eutectic with a melting temperature of 4350°F (2672 K).

In general, the calculations whose results are represented in this paper were carried out on a best-estimate basis. This includes the representation of the decay heat power as a function of time. The fuel models are appropriate for conventional GE 8X8R BWR fuel assemblies.

II. BWRSAR Models for Events After the Onset of Core Degradation

A. Core plate failure

The primary alignment function of the BWR core plate is to provide lateral guidance for the upper portion of the control rod guide tubes, as shown in Fig. 1. Each of the 185 control rod guide tubes supports four fuel assemblies grouped around a cruciform opening for the control rod blade. The core plate, which is two inches (5.1 cm) thick and weighs 20,500 lb (9300 Kg) supports only the outermost 24 assemblies of the 764 assemblies that make up the total core. [Dimensions pertain to the 251-in. ID BWR 4 reactor vessel installed at 1067 MW_e plants such as Peach Bottom or Browns Ferry.] The core plate is characterized by large holes provided for passage of the control rod guide tubes and smaller

holes for the in-core instrument guide tubes as shown in the plan view of Fig. 2. In the BWRSAR models, molten materials moving downward during the early period of the core relocation phase of a severe accident attack and fail individual radial regions of the core plate, opening pathways for follow-on relocating debris to fall directly into the reactor vessel bottom head. Debris relocation and the effect upon the core plate are described in detail in the following paragraphs.

The models for candling of fuel rod cladding that have been incorporated into BWRSAR are essentially identical to those developed by R. M. Summers[2] for MELCOR and discussed by Dingman et al.[3] In the BWRSAR code, the candling of molten clad and its associated mass of dissolved UO_2 leaves the upper portions of the fuel pellet stacks standing encased in thin ZrO_2 sheaths after all of the Zr metal has relocated downward. As the downward-moving candled material freezes, remelts, and freezes again on subsequently lower nodes, the lower portion of the core undergoes a thermal escalation due to the associated energy transport and to the increased metal/steam reaction, enhanced by the continual presentation of a fresh, unoxided material surface to the steam in the local environment. Eventually, the candling material contacts any remaining water above the core plate causing increased steaming, buildup of a quenched mass upon the core plate surface, and, after core plate dryout, rapid core plate heatup.

Since calculations and available experimental evidence[4] indicate that the control blade and channel box material of the BWR core would relocate uniformly and rapidly over a time scale of seconds once the stainless steel and zirconium metal melting points are reached under severe accident conditions, candling models are not employed in the BWRSAR code for the molten control blade or channel box nodes. Rather, upon reaching the molten state, the nodal control blade or channel box material is transferred immediately downward onto the core plate. As long as water remains above the core plate, the molten material is quenched, causing an increased steaming rate. Eventually, if there is no water injection into the reactor vessel, core plate dryout will occur and there will be a temporary cessation of steam generation into the core region.

After core plate dryout, mass continues to build up on the core plate from the candling process and from relocated molten canister or control blade nodes, with associated core plate heatup. Each radial region of the core plate is predicted to fail due to the accumulated load and loss of strength when the regionally calculated mass-averaged debris/core plate temperature exceeds a user-specified temperature, usually 2000°F (1367K). In practice, the mass-averaged temperature increases so rapidly after core plate dryout that adjusting the assumed failure temperature has little effect on the calculated time of failure.

Each failed core plate region and its accumulated debris fall into the lower plenum producing a burst of steam as the fallen material is quenched. However, it is expected that the fuel pellet columns, encased in ZrO_2 sheaths, would remain standing since the weight of the fuel is

supported by the control rod guide tubes, not by the core plate. After failure of a core plate region, additional relocating material in that region falls directly into the lower plenum. During the relocation process, material balances are performed to keep track of chemical species (such as Fe, Cr_2O_3, Zr, UO_2) as they accumulate on the core plate and in the lower plenum.

The rationale for the BWRSAR code methodology with respect to core debris relocation onto the core plate is supported by the results of the DF-4 experiment[4] conducted in the Annular Core Research Reactor (ACRR) at Sandia National Laboratories in November 1986, which confirm the predictions of earlier calculations with the BWRSAR models. In the experiment, the control blade melted first (as predicted in pretest calculations by BWRSAR models) and progressively and rapidly relocated to the bottom of the test section. In a post-test cross-section, the relocated control blade material was found in the form of an ingot cast in the shape of the zircaloy channel box at the very bottom of the test section, which is below the bottom of active fuel. Both the control blade and channel box wall portions of the DF-4 test section were more than 90% destroyed due to melting and relocation during the experiment, but the fuel pellet stacks are predominantly still standing. Relocated cladding blocks the base of the fuel rod regions of the experiment.

The DF-4 experiment, which had to fit within the ACRR, was designed to represent a short (0.5-m) length of uncovered fuel, channel box, and control blade in the upper region of a BWR core undergoing an unmitigated severe accident. It can be argued that in a full-length test section, the relocating molten control blade and channel box material might not travel all of the way to the experiment base before freezing. However, BWRSAR code predictions indicate that all axial sections of the control blades above the core water level would reach their melting points almost simultaneously as the temperature of the uncovered region of the core increases, and the same is true for the axial sections of the channel box walls. (It is a matter of relatively low-melting-point material sandwiched between higher-melting-point materials whose temperatures are rapidly rising: the very low thermal capacitance of the thin channel box walls also contributes to the observed phenomena.) There is no question, however, that the execution of an experiment using full length representation of BWR control blade, channel box, and fuel rods is highly desirable to confirm these calculated results. If much of the relocated molten core debris were to not reach the core plate, but instead were to form a frozen crust above the plate, subsequent debris bed formation and melting above the core plate would lead to an accident event sequence more like the Three Mile Island experience (PWR) than the sequence predicted by BWRSAR. Thus, the question of core plate survival in the BWR severe accident sequence is pivotal.

It should be noted that the BWRSAR models do predict retention and buildup of a debris bed above the core plate for cases in which the core plate is sufficiently cooled by reactor vessel water injection to forestall dryout, heatup, and structural failure. The required water injection rate is small if continuous, larger if the flow is intermittent and

in both cases the integrated effect must be sufficient to prevent core plate failure but insufficient to terminate the accident. This scenario seems most unlikely for prolonged BWR severe accident sequences since any injection system, if available, is capable of injection rates ample to recover the core and terminate the accident although operator action (specified in existing written procedures) would be necessary to enhance the flow in some cases. For this reason, the BWRSAR models for the progression of the unmitigated severe accident are based upon the assumption of a total loss of injection such as would occur in short-term station blackout.

B. Debris bed formation in the BWR bottom head

After regional failures of the core plate structure occur, debris including the failed portions of the core plate itself accumulates in the reactor vessel bottom head. The standing portions of the fuel pellet stacks are modeled to fall into the bottom head by radial column. Each of the radial columns collapses if and when its axially-averaged ZrO_2 temperature reaches a user-input value [currently 4400°F (2700K)], at which very little of the fuel mass in the column has become molten. The envisioned failure mechanism is weakening, by overtemperature, of the ZrO_2 sheaths surrounding the fuel pellets and of the previously molten material that tends to weld the fuel pellet stack together. The falling masses are quenched by the water in the bottom head until the time of bottom head dryout.

The argument that the falling heated masses of core debris would be quenched in the reactor vessel bottom head is buttressed by the geometry of the structures and the large water mass present in the BWR lower head. For example, at the Browns Ferry nuclear plant there are 185 control rod guide tubes [11-inch (0.2794-m) outer diameter on a 12-inch (0.3048-m) pitch] in the vessel lower head; thus within a unit cell the debris must pass through a 0.340 ft^2 (0.032-m^2) opening (see Fig. 3) that is 12 ft (3.7 m) in length. This, plus the fact that there is sufficient water in the bottom head [160,000-210,000 lbs (72,000-95,000 kg) depending on the temperature] to completely quench more than one molten core, leads to the assumption employed in BWRSAR that the relocated debris is quenched. It should be noted, given the progressive relocation methodology outlined above, that the majority of the debris (failed core plate regions or collapsed fuel columns) entering the lower plenum would be solid when it enters the water. The rate of quench of the relocated debris is determined by state-of-the-art debris bed models (normally Lipinski's).

Displacement of water in the lower head by the accumulated debris is modeled by BWRSAR. Depending on the accident sequence, this displacement can result in water being forced into the core region even after core plate dryout has occurred; the core plate is cooled whenever this happens, however, given the state of the core, the water displaced above the core plate is rapidly boiled off.

As the relocated core material accumulates in the BWR reactor vessel bottom head, the BWRSAR models recognize three layers of debris. The bottom layer is comprised of mostly metallic debris (control blades, canisters, candled clad and dissolved fuel) that either had originally accumulated on the core plate before failure, or had subsequently relocated within the failed core plate regions before fuel pellet stack collapse. The middle layer is initiated by the first collapse of the fuel pellet stacks in a radial fuel column. Subsequent relocated materials, including failed core plate regions or additional collapsed fuel columns, are then added to the middle layer. The initial failure of the core plate and the formation of the bottom debris layer causes temporary bursts of steaming as the relocated debris is quenched; however, with the initiation of the middle layer, a constant heat source (the decay heat from the collapsed fuel columns) is introduced to the lower plenum reservoir. This results in a rapid continuous boiloff of the lower head water.

After bottom head dryout, the debris in the bottom and middle debris layers begins to heat up, and it is assumed that the debris thermally attacks and fails (at a user input debris temperature) the control rod guide tubes, which the debris completely surrounds to a depth of 6 to 9 ft (2-3 m). Since the control rod drive mechanism assemblies and the control rod guide tubes support the core, the remaining standing regions of the core collapse into the bottom head when these support structures fail. Thus, the top layer of the debris bed is formed when the control rod guide tubes fail. The material (stainless steel) of the control rod guide tubes is assumed to be subsumed into the surrounding debris of the bottom, middle, and upper layers, as appropriate.

The upper debris layer consists of the collapsed outer portion of the core, any unfailed core plate regions and accumulated debris remaining at the time of control rod guide tube failure, the top guide (which is normally calculated to melt during core heatup, but is not added to the debris until control rod guide tube failure), and the portion of the control rod guide tubes that is not subsumed into the bottom and middle debris layers. The vessel structural masses as they exist at the initiation of the calculation (prior to oxidation) that are normally included in the formation of the bottom head debris bed are outlined in Table 1.

With control rod guide tube failure and collapse of the outer regions of the core, the formation of the bottom head debris bed is complete. As described, it is discretized on formation into three layers separated vertically; additionally, each layer is discretized into radial nodes resulting in the debris bed nodalization illustrated in Fig. 4. The lower head of the vessel is modeled at each debris node in contact with the wall; each wall segment is also discretized radially into nodes with the outside nodes having the capability of transferring heat to the drywell atmosphere. Heat generation within the debris bed is associated with the decay heat of the fuel and the chemical reaction of steam from the vessel atmosphere with the zirconium metal of the debris.

In the heat balances for each debris node, normal heat transfer mechanisms are employed for node-to-node and node-to-wall transfer. Additionally, radiation and convection from the surface nodes to the vessel gaseous contents and to structures above the debris bed are considered. Radiation to the shroud and axial conduction along the vessel wall causes boiloff of water remaining in the downcomer jet pump region. Also included in the nodal heat balances are the change-of-phase heat of fusion of species (or eutectics) as they melt or refreeze within the bed. Mass balances track species as they melt, migrate, refreeze, and eventually egress from the vessel.

C. Reactor vessel bottom head penetration failure

As the temperature of the debris bed increases, materials begin to melt, migrate, freeze, and remelt. Eventually, temperatures near the wall are such that penetrations fail and a path is opened for gas blowdown and passage of molten material from the vessel. In general, most of the debris bed is still solid when penetration failure and vessel blowdown occur, so that relatively little of the debris is expelled during blowdown.

There are more than 200 reactor vessel bottom head penetrations in a BWR reactor vessel of the size employed at Browns Ferry, where there are 185 control rod drive mechanism assembly penetrations, 55 instrument guide tube penetrations, and a drain line near the low point in the bottom head. It seems certain that the initial pressure boundary failure under the conditions of bottom head debris dryout would occur through the vessel penetrations, not by melt-through of the bottom head itself. The lower head of a BWR is clad with Inconel while the penetrations are stainless steel. Cross sections of the control rod drive mechanism assembly and instrument tube penetrations and their weldments are illustrated in Fig. 5. The assumed method of failure of the penetration structure is by creep/rupture of the Inconel/stainless steel welds by which the penetration assemblies are held within the reactor vessel.

The BWRSAR models also provide for a loss of the reactor vessel pressure boundary that is initiated by failure of the in-core housing guide tubes associated with the local power range detectors (Fig. 6) and the source and intermediate range detectors (Fig. 7). Melting of upper portions of these guide tubes within the bottom head debris bed would provide an annular flow path within the tubes by which molten metals could pour through the reactor vessel wall. Passage of molten metal into the ex-vessel portion of a guide tube is assumed sufficient to cause immediate failure of the tube pressure boundary.

Since the bottom layer of debris is comprised almost entirely of metals while UO_2 constitutes more than half of the middle layer, the middle layer heats up much more rapidly after bottom head dryout than does the bottom layer. For this reason, melting of the in-core housing guide tubes would occur first in the middle layer. The criteria

employed in BWRSAR for initiation of reactor vessel blowdown through the in-core instrument housing guide tubes are first, that the middle layer debris bed temperature be above the melting point of stainless steel and second, that the level of liquid metal within the reactor vessel has risen into the middle debris layer so that molten metal is available to pour into the failed portion of the tubes.

After failure of the penetrations, a leak path from the vessel to the drywell atmosphere is created. Subsequently, the vessel gaseous content blows down if the reactor vessel is at pressure or, if the vessel is depressurized, slowly leaks out as the gas temperature increases and the water in the reactor vessel downcomer region surrounding the jet pumps is boiled off. The leak path for the steam generated from the water surrounding the jet pumps is up through the downcomer region, down through the core region, and out through the debris bed. Thus, the steam available in the vessel at the time of penetration failure would pass through the debris and would react with the zirconium metal during its passage. Only the steam/zirconium reaction is modeled in the debris bed models, but this is a major heat source in the nodal energy balances, particularly for cases in which the reactor vessel is pressurized at the time of penetration failure. Stainless steel oxidation in the bottom head debris is not modeled since this is expected to be a secondary effect and because the temperatures at which rapid stainless steel oxidation occurs are close to the melting point; thus stainless steel tends to relocate rather than to undergo excessive oxidation. The result is that much of this metal is expected to leave the vessel in a molten state without oxidizing. Obviously, there are uncertainties in this area. These concerns definitely indicate the need for experimental resolution because a great amount of hydrogen is predicted to be generated in the vessel bottom head via the BWRSAR modeling approach.

Application of the current BWRSAR models leads to a protracted, time-dependent pour of debris from the reactor vessel. Molten material moves downward from one node to another within the debris bed as long as void space remains within the lower node. Once the interstitial spaces in the lower nodes are filled, the molten liquid can move horizontally within the bed as necessary to keep the liquid level approximately constant within a layer. An exception occurs in the case of the two middle layer outermost nodes after penetration failure occurs in this layer; for these two nodes, simultaneous movement downward to the void space in the (single) underlying node and horizontally to exit the vessel through the failed penetration can occur. In all cases, the rate of movement of molten material through the debris bed is controlled by a user-input time constant, usually set at one minute. Thus, for example, if the calculational timestep is 0.2 minute, 20% of the molten material within a node can move horizontally or vertically (or both, for the outermost middle layer nodes) each timestep.

II. The Short-Term Station Blackout Accident Sequence

Much of the impetus for these new studies of Peach Bottom Station Blackout has derived from the most recent findings of the NRC-sponsored Accident Sequence Evaluation Program (ASEP) in support of the NUREG-1150 effort.[1] The final results of the ASEP Program provide the estimate that 60% of the overall risk of core melt for Peach Bottom can be attributed to the overall threat of Station Blackout. (The remaining risk is allocated as 31% for ATWS and 9% for all other possible accident sequences.) Historically, the station blackout accident sequence has been considered to be loss of offsite power and reactor scram combined with failure of the station diesels to start and load. In this (long-term) accident sequence, water is injected into the reactor vessel by the steam turbine-driven HPCI or RCIC systems as necessary to keep the core covered for as long as dc power for turbine governor control remains available from the unit batteries, a period of about six hours. However, the definition of Station Blackout implemented by the ASEP Program has been expanded to include two cases that heretofore would have been classified as Loss of Injection, or TQUV in WASH-1400 parlance. In these short-term station blackout sequences, the capability for water injection to the reactor vessel is lost at the inception of the accident sequence. (The short-term designation derives from the fact that the core is uncovered relatively quickly in these sequences.)

The early total loss of injection hallmark of Peach Bottom Short-Term Station Blackout might be initiated in either of two ways. First, there might be independent failures of both the HPCI and RCIC systems when they are called upon to keep the core covered during the period while dc power remains available. Second, there might have been a common-mode failure of the dc battery systems that, upon loss of offsite power, had precluded starting of the diesel generators and thereby was the cause of the Station Blackout; without dc power for valve operation and turbine governor control, the steam turbine-driven injection systems also would not be operable. The ASEP program results assign 17% of the overall core melt frequency for Peach Bottom to the case of Short-Term Station Blackout with independent failure of HPCI and RCIC and 3% of the frequency to the case initiated by common-mode failure of the station batteries. The calculations discussed in the remainder of this paper are based upon the case with independent failure of HPCI and RCIC.

III. The Calculated Sequence of Events

The sequence of events and event timing for the Peach Bottom short-term station blackout with ADS actuation accident sequence as calculated by the BWRSAR code are provided in Table 3. It is assumed that the reactor had been operating at 100% power at the time of scram and that no injection source is ever recovered.

Plots of key parameters representing events within the reactor vessel as predicted by the BWRSAR code are provided in Fig. 8. These plots represent events from time 35 minutes when the BWRSAR calculation is

initiated until time 300 minutes, which is about 45 minutes after reactor vessel bottom head penetration failure. As indicated in Fig. 8a, the ADS system is activated at time 80.0 min, when the reactor vessel water level is near the bottom of the core; this causes the opening of five safety/relief valves (SRVs). The open SRVs subsequently close whenever the reactor vessel falls to within 20 psi (0.138 MPa) of the drywell pressure and then reopen when the reactor vessel pressure has increased to 50 psi (0.345 MPa) above drywell pressure. The corresponding relief valve flows are shown in Fig. 8d.

The swollen reactor vessel water level, the calculation of which includes consideration of the effects of voids, is shown in Fig. 8b. The calculated water level rapidly falls below the core plate as a result of the water loss by flashing when the ADS valves are opened. Small temporary increases in level occur because of displacement of water in the bottom head when large masses of core debris are introduced after core plate failure. The decay heat associated with the fuel pellets relocated into the bottom head at time 222.8 min causes a boiloff of the remaining water in the reactor vessel; bottom head dryout occurs at time 254.9 min.

Plot 8c shows the extent of hydrogen generation by metal-steam reaction in the core region. Approximately 23% of the clad, 12% of the channel box walls, and 3% of the control blade stainless steel is predicted to be oxidized during the accident sequence, producing about 1137 lb (516 kg) of hydrogen in the core region within the reactor vessel.

Selected primary containment response characteristics predicted by the BWRSAR code for the period up to one-half hour after reactor vessel bottom head penetration failure are provided in the individual plots provided in Figs. 9 and 10. As indicated in Fig. 9a, ADS actuation causes a small pressure increase, but this pressure increase is erased as the containment heat sinks soak up energy after core plate dryout. The containment pressure increases significantly in response to debris relocation into the reactor vessel bottom head and after collapse of the central fuel pellet stacks. Bottom head penetration failure does not significantly increase the containment pressure because the reactor vessel was previously depressurized by means of the ADS actuation.

The drywell atmosphere temperature, shown in Fig. 9b, increases due to increased heat transfer from the reactor vessel whenever flow is initiated from the safety/relief valves (Fig. 8d), then decreases as the drywell heat sinks absorb the energy to the atmosphere. The effect of bottom head penetration failure is slight. At the completion of the reactor vessel blowdown, neither the drywell pressure nor the calculated drywell shell temperature (Fig. 9c) is of sufficient magnitude to threaten the integrity of the drywell shell pressure boundary.

The temperatures of the wetwell atmosphere and the torus shell respond to events within the reactor vessel as shown in Figs. 10a and 10b, but do not increase to threatening values. The wetwell atmosphere temperature increases after reactor vessel bottom head penetration

failure because of the hot gases entering the pressure suppression pool from the drywell via the vent lines and downcomers. (The pool remains subcooled, however. Its response is shown in Fig. 10d.)

A large amount of hydrogen has accumulated within the wetwell airspace (Fig. 10c) and the drywell (Fig. 10d) at the time of reactor vessel bottom head penetration failure. Some additional hydrogen [about 247 lb (112 kg)] is generated by the passage of steam through the bottom head debris bed during the first 60 minutes after penetration failure. A slow rate of hydrogen generation by this mechanism continues as long as water remains in the downcomer region of the reactor vessel. This water is boiled by radiative and conductive (through the vessel wall) heat transfer from the bottom head debris; the steam passes through the debris bed on its way out of the vessel.

The characteristics of the debris pours from the reactor vessel bottom head as calculated by the BWRSAR code are shown in Fig. 11. Figure 11a indicates the rate of molten material release from the reactor vessel as a function of time. Although bottom head penetration failure occurs at 255 minutes, the initial pour does not occur until time 263 minutes because of the time interval required for the metallic debris to heat to its assumed melting temperature of 2750°F (1783 K). The mass-averaged temperature of the release is shown in Fig. 11b.

The integrated mass of debris released from the reactor vessel is indicated in Fig. 12a, where it is shown that about 875,000 lbs (397,000 kg) has left the vessel by the end of the calculation, at time 900 min. This is equivalent to about 98% of the total mass of bottom head debris. The decay heat (proportional to the mass of UO_2) included in the released debris is shown in Fig. 12b.

It should be noted that the BWRSAR code predicts that the portion of the reactor vessel bottom head beneath the point of attachment of the support skirt is completely melted through at time 483 minutes. There are no specific models within BWRSAR to address this phenomenon since it is believed that the 340,000 lbs (154,000 kg) of debris remaining within the vessel at this time would merely relocate downward about three feet (0.91 m) onto the control rod drive housing support structure (see Fig. 13). After relocation, the debris would continue to melt, with the molten portion flowing down onto the drywell floor in the same manner as if the reactor vessel had remained intact. Heat transfer from the debris to the reactor vessel by convection and conduction is discontinued at the time of debris relocation.

IV. CONTAIN Calculations of Primary Containment Response

The reactor vessel debris pours shown in Figs. 11 and 12 have been used to drive CONTAIN code calculations to estimate the primary containment response. The results of these primary containment calculations are presented at this meeting by C. R. Hyman in the paper "CONTAIN Calculations of Debris Conditions Adjacent to the BWR Mark I Drywell Shell During the Later Phases of a Severe Accident."

V. References

1. Personal communication with Alan Kolaczkowski of the ASEP Program, July 6, 1988.

2. R. M. Summers, "Degraded Core Modeling in MELCOR," Proceedings of the Topical Meeting on Reactor Physics and Safety, Saratoga Springs, NY, September 1986.

3. S. E. Dingman et al., "Analysis of Peach Bottom Station Blackout with MELCOR," Fourteenth Water Reactor Safety Research Information Meeting, National Bureau of Standards, Gaithersburg, MD, October 30, 1986.

4. R. O. Gauntt, DF-4 BWR Control Blade/Channel Box Fuel Damage Experiment, Reactor Safety Research Semiannual Report, January-June 1987, Volume 37, Chapter 3, NUREG/CR-5039 (1 of 2) SAND87-2411 (1 of 2), January 1988.

Table 1. BWR reactor vessel structures included in bottom head debris bed formation

	Initial Masses kg	Initial Masses lbs
Core constituents:		
a. Zircaloy		
1. Cladding	37,000	81,500
2. Channel box	22,900	50,400
3. Spacers	2,700	5,900
b. UO_2 fuel	172,500	380,300
c. Stainless steel control blades	16,300	35,800
d. B_4C powder	1,150	2,500
Stainless steel structures:		
a. Top guide	6,900	15,200
b. Core plate	9,300	20,500
c. Control rod guide tubes	88,680	195,500
Total	357,430	787,600

Table 2. Default values for eutectic mixture and constituent melting points provided within the BWRSAR code

Constituent/Eutectic	Melting Temperature K	Melting Temperature °F
SS/B/Zr	1422	2100
SS/Zr	1589	2400
SS	1672	2550
Zr/B	2033	3200
$Zr(O)/UO_2$ #1	2125	3365
$Zr(O)/UO_2$ #2	2673	4350
ZrO_2	2978	4900
UO_2	3070	5066

Table 3. Calculated sequence of events for Peach Bottom Short-Term Station Blackout with ADS Actuation. The bottom head debris is modeled to separate into a mixture of metals melting at 2750°F and a mixture of oxides melting at 4750°F

Event	Time (min)
Station blackout-initiated scram from 100% power. Independent loss of the steam turbine-driven HPCI and RCIC injection systems	0.0
Swollen water level falls below top of core	40.2
Open one SRV	77.0
ADS system actuation	80.0
Core plate dryout	80.9
Relocation of core debris begins	132.4
First local core plate failure	132.7
Collapse of fuel pellet stacks in central core	222.8
Reactor vessel bottom head dryout; structural support by control rod guide tubes fails; remainder of core falls into reactor vessel bottom head	254.9
Bottom head penetrations fail	255.0
Pour of molten debris from reactor vessel begins	263.1
First UO_2 leaves reactor vessel	355.0
Bottom head melt-through	483.0

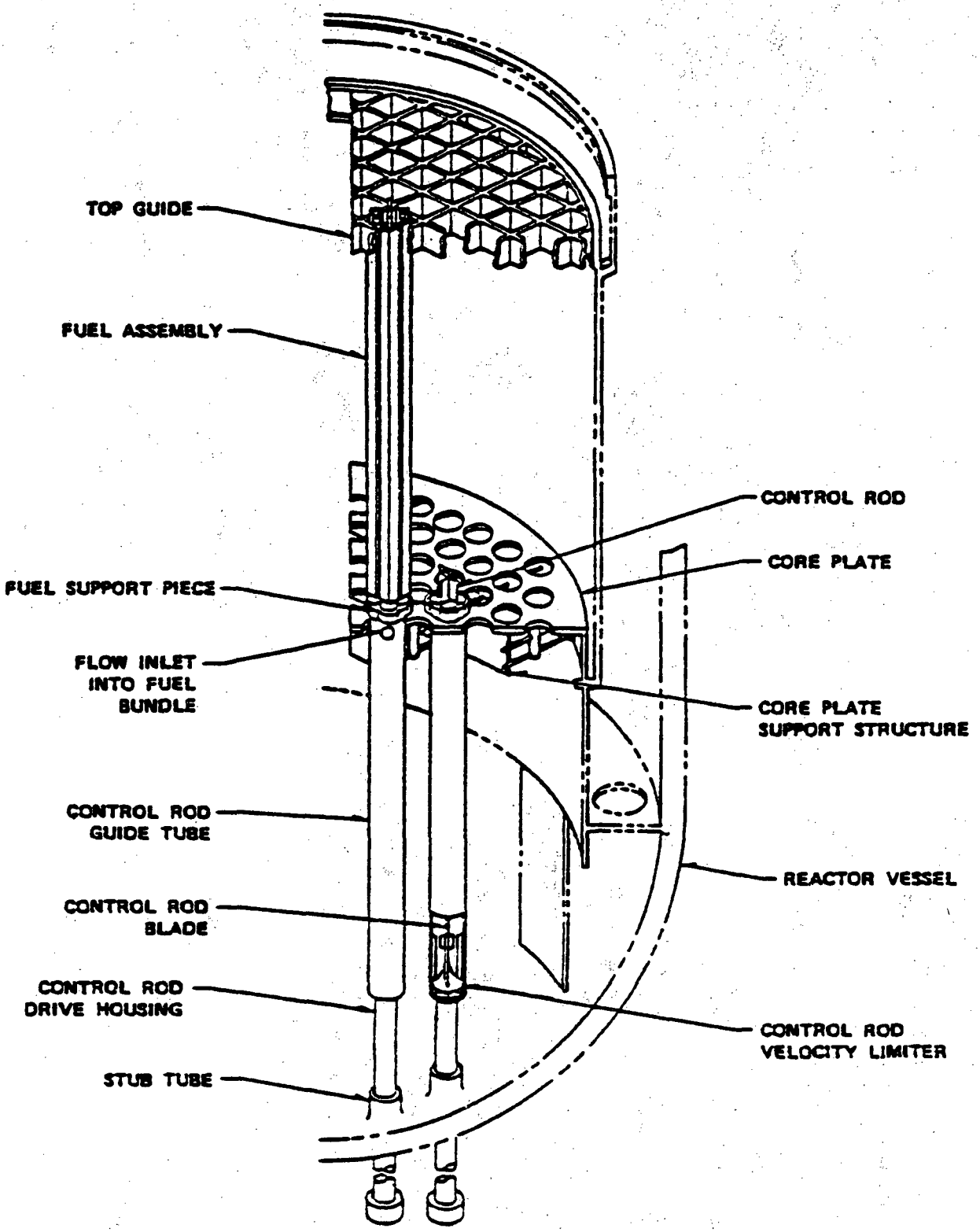


Fig. 1. The BWR core plate separates the core region from the reactor vessel bottom head. The core fuel assemblies are supported by the fuel support pieces, the control rod guide tubes, the control rod drive housings, and the stub tube welds.

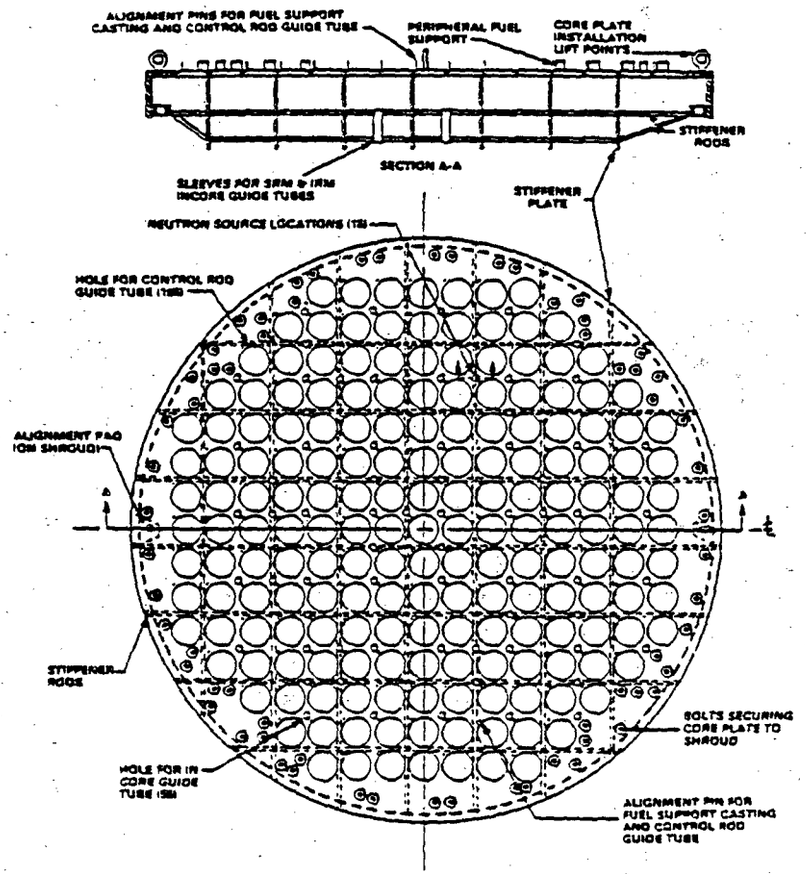


Fig. 2. Elevation and plan views of the core plate.

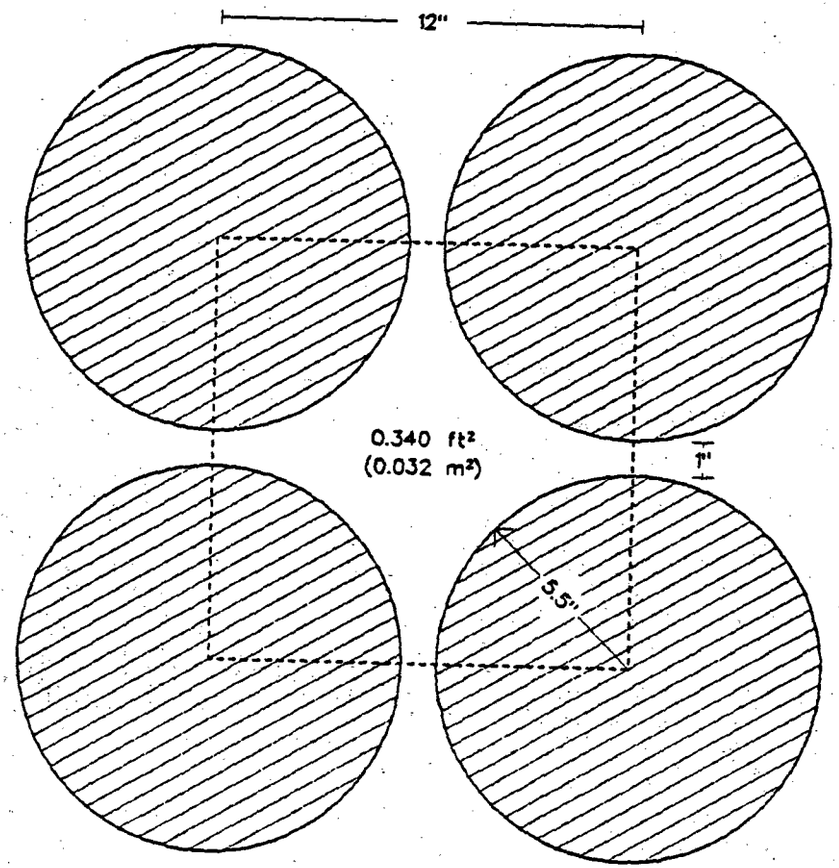


Fig. 3. Control rod guide tube spacing and available open flow area in the BWR reactor vessel bottom head.

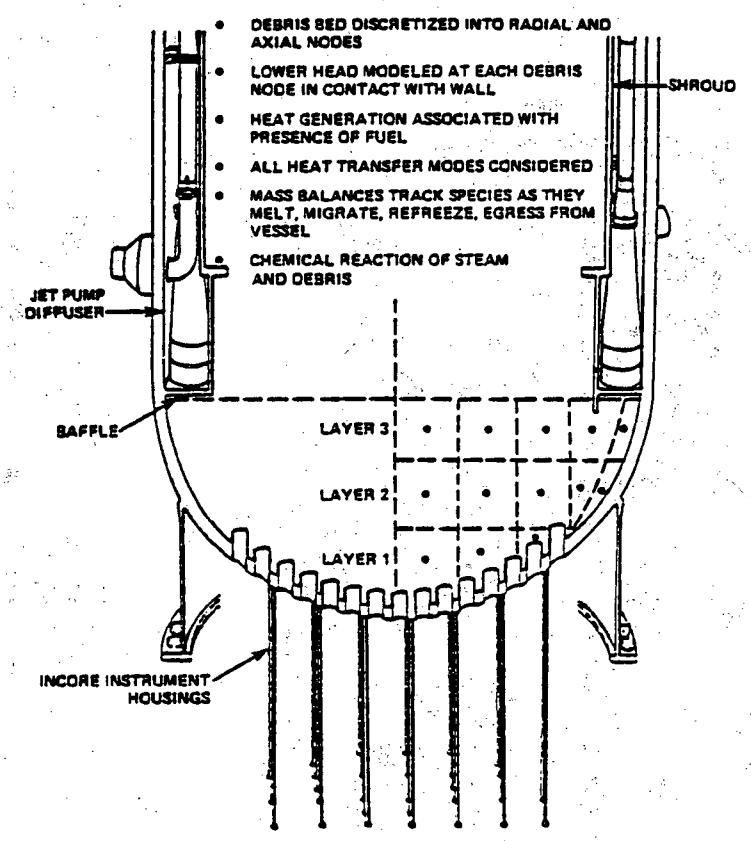


Fig. 4. Description of models and illustration of noding employed for the BWR reactor vessel bottom head debris bed.

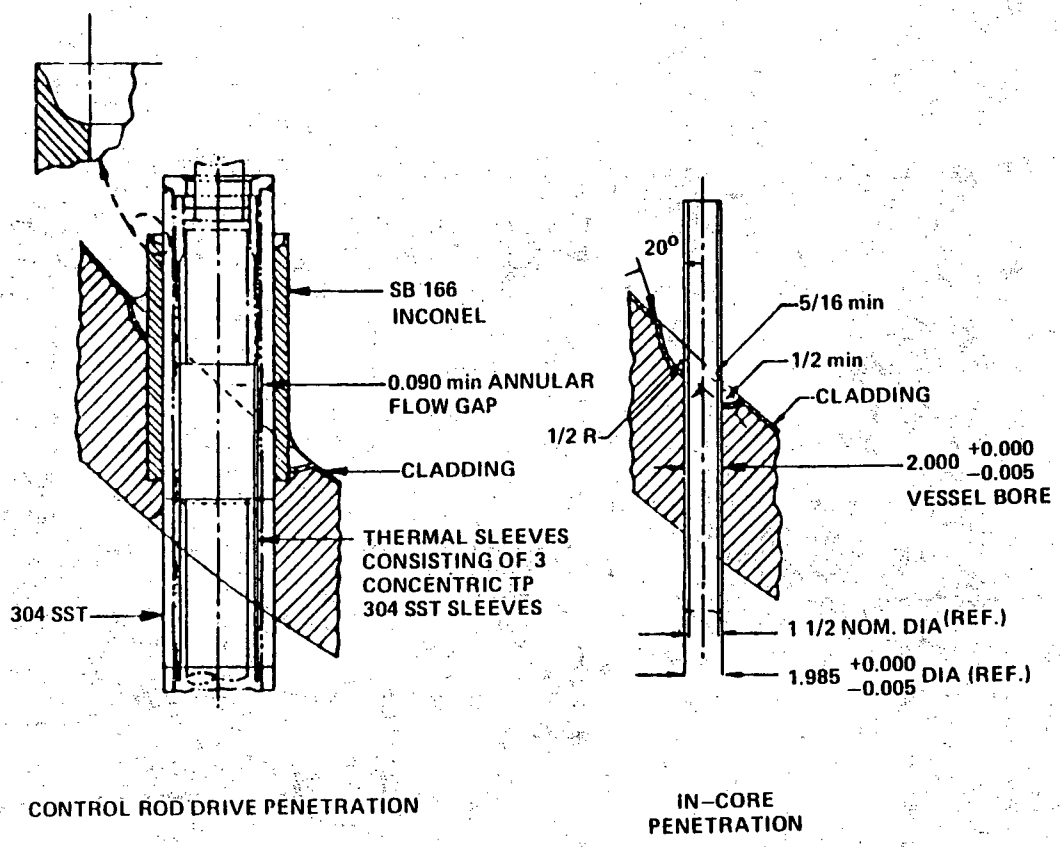


Fig. 5. Control rod drive mechanism assembly and in-core instrument guide tube penetrations through the BWR reactor vessel bottom head. Dimensions are given in inches.

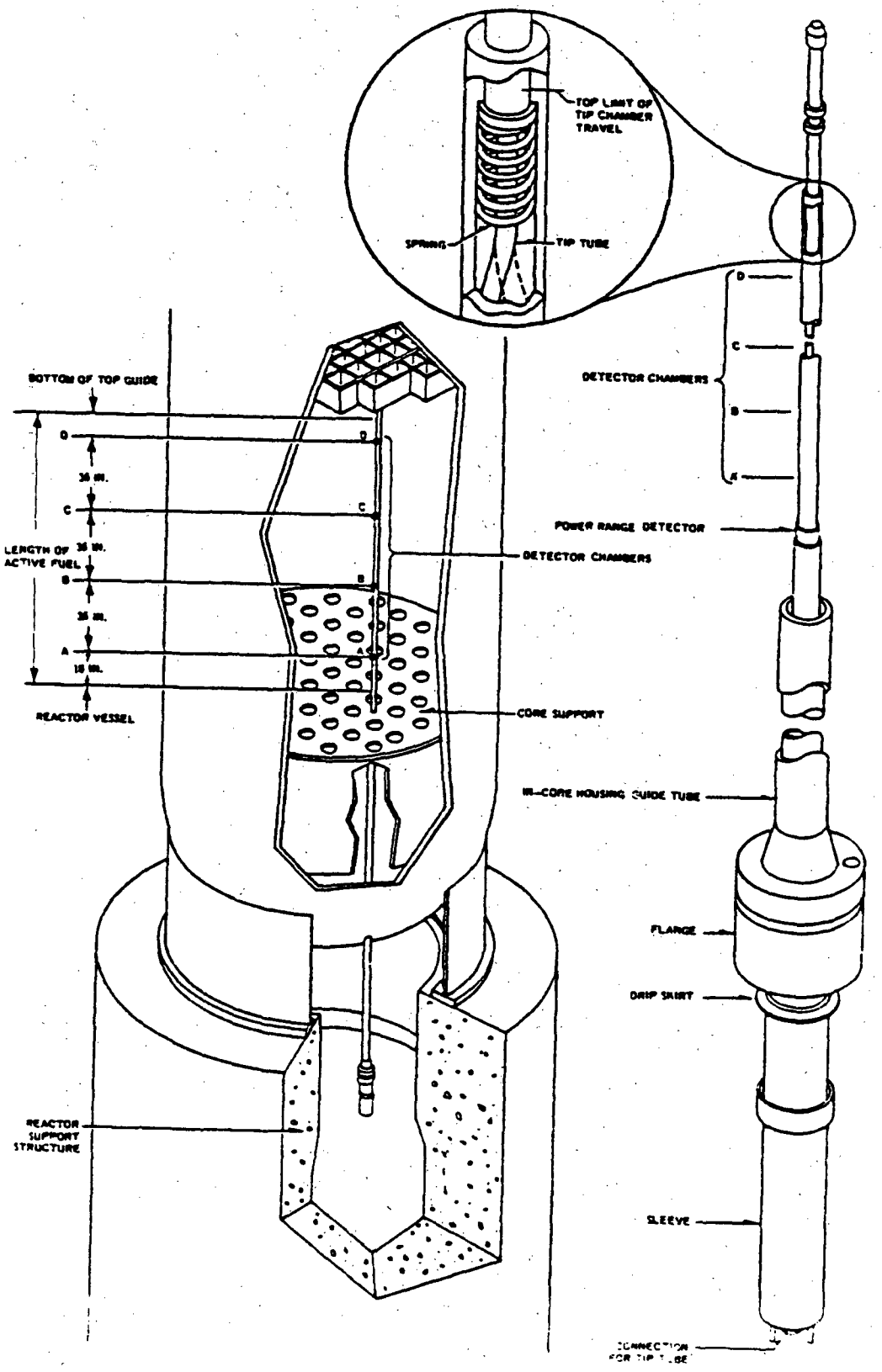


Fig. 6. Mechanical arrangement of one of the 43 Local Power Range Detector assemblies. The annular gap clearance between the in-core housing guide tube and the instrument tube is specified as 0.40 inches.

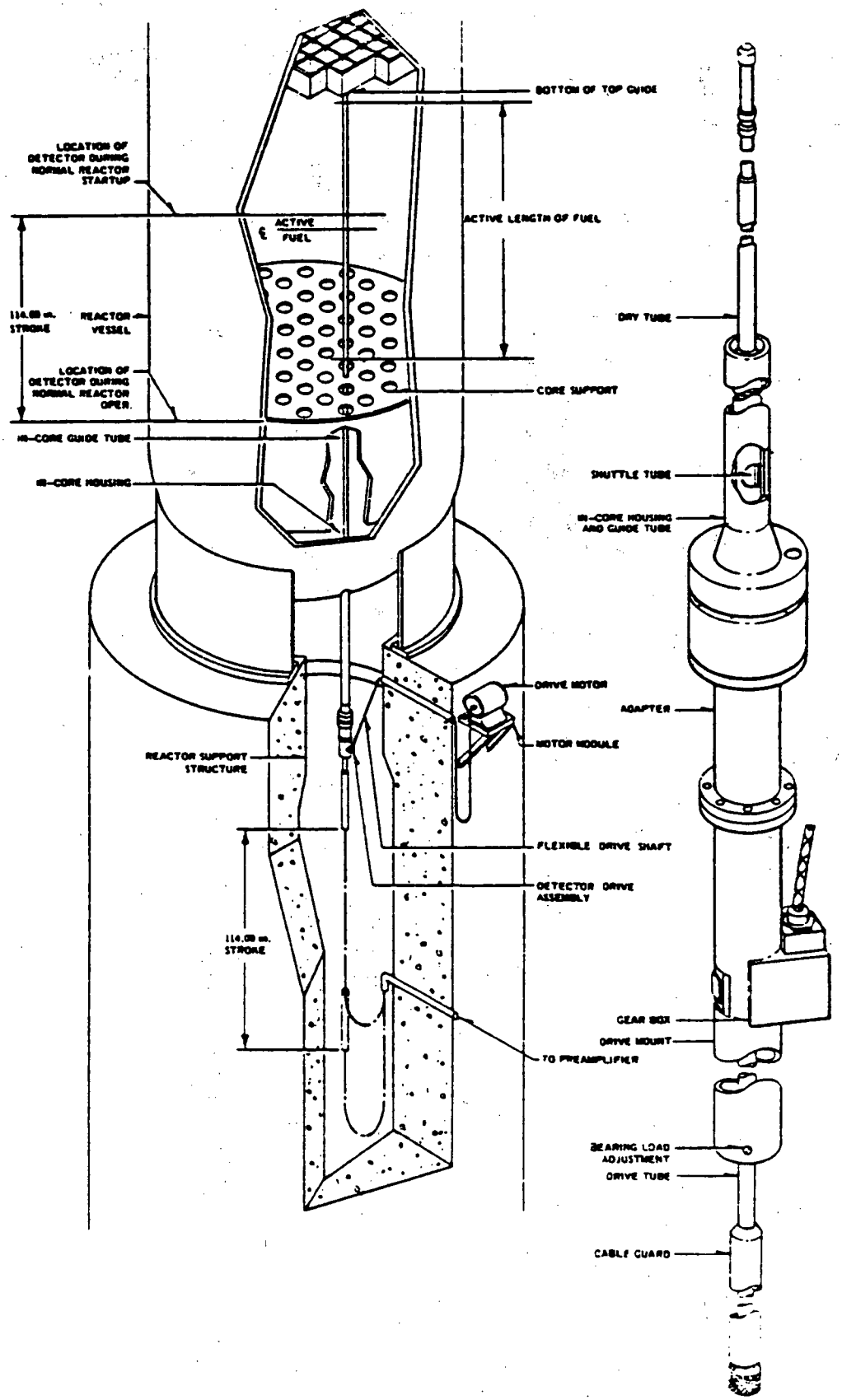


Fig. 7. Mechanical arrangement of the four source range and eight intermediate range detector in-core instrument assemblies.

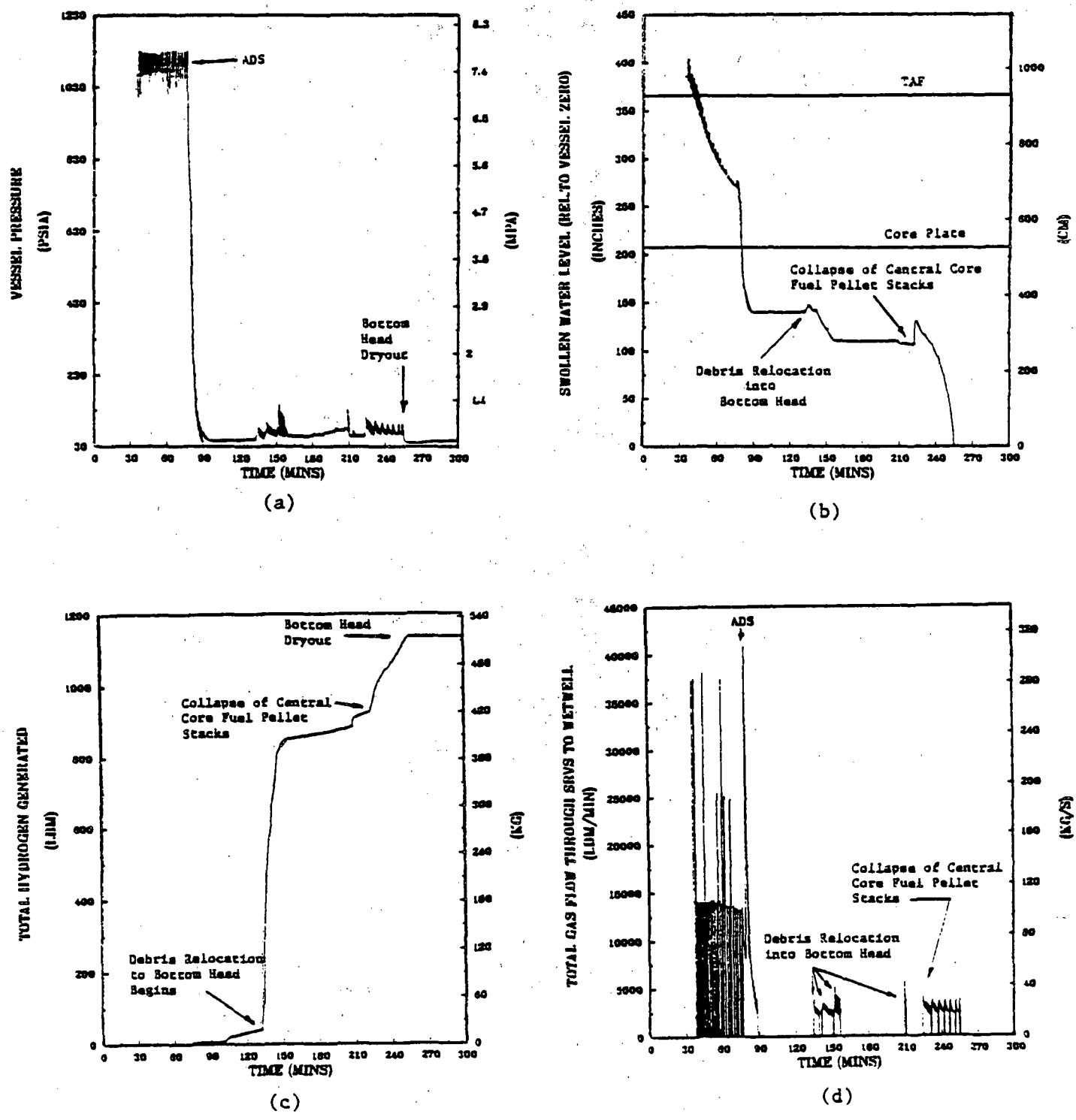


Fig. 8. Accident signatures for events within the reactor vessel as predicted by the BWRSAR code for the Peach Bottom short-term station blackout accident sequence with ADS.

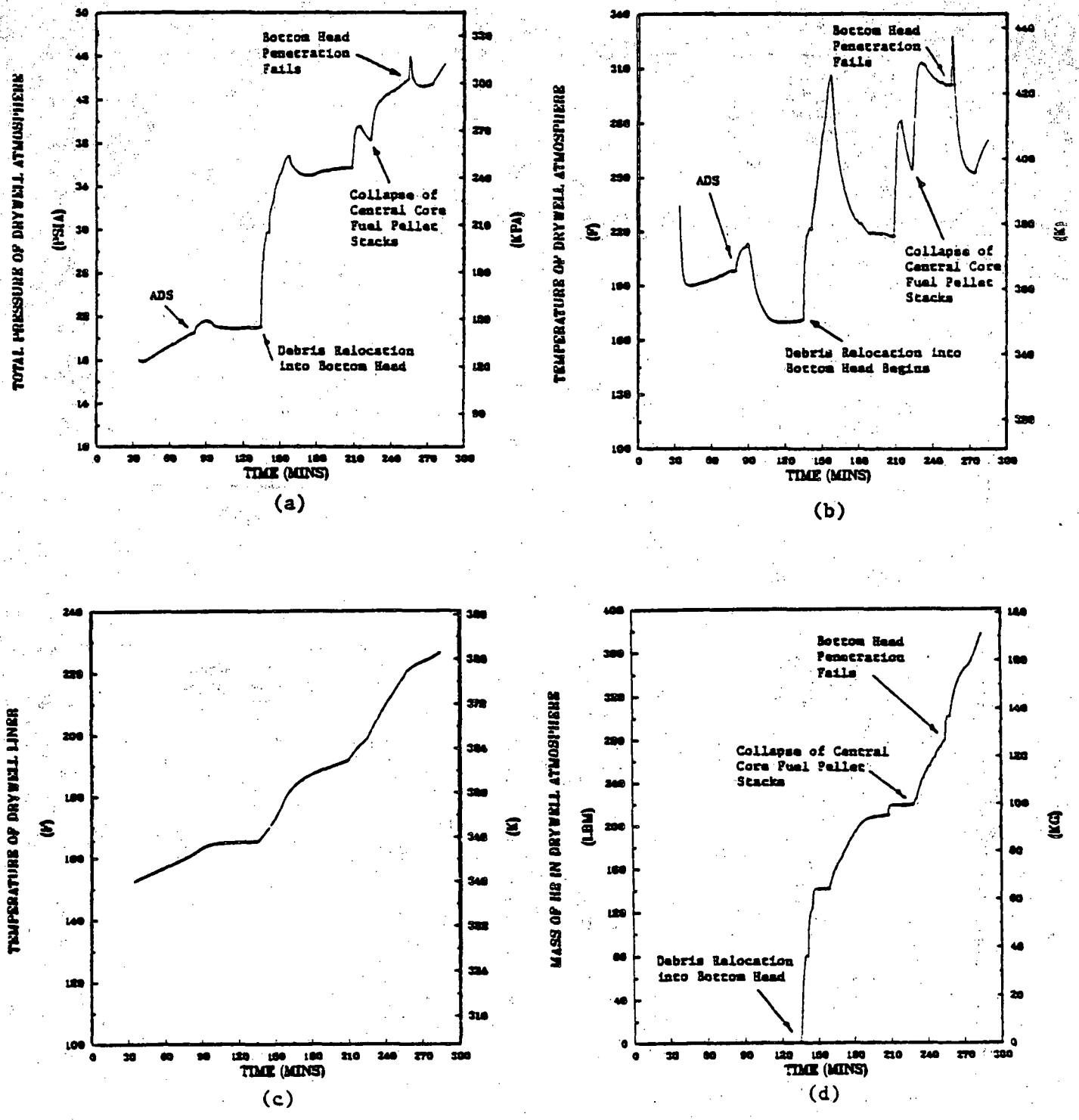


Fig. 9. Accident signatures for response of the drywell as predicted by the BWRSAR code for the Peach Bottom short-term station blackout accident sequence with ADS.

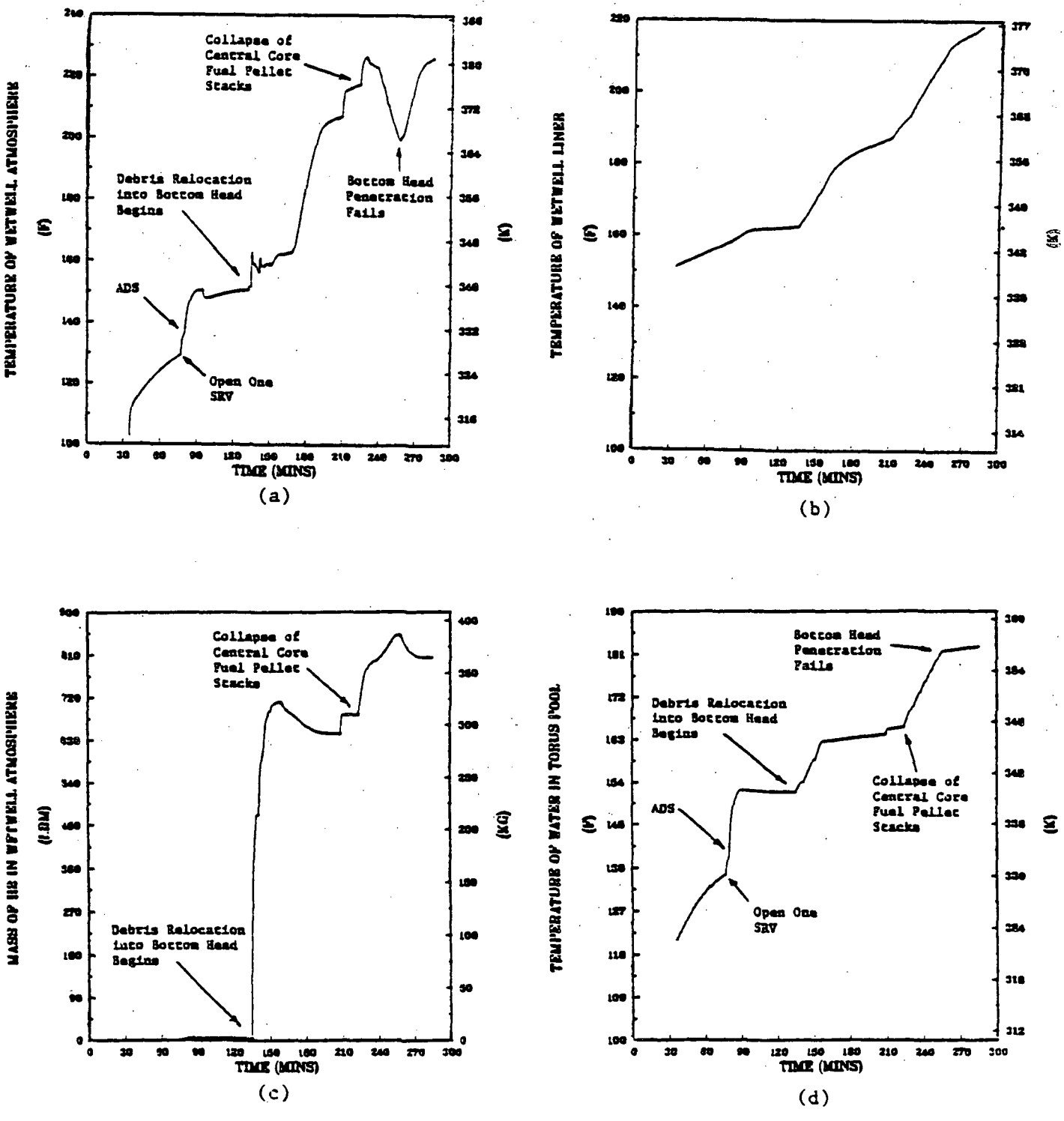


Fig. 10. Accident signatures for response of the wetwell as predicted by the BWRSAR code for the Peach Bottom short-term station blackout accident sequence with ADS.

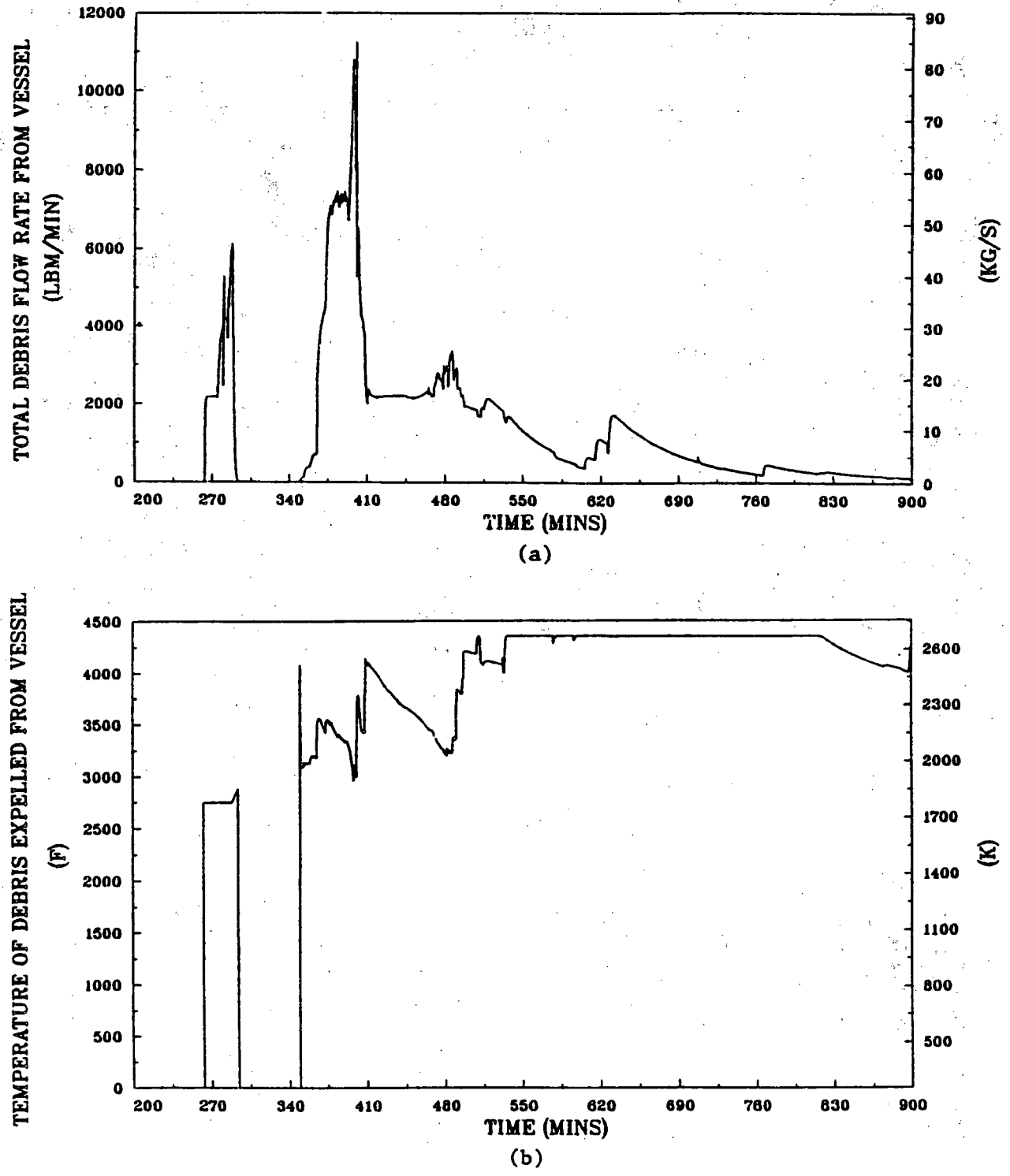


Fig. 11. Flow rates and temperatures of debris pours from the reactor vessel bottom head as predicted by the BWRSAR code for the short-term station blackout accident sequence with ADS at a unit of the Peach Bottom Atomic Power Station.

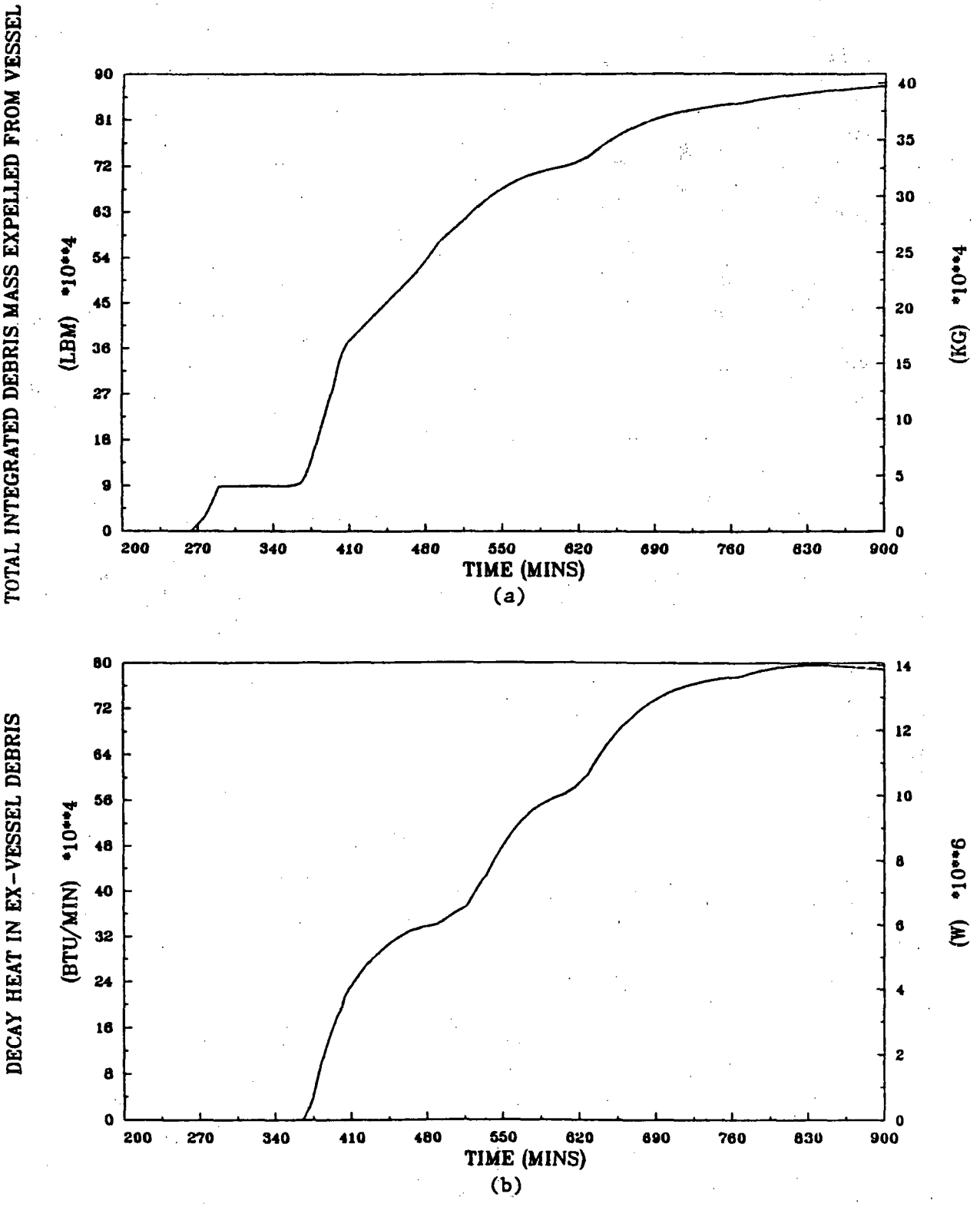


Fig. 12. Integrated debris mass expelled from the reactor vessel and decay heat power in the ex-vessel debris as calculated by the BWRSAR code for the short-term station blackout accident sequence with ADS at a unit of the Peach Bottom Atomic Power Station.

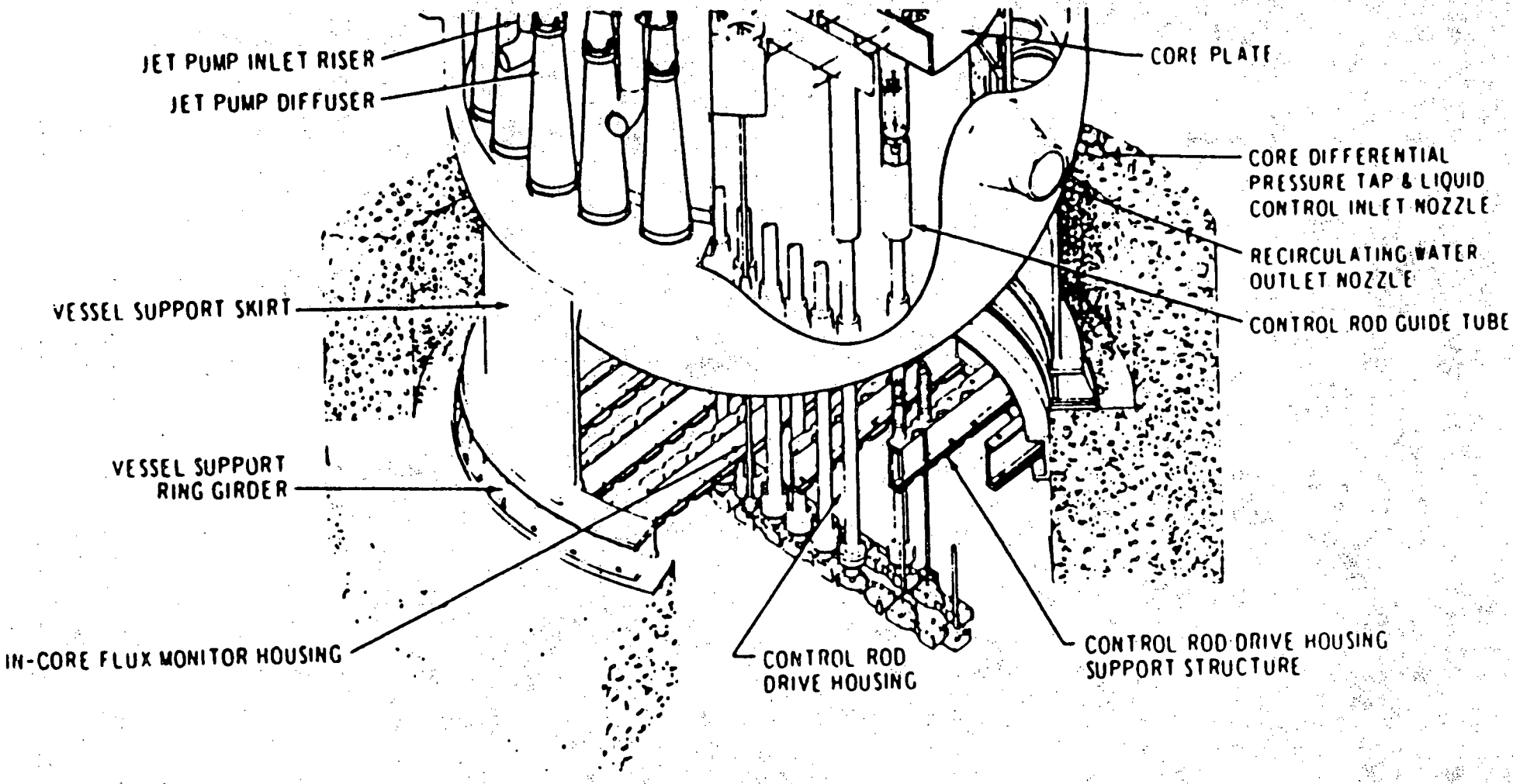


Fig. 13. Downward movement of separated portions of the bottom head beneath the skirt would be limited to about 34 inches by the CRD housing support structure.

CONTAIN CALCULATIONS OF DEBRIS CONDITIONS ADJACENT TO THE BWR MARK I DRYWELL SHELL DURING THE LATER PHASES OF A SEVERE ACCIDENT

C. R. Hyman

Oak Ridge National Laboratory
Oak Ridge, Tennessee 37831

ABSTRACT

Best estimate CONTAIN calculations have recently been performed by the BWR Severe Accident Technology (BWRSAT) Program at Oak Ridge National Laboratory to predict the primary containment response during the later phases of an unmitigated low-pressure Short Term Station Blackout at the Peach Bottom Atomic Power Station. Debris pour conditions leaving the failed reactor vessel are taken from the results of best estimate BWRSAR analyses that are based upon an assumed metallic debris melting temperature of 2750°F (1783 K) and an oxide debris melting temperature of 4350°F (2672 K). Results of the CONTAIN analysis for the case without sprays indicate failure of the drywell head seals due to the extremely hot atmospheric conditions extant in the drywell. The maximum calculated temperature of the debris adjacent to the drywell shell is less than the melting temperature of the shell, yet the sustained temperatures may be sufficient to induce primary containment pressure boundary failure by the mechanism of creep-rupture. It is also predicted that a significant portion of the reactor pedestal wall is ablated during the period of the calculation. Nevertheless, the calculated results are recognized to be influenced by large modeling uncertainties. Several deficiencies in the application of the CORCON module within the CONTAIN code to BWR severe accident sequences are identified and discussed.

1. INTRODUCTION

This paper provides a discussion of recent containment analyses performed by the ORNL BWRSAT Program to estimate the primary containment response during the later phases of an unmitigated Short-Term Station Blackout at Peach Bottom. The work was performed at the request of Dr. Thomas J. Walker, Leader of the Task Group on the BWR Mark I Shell Melt-Through Issue established by the Accident Evaluation Branch of the Nuclear Regulatory Commission (NRC) Office of Nuclear Regulatory Research. The tool used to perform this containment analysis is a modified version of the most recent release of the CONTAIN code.[1]

"The submitted manuscript has been authored by a contractor of the U.S. Government under contract No. DE-AC05-84OR21400. Accordingly, the U.S. Government retains a nonexclusive, royalty-free license to publish or reproduce the published form of this contribution, or allow others to do so, for U.S. Government purposes."

The invessel and debris release portions of this accident sequence were analyzed by the BWRSAR code and provide the subject of a separate paper presented at this meeting.[2] The debris pours and the primary containment initial conditions used in the CONTAIN analysis were taken from the BWRSAR results. Principal characteristics of the BWRSAR calculated debris pours are: (1) the debris leaves the reactor vessel in a discontinuous manner over a period of 11 h, (2) early debris pours are mainly metallic (Fe, Cr, Ni, Zr) with a characteristic melting temperature of 2750°F (1783 K), and (3) later debris pours are primarily oxide (ZrO_2, UO_2) with a melting temperature of 4350°F (2672 K). Figure 1 shows the calculated total mass flow and temperature of the debris as it leaves the reactor vessel. This information was taken from Reference 2.

The following Section describes the modeling approach used to perform the containment analysis with CONTAIN, Section 3 presents results, Section 4 provides a discussion of current deficiencies in the CONTAIN/CORCON linkage with respect to BWR accident analyses, while Section 5 presents a summary.

2. BWR MARK I PRIMARY CONTAINMENT MODELING APPROACH

2.1 ORNL CONTAIN Model

The BWRSAT Program at ORNL has developed a 12-cell CONTAIN model for use in analysis of the response of the BWR Mark I primary containment under severe accident conditions. The model is shown in Fig. 2. Cells one through nine are used to represent the free volume of the drywell. Core debris/concrete interactions are calculated with the CORCON module of CONTAIN for the floor of Cell 1 after the initial debris pour from the reactor vessel and also for the floor of Cell 6 when the debris has spread into the expedestal region. Cell 7 represents the one-foot (0.305 m) wide annular region between the outer surface of the reactor insulation and the inner surface of the concrete biological shield. Flow paths through the reactor pedestal and biological shield are indicated by dotted lines; as shown, they connect Cells 1 and 6, 2 and 5, 3 and 4, 7 and 4, and 7 and 9.

Cell 10 of the model is a large single-cell representation of the secondary containment, both reactor building and refueling bay. Its purpose is to trap leakage flows from the drywell shell either by temporary lifting of the drywell head or by temperature-induced failure of the drywell shell at the level of the floor. Cell 11 represents the outside environment and collects any gases that escape from the secondary containment (cell 10) or are vented from the primary containment via the wetwell airspace, which constitutes Cell 12 of the model.

2.2 Debris Spreading Methodology

The currently released version of the CONTAIN code allows for the time dependent addition of debris mass onto the drywell floor and the calculation of the subsequent debris/concrete interaction via the CORCON module. The

debris/concrete reaction is calculated for a well-defined user input "crucible" geometry, but no allowance is made for consideration of a time dependent lateral spreading of molten core debris across a flat floor, such as would be expected to occur in the BWR Mark I drywell. Accordingly, the code user must attempt to simulate debris spreading by stopping and restarting the calculation. It is the purpose of this Section to explain the rationale behind performing multiple CONTAIN calculations, with each calculation considering increasing areas of the drywell floor being affected by the debris/ concrete interaction.

Because the initial debris pour from the reactor vessel as defined by the BWRSAR calculation is metallic, lasts for only 30 minutes, and has very little superheat [Temp = 2750°F (1783 K)], the debris freezes on the drywell floor and is not able to spread. In addition, the initial debris pour barely fills the drywell sump [Volume = 206 ft^3 (5.83 m^3)] and thus physically would not be able to spread throughout the drywell. The time between termination of the first pour and the beginning of the second pour is approximately 1 h. It is reasonable therefore to consider an initial debris/concrete interaction that is confined to the inpedestal region of the drywell. Thus, for the purpose of analyzing the initial debris/concrete reaction, a "crucible" geometry representative of the inpedestal region of the drywell floor was assumed.

According to the BWRSAR calculation, the initial pour begins at time 263 min. after scram and is terminated at time 298 minutes. Starting at about 360 min., a second debris pour is predicted; this pour is a mixture of oxides and metals that exits the vessel at a temperature higher than that of the first pour. The second debris pour is added to the floor debris already present, and the mixed debris temperature begins to rise rapidly.

By time 375 min., the height of the debris in the inpedestal region extends 3.1 in. (0.08 m) above the drywell floor level. In addition, the oxide portion of the debris has been sufficiently diluted by concrete slag oxides (SiO_2,CaO) so that the oxide solidus temperature is lowered to 2523°F (1657 K). The oxide temperature at this time is 2655°F (1730 K). Thus, a reason exists for increasing the debris/concrete interaction area being analyzed by CORCON in order to simulate the increased interaction area caused by probable debris spreading into the expedestal area of the drywell floor. The question that remains to be answered is: How large a radius is appropriate for initial debris spreading into the expedestal area? Also, once the extent of initial expedestal debris spreading has been determined, a separate CONTAIN calculation must be initiated as CONTAIN cannot be instructed by user input to perform the simple maneuver of moving debris from the debris/concrete interaction occurring in one cell to another cell and to begin a new debris/ concrete interaction calculation in the new cell.

Using the method proposed by Kazimi[3] to estimate the extent of initial debris spreading over the expedestal floor, it was determined for these calculations that the initial spread area in the expedestal region should be 800 $ft.^2$ (74.3 m^2). Therefore, a second CONTAIN calculation was initiated with debris/concrete interactions continuing on the inpedestal floor [322 ft^2 (27.9 m^2) - Cell 1] and beginning on the expedestal floor [800 ft^2 (74.3 m^2) -

Cell 6]. The results of this calculation showed that after only three additional minutes the debris conditions on the expedestal floor were appropriate for further spreading over the remaining 300 ft^2 (27.9 m^2) of the expedestal region.

The short duration of the second calculation is caused by the very rapid pour from the failed reactor vessel during this period (Fig. 1), the large superheat of the molten metals assumed to flow into the expedestal area, and the large expedestal energy release from chemical reaction of zirconium with gases released by the ablation of concrete. Thus, the expedestal debris is predicted to accumulate rapidly and to remain molten.

During the three minute period of the initial debris spread into the expedestal region, the metals portion of the continuing pour from the reactor vessel is predicted by BWRSAR to be molten and superheated, while the oxide portion of the pour is frozen. Accordingly, it was assumed that 80% of the oxide pour remained inpedestal while 20% of the oxide pour was injected directly into the expedestal region. For the metals, it was assumed that one percent was kept inpedestal due to adhesion upon the surfaces of the frozen oxides. An exception was made for the zirconium metal to model its eutectic formation with the oxides; an additional 10% of the zirconium metal was kept inpedestal so that only 89% of this metal was directed into the expedestal region.

After time 378 min., when the debris expedestal is modeled to spread over the entire 1100 ft^2 (102.2 m^2) of expedestal floor area, the apportionment of the continuing debris pour from the reactor vessel between the inpedestal and expedestal areas remained the same as before; the basis being that the metals continued to be molten and superheated while the oxides were frozen.

After time 515 min., the oxide debris pour is molten as well as the metals. Thus, there is no reason to preferentially retain oxides in the inpedestal region. From this time until the end of the calculation at 900 min., the apportionment of the predicted debris pour was made strictly according to the respective floor areas; thus, 23% was kept inpedestal and 77% was introduced into the expedestal region.

As a summary of the above, three CONTAIN calculations were required to perform the analyses discussed in this paper. The first CONTAIN calculation is used to estimate events during the period from 255 to 375 min. and corresponds to the debris/concrete interaction period when the debris resides on the inpedestal region of the drywell floor. The second CONTAIN calculation, only three minutes long (375 to 378 min.), corresponds to the initial spreading of debris onto the expedestal floor. Simultaneous debris/concrete interactions are analyzed both inpedestal and expedestal with CORCON being independently active in both Cells 1 and 6 (see Fig. 2). As modeled by user input to the BWRSAR calculation that allocates the pours between the inpedestal and expedestal regions, inpedestal debris sources are rich in frozen oxides while expedestal sources are rich in molten metals.

The final calculational period from 378 until 900 min. constitutes the domain of the third CONTAIN calculation. Again, simultaneous but independent inpedestal and expedestal debris/concrete interactions were calculated, but this time the debris/concrete interaction area for the expedestal calculations was increased from 800 ft^2 (74.3 m^2) to the full expedestal floor area of 1100 ft^2 (102.2 m^2). For times prior to 515 min., the reactor vessel debris pours predicted by BWRSAR are comprised of frozen oxides and molten metals. Therefore, the inpedestal debris sources again are rich in frozen oxides while the expedestal sources are rich in molten metals. After 515 min., both the metal and oxide flows from the vessel are molten, and debris sources of uniform composition are added to the inpedestal and expedestal floor areas.

2.3 Assumptions Regarding Lifting of the Drywell Head

The model for lifting of the drywell head is taken from the discussion beginning on page 58 of the recently completed Chicago Bridge and Iron Company study of Peach Bottom containment strength (Ref. 4). In recent gasket tests at Idaho National Engineering Laboratory (Ref. 5), gaskets similar to those used at Peach Bottom withstood differential pressures of 160 psi (1.103 MPa) combined with temperatures of 700°F (644 K), but then failed catastrophically as the temperature was increased to 730°F (661 K). Greg Krueger of PECo has confirmed that the drywell head gaskets at Peach Bottom are replaced each refueling. Then, with the assumption of normal (0.04 in.) gasket springback, a leakage area would not ordinarily begin to open until the drywell pressure reached 175 psia (1.207 MPa).[4] However, recognizing that the results of the CONTAIN calculations discussed here involve drywell head temperatures well in excess of 700°F (644 K), a leakage area is assumed to open for these calculations when the temperature of the drywell head reaches 730°F (661 K). As modeled, the leakage area increases linearly from zero at 97 psia (0.669 MPa) to a value of 62 $in.^2$ (0.04 m^2) as the pressure increases to 215 psia (1.482 MPa).

3. CALCULATED RESULTS

Table 1 presents the limestone common sand concrete composition used at Peach Bottom and the composition of high limestone concrete. As seen from this table, limestone common sand concrete contains less carbon dioxide than high limestone concrete. In addition, it has an ablation temperature [2246°F (1503 K)] significantly lower than that of high limestone concrete [2694°F (1752 K)]. The reader should keep these considerations in mind as the results presented in this section would be significantly altered by a change in concrete types.

The CONTAIN calculation was initiated just before reactor vessel bottom head penetration failure (255 min.) with the initial drywell cell temperatures taken from BWRSAR code results, and the CORCON calculation of the debris/concrete interaction was initiated 10 minutes later. The intercell flows and cell temperatures 10 min. after bottom head penetration failure and the beginning of gas release from the depressurized reactor vessel into the drywell are

shown in Figs. 3a and 3b, respectively. The highest atmosphere temperature, as expected, is in the uppermost inpedestal cell, immediately beneath the reactor vessel. As shown in Fig. 3a, two natural circulation flows are set up by the calculation: a clockwise flow between the inpedestal and lower expedestal region, and a counter-clockwise flow between the upper expedestal region and annular Cell 7 that represents the volume between the reactor vessel and the biological shield.

Primary containment atmospheric temperatures and flows at time 593 min., which is immediately after leakage from the drywell head flange seals is expected to begin, are shown in Fig. 4. The high temperatures that occur at this time are due to continuous concrete ablation, the associated gas release into the debris, the metal oxidation therein, and the escape into the atmosphere of gases sparged through the debris. The gas temperature in Cell 8 is high enough at this time that the temperature of the heat sink representing the drywell head is predicted to exceed 730°F (661 K).

As explained in Section 2.3, the drywell head seals are modeled to fail catastrophically once they reach 730°F (661 K). Because the drywell pressure, Fig. 5, is 126 psia (0.869 MPa), the head is modeled to be lifted at this time so that a leakage area of 15.5 in.^{2} (0.010 m^2) ensues when the seals fail. This leakage directly enters the refueling bay and therefore bypasses the reactor building. It is represented in Fig. 4a as an arrow leaving Cell 8. Once the head seals fail, the drywell pressure decreases to about 98 psia (0.68 MPa). This pressure is representative of the maximum pressure that could be maintained if the drywell head had no seals. A small leakage flow continues to occur until the end of the calculation at 900 min. as the debris/concrete interaction continues to release gas into the drywell atmosphere and thus provides a continuous pressure source to maintain a small flange separation.

The configurations of the debris layers on the drywell floor just before and just after initial spreading into the expedestal region are shown in Table 3. In particular, it can be noted that ablation of the inpedestal concrete is significant. The bottom of the debris sinks from −7.71 inches (floor of the original sump configuration) to −16.26 inches during the period 265–375 min.

Radial concrete ablation in the inpedestal region as calculated by CONTAIN is significant, as shown in Fig. 6, which indicates the maximum radius of the lowest inpedestal cell as a function of time. The plotted curve begins when the CORCON calculation is initiated, at time 265 min. The initial value of 10.125 ft (3.09 m) is the radius to the inner pedestal in its original configuration. Pedestal ablation is most rapid during the early part of the calculation, when zirconium oxidation is occurring. About seven percent of the original pedestal width is predicted to be consumed during the period prior to the initial spread into the expedestal region.

Comparison of the radial concrete ablation shown in Fig. 6 to the axial ablation shown in Table 3 reveals that the predicted radial ablation at the time (375 min.) of initial spread into the expedestal region is much less than the predicted axial ablation (0.2 ft radial vs 0.7 ft axial).

There are two reasons for this. First, the lower portion of the inpedestal debris consists of a relatively thin layer of frozen metals so that the resistance to heat transfer by conduction in the radial direction is much larger than the resistance in the axial direction. Second, although there is no appreciable radial crust in the partially liquefied layer of oxides overlying the metals, the convective heat transfer in the radial direction is limited in this layer by the stable gas film maintained at the interface between the debris and the concrete. Because the gas flow in this vertical film at the outer radius of the debris is laminar, the CORCON module assigns a Nusselt number (1.0) close to the Nusselt number (0.804) used for the horizontal gas film at the base of the frozen metallic layer. Since both of these Nusselt numbers are defined directly in terms of the gas film thickness, the thicker gas film at the vertical interface results in a convective heat transfer coefficient smaller than that for the horizontal interface, where the gas film is much thinner. Thus, the predicted downward heat transfer and ablation exceed the radial heat transfer and ablation.

The debris/concrete interaction begins in the expedestal region at 375 min., just after the debris inpedestal has accumulated to a sufficient depth and molten state to be modeled to flow through the pedestal doorway. As explained in Section 2.2, the initial expedestal area covered by this debris flow is 800 ft^2 (74.3 m^2). Since the entire expedestal floor area is only 1100 ft^2 (102.2 m^2), this initial spreading area supports the contention that the entire expedestal floor area would be covered quickly, especially in light of the large debris pour rate leaving the reactor vessel at this time and the large amount of superheat associated with the metals flowing to the expedestal region of the floor. Indeed, only three additional minutes of pour produce conditions for which the spreading debris would completely cover the expedestal floor.

The expedestal debris temperatures are shown in Fig. 7. They reach their maximum values during the period from 375 to 430 min. These high temperatures are calculated because of the oxidation of zirconium metal as it is being added to the expedestal floor area. A comparison of energy release rates due to chemical and decay heat sources is provided in Fig. 8. Chemical power is much larger than decay power during the period before exhaustion of the zirconium metal at time 435 min. and clearly is the reason for the calculated high debris temperatures expedestal during this period.

As discussed in Section 2, the debris source to the expedestal region of the drywell floor is metals-rich during the period between the initial spread into this region and the time when the temperature of the vessel pour is sufficient to result in molten oxides. During this 140-min. period from time 375 to time 515 min., 89% of the zirconium and 99% of the other metals in the ongoing pour are directed into the expedestal region. For the oxides in the pour, which are frozen during this period, 80% are modeled by CONTAIN code input to flow into the inpedestal region while 20%, assumed to be carried into the expedestal region with the molten metal flow, are directed into the expedestal region.

It is obviously important to consider to what extent the calculated debris temperatures in the expedestal region are dependent upon the assumed division of metals and oxides between the inpedestal and expedestal regions of the drywell floor. To this end, the pour partitioning was redone so that both metals and oxides were split between the inpedestal and expedestal regions strictly on the basis of the respective floor areas and the CONTAIN calculation of the drywell response was repeated. This exercise was performed both for the three-minute period immediately following the initial spread into the expedestal region, when the pour is divided between the 322 ft^2 (29.9 m^2) of the inpedestal region and 800 ft^2 (74.3 m^2) of the expedestal region, and for the final spread over the entire expedestal region.

The expedestal debris temperatures for this uniform debris composition case are shown on Fig. 9a and 9b, together with the temperatures for the best-estimate case. The overall temperature profiles for the two predictions have similar shapes. For the metal layer (Fig. 9a), the peak temperature is slightly higher for the uniformly distributed case, but the period during which the temperature remains elevated is correspondingly shorter. This is consistent with the assumed partitioning of the debris pours.

From time 378 to 515 min., the best-estimate expedestal debris pour is rich in metals, incorporating 89% of the molten zirconium and 99% of the molten stainless steel leaving the reactor vessel, but only 20% of the frozen oxides. During the same period, 77% of the metals and 77% of the oxides in the ongoing pour are directed into the expedestal region for the uniform composition case. Thus, the best-estimate calculation places more zirconium metal in the expedestal region and the predicted chemical energy source and the debris temperatures remain elevated longer than in the uniform case calculation.

On the other hand, the additional oxides added to the expedestal region in the uniform composition case overlie the metals and reduce the heat loss from the metal layer to the atmosphere. This causes the peak metal layer temperature to be slightly higher for the uniform composition case and, over the long term, the predicted temperature of the metal layer for this case remains about 50°F (28 K) higher than the metal layer temperature for the best-estimate metals-rich case.

In neither calculation does the predicted expedestal debris temperature exceed the melting temperature of the carbon steel drywell shell [2800°F (1810 K)] and, as indicated on Figs. 9a and 9b, the calculated temperature profiles are similar. Thus, although assumptions regarding the degree of lateral separation of the molten metals from the frozen oxides have some effect upon the calculated expedestal debris temperatures, these assumptions clearly are not the dominant parameters in determining the question of shell survivability.

The cumulative gas release from the concrete is provided in Table 2 for the limestone common sand concrete considered in this paper. It should be noted that most of the carbon dioxide and steam released from the concrete is consumed in metal-gas reactions within the debris; relatively little of these

gases escapes from the debris surface to enter the drywell atmosphere. It should also be noted that of the 1717 lb-moles released from the debris, 66% is hydrogen and 28% is CO. Thus, 94% of the released debris gas is combustible. This has important ramifications regarding the performance of the secondary containment if the primary containment fails.

A final threat to primary containment integrity is posed by the significant predicted erosion of the reactor pedestal illustrated by Fig. 6. As discussed earlier, about seven percent of the reactor pedestal is predicted to be eroded at the time of initial spreading of debris into the expedestal region. An additional 23% of the original pedestal is predicted to be eroded by the end of the calculation. However, this predicted 30% reduction in pedestal wall thickness is probably a minimum estimate since the attack upon the pedestal wall from the other side by the expedestal debris (after time 375 min.) is not considered in the calculation.

Table 4 provides the time-history of the conditions at the debris-shell interface as calculated by CONTAIN for the periods during which the metal and oxide temperatures in the expedestal region are sufficiently high to challenge the integrity of the shell. As shown on Fig. 7, these temperatures approach the melting temperature of carbon steel [2800°F (1810 K)] during the one hour period 375–435 min. after scram. The maximum debris temperature predicted for the expedestal region during this period is 2706°F (1759 K) for the metal layer at time 418 min.; the calculated debris temperatures decrease rapidly after this peak.

Conclusions regarding the effect of the debris-shell interface upon continued integrity of the drywell shell pressure boundary cannot be reached without additional calculations to determine the thermal response of the shell. Although the predicted debris temperatures are clearly not high enough to cause shell melt-through, failure of the shell pressure boundary through loss of strength is possible. [Because of the uncertainty of this failure mechanism, a flow path between Cells 6 and 10 (lower expedestal region to secondary containment) modeling this failure was not allowed in the current analysis. As described earlier, thermally induced failure of the drywell head seals is modeled and is calculated to occur at time 593 min.] A detailed thermal and stress analysis should be performed for the drywell shell throughout the region of contact with the hot debris to address this issue. It is for this purpose that the time-dependent debris conditions in the expedestal region together with the internal pressure loading of the drywell shell as calculated in this study are provided in Table 4. In particular, this detailed information pertaining to the calculated conditions at the interface during the period of elevated debris temperature is intended for use by interested parties who desire to perform shell response calculations with codes such as HEATING-6 or TAC-2D.

As mentioned previously, the CONTAIN calculations for this case without drywell sprays were terminated at time 900 min. (15 h) after scram. Approximately 98% of the reactor vessel bottom head debris has become molten and left the vessel by this time, and most of the lower portion of the bottom head wall has been subsumed into the debris on the drywell floor. In the

expedestal region, the base of the metal layer is predicted to have sunk 12.9 inches (32.7 cm) beneath the original level of the floor. All of the zirconium metal has long since oxidized, and the metal layer consists only of the frozen (but still very hot) constituents of stainless steel, whose oxidization by gases released by the continued ablation of concrete is slow. Overlying the 9.5-inch (24.2-cm) thickness of frozen metal is a 15.6-inch (39.6 cm) thickness of oxide slurry at a temperature of 2471°F (1628 K), extending to a height of 12.3 in. (31.1 cm) above the original level of the floor. Since the debris pour from the reactor vessel is for all practical purposes terminated at this point, it is reasonable to assume that this is the maximum height that the debris would reach against the drywell shell. Continuation of the CONTAIN calculation to times beyond 900 min. would be expected only to predict that the frozen metal slug and its overlying oxide slurry would continue to slowly sink into the concrete remaining beneath the debris.

4. REMAINING DEFICIENCIES AND UNCERTAINTIES IN CURRENT ANALYSIS

Although the advanced capabilities provided by CONTAIN Version 1.1 greatly improve the efficacy of the code for BWR severe accident applications, the results of this work have made it clear that there are several remaining areas where the present capability must again be expanded if the code is to become adequate for BWR Mark I containment severe accident calculations. Major areas include:

1. Improved representation of concrete degassing. Within the latest released version (1.1) of CONTAIN, none of the gas (H_2O and CO_2) stored in the concrete is released unless and until the temperature of the overlying debris is sufficient to cause ablation. Clearly, this is inadequate during certain times during the accident sequence when the debris cools to below the ablation temperature. It is expected that some degassing of the concrete would occur and would indirectly provide an energy source to the debris via chemical reaction of the gas with unoxidized zirconium.

   The calculations discussed in this paper were performed with an advanced version of CONTAIN provided to the BWRSAT Program at ORNL by the code development staff at SNL. This advanced version partially corrects for the above degassing deficiency. It allows for degassing in the absence of ablation via the use of calculated 1-dimensional concrete temperature profiles and user prescribed temperature release ranges for H_2O (bound and evaporable) and CO_2. While this is a large step forward, it is also desirable that the CONTAIN code be further improved to provide accurate representation of the effects of concrete degassing ahead of the ablation front during periods of unsteady concrete ablation. Although the additional gas release due to accurate modeling of degassing during periods of rapidly increasing debris temperature may be only a fraction of the gas release due to ablation, there are significant periods of time during the present calculation when the metal oxidation reactions in the debris are gas-starved. Therefore, any additional gas release from the

concrete during these periods would be reflected in higher metal oxidation rates and higher temperatures. It is recommended that these advanced degassing models be included in future released versions of CONTAIN.

2. Representation of debris melting. The algorithms for determination of the state of the debris components in the CORCON module of the current released version of CONTAIN are very deficient for BWR severe accident applications. Debris melting is characterized by a determination of solidus and liquidus temperatures applicable only to the vertically separated layer configuration assumed by the CORCON model. Within the metal layer, a tertiary phase diagram is used to determine the melting temperature of the stainless steel according to the relative amounts of its constituent iron, nickel, and chromium. As long as stainless steel is present (there would be an enormous amount of stainless steel in BWR debris), the presence of zirconium metal is ignored and the melting temperature of the metal layer is set equal to the melting temperature of the stainless steel. In actuality, the zirconium metal would be expected to enter into the formation of a eutectic mixture with much of the stainless steel.

   For the oxide layer, the ZrO_2 and UO_2 components are grouped as "fuel" oxides while the oxides created by concrete decomposition are treated separately. A simple phase diagram that provides a melting temperature for a ZrO_2-UO_2 mixture based upon the relative mole fractions is provided within the code for the fuel oxides. The composition and melting temperature of the fuel oxides is combined with that of the concrete oxides to determine the resulting solidus and liquidus temperatures of the oxide layer.

   Difficulty arises with the simple CORCON phase representation for the ZrO_2-UO_2 mixture in that the lowest melting temperature on the diagram is 4625°F (2825 K), which occurs at 56 mole percent ZrO_2. For example, if the BWRSAR code were to predict a pour of molten ZrO_2-UO_2 eutectic at 4352°F (2673 K), the CORCON module within CONTAIN would, upon receipt of this pour, recognize it to be frozen. Thus, the latent heat of fusion for the pour would be lost from the calculation.

   Therefore, in order to perform the calculations reported here, it was necessary to implement a local (ORNL) code modification to reduce the melting temperature of the ZrO_2-UO_2 mixture recognized by CONTAIN/CORCON to 4350°F (2672 K). With this local modification, CONTAIN/CORCON recognizes the molten oxides pouring from the reactor vessel to be molten. It is recommended that modifications be installed in future versions of CONTAIN/CORCON to provide a more realistic representation of the Zr-UO_2 phase diagram or at least, to provide the code user with the ability to set the oxide mixture melting temperature by code input.

3. Representation of B_4C powder. Although there is a significant amount of B_4C powder within the BWR control blades [about 12 lbs (5.4 kg) per blade], the current CONTAIN/CORCON module gives no consideration to the

effect of boron carbide powder upon the core debris or its interaction with the concrete floor. It is recommended that appropriate models, based upon available experimental data, be implemented.

4. Spreading of debris on the drywell floor. There are no models in the current version of CONTAIN to simulate the lateral spreading over the drywell floor of molten bottom head debris released from the reactor vessel. Such a capability should be developed and implemented into CONTAIN. The most important benefit to be gained from a mechanistic debris spreading model is the improved calculation of the oxidation of metals on the drywell floor. As discussed in Section 2 of this paper, metal and oxide debris pours were prescribed for the various regions of the drywell floor based on the spreading analysis developed by Kazimi and the physical state of the debris as it left the failed reactor vessel. For the metals leaving the reactor vessel, this means that independent but simultaneous metal sources appear in the CORCON calculations for inpedestal and expedestal areas. This is nonrealistic because fresh metal would appear first in the inpedestal region beneath the failed reactor vessel and then flow through the pedestal doorway into and around the expedestal region, becoming progressively oxidized along the way. Thus, the chemical energy release in the expedestal region would be greater in the vicinity of the expedestal doorway and less in the more remote areas of the drywell floor. As shown in Section 3, it is this chemical energy release that establishes the maximum temperature of the bulk debris adjacent to the drywell shell.

5. Debris Layer Structure.

   a. The debris layer structure as currently modeled in CORCON is based upon an assumption that individual layers of oxides and metals always exist. During periods of rapid ablation, gas sparging through molten debris makes this debris layering assumption questionable. It is recommended that the CORCON module be modified so that the mixing of the metals and oxides can be calculated automatically or at least controlled with user input. It should be recognized that this in turn will lead to questions concerning the large uncertainties in the chemical and thermophysical environment existing in such a mixture of metals and oxides.

   b. A second change should be implemented in CORCON with respect to the processing of debris added via debris source tables. At present, the new debris is added to the uppermost layer of the previous debris and the temperature of the added debris is immediately equilibrated with the average temperature of the upper layer. For massive upper layers that are calculated to be completely frozen, addition of debris sources in this manner results in temperature gradients in the upper layer crust that are of incorrect sign. This is because the CORCON model prescribes that melting of the uppermost layer be from the interior of that layer. This is inconsistent with the physical situation in which the added debris would reside on top of the upper frozen layer, and thus melting of that layer would not be from the interior

but would occur from the upper surface in contact with the newly added debris.

A potential solution to this problem would be to create a new layer within the existing CORCON layering scheme. This new layer should be thin and located at the top of the debris. Heat and mass transfer should be across the interface of the thin layer with the underlying thick layer.

c. A third change in the CORCON layering scheme should be implemented to address a problem associated with modeling the BWR drywell sumps. The BWR Mark I drywell sumps are small (~6 m^3) and hold roughly 10% of the debris expected to leave a failed BWR reactor vessel. Thus, it is probable that the sumps would be completely filled with metallic debris during the initial metallic pours with some metals remaining to overflow onto the rest of the inpedestal drywell floor. When this occurs, there are two radically different characteristic geometries with which the metal layer is simultaneously associated. The problem in the current application of CORCON is the way in which the crusting model is implemented. The crusting model considers individual debris layers and represents them as cylindrical in shape, using layer thickness and layer volume to calculate an equivalent layer cross sectional area and thus an equivalent layer radius. For the situation described previously with the metals overflowing the sumps, the code simply adopts a cross-sectional area between that of the sumps and that of the inpedestal floor area. As a result of this approach, the crusting model cannot arrive at crusting estimates appropriate for either the sump or the inpedestal geometry. Since debris crusting is a dominant resistance to heat loss from the debris, a deficiency in this model is not of a minor nature. For the calculations performed for this paper, the sump volume was conserved by user input, but the floor area was set to 322 ft^2 (29.9 m^2) – the inpedestal cross-sectional area.

A potential solution to this problem of similar materials in different geometries would be to allow for multiple layers for the same debris. For material filling the sumps and overflowing onto the drywell floor, it seems reasonable to place the material in the sump in one layer and to place the remainder of the debris that overflows onto the floor in another layer. In this way the crusting model as implemented in CORCON would calculate two characteristic crusts for that material – one appropriate for the geometry of the sump and the other appropriate for the inpedestal floor area.

5. SUMMARY

CONTAIN calculations of primary containment response have recently been completed for the Peach Bottom Short Term Station Blackout accident scenario. The specific calculations performed address the debris/concrete interactions that would occur on the floor of the Mark I drywell for the case without drywell sprays. Debris pours from the failed reactor vessel were taken from BWRSAR analyses of the in-vessel response during this scenario.

Three separate CONTAIN calculations were required in order to perform the containment response analysis. The initial CONTAIN calculation addresses the containment response during the time frame 255–375 min. when the debris leaving the reactor vessel via failed bottom head penetrations is expected to remain in the inpedestal region of the drywell floor. The second CONTAIN calculation concerns the time frame of the initial debris spread into the expedestal area, 375–378 min. The extent of initial debris spreading over the expedestal floor was estimated to be 800 ft^2 (74.3 m^2) and was based on a method proposed by Kazimi.

The reason for the short duration of the second CONTAIN calculation is the rapid pour of debris from the failed reactor vessel during this period and the growing superheat of the metallic debris assumed to spread into the expedestal area. The oxidic debris is initially frozen as it leaves the reactor vessel, and for the period of the second CONTAIN calculation, 80% of the oxidic core debris is retained in the inpedestal area with only 20% assumed to flow into the expedestal area. For the metals, it was assumed that one percent was kept inpedestal due to adhesion upon the surfaces of the frozen oxides. An exception was made for the zirconium metal to model its mixing with the oxides; an additional 10% of the zirconium metal was kept inpedestal so that only 89% of this metal was directed into the expedestal region.

The third CONTAIN calculation concerns the time frame 378 to 900 min., for which debris was spread over the remaining 300 ft^2 (27.9 m^2) of the expedestal area. By 515 min., the oxidic debris leaving the reactor vessel was molten along with the metals so that debris partitioning between the inpedestal and expedestal floor areas was based strictly on the floor areas involved. Thus, 77% of all the oxides and metals was placed expedestal (1100 ft^2) while 23% of all the metals and oxides was placed inpedestal (322 ft^2). Prior to time 515 min., debris partitioning was the same as the second CONTAIN calculation.

Results of the CONTAIN analysis indicate that the drywell head flange seals would fail due to thermal degradation at time 593 min. Because the drywell pressure is 126 psia at the time of predicted head seal failure, the head is calculated to lift with the resulting leakage area of 15.5 $in.^2$ (0.010 m^2). The resulting leakage flow would proceed directly into the refueling floor. Smaller leakage flows were calculated after this time due to the pressurization provided by the continuous gas release from the debris/concrete reactions.

Expedestal debris temperatures reach a maximum of 2706°F (1759 K), somewhat below the melting temperature of 2800°F (1810 K) for the carbon steel drywell shell. Although shell burn-through is not indicated, shell integrity is still in question as failure may occur by loss of strength. The debris conditions adjacent to the shell as well as the containment pressure are reported so that more detailed thermal and stress analysis may be performed.

Ablation of the reactor pedestal wall is significant. Results indicate that about 30% of the reactor pedestal thickness is consumed by ablation from

the inpedestal debris. Although not calculated by the expedestal debris/concrete analysis, it is believed that a similar amount of ablation may occur on the outer surface of the pedestal due to attack by expedestal debris.

Cumulative gas release from the debris at the end of the calculation totals 1717 lb-moles. Of this, 1135 lb-moles or 66% of the released gas is H_2 while 485 lb-moles or 28% is CO. Thus, 94% of the released gas from the debris entering the drywell atmosphere is combustible. This has some important ramifications regarding the performance of the secondary containment should the primary containment fail.

Finally, several deficiencies have been identified in the CONTAIN adaptation of CORCON that should be addressed for future best-estimate BWR applications. These include: (1) representation of concrete degassing during periods of unsteady concrete ablation, (2) improved representation of debris melting behavior, (3) chemical and thermophysical representation of boron carbide, and (4) development of an automatic debris spreading model. In addition, three deficiencies have been identified concerning the layer structuring assumed by the CORCON module of CONTAIN. First is the strict adherence to the layering approach during periods of rapid gas sparging through the debris; it is probable that the debris is uniformly mixed. Second is the way in which debris sources are added to the upper layer of the debris. If the upper layer is thick and completely crusted (i.e., frozen), incorrect temperature profiles may be calculated in the frozen layer. A third deficiency concerns the inappropriate method used by CORCON in the determination of radial crusts for layers that experience drastic changes in geometry. The particular BWR application where this problem is most apparent occurs when trying to model the small drywell sumps. In this situation, it may be possible for either metallic debris or oxidic debris to completely fill the sumps and to overflow onto the inpedestal drywell floor. However, the crusting model calculates radial crusts that are not appropriate for either the sumps or for the inpedestal floor. Clearly, the way to resolve this problem is to allow for multiple layers of the same debris.

6. REFERENCES

1. K. K. Murata et al., *Users Manual for CONTAIN 1.1 - A Computer Code for Severe Nuclear Reactor Accident Containment Analysis*, SAND 87-2309 (to be published).

2. S. A. Hodge and L. J. Ott, *BWRSAR Calculations of Reactor Vessel Debris Pours for Peach Bottom Short-Term Station Blackout*, presented at 16th Water Reactor Safety Information Meeting, October 27, 1988.

3. M. S. Kazimi, "On the Liner Failure Potential in Mark-I BWRs," Department of Nuclear Engineering, Massachusetts Institute of Technology, (to be published in *Nuclear Science and Engineering*).

4. CBI NA-CON, Inc., "Mark I Containment Severe Accident Analysis," for the Mark I Owners Group (April 1987).

5. T. L. Bridges, "Containment Penetration Elastomer Seal Leak Rate Tests," NUREG/CR-4944, SAND87-7118, July 1987.

Table 1. Comparison of the constituent weight fractions of Peach Bottom concrete vs high limestone concrete

Constituent	Peach Bottom	High Limestone
Al_2O_3	0.009	0.016
CaO	0.338	0.454
CO_2	0.206	0.357
SiO_2	0.358	0.036
Free H_2O	0.045	0.039
Bound H_2O	0.027	0.020
Other	0.017	0.078
	1.000	1.000

Table 2. Cumulative gas release at termination of calculation for Peach Bottom Station Blackout with ADS actuation and limestone common sand concrete Time 900 min.

	lbs	lb-moles
Gas release from concrete		
CO_2	61,555	1399
H_2O	21,339	1184
	82,894	2583
Gas release from debris surface		
CO_2	2,180	49.5
H_2O	847	47.0
CO	13,592	485.3
H_2	2,289	1135.6
	18,908	1717.4

Table 3. Debris configurations before and after spreading at time 375.0 min for Peach Bottom Short-Term Station Blackout with ADS actuation and limestone common sand concrete

Before Spreading
Inpedestal only (322 ft²)

(Inches)

3.13 _____ Tsolidus

oxides 2522°F
metals 2690°F

Floor 0.00 -----Oxides----- Toxide = 2654°F
Tmetal = 2536°F

Mass oxides = 73,971 lbm
Mass metals = 101,610 lbm

-7.01 _____

Metals

-16.26 _____

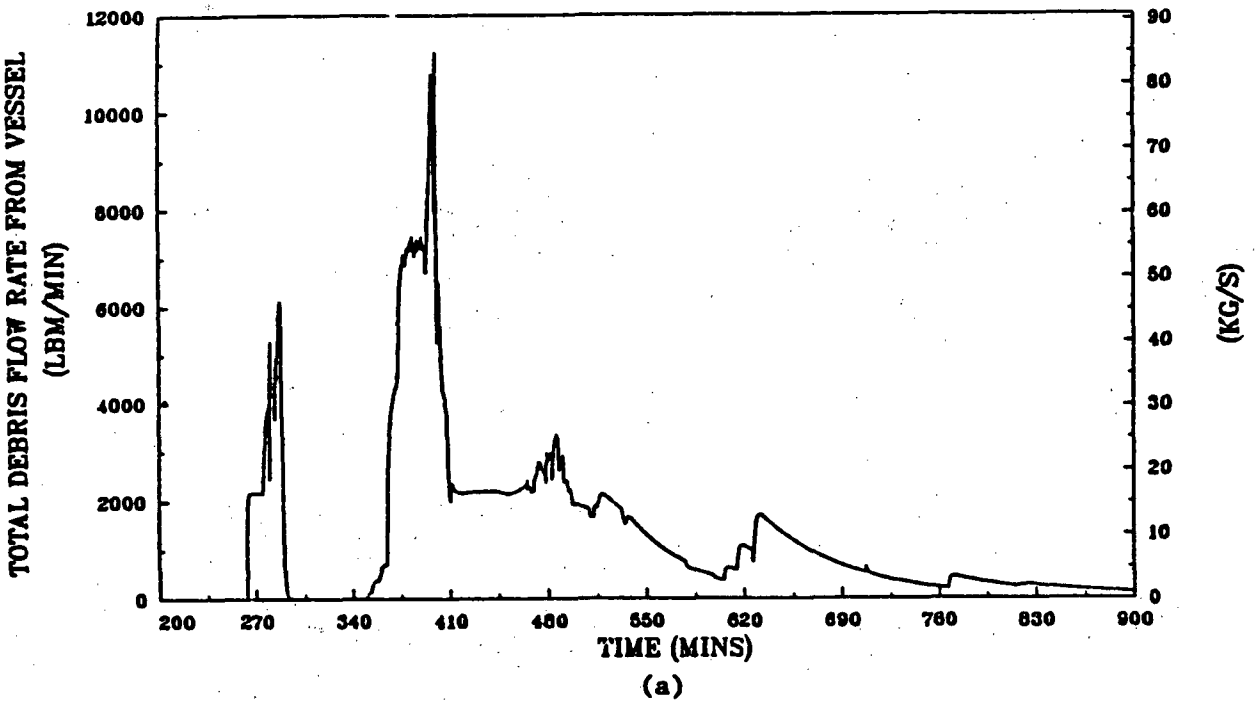
After Spreading:

Inpedestal (322 ft²)		**Expedestal (800 ft²)**	
0.98	_____	_____	.94
		Oxides	
		_____	.45
Floor 0.00	-----Oxides-----	-----Metals-----	0.00 Floor
		_____	-.01
-7.98	_____		
	Metals		
-16.27	_____		
Toxide = 2586°F		Toxide = 2592°F	
Tmetal = 2586°F		Tmetal = 2590°F	
Mass oxides = 65,847 lbm		Mass oxides = 8,442 lbm	
Mass metals = 90,199 lbm		Mass metals = 11,612 lbm	

Table 4. Expedestal debris conditions for Peach Bottom Short Term Station Blackout with ADS actuation and limestone common sand concrete

Time (min)	Zbot (in.)	$Z_{MET/LOX}$ (in.)	$Z_{LOX/ATM}$ (in.)	Mass metals (lbs)	T_{METALS} (°F)	$T_{SOLIDUS}$ METALS (°F)	LOX-mass light oxides (lbs)	T_{LOX} (°F)	$T_{SOLIDUS}$ (LOX) (°F)	Drywell Pressure (psia)
375.0	0.00	0.45	0.94	11,610	2590	2690	8,442	2592	2523	62.0
375.5	-0.04	0.46	1.00	12,860	2622	2690	9,298	2628	2526	63.7
376.0	-0.09	0.47	1.06	14,290	2654	2691	10,340	2659	2529	64.3
376.5	-0.14	0.48	1.14	15,810	2681	2691	11,430	2687	2531	64.6
377.0	-0.20	0.48	1.21	17,300	2693	2691	12,610	2692	2831	64.8
377.5	-0.26	0.48	1.28	18,810	2694	2692	13,830	2693	2531	65.0
378.0	-0.32	0.48	1.35	20,310	2695	2692	15,060	2695	2531	65.2
379.0	-0.42	0.40	1.20	25,450	2677	2692	19,610	2679	2538	65.7
380.0	-0.52	0.39	1.31	28,600	2685	2692	22,160	2685	2536	66.1
381.0	-0.63	0.39	1.42	31,890	2691	2692	24,770	2692	2534	66.5
382.0	-0.75	0.39	1.54	35,340	2693	2693	27,520	2692	2531	66.9
383.0	-0.87	0.39	1.66	38,970	2694	2693	30,310	2693	2528	67.2
384.0	-0.99	0.39	1.78	42,740	2696	2694	33,100	2695	2526	67.6
385.0	-1.11	0.38	1.90	46,460	2697	2694	35,880	2695	2523	68.0
386.0	-1.23	0.38	2.02	50,140	2697	2695	38,660	2696	2521	68.3
387.0	-1.35	0.38	2.14	54,010	2698	2695	41,440	2697	2519	68.7
388.0	-1.47	0.38	2.26	57,830	2699	2695	44,210	2697	2518	69.1
393.0	-2.07	0.40	2.89	77,700	2701	2696	58,030	2699	2510	70.5
398.0	-2.68	0.59	3.69	100,360	2701	2696	71,700	2698	2505	72.2
403.0	-3.28	0.70	4.42	127,000	2702	2696	85,720	2699	2504	74.3
408.0	-3.89	0.43	4.75	136,100	2703	2699	99,190	2700	2499	76.5
413.0	-4.50	-0.03	4.89	138,300	2704	2702	112,200	2702	2493	78.8
418.0	-5.10	-0.51	4.98	139,500	2706	2706	125,200	2695	2489	80.9
423.0	-5.54	-0.86	4.99	142,300	2680	2709	134,500	2651	2486	83.2
428.0	-5.87	-0.71	5.08	146,500	2647	2713	141,100	2609	2483	85.0
433.0	-6.16	-0.86	5.20	151,300	2630	2716	147,000	2575	2482	86.8
438.0	-6.41	-0.95	5.33	157,300	2538	2719	151,300	2545	2475	88.8
443.0	-6.59	-0.96	5.42	169,900	2472	2723	154,500	2509	2467	90.5

$T_{SOLIDUS}$ = Mixture temperature at which melting begins
LOX = Light oxides
HOX = Heavy oxides
Z = Elevation relative to original floor surface
MET/LOX = metal - light oxide interface
LOX/ATM = light oxide - atmosphere interface



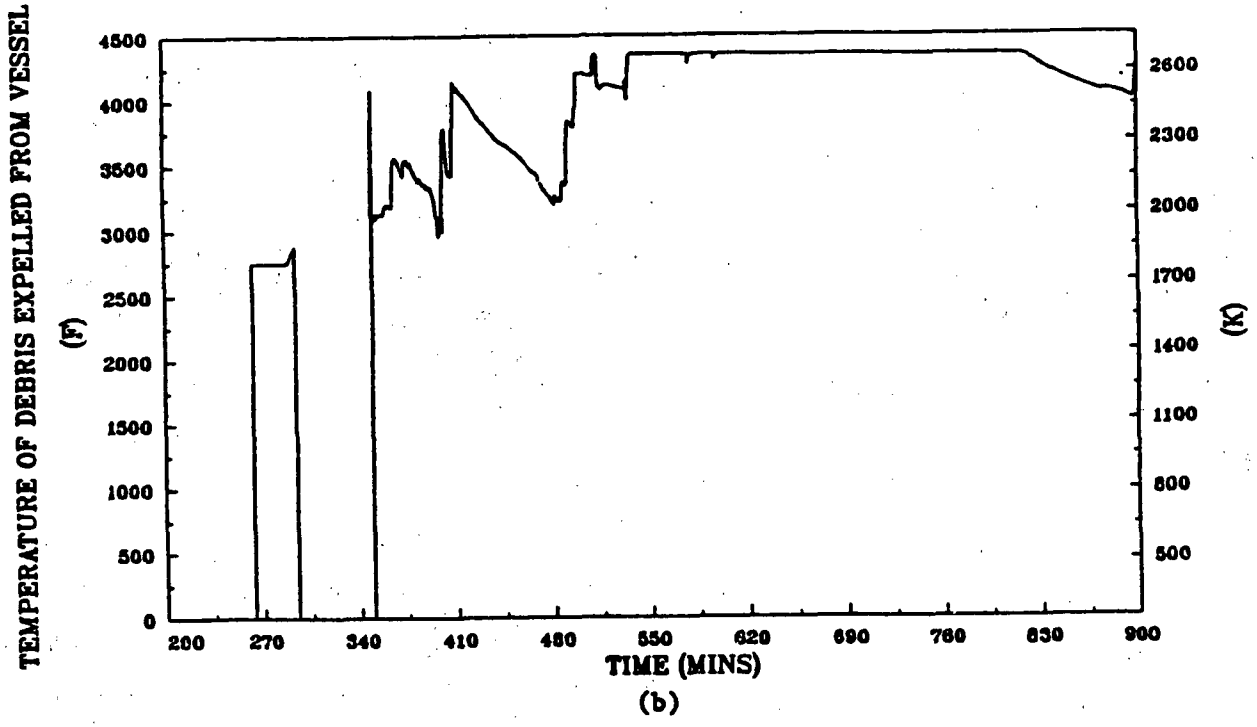


Fig. 1. Flow rates and temperatures of debris pours from the reactor vessel bottom head as predicted by the BWRSAR code for the short-term station blackout accident sequence with ADS at a unit of the Peach Bottom Atomic Power Station.

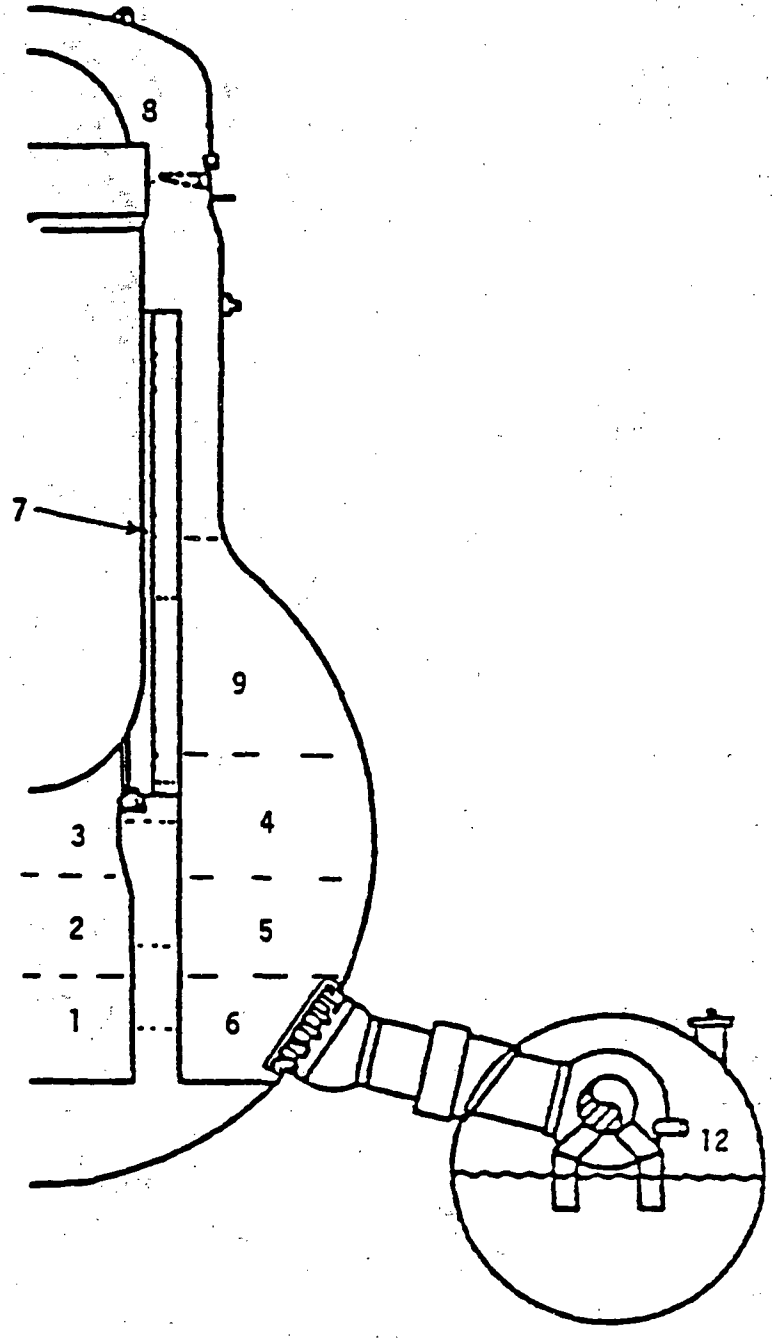
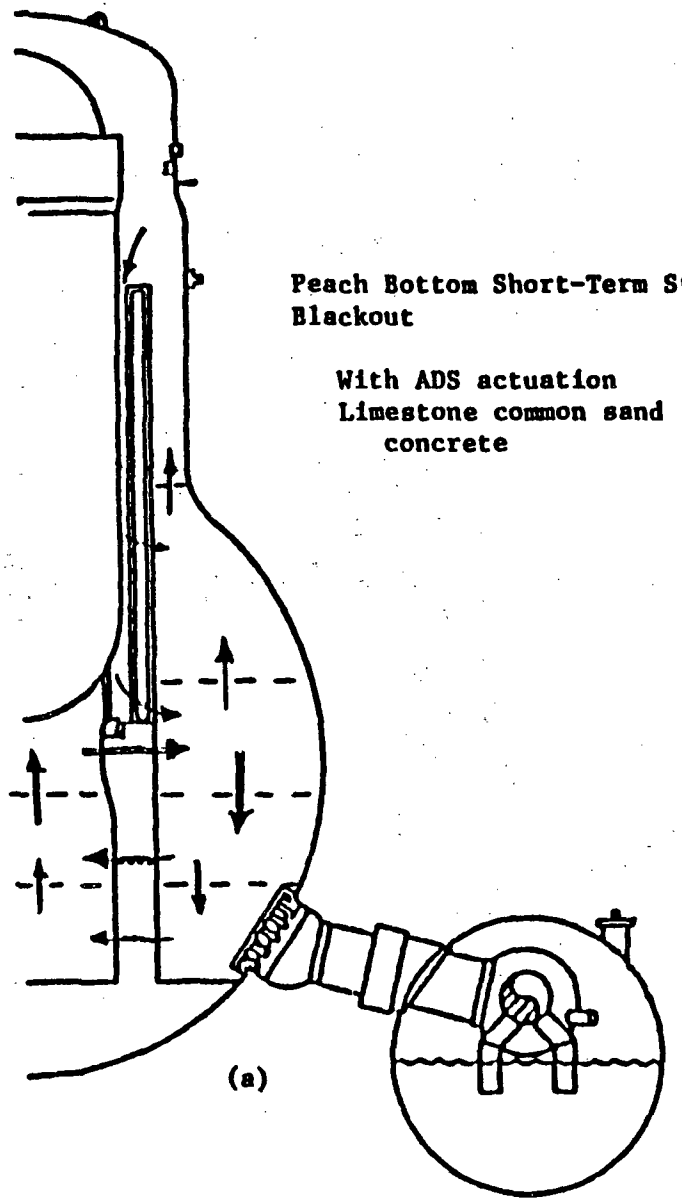


Fig. 2. BWRSAT Program Nodalization for the BWR Mark I Primary Containment. Not shown are cells 10 (secondary containment) and 11 (outside environment), which make up the balance of the complete CONTAIN model used for the Peach Bottom Calculations.



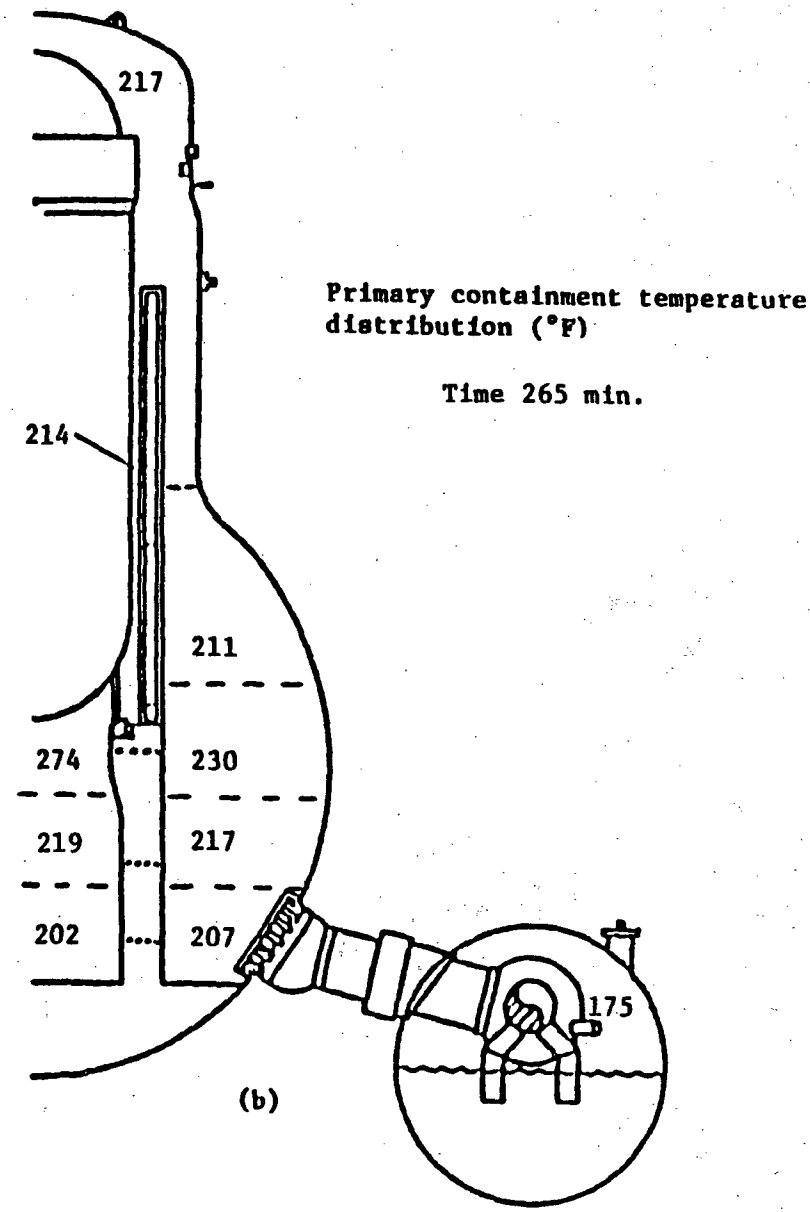
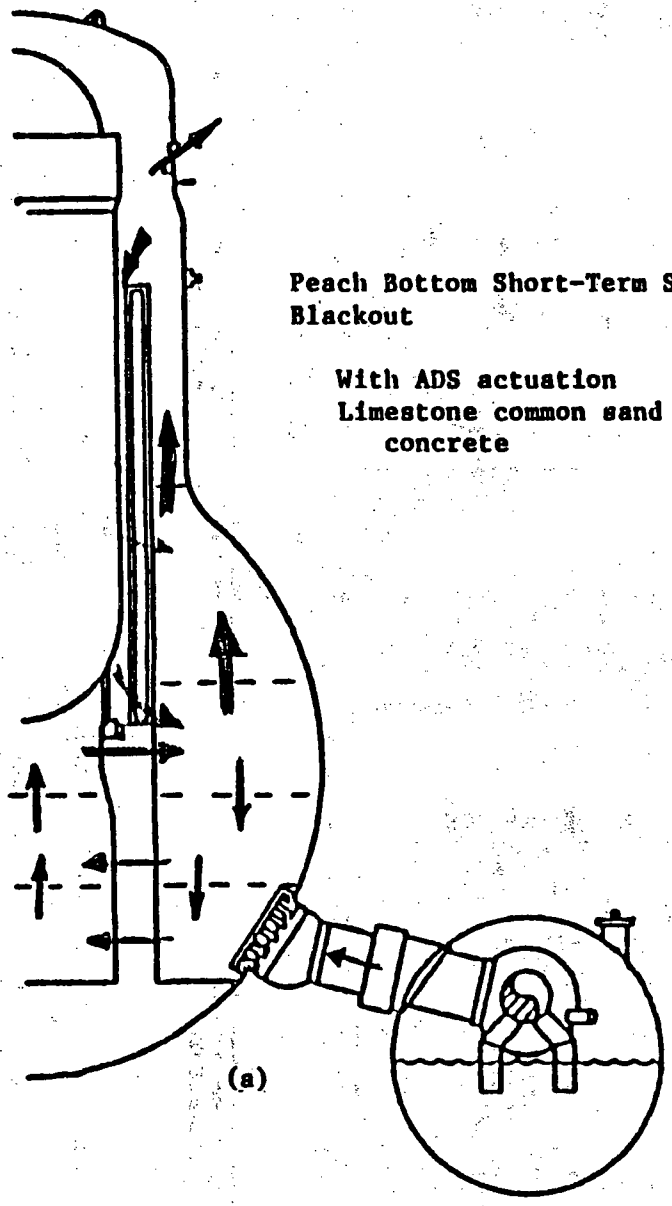


Fig. 3. Drywell intercell flows and cell temperatures as predicted by CONTAIN at 10 minutes after reactor vessel bottom head penetration failure and just before the inpedestal CORCON calculation is initiated.



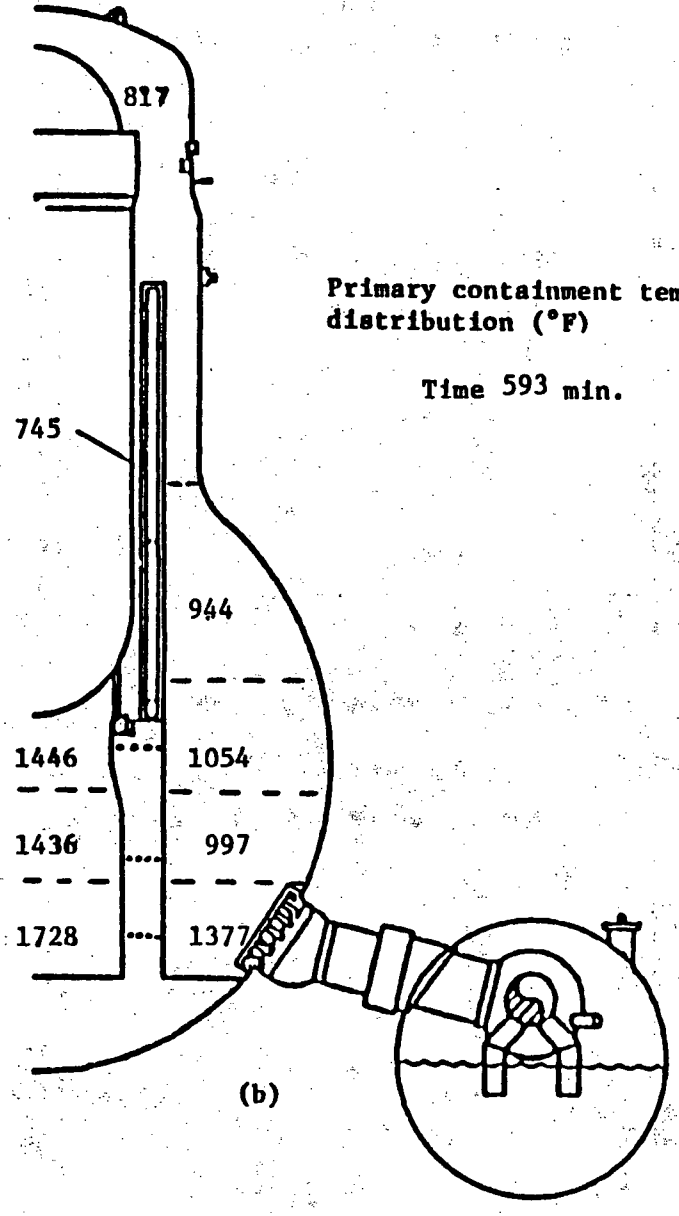
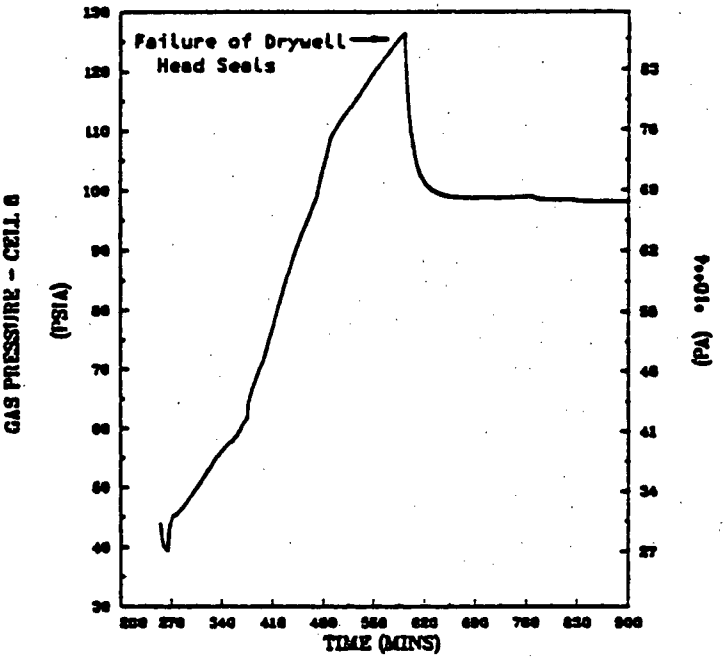
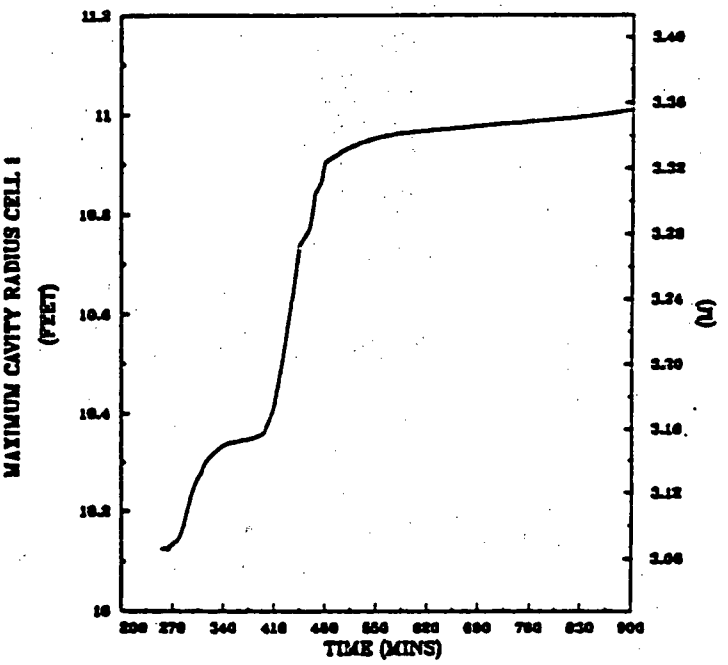


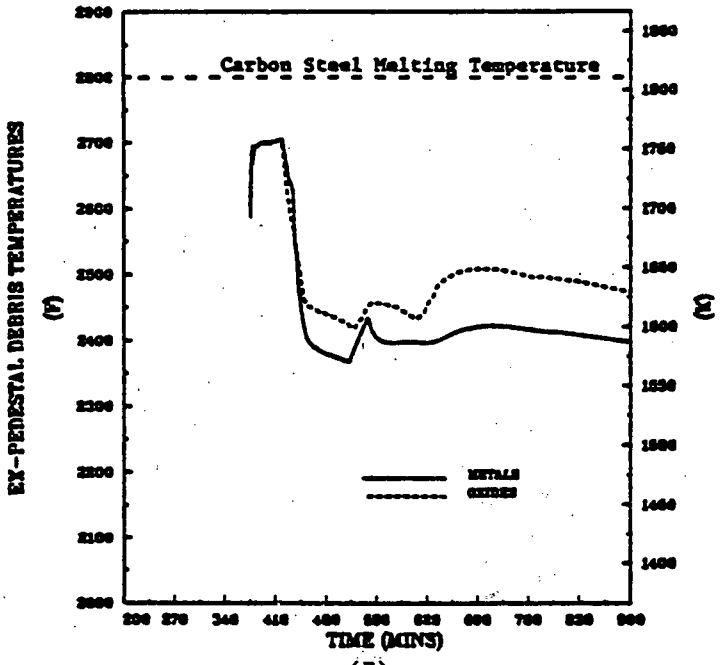
Fig. 4. Drywell intercell flows and cell temperatures as predicted by CONTAIN 0.8 minutes after drywell head flange leakage begins. The leakage is induced by a combination of high drywell pressure, which lifts the head and high temperature, which degrades the seals.



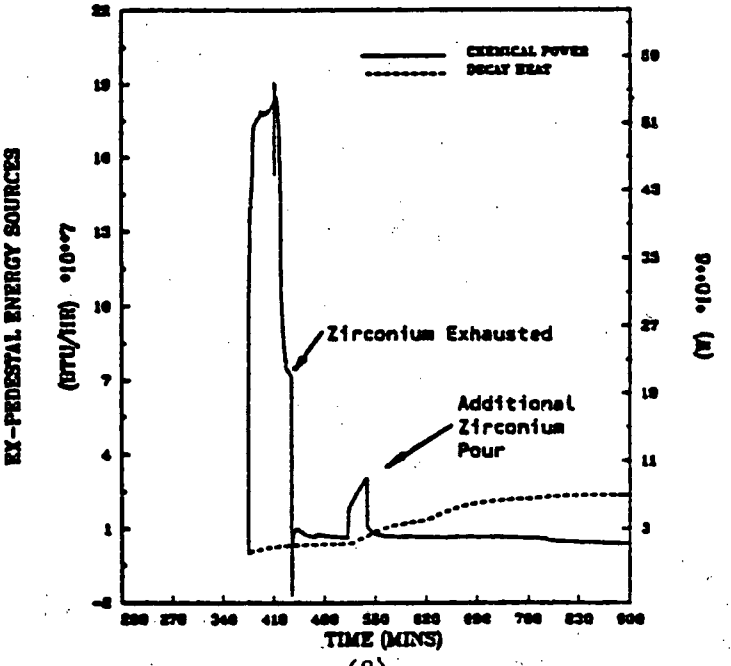
(5)



(6)

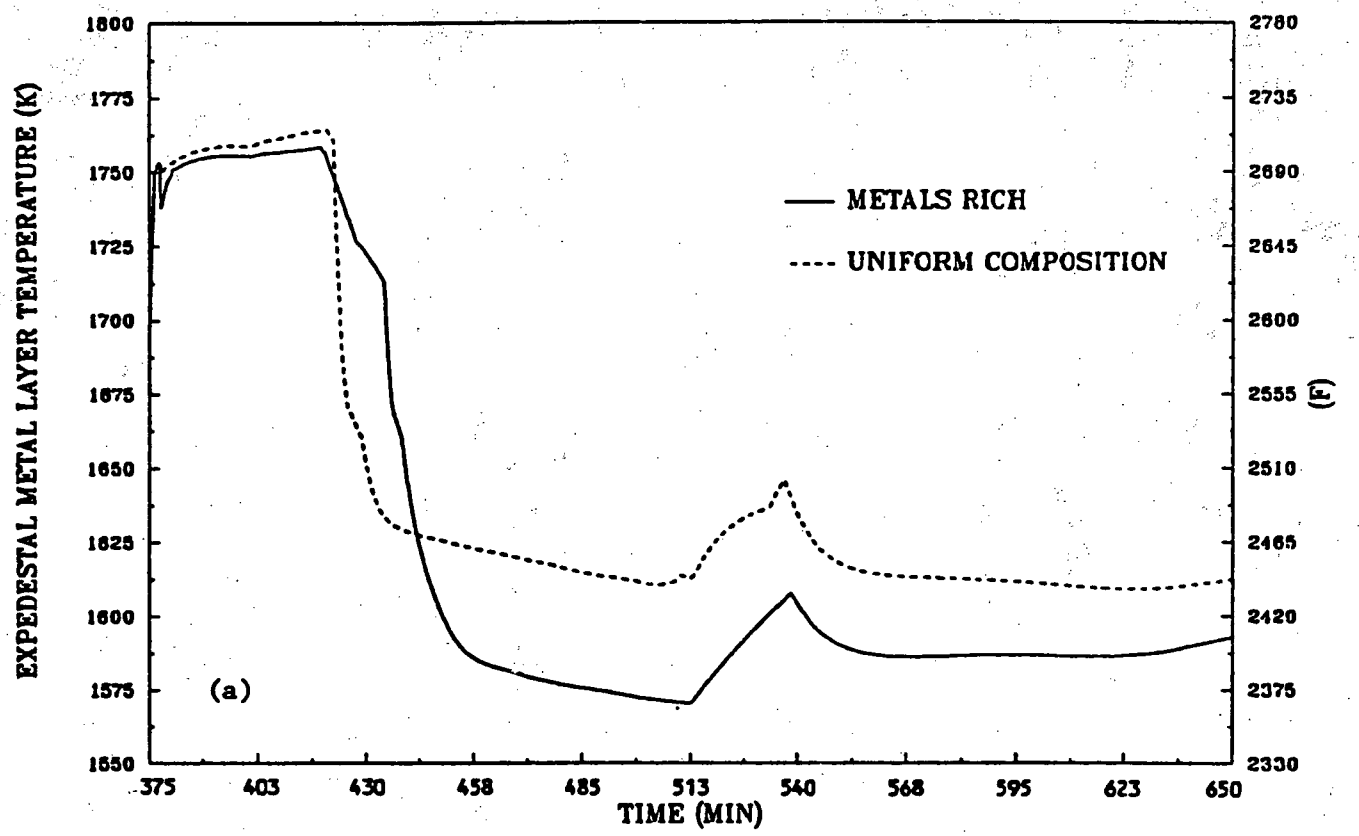


(7)



(8)

Figs. 5–8. Selected parameters relative to maintenance of drywell shell pressure boundary integrity for Peach Bottom Short-Term Station Blackout with ADS actuation. The first spread of debris into the expedestal region occurs at time 375 minutes. The floor is modeled as limestone common sand concrete without overlying water.



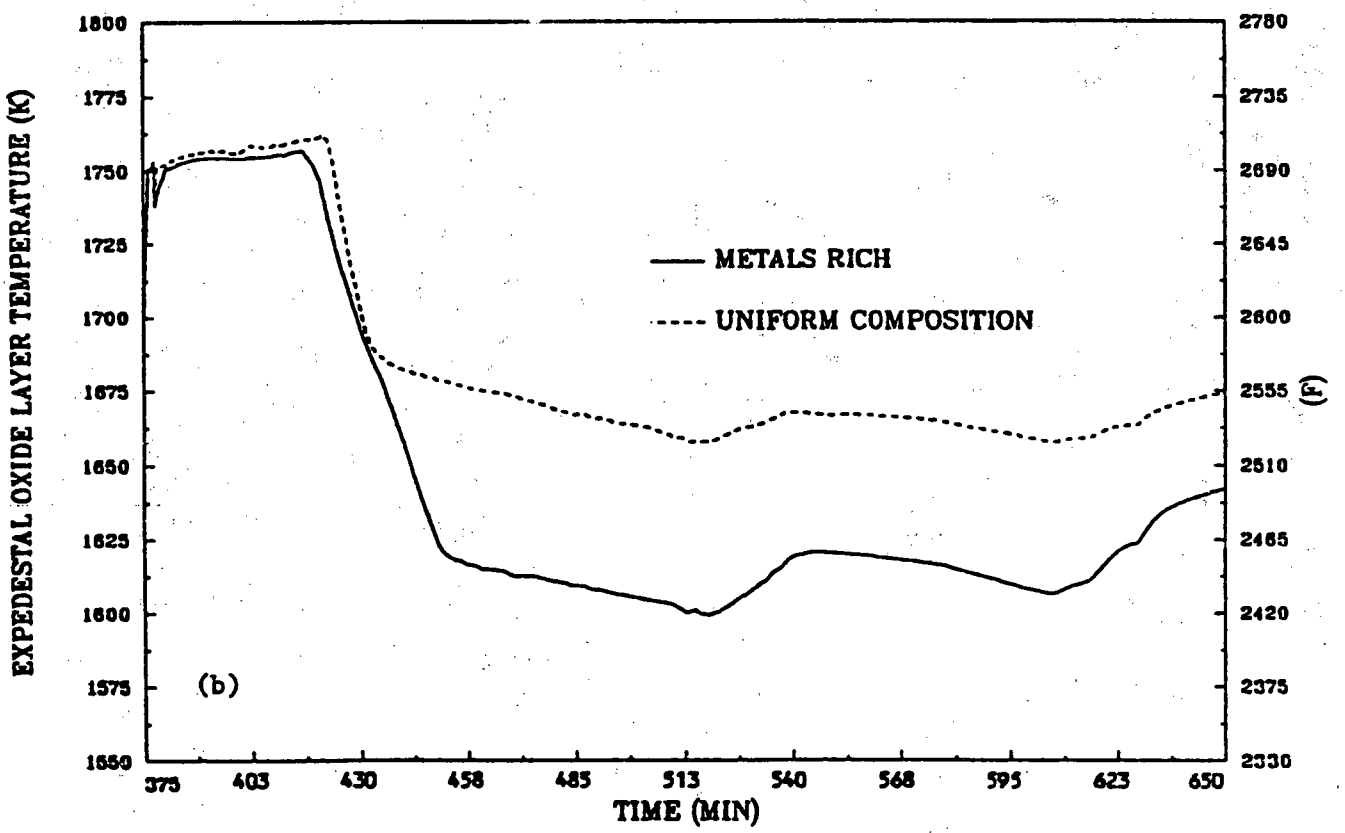


Fig. 9. Comparison of the debris layer temperatures in the expedestal region for the case of best-estimate (metals rich) spreading vs. the case with equal spreading of oxides and metals.

ANALYSIS OF THE THERMAL RESPONSE OF A BWR MARK-I CONTAINMENT SHELL TO DIRECT CONTACT BY MOLTEN CORE MATERIALS*

T. S. Kress and J. C. Cleveland
Oak Ridge National Laboratory
Oak Ridge, Tennessee 37831

ABSTRACT

This study was undertaken to evaluate the thermal response of a BWR Mark-I containment shell in the event of an accident severe enough for molten core materials to fall into the cavity beneath the reactor vessel and eventually come into direct contact with the shell. An existing ORNL three-dimensional transient heat transport computer code, HEATING-6, was used for a specific 2-D case (and variations) for which representative melt/shell boundary conditions required as input were available from other studies.

In addition to the use of HEATING-6, a simplified analytical steady-state correlation was developed and given the name BWR Liner Analysis Program (BWRLAP). BWRLAP was "benchmarked" by comparison with HEATING-6 and was then used to make a number of parametric calculations to investigate the sensitivities of the results to the inputs.

INTRODUCTION

A mode of early containment failure for BWR Mark-I systems has been identified to result from heating of the containment steel shell by the direct contact of molten core materials (Ref. 1). The issue in question is whether or not the shell would actually fail as a result of this contact. The present study was undertaken to develop a means to evaluate the thermal response of the shell for initial and boundary conditions at contact that are predicted by other studies that use melt progression (MP) and molten core concrete interaction (MCCI) codes.

The geometric aspects of the problem are illustrated in Figure 1 which is a diagram of our representation of the Peach Bottom system (although Figure 1 treats the shell as being vertical for computational convenience, it is actually imbedded in the floor at a 45° angle). Above the floor level, there is an air gap between the back side of the shell and the surrounding concrete. Below the floor level, this gap is filled with sand (there are plant-specific differences in these details).

---

*Research sponsored by the Office of Nuclear Regulatory Research, U.S. Nuclear Regulatory Commission under Interagency Agreement DOE 0551-0551-A1 with the U.S. Department of Energy under contract DE-AC05-840R21400 with the Martin Marietta Energy Systems, Inc.

"The submitted manuscript has been authored by a contractor of the U.S. Government under contract No. DE-AC05-84OR21400. Accordingly, the U.S. Government retains a nonexclusive, royalty-free license to publish or reproduce the published form of this contribution, or allow others to do so, for U.S. Government purposes."

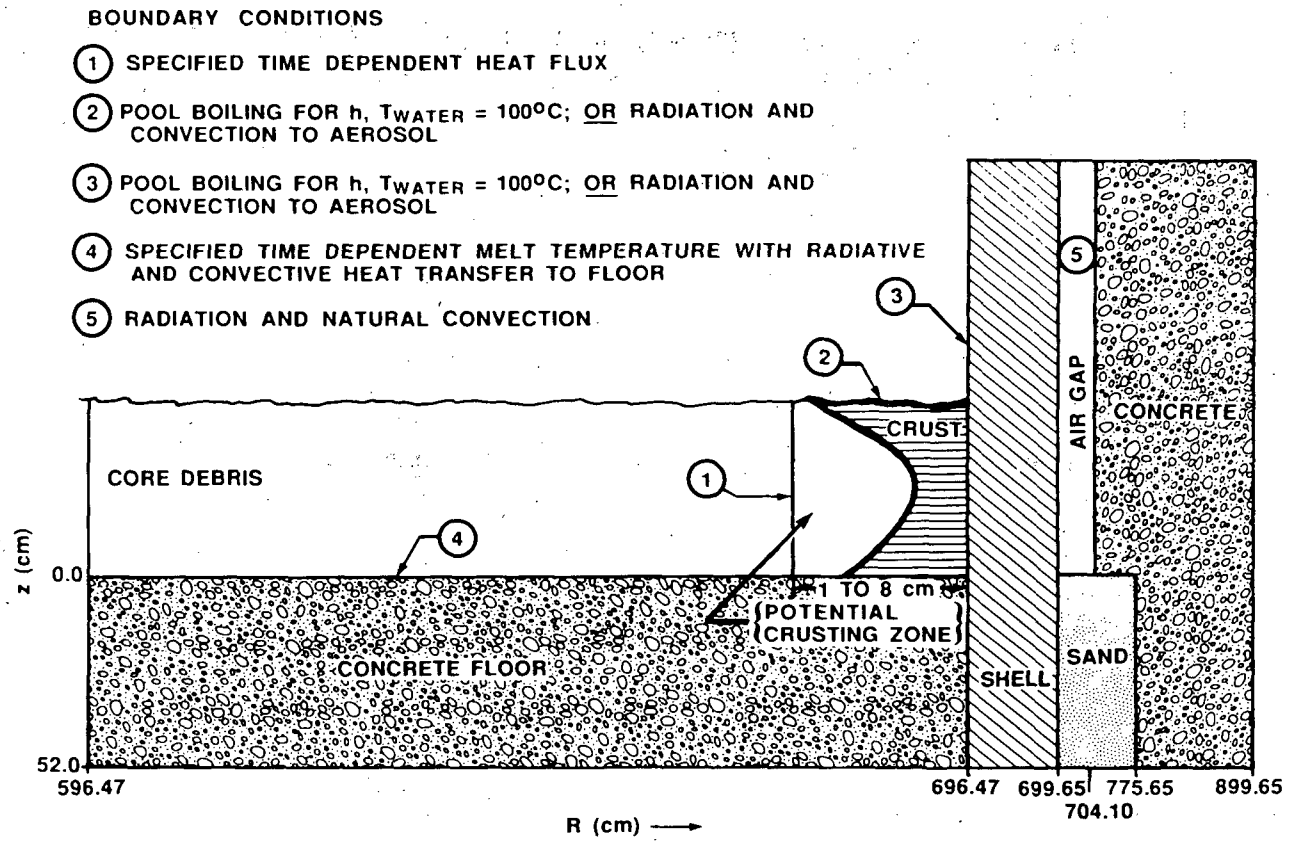


Fig. 1. Mark-1 Containment shell model for heatup analysis.

Our qualitative view of what occurs when the melt contacts the shell is that the interface between the melt and the shell immediately acquires the classical "perfect contact" interfacial temperature given by:

$$T_i = \frac{T_m + T_s[(kdC_p)_s/(kdC_p)_m]^{1/2}}{1 + [(kdC_p)_s/(kdC_p)_m]^{1/2}} .$$

Under essentially all circumstances of interest to this issue, this interfacial temperature will be well below the melt solidification temperature, and, therefore, it would be expected that a crust would quickly form at the melt/shell interface and would begin to grow in thickness as the thermal wave moves backward into the melt. If there is water overlying the melt, this crust growth would be enhanced by heat transfer from the crust top surface to the boiling water. The water would also cool the region of the shell just above the melt/crust providing a sink for the heat transferred through the crust to the shell. Heat will also be transferred from the backside of the shell in the region of the air gap via radiation and natural convection to the surrounding concrete. Below the floor level, heat will be conducted from the

shell through the sand into the concrete. Heat will also be transferred downward from the melt into the concrete floor. Any crust that is formed could exhibit a dynamic behavior – first growing and then shrinking again as the shell undergoes its transient heat-up. If the melt conditions are constant, an equilibrium crust thickness could be attained.

The concrete behind the shell would serve as a large heat capacitance to absorb energy as it slowly heats up. The thermal response of the shell is rapid compared to the concrete thermal response. For constant melt conditions, a quasi-equilibrium state will likely be achieved in which the shell arrives at a quasi-steady temperature distribution. The major heat sink prior to the quasi-steady condition would be the water cooling the shell above the melt (or, if water is not present, convective and radiative heat transfer into the drywell atmosphere). The melt itself is expected to decrease in temperature with time, perhaps allowing the shell temperature to reach a maximum (if failure does not occur) and subsequently to decrease as the melt cools.

The above qualitative description implies that the shell essentially stays in place at its original location. It is likely that the shell will fail if its temperature approaches 1000 K. Stress analyses are needed to confirm this supposition.

APPROACH

The Heating-6 Model

To address this issue, we used an existing ORNL three-dimensional transient heat transport computer program called HEATING-6. This code uses finite difference techniques to solve the general heat conduction equation with internal heat generation. With HEATING-6, the "volume" to be modeled can be divided into any number of arbitrary regions each of which can have its own individual thermal properties as functions of both time and temperature. The boundaries between regions and between internal nodes can be connected to each other by conduction or by radiation and convection to simulate an air gap. Phase changes can be simulated by temporarily specifying properties in such a way that a node will absorb a given amount of energy (the latent heat) with small increase in temperature. After the phase change, the node properties can be internally re-specified to represent the new phase.

Options for boundary nodes include specification of: temperatures that can be functions of time, radiative heat transfer to any sink (which can also have a specified time variable temperature), convective heat transfer with a specified heat transfer coefficient that can be either an arbitrary function of time or some specified function of the average of the boundary temperature and the sink temperature. Alternatively, the code will allow the specification of a time-variable heat flux across any boundary. The HEATING-6 code is fully documented (Ref. 2), has undergone all ORNL quality assurance requirements, and has been extensively verified (Refs. 3, 4, and 5).

The melt/shell region of the Mark I drywell was modelled with HEATING-6 using R-Z geometry as shown in Figure 1. To simplify the noding procedure, the shell was treated as being vertical and the melt depth was increased to a value equal to the full contact distance (i.e., the slant height).

Moving boundaries are not explicitly modeled in HEATING-6. Consequently, to simulate the dynamic crust behavior, the following procedure was used. A potential crusting region was initially defined having a size selected to be slightly larger than the expected real maximum crust thickness (iteration on this was necessary). The heat flux at the melt/crust interface [determined in our study by the prior use of CORCON as given by $h_m(T_m - T_c)$] was specified as input into the face of the potential crusting region. The crust region was given property specifications such that, for temperatures at or below T_c (the "crusting temperature"), the nodes would have thermal properties representative of the solidified melt. Nodes in the potential crusting region with temperatures above the crusting temperature were specified to have an arbitrarily high thermal conductivity and a low specific heat.

The practical effect of this procedure is the same as if there were a crust with a moving interface that is heated by convective transfer from a melt region so long as the specific heat of the "melt" portion of the potential crusting region is low enough that the stored energy change is negligible compared to the through-put heat flux.

The crust region is allowed to have internal volumetric heat generation that is input as a function of time. This input is also obtained from the MCCI code and can be specified to represent any combination of the decay heat and the chemical energy generated as a result of the melt-concrete interaction. Heat transfer out of the crust is by conduction into the shell, into the concrete floor, and into the overlying water undergoing pool boiling. For this boiling heat transfer, the full flat plate pool-boiling curve is used in which the temperature difference between the crust and the water determines the heat flux as well as whether or not the boiling regime is nucleate or film. The same pool boiling relationship is also used to determine the direct contact cooling of the shell by the water pool.

The heat flux from the melt region downward into the concrete floor as determined by CORCON is also an input parameter.

The heat-loss from the exterior side of the shell across the air gap to the concrete is specified to be natural convection plus radiation. In order to close the problem, an adiabatic boundary is placed at a sufficiently large distance around the modelled region.

As the HEATING-6 code does not recognize possible failure and movement of the shell due to reduced strength at high temperatures, our model allows the temperature of any node in the shell to increase to its melting point and absorb the phase change energy at essentially constant temperature. The material in the node is then assumed to be instantaneously replaced with the pseudo-melt material of the potential crusting region. This material is

allowed to subsequently freeze into an internal crust if so dictated by the subsequent heat transfer and temperatures.

The BWRLAP Model

Because of the modeling complexity, the time required (for example, 2 CPU hours on the IBM 3033 computer), and the expense, it is sometimes difficult to use an extensive code such as HEATING-6 for the large number of cases that would be needed to fully examine the sensitivity of the results to the input parameters. Consequently, to develop insight into the issue, provide guidance for running HEATING-6, and to investigate the sensitivity of the results to the assumptions and the input values, a simplified (but qualitatively and quantitatively representative) correlational model was developed for application on a PC and given the name BWR Liner Analysis Program (BWRLAP). A detailed description and derivation of BWRLAP is presented in Appendix I. BWRLAP calculates the shell maximum temperature for an assumed quasi-steady state condition as discussed in the introduction. The shell is treated as a fin with heat input along its length by convection from the melt to the crust interface and series conduction in the crust to the shell. BWRLAP allows heat to be lost from the exterior side of the shell by radiation and natural convection to the concrete and by conduction along its length to its interface with the water pool. Heat losses from the crust to the water and to the concrete floor are accounted for by benchmarking the correlation with the HEATING-6 results.

The BWRLAP model should not be viewed as a solution to the 2-D conduction problem but, rather, as a correlational algorithm for the HEATING-6 results. There are essentially two effects of the crust that must be accounted for:

1. The crust allows some fraction of the heat it receives from the melt to be lost off its top and bottom surfaces and to not be delivered to the shell directly.

2. Because of the 2-D nature of the heat transport through the crust, some of the heat is "shunted" upward and enters the shell at a higher position. For a given total transfer of heat into the shell, this will have the effect of lowering the maximum shell temperature.

BWRLAP accounts for both of these effects by utilizing a semi-mechanistic heat transfer algorithm for the heat passing from the melt and through the crust into the shell at each elevation (see Appendix I). Consequently, the BWRLAP correlation must be benchmarked directly to the "true" HEATING-6 results. To accomplish this benchmarking, the following expedient is used. An effective melt depth is used in the BWRLAP model that consists of the actual depth divided by the product of cos 45° (to correct for the slant height) and a correlating parameter that is greater than 1.0. The product is called an "effectiveness factor" (EF).

RESULTS OF CALCULATIONS

HEATING-6 Cases

Five cases were run with the HEATING-6 model, and results are reported here. The input for the first three cases primarily came from early results of the ORNL BWRSAT Programs' application of MP and MCCI codes. The other two cases were designed to benchmark BWRLAP.

CASE-1:

This case is designated as the "base" case to be consistent with the designation given to it by the BWRSAT staff who used their state-of-the-art code called BWRSAR to calculate the melt conditions upon exiting the reactor vessel and then creatively used CORCON (by a method described in a companion paper in these proceedings) to determine the conditions of the melt as it spreads out over the cavity floor and interacts with the concrete. An important feature of this case is that, in the use of BWRSAR, the core materials were arbitrarily held in place inside the reactor vessel until substantial quantities (75%) were molten and at a high temperature. High limestone concrete was assumed for these CORCON calculations. Input for HEATING-6 for this case and subsequent cases is shown in Table 1.

The HEATING-6 results for Case-1 are presented in Figure 2 which shows isotherms in the crust at successive time periods illustrating the crust dynamic behavior, and in Figure 3 which shows isotherms in the shell itself. For the boundary conditions supplied for this case, a crust first grows to a maximum thickness of only about 1 cm (Fig. 2A) and then shrinks again to zero thickness (Fig. 2C). The shell quickly heats to 1000 K where it would be expected to fail due to lack of strength. Under the unrealistic assumption that it would stay in place, it further heats up to its melting temperature (assumed to be 1750 K). The melting interface is seen to move across the entire cross-section.

CASE-2:

Case-2 is a variation on Case-1 in which the melt depth was arbitrarily decreased to approximately two-thirds of the value of Case-1 to assess the effects of that parameter. The input crusting temperature was also reduced to 2050 K (this was not expected to have a significant impact on the results). The results are shown in Figure 4 which is a plot of the transient temperatures at various distances into the shell at the location of the maximum shell temperature. It is seen that, for the otherwise identical initial conditions, reducing the melt depth to this value is still not sufficient to prevent the prediction of temperatures at which the shell would be expected to fail.

Table 1. Heating-6 input values for cases 1-3

Transient input from CORCON		Input for both Cases 1 and 2	
Time (sec)[a]	Heat flux (W/m^2) melt-to-crust[b] ($\times 10^{-4}$)	Melt temperature (K)	Power density (W/m^3) decay + chem rx[c] ($\times 10^{-6}$)
0	18.3	2382	0.4
1	20.8	2379	22.1
31	75.5	2335	17.5
61	211.7	2352	15.5
91	376.6	2368	13.3
121	199.6	2339	7.7
151	144.9	2283	1.7
181	78.0	2216	0[d]
211	40.1	2163	0[d]
241	20.6	2121	0[d]
271	13.3	2089	0.16
301	10.4	2065	6.2
331	6.2	2043	0.3
361	5.1	2030	0.9
391	4.5	2021	0.9
421	3.8	2013	0.9
451	3.3	2006	0.9
481	2.8	1999	0.8
511	2.4	1993	0.8
541	2.1	1988	0.8
571	1.8	1983	0.8

Other Parameters

	Case 1	Case 2	Case 3
Melt-to-crust heat flux (W/M^2)	see above	see above	5×10^5
Melt temperature (K)	see above	see above	2150
Crusting temperature (K)	2150	2050	2100
Power density in crust (W/M^3)	see above	see above	1.07×10^5[e]
Debris depth (M) (vertical)	0.118	0.078	0.118
Crust thermal conductivity (W/M-K)	4.7	4.7	3.0 (UO_2)
Crust density	UO_2	UO_2	UO_2
Crust specific heat (J/g-K)	0.74	0.74	UO_2
Shell emissivity	0.3	0.3	0.7
Concrete emissivity	0.3	0.3	0.7

[a]Time = 0 sec at melt-shell contact.

[b]Computed from CORCON as $Q/A = hl_{iq\ side}(T_{melt} - T_{solidus})$.

[c]Used only where HEATING-6 determines crust existence.

[d]CORCON computed endothermic reactions with energy absorption rates larger in magnitude than decay power. Power density input as 0.0 for conservatism.

[e]Decay power only.

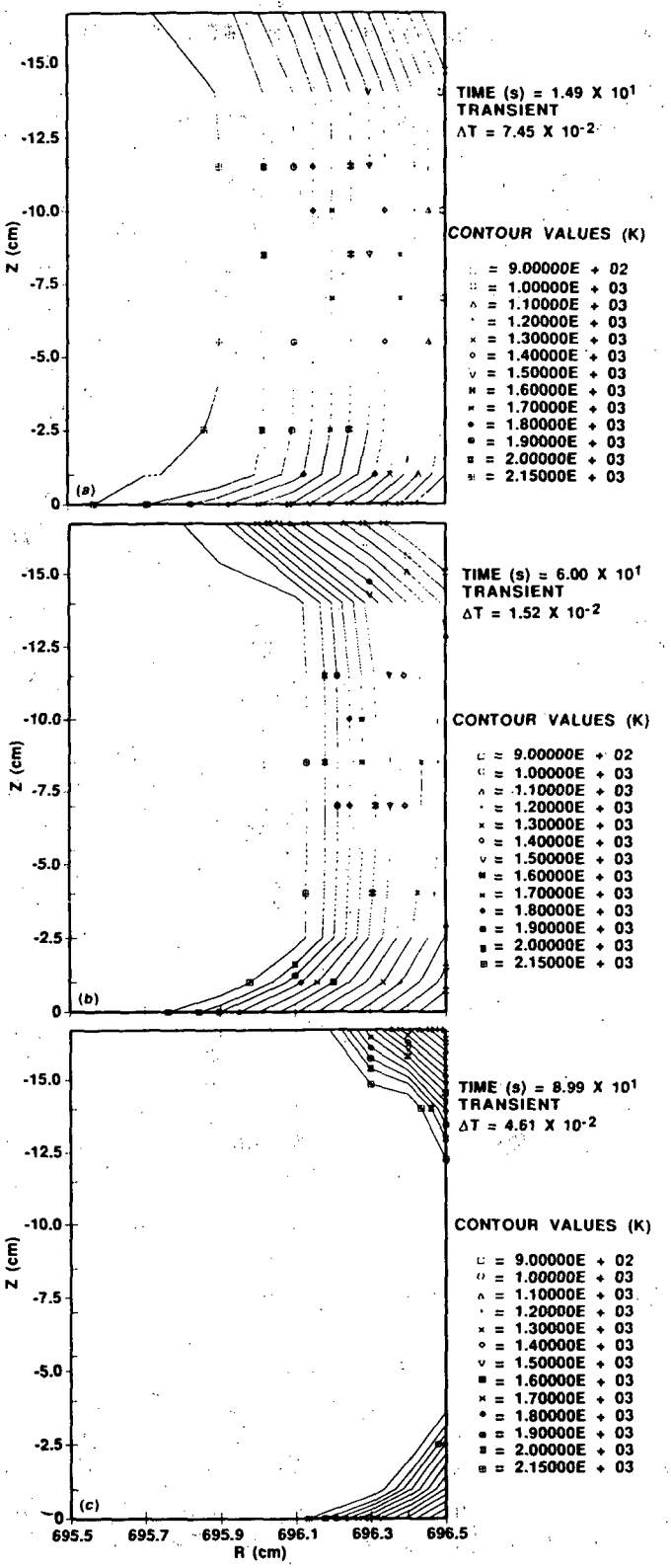


Fig. 2. Isotherms in crust at different times.

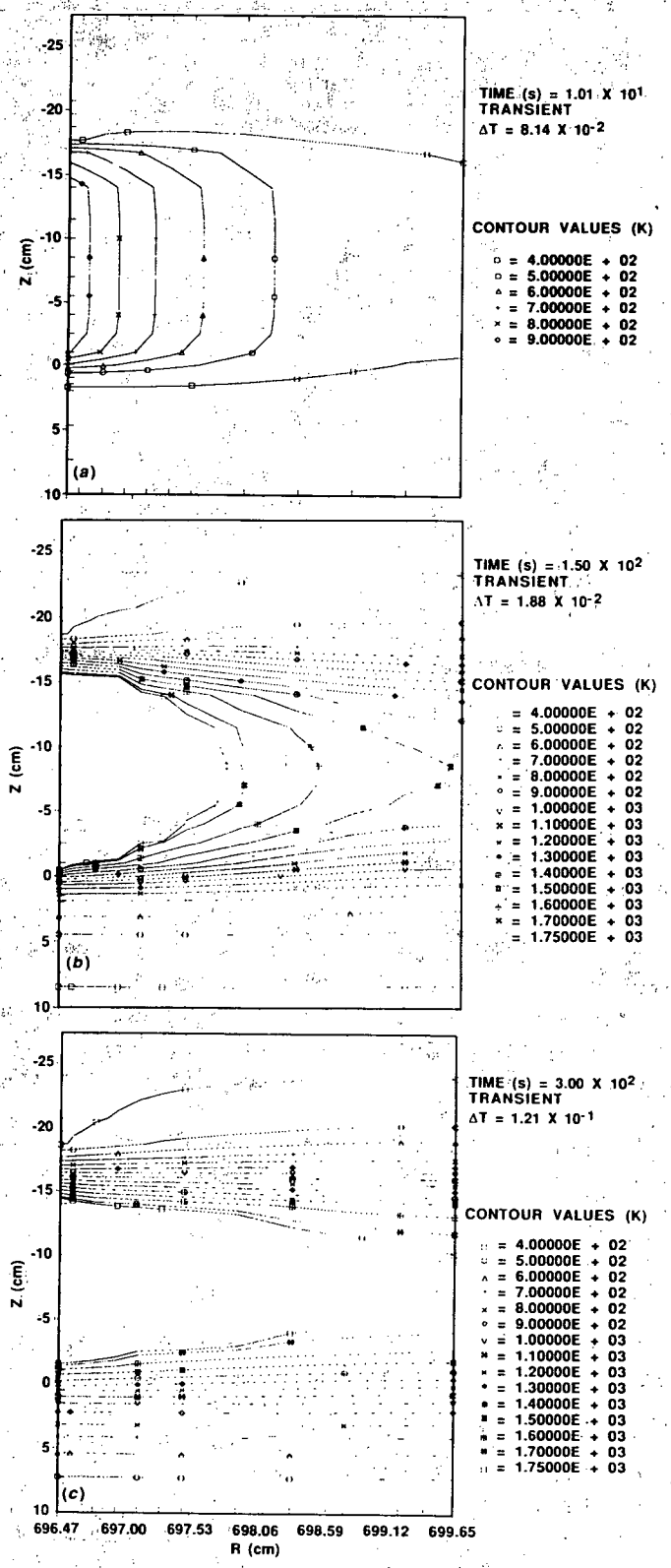


Fig. 3. Isotherms in containment shell at different times.

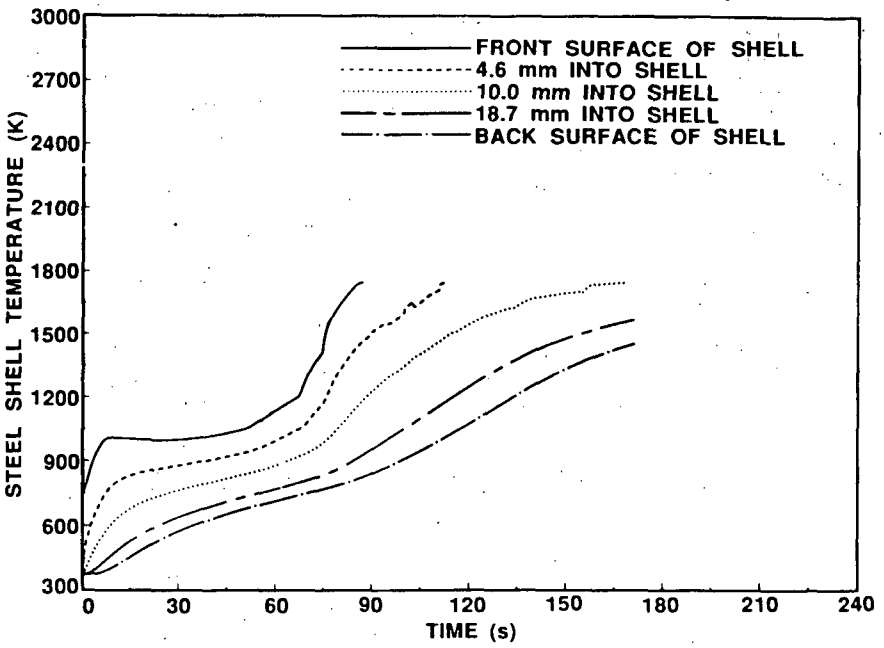


Fig. 4. Transient temperatures in containment shell (case 2).

CASE-3:

Case-3 is another variation of the base case performed in an attempt to investigate the effect of assumed parameters that are more favorable for the shell survival. The changes made to the base case for this variation included: The surface emissivities of the shell and of the concrete were increased from 0.3 to 0.7. The heat flux at the melt/crust interface was input at a constant value of 5×10^5 W/M^2 compared to the transient values for Case 1, some of which were above 2×10^6 W/M^2. The crust thermal conductivity was given the lower values representative of UO_2 (3.0 W/M-K) rather than the higher values (up to 6 W/M-K) given in CORCON for the melt mixture.

The results for this case are presented in Figure 5. It is seen that shell temperatures are still above the 1000 K level and are approaching melting after ~500 s.

CASE-4 and -5:

The development of the BWRLAP correlation was done in such a way as to allow it to be "benchmarked" to the HEATING-6 code through specification of the effectiveness factor (EF) previously discussed. Case-4 and -5 were run specifically for this purpose. Both cases were deliberately chosen to result in shell maximum temperatures that were below the melting value so as to be within the range of validity of the BWRLAP model. Case-4 assumed a high crusting temperature (2600 K) and a high melt-to-crust heat transfer coefficient of 10000 W/M^2-K, but used a low melt superheat (10 K) that would allow a very thick crust to develop (approximately 8 cm). Figure 6 presents the Heating-6 results compared with the prediction of BWRLAP for an EF of 0.85.

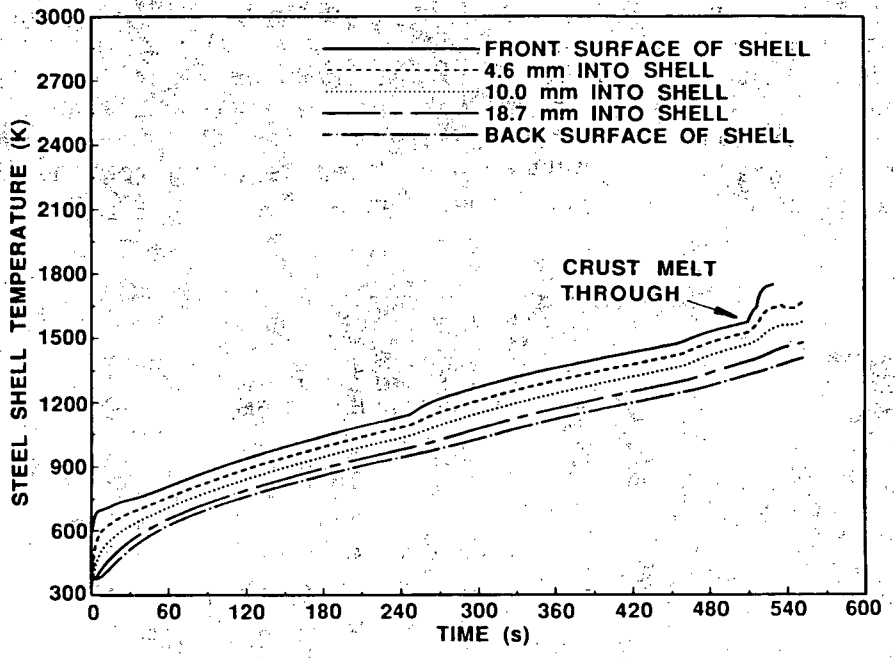


Fig. 5. Transient temperatures in containment shell (case 3).

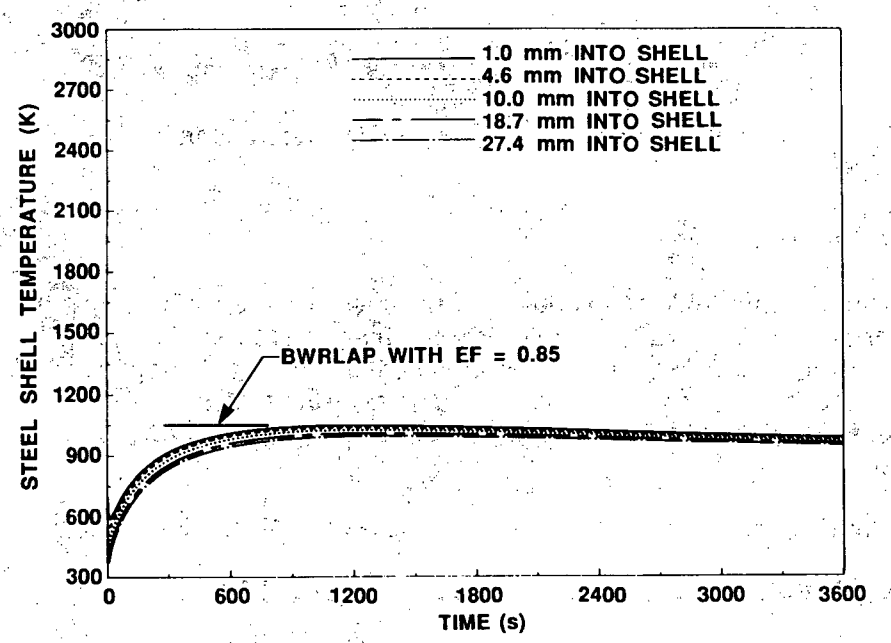


Fig. 6. Transient temperatures in containment shell (case 4).

Case-5 assumed a lower crusting temperature (2100 K), a lower heat transfer coefficient (5000 W/M²-K), but a larger melt superheat (50 K) resulting in a much thinner crust (approximately 1 to 2 cm) thereby providing a significant "stressing" range for the BWRLAP correlation. The results compared with the BWRLAP calculation for the same EF of 0.85 are shown on Figure 7. It is seen in Figures 6 and 7 that the BWRLAP model compares well with HEATING-6 (this is true for both the maximum liner temperature and for the crust thickness). This provides confidence in the BWRLAP correlation as being reasonably representative of the important features of the problem.

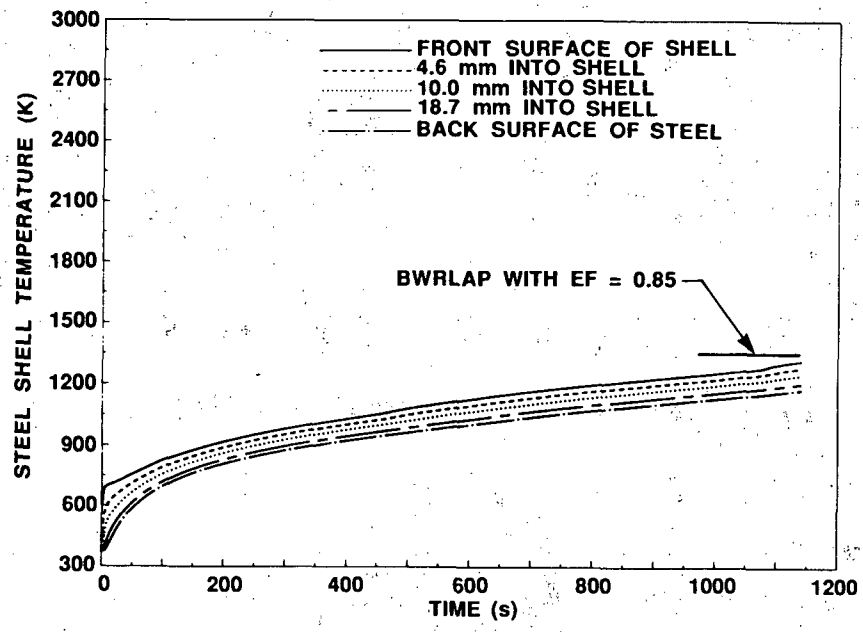


Fig. 7. Transient temperatures in containment shell (case 5).

BWRLAP Parametric Study

Both HEATING-6 and BWRLAP require (in one form or another) input of the following parameters the values of which are believed to be highly uncertain: the crusting temperature, the superheat, the melt depth, and the melt-to-crust heat transfer coefficient. To determine the sensitivity of the results to these inputs, calculations were made with BWRLAP for the following parameter values:

- crusting temperature (K) ..... 1800; 2200; 2600.
- melt depth (cm) ..... 5; 10; 15; 20.
- heat transfer coefficient (W/M²-K) 5000; 10000
- superheat (K) .... [varied systematically until the shell melt temperature (1750 K) was reached].

The results of the parameter study are presented in Figure 8 (for h = 10000) and Figure 9 (for h = 5000). It can be seen from these figures that the shell maximum temperature is relatively insensitive to the absolute level of the crusting temperature (and therefore the melt temperature) but is very sensitive to the superheat (the difference between the melt temperature and the crusting temperature) especially for melt depths of 10 cm or greater where the curves are very steep. There is moderate sensitivity to the melt-to-crust heat transfer coefficient. Reducing the value from 10000 to 5000 W/M²-K basically allows the superheat to double for a given shell maximum temperature. This is better illustrated on Figure 10 which presents the maximum superheat values allowed before the liner maximum temperature exceeds 1000 K (failure) as a function of melt depth for two values for the melt-to-crust heat transfer coefficient (10000 and 5000 W/M²-K).

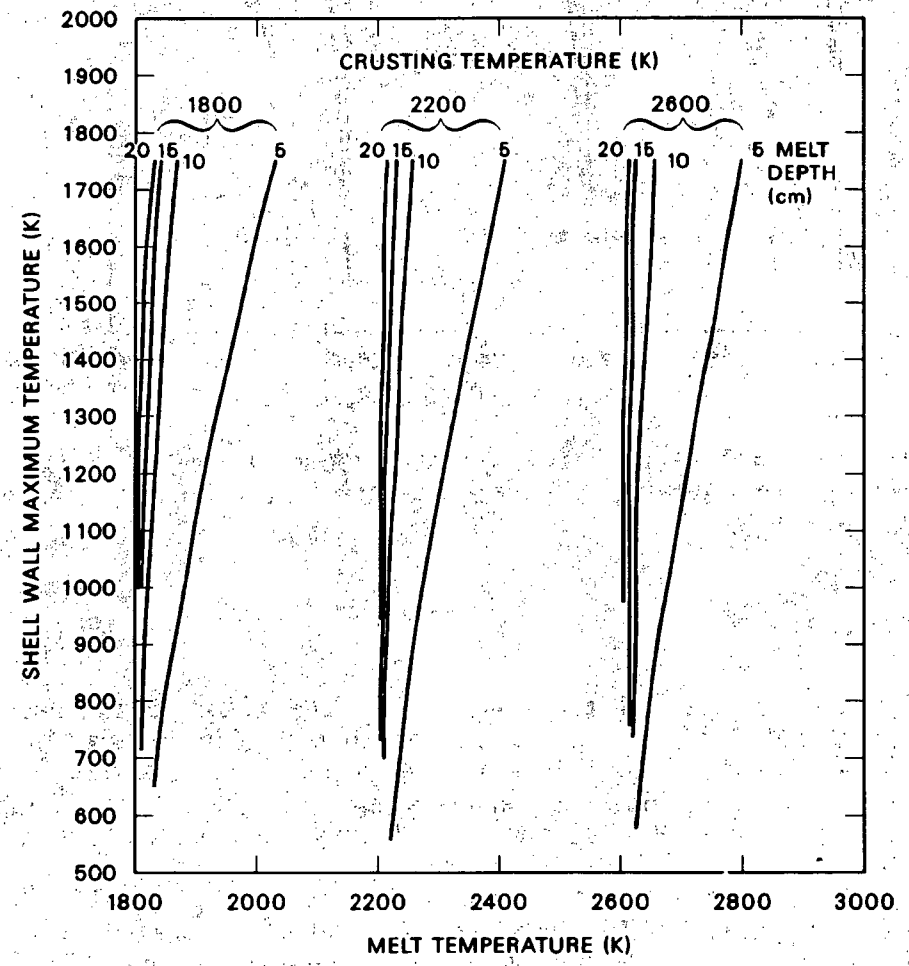


Fig. 8. Maximum shell temperature vs melt temperature as a function of crusting temperature and melt depth for a melt convective heat transfer coefficient of 10,000 (W/M²-K).

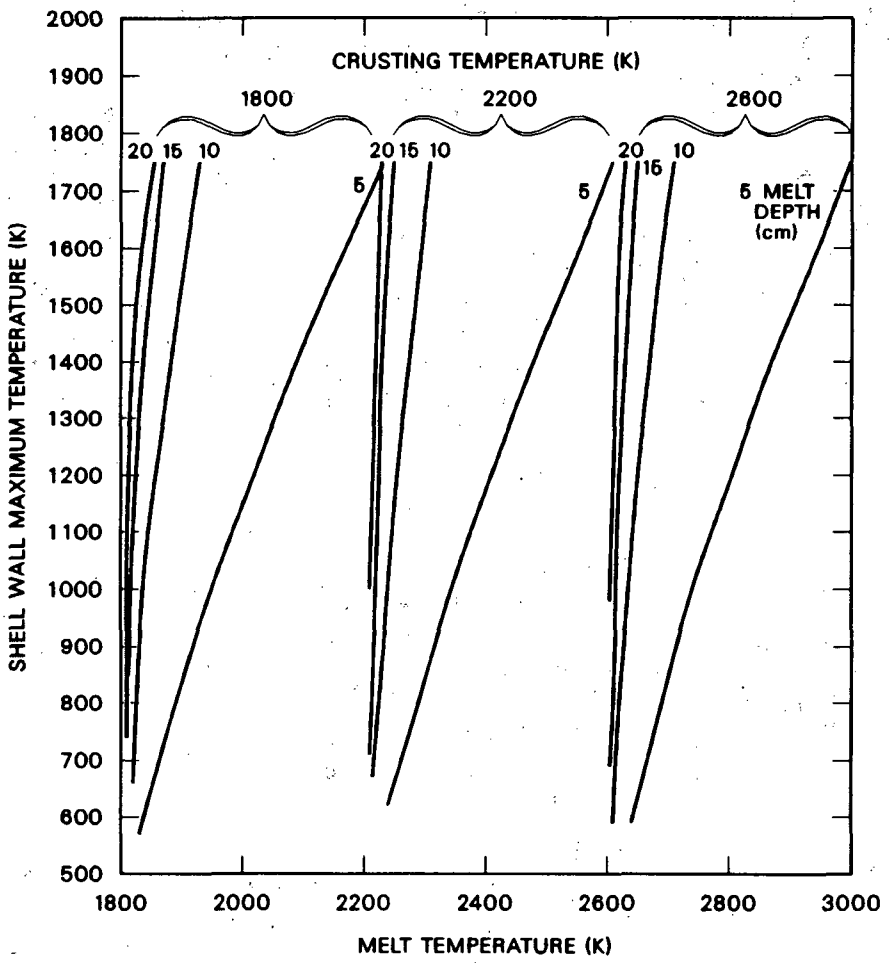


Fig. 9. Maximum shell temperature vs melt temperature as a function of crusting temperature and melt depth for a melt convective heat transfer coefficient of 5,000 ($W/M^2/K$).

Figure 11 shows the calculated values for the crust thicknesses as a function of the superheat for a crusting temperature of 2600 K and for the two values for the heat transfer coefficient. As would be expected, the crust thickness gets very large at small superheats and small at large superheats. This result is not very sensitive to the actual crusting temperature.

The sensitivity of the results to the thickness of the shell itself can easily be addressed by the BWRLAP correlation. Table 2 compares the results for shell thicknesses of 2.16 cm and 3.18 cm. Moderate sensitivity to this parameter is noted in that at a melt depth of 10 cm, the 32% reduction in thickness resulted in a 25% reduction in the limiting superheat before melting temperature was exceeded.

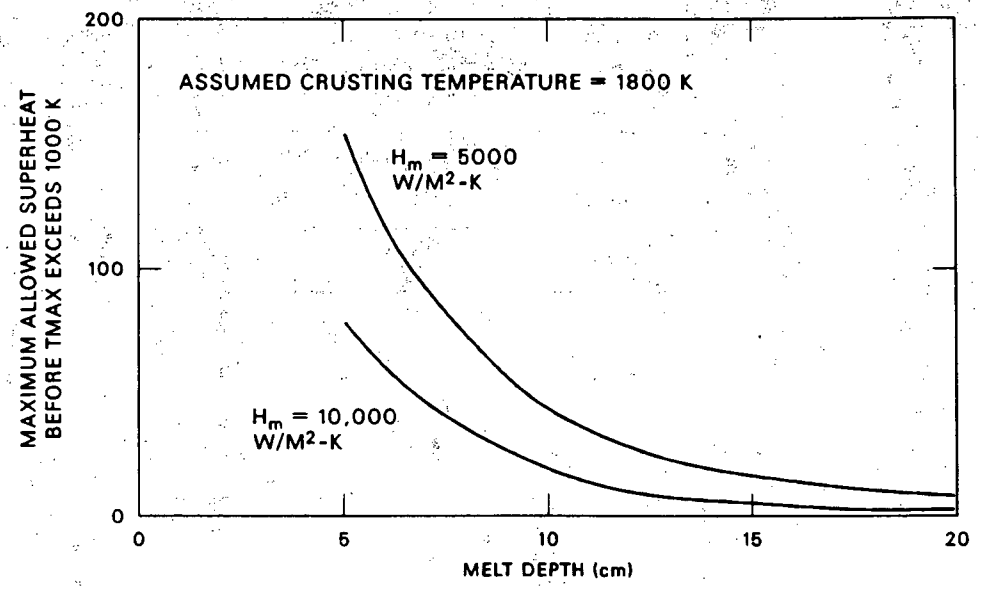


Fig. 10. Superheat (melt temperature – crusting temperature) above which th shell maximum temperature exceeds 1,000 K as a function of the melt depth and the melt-to-crust heat transfer coefficient.

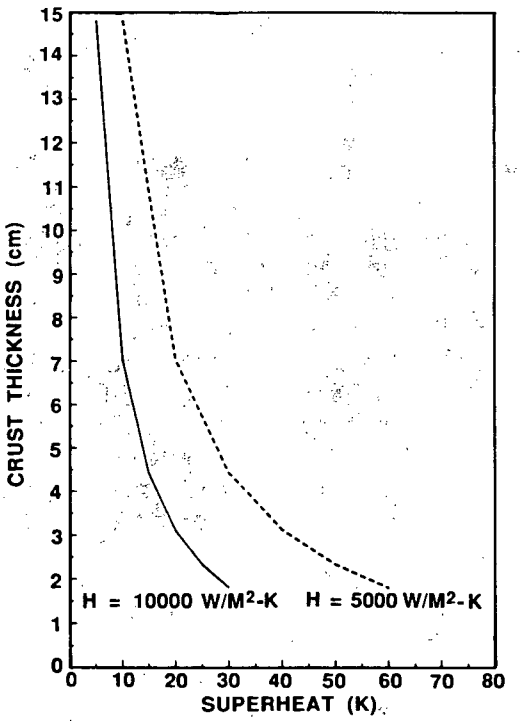


Fig. 11. Crust thickness vs superheat (melt temperature – crusting temperature), for a crusting temperature of 2,600 K, melt-to-crust heat transfer coefficients of 10,000 and 5,000 (W/M²-K), and melt depth of 15 cm.

Table 2. Superheat required to produce shell maximum temperature of 1750 K for the indicated shell thickness

Melt depth (cm)	Superheat (K) for shell thickness (cm)	
	3.18	2.16
5	235	170
10	75	55
15	40	33
20	31	27

CONCLUSIONS

This study provides a clear understanding of the dominant parameters that influence the thermal response of the BWR MARK-I containment shell upon contact with molten core materials. The important parameters are:

- melt superheat.
- melt depth.
- melt-to-crust heat transfer coefficient.

These parameters are generally determined by computer codes that treat the melt progression (MP) and molten-core/concrete interaction (MCCI) phases of a severe accident. These required inputs from the MP and MCCI codes are believed to be subject to much uncertainty, particularly with respect to the melt spreading behavior and the effects of existing water within the reactor cavity. Without a clearer understanding of these uncertainties and their quantification, it is not possible to provide an unqualified resolution to this issue at this time. The HEATING-6 model is now available and can provide a credible evaluation of the containment shell thermal response when new and less uncertain contact boundary conditions become available.

REFERENCES

1. G. A. Greene, K. R. Perkins, and S. A. Hodge, "Mark I Containment Drywell: Impact of Core-Concrete Interactions on Containment Integrity and Failure of the Drywell Liner," Proceedings of the International Symposium on Source Term Evaluation for Accident Conditions, IAEA (October 1985).

2. D. C. Elrod, G. E. Giles, and W. D. Turner, "HEATING-6, A Multidimensional Heat Conduction Analysis with Finite Difference Formulation. In Scale, A Modular Code System for Performing Standardized Computer Analyses for Licensing Evaluations," NUREG/CR-0200, ORNL/NUREG/CSD-2/R1.

3. C. B. Byran, K. W. Childs, G. E. Giles, "HEATING-6 Verification," K/CSD/TM-61, December 1986.

4. K. W. Childs, C. B. Byran, "HEATING-6 Analysis of International Thermal Benchmark Problem Sets 1 and 2," ORNL/CSD/TM-239, October 1986.

5. C. B. Byran and K. W. Childs, "Thermal Codes Benchmarking — HEATING-6 Results," K/CSD/TM-57, August 1985.

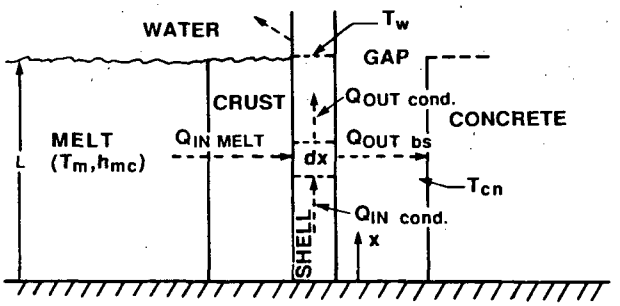
APPENDIX I

DESCRIPTION AND DERIVATION OF THE BWRLAP CORRELATION

The objective of the BWR Liner Analysis Program (BWRLAP) is to correlate the steady-state temperature distribution in a BWR MARK-I containment steel shell when contacted by molten core materials. The shell is assumed to be cooled by water overlying the melt and by radiative and convective heat transfer off its back side to surrounding concrete. A crust is assumed to have formed between the shell and the melt of a thickness to be determined by the solution of the problem itself.

Derivation of the governing equations:

Refer to the geometric representation of the BWRLAP model shown below for the derivation that follows.



The derivation of the BWRLAP model is based on the following implied assumptions:

- The temperature gradient across the shell (in the R-direction) is small enough to be neglected.

- The cooling of the shell in its region of contact with the water overlying the melt is so effective that a low value (near the water temperature) can be assumed for the temperature at that interface.

- The rate of heat-up of the concrete surrounding the backside of the shell is slow compared to the initial response of the shell so that a quasi-steady state solution is sufficient and the concrete temperature can be assumed to have small effect on the radiative losses from the back side of the shell.

- The heat transfer from the melt to the crust is given by the product of a heat transfer coefficient h_m and the difference between the melt temperature T_m and the crusting temperature T_c, all of which are assumed constant in this model. The portions of this heat that are lost to the

overlying water and to the underlying floor are represented in the correlation by utilizing an "effectiveness factor" (EF) to decrease the heat transfer calculated by a series conduction-like fin equation that must be calibrated to a known solution.

A heat balance at any vertical axial location, x, in the shell can be made as follows:

$$Q_{in\ cond} + Q_{in\ melt} = Q_{out\ bs} + Q_{out\ cond} \cdot$$

The relationships used for the above heat flow quantities are given below:

$$Q_{in\ cond} = -k\ A_{cs}\ (dT/dx)$$

$$Q_{out\ cond} = -k\ A_{cs}\ [dT/dx + (d^2T/dx^2)(dx)]$$

$$Q_{in\ melt} = h_{eff}\ A_p\ (T_m - T)$$

$$Q_{out\ bs} = h_{bs}\ A_p\ (T - T_{cn})$$

where

$h_{eff} = [1/h_{mc} + Th_c/k_c]$

$h_{bs} = h_{nc} + h_r$

h_{mc} = The melt-to-crust convective heat transfer coefficient.

Th_c = The crust thickness in the R-direction.

k_c = The crust thermal conductivity.

h_{nc} = The natural convection heat transfer coefficient in the air gap behind the shell.

h_r = An "effective" radiation heat transfer coefficient between the shell and the concrete (to be discussed later).

k = The shell thermal conductivity.

A_{cs} = The cross-sectional area of the shell per unit circumferential distance.

A_p = The surface area of element dx for unit circumferential distance.

T = The shell temperature.

T_m = The melt temperature.

T_{cn} = The temperature of the concrete behind the shell.

It is noted here that the use of h_{eff} is not the normal series conduction concept. In the BWRLAP correlation it is used as a convenient means to account for the heat losses from the crust top and bottom surfaces. The implied assumption is that these losses are essentially proportional to the crust thickness. Substituting the above into the heat balance equation gives:

$$kA_{cs}(d^2T/dx^2) + h_{eff}(T_m - T) - h_{bs}(T - T_c) = 0 \ . \qquad \text{(Eq. I-1)}$$

Note that, for zero crust thickness, the above reduces to the exact "fin" equation with a heat source on one side and a heat sink on the other.

Defining T' as $(T_m - T)$, Eq. I-1 becomes

$$d^2T'/dx^2 - A\ T' = B \ , \qquad \text{(Eq. I-2)}$$

where

$$A = (h_{eff} + h_{bs})/(kt_w)$$

$$B = -(h_{bs})(T_m - T_{cn})/(kt_w)$$

t_w = shell wall thickness

and the boundary conditions are

at $x = 0$; $dT'/dx = 0$,

at $x = L$; $T' = (T_m - T_w)$.

In these boundary conditions, T_w is the temperature of the wall at the location of its interface with the water coolant. It is presumed that this can be arbitrarily specified to be a low value near the water temperature itself. The distance "L", while nominally considered to be the "slant depth" or contact length of the melt with the shell is left here as an unspecified length less than this value. This allows "benchmarking" the BWRLAP correlation to the more exact 2-D analysis of HEATING-6 that accounts for the heat losses to the water as well as for heat to be transferred downward through the shell into the concrete below the floor. This "benchmarking" will also allow folding in the effects of using a convective-like equation to model radiation heat transfer off the side of the shell facing the concrete.

The homogeneous solution to Eq. I-2 is

$$T' = C_1 \exp(A^{1/2}x) + C_2 \exp(-A^{1/2}x) \ .$$

A particular solution is

$$T' = -B/A \ .$$

Therefore, the full general solution is

$$T' = C_1 \exp(A^{1/2}x) + C_2 \exp(-A^{1/2}x) - B/A \ .$$

Applying the boundary conditions, this becomes

$$T' = \frac{(T_m - T_w + B/A)}{[\exp(A^{1/2}L) + \exp(-A^{1/2}L)]} [\exp(A^{1/2}x) + \exp(-A^{1/2})] - B/A \qquad \text{(Eq. I-3)}$$

The maximum temperature in the shell will occur at the location of $x = 0$. The value of T' at this location (designated T'_{max}) is given by

$$T'_{max} = (2)\ (T_m - T_w + B/A)/[\exp(A^{1/2}L) + \exp(-A^{1/2}L)] - B/A \ . \qquad \text{(Eq. I-4)}$$

The maximum shell temperature itself, from our definition of T', is

$$T_{max} = T_m - T'_{max} \ .$$

Equations I-3 and I-4 form the fundamental basis of the BWRLAP correlation. In the BWRLAP application, the melt depth is divided by an "effectiveness factor" (EF) to correct for the slant height (cos 45°), to account for heat losses from the top and bottom of the crust, and to account for the 2-D shunting effects of the crust. However, these do not yet represent a completely closed solution because we have left unspecified the exact crust thickness. In addition, the back-side radiation heat transfer is a function of the fourth power of the as yet undetermined liner temperature distribution. Consequently, the above equations were programmed into a PC and an iterative procedure was used to establish both the crust thickness, Th_c, and the back-side heat transfer coefficient, h_{bs}.

Procedure for determining crust thickness and the back-side equivalent radiative heat transfer coefficient

The crust thickness is determined by an iterative procedure that balances the heat going from the melt into the EF corrected melt/crust interface with the heat going from the interface to the shell itself. Recall that this EF reduces the magnitude of the heat to the shell as a way of accounting for losses at the crust upper and lower surfaces.

The heat (per unit circumferential distance) going from the melt into the melt/crust interface is given by

$$Q_{mc} = h_{mc}L(T_m - T_c) \ , \qquad \text{(Eq. I-5)}$$

where T_c = the crusting temperature of the melt.

The heat (per unit circumferential distance) going from the crust interface into the shell is given by

$$Q_1 = \int_0^{L/EF} (k_c/Th_c)\ (T_c - T)dx \ . \qquad \text{(Eq. I-6)}$$

The following algorithm is used:

- An arbitrary crust thickness is assumed.
- An arbitrary h_{bs} is assumed.
- Equation I-3 is solved for the temperature distribution in the shell.
- Equation I-6 is integrated for this temperature distribution to obtain Q_1.
- The crust thickness is iterated upon until Q_{mc} (Eq. I-5) equals Q_1 (Eq. I-6).
- A second level iteration is then made on h_{bs} as discussed below until convergence is achieved for both Th_c and h_{bs}.

The heat transfer from the back-side of the shell to the concrete is considered to be by both radiation and natural convection. BWRLAP uses an effective convective relationship for this,

$$Q_{bs} = (h_{nc} + h_{rad})\ (T - T_{cn}) \ .$$

Preliminary calculations have indicated that the radiation contribution dominates over the natural convection. Therefore, a constant representative value is input for h_{nc}. The effective radiation coefficient is calculated internally by the relationship

$$h_{rad} = [C/(1/e_1 + 1/e_{cn} - 1)][1/L \int_0^L (T^3 + T^2T_{cn} + TT_{cn}^2 + Tcn^3)dx] \ .$$

This "averaging" assures that the radiation heat transfer off the back side has the correct total amount but distributes it differently along the shell length. This is not considered to introduce a serious error in the determination of the maximum shell temperature.

Assessment of Models for Steam Release from Concrete and Implications for Modeling Corium Behavior in Reactor Cavities*

Kenneth E. Washington and Daniel E. Carroll
Sandia National Laboratories
Albuquerque, NM 87185

ABSTRACT

Models for concrete outgassing have been developed and incorporated into a developmental version of the CONTAIN code for the assessment of corium behavior in reactor cavities. The resultant code, referred to as CONTAIN/OR in order to distinguish it from the released version of CONTAIN, has the capability to model transient heat conduction and concrete outgassing in core-concrete interaction problems. This study focused on validation and assessment of the outgassing model through comparisons with other concrete response codes. In general, the model is not mechanistic; however, there are certain important processes and feedback effects that are treated rigorously. The CONTAIN outgassing model was compared against two mechanistic concrete response codes (USINT and SLAM). Gas release and temperature profile predictions for several concrete thicknesses and heating rates were performed with acceptable agreement seen in each case. The model was also applied to predict corium behavior in a reactor cavity for a hypothetical severe accident scenario. In this calculation, gases evolving from the concrete during nonablating periods fueled exothermic Zr chemical reactions in the corium. Higher corium temperatures and more concrete ablation were observed when compared with that seen when concrete outgassing was neglected. Even though this result depends somewhat upon the makeup of the corium sources and the concrete type in the cavity, it does show that concrete outgassing can be important in the modeling of corium behavior in reactor cavities. In particular, the need to expand the traditional role of CORCON from steady-state ablation to the consideration of more transient events is clearly evident as a result of this work.

I. INTRODUCTION

Traditional methods for modeling molten core concrete interactions (e.g., [Co84]) neglect the transient response of the concrete when corium first encounters the surface. For some important reactor safety issues, this assumption may not be adequate. An example is the issue of drywell

* This work supported by the United States Nuclear Regulatory Commission and performed at Sandia National Laboratories, which is operated for the U.S. Department of Energy under contract number DE-AC-04-76DP00789.

shell melt-through in BWR Mark I reactors. Workers at Oak Ridge National Laboratory (ORNL) have studied this issue using a combination of the BWRSAR [Ho88] in-vessel code and the CONTAIN [Mu87] containment analysis code to model corium behavior in the BWR Mark I cavity. In these calculations, the BWRSAR code provided time-dependent sources of corium to the CORCON [Co84] model that is integrated into the CONTAIN code. In some scenarios studied to date, metals with relatively low superheat are first released from the vessel, while solid oxides are held in the vessel until they melt at a later time. Metal freezing accompanied by relatively little ablation was exhibited in these calculations up to the time of the higher temperature oxide pour. This behavior is, in part, attributed to the makeup of the BWRSAR sources and the high ablation temperature of the concrete; however, certain modeling deficiencies have also been identified as causing artificially cool conditions in the melt.

In the stand-alone version of CORCON (CORCON-MOD2), and the version of this model incorporated into the released version of CONTAIN (CONTAIN 1.10), heat loss to the concrete occurs only during ablating circumstances. If the melt-concrete interface temperature is below the specified ablation temperature, the interface is treated adiabatically. This assumption can have a profound effect upon scenarios involving long-term periods of non-ablation, such as the ORNL application, wherein liquid metals are first introduced into a cavity made of concrete with a high ablation temperature. The reduced heat loss results in an artificially high temperature of the melt and can lead to periods of ablation that would not occur if the heat were properly removed. A more realistic treatment, however, would not necessarily lead to overall lower corium temperatures nor less ablation in some scenarios, since heat loss to the concrete during such periods can result in a considerable amount of concrete outgassing. If chemically reactive metals (e.g., Zr and Fe) are present in the corium pool, the introduction of these gases will lead to or accelerate exothermic chemical reactions in the melt. The energy release from these reactions can be quite substantial, and can exceed the fission product decay heating rate by many times. The gas release and chemical heating processes contribute to one another in a positive feedback fashion. The absence of models for these processes in the default CORCON treatment has therefore been identified as potentially important for modeling corium behavior in certain severe accident scenarios.

The modeling limitations described above suggest that the behavior of the corium in the earlier calculations to assess corium behavior in the Mark I drywell were unrealistic. More precisely, it has been suggested that the chemical energy resulting from the reaction of evolved gases with metals in the corium would be sufficient to sustain the molten state of the corium that is in thermal contact with the shell. It is not clear, however, whether the chemical heating in the corium pool would outweigh the heat lost to the concrete.

A cooperative effort between workers at Sandia National Laboratories (SNL) and Oak Ridge National Laboratory (ORNL) was initiated to address these concerns, and assess the importance of the modeling limitations for scenarios

involving corium behavior in reactor cavities. This involved the development of a concrete outgassing model and appropriate interfaces between this model and the CORCON model embedded in the CONTAIN code. The result of this merger is the CONTAIN/OR code, a variant of the standard released version of CONTAIN which has been made available to ORNL for scoping calculations related to the Mark I Drywell Shell Attack issue. An important aspect of this effort has been the development, implementation, and assessment of the new concrete outgassing and thermal response model. The focus of this report will be on these efforts.

The outgassing model is described in Section II. This includes a description of the outgassing model itself and the model interfaces in the CONTAIN/OR code. A number of calculations assessing the validity of the CONTAIN outgassing model are given in Section III, where comparisons are made against the SLAM [Su84] and USINT [Be80] mechanistic concrete response codes. A demonstrational cavity response calculation to illustrate the effects of heat loss to the concrete and outgassing in a somewhat realistic accident sequence is presented in Section IV. A few concluding remarks are given in the final section.

II. MODEL DESCRIPTION

For discussion purposes, the CONTAIN outgassing model is divided into two parts: the outgassing model, and the CORCON interface. The outgassing model describes the release of gases in conjunction with the thermal response of the concrete. In keeping with the integrated analysis approach in CONTAIN, important coupling effects between the concrete response and the corium behavior are treated. The CORCON interface serves this purpose. The following two sections describe the concrete response model and the CORCON interface in turn. Even though these two portions of the outgassing model are discussed separately, the integrated nature of the model should be kept in mind.

II.A. Concrete Response Model

Three types of gases evolve when concrete is heated: unbound water, bound water, and carbon dioxide. Unbound water (also called evaporable water) evaporates and is expelled when concrete is heated to relatively low temperatures (~375 K). Calcium and magnesium compounds decompose at higher temperatures (> ~500 K), giving rise to the release of previously bound H_2O and CO_2. The CONTAIN outgassing model treats all three of these gas release processes. The gas release models are not completely mechanistic; however, certain important aspects of the governing physical processes are treated in a rigorous manner. The evaporable H_2O model differs from the bound gas release model, with the latter being the more rigorous. These two models are discussed below in turn. Important coupling effects between the outgassing model and the concrete heat conduction model are discussed in the last part of this section.

Evaporable water. The evaporable H_2O release model is based on a thermal penetration approach. In this approach, it is assumed that concrete begins to dry out when it reaches a certain temperature, and is completely dry when it has been heated to a predetermined temperature above that point. This non-mechanistic approach is founded on the observation that mechanistic concrete outgassing codes predict relatively constant temperatures at the wet/dry interface for a wide class of problems. This is particularly true if the pressure at the surface is steady, and if the dryout front has not receded too deeply (> 1 m) into the concrete.

The gas release is computed on a node-by-node basis as a function of temperature. The total amount of steam released in a given time step is the sum over all nodes of the gas release from each node as given by the following expression.

$$G = \sum_{k=1}^{N} \frac{M_k \, \theta(T_k, T_{mk}) \, (T_k - T_{mk})}{(T_{hi} - T_{lo})} \qquad (1)$$

where,

G	=	Gas mass released (Kg) in one time step
M_k	=	Initial liquid H_2O content in node k
T_k	=	Temperature of node k
T_{mk}	=	Highest previous temperature of node k
T_{lo}	=	User specified initiation temperature
T_{hi}	=	User specified temperature for complete dryout
θ	=	Heaviside step function
N	=	Number of concrete nodes

In practice, only a few nodes will actually release steam in any one time step, since a large fraction of the concrete will either be too cold, or will have already completely dried out.

The accuracy of this model undoubtedly depends on the value of the user-selected initiation and dryout temperatures, T_{lo} and T_{hi}. Experience with the model indicates that T_{lo}=373 K and T_{hi}=473 K work well for a wide variety of applications. These temperatures also correspond closely with the liquid saturation temperature (at 1 bar), and the observed temperature at the wet/dry interface in many SLAM and USINT calculations, respectively. These values are therefore used as the defaults.

Bound gas release. The bound H_2O and CO_2 release models are more mechanistic than the evaporable H_2O release model. This is a reflection of the fact that the governing equation that describes the decomposition of chemical

compounds is considerably more straightforward than those for liquid and gas transport through porous media. It is generally accepted that the decomposition of chemical compounds can be reasonably described by the following Arrhenius rate law,

$$\frac{dC}{dt} = - C \kappa e^{-E/(RT)} \qquad (2)$$

where,

C = Mass concentration of a chemical compound, Kg/m^3,
κ = Decomposition rate constant, s^{-1},
E/R = Activation energy divided by the gas constant, Kelvin, and
T = Temperature, Kelvin.

This expression is integrated over successive time steps to determine the bound H_2O and CO_2 release from the concrete. C in Eq. 2 denotes the concentration of magnesium or calcium compounds which, upon decomposition, release H_2O and CO_2. A separate expression is written for the compounds that decompose into H_2O and CO_2 respectively. The gas release is then determined by the change in the compound mass. The temperature in Eq. 2 is the end of time step value, determined through a simple iterative procedure. This implicit approach was adopted to avoid unrealistically large gas releases and temperature swings, particularly when large time steps are used.

The bound gas release model is limited to the decomposition of only one compound for bound H_2O, and another one for bound CO_2. For example, the decomposition of $MgCO_3$ and $CaCO_3$, both of which produce CO_2 gas, cannot be represented by separate rate equations of the type given by Eq. 2. The user does, however, have complete control over the selection of the rate constant, κ, and the activation energy, E/R, so that appropriate average parameters can be chosen.

A simpler model, identical to the evaporable H_2O release model described earlier, can also be used in such situations. This temperature range approach is provided for the study of certain parameter sensitivities, such as disabling a particular type of gas release.

Heat conduction. A key aspect of the concrete response model is the manner in which the concrete outgassing and heat conduction models are integrated. Concrete thermal response is modeled in CONTAIN using a relatively straightforward one-dimensional finite-difference heat conduction formalism. Changes have been made to this model to accommodate the gas release model. First, the energy required to decompose compounds in the concrete and/or evaporate water from the pores is accounted for in the heat conduction equation with appropriate energy sink terms. This is done so that gases released during a time step have an immediate impact on the temperature at the end of the same time step. Likewise, the end of time step temperature is used in the gas

release expressions given in Eq. 1 and Eq. 2. An iterative solution technique is used for this rigorous partitioning of the heat input between the gas release and the heating of the concrete. Second, the thermo-physical properties of the concrete are modeled as a function of temperature and concrete composition. As gases evolve, the heat capacity and thermal conductivity change due to an increase in the concrete porosity. Mass weighting is used to calculate the heat capacity, and volume weighting is used to determine the thermal conductivity for each node in the concrete. Composition and porosity are tracked for each concrete node throughout the calculation for this reason.

II.B. CORCON Interface

There are three main areas where the outgassing and CORCON models must interface. First, the gases evolved from the concrete must be introduced into the CORCON corium layers. Secondly, the concrete being ablated by CORCON must reflect the composition changes that take place as a result of outgassing. Finally, the heat lost from the corium to the concrete must be accounted for in CONTAIN's concrete response model in order to drive the gas release. Each of these areas will be discussed in turn. A general familiarity with the CORCON code and terminology is assumed in the following discussion. A discussion of the CORCON code and the models included therein is available in reference [Co84].

Gas exchange. Gases released from concrete are introduced into CORCON in a manner that is analogous to the treatment of gases that result from ablation. Thus, released gases contribute to both the film layer, which CORCON assumes to exist between the corium and the concrete, and the gas flux sparging the melt. While the CORCON cavity model is two-dimensional, the CONTAIN concrete response model is one-dimensional. In order to accommodate this difference, the interaction between the CONTAIN concrete layer and CORCON is restricted to the lowest CORCON corium layer. Gas masses from the concrete are converted to fluxes and applied at each ray location along the melt-concrete interface of this lowest layer. Since concrete gases contribute to the film thickness at the corium-concrete interface, they have an effect on the heat transfer rate between the corium and the concrete.

Effect of gas release on ablation. To achieve a consistent calculation, the composition of the concrete nodes is tracked in CONTAIN/OR and is used to obtain ablation products for CORCON. Thus, the amount of water and CO_2 being released by ablation along the lowest CORCON layer is dependent upon the location of the ablation front relative to the dryout fronts in the concrete. Ablation of layers other than the lowest utilizes properties of wet concrete and corresponds exactly to the default CORCON model calculation. This treatment of the upper layers is done to maintain consistency between the one-dimensional concrete response model and the two-dimensional CORCON cavity model. All applications made to date with the code have employed the "flat-bottom cylinder" shape for the cavity. For this geometry, the CONTAIN/OR treatment is quite acceptable, since ablation primarily takes place at the interface of the lowest melt layer and the concrete.

The specific energy required to ablate concrete is modified to reflect the altered concrete composition. This energy is made up of three components: the energy required to release any bound or evaporable gases, the sensible heat needed to raise the concrete to the ablation temperature and the heat of fusion needed to melt the concrete. In the CORCON system, the later two are accounted for together. In CONTAIN/OR these two components are separated, since they are needed at different points in the calculation. The sensible heat component depends upon the "pre-ablation" temperature of the concrete. This temperature is that obtained by a node during a preceding nonablating period. In this manner, an accounting is made of the amount of energy that has been transmitted into the concrete during such periods.

Heat loss from the corium. Accounting for the heat loss into concrete from the corium is a crucial portion of CONTAIN/OR. In the stand-alone version of the CORCON model and in the version of CORCON incorporated into the released version of CONTAIN, heat transfer to the concrete occurs only during ablating circumstances. As stated in the Section I, this assumption can be important for calculations involving long-term periods of non-ablation. Experience with CONTAIN/OR for scenarios involving high limestone concrete has shown that introducing liquid metals into the concrete cavity results in an extended period when no ablation takes place. The relatively high ablation temperature of high limestone concrete, 1750 K, and the lack of any significant decay heat in the liquid metal pour (predicted by the ORNL BWRSAR in-vessel code), account for this type of behavior. During the non-ablation periods, heat is driven into the concrete, establishing a thermal profile as deep as tens of centimeters into the concrete. This energy exchange is the driving force behind the concrete outgassing.

In an effort to simplify the interface as much as possible, heat transfer from the corium into the concrete is allowed to take place only during non-ablating periods. During these periods, the CONTAIN conduction solver is furnished with the thicknesses and averaged material properties of the CORCON layers. Energy source rates from chemical reactions and decay heating in the CORCON layers are also included in CONTAIN's conduction solution. The heat flux into the concrete is determined from a one-dimensional axial heat conduction calculation that is performed in conjunction with the concrete outgassing. The corresponding amount of energy is removed from the lowest CORCON layer in a volumetric manner. The temperatures of the CORCON layers and interfaces are still obtained with CORCON's heat conduction algorithm.

Energy transfered from the corium to the concrete during ablating periods is used exclusively for concrete ablation. By imposing this restriction, the difficulty is avoided of trying to partition the heat leaving CORCON into that going to ablation and that responsible for further propagation of the thermal profile and outgassing fronts. This treatment implies that during ablation periods, any thermal profile established in the concrete during preceding non-ablation periods will simply relax. Also, under this restriction CONTAIN/OR behavior limits to that of standard CORCON, once all dry and partially dried concrete nodes have been ablated away and steady-state ablation has been achieved.

II.C. Model Limitations

A few simplifying assumptions and modeling limitations believed to be most important are noted below. This discussion applies to both the gas release and CORCON interface models.

The evaporable water release model is not mechanistic. The thermal penetration, or temperature range, approach is related to the assumption that liquid initially present in the concrete pores is stationary until it evaporates. It is also assumed that gases released locally evolve instantaneously at the heated surface. A more mechanistic treatment would require the solution of mass continuity and flow equations for liquid and gas phases in parallel with energy balance equations in both wet and dry regions of the concrete. The decision was made to implement the simpler temperature range model because a number of applications requiring use of the outgassing model in multiple locations for long time periods would not feasibly permit the computational overhead associated with a more detailed model. Finally, the parametric model greatly simplified the challenging task of interfacing the concrete response model to the CORCON model in the code.

With regard to the CORCON interface, accounting for the heat loss from the corium to the concrete during non-ablating periods is done approximately. In this treatment, the two-dimensional cavity is temporarily converted into an equivalent-area one-dimensional corium/concrete slab for the conduction calculation. This is done in order to account for the mismatch between the one-dimensional concrete response model and the two-dimension CORCON model. A more rigorous approach would involve a two-dimensional ray-by-ray coupling of the heat-transfer/outgassing model with the thermal-conduction/crust-formation model of CORCON. This ambitious task is being addressed by other projects supported by the NRC. At the time of this study, however, none of these efforts had yet come to fruition.

III. MODEL VALIDATION

The primary objective of this aspect of the work was to validate the CONTAIN outgassing model for predicting gas release and temperature response of heated concrete for a variety of heating conditions. This was done by comparing CONTAIN results against the results of more mechanistic concrete response codes. It should be pointed out that no attempt was made to assess the validity of the CORCON interface described in Section II.B. It is not the intent of the CORCON interface treatment to provide a mechanistic model, but rather to allow the assessment of the possible importance of concrete outgassing effects on corium-concrete interactions. It was quite clear from the results presented later (see Section IV) that the CORCON interface adequately served this purpose.

Two mechanistic codes that model heat and mass transfer in concrete were employed in this study: USINT and SLAM. These codes were chosen for their proven history of successful benchmarking against experimental data. Both

codes are similar in capabilities; however, USINT treats steam release but does not model CO_2 release. Minor differences exist between USINT and SLAM in the implementation of the models from a numerical standpoint. The most important difference is that USINT uses a fixed node scheme, while SLAM uses a moving node approach. SLAM also has models for the ablation of concrete by molten sodium; however, these models were deactivated in the version of the code used in this study. Both codes solve realistic mass flow and conservation equations for liquid and gas transport in both the dry and wet zones of the concrete (i.e., the evaporable H_2O release is treated in a mechanistic manner). Both codes use expressions similar to Eq. 2 to describe the local liberation of bound H_2O and CO_2. Unlike the CONTAIN approach, however, these gases are not assumed to instantaneously evolve from the heated surface. More information about these two codes can be found in references [Be80] and [Su83].

Table 1
Case Description and Gas Release Result Summary

Case	Boundary Condition (T, W/m^2)	Problem Duration	Active Depth (m)	Other Code	Cumulative H_2O Release Other/CONTAIN (Kg)	Cumulative CO_2 Release Other/CONTAIN (Kg)
1a[1]	T=1000	48 hrs	1.2	SLAM	67.3/66.1	83.1/61.7
1b	T=1000	48 hrs	1.2	SLAM	67.3/74.4	83.1/77.8
1c[2]	T=1000	48 hrs	1.2	SLAM	67.3/68.3	83.1/77.8
2a	Q=0.15	500 s	0.02	USINT	2.85/2.72	N/A
2b[3]	Q=0.15	500 s	0.02	USINT	2.85/2.82	N/A
3a	T=1500	3600 s	0.2	SLAM	12.4/13.4	20.2/19.2
3b	T=2000	3600 s	0.2	SLAM	14.0/14.9	29.1/28.1

Notes

1. In this calculation, K was a function of gas release, or porosity. Thermal conductivity was strictly constant in all other cases for reasons that are discussed in the following subsection.

2. T_{lo}=450, and T_{hi}=475. The default values of 373 and 473 were used in all other calculations.

3. The temperature range approach was used to model bound H_2O release in this calculation, with T_{lo}=500 and T_{hi}=800. The default Arrhenius rate law approach was used in all the others for bound gas release.

Seven representative test cases, divided into three groups, are presented in this section. A semi-infinite concrete slab is heated for 48 hours in cases 1a, 1b, and 1c to validate the long-term response capabilities of the model. Short-term response is addressed in cases 2a and 2b, where a thin concrete slab is heated for 500 seconds. Cases 3a and 3b involve exposing a concrete slab for one hour to temperatures typically seen in reactor cavities under severe accident conditions. The concrete used in all cases consisted of the following mass percentages: 20% bound CO_2, 2% bound H_2O, and 3% evaporable H_2O. Magnetite concrete was used in all calculations, with a density (including the gases initially present) of 3739 Kg/m^3. The heat capacity and thermal conductivity were fixed at 1000 J/Kg-K and 2.0 W/m-K respectively. More details are given in Table 1, along with the cumulative gas release results for each case.

As a result of the long problem time, appreciable CO_2 release was expected in the first three calculations; therefore, USINT comparisons were not made. CONTAIN and SLAM temperature profiles at 1, 12, and 48 hours and cumulative gas release as a function of time are presented in Figure 1. The differences observed in temperature profiles and CO_2 release are due to CONTAIN's treatment of concrete properties. In the CONTAIN outgassing model, the concrete thermal conductivity (K) decreases as the concrete dries out according to the

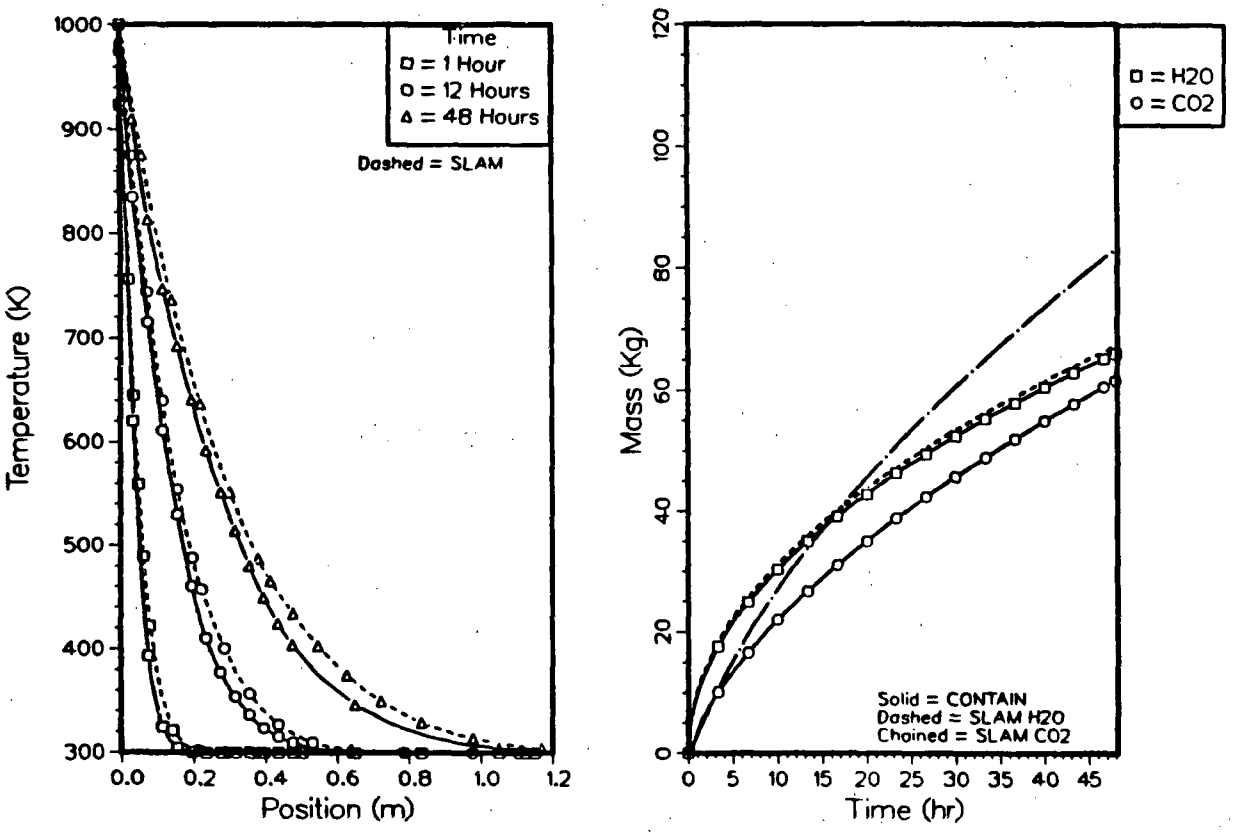


Figure 1 CONTAIN and SLAM Concrete Response Comparison for Case 1a

associated void fraction increase. The SLAM code includes no such treatment (it can however model K as a function of temperature). The change in K is particularly prominent at the surface of the concrete, where the temperatures are highest. Because a constant temperature boundary condition is imposed, the cumulative heat fluence to the slab in the CONTAIN case is considerably less than in the SLAM case. Over a 48-hour period, approximately 1.4×10^9 J were conducted into the concrete in the SLAM calculation, while only 1.1×10^9 J were conducted into the concrete in the CONTAIN calculation. The lower heat input in the CONTAIN calculation resulted in lower temperatures and gas releases. The excellent agreement shown in Figure 1 (also see Table 1) for the H_2O release is somewhat misleading, because an underprediction of the bound H_2O release was compensated by an overprediction of the evaporable H_2O release. These results demonstrate that concrete properties can have a noticeable effect on the thermal response and gas release for long-term problems.

A special version of the CONTAIN outgassing model, where concrete properties were assumed to be independent of gas content, was developed to avoid this inconsistency in the model validation. This version was only used in order to perform calculations for comparison against SLAM and USINT results.

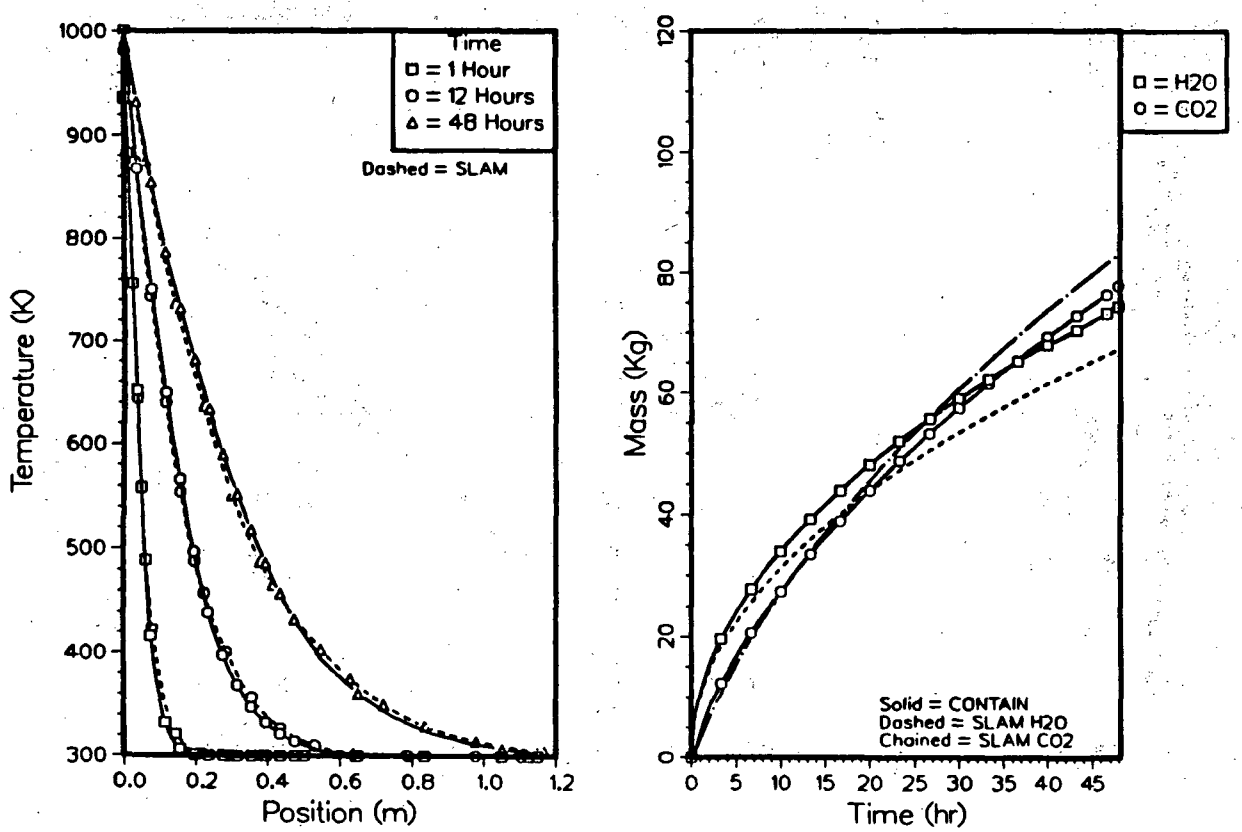


Figure 2 CONTAIN and SLAM Concrete Response Comparison for Case 1b

The CONTAIN/OR code was used without this modification for the sample calculation presented in Section IV. Case 1b represents a repeat of case 1a using the modified version of CONTAIN. As seen in Figure 2, the temperature profile and CO_2 release results for this case are in much better agreement with those of SLAM. This improvement is a result of a closer match between the total heat input to the concrete, which is 1.3×10^9 in CONTAIN for case 1b. The overall steam release agreement in case 1b, however, is worse. This is explained by the fact that the overpredicted evaporable H_2O release is no longer compensated by an underprediction of the bound H_2O release. The temperature range for evaporable H_2O was adjusted in case 1c in an attempt to improve upon this result. The values for T_{lo} (450 K) and T_{hi} (475 K) used in this calculation were derived by numerical experimentation. As seen in Figure 3, the steam release for this case are in excellent agreement with the SLAM result. Unfortunately, no basic guidelines can be offered by the authors for the selection of the temperature range for more generalized long-term applications.

Cases 2a and 2b address the model's ability to predict short-term gas releases. In these calculations a thin concrete slab (0.02 m) is rapidly heated by imposing a fixed surface heat flux of 0.15 MW/m^2. In case 2a, the

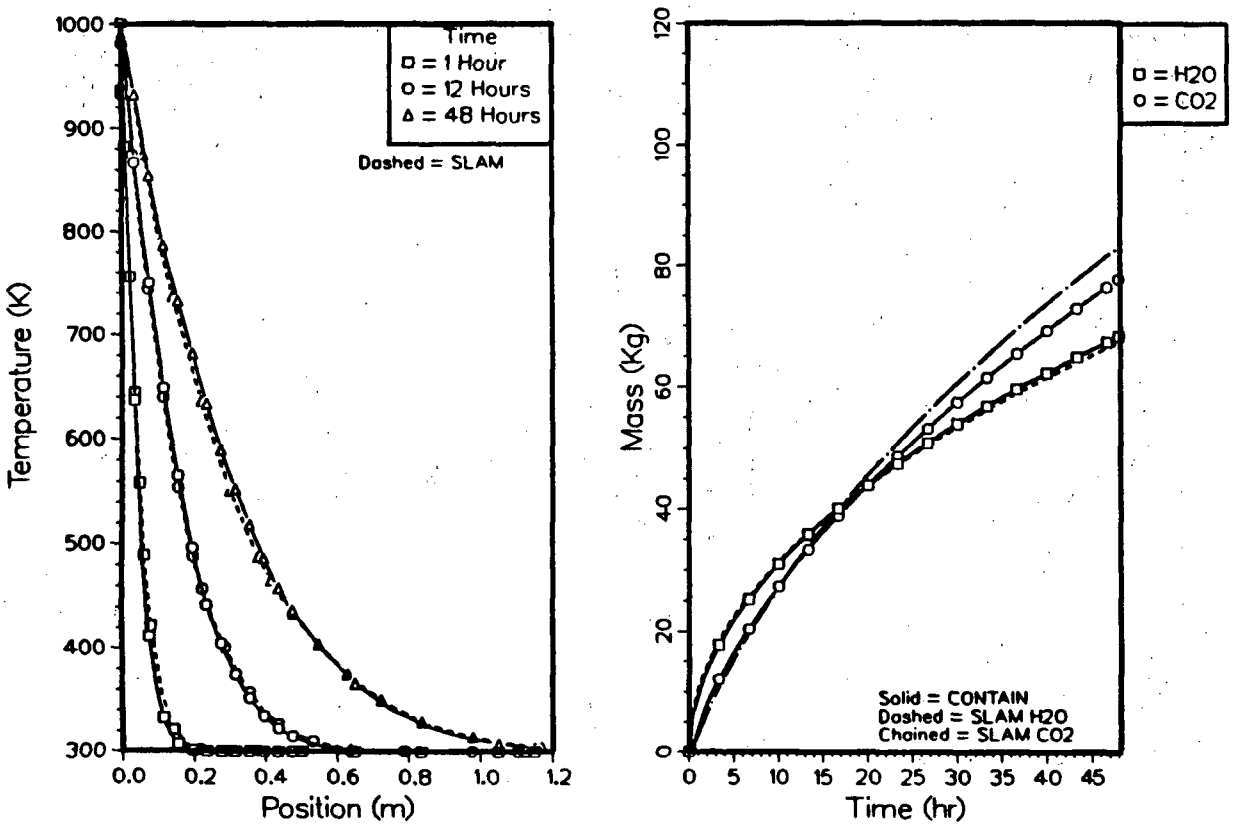


Figure 3 CONTAIN and SLAM Concrete Response Comparison for Case 1c

more mechanistic Arrhenius rate model is used to describe the release of bound H_2O, and in case 2b, the temperature range approach is used. USINT calculations for these cases were performed and compared against the CONTAIN results. SLAM calculations were not performed, since it does not provide for the specification of a constant heat flux boundary condition. Therefore, only H_2O release was considered, since USINT does not model CO_2 release. The results for cases 2a and 2b are given in Figures 4 and 5 respectively. In both cases, the agreement between the CONTAIN and USINT is excellent. This result indicates that, for short-term applications, the temperature range option performs well, despite its non-mechanistic nature.

CONTAIN results for Case 2a and 2b are shown in Figures 4 and 5, along with corresponding results from USINT. In reality, a finite amount of time is required for liberated steam to travel to the heated surface. This is accounted for in the USINT model but not in CONTAIN. As seen in Figures 4 and 5, however, this is not a major effect. It is seen that the USINT steam release prediction shown in Figures 4 and 5 is not a smooth function of time.

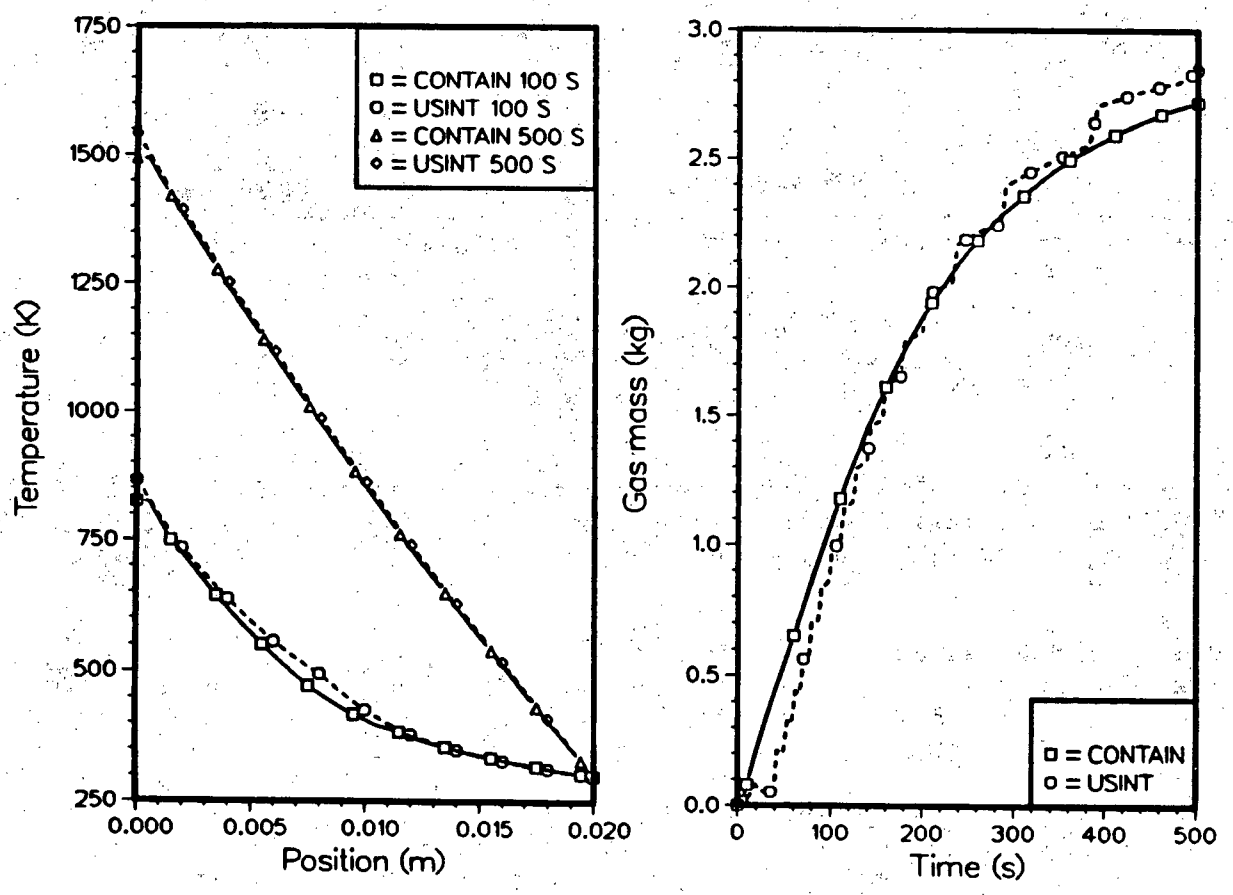


Figure 4 CONTAIN and USINT Concrete Response Comparison for Case 2a (Arrhenius)

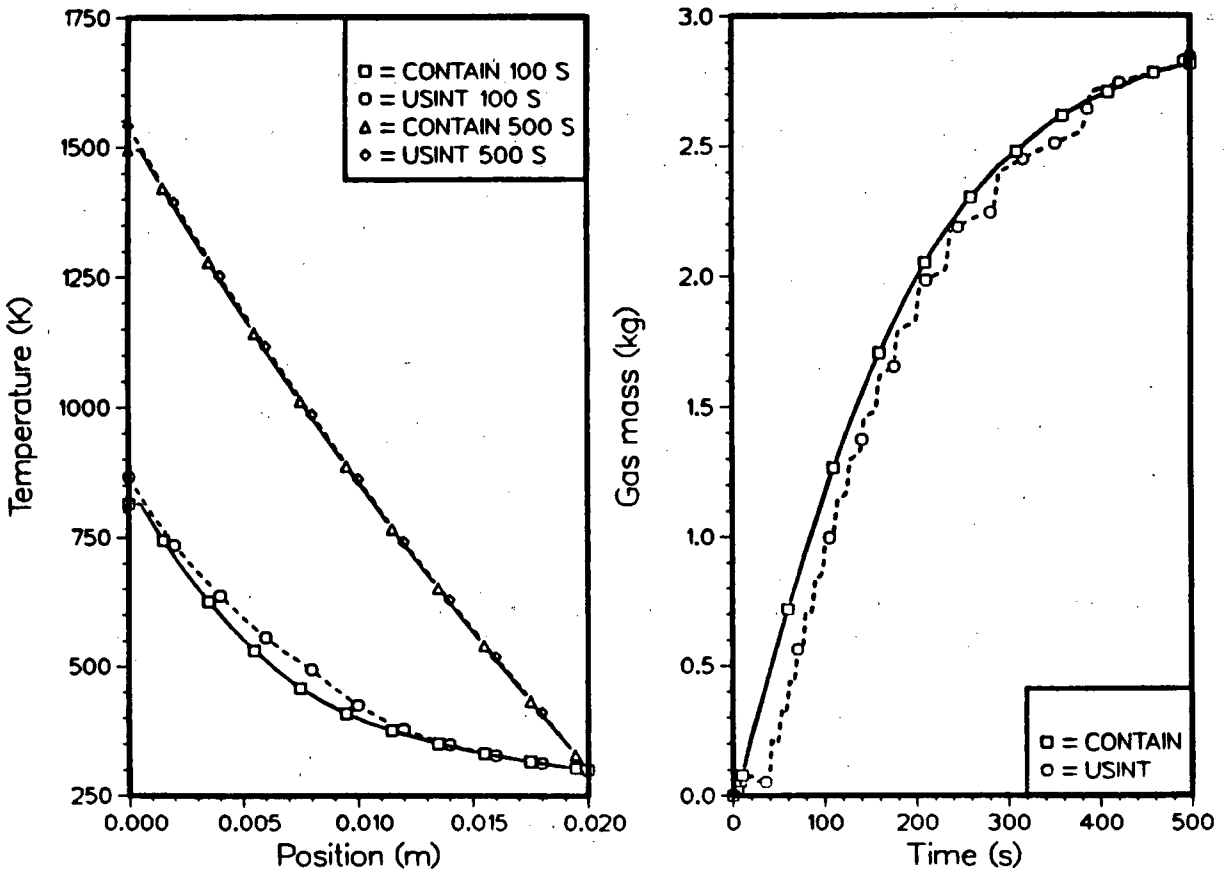


Figure 5 CONTAIN and USINT Concrete Response Comparison for Case 2b (Temp. range)

This somewhat unrealistic behavior is believed to be caused by explicit coupling between the gas release and heat transfer processes in the USINT code. In the CONTAIN model, these two processes are treated together in an implicit manner; therefore, the CONTAIN steam release prediction is a smooth function of time.

In cases 3a and 3b a semi-infinite concrete slab was heated for one hour by holding one surface at 1500 K and 2000 K respectively. Temperature profiles at 900 seconds and one hour for these two cases are presented in Figures 6 and 7. In both calculations, the CONTAIN temperature profiles are in excellent agreement with those predicted by SLAM. The gas release shown in Figure 6 is also in good agreement with the SLAM results. The gas release rate (the slope of the transient response curve) is in particularly good agreement. As seen in Figure 7, the gas release for the higher surface temperature case is also in very good agreement with the SLAM prediction. This result is viewed as particularly significant, because 2000 K is well above the ablation temperature of most concrete types used in reactor cavities.

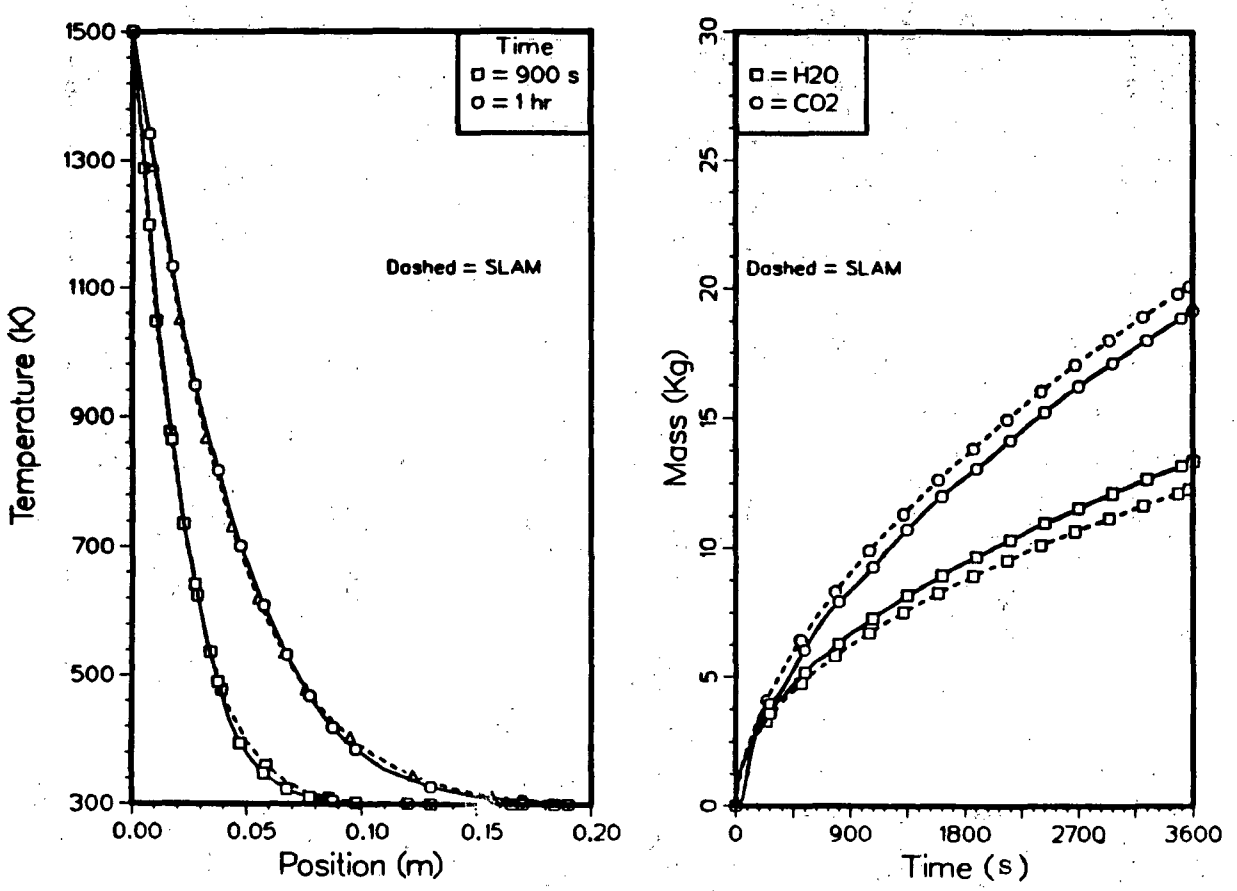


Figure 6 CONTAIN and SLAM Concrete Response Comparison for Case 3a

IV. A SAMPLE CALCULATION

To demonstrate the possible importance of improved concrete behavior models, the results of a sample calculation are presented in this section. The problem consists of a simple two-cell version of the more detailed nodalization developed by ORNL for the corium spread calculations. The cavity compartment of the two-cell problem represents the in-pedestal region of a BWR Mark I primary containment. The second cell is a large compartment to represent the balance of the containment. The sources used in this problem were obtained from the ORNL BWRSAR code [Ho88]. The cavity concrete type is high limestone, with an ablation temperature of 1750 K.

The use of the BWRSAR sources is one of the key elements in determining the outcome of the calculations presented here. The sources from the primary vessel are unique in that they dictate that the first materials to enter the cavity are liquid metals with a low superheat. Important features of this source include the presence of reactive zirconium in the pour and the absence

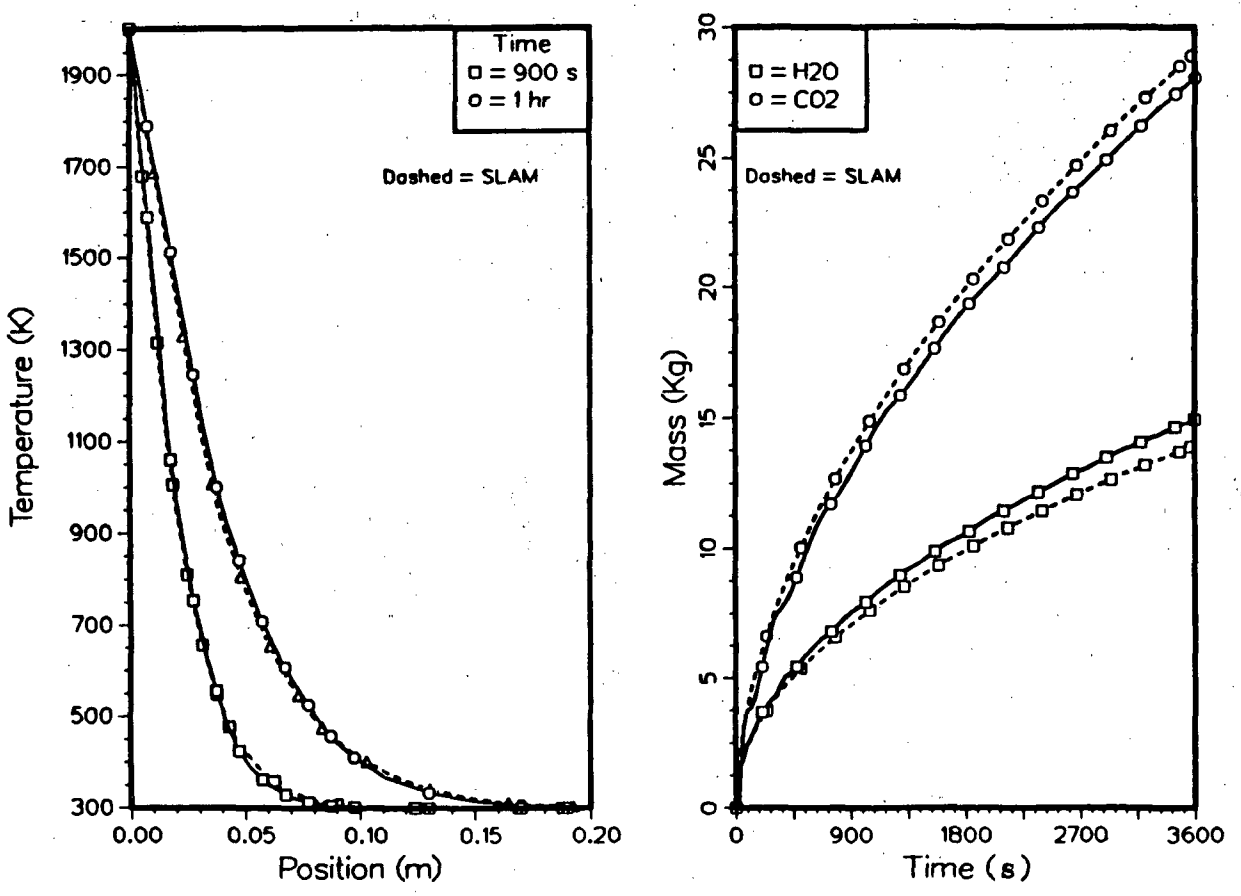


Figure 7 CONTAIN and SLAM Concrete Response Comparison for Case 3b

of any significant decay heating source. An additional key element of this problem specification is the use of high-limestone concrete. It has been observed that for concrete types with lower ablation temperatures, concrete outgassing has little effect, since steady-state ablation begins almost immediately. A third determining factor in this application is the absence of water in the cavity.

Figure 8 presents the metallic sources to the cavity from the failed primary vessel, as computed by BWRSAR. An initial pour of metal at a temperature of 1783 K lasts for 2400 seconds, followed by a hiatus of 1200 seconds. The second metal pour consists primarily of iron at a temperature that ranges from 2204 K to 2672 K. Figure 9 shows the oxide pour from the primary vessel, consisting primarily of UO and ZrO. The temperature of these materials is 2672 K. The initial pour of metals is very important for this scenario. While deprived of significant decay heating, these metals contain

substantial amounts of chemically reactive materials which, when exposed to gases from the concrete, reduce these gases in exothermic reactions. The energy from these reactions drives the concrete outgassing. These two processes contribute to each other in a positive feedback fashion.

Three different calculations are presented here. In situations where the outgassing model is used, the thermal penetration version is employed. Thus, evaporable water and chemically bound water and CO_2 are released from heated concrete within a given temperature range, the limits of which are user-defined. As seen by the earlier model validation study (see cases 2a and 2b), this treatment produces results which are acceptable for scoping calculations.

In the first case, the standard version of the CORCON model is used. As mentioned previously, in this configuration the CORCON model uses an adiabatic lower boundary in nonablating circumstances and there is no treatment of gas release from heated concrete. In the following figures, values from this calculation are labeled as "STND. CORCON." The second case consists of activating the CONTAIN conduction/gas-release model with its CORCON interface, but specifying a very high release temperature for the gases. This has the effect of removing the assumption of an adiabatic boundary during nonablating periods, but does not include the effects of gases released from the concrete. Values from this calculation are denoted "WITH HEAT LOSS" in the following figures. The final case has the concrete response model fully

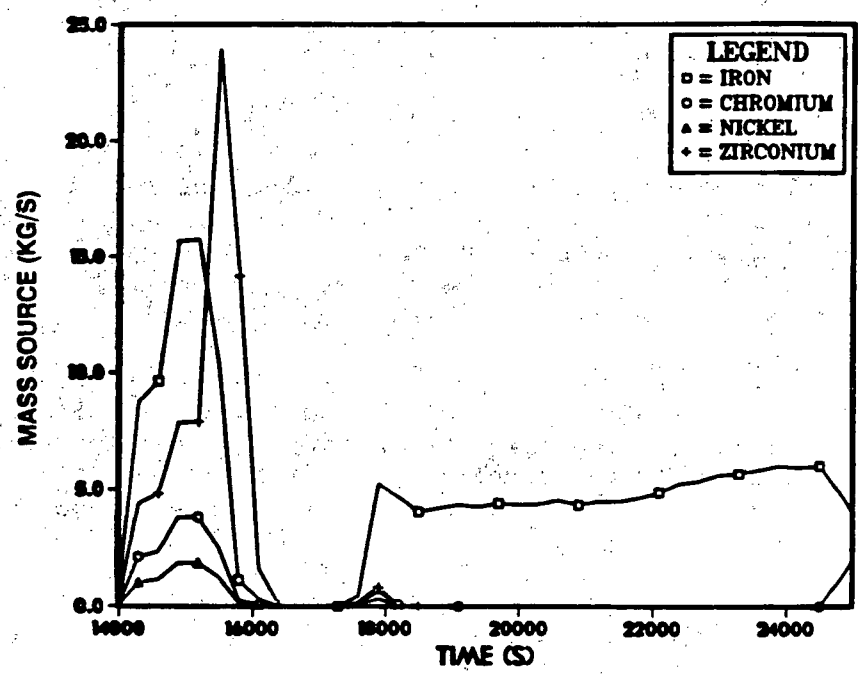


Figure 8 Metallic Sources to the Cavity Predicted by BWRSAR [Ho88]

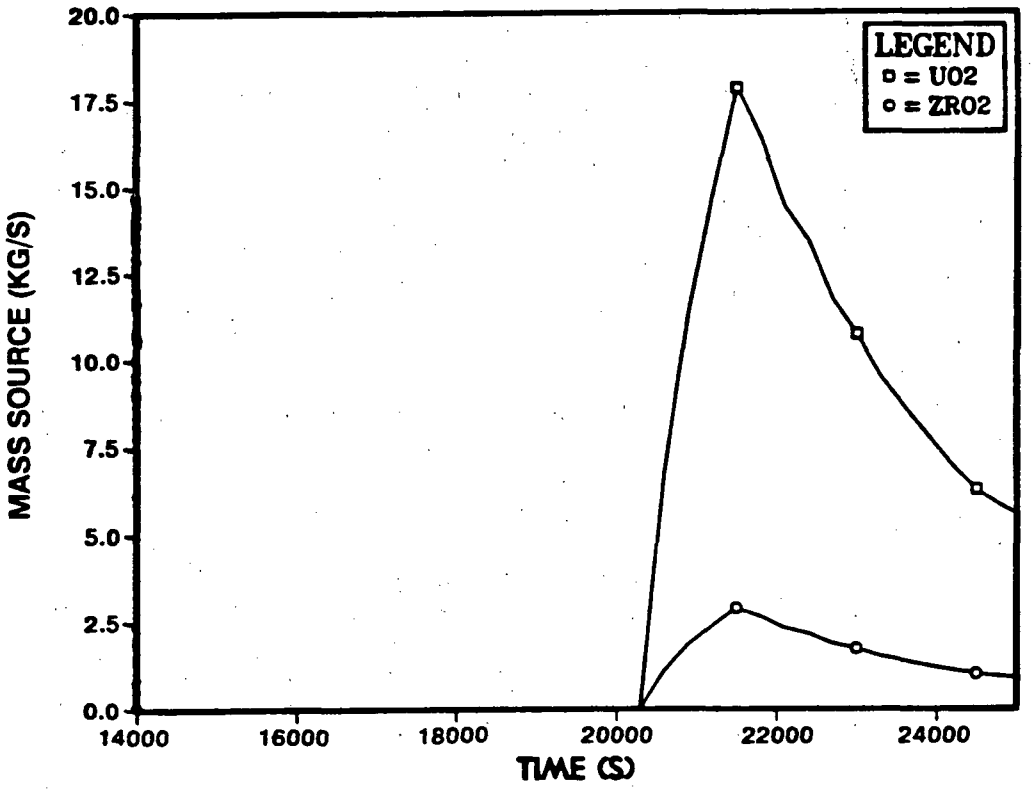


Figure 9 Oxidic Sources to the Cavity Predicted by BWRSAR [Ho88]

operational, with outgassing modeled and its effects taken into account in the CORCON model. The temperature ranges for gas release were based upon experience gained from the model validation exercise discussed earlier: evaporable H_2O (373 K - 500 K); bound H_2O (400 K - 800 K), and CO_2 (673 K -1800 K). Results from this calculation are labeled "WITH O.G."

Figure 10 presents a time history of the CORCON metal layer average temperature for the three cases described above. The most important feature of this plot is the behavior of the case with outgassing. The temperature initially settles at about 1750 K, the temperature of the solidus-liquidus transition. Ablation does not begin until about 18000 seconds. Before this time, the metal layer, which in this case is on the bottom of the CORCON configuration during the entire duration of the problem, maintains its temperature in the range of the solidus-liquidus transition. This temperature range is very close to the ablation temperature, and a situation is arrived at whereby the energy source due to the reaction of concrete gases with zirconium balances the heat lost from the melt. The temperature slowly rises and eventually the concrete ablation temperature is exceeded. Ablation starts at the modest rate of 3.6 cm/hr.

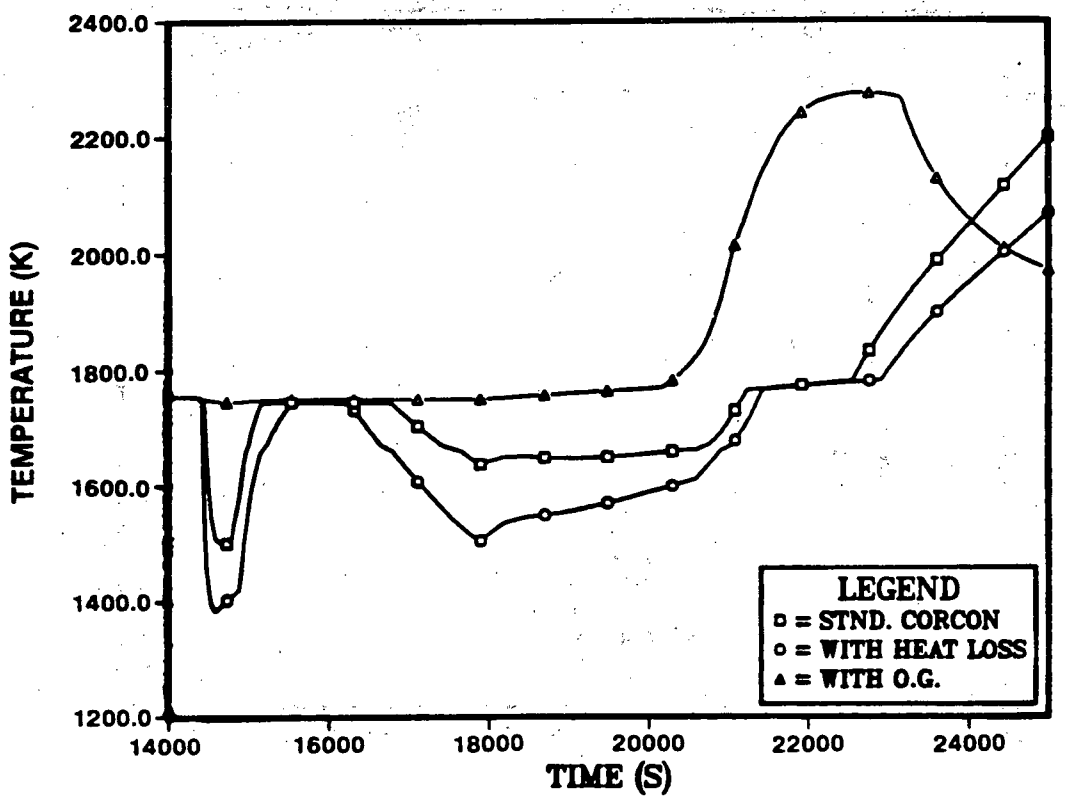


Figure 10 CORCON Metal Layer Average Temperature for Three Cases

The abrupt rise in metal layer temperature just prior to 20000 seconds is the result of the metal liquidus point finally being exceeded. The layer is fully molten and heat transfer to the concrete is increased. This results in an increased ablation rate and, with the enhanced flux of gases from ablation, the zirconium reaction is accelerated. Energy from these reactions raises the metal temperature and a positive feedback cycle is begun. As shown in Figure 11, the total inventory of zirconium metal is exhausted in about 3000 seconds. The feedback cycle is enhanced by the addition of the hot oxides from the primary vessel at a time of 20592 seconds. The burst of reaction results in a large amount of ablation and the final ablation depth in the case with outgassing is more than 30 times greater than that which takes place in either of the other two cases.

For the case with the outgassing model fully operational, the oxidic materials from the primary vessel reside in CORCON's light oxide layer. For the other two cases, the oxides move to a position below the metal layer, in the heavy oxide layer. The difference in behavior is due to the presence of a large light oxide layer in the outgassing calculation at the time of the heavy oxide pour. This material results from the earlier chemical reaction

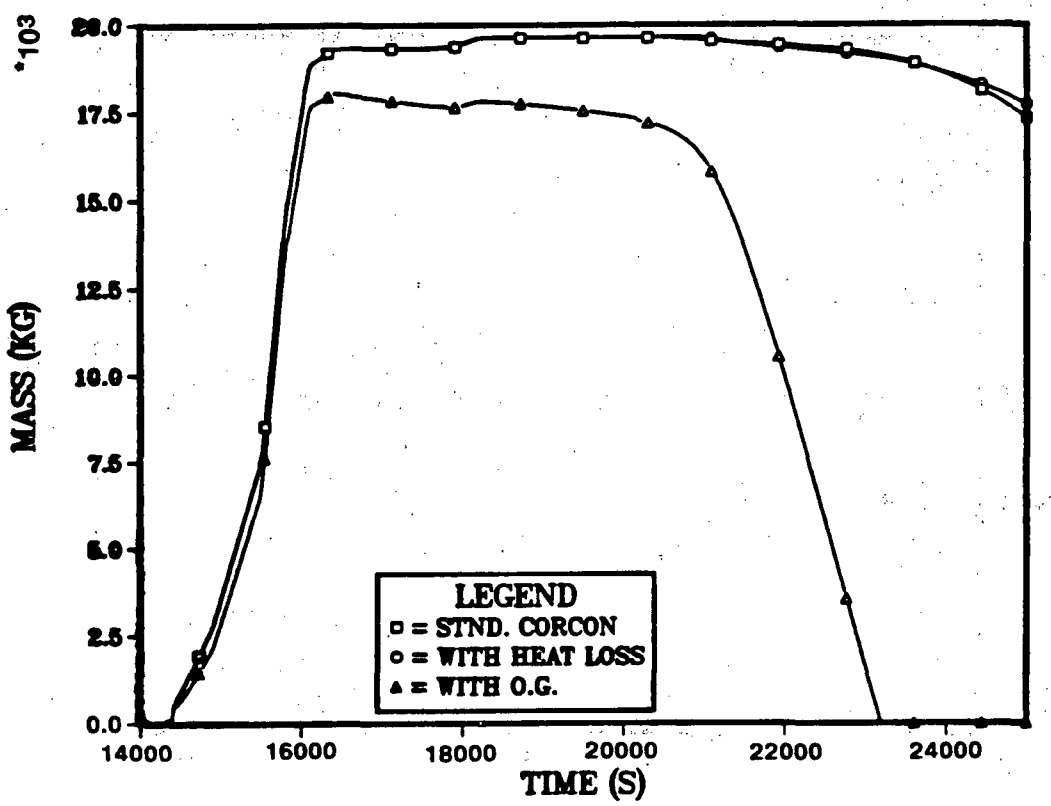


Figure 11 Zirconium Inventory in CORCON Metal Layer for Three Cases

of concrete gases with zirconium in the metal layer. These materials, as well as the products of the rapid burst of ablation, are sufficient to dilute the oxides from the vessel and maintain the light oxide layer above the metal layer. The ablation products contribute to this effect since CORCON is ablating dry concrete during this period and the products of ablation are less dense than would be the case for wet concrete. It must be noted that this behavior of the oxidic materials from the vessel is a result of the current model for source addition to the CORCON layers. The final disposition of the oxide materials from the vessel is a matter of uncertainty.

A comparison of results presented in Figure 10 for the first and second case, with the standard CORCON model and with heat loss from the bottom interface during nonablation periods, shows that the inclusion of bottom heat loss results in lower temperatures. While the standard CORCON case does show slow ablation during the period around 16000 seconds, the extra heat loss in the second case prevents all ablation until later time. Both of these cases show the start of steady- state ablation at the time of the oxide pour from the vessel. The oxide materials gravitate to the heavy oxide layer and form

a frozen layer with limited heat transfer to the concrete. No rapid zirconium oxidation takes place in these cases.

The initial drop of the metal layer temperature in the two cases without outgassing is due to heat loss to the concrete and from the surface, which is not compensated by any chemical energy source term. As continuing sources of metal are added to the layer, enough energy is retained to raise the temperature. Note that the case with heat loss but no gas release shows the metal layer temperature dropping immediately upon the cessation of the molten metal source from the primary vessel. The case with standard CORCON shows some extended period at elevated temperature after the cessation of the source. This is due to continuing slow ablation which introduces gases to the metal and thus supplies reaction energy. The termination of the downward trend in layer temperature at about 18000 seconds is due to a resumption of the metal layer pours.

These results have shown the importance in some accident calculations of not only removing CORCON's adiabatic lower boundary, but also including gases generated from heated concrete. The most significant aspects of the accident scenario studied here which dictate the importance of these effects are the presence in the cavity of reactive metals with low amounts of superheat, followed by an influx of oxidic materials at higher temperature, carrying decay heating energy sources. The type of concrete is also crucial to this behavior, requiring high ablation temperatures to observe the effects shown here. The absence of cavity water is an important part of the scenario presented. Many of the details of the calculational results shown here are dictated by the present state of the CORCON model and may change significantly with continued improvement of the models incorporated in this code.

V. SUMMARY

The model assessment results presented in Section III showed good agreement between the CONTAIN outgassing model and the USINT and SLAM mechanistic codes. This agreement was seen for short-term problems as well as for long-term problems. For the long-term cases, it was shown that the model slightly overpredicted the evaporable H_2O gas release. This inherent model deficiency was compensated somewhat by specifying higher temperatures for the initiation and dryout of the concrete. Finally, it was shown that the treatment of the thermophysical concrete properties as a function of temperature and gas release is important in long-term problems.

While originally motivated by the BWR Mark I drywell shell attack issue, the models introduced into CONTAIN/OR demonstrate in a general fashion the importance of treating gas release from concrete in those scenarios which do not result in immediate steady-state ablation of the concrete. The results shown in Section IV clearly demonstrate the need in such scenarios to expand the traditional role of the core concrete interaction models from steady-state ablation to the consideration of more transient events.

VI. REFERENCES

Be80 J. Beck and R. Knight, "User's Manual for USINT: A Program for Calculating Heat and Mass Transfer in Concrete Subjected to High Heat Fluxes," NUREG/CR-1375, SAND79-1694, Albuquerque, NM, 1980.

Co84 R. K. Cole, D. P. Kelly, and M. A. Ellis, "CORCON-MOD2: A Computer Program for Analysis of Molten-Core Concrete Interactions," NUREG/CR-3920, SAND84-1246, Sandia National Laboratories, Albuquerque, NM, 1984.

Ho88 S. A. Hodge, "BWRSAR Calculations of Debris Pours From the Reactor Vessel for Peach Bottom Short-Term Station Blackout," (published elsewhere in these proceedings), Proceedings of the 16th WRS Information Meeting, Gaithersburg, MD, 1988.

Mu87 K. K. Murata, et al, "User's Manual for CONTAIN 1.1, A Computer Code for Severe Nuclear Reactor Accident Containment Analysis," DRAFT, SAND87-2309, Sandia National Laboratories, Albuquerque, NM, 1987.

Su83 A. J. Suo-Anttila, "SLAM - A Sodium-Limestone Concrete Ablation Model," NUREG/CR-3379, SAND83-7114, Albuquerque, NM, 1983.

The Influence of Conventional PRA Conservatisms on The Assessment of BWR Accident Sequences

P. R. Hill and C. A. Kukielka
Pennsylvania Power & Light Company

Abstract

The Susquehanna Steam Electric Station is a two unit BWR4 plant using a Mark II containment. These 3293 MWt units have been in operation since 1982 for Unit 1 and 1984 for Unit 2. PP&L has devoted considerable resources to evaluation of the plant's capability to survive severe equipment failures such as ATWS and Station Blackout. These studies not only considered such severe events, but also considered the effects of additional equipment failures. In the evaluations the unconventional use of plant equipment was considered in order to assure a minimum level of plant damage for each succeeding level of equipment failure considered.

In mid-1985 PP&L performed an Individual Plant Evaluation for Susquehanna using a modified version of the IDCOR IPE Methodology for the BWR plant. In the performance of the IPE the same principle of considering what could be done with existing equipment was followed for all initiating events. The result was a drastic reduction in the calculated frequency of plant damage and the severity of the damage in comparison with previous PRA results. We have examined our Emergency Operating Procedures to determine whether the operators could be expected to make use of the equipment as assumed and found that with only a few problem areas that the actions would be indicated. Measurements of our operating crews' performance on simulator experiements to test the quality of our EOPs and training have indicated that we can expect our operators to utilize the full capabilities of the plant with a high degree of success.

This expectation has lead us to question the validity of several conventional PRA assumptions for the BWR plant. This presentation is intended to identify the most important of these and to demonstrate why we believe they are inappropriate for a plant with procedures that attempt to make maximum use of existing plant equipment.

THE PRIMARY PP&L OBJECTIVES
FOR
PROBABILISTIC RISK ASSESSMENT

- OUR PRIMARY OBJECTIVE IS TO ASSURE THAT ALL POSSIBLE CAPABILITY OF THE PLANT TO PREVENT OR MINIMIZE THE CONSEQUENCES OF PLANT DAMAGE WILL BE EFFICIENTLY AND EFFECTIVELY APPLIED FOR ANY INITIATING EVENT AND ANY COMBINATION OF EQUIPMENT FAILURES.

- THIS OBJECTIVE IS ACHIEVED BY:
  - TRANSIENT ANALYSIS OF ALL CRITICAL ACCIDENT SEQUENCES TO DETERMINE THE TIME AVAILABLE FOR OPERATOR ACTION,
  - APPLICATION OF EOPs TO EACH ACCIDENT SEQUENCE TO ASSURE OPTIMAL USE OF AVAILABLE EQUIPMENT,
  - OPERATOR TRAINING IN THE BASIS FOR AND USE OF EOPs, AND
  - CONFORMANCE OF ALL ACCIDENT SEQUENCES TO PP&L DEFENSE IN DEPTH CRITERIA.

- THE RESULT IS:
  - A TWO DECADE REDUCTION IN CALCULATED TOTAL PLANT DAMAGE FREQUENCEY, AND
  - A ONE TO TWO DECADE CALCULATED REDUCTION IN CONDITIONAL CONTAINMENT FAILURE PROBABILITY.

The Primary PP&L Objective for Probabilistic Risk Assessment

The BWR4 plant has a wealth of redundancy in equipment to serve the three basic front line functions required to avoid damage to the plant. PP&L wishes to assure that our operators at Susquehanna will make optimal use of this equipment for any initiating event with any combination of additional equipment failures. Fulfilling this objective requires that a realistic analysis of all accident sequences be performed in order to determine the time available for operator action to use the equipment, the degree of success permitted by various equipment combinations, and the occurrence of unambiguous symptoms which will trigger the operator actions.

In addition, it is necessary to have developed a comprehensive set of Emergency Operating Procedures (EOPs) which have considered all of the credible initiators that can threaten the plant. The EOPs which result are quite complex and are vulnerable to misinterpretation because of ambiguities or excessive complexity. Complexity can be greatly reduced by use of a flow chart format which references the specific details for actions taken to supplemental written procedures. Ambiguity is addressed by testing operator performance in use of the EOPs in simulator exercises involving a variety of severe accident scenarios designed to exercise as much of the EOPs as possible. The effectiveness of the EOPs is determined by an analysis of the accident transient which considers the actions specified by the EOPs.

We believe that, with effective operator training the contribution of operator failure to follow a procedural step will be dominated by equipment failure rates in all cases where adequate time is available to take the action. This view is supported by the results of the program of measurement of operator performance on the Susquehanna simulator. This level of performance is critically dependent on the organization and clarity of the EOPs and the thoroughness of operator training in their use.

The overall adequacy of plant equipment to respond to all credible initiating events is tested by application of a set of procedural and equipment defense in depth criteria. These criteria were presented at this meeting by R. A. Cushman in Session 6, Industry Safety Research. With the exception of a wetwell vent capability PP&L has found that very simple, low cost modifications can be made to existing equipment to assure defense in depth can be met. Examples are:

1) provision for connection of the Fire Main System to the RHR Service Water System by fire hose,

2) connection of the SLCS boron solution tank to the RCIC suction by fire hose, and

3) provision of a back up AC generator for connection to battery chargers in long term Station Blackout events.

CONVENTIONAL PRA CONSERVATISMS

- o FAILURE TO:
  - INITIATE SLCS
  - CONTROL WATER LEVE IN ATWS
  - PREVENT HPCI/RCIC SUCTION TRANSFER AND HIGH BACK PRESSURE TRIP
  - DEPRESSURIZE WHEN THE HEAT CAPACITY TEMPERATURE LIMIT (HCTL) IS REACHED IN ATWS
  - SHUTDOWN BY MANUAL ROD INSERTION FOR SLCS FAILURE IN ATWS
  - INCREASE THE HEAT CAPACITY TEMPERATURE LIMIT (HCTL) CURVE FOR ATWS
  - PARTITION ATWS EVENTS
  - ACCOUNT FOR SAVING THE REACTOR PRESSURE VESSEL
  - PROVIDE BACKUP WATER INVENTORY FOR CONDENSATE STORAGE TANK
  - STRIP NON-ESSENTIAL DC LOADS IN STATION BLACKOUT
  - DEPRESSURIZE EARLY IN STATION BLACKOUT TO ALLOW SUCCESSFUL FIRE MAIN INJECTION
  - MAKE EARLY FIRE MAIN CONNECTION TO RHR SERVICE WATER (RHRSW)
  - USE ALTERNATE WATER INJECTION SOURCES
  - USE ALTERNATE DEPRESSURIZATION METHODS
  - USE REACTOR WATER CLEANUP (RWCU) BLOWDOWN FOR DHR IN TRANSIENTS WITH RHR FAILURE
- o USE OF UNREALISTIC COMMON MODE FAILURE (CMF) TREATMENT

The provision of a wetwell vent capability at Susquehanna that has acceptable characteristics appears to be a rather expensive modification, but the venting issue has not yet been resolved at PP&L.

This use of PRA techniques is much more important than use of it for conservative assessment of plant damage frequency and public risk. The use of realistic PRA as discussed above results in a very sharp reduction in calculated plant damage frequencies. We believe that the reduction is real, particularly with regard to protection of containment integrity.

Conventional PRA Conservatisms

If the process discussed in the previous viewgraph is adopted, many of the assumed causes of loss of a front line function found in conventional PRA treatments become unrealistic and lead to an improper view of the dominant accident sequences for the BWR4 plant.

ATWS represents a severe (but low frequency) threat to the BWR plant. Nevertheless, if the operator takes prompt response and anticipatory actions, given occurrence of ATWS, the expected frequency of severe consequences of ATWS can be held at an extremely low level. The first seven of the actions (and analysis assumptions) listed in this viewgraph represent actions which can assure a very high level of success at minimizing plant damage as a result of an ATWS event.

While time is limited for operator response in ATWS events, our analysis shows that the most frequent ATWS event of a serious magnitude is result of a single Scram Discharge Volume failure which results in the rods on only one side of the core failing to insert. The reduced power generation of this type of ATWS provides sufficient time for operator action to assure a very high level of success even for isolation events in which SLCS or HPCI fail. The operator actions are important as follows.

1) Timely SLCS initiation terminates the threat of the ATWS event and assures shutdown without plant damage.

2) Actions to control water level are minimized at Susquehanna and require only HPCI to run at full flow in isolation events or feedwater run back to an equivalent flow in non-isolation events.

3) Depressurization to the 150 to 200 psia range is required for power reduction if SLCS fails. This power reduction allows time for manual insertion of 46 control rods to reach hot shutdown.

4) Since high pool temperatures may be reached, prevention of HPCI suction transfer or high back pressure trip is important (but not essential) to minimize the threat of inadequate core cooling or severe reactivity transients.

BWR FRONT LINE FUNCTIONS

- o REACTOR VESSEL MAKE UP
  - ASSURES ADEQUATE CORE COOLING AND ABSENCE OF FUEL DAMAGE EXCEPT FOR DEGRADED ATWS EVENTS.
- o DECAY HEAT REMOVAL
  - IN THE ABSENCE OF CORE DAMAGE, ASSURES PROTECTION AGAINST CONTAINMENT OVERPRESSURE FAILURE.
- o REACTOR SHUTDOWN
  - REDUCES HEAT GENERATION RATE TO WITHIN DHR SYSTEM CAPABILITY.
- o DEBRIS COOLING
  - RESTORE VESSEL INJECTION TO PREVENT REACTOR VESSEL FAILURE.
  - OPERATE VESSEL INJECTION OR DRYWELL SPRAYS TO COOL EX-VESSEL CORE DEBRIS

With these provisions, the frequency of plant damage from ATWS is sharply reduced and the dominant form of plant damage is postulated mechanical clad damage resulting from reactivity excursions or unstable operation in a low pressure regime.

The level of success is also very high even for full ATWS events where time constraints are much shorter. While mechanical clad damage is postulated to be nearly certain, unless SLCS functions properly, containment over pressure failure is always avoided except in cases of very massive equipment loss.

Similar results can be achieved for Station Blackout by:

1) assuring adequate CST inventory for vessel injection,

2) stripping non-essential DC loads or by backing up the DC supply, and

3) early depressurization to prepare for vessel injection from the Fire Main System in the event of HPCI or RCIC failure.

Similar improvements can also be made for transients by:

1) utilization of alternate water sources,

2) use of alternative depressurization methods, and

3) use of RWCU blowdown mode for decay heat removal

in sequences which benefit from such actions.

Finally, it is essential to avoid unrealistic treatment of common mode failure. We believe that loss of redundant system function is dominated by one division being out of service for maintenance accompanied by independent failures in the other division or by loss of common support systems such as loss of all AC power in Station Blackout.

BWR Front Line Functions

The first three functions listed in the viewgraph are the basic BWR front line functions, which, if satisfied, will assure safe shutdown of the plant with no plant damage. There are a variety of plant systems which can satisfy the requirements of these functions.

When severe accidents are to be considered, it is important, in addition, to consider a fourth "front line function" that will stabilize the core debris and halt the damage progression even when the prime function of reactor vessel make up has initially failed. Most important is terminating the damage progression prior to reactor vessel failure. PP&L uses the ORNL BWRSAR code and criteria developed by Steve Hodge and his co-workers at ORNL for determining the level of success for this objective.

EVENT CODES

A - NORMAL SYSTEM

B - AVAILABLE, NOT REQUIRED

C - ALTERNATE SYSTEM

D - AVAILABLE BUT NOT ADEQUATE

E - EXTENDS TIME AVAILABLE FOR EQUIPMENT RECOVERY OR SHUTDOWN

F - SAVES REACTOR VESSEL

X - AVAILABLE FOR DEGRADED CONDITIONS

	APPROXIMATE FREQUENCEY OF OCCURRENCE
1. NON-ISOLATION TRANSIENT	3^{+} YR^{-1}
2. ISOLATION TRANSIENT	1 YR^{-1}
3. LOSS OF OFFSITE POWER	0.06 YR^{-1}
4. STATION BLACKOUT	2×10^{-4} YR^{-1}
5. LOCA (LARGE AND MEDIUM)	3×10^{-3} YR^{-1}
6. PARTIAL ATWS	5×10^{-5} YR^{-1}
7. PARTIAL ATWS + STATION BLACKOUT	4×10^{-9} YR^{-1}
8. PARTIAL ATWS + LOCA	6×10^{-8} YR^{-1}
9. FULL ATWS	6×10^{-7} YR^{-1}
10. FULL ATWS + STATION BLACKOUT	4×10^{-11} YR^{-1}
11. FULL ATWS + LOCA	6×10^{-10} YR^{-1}

+ INCLUDES ONLY TRANSIENTS IMPORTANT TO ATWS.

If the reactor vessel has failed, actions can be taken to flood the drywell floor before vessel failure and operate drywell sprays or vessel injection sources after vessel failure to reduce the threat of core debris to the containment integrity. PP&L intends to use the CONTAIN code recently acquired from Sandia National Laboratories for these calculations. This code is not yet operational at PP&L, but preliminary information obtained from various investigations of the behavior of core debris falling into the under-pedestal region, in combination with the available equipment, leads us to expect a high level of success in protecting containment integrity even in this severe condition of the plant.

Event Codes

The complexity of the next two viewgraphs has made it necessary to provide a separate list of the event codes necessary to interpret the tables. This viewgraph presents the codes for constraints on availability of systems and defines the events which have been considered. While this list is not complete it does include the most important and the most severe event types in order to demonstrate the influence of the event type on equipment availability and effectiveness.

FRONT LINE FUNCTION

VESSEL MAKEUP

HAVE	FRONT LINE SYSTEM	NEED	EVENT										
			1	2	3	4	5	6	7	8	9	10	11
3	FEEDWATER (0,1 FOR 1)	1	A					A			A		
1	HPCI } (3×10^{-3})	1	X	C	C	C		C	A		C	A	
1	RCIC } (3×10^{-3})	1	X	A	A	A		D	D		D	D	
2	CRD (0,01)	2	X	X	X		F	D		F	D		F
2	SLCS (0,01 FOR 2 PUMPS)	2	F	F	F		F	X		F	X		F
16	SRVs (6×10^{-6})	1	X	X	X	X	X	X	X	X	X	X	X
4	LPCI } (10^{-5})	1	X	X	X		A	X		X	X		X
4	LPCS } (10^{-5})	1	X	X	X		A	X		X	X		X
4	CONDENSATE (0,01)	1	X	X			C	X		A	X		A
4	RHR SERVICE WATER (4×10^{-5})	1	X	X	X		X	X		X	X		X
2	FIRE PUMP (0,03)	1	X	X	X	F	F		F	F	F	F	F

Front Line Function
Vessel Make Up

In this viewgraph a matrix of the front line systems which can supply make up to the reactor vessel are listed down the left hand side of the matrix and the various events which can challenge these systems are listed across the top. Unavailability of a system for a given event is depicted by a blank space. Systems which are available are denoted by a letter code which denotes various considerations related to the availability.

A variety of quantitative information is given in this viewgraph including,

1) the number of components available,

2) the number of components required to perform the function,

3) the frequency of the various events, and

4) the unavailability or failure rate of the front line systems where applicable.

Examination of this matrix quickly shows that loss of vessel make up capability is an extremely improbable event for all transients, LOCAs, and loss of off site power. Except for the low pressure ECCS injection permissive which reduces 8 pumps with 4 independent power sources to an unavailability of 10^{-5}, there are no important common cause losses of equipment to threaten inadequate core cooling except loss of all AC power, Station Blackout. Even in this case, however, there are two independent reactor steam driven pumping systems available which, when combined with the low frequency of the Station Blackout event, results in a core damage frequency in the 10^{-7} range. The causes of core damage in Station Blackout in the long term are sharply reduced by operator actions to avoid them. These include:

1) back up of DC power,

2) early depressurization and connection to the Fire Main System to permit injection if HPCI and RCIC are lost after the first hour.

3) addition of water to the suppression pool from the Fire Main System to reduce the rate of pressure increase in the containment due to pool heat up, and

4) operation of the wetwell vent as a last resort to preserve containment integrity.

Even in the case of HPCI/RCIC failure to start (the dominant core damage sequence) the Fire Main connection can save the reactor vessel and greatly reduce the threat to containment integrity.

FRONT LINE FUNCTION

DECAY HEAT REMOVAL AND REACTOR SHUTDOWN

HAVE	FRONTLINE FUNCTION FRONTLINE SYSTEM	NEED	EVENT										
			1	2	3	4	5	6	7	8	9	10	11
	DECAY HEAT REMOVAL												
1	MAIN CONDENSER	1	A					A			A		
2	SUPPRESSION POOL COOLING (6×10^{-6})	1	B	A	A		A	D		D	D		D
1	RWCU BLOWDOWN (4×10^{-3})	1	X	X									
-	POOL MASS ADDITION & RECOVERY	-	B	E	E	E	E	E		E	E		E
1	WETWELL VENT (0.01)	1	B	X	X	C	X	D	D	D	D	D	D
	REACTOR SHUTDOWN												
185	SCRAM SYSTEM RODS (6×10^{-5})	93	C	A	A	A	A						
2	STANDBY LIQUID CONTROL SYSTEM (0.003)	1	X	X	X			A		A	A		A
185	MANUAL ROD INSERTION (0.01)	93	A	X	X		X	C		C	C		C
1	RCIC - SLCS CONNECTION	1	X	X	X		X	X		X	X		X

Inadequate core cooling in transients, LOCAs, and ATWS is believed to be a much less probable occurrence due to the numerous systems available which can provide adequate make up flow. The primary risk in these sequences is believed to involve ATWS sequences in which reactor depressurization is required while the reactor is still critical and at power levels well above the decay heat level. Our concern in such cases is postulated mechanical clad damage due to reactivity transients rather than inadequate core cooling however.

Assurance that operators will properly make use of the equipment available for the events shown here must be the first priority in structuring EOPs, operator training, and evaluation of plant capabilities.

The Susquehanna IPE contains detailed descriptions of the various actions, commonalities, and success criteria for this function.

Front Line Functions
Decay Heat Removal and Reactor Shutdown

The system-event matrix for the front line functions Decay Heat Removal and Reactor Shutdown are presented in this viewgraph. For Decay Heat Removal (DHR) a response action used when normal systems are unavailable has been included. This action involves adding water to the suppression pool by means of any one of several systems which can do this. The primary purpose of this action is to avoid the necessity of venting and to provide time to reacquire the condenser or suppression pool cooling capability. In the case of transients this can extend the time to venting pressure out to beyond 40 hours and the time to containment failure out to about 60 hours given no core damage. This capability can greatly enhance the likelihood of regaining suppression pool cooling capability.

This capability combined with the introduction of RWCU blowdown for transient events virtually eliminates the need to vent as a response to loss of other forms of Decay Heat Removal. The addition of mass to the pool also provides a greatly increased time margin for operator action in other events and can be particularly important for Station Blackout and ATWS. Use of this capability for full ATWS cases with failure of SLCS to inject boron would virtually assure operator success at reaching hot shutdown before reaching containment failure pressure. If this is also reinforced by operation of full suppression pool cooling capability and operation of the wetwell vent, even greater time margin can be provided. The acceptability of venting during degraded ATWS sequences is still under investigation at PP&L since mechanical clad damage and noble gas release are possible early in the event.

The limiting accidents for Decay Heat Removal are clearly Station Blackout and ATWS. The threat from transient events is clearly negligible as a consequence of the redundant and diverse means of Decay Heat Removal. In the case of Station Blackout, AC power recovery becomes the prime objective for recovering

SUMMARY

- PROVIDING EXPLICIT GUIDANCE AND TRAINING TO ASSURE OPERATOR USE OF ALL AVAILABLE PLANT CAPABILITY IN AN ACCIDENT SEQUENCE CAN REDUCE CORE DAMAGE FREQUENCY BY TWO DECADES AND CONDITIONAL CONTAINMENT FAILURE PROBABILITY BY OVER ONE DECADE.

- A HIGH PRIORITY MUST BE ASSIGNED TO:

  - SAVING THE REACTOR VESSEL,
  - AVOIDING LOSS OF CRITICAL EQUIPMENT,
  - UTILIZING ALL AVAILABLE RESOURCES FOR VESSEL MAKE UP AND DECAY HEAT REMOVAL,
  - ASSURING PROPER OPERATOR RESPONSE IN ALL ATWS EVENTS.

- EOPs MUST BE COMPREHENSIVE AND THOROUGHLY REVIEWED AND TESTED FOR EFFECTIVENESS.

- OPERATOR TRAINING MUST BE THOROUGH AND INCLUDE BOTH UNDERSTANDING OF THE REASONS FOR ACTIONS AND PRACTICE IN EXECUTION.

- THIS APPROACH OFFERS BY FAR THE MOST CREDIBLE, DEPENDABLE, AND COST EFFECTIVE APPROACH TO TRUE OPERATIONAL RISK REDUCTION.

DHR with wetwell venting being a last ditch action. In the case of ATWS the hierarchy of actions to achieve adequate DHR capability involves reducing the heat generation rate by injecting boron or, failing that, by manual rod insertion. Reactor pressure reduction, suppression pool mass addition, and possibly wetwell vent operation can all extend the time available to succeed at these actions.

As a result of these capabilities a proper set of EOP instructions and operator training in their use can sharply reduce the greatest threats to containment integrity from Station Blackout and ATWS.

In the case of achieving Reactor Shutdown, one additional capability exists at Susquehanna - connecting the RCIC suction to the SLCS boron solution tank by means of a fire hose. While this capability exists it is very time consuming due to the physical elevation separation of these systems and requires on the order of one to two hours to make the connection. Nevertheless, this capability could be extremely important in severely degraded cases where CRD pumps were not available.

Summary

The preceding discussion has shown that considerable capability exists in the BWR4 plant to achieve a dramatic reduction in the calculated values of plant damage frequency and a reduction in the severity of that damage in comparison with conventional PRA treatment of the BWR plant. Accomplishing such a reduction does impose strict demands on the quality and comprehensiveness of EOPs and operator training in their use. This process will require far more realism and rigor in the calculation of accident transients and the translation of the information derived into practical and demonstrably effective EOPs. In addition to developing procedures strictly directed toward avoiding core damage, the process must be extended to terminating the damage progression, preferably in-vessel.

It is important to test the procedures and operator capability for execution of them using a plant simulator if possible. Only in this way can it be determined that the EOPs will actually result in the operator actions envisioned when they were written. It is by far the most effective way to assure the absence of ambiguity, the practicality of the procedures, and the adequacy of the operator's knowledge to use them effectively.

While this approach imposes a heavy demand on analytical, documentation, and training capabilities of the organization it is by far the most credible, dependable, and cost effective approach to true operational risk reduction for a nuclear plant.

Toward Estimating
MARK-I
LINER-FAILURE PROBABILITY

by

T.G. Theofanous, U. Ratnam and A. S. Wanniarachchi
Department of Chemical and Nuclear Engineering
University of California
Santa Barbara, CA 93106

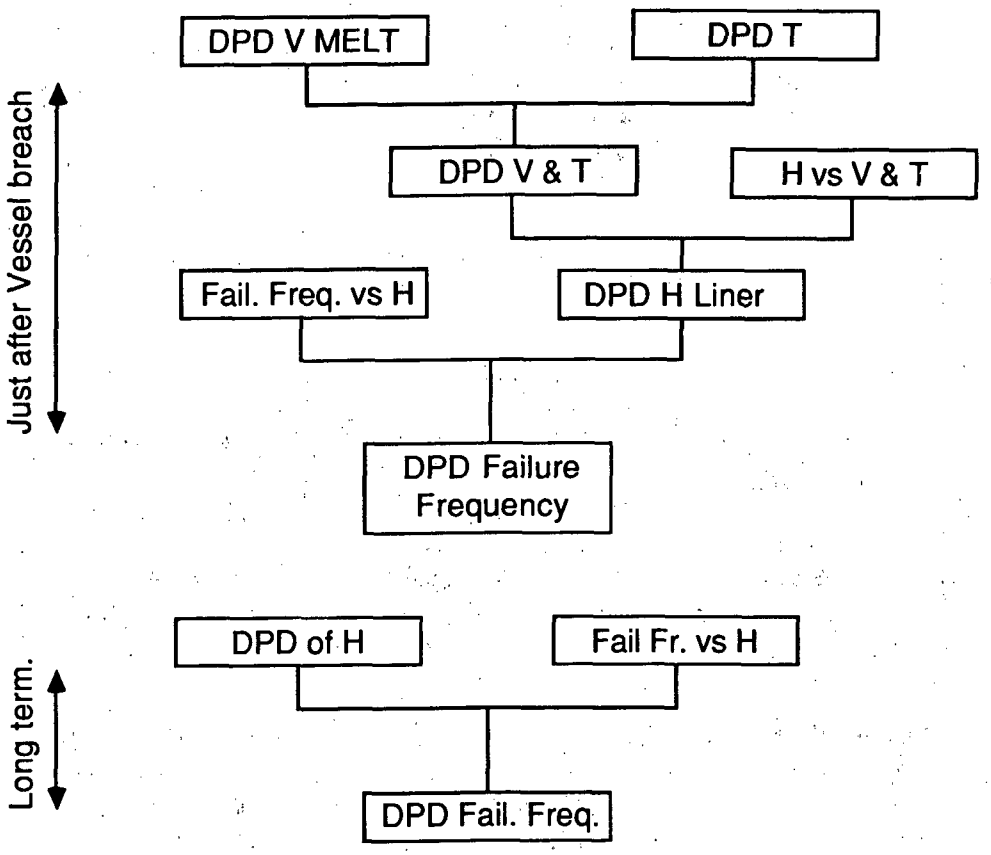
ABSTRACT

This paper is the first installment of a comprehensive probabilistic/phenomenological approach to estimating the Mark-I liner-attack-failure probability. Only wet (flooded) drywells and low-pressure scenarios are considered here. The probabilistic framework is based on ideas of probabilistic modelling on the basis of causal relations as initially developed and applied to the α-mode failure problem (Theofanous et al. 1987, Theofanous 1988b). The framework recognizes an initial phase associated with the quantity of melt released at vessel failure and a long-term (or final) phase obtained eventually after all material relocation has been completed.

Two (probably the key) of the phenomenological aspects are addressed. One aspect considers corium debris heat up in contact with the lower head. A closed-form solution is obtained, which indicates creep rupture of the head prior to significant debris melting. If confirmed by more detailed modelling and for all relevant scenarios, this aspect alone will make the liner-failure event physically unreasonable.

The other aspect is related to the development of the causal relation between the height of the corium layer against the liner and the likelihood of its failure (by overheating). To a very large extent, the thermal load to the liner is dependent upon the heat transfer coefficient on the corium pool side. Our view expressed in the NRC Baltimore Mark-I Workshop (Theofanous 1988a) that the 45°angle of the liner with the concrete basemat is essential to the phenomenology that controls the values of the heat transfer coefficient is demonstrated experimentally. Furthermore, its evaluation is reduced to the determination of the velocity of the single-phase film flow created by the two-phase "lift" and associated recirculation pattern. Finally, our integrated corium-concrete-interaction/liner-heat-up model is briefly described. We find that the transient aspects of the behavior are essential to the accuracy of the results. Both experiments and analyses are continuing.

PROBABILISTIC FRAMEWORK



Note: H is height of molten pool, V is volume, T is temperature, and DPD is Discrete Probability Distribution

Slide 1

The probabilistic framework first proposed and illustrated for a specific example in the Baltimore Workshop (Theofanous 1988a) is another application of the ideas originally developed for dealing with the α-mode failure problem (Theofanous et al. 1987, Theofanous 1988b). In it, probability is used to express degrees of belief based on appropriately supported mechanistic analyses. The framework recognizes explicitly an initial phase associated with the quantity of melt released immediately following vessel failure (i.e., the quantity already molten and having access to spread upon the drywell floor) and a long-term (or final) phase obtained eventually after all material relocation has been completed.

For the initial phase, we show that probability distributions of the volume and temperature of the melt are to be combined to obtain a joint probability distribution of these two important quantities. These probability distributions are to be obtained (see below) from considerations of debris heatup in contact with the lower head and the lower-head-failure event. These two distributions are not independent; furthermore, they have the melt composition (i.e., % of metallic components) associated with them and exemplify the "state" of the released melt. Depending on the detailed examination of various meltdown scenarios, it may become necessary that the composition variable shows explicitly in the framework. Because of the presence of the control rod guides and the large amount of water in the lower plenum, there is a tremendous quenching capacity, and lower head failure becomes, to a large extent, decoupled from the details of the core meltdown and slumping process.

The framework also contains two causal relations. The one relates the "state" of the melt to the height of the pool adjacent to the liner and will be obtained from consideration of spreading on the concrete floor and associated heat transfer phenomena. The other relates liner failure frequency to the height of the pool adjacent to the liner and is to be obtained from mechanistic analyses of the liner thermal loading. Combining these inputs as shown will produce a probability distribution for the liner-failure frequency. Again, some refinement may be necessary here if melt composition needs to be shown explicitly.

For the long term, the probability distribution of melt height is to be obtained from consideration of the long-term, gradual spreading of an initially solid corium mass from within the pedestal region until it reaches a stably coolable configuration.

MELT VOLUME AND TEMPERATURE AT VESSEL BREACH

- Heat up in lower plenum will be gradual and will heat vessel head, too.

$$T - T_o = \frac{\dot{Q}}{\rho c_p} t - \frac{\dot{Q}}{h^2 k} \left\{ 2h\sqrt{\frac{\alpha t}{\pi}} + e^{\alpha h^2 t} erfc(h\sqrt{\alpha t}) - 1 \right\}$$

where: $h = \frac{\rho c_p}{\ell \rho_s c_{ps}}$

in ~ 1 hr $\quad (T\text{-}T_o)_{/head} = 548\ ^\circ C$

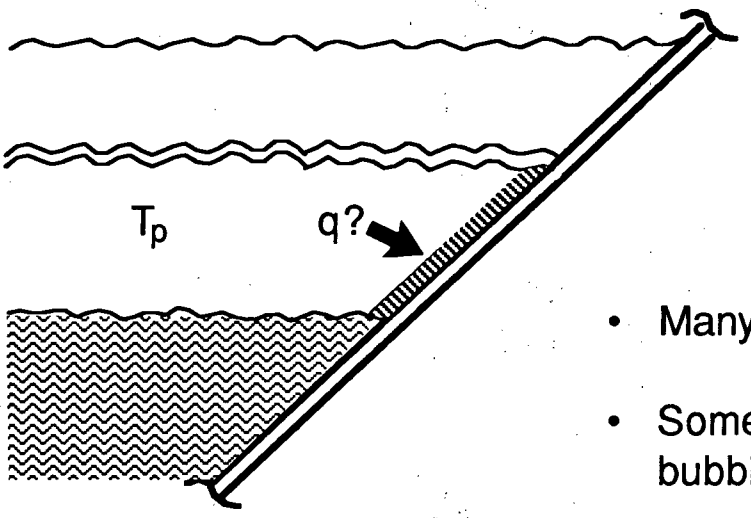
$\quad (T\text{-}T_o)_{/fuel} = 1749\ ^\circ C$

Steel loses structural strength @ 600-700 °C

Slide 2

In the lower plenum of a BWR, there are ~100 tons of steel and ~90 tons of water. The control rod guides are ~1 ft in diameter and are on a square grid with 1-inch spacing between them. Clearly, the core debris will be fully quenched independently of the details of the meltdown and slumping sequence. This is also borne out by detailed calculations at ORNL. After lower plenum dryout, the debris will begin to heat up, while, at the same time, heating up the lower head in contact with it. The geometry is rather complicated, but as an initial attempt to scope this heat-up process, we consider a semi-infinite space of debris in contact with a steel wall of thickness ℓ. The other side of the steel wall (lower head) is considered well insultated. The effective properties of the debris are as follows: thermal diffusivity α, thermal conductivity k, density ρ, and heat capacity c_p. The respective steel properties are denoted by ρ_s and c_{ps}. The volumetric heat generation rate in the debris space is $\dot{Q}$. The lower head temperature can be obtained from the equation shown above. For the debris in the bulk (away from the wall), the solution is given by eliminating the term in the brackets above. Using rough, representative values, we obtain the heat up estimates shown above. Considering that carbon steel loses structural strength at ~600–700 °C, the above estimates indicate that lower head creep rupture will occur prior to significant fuel melting. If most of the metallic component is found stratified down/against the lower head, it also will be solid at the time of failure. In the interior, both instrument tubes and control rod guides will melt; however, such failure cannot provide escape paths for any of the debris. More detailed considerations of the role of control rod guides and of melting/relocation of any metallic components distributed in the debris volume would appear to further support the above conclusions. We are pursuing such refinements.

DEFINITION OF THE PROBLEM



?

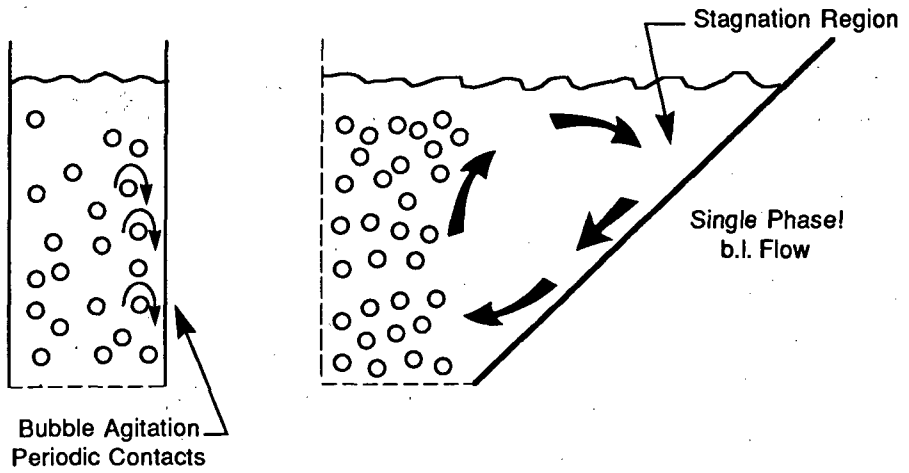
$q = h\,(T_p - T_m)$

- Many parametric analyses
- Some experiments for h with bubbling in vertical cylinders

Slide 3

There have been a number of analyses aimed at assessing liner thermal response, a good representation of which is found in this session. They are in the main part parametric, particularly with reference to the pool-to-liner heat flux (some use the corresponding heat transfer coefficient as the parameter). This, of course, is a fundamental limitation in making any sort of quantitative predictions. Unfortunately, the few experiments aiming to fulfill this limitation missed a key aspect of the flow regime and, therefore, they are not very helpful. Specifically, both the BNL (simulant fluids) and the SNL (reactor materials) experiments were conducted in vertical geometries (i.e., vertical side walls), while the geometry as shown above involves a 45° angle. We have argued previously (Theofanous 1988a) that the inclined side wall will have a crucial effect on the flow patterns, as created by the two-phase flow resulting from the concrete decomposition gases. Here we will demonstrate experimentally that, indeed, this is the case.

MECHANISMS



h: Uniform
?

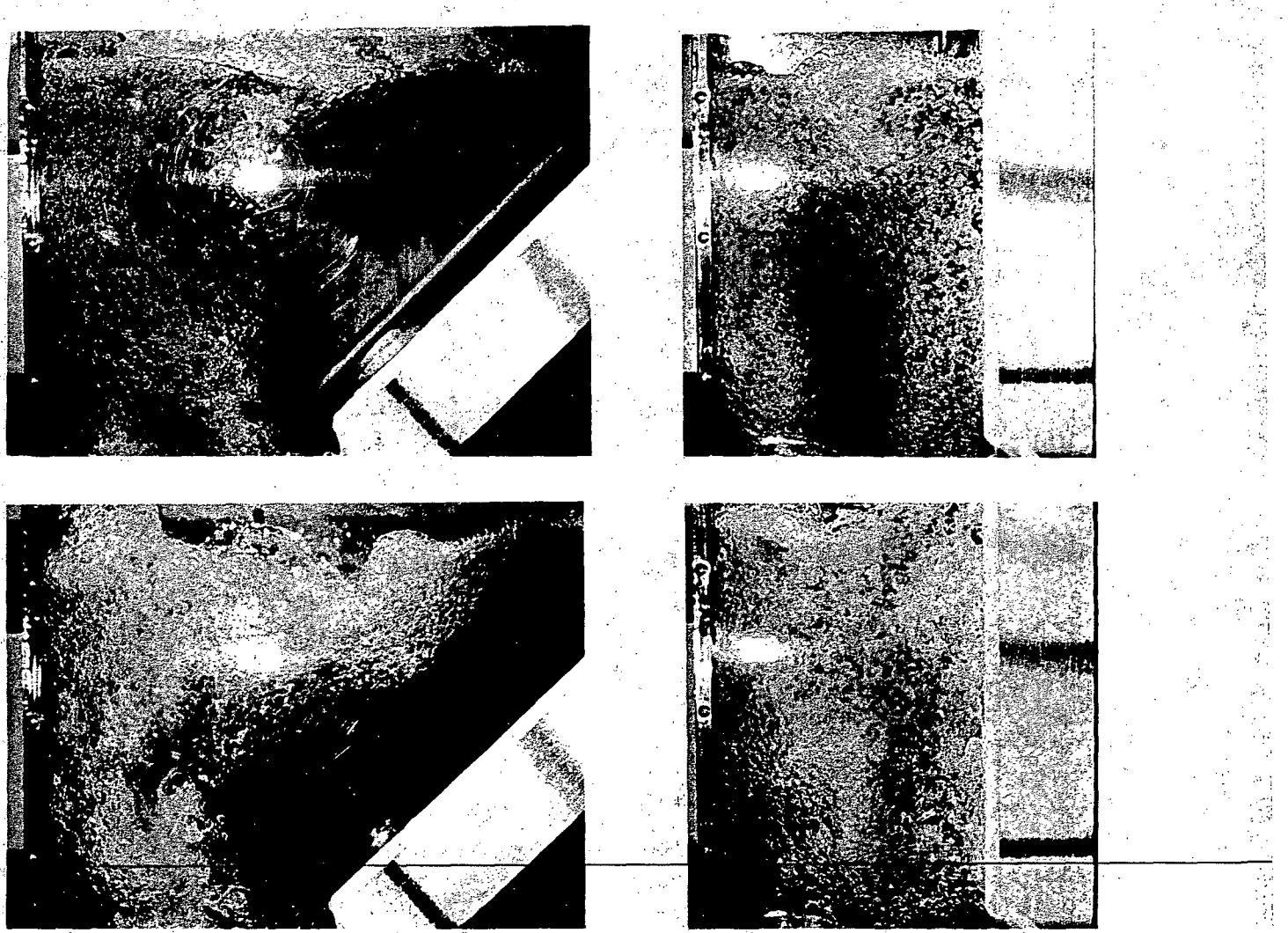
Non-Uniform
Predictable!

Slide 4

But first, let us examine the mechanisms and their effect in more detail. As shown above, a vertical geometry involves a local agitation mechanism as bubbles pass by and bounce around the vertical walls. Under this condition, we expect a more-or-less uniform heat transfer coefficient, and we would need substantial elucidation of the local mechanisms to affect a theoretical prediction. In contrast, for an inclined side wall, we expect that the two-phase flow will be largely confined and directed as shown, causing significant side entrainment and a *single-phase* (liquid only) region in recirculation making up the fluid entrained in the two-phase flow. That is, we have something analogous to a two-phase "lift." Under such conditions, the heat transfer coefficient should be highly non-uniform, being maximum near the top around the forward stagnation flow and minimum near the bottom around the backward stagnation flow. Furthermore, we expect standard (single-phase) boundary-layer heat transfer correlations to be applicable once the velocity in the liquid "film" can be estimated. In this fashion, the problem can be reduced to fluid mechanics with obvious advantages in scaling and experimentation.

It also should be noted that in the vertical geometry, whether on a side wall (BNL) or on an immersion probe (SNL), the heat flux will be directly controlled by two-phase flow regimes and phase mal-distribution effects that would add considerable difficulties for interpretation, while they have nothing to do with the problem at hand.

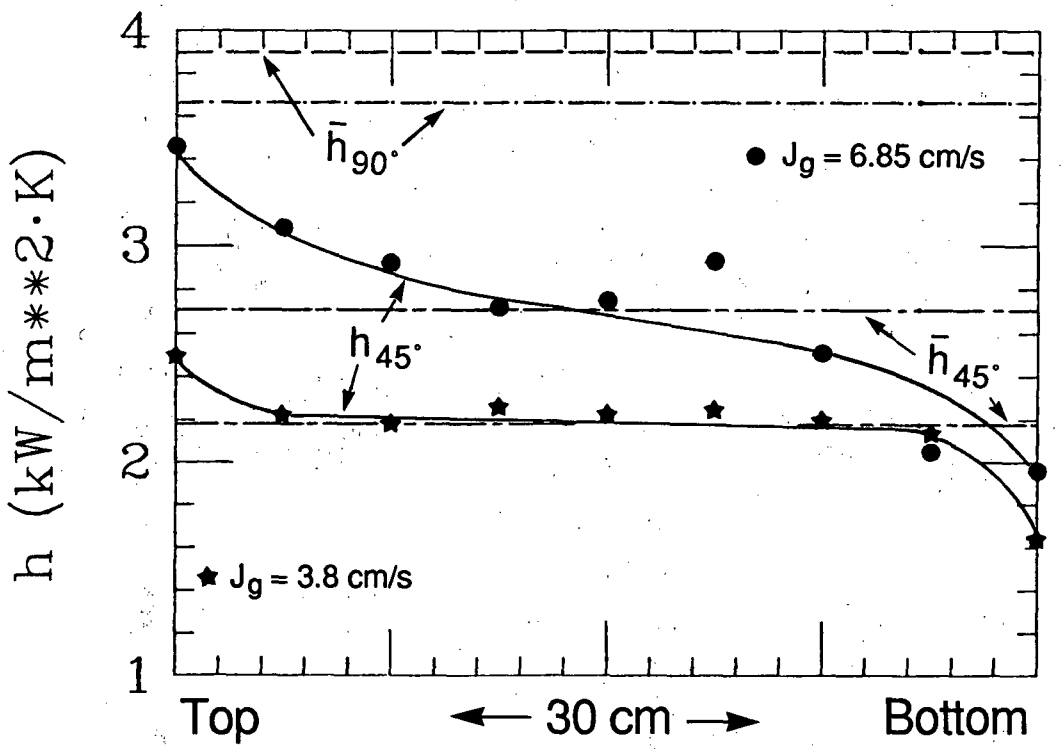
EXPERIMENTALLY OBSERVED FLOW REGIMES



Slide 5

An initial series of experiments were carried out in the apparatus shown in the slide. The apparatus consists of a Plexiglas box with a porous plate as a bottom. The box is 30 cm at the base, 30 cm in height, and 30 cm in width. The inclination of the side wall can change between 90° (vertical) and 45° with the horizontal. In the present series of experiments, a 20 cm (collapsed level) water layer was sparged with air at superficial velocities of 2, 3.8, and 6.85 cm/s. The regimes discussed above are clearly evident. We also have carried out a series of experiments in an initial attempt to relate the intensity of recirculating liquid flow to the superficial gas velocity. This series was with a 10 cm collapsed water layer and superficial gas velocities of up to 30 cm/s.

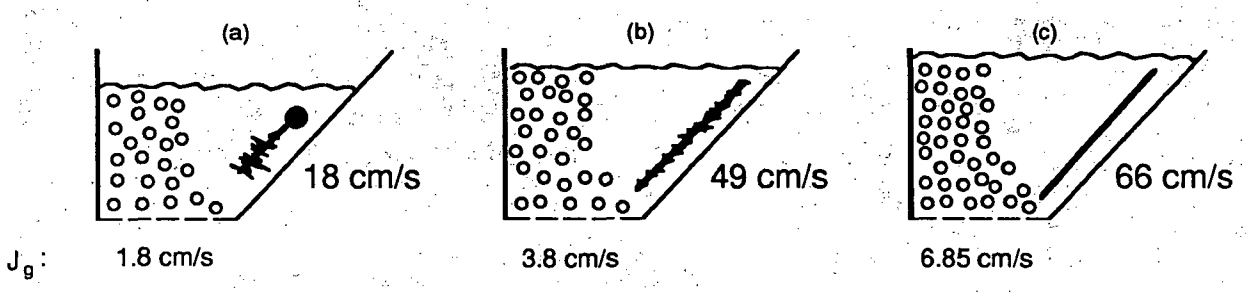
MEASURED HEAT TRANSFER COEFFICIENTS



Slide 6

The inclinable side wall was made out of a copper plate, chilled externally with a conforming helix of copper tubing fed with an ethylene-glycol/water flow maintained at −25 °C by a refrigeration unit. This plate was invariably covered with ice during an experimental run. By adjusting a small amount of heat input to the water pool (immersion heaters), the system could be brought to steady state. At steady state, the thickness of the ice crust was measured using a traversing dial-gauge arrangement. The pool temperatures (found to be uniform) and the plate temperatures on the pool side were measured using 4 and 19 thermocouples, respectively. The temperature rise of the ethylene glycol/water coolant was measured by a series-connected thermopile (±0.001 K) having ten junctions on either end. The flow rate of the coolant was measured by means of a calibrated rotameter. Deduced local and average heat transfer coefficients are shown in the slide above. The vertical geometries produced essentially uniform results (± 15%), so they are simply indicated by the average values ($\bar{h}$) in the figure. The expected, as discussed above, trends of non-uniformity are clearly evident. In addition, we note that vertical geometries in these experiments produced significantly higher heat transfer coefficients. This again is quite expected in terms of the mechanisms involved.

THEORETICAL ESTIMATES

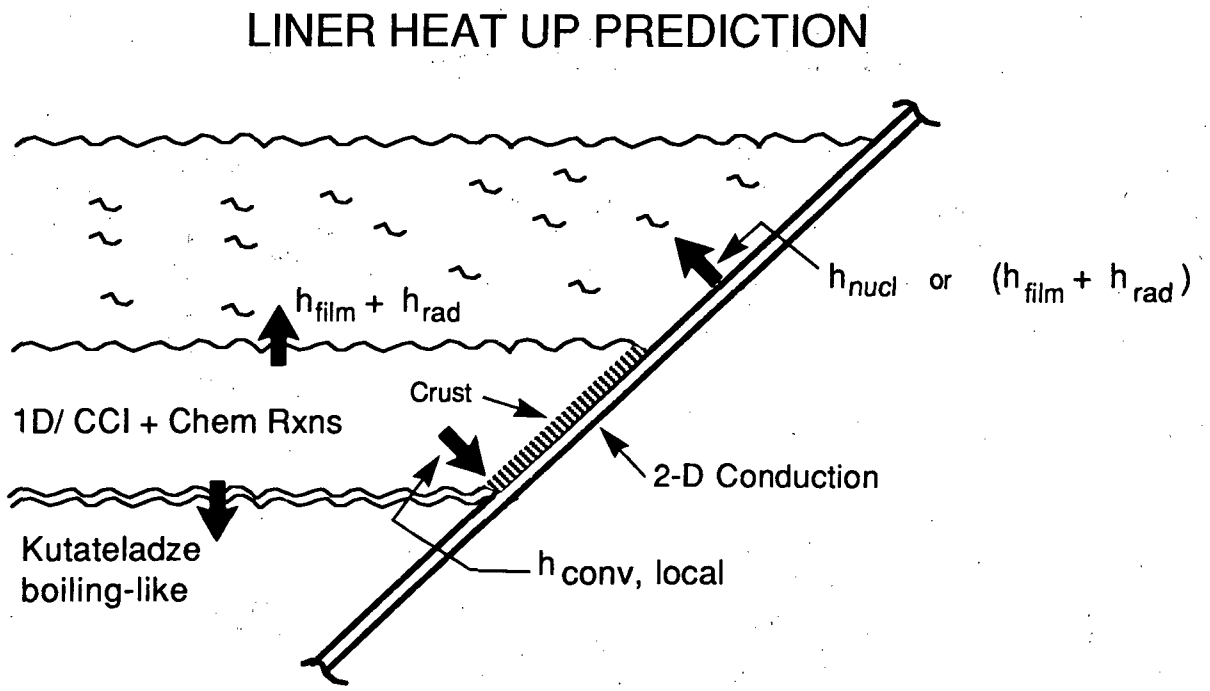


$$St_x = \frac{0.0297\ \mathrm{Re}_x^{-0.2}}{1 + 1.48\ \mathrm{Re}_x^{-0.1}\ \mathrm{Pr}^{-0.16}\ (\mathrm{Pr}\text{-}1)}$$

$$\overline{Nu}_x = 0.037\ \mathrm{Re}_x^{0.8}\ \mathrm{Pr}^{0.33}$$

Slide 7

In this slide, we show liquid film velocities roughly estimated from tracer (dye injection) studies for each of the three conditions utilized in the heat transfer runs. The well-known expressions for the local Stanton numbers, and the Nusselt number approximately averaged over a length x, for turbulent boundary layer flow over a flat plate are also indicated. The plate averaged values are 1623 and 2141 W/m^2 K for cases (b) and (c) above, respectively. These are to be compared to the measured average values of 2200 and 2700 W/m^2 K, respectively. For the top of the plate, we calculate (average over the top 5 cm) 2292 and 3022 W/m^2 as compared to measured values of 2500 and 3500, respectively. As a first attempt, these comparisons show that this is a promising path toward a predictive tool. We should further note that these favorable comparisons were obtained with turbulent boundary layer mechanism although the Reynold's number (based on plate length) is barely indicating transition. Clearly, free stream turbulence has been able to destabilize the boundary layer right from the start!



Slide 8

As illustrated in this slide, the liner heat up calculation is carried out by coupling a corium-concrete interaction calculation with a two-dimensional conduction calculation involving the steel liner (and any crust on it) and the concrete basemat. The corium-concrete interaction in the high-temperature regime of interest here is controlled by (a) a Kutateladze boiling-like heat transfer correlation to both upper and lower pool interfaces, (b) radiation and film boiling to the water above the corium pool, and (c) chemical reactions in the corium pool with the gases released from concrete decomposition. On the liner, heat loss to the water is controlled either by nucleate boiling or, if CHF is exceeded, by the combination of radiation and film boiling. On the corium pool interface, crust formation is calculated by a usual heat balance, and the heat transfer coefficient is taken to vary in the manner observed experimentally. The absolute value was estimated from the approach of Slide 7, with a rough variation of the film velocity as a function of the gas sparging velocity obtained in a series of tracer experiments with up to 30 cm/s superficial gas velocity. It is emphasized, however, that the purpose here is to show the general nature of this computation, rather than to make final predictions.

CONCLUDING REMARKS

We have demonstrated that the 45° liner inclination with the horizontal is an essential feature to the flow and heat transfer regime. These initial data indicate that we can expect heat transfer coefficients easily interpretable in terms of well-known single-phase heat transfer correlations and liquid recirculating velocities. The latter depend on the hydrodynamics of the two-phase layer, and still need to be defined in terms of the liquid height, superficial gas velocities, and appropriate fluid properties. We are continuing work in this area. In addition, refinements of the heat transfer aspects, including the effects of free-stream turbulence, are being pursued.

Implementation of the integral liner heat up model will have to await definition of the local heat transfer coefficients, i.e., completion of the above work. Meanwhile, we have benchmarked the corium-concrete interaction aspects with available SURC and BETA experiments.

One of the key inputs to the probabilistic model, namely, failure frequency related to melt pool depth (and associated parameters), will follow production-type runs with the integral liner model, once ready for implementation as described above. The other key input providing probability distributions for the quantity and state of melt released will be developed on the basis of our simple calculations presented here and in conjunction with available code results. Our approach for the rest of the input required, that is the spreading dynamics, is presently being developed.

ACKNOWLEDGMENTS

This work was supported by the US Nuclear Regulatory Commission under Contract No. 04-87-396. We are grateful to Dr. F. El-Tawila (US Nuclear Regulatory Commission) for his cooperation and help with many aspects of this work. We are all grateful to Mr. M. Vandenbroek and Mr. J. Beecher, who made it possible to meet an extremely tight schedule with the experiments and Ms. E. Horton, similarly with this manuscript.

REFERENCES

1. T.G. Theofanous, B. Najafi and E. Rumble, "An Assessment of Steam-Explosion-Induced-Containment Failure. Part I: Probabilistic Aspects," *Nuclear Science & Engineering*, **97**, 259-281 (1987).

2. T.G. Theofanous, "Mark-I Liner-Attack Probability," NRC Mark-I Workshop, Baltimore, MD, Feb. 24–26, 1988.

3. T.G. Theofanous, "Dealing with Phenomenological Uncertainties in Severe Accident Assessments and Probabilistic Risk Assessments," Proceedings of the Third International Topical Meeting on Nuclear Power Plant Thermal Hydraulics and Operations, Seoul, Korea, Nov. 14–17, 1988.

Is Mark I Shell Failure Really Important?

Herschel Specter, New York Power Authority
and
Peter Bieniarz, Risk Management Associates

Abstract

Results are presented for several station blackout source term analyses using the Peach Bottom plant as a reference Mark I design. An advanced suite of codes was used which included modeling of revaporization. These analyses showed that releases of iodine, tellurium, and cesium would be small, in the order of a few percent of the core inventory. If use of the automatic depressurization system is assumed, then such releases are reduced by about an order of magnitude. These results indicate that even if the drywell shell failed during Mark I blackout sequences, releases of radioactive material would be limited. Based on these results and other progress in reducing the core melt frequency, regulatory actions to significantly modify Mark I containments do not appear to be warranted at this time.

I. Introduction

A principle concern for nuclear power plants with Mark I containments is the possibility that in a severe accident molten core material will penetrate the reactor vessel, spread across the drywell floor, and then attack the drywell shell. This high temperature attack might lead to shell failure and releases of radioactive material into the environment.

It may be some time before additional experiments and further development of our analytical capabilities can describe the drywell shell failure process with much greater certainty. What safety actions should be taken in the meanwhile? That depends on how well we can answer the question: "Is Mark I shell failure really important?"

In one fundamental respect we already have the answer to this question. Even if Mark I shell failure is assumed to occur each time there is a core melt, nuclear health risks would still be quite small. This is because all U.S. LWR nuclear power plants, when properly analyzed, meet the NRC's early and latent fatality safety goals.

Furthermore, this can be shown without reliance on smaller, but more realistic, source terms or on the use of PRA. For example, assuming large, WASH-1400 type, releases of radioactive material

into the environment, virtually no early fatalities would be expected, provided an efficient emergency response was taken. A highly efficient emergency response is the "Graded Response" which utilizes a combination of prompt evacuation of a two mile or so inner zone near the plant and sheltering elsewhere in the EPZ. Some sheltered people might be relocated later if the results of radiation monitoring showed that they were in areas of unacceptably high dose rates [Figure 1]. Analyses by the NRC[1], DOE[2], EPRI[3] and others[4] show that if the Graded Response were fully utilized, essentially zero early fatalities would be expected, even at our most populated sites. Thus the NRC's early fatality safety goal can be met at any site and with any LWR design even assuming severe releases. This conclusion is reached independent of core melt or containment failure frequency, and without reliance on PRA's or IPE's.

All plants and sites also meet the NRC's latent fatality safety goal, again assuming severe releases of radioactive material. All published comparisons that we are aware of show wide margins between the calculated latent fatality risk and this safety goal [Figure 2]. Testimony provided by the NRC in connection with the Indian Point hearing showed that even at the nation's most populated site, the latent fatality safety goal would be met with WASH-1400 type source terms, even if there were no containment. One would need a severe release frequency on the order of 10^{-3}/RY to possibly exceed this goal. After about 1100 operating - years of experience in the United States without any severe releases to the environment there is considerable confidence that the U.S. nuclear national average severe release frequency is well below 1×10^{-3}/Reactor year. The consequences of actual large releases of radioactive material are also of interest. The most serious release of radioactive material from a nuclear power plant ever came from the accident at Chernobyl. Yet DOE analyses[5] indicate that over the next 70 years the increment in latent fatal cancers in the Northern Hemisphere due to Chernobyl would be 0.00004. Stated differently, where there might be 100,000 latent cancer fatalities from non-nuclear causes, Chernobyl might raise it to 100,004. More recent data indicate that this small calculated increment should be revised in a downward direction.

Therefore our starting point is the recognition that health risks from all U.S. LWR nuclear power plants are quite small and well within the NRC's safety goals. This includes all Mark I plants, regardless of drywell shell failure concerns.

Suppose, however, we want to look beyond the safety goals. Assuming a core damage situation were in progress, do we have additional information that bears on the following questions:

1. Will the reactor vessel fail, and if so, how and when,

2. Will the corium freeze before it reaches the drywell shell,

3. Will the shell fail, assuming it is attacked by molten material,

4. Even if the shell fails, will the releases of radioactive material be large, and

5. Can the operator take actions to reduce the drywell shell failure probability and/or source term?

Some severe accident management studies conclude, particularly in conjunction with more refined core melt progression analyses such as Oak Ridge's BWRSAR code, that there are many opportunities to terminate core damage sequences. Such core melt progression analyses indicate that core melts might progress more slowly than earlier analyses predicted. This additional time translates into greater opportunities for operator intervention to arrest the accident. For example, analyses performed on the Susquehanna Plant by the Pennsylvania Power and Light Company resulted in a calculated core melt frequency about two orders of magnitude smaller than typical BWR core melt figures. Backing this up is intensive operator training and full use of safety and non-safety plant equipment. Thus lower core melt frequencies are accomplished by identifying more "success paths" through more refined analyses, by more extensive severe accident training of plant operators, and by extensive use of existing plant equipment.

To the extent that these actions reduce the core melt frequency, concerns about Mark I shell failure become less important.

Ongoing research and development on core melt progression analyses may also result in calculating a much slower rate at which molten material might fall onto the drywell floor from the failed reactor vessel. Slower rates enhance the possibility that freezing of the molten core material would take place before the shell is reached, thereby eliminating the shell attack containment failure mode.

Other research is directed at determining the influence of water in the drywell. Enough heat may be transferred from the molten material to an overlying layer of water so that shell penetration is prevented. This layer of overlying water may be there as a result of the accident itself and/or brought about by spraying into the drywell. If water sprays are used this would also reduce the source term, should shell failure nonetheless occur.

Each of the possibilities described above has the potential for minimizing the importance of Mark I shell failure. Another possibility, the principal subject of this paper, is that even if containment integrity is lost immediately after the reactor vessel fails, the source term is rather small. Therefore the safety significance of shell failure is correspondingly limited. This paper reports on station blackout source term analyses which did not assume improved operator procedures, any core or

containment cooling modifications, or credit for a more gradual core melt progression. The Peach Bottom plant was used as the reference plant in these analyses.

In addition to the above calculations, a second set of source term analyses was performed in which it was assumed that the automatic depressurization system (ADS) was available. This second set of analyses showed that extended use of the automatic depressurization system (ADS) would reduce the above small source term by about an order of magnitude, would delay containment failure via overpressurization, and would reduce direct containment heating concerns. A systematic review of what would be required to assure extended use of the ADS during station blackout conditions was not performed other than to determine that the electrical power needs would be minimal.

The computer code set that was used is an advanced version of NRC's Source Term Code Package (STCP) which accounted for revaporization of deposited volatile radionuclides, thereby eliminating the major contributor to source term uncertainty for station blackout sequences in Mark I's.

II. Background

During 1987 the New York Power Authority (NYPA), with the support of its consultant, Risk Management Associates (RMA), submitted extensive comments on the draft version of NUREG-1150[6], "The Reactor Risk Reference Document".

The basis of these comments was an independent reanalysis of certain important accident sequences of NUREG-1150's reference Mark I plant, Peach Bottom. The Philadelphia Electric Company assisted us in this effort by verifying that the code input parameters accurately represented the Peach Bottom plant.

The roots of the RMA code suite is the NRC's Source Term Code Package (STCP). However, numerous improvements over the STCP have been made including a much more comprehensive treatment of plant systems (e.g., ECCS, SRV's, ADS in BWR's), and the modeling of important physical phenomena such as revaporization of desposited radionuclides. Structural improvements among the individual codes permit the exchange of data at each time step which results in a truly integrated package that more accurately represents accident conditions and processes.

Our NUREG-1150 reanalysis of Peach Bottom covered two important ATWS sequences, TC1 and TC3, and several station blackout sequences. In NUREG-1150, station blackout sequences account for about 85% of Peach Bottom's calculated risks. These reanalyses not only served as the basis for commentary on NUREG-1150, they yielded important insights on the usefulness of various potential plant safety additions, such as filtered vents. Further, the importance of design differences between various BWR's became more apparent when the Peach Bottom analyses were compared to similar sequences in other BWR's.

This paper does not attempt to fully describe either our NUREG-1150 comments or the features of the RMA code set. The purpose of this paper is to report on what we learned from three station blackout sequences and the implications of these analyses on the Mark I shell failure issue.

III. Station Blackout Analyses

Three different station blackout analyses were made using the RMA code set:

1. TB1, Battery Failure After 6 hours, no ADS available

2. TB1A, Battery Failure After 6 hours, ADS available

3. TB1E, Battery Failure at T=0 hours, ADS available

Immediate battery failure, case TB1E, might be postulated for extreme external events, such as earthquakes. Comparisons of TB1A and TB1E do not show any significant differences once battery power becomes unavailable. Although the decay energy is somewhat smaller in the case of TB1A compared to TB1E, the dominant source of accident energy, metal-water reactions, is the same. Therefore it is to be expected that once core cooling ceases, TB1A and TB1E proceed in very similar ways. Except for providing limited number of curves and the accident chronology, the discussion of TB1E is encompassed within the review of case TB1A. [See Figures 11, 12 and Table 3]

Table 1 and Figures 3 to 6 provide detailed information about the results of the TB1 analysis. It is important to note that this calculation resulted in sufficiently high containment pressure at the time the reactor vessel was breached, that containment integrity was assumed to be lost. Such a prompt containment failure assumption maximizes the release of radioactive material, thereby presenting a source term equal to or greater than one that might occur if the containment failure mode was through the loss of the drywell shell. The RMA calculated core release fractions for this prompt containment failure sequence for three important elements were:

Iodine	.030
Tellurium	.014
Cesium	.020

Iodine and tellurium are important in terms of affecting early injury and early fatality health risks. Cesium is important in determining latent cancer health effects, offsite economic losses, and as a surrogate for evaluating the number of person-rems per release. Backfit analyses, which determine the amount of money justified to modify a plant, are proportional to the number of averted person-rems.

As stated earlier, even with WASH-1400 type source terms, an efficient emergency response would result in virtually no early fatality risk. With iodine and tellurium releases of the above

magnitude, early fatalities would be very unlikely with almost any kind of emergency response.

With regard to the cesium release fraction of 0.020, offsite costs at an average population site would be in the range of .04 to 0.9 billion dollars, well within present Price-Anderson coverage.

Assuming a radioactive release frequency of 10^{-5}/RY, a frequency ten times larger than SECY-88-147's screening criterion, a cesium release fraction of 0.020 only justifies about $12,000 to $270,000 for backfits for the average site*. Thus if the backfit policy is strictly applied, very few dollars would be available to modify Mark I plants. This infers that most emphasis would be placed on procedural improvements and better use of existing plant equipment.

Further insights were gained on Mark I risks by running an additional set of analyses; one where it was assumed that the automatic depressurization system (ADS) was operational even though a station blackout had occurred. By assuming a functional ADS, source terms were further reduced by about an order of magnitude, yielding the following core fractions:

Iodine	<.004
Tellurium	<.014
Cesium	<.004

There are several benefits to extended use of the ADS:

1. It lowers surface temperatures inside the reactor vessel. Cooler surfaces are more effective in trapping volatile radionuclides.

2. It provides a pathway for volatile radionuclides from the reactor vessel to the suppression pool prior to vessel breach.

3. It reduces the energy available for release at the time of reactor vessel failure. Because of this, the containment was not calculated to promptly fail through overpressure when the vessel was breached. The lower reactor pressure at the time of vessel breach also minimizes direct heating concerns.

A comparison of temperature - time plots, with and without extended use of the ADS, shows that reactor surface temperatures are hundreds of degrees cooler when the ADS is used. Additionally, the time of containment overpressure is extended by about 4 hours compared to the case when no ADS is used. Results of the extended ADS analyses can be found in Table 2 and Figures 7 to 10.

*Based on a 30 year remaining plant life, no discounting of offsite health costs or property values, and the data in NUREG-0880, Rev. 1

IV. CONCLUSIONS

Much of the attention that has been focused on Mark I BWR's is because of the perception that such plants may lack the inherent capabilities of other containment designs, particularly those of the large dry PWR containments. We believe that such views are no more appropriate than ones that would be critical of large dry PWR containments because they do not have suppression pools. Both reactor types have inherent capabilities, albeit sometimes different ones. BWR's have many ways of getting cooling water to heated surfaces and therefore they often exhibit low core melt frequencies. Based on the pioneering work of PP&L and Oak Ridge, even lower core melt frequencies appear to be achievable.

The BWR suppression pool is also an inherent capability. Station blackout sequences, in effect, cut the pathway between the reactor and the suppression pool. Once this is done, severe accidents generally proceed rather like a PWR with a very small containment volume. However if there is a functional ADS, the link between the reactor and the suppression pool is reestablished. Because of this containment overpressure failure times are later and source terms are even smaller.

Based on the above, it appears that a successful severe accident management program for BWR's is one that maximizes on its inherent capabilities, such as core coolability and use of the suppression pool, rather than seeking major plant modifications.

The NYPA/RMA analyses exhibit small source terms even for station blackout sequences. A detailed uncertainty analysis of these analyses has not been done. However, since the RMA code set has modeled important phenomena absent in the STCP and since expert panels have assigned the bulk of the station blackout source term uncertainty to such missing models, it is anticipated that the uncertainty bands on these results are comparatively narrow. The NYPA/RMA results, codes, tapes, etc. have been submitted in full to NRC's research division who are in the process of reviewing this effort.

In summary, there appears to be ample technical justification to consider Mark I shell failure as small enough risk so that major regulatory actions are not warranted at this time. A more balanced approach appears to be one where the various IPE's go forward, use is made of the insights from the PP&L, NYPA, and RMA analyses, and plant modifications, if any, are limited. By the time most of the IPE's are concluded, the various analytical work and experiments directed at this issue should also be completed and final resolution of the Mark I shell failure concern can be meaningfully achieved.

References

1. "A Perspective on Emergency Planning, Risk, and the Source Term Issue", James Martin, USNRC, April 13, 1983

2. "Issues, Information Needs, and Programs for Improved Emergency Preparedness", DOE Working Group on Emergency Preparedness, November, 1984, Draft Version

3. "Risk Based Evaluation of Emergency Response Planning", Nuclear Safety Analysis Center, Electric Power Research Institute, NSAC 115, November, 1988

4. "Graded Response: The Preferred Evacuation Strategy For Nuclear Power Plants", Nuclear Management and Resource Council, to be published

5. "Health and Environmental Consequences of the Chernobyl Nuclear Power Plant Accident", DOE/ER-0332, June, 1987

6. "Reactor Risk Reference Document". NUREG-1150, Draft For Comment, USNRC, February, 1987

List Of Tables

Table 1 Accident Chronology, Battery Failure At 6 Hours, No ADS (TB1)

Table 2 Accident Chronology, Battery Failure At 6 Hours, With ADS (TB1A)

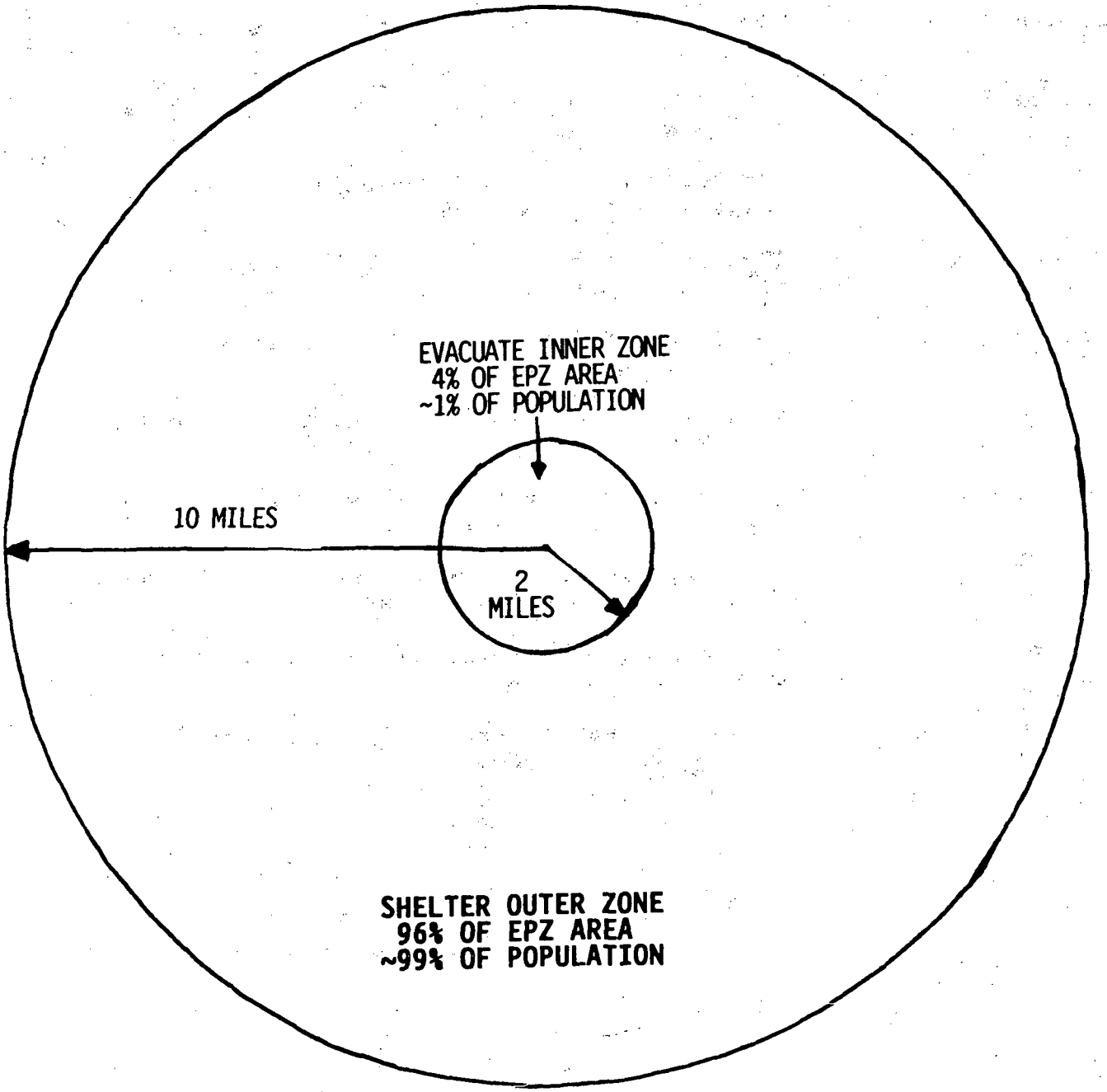
Table 3 Accident Chronology, Battery Failure At 0 Hours, With ADS (TB1E)

List of Figures

Figure One	Graded Response Strategy
Figure Two	Latent Cancer Fatality Risks
Figure Three	RCS Temperatures Versus Time, Battery Fails At 6 Hrs, No ADS
Figure Four	Drywell Pressure Versus Time, Battery Fails At 6 Hrs, No ADS
Figure Five	CSI Deposition In RCS Versus Time, Battery Fails At 6 Hrs, No ADS
Figure Six	CSOH Deposition In RCS Versus Time, Battery Fails At 6 Hours, No ADS
Figure Seven	RCS Temperatures Versus Time, Battery Fails At 6 Hrs, With ADS
Figure Eight	Drywell Pressure Versus Time, Battery Fails At 6 Hrs, With ADS
Figure Nine	CSI Deposition In RCS Versus Time, Battery Fails At 6 Hours, With ADS
Figure Ten	CSOH Deposition In RCS Versus Time, Battery Fails At 6 Hours, With ADS
Figure Eleven	RCS Temperatures Versus Time, Battery Fails At 0 Hours, With ADS
Figure Twelve	Drywell Pressure Versus Time, Battery Fails At 0 Hours, With ADS

FIGURE ONE

GRADED RESPONSE STRATEGY



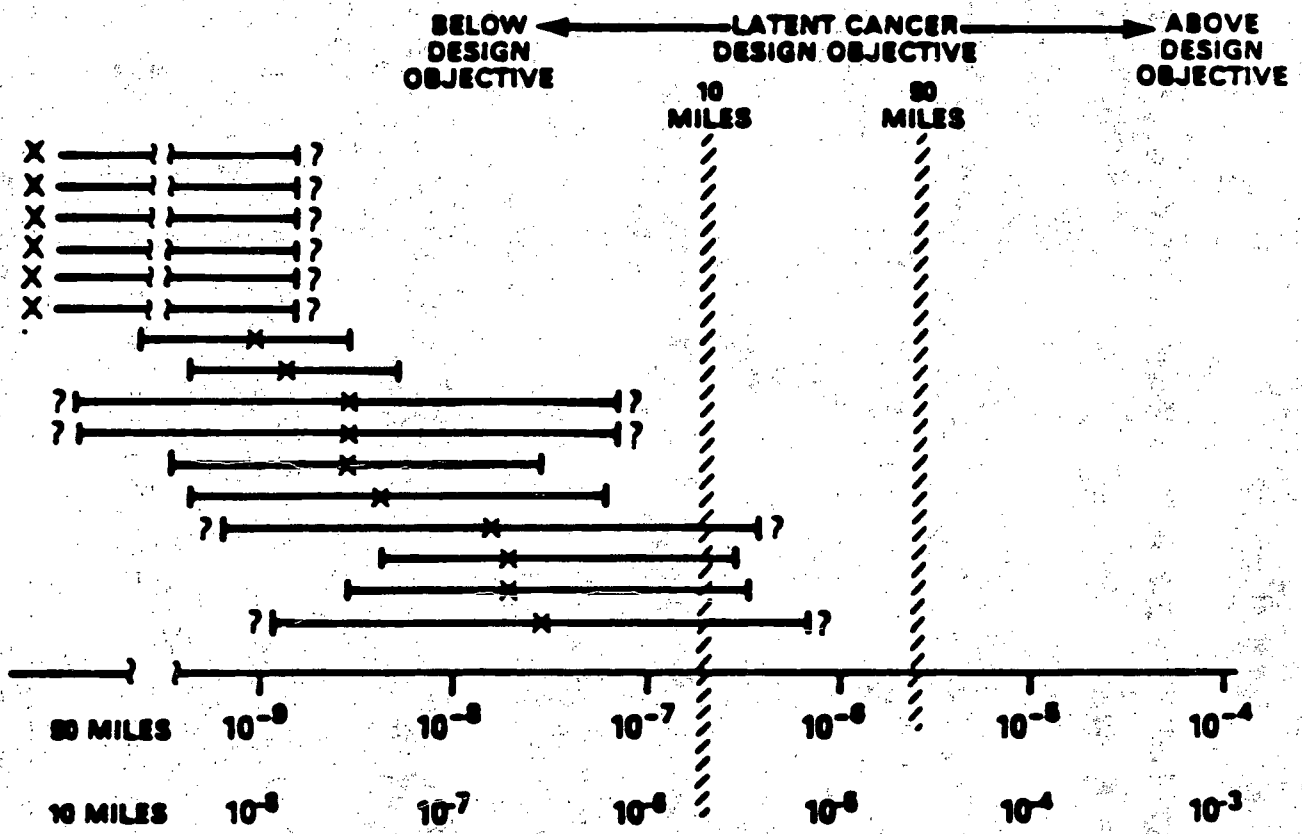
PHASE #1: NOTIFY PUBLIC TO EVACUATE AN INNER ZONE OF ABOUT A 2-MILE RADIUS AND TO SHELTER IN THE REST OF THE 10-MILE EPZ.

PHASE #2: MONITOR RADIATION LEVELS.

PHASE #3: NOTIFY SHELTERED PEOPLE IN PLUME PATHWAY TO RELOCATE IF MEASURED RADIATION LEVELS ARE TOO HIGH.

FIGURE TWO

LATENT CANCER FATALITY RISKS



LATENT CANCER FATALITY RISK
(Events per Reactor Year)
(To Average Individual Within 10 and 50 Miles)

Figure Three

RCS Temperatures Versus Time, Battery Fails At 6 Hrs, No ADS

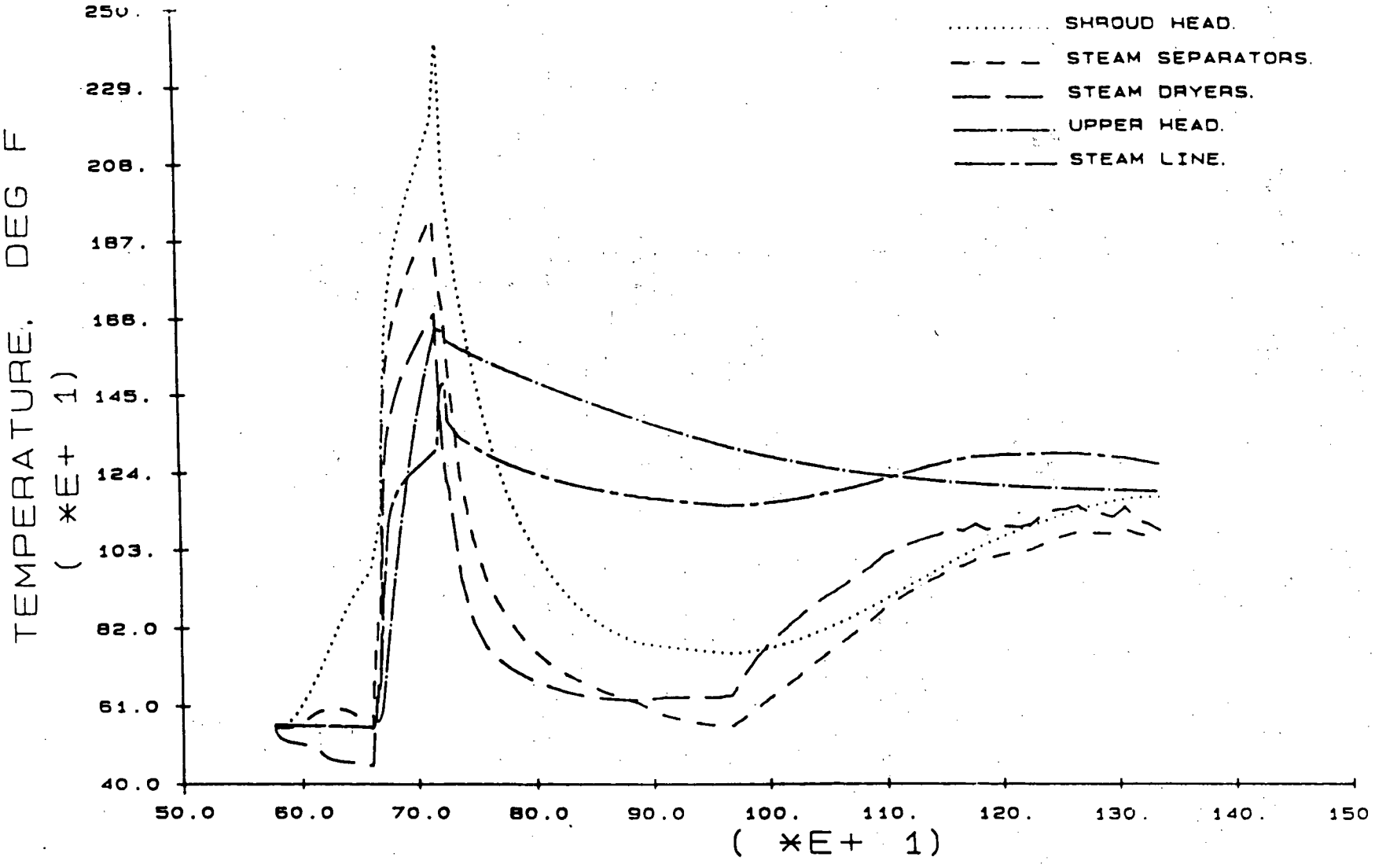


Figure Four

Drywell Pressure Versus Time, Battery Fails At 6 Hrs, No ADS

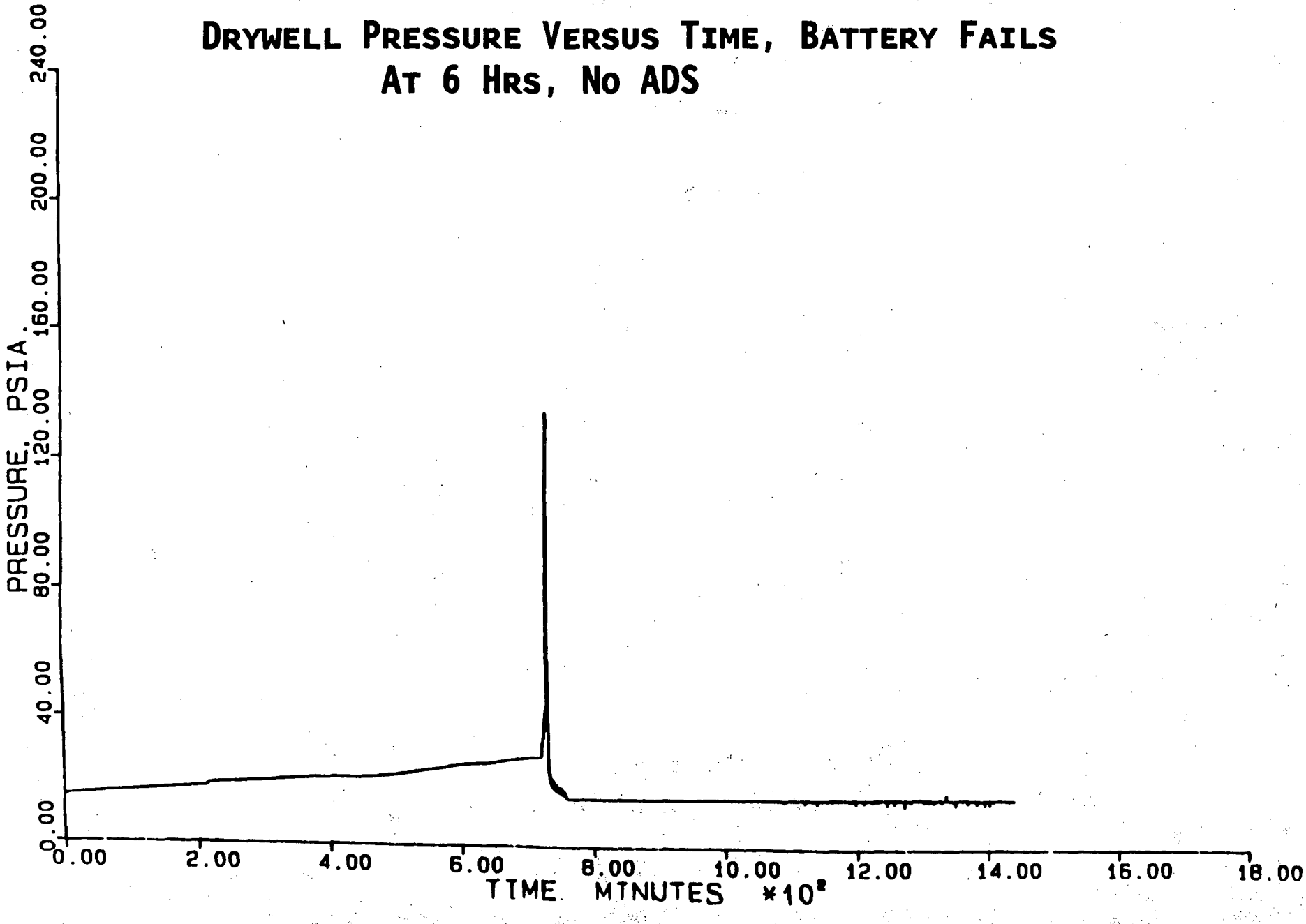


Figure Five

CSI Deposition In RCS Versus Time, Battery Fails At 6 Hrs, No ADS

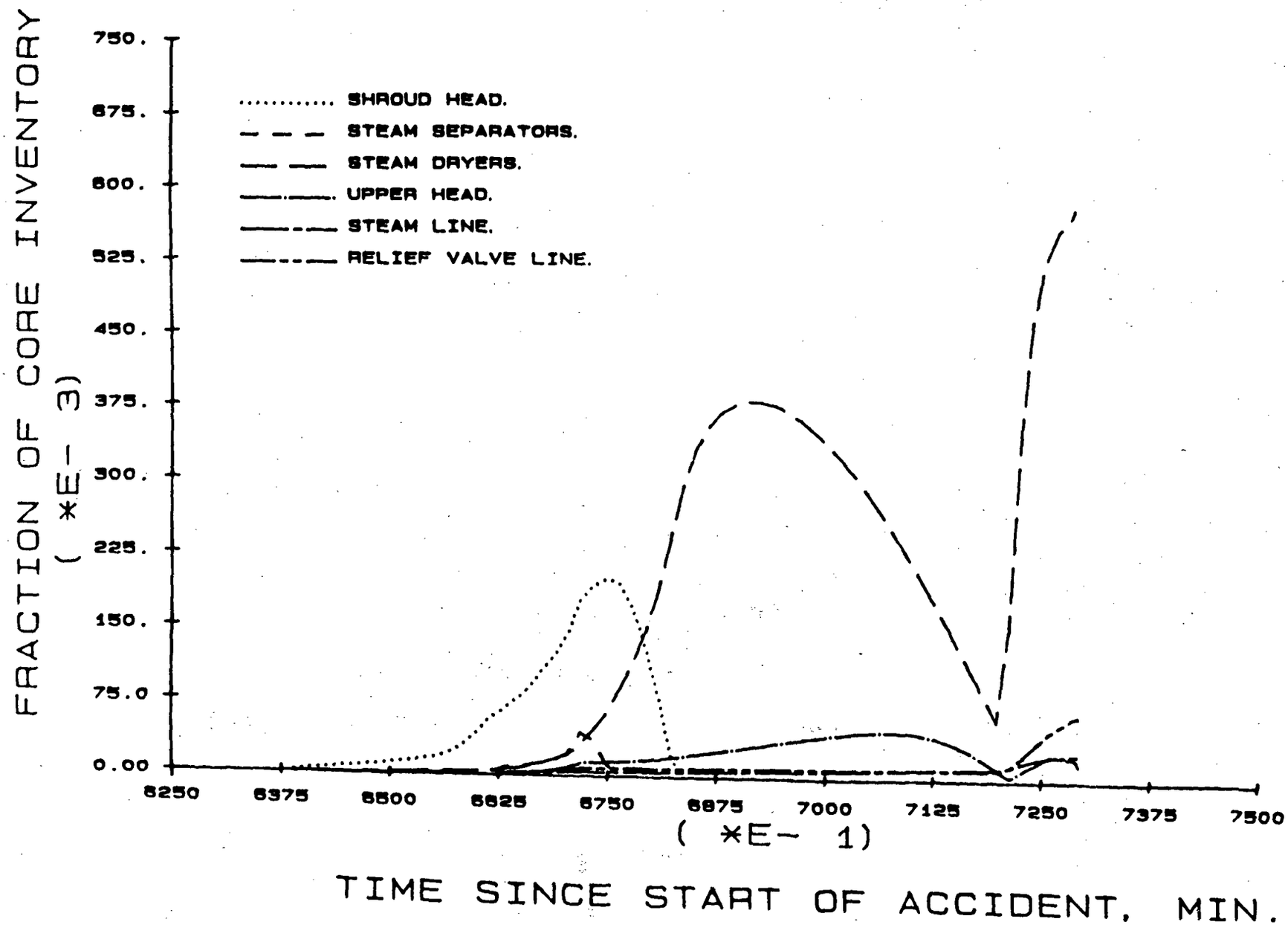


Figure Six

CSOH Deposition In RCS Versus Time, Battery Fails At 6 Hours, No ADS

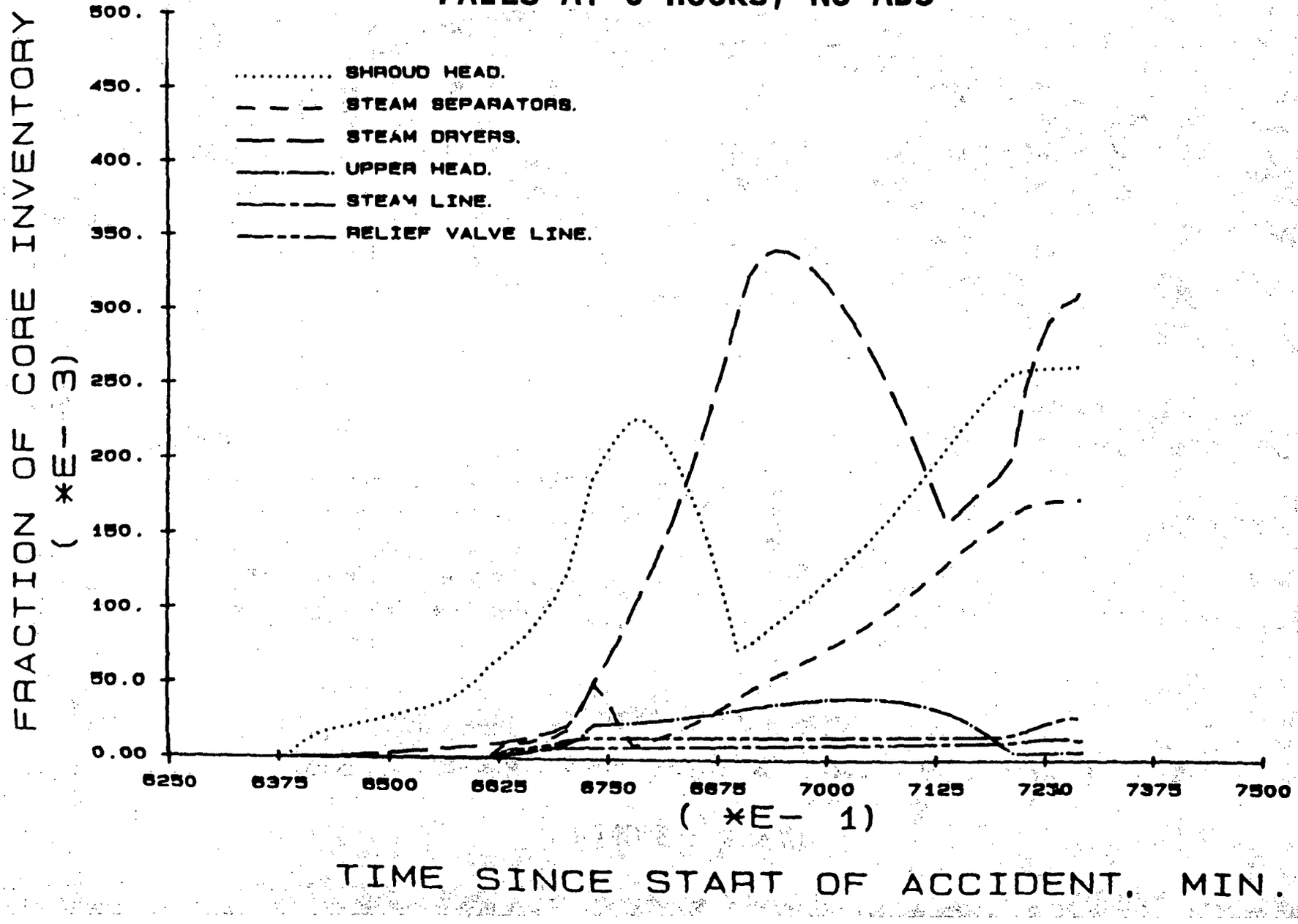


Figure Seven

RCS Temperatures Versus Time, Battery Fails At 6 Hrs, With ADS

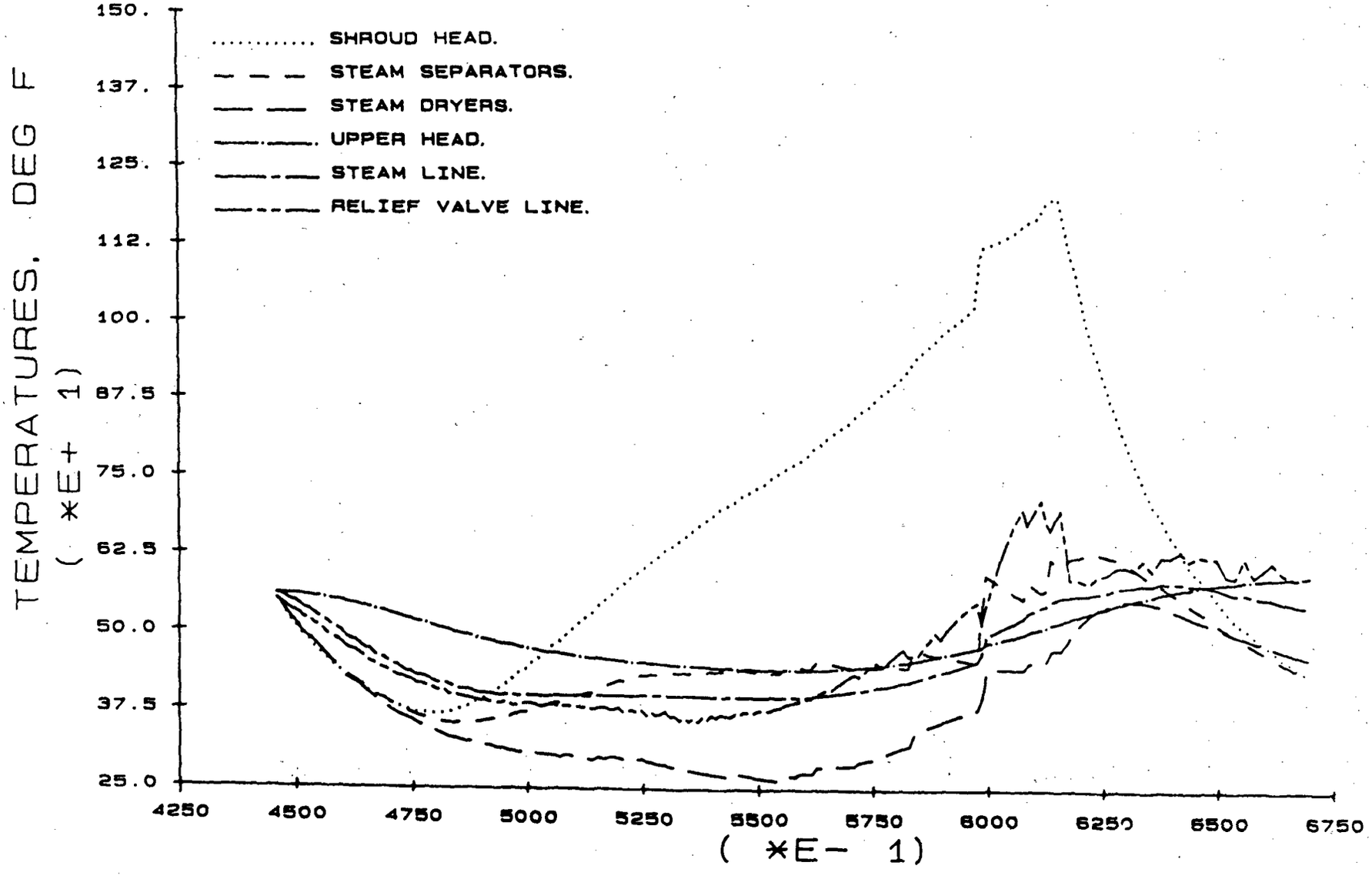


Figure Eight

Drywell Pressure Versus Time, Battery Fails At 6 Hrs, With ADS

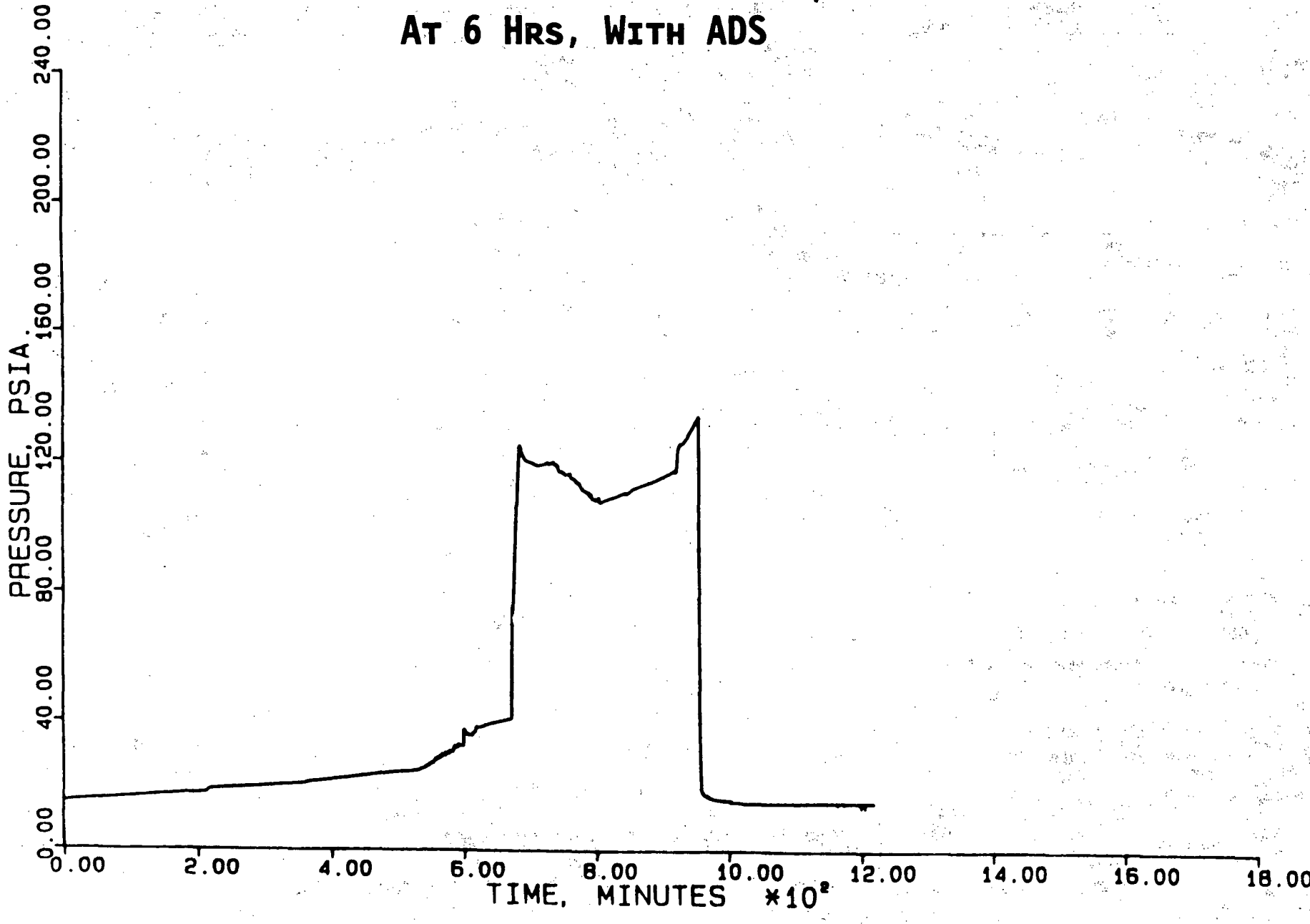


Figure Nine

CSI Deposition In RCS Versus Time, Battery Fails At 6 Hours, With ADS

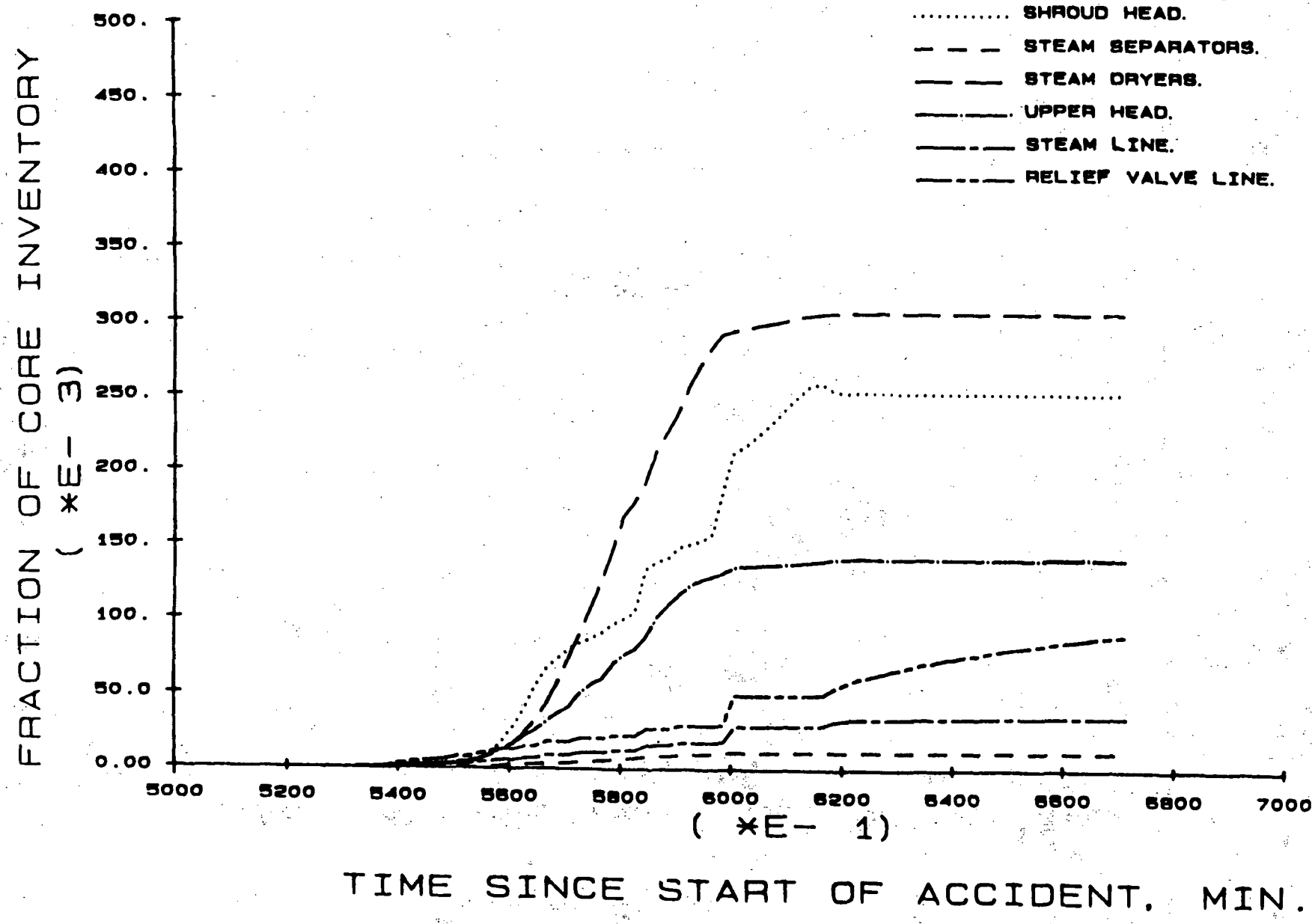


Figure Ten

CSOH Deposition In RCS Versus Time, Battery Fails At 6 Hours, With ADS

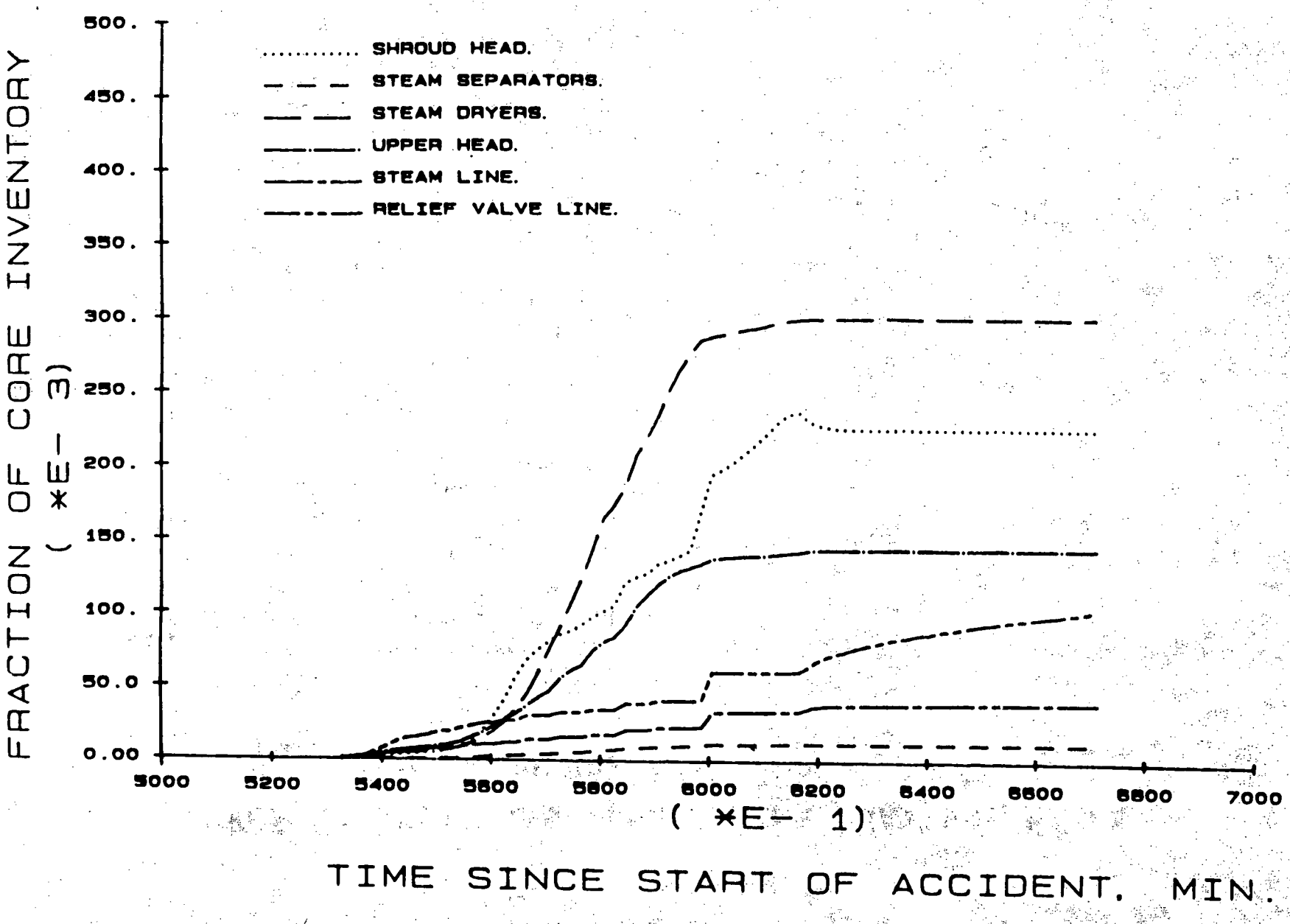


Figure Eleven

RCS Temperatures Versus Time, Battery Fails At 0 Hours, With ADS

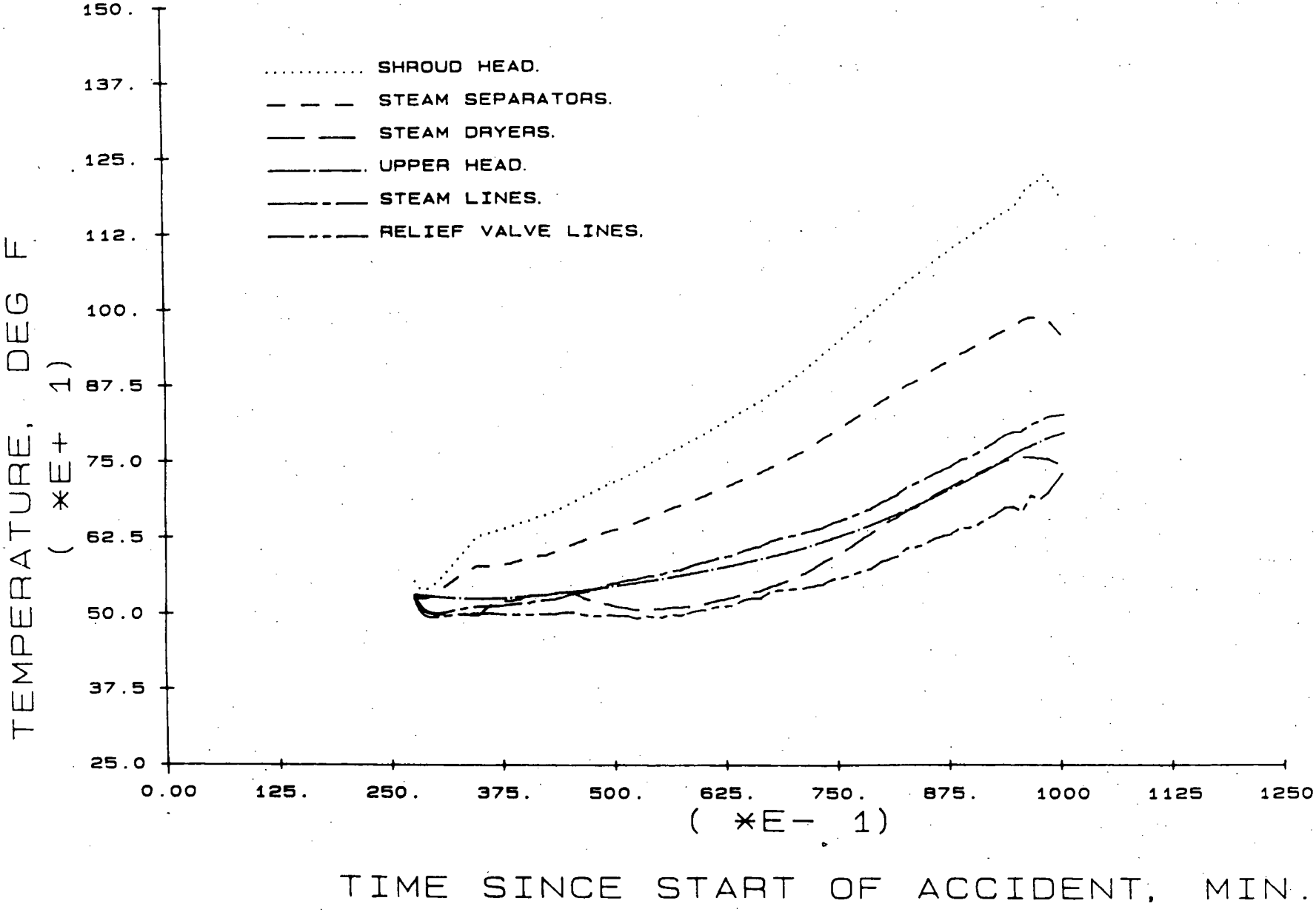
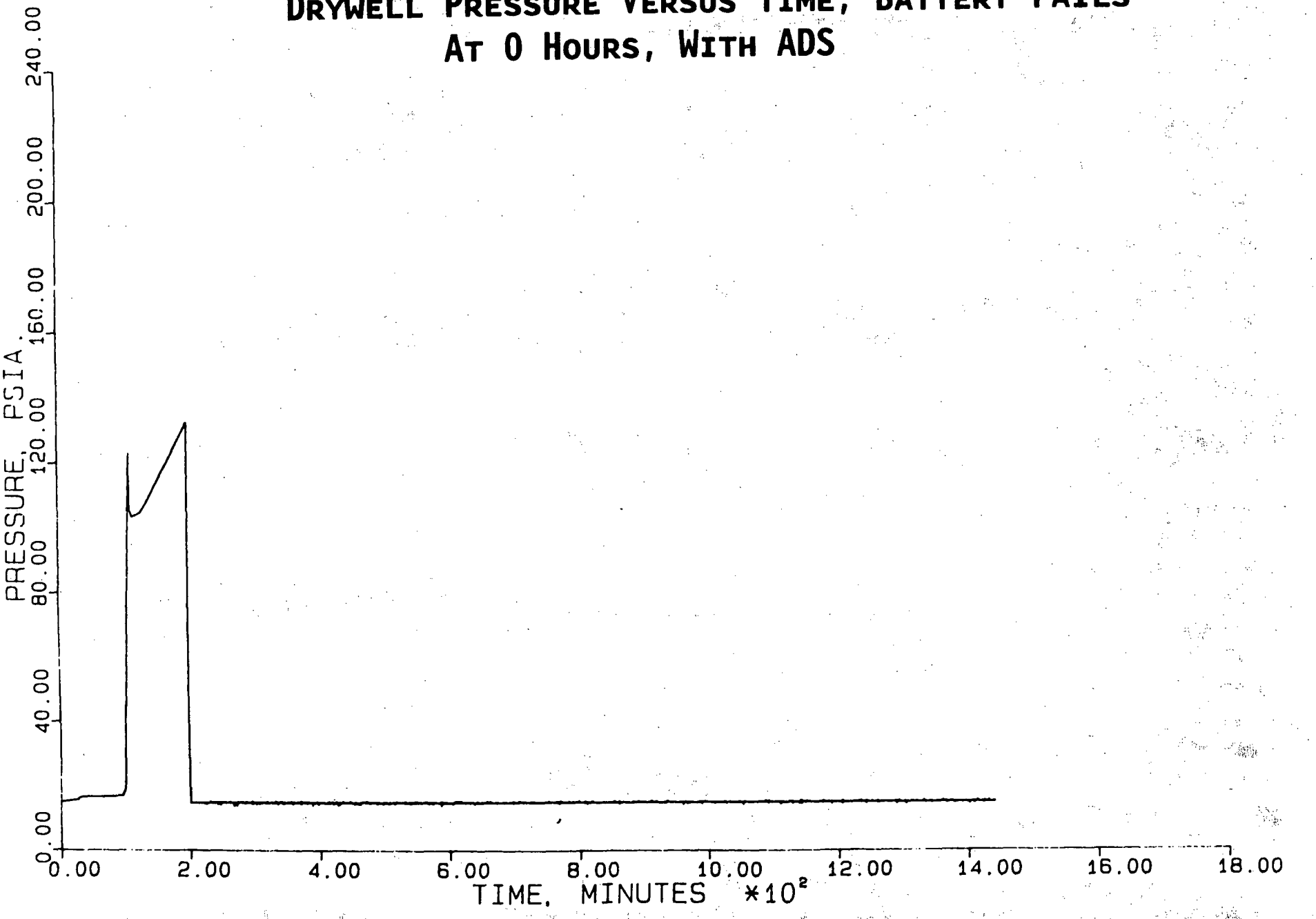


Figure Twelve

Drywell Pressure Versus Time, Battery Fails At 0 Hours, With ADS



MARK I DRYWELL SHELL TEMPERATURE RESPONSE IN A SEVERE ACCIDENT

by

F. J. Moody
R. Muralidharan
S. S. Dua

GE Nuclear Energy, San Jose, California

ABSTRACT

This study describes methods for estimating the maximum temperature of a Mark I steel shell in response to the arrival of molten corium, discharged from a breached reactor during a postulated severe accident. Theoretical formulations are described, which display the influence of important parameters on shell temperature. Recent numerical simulation for corium discharge rate, composition, and chemical heating from concrete gases were employed as basic inputs for a typical example case in this study.

Calculations show that for a water layer over the corium with a cooling range between nucleate and enhanced film boiling, the estimated shell maximum temperature is between 600 and 1000°K below the melting value. It was concluded that creep rupture failure of the shell was not a concern for the calculated shell hot spot temperature transient and corresponding drywell pressure.

NOMENCLATURE

Major Symbols

A	Area
c	Specific heat capacity
D	Distance into page
E, e	Internal thermal energy, specific internal energy
F	Cooling factor, Eq. (25)
g_o	Newton's constant in $F = Ma/g_o$
g	Acceleration of gravity
h	Convective heat transfer coefficient
K	Thermal conductivity
$\dot{m}_g$	Gas mass flow rate
P	Pressure
Q	Volume flow rate
q, q", q'''	Heat transfer rate, flux, volume generation
R, r	Sector radius, radial coordinate
T	Temperature
t	Time
V	Volume

$\underline{V}$	Velocity vector, components (u, v, w)
x, y, z	Rectangular coordinates
Y	Corium Depth
α	Thermal Diffusivity
α_g	Gas void fraction
ρ	Density
τ	Time Constant
σ	Stress
δ	Shell thickness
ν	Kinematic Viscosity
π_n	Non-dimensional groups, n = 1, 2, ---, 7, Eq. (A.14)

Subscripts and other symbols

front	Front of flowing corium
h	Convection
i	Initial Value
cs	contact with the shell
c	Concrete
L-S	Freezing property (liquid to solid)
Liq	Liquidus
M	Shell Hot Spot
Sol	Solidus
s	Shell
R	Rectangular Region
w	Triangular Wedge Region
Y	Corium Surface
α	Internal conduction
∞	Ambient Condition
(_)	Vector

INTRODUCTION

The discharge of molten corium following a breached reactor vessel during certain postulated severe accident sequences, indicated in Figure 1, has raised questions about the Mark-I drywell shell integrity. This subject is the focus of several current experimental and theoretical studies, much of which are summarized in Reference [1]. Various state-of-the-art computer models are being used to predict core melt progression and containment response (for example, see References [2-6]). However, the sensitivity of containment temperature to various accident parameters is often obscured in these calculations.

Studies of postulated severe accidents due to inadequate cooling of the reactor core have been performed by scientists and engineers for over 20 years. The present state-of-the-art provides a technological base for understanding and estimating basic phenomena of severe accidents.

Several theoretical models have been formulated to describe the basic phenomena, and have been incorporated into complex system programs for predicting the heat up, melting, and flow progression of core material in the reactor vessel, vessel failure, and resulting discharge of corium into the

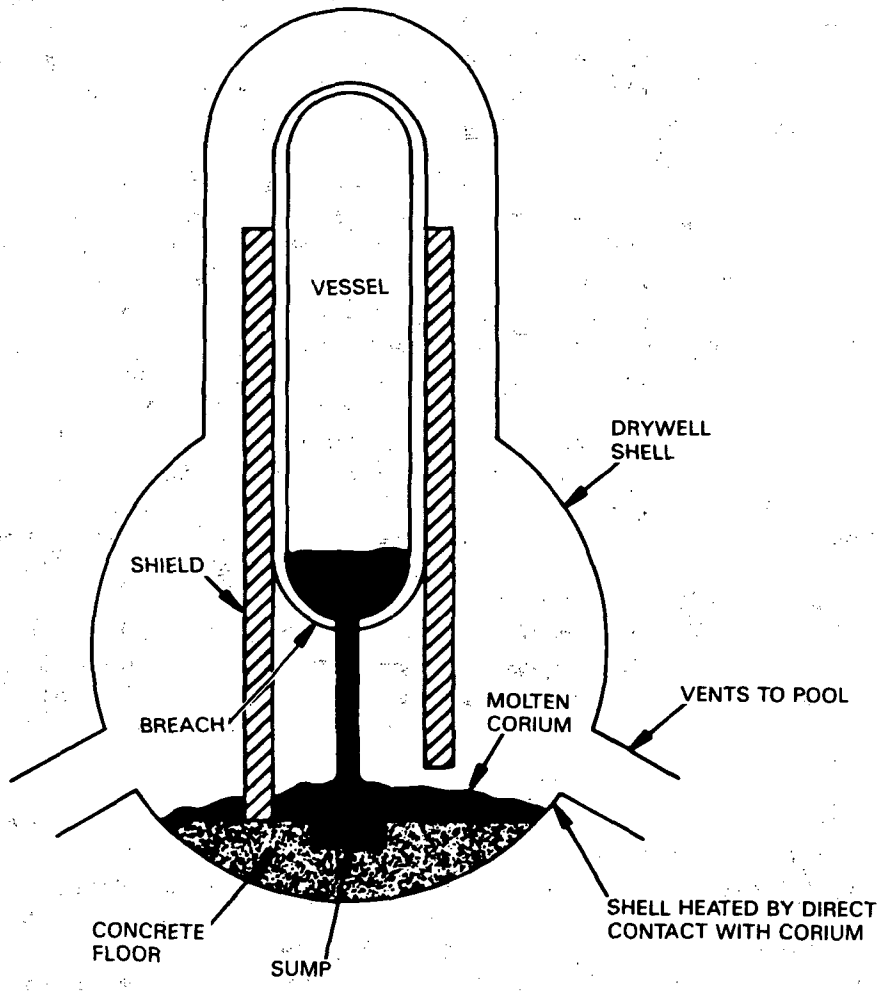


Figure 1. Molten Corium Discharge into Drywell

containment. The BWRSAR Code [2], developed by Oak Ridge National Laboratory (ORNL), uses such phenomena modeling to determine core melt progression and corium discharge into the drywell in the case of an unrecovered severe accident. BWRSAR is employed in this study to provide the time-dependent accumulation of corium and its composition in the pedestal and drywell area.

Computational models for corium progression in the containment focus on concrete interaction, e.g., the CONTAIN code [5], with less emphasis on spreading and thermal response following arrival at the Mark-I drywell shell. However, additional analyses have been employed by various investigators for estimating corium-steel shell heat transfer in Mark-I drywells to determine if the shell temperature approaches that of melting. The results yield conclusions which range from the possibility of early shell melting to maximum temperatures well below the melting value. This range of conclusions appears to be the result of major assumptions which differ in the following:

1. The rate of corium discharge onto the drywell floor;
2. The corium discharge temperature and composition;
3. The amount of chemical heat generation by zirconium reaction with water and carbon dioxide released from concrete;
4. The amount of heat transfer from the steel shell to the concrete shield wall and containment environment;
5. The heat transfer rate to overlying water on corium.

It is difficult to tell a-priori which parameters implied in the above assumptions dominate a given containment thermal response. This study was performed to provide simplified, reasonable-estimate formulations which display the relative dependence of drywell shell thermal response to important severe accident parameters. The shell temperature response in a Mark-I drywell for a typical severe accident also is discussed. Results indicate that the shell temperature remains well below the melting value for a state-of-the-art calculated discharge of corium from a breached reactor. It was found that for the example case considered, creep-rupture failure of the shell is not a concern.

OVERVIEW OF THE ANALYSIS

The various analyses described in this study involve the thermal-hydraulics of molten corium flow across the drywell floor, its arrival at the steel shell, and the resulting temperature response. Results are offered to help ascertain how various accident parameters affect corium and shell thermal response without the complexity of detailed computer models.

It is assumed that molten corium discharge rates and composition, and release rates of steam and carbon dioxide from concrete, are available from modern computer simulation. Internal heat generation from radioactive decay and chemical reactions takes the simple form of a uniform total volumetric heat generation rate q'''. The corium is assumed to be a homogeneous liquid mixture of released components spreading on the floor. A typical volume discharge rate of 0.5 m^3/min results in a spreading front velocity of 20 cm/s at a depth of 8 mm for a frontal width of 5 m.

Corium internal heat generation and cooling heat transfer rates to the concrete below and the environment above are discussed, and estimated flow rates are employed to predict the corium temperature as it spreads on the

drywell floor. Predictions show that for corium introduction at the liquidus temperature of 2600°K, the frontal temperature for spreading under water would be cooled to 2288°K by the time it reached the shell. It was found that the shell temperature, initially at 373°K, would rise to 795°K at the instant of contact with the arriving 2288°K corium.

It is assumed that after arrival at the shell, the corium continues to rise as a liquid pool on the drywell floor, even if it has been cooled below the solidus temperature. Shell temperatures were estimated from a quasi-steady heat transfer analysis for which temperature fields closely approach equilibrium. This analysis, which displays important parameter effects on the shell maximum or hot spot temperature, is shown to be a reasonable approximation for typical conditions analyzed where the corium energy inflow rate is less than the heat removal rate. If a higher pouring rate should occur, an unsteady thermal analysis would be required.

Graphs are included which show the effect of various severe accident parameters on the Mark-I steel shell hot spot temperature. Calculations for a typical Mark-I system with overlying water and a heat transfer rate between nucleate boiling and film boiling which is enhanced by gas bubbling (three times the film boiling coefficient of Berensen [7]), yield shell hot spot temperatures between 600 and 1000°K below the melting value of 1672°K.

The phenomenon of creep-rupture was considered for the shell hot spot temperature predicted in this study and corresponding drywell pressure obtained from the CONTAIN code [5]. It was found that for corium heat transfer to overlying water, the shell creep-rupture life would exceed several days.

The following sections give details on the methodology employed to predict corium spreading, cooling, and the shell temperature.

MOLTEN CORIUM SPREADING

The continued flow of molten corium from a breached reactor vessel will fill the in-pedestal sumps, and ultimately begin to cover the concrete floor. The arrival time and corium state at initial contact with the shell depends on the spreading flow rate and depth.

The gravity-driven spreading velocity and depth of corium is governed by the liquid mass conservation and momentum principles [e.g., 8]

$$\nabla \cdot \underline{V} = 0 \tag{1}$$

and

$$\frac{\partial \underline{V}}{\partial t} + \underline{V} \cdot \nabla \underline{V} + \frac{g_o}{\rho} \nabla p + g\underline{j} = \nu \nabla^2 \underline{V} \tag{2}$$

The two dimensional flow case is considered here for flow in a channel of width D. An approximate value of D for spreading on a curved arc is simply the frontmost perimeter. The velocity vector in x,y geometry is

$$\underline{V} = u\underline{i} + v\underline{j} \tag{3}$$

Since the vertical velocity component v is much less than the horizontal component u, Eqs. (1) and (2) can be simplified by setting v = 0. Also, the

kinematic viscosity of molten corium [3] is about 6.7×10^{-7} m^2/s, which is close to that of water, 4×10^{-7} m^2/s, for which viscous effects can be neglected. Pressure variation in the corium is nearly hydrostatic, except on the advancing front, where the pressure is ambient. It follows from Eq. (1) that $\partial u/\partial x \approx 0$, and from (2) that for steady flow, the front surface condition is

$$\nabla \left(\frac{u^2}{2g} + Y \right) = 0 \tag{4}$$

That is, the corium layer kinetic and potential energy sum tends toward an extremum. If the volume rate of corium supplied is

$$Q = DuY \tag{5}$$

then Eq. (4) yields the spreading velocity and depth as

$$u = \left(\frac{g}{2} \frac{Q}{D} \right)^{1/3} \tag{6}$$

and

$$Y = \left(\frac{2}{g} \frac{Q^2}{D^2} \right)^{1/3} \tag{7}$$

It is seen that the velocity is proportional to the cube root of Q, whereas the depth varies with $Q^{2/3}$. An example corium volume pouring rate of Q = 0.5 m^3/min with an advancing front of D = 5 m would flow at a velocity of 20 cm/s and a depth of 8 mm.

THERMAL RESPONSE TIMES, CORIUM COOLING

A comparison of the relative times associated with corium cooling is made next for the purpose of determining when various heat transfer effects dominate the thermal response.

Consider a corium section of depth Y, horizontal cross-sectional area A, and uniform temperature T, insulated at the bottom, but cooled by convection at the top surface, according to

$$q = hA(T - T_\infty) \tag{8}$$

The corium thermal energy, relative to ambient T_∞, is

$$E = \rho AYc(T - T_\infty) \tag{9}$$

If internal heat generation is neglected, the corium initial temperature is T_i, and its temperature is uniform, energy conservation yields

$$T - T_\infty = (T_i - T_\infty)e^{-(h/\rho cY)t} \tag{10}$$

That is, the thermal response time for cooling by convection at the top surface is

$$\tau_h = \frac{\rho c Y}{h} \tag{11}$$

Let the same section of corium be insulated at the top surface and cooled by conduction to concrete on the bottom. The cooling rate is approximated by heat transfer to a semi-infinite slab [9] at temperature T_∞, suddenly placed in contact with an environment at temperature T_i at its surface, given by

$$q = (T_i - T_\infty)A \frac{K}{\sqrt{\pi\alpha}} \frac{1}{\sqrt{t}} \tag{12}$$

An energy conservation analysis with $K = K_c$ and $\alpha = \alpha_c$ in Eq. (12), and uniform corium temperature gives the thermal response time for cooling by the concrete as

$$\tau_c = \frac{\pi}{4} \frac{1}{\alpha_c} Y^2 \tag{13}$$

Equations (11) and (13) give approximate cooling response times of a corium layer for convective cooling at the top surface, or conductive cooling at the bottom surface. These results are based on uniform temperature in the corium. However, heat conduction within the corium may actually be the limiting phenomenon for thermal response. The importance of internal conduction is estimated by considering a corium layer of depth Y and temperature T_i with one face at y = 0 insulated, and the other face at y = Y suddenly cooled to T_∞. The eigenvalue solution for unsteady temperature, neglecting internal heat generation [9] yields the approximate thermal response time,

$$\tau_\alpha \approx \frac{1}{\alpha} \left(\frac{2Y}{\pi}\right)^2 \tag{14}$$

Typical severe accident parameters are listed in Table 1 for use in estimating the various response times and thermal behavior. It is assumed that corium of depth Y suddenly falls onto the concrete floor, for which the corresponding thermal response times are given in Table 2. A comparison of these typical response times shows that corium cooling by the concrete takes about six times longer than convective cooling by an overlying water layer. Heat conduction through the corium requires an order of magnitude less time than the example cooling times of convection or conduction at the surface. Therefore, cooling of the corium for the parameters of Table 1 is dominated by convection at the top surface.

Table 1

TYPICAL SEVERE ACCIDENT PARAMETERS

Corium

K	= 30 W/M-°K	q'''	= { 4.0 Mw/m^3 chem. & decay heat until zirconium is depleted; 1.0 Mw/m^3 decay heat only
ρ	= 9000 kg/m^3	Q	= 0.5 m^3/min
c	= 0.48 J/gm-°K	Y	= 0.01 m
α	= 0.07 cm^2/s	T_{liq}	= 2600°K
E_{L-s}	= 250 J/gm	T_{sol}	= 2100°K
V	= 0.2 m/s	T_∞	= 373°K
h	= 390 W/m^2-°K	(Berensen film boiling coefficient [7], enhanced by a factor of 3)	

Concrete

K_c	= 1.3 W/m-°K	c_c	= 0.835 J/gm-°K
ρ_c	= 2300 kg/m^3	α_c	= 0.0068 cm^2/s
$R_{in-pedestal}$	= 4 m	$R_{ex-pedestal}$	= 7 m
V_{sump}	= 5.8 m^3		

Shell

K_s	= 50 W/m-°K	δ	= 3.0 cm
α_s	= 0.14 cm^2/s		

Table 2

THERMAL RESPONSE TIMES, CORIUM COOLING

τ_h = 100 s

τ_c = 600 s

τ_α = 10 s

HEAT TRANSFER IN SPREADING CORIUM

The state of a molten corium layer spreading on the floor and arriving at the drywell shell depends on heat transfer from the top and bottom surfaces and the internal heat generation. The top surface convective heat transfer can be to overlying water, or it can be to air and drywell structures if an equivalent coefficient is used which includes radiation effects. Heat conduction to the concrete was shown to be small for the parameters of Table 1, but the relative effect could be important for other sets of parameters. Decay heat from UO_2 and the chemical heat generation of Zr reaction with steam and CO_2 released from the concrete produce internal heating of the corium. The physical state of spreading corium depends on its local temperature, which is estimated next.

The time-dependent energy equation for temperature T(x,y,t) in flowing, inviscid, incompressible liquid with internal volumetric heat generation is given by (Appendix A),

$$\frac{\partial T}{\partial t} + \underline{V} \cdot \nabla T = \frac{1}{\rho c} (q''' + K\nabla^2 T) \qquad (15)$$

The corium surface on the concrete is assumed to be insulated because of the relatively long thermal response time for concrete heat absorption in Table 2. A convective boundary condition is imposed at the top surface. The internal conduction response time in Table 2 for a thin layer of corium is sufficiently rapid to justify the assumption of a uniform temperature at each vertical plane. The horizontal conduction is neglected because it is much slower than energy transport by corium flow. Solution details for the corium temperature as it spreads are given in Appendix A.

The corium front temperature is graphed in Figure 2 for corium entering at T_o with volumetric heat generation. Other parameter effects included are the corium density, specific heat, convective heat transfer coefficient, the flowing depth and velocity, and the distance traveled. It is seen that the corium front will be cooled as it flows for values of the parameter $q'''Y/h(T_o - T_\infty) < 1.0$. Consider a case where corium enters at the liquidus temperature, $T_o = 2600°K$, with internal heat generation $q''' = 4$ Mw/m^3 which includes both zirconium reaction and radioactive decay. Use of additional properties of Table 1 in Figure 2 show that when the front travels a distance x = 3 m across the ex-pedestal floor to the shell, its temperature will drop to 2288°K for an enhanced film boiling coefficient of h = 390 W/m^2-K. If nucleate boiling occurred with h = 60,000 W/m^2-K, the corium front would reach the 2100°K solidus temperature before it traveled 5 cm. Therefore, there are ranges of accident parameters which would result in corium freezing before it reached the shell. The following sections are based on the assumption that the corium remains liquid, contacts the shell, and continues to rise in depth as pouring from the breached reactor continues.

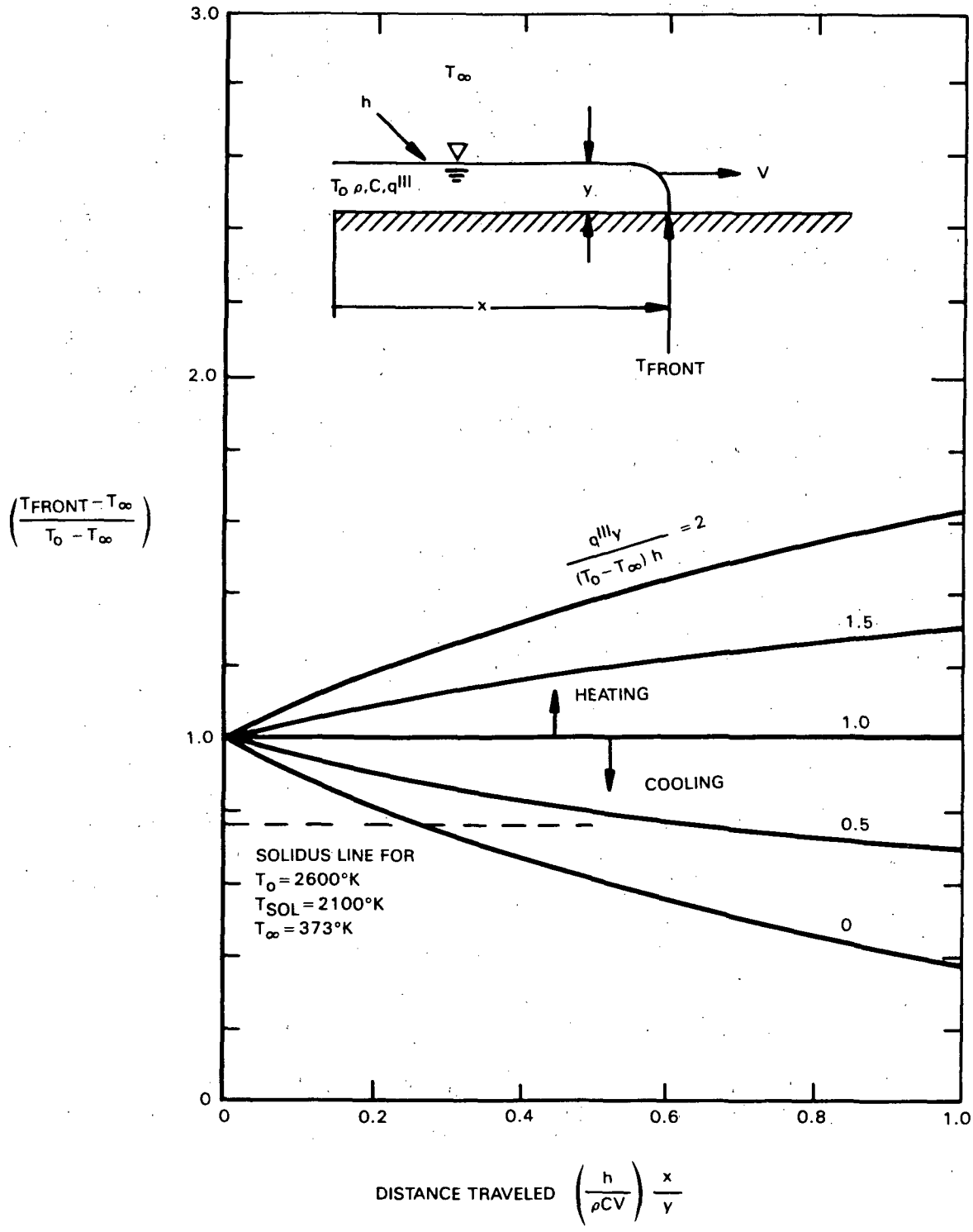


Figure 2. Corium Advancing Front Temperature

CORIUM-SHELL INITIAL CONTACT TEMPERATURE

When molten corium at temperature T_{front} initially contacts the shell at T_∞, the shell surface immediately changes to the so-called contact temperature, T_{cs}, which is between T_{front} and T_∞. The value of T_{cs} is important because if it is close to the shell melting value, early shell failure would be expected.

The contact temperature is obtained by treating the corium layer of depth Y and the shell of thickness δ as two semi-infinite bars suddenly in perfect thermal contact. Heat transfer across the interface can be written from Eq. (12) for both the corium and shell with the contact surface at T_{cs}, which gives

$$\frac{T_{cs} - T_\infty}{T_{front} - T_\infty} = \frac{1}{1 + \left(\frac{K_s}{K}\sqrt{\frac{\alpha}{\alpha_s}}\,\frac{\delta}{Y}\right)} \tag{16}$$

The contact temperature for parameters of Table 1 with a value of T_{front} = 2288°K is T_{cs} = 795°K, which is below the corium solidus temperature of 2100°K

Equation (16) is based on constant specific heat of corium. A pure substance would maintain higher contact temperature during phase change from liquid to solid. However, corium generally is not a pure substance, and its temperature changes during solidification. An equivalent specific heat was obtained by employing the heat of fusion in the definition of specific heat, giving

$$c = \left(\frac{\partial e}{\partial T}\right)_p = \frac{e_{L-s}}{T_{Liq} - T_{sol}} = 0.5 \text{ J/gm-°K}$$

This value of specific heat is essentially equal to the liquid value of Table 1. Therefore, the contact temperature analysis is based on a constant value of specific heat in the corium.

QUASI-STEADY SHELL TEMPERATURE

When the thermal energy rate of corium discharge from the reactor can be removed by cooling mechanisms, the temperature field can be estimated by a quasi-steady analysis for the continuously increasing depth. The thermal energy addition rate, based on T_∞ as a datum, is $\dot{E} = \rho Q c(T - T_\infty)$. If the controlling heat removal mechanism is convection from the top surface at a rate $q = hA(T - T_\infty)$, a quasi-steady analysis is appropriate when $q > \dot{E}$, or when

$$Q < \frac{Ah}{\rho c} \tag{17}$$

The parameters of Table 1 for molten corium spread over the total drywell floor area give a maximum pouring rate of $Q < 0.7\ m^3/min$ for a quasi-steady thermal analysis to apply.

Figure 3 shows the model employed for estimating a temperature field in corium and the shell. Separate analyses for the rectangular and triangular region of corium are matched at the common dotted boundary to determine the maximum shell temperature.

Temperature in the rectangular region is based on an insulated bottom surface, convection cooling at the top, uniform internal heat generation, and an unknown temperature profile, assumed to be quadratic in form, on the dotted boundary. The eigenvalue problem is summarized below:

$$\text{DE} \quad \left(\frac{\partial^2}{\partial x^2} + \frac{\partial^2}{\partial y^2}\right) (T - T_\infty) = - \frac{q'''}{K} \tag{18}$$

$$\text{BC's} \quad T(0,y) - T_\infty = T_m - T_\infty - (T_m - T_Y) \left(\frac{y}{Y}\right)^2 \tag{19}$$

$$T(\infty,y) - T_\infty = \frac{q'''Y}{h} + \frac{q'''}{2K} (Y^2 - y^2) \tag{20}$$

$$\frac{\partial T(x,0)}{\partial y} = 0 \tag{21}$$

$$\frac{\partial T(x,Y)}{\partial y} + \frac{h}{K} [\ T(x,Y) - T_\infty\ ] = 0 \tag{22}$$

The quadratic temperature profile assumed in Eq. (19) is based on the form of Eq. (20), which is a solution to (18), (21), and (22) at $x \to \infty$.

The triangular wedge region is bounded by an angle of $\pi/4$ between the vertical dotted line and the shell. It is idealized in Figure 3 to a circular segment of radius.

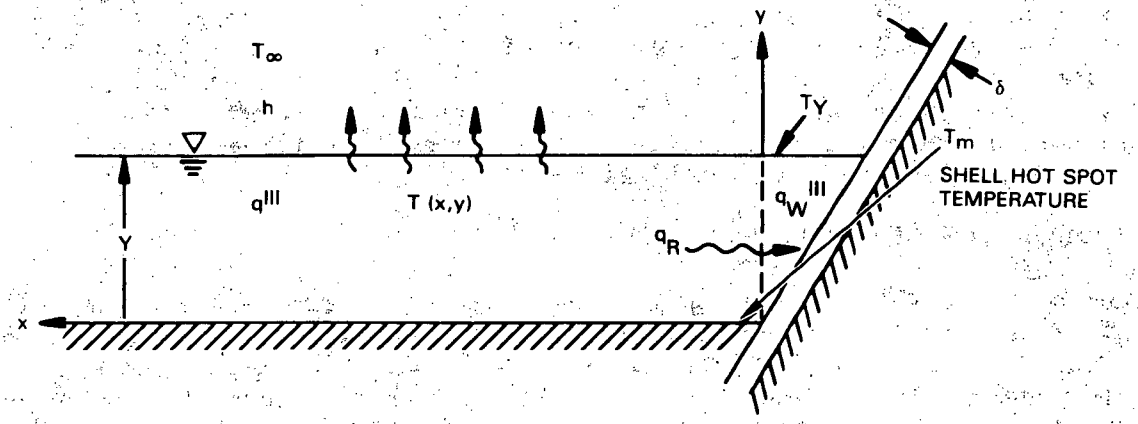
$$R = \frac{2}{\sqrt{\pi}}\ Y \tag{23}$$

to maintain its volume. It is assumed that the heat transfer rate q_r entering from the rectangular region blends with the uniform internal heat generation of the triangular wedge. Since the wedge volume is $DY^2/2$, the total volumetric heat generation rate is

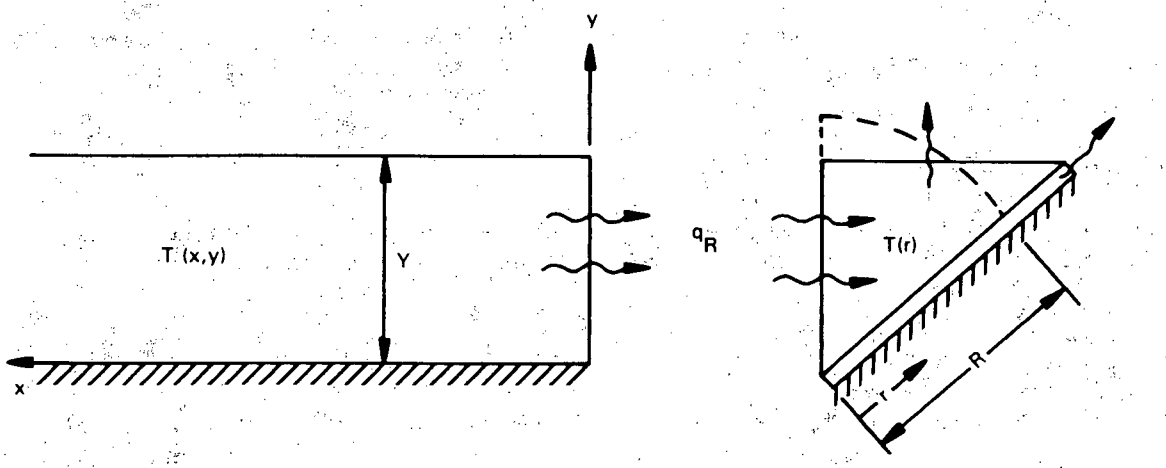
$$q_+''' = q_w''' + \frac{2q_R}{DY^2} \tag{24}$$

where q_w''' is due to decay and chemical heating.

Heat generation in the wedge is transferred to the surroundings through the top surface by convection from the corium and shell. It is assumed that the wedge and shell temperature profiles T(r) are the same. Furthermore,



FORMULATED BY TWO PROBLEMS



RECTANGULAR REGION

TRIANGULAR WEDGE REGION

Figure 3. Model for Shell Hot Spot Temperature

total heat generation in the triangular region, $q_+'''\pi R^2 D/8$, must be transferred from the top surface by the convective flow $h_w(\pi RD/4 + \delta D)(T_Y - T_\infty)$, based on the assumption that both the shell area δD and corium surface area $\pi RD/4$ transfer heat to the surroundings with the convection coefficient h_w. This assumption neglects the extended fin heat transfer aspects of the shell, which would cause higher heat removal. Repre- sentative solutions are graphed in Figures 4(a) and 4(b), which contain the functional dependence of shell maximum temperature on corium depth Y, internal volumetric heat generation in the rectangular region q''' and in the triangular wedge region q_w''', shell and corium thermal conductivities K_s and K, shell thickness δ, and the top surface heat transfer coefficient h.

RELATIVE IMPORTANCE OF SEVERE ACCIDENT PARAMETERS

Figures 4(a) and 4(b) show how the shell hot spot temperature varies with important severe accident parameters. The ratio K_s/K was held constant. The ratio of internal heat generation rates q_w'''/q''' was set equal to 0.0 in Figure 4(a) where internal heat generation in the rectangular region of corium is dominated by chemical reaction with concrete gases, but relatively small decay heat occurs in the triangular region, which is not expected to participate in bubbling from below. Figure 4(b) is for cases where decay heat is the only source. It is seen that higher values of the convective heat transfer parameter $h\delta/K$ result in lower maximum shell temperature T_m. However, T_m reaches a limit as $h\delta/K \to \infty$. The cooling factor

$$F = \frac{h}{h_{\text{film boiling}}} \tag{25}$$

is employed to display the effect of h relative to the case of ordinary film boiling. Nucleate boiling corresponds to about F = 460 ($F \geq 10$) in Figures 4(a) and (b).

CORIUM VOID FRACTION

Gas released from the concrete will bubble upward through the liquid corium, which results in a swollen depth. Gas mass flux can be written as

$$\dot{m}_g'' = \rho_g d_g V_b \tag{26}$$

where ρ_g is the gas density, α_g is the gas volume or void fraction in the corium, and V_b is the bubble rise velocity. Liquid volume contained in a corium-gas mixture is $(1 - \alpha_g)AY_\alpha$ where A is a section of floor area and Y_α is the swollen depth. The liquid volume is AY where Y is the collapsed level without voids. It follows that the swollen level is

$$Y_\alpha = \frac{Y}{1 - \alpha_g} \tag{27}$$

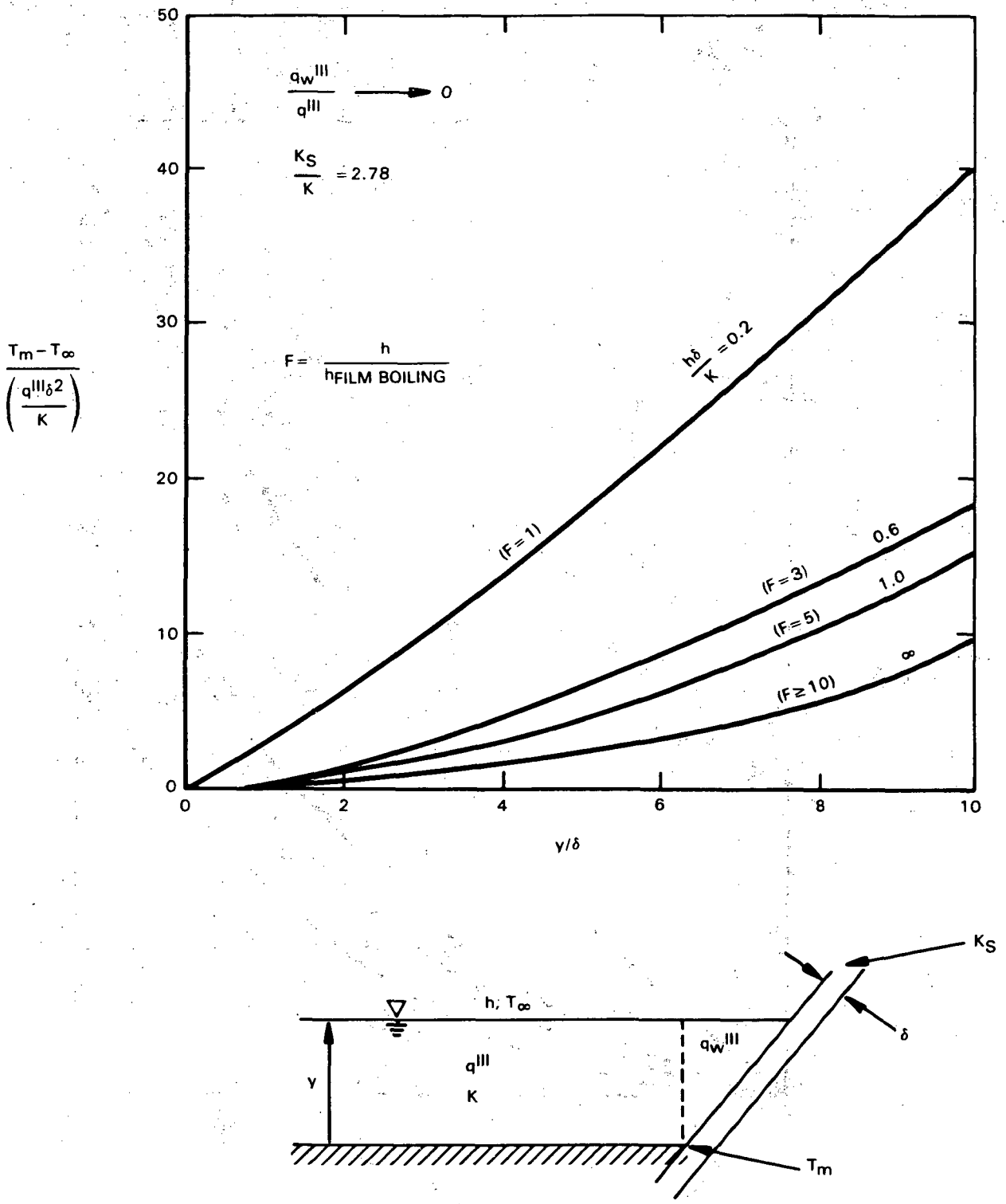


Figure 4(a). Shell Hot Spot Temperature; High Internal Heat Generation in Rectangular Region

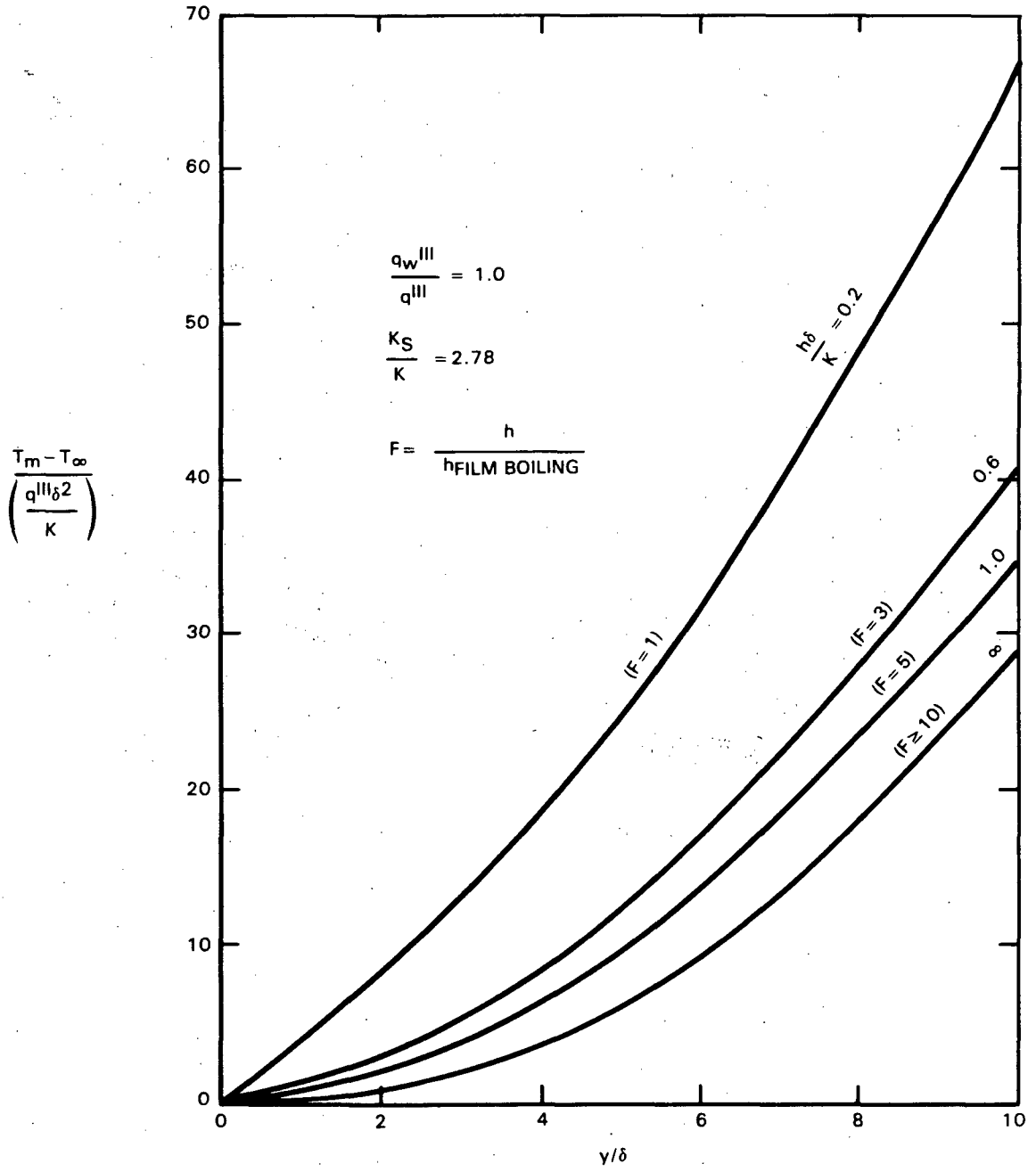


Figure 4(b). Shell Hot Spot Temperature; Equal Heat Generation Rates, Rectangular and Wedge Regions

Equation (27) is used to show that the volume ratio of a bubbly corium mixture to that of the liquid is $1/(1 - \alpha_g)$. It follows that the volumetric heat generation rate for a bubbly mixture becomes

$$q_\alpha''' = q'''(1 - \alpha_g) \tag{28}$$

The conductive heat transfer rate across an area A in the liquid corium is $q = - KA\ \partial T/\partial n$. The liquid area fraction of A in a bubbly mixture is $A_L/A = 1 - \alpha_g$, across which the heat conduction is $q = - KA_L \partial T/\partial n = - K_\alpha A \partial T/\partial n$ where the effective thermal conductivity for the bubbly mixture is

$$K_\alpha = K(1 - \alpha_g) \tag{29}$$

Equations (27), (28), and (29) show that the effect of voids is to increase the corium depth Y, decrease the volumetric heat generation rate q''', and decrease the thermal conductivity K. Therefore, the ratio q'''/K remains unchanged by voids in Figures 4(a) and (b). Also, the parameter $h\delta/K$ increases with α_g, an effect which is largely offset by the increased Y. It follows that the effect of corium swelling from bubbling gas has a relatively small effect on shell temperature.

CREEP-RUPTURE CONSIDERATIONS

A metal sample under tensile stress at elevated temperature may undergo creep elongation until failure occurs. Typical stress rupture data is shown in Figure 5 [10], giving the rupture life in terms of applied stress σ and temperature. The stress in a spherical steel shell of radius R and wall thickness δ with internal gauge pressure P is

$$\sigma = \frac{PR}{2\delta} \tag{30}$$

When the stress and temperature vary with time, integration of life fraction used over a period of time determine the fraction of rupture life remaining.

EXAMPLE CALCULATION

The postulated severe accident used in a typical example case involved station blackout with automatic vessel depressurization. Important corium properties are listed in Table 3. The major corium discharge inputs, chemical heating values, and drywell pressure were extracted from BWRSAR [2] and CONTAIN [5] runs, and are given in Table 4. Figure 6 shows the shell hot spot temperature as a function of time and the cooling factor F.

The drywell sumps are filled with molten corium at 350 minutes, and continued discharge begins to flow over the floor. The temperature rise is rapid between 350 and 400 minutes because a large mass of zirconium is released which reacts with water and gas released from the concrete. This zirconium is depleted at 400 minutes, according to CONTAIN calculations. A smaller zirconium discharge occurs between 510 and 540 minutes.

Table 3

CORIUM PROPERTIES

Component	Density (kg/m^3)	Thermal Conductivity (W/m-K)
ZR	6500	18
FE	8500	66
UO_2	10100	3.3

Table 4

BWR-SAR, CONTAIN OUTPUT, CORIUM DISCHARGE AND VOLUMETRIC HEATING, TYPICAL CASE

Time (min)	P (KPa)	ZR (kg)	FE (kg)	UO_2 (kg)	q''' (MW/m^3)	K_{mix} (W/m-K)
260	230	0	0	0	0	0
285	260	19000	61000	0	0	54.6
350	300	19000	61000	0	0	54.6
350	300	19000	61000	0	3.6	54.6
400	500	43000	86000	36000	3.6	39.8
510	760	44000	113905	117095	0.3	31.6
510	760	44000	113905	117095	0.3	31.6
540	830	45500	113905	120300	0.3	31.9
540	830	45500	113905	130505	0.3	32.1
600	880	45550	143986	140514	0.3	32.7
700	970	45500	166954	157546	0.3	33.4
800	1060	45500	178438	166062	0.3	34.6
900	1160	45500	184179	170320	0.3	33.8

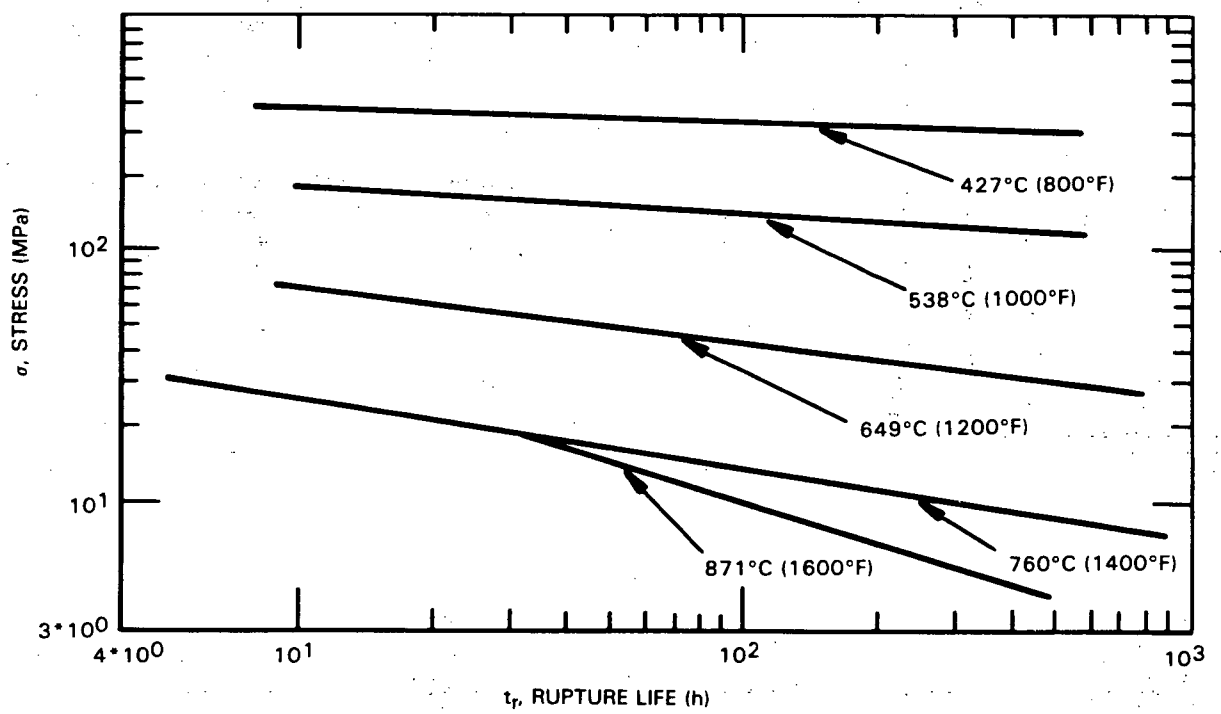


Figure 5. Creep-Rupture Design Data SA-516 Grade 55 Carbon Steel [10]

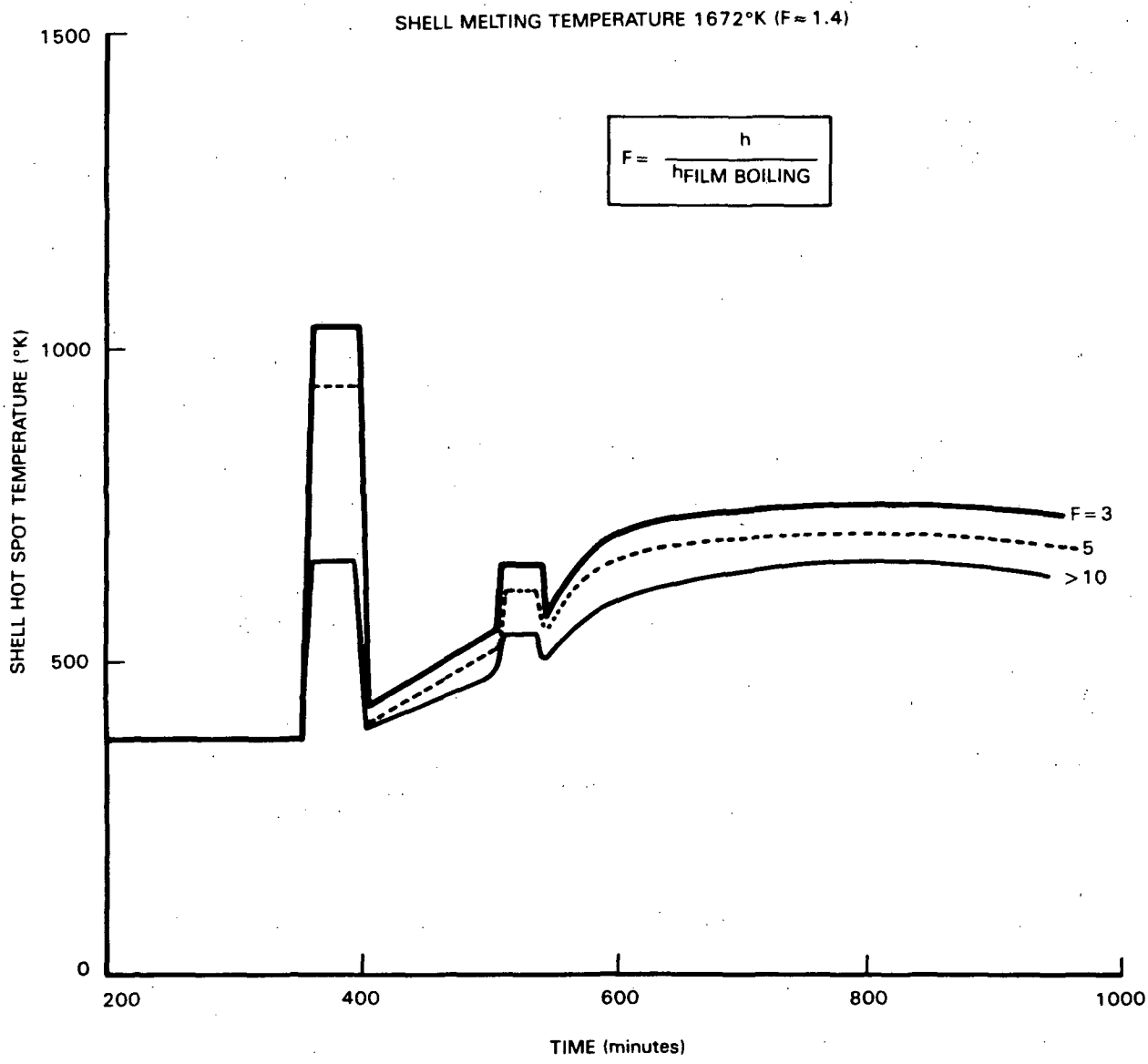


Figure 6. Calculated Shell Hot Spot Temperature, Typical Mark-I System

A cooling factor of F = 3 corresponds to enhanced film boiling, and results in an estimated maximum shell temperature about 600°K below the melting value of 1672°K. Corium heat transfer enhancement with a cooling factor F from 6 to 10 are unofficially being suggested for bubbling corium-water interfaces. The value of $F \geq 10$, which corresponds to nucleate boiling, results in a maximum shell hot spot temperature about 1000°K below melting. The entire mass of corium is in the drywell at 900 minutes, after which the maximum shell hot spot temperature declines with decay heat.

CONCLUSIONS

The simplified theoretical formulations described in this study make it possible to estimate the effect of important severe accident parameters on the shell hot spot temperature in a Mark-I containment system. It was found that the maximum shell temperature is directly proportional to the volumetric heat generation rate. Convective heat transfer to overlying water is effective in preventing temperatures from reaching the steel shell melting value if a film boiling enhancement factor of 3.0 occurs from concrete gas bubbling at the corium-water interface. Increased thermal conductivity of the corium mixture cause the maximum shell temperature to be reduced, whereas increased corium depth causes it to increase. A typical example case, with corium discharge rate, properties, and chemical heating obtained from BWR-SAR and CONTAIN outputs, showed that for a film boiling enhancement factor of 3.0, shell maximum temperatures are more than 400 K below the steel melting value. It was concluded that shell creep-rupture failure was not a concern for the example case considered.

REFERENCES

1. Workshop on BWR/Mark-I Containment Issues, Feb. 24-26, 1988, Baltimore, MD.

2. BWRSAR, Calculations for Peach Bottom, Private Communications, S. A. Hodge, 1987-1988.

3. MAAP-Modular Accident Analysis Program, Fauske & Associates, Inc., 1985 (User's Manual, Vols. 1 & 2).

4. APRIL.MOD 2, A Computer Code for Core Meltdown Accident Analysis of Boiling Water Nuclear Reactors, S. H. Kim, et. al., RPI, N.Y., 1987.

5. CONTAIN Code, C. R. Hyman, Private Communication, 1988.

6. R. K. Cole, et. al., "CORCON/Mod 2, A Computer Program for Analysis of Molten Core-Concrete Interaction," NUREG/CR-3920, Aug. 1984.

7. Berenson, P. J., "Film Boiling Heat Transfer From a Horizontal Surface," Trans. ASME, Ser. c, Vol. 83 (1961).

8. Landau, L.D., and Lifshitz, E. M., Fluid Mechanics, Pergamon Press, 1959.

9. Kreith, F., Principles of Heat Transfer, 3rd Ed., IEP - A Dun-Donnelley Publisher, N.Y., 1976.

10. Nuclear Systems Materials Handbook, Vol. 1, TID 26666.

APPENDIX A

Temperature in Spreading Corium

Figure A.1 shows an elemental volume of corium with dimensions dx, dy, and dz. Conductive heat transfer rates q_x q_y, and q_z flow in each of the coordinate directions, while an internal heat generation rate q'''dx dy dz is occurring. The element has mass M = ρ dx dy dz and stored thermal energy E = McT. Conservation of energy for the volume element yields

$$\frac{\partial q_x}{\partial x} dx + \frac{\partial q_y}{\partial y} dy + \frac{\partial q_z}{\partial z} dz - q'''dx\, dy\, dz + \rho c \frac{dT}{dt} dx\, dy\, dz = 0 \qquad (A.1)$$

The heat flux vector

$$\underline{q}'' = - K \nabla T \qquad (A.2)$$

and the total derivative of temperature for the moving fluid increment,

$$\frac{dT}{dt} = \frac{\partial T}{\partial t} + \underline{V} \cdot \nabla T \qquad (A.3)$$

are employed to obtain,

$$\frac{\partial T}{\partial t} + \underline{V} \cdot \nabla T = \frac{1}{\rho c} (q''' - \nabla \cdot \underline{q}'') = \frac{1}{\rho c} (q''' + K \nabla^2 T) \qquad (A.4)$$

The top surface heat flux is given by

$$\underline{q}''\Big|_{y=Y} = h[\, T(x,Y,t) - T_\infty \,]\, \underline{j} \qquad (A.5)$$

Heat transfer from the corium bottom surface corresponds to diffusion into the concrete, which is governed by

$$\frac{\partial T_c}{\partial t} = - \frac{1}{\rho_c c_c} \nabla \cdot \underline{q}''_c \qquad (A.6)$$

where

$$\underline{q}''_c = - K_c \nabla T_c \qquad (A.7)$$

The concrete and containment space initial temperature is T_∞. Molten corium enters at T_o. The boundary condition for thermal contact between corium and concrete is based on temperature continuity $T(x,0,t) = T_c(x,0,t)$, and equal normal heat fluxes, $\underline{j} \cdot \underline{q}'' = \underline{J} \cdot \underline{q}''_c$.

The relative importance of terms in Eqs. (A.4) through (A.7) can be determined by first normalizing so that the non-dimensional variables and derivatives are of order of magnitude 1. A comparison of the resulting

coefficients then can be made to determine which effects are small enough to neglect.

It is assumed that cooing of the corium is dominated by heat transfer to the overlying water layer, for which a reference time interval $\Delta t = \tau_h$ from Eq. (11) is employed for normalizing the time scale. An appropriate horizontal reference length during corium spreading is the distance a liquid particle travels during Δt, or $\Delta x = \tau_h V$. Unsteady temperature in the concrete floor, treated like a semi-infinite slab, is a function of the similarity variable $\eta = Y_c / 2\sqrt{\alpha_c t}$ [9]. The penetration depth of the surface temperature disturbance approximately corresponds to $\eta = 1$, or $y_c \approx 2\sqrt{\alpha_c t}$. Therefore, a reference length for heat absorption in the concrete during time Δt is $\Delta y_c = 2\sqrt{\alpha_c \tau_h}$. Similarly, a reference length for vertical conduction in the corium is $\Delta y \approx 2\sqrt{\alpha \tau_h}$. Finally, a reference temperature difference for both corium and concrete is $\Delta T = T_o - T_\infty$. The normalized variables are summarized below:

$$
\left.
\begin{aligned}
T^* &= \frac{T - T_\infty}{T_o - T_\infty} & u^* &= \frac{u}{V} \\
T_c^* &= \frac{T_c - T_\infty}{T_o - T_\infty} & v^* &= \frac{v}{V} \\
x^* &= \frac{x}{\tau_h V} = \frac{h}{\rho c Y V}\, x & q''^* &= \frac{q''}{h(T_o - T_\infty)} \\
y^* &= \frac{Y}{2\sqrt{\alpha \tau_h}} & q''^* &= \frac{q''}{h(T_o - T_\infty)} \\
y_c^* &= \frac{y_c}{2\sqrt{\alpha_c \tau_h}} & q_c''^* &= \frac{q_c''}{h(T_o - T_\infty)} \\
t^* &= \frac{t}{\tau_h} = \frac{h}{\rho c Y}\, t
\end{aligned}
\right\} \qquad (A.8)
$$

The heat transfer equations become

Flowing Corium

$$
\frac{\partial T^*}{\partial t^*} + u^* \frac{\partial T^*}{\partial x^*} = \pi_1 - \pi_2 \left(\pi_3 \, \underline{i} \frac{\partial}{\partial x^*} + \underline{j} \frac{\partial}{\partial y^*} \right) \cdot \underline{q}''^* \qquad (A.9)
$$

Heat Flux in Corium

$$
\underline{q}''^* = - \pi_4 \left(\pi_3 \, \underline{i} \frac{\partial}{\partial x^*} + \underline{j} \frac{\partial}{\partial y^*} \right) T^* \qquad (A.10)
$$

Top Surface Heat Flux

$$\underline{q}''^* = T^* \underline{i} \tag{A.11}$$

Concrete Heat Transfer

$$\frac{\partial T_c^*}{\partial t^*} = -\pi_5 \left(\pi_6 \underline{i} \frac{\partial}{\partial x^*} + \underline{j} \frac{\partial}{\partial y^*} \right) \cdot \underline{q}_c''^* \tag{A.12}$$

$$\underline{q}_c''^* = -\pi_7 \left(\pi_6 \underline{i} \frac{\partial}{\partial x^*} + \underline{j} \frac{\partial}{\partial y^*} \right) T_c^* \tag{A.13}$$

where

$$\left.\begin{aligned} \pi_1 &= \frac{q'''Y}{(T_o - T_\infty)h} & \pi_5 &= \frac{1}{2}\sqrt{\frac{\tau_h}{\alpha_c}}\ \frac{h}{\rho_c c_c} \\ \pi_2 &= \frac{1}{2}\sqrt{\frac{\tau_h}{\alpha}}\ \frac{h}{\rho c} & \pi_6 &= \frac{2}{V}\sqrt{\frac{\alpha_c}{\tau_h}} \\ \pi_3 &= \frac{2}{V}\sqrt{\frac{\alpha}{\tau_h}} & \pi_7 &= \frac{K_c}{2h\sqrt{\alpha_c \tau_h}} \\ \pi_4 &= \frac{K}{2h\sqrt{\alpha\, \tau_h}} \end{aligned}\right\} \tag{A.14}$$

The nondimensional variables and first derivatives are of order 1.0 in magnitude, that is, their values generally fall between 0.0 and 1.0. Therefore, the magnitude of the non-dimensional groups $\pi_1, \ldots, \pi_7$ show the relative importance of terms in Eqs. (A.9) through (A.13). Example parameters of Table 1 yield

Internal heat generation (decay heat only)	$\pi_1 = 0.01$
Corium heat diffusion in y	$\pi_2 = 0.23$
Corium heat diffusion in x	$\pi_2\pi_3 = 0.00046$
Corium heat flux in y	$\pi_4 = 2.13$
Corium heat flux in x	$\pi_3\pi_4 = .00426$
Concrete heat diffusion in y	$\pi_5 = 1.3$
Concrete heat diffusion in x	$\pi_5\pi_6 = 0.001$
Concrete heat flux in y	$\pi_7 = 0.19$
Concrete heat flux in x	$\pi_6\pi_7 = 0.00015$

The small value of π_1 implies that internal heat generation is negligible during the initial flow. Corium heat diffusion in the flow direction also is negligible, as seen by the small value of $\pi_2\pi_3$. The small value of $\pi_5\pi_6$ shows that concrete heat diffusion in the flow direction is negligible. A comparison of heat flux values at the corium top surface and into the concrete shows that

because π_7 is small, cooling by concrete heat transfer can be neglected during the initial flow. Therefore, Eq. (A.9) can be written without the π_3 term, integrated with respect to y^* between $y^* = 0$ at the concrete where heat flux is zero, to $y^* = Y/2\sqrt{\alpha\tau_h}$ at the top surface where the heat flux is $\underline{j} \cdot \underline{q}''^* = \underline{j} \cdot (\underline{j}\, T^*) = T^*$. It follows that the corium temperature during initial flow can be estimated from a solution to

$$\frac{\partial T^*}{\partial t^*} + u^* \frac{\partial T^*}{\partial x^*} + T^* = \pi_1 \quad ; \quad T^* = T^*(x^*, t^*) \tag{A.15}$$

with the initial and boundary conditions,

$$T^*(x^*, 0) = 0 \tag{A.16}$$

$$T^*(0, t^*) = 1.0 \tag{A.17}$$

A solution for the corium unsteady temperature is given by

$$T^*(x^*, t^*) = \pi_1 (1 - e^{-t^*}) + e^{-x^*} \left\{ 1 - \pi_1 \left[1 - e^{-(t^* - x^*)} \right] \right\} H_s(t^* - x^*) \tag{A.18}$$

where H_s is the Heaviside unit step, which is 1.0 for positive values of its argument, and otherwise is zero. Temperature of the advancing corium front corresponds to $x = Vt$, or $t^* = x^*$, for which Eq. (A.18) yields

$$T^*_{front} = e^{-x^*} + \pi_1 (1 - e^{-x^*}) \tag{A.19}$$

Equation (A.19) is graphed in Figure 2.

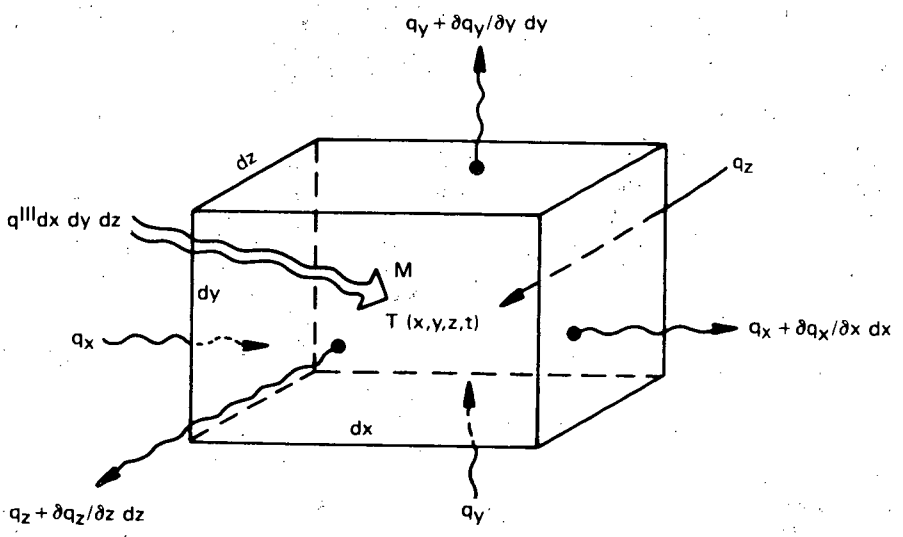


Figure A.1. Heat Transfer, Corium Element

EXPERIMENTS TO ASSESS THE THERMAL RESPONSE OF THE MARK I DRYWELL SHELL

by

D. R. Bradley
E. R. Copus
J. E. Brockmann
D. A. Powers

Sandia National Laboratories
Albuquerque, NM

ABSTRACT

Early failure of BWR Mark I containment shells when contacted by core debris has become a crucial issue in severe accident research. Two series of experiments, LINERQT and WITCH-LINER, have been performed to assist in the development and validation of models for the thermal response of the shell. The LINERQT tests were integral experiments involving molten steel melts simultaneously interacting with concrete and a vertical steel wall. The WITCH-LINER tests were separate effects tests which examined heat transfer from a steel melt to a steel surface under a controlled gas sparging rate. The results from the experiments are described. The results show that heat transfer was initially controlled by crust formation on the steel surface. Eventually, however, heat transfer was controlled by convection within the bubbling melt. Heat transfer coefficients during the convection-controlled phase were found to be in the range of 4000 W/m^2 K to greater than 13000 W/m^2 K, depending on the supplied gas flux. A model is proposed to describe the crust growth phase of the interaction. The model compares favorably with the observed experiment results.

NOMENCLATURE

Major Symbols

A, B, C	constants of integration
c	specific heat
k	thermal conductivity
L	enthalpy of fusion
T	temperature
t	time
X	position of solidification and melting fronts
x	spatial location
α	thermal diffusivity
β, Λ, σ, θ	defined property groupings
λ	growth constants for solidification and melting
π	pi = 3.14159...

ρ	density

Subscripts

i	interface
m	molten phase
mp	melting point
s	solid phase
0	initial condition
1	melt pool
2	solid substrate

BACKGROUND

In boiling water reactors (BWR's) with Mark I containments, the containment pressure boundary is provided by a steel vessel surrounding the reactor drywell. A typical Mark I containment configuration is shown in Figure 1. The steel found in different plants is of various thicknesses, but the nominal thickness in the vicinity of the drywell floor is about 3 cm. Many analyses of severe reactor accidents at these BWR plants have considered failure of the Mark I containment due to overpressurization, loss of strength by overheating, or shear stresses caused by differential thermal expansion around penetrations [1,2]. Such failures of the drywell shell usually are predicted to occur many hours after the start of a severe reactor accident [2]. Radioactivity releases associated with these late failures are likely to occur after significant emergency actions have been taken, including evacuation of the vulnerable population.

In 1983, Greene identified a vulnerability of Mark I containments that had not been considered in past analyses [2,3]. Greene recognized that as a severe reactor accident progressed, molten core debris would drain from the reactor pressure vessel, flow across the drywell floor, and contact the drywell shell. He coupled simple calculations of the thermal response of the steel shell with results obtained from the CORCON model [4] of core debris interactions with concrete in the reactor cavity. In general, Greene found that for many circumstances, core debris would penetrate the drywell shell in less than one hour. Penetration of the drywell shell opens a path for the release of radionuclides to the weak upper containment structure and subsequently to the environment. Because this mode of containment failure occurs early in the accident when radionuclide release is high, the consequences of the accident may be much more severe than for those accidents with delayed containment failure.

In the Severe Accident Risk Reduction Program report on the Peach Bottom, Unit 2 reactor [5], the probability of drywell shell failure was considered and was found to be a major contributor to the overall risk from severe accidents. Following the publication of this result and its subsequent implementation into the draft NUREG-1150 report [6], there was a period of intense activity during which a variety of analyses were proposed to evaluate failure of the drywell shell [7,8,9]. Unfortunately, these analyses have

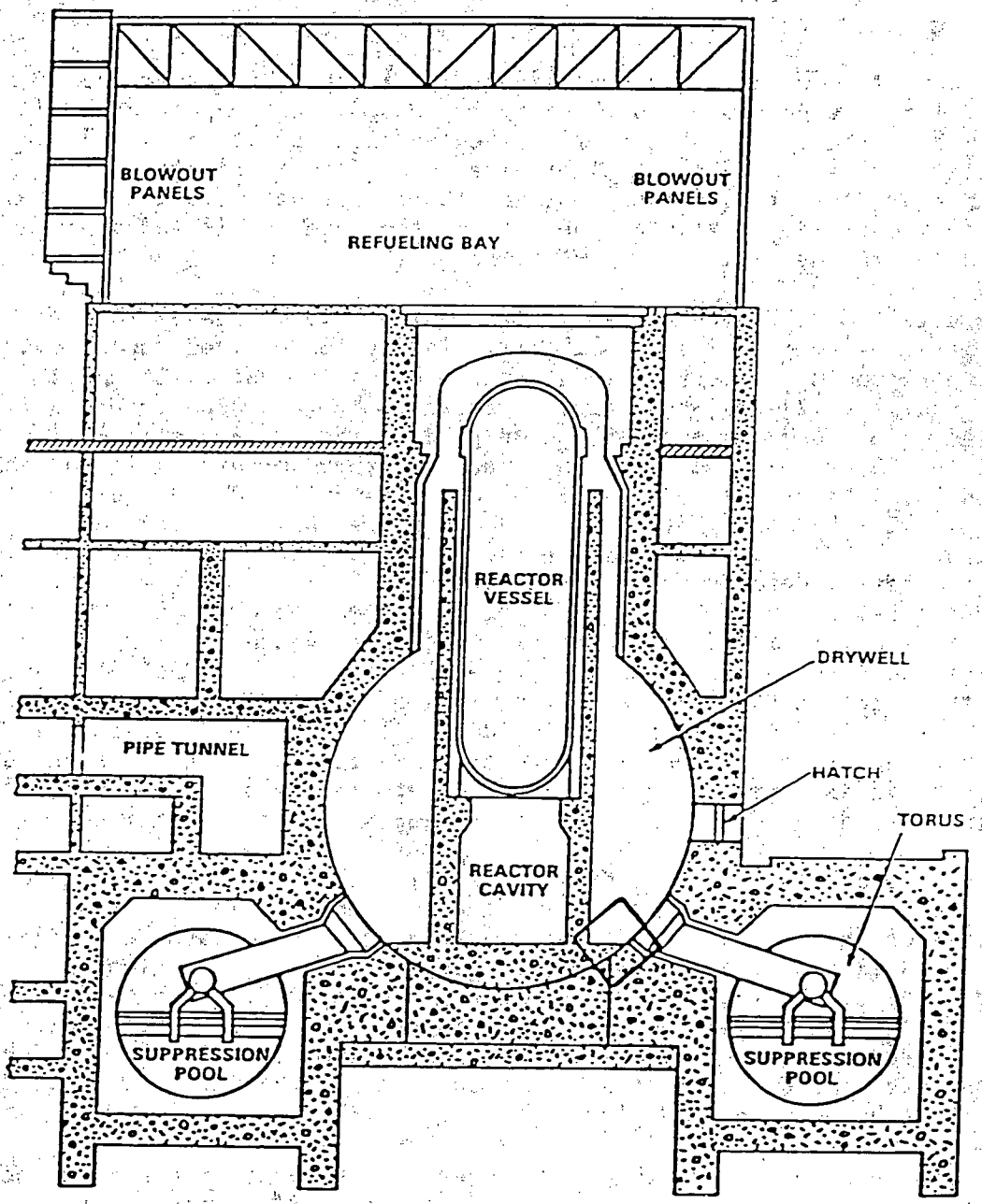


Figure 1. Diagram of the BWR Mark I Containment

yielded vastly different results due to uncertainties in the modelling of the controlling phenomena.

The key factors that have been identified in these analyses include: the rate at which core debris exits the reactor vessel, the temperature and composition of the core debris exiting the vessel, the rate at which the core debris flows across the drywell floor, the rate of heat transfer to the shell following contact by the core debris, and the effect of water which may be present in the reactor cavity on the flow of the core debris and subsequent heat transfer to the shell.

The nature of core debris expelled from the reactor vessel into the drywell is a challenging issue which will finally be resolved once there is a better understanding of core degradation processes in BWR's. Greene's original analyses [2] utilized results predicted by the MARCH code [10]. The simplified models used in the MARCH code predict that a substantial fraction of the core (including fuel, cladding, and structural material) is suddenly deposited into the drywell at vessel failure. Recently, Ott and others at Oak Ridge National Laboratory have developed a more refined model of core degradation in BWR's, BWRSAR [11]. Although the nature of the core debris exiting the vessel depends on the details of the accident progression, the BWRSAR model usually predicts that a large mass (on the order of 50 tons) of mostly metallic material is expelled at the time of vessel failure. The balance of the core debris is expelled over several hours. MAAP [12] analyses done by the Electric Power Research Institute predict qualitatively similar behavior. That is, there is an initial deposition of core material followed by slow drainage from the vessel. However, the details of the MAAP and BWRSAR predictions differ from one another in terms of the composition, mass, and temperature of the core debris involved in each stage of the accident.

Once core debris is in the drywell, it will begin to migrate toward the drywell shell. If the core debris is molten, it should flow readily since the viscosities of the molten core debris constituents are comparable to that of water. Rapid flow of metallic materials has been observed in simulant experiments by Greene [13] and in experiments by Copus [14] and Henry [15] which used melts which were predominantly iron. The experiments by Greene also considered the effect of water on the spreading of the melt. He found that water has a significant effect only when the depth of the water is greater than the depth of the flowing melt.

If heat transfer during the flow process is sufficient to remove the available sensible heat of the melt, solidification will begin. Subsequent removal of the available latent heat of the core debris may stop the flow. However, if complete solidification occurs only at the leading edge of the flow, the still molten material behind the leading edge may simply surge over this barrier and continue to flow. It is important to accurately model the hydrodynamics and heat transfer during the flow since these factors control the rate of spreading of the core debris and the condition of the core debris when it contacts the drywell shell. As yet, adequate models for these processes have not been developed.

Uncertainties in the modelling of core degradation, reactor vessel failure, and melt spreading across the drywell floor lead to uncertainties in the condition of the core debris in contact with the drywell shell. Equally important are the uncertainties involved in the modelling of the subsequent heat transfer between the core debris and the shell. Here, some of the important questions include:

* How rapidly does a crust form on the surface of the drywell shell?

* What are the rate-controlling mechanisms for heat transfer to the shell and what is the resulting time-dependent heat flux to the shell?

Formation of a crust on the surface of the shell is likely given the relatively cold initial temperature of the steel. If a thick crust forms on the shell surface or if the crust that forms is of a low thermal conductivity material, heat transfer to the shell may be limited by conduction through the crust rather than by convection in the molten core debris. In this case, failure of the shell may be significantly delayed or, in fact, may be prevented. If, on the other hand, a thin or high thermal conductivity crust forms, heat transfer may be little affected by the crust. In this case, heat transfer to the shell would be controlled by convection. The higher heat transfer rates associated with convective heat transfer processes would lead to much earlier failure of the drywell shell.

The research reported here is focused on answering the important heat transfer questions using a combined experimental and analytical approach. In the discussion which follows, the experimental apparatus are described first. Next the results from the experiments are discussed and analytical models are then proposed to explain some of the observed results. Finally, the implications of the results to the evaluation of Mark I containment failure are discussed.

DESCRIPTION OF THE EXPERIMENTS

Two sets of experiments, LINERQT and WITCH-LINER, have been performed at Sandia National Laboratories to investigate heat transfer to the drywell shell. The LINERQT experiments were integral studies of the simultaneous interactions of metallic melts (primarily mild or stainless steel) with a vertical steel surface and a concrete substrate. The WITCH-LINER experiments were separate effects experiments designed to examine heat transfer from steel melts to vertical steel surfaces under controlled gas sparging rates.

Metallic melts were chosen for these experiments for two reasons. First, they are relatively easy to prepare using induction heating techniques. Second, the most recent analyses of BWR reactor accidents using the BWRSAR code [10] indicate that the molten material initially deposited into the drywell will be mostly metallic. Thus, the melts used in the experiments are believed to be prototypic of the molten core debris which would be initially in contact with the drywell shell in a reactor accident.

The experimental apparatus, procedures, and results for the LINERQT and

WITCH-LINER tests are described below.

The LINERQT Tests:

A schematic diagram of the test apparatus employed in the LINERQT experiments is shown in Figure 2. Metallic melts weighing 20 to 30 kg were prepared in a tilting furnace using a 3000 Hz Inductotherm induction heating unit. During the melting process, the temperature of the melt was monitored using a two-color pyrometer. Once the temperature reached the desired value, the melt was teemed into the interaction crucible. The time required for the pour was about three seconds. The fall distance for the pour was approximately 50 cm.

The interaction crucibles used in the LINERQT tests consisted of a 61 cm length of 30.5 cm diameter mild steel pipe into which a depth of 30.5 cm of concrete had been poured and subsequently cured. The wall thickness of the pipe was approximately 0.95 cm. The outside of the tubes were wrapped with about 2.5 cm of Fibrefax insulation to establish a nearly adiabatic boundary.

To monitor the thermal response of the steel wall following contact by the melt, stainless steel sheathed, 1/16 inch, type K thermocouples were peened into 1.5 mm deep holes on the outside of the pipe. The thermocouples were mounted in two axial arrays placed at 90 degrees to the left and to the right of the direction of the pour. The thermocouples were oriented in this manner to minimize the effect of the pour on the thermal response of the steel wall. The thermocouples were spaced at 1.27 cm intervals starting at the level of the top surface of the concrete and going up 8.9 cm and down 3.8 cm. Temperature measurements were recorded at 100 millisecond intervals.

Four LINERQT experiments have been performed. The important test parameters for these experiments are listed in Table 1.

Table 1.
Experiment Parameters of the LINERQT Tests

Test	Melt Composition	Mass of Melt (kg)	Initial Temperature (K)
LINERQT-1	Mild Steel	23	1950
LINERQT-1A	Mild Steel	20	1850
LINERQT-2	Stainless Steel	20	1800
LINERQT-3	Mild Steel with 1 kg of Zirconium	30	1950

The WITCH-LINER Tests:

A schematic diagram of the apparatus employed in the WITCH-LINER experiments is shown in Figure 3. These experiments utilized the WITCH

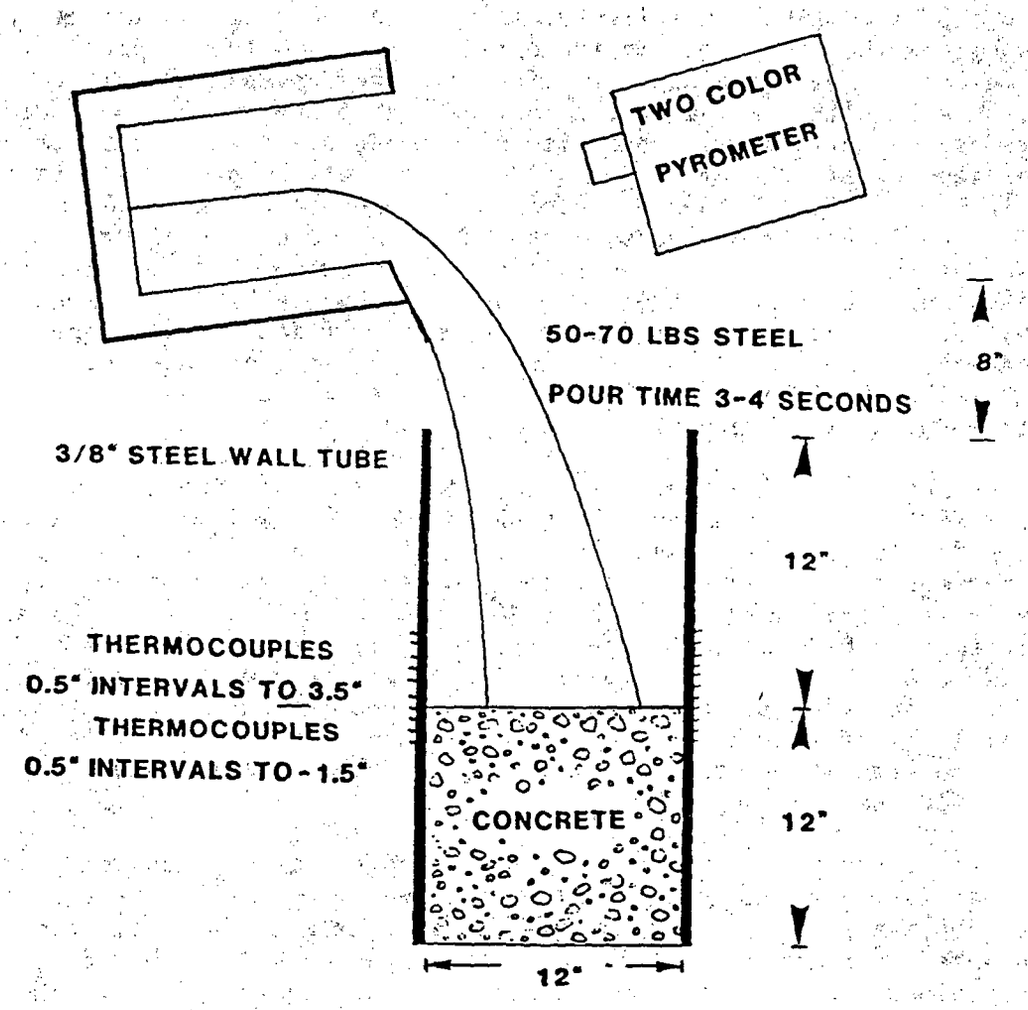


Figure 2. Schematic Diagram of the LINERQT Apparatus

apparatus [16] which was designed originally to study gas holdup and mechanical aerosol formation from prototypic reactor melts under controlled gas sparging rates. The apparatus consists of a crucible which is constructed of a castable alumina ceramic. The crucible inside diameter is 16.5 cm and the wall thickness is 1.9 cm. The height of the crucible is 91.4 cm. A gas sparger plate with 1 hole/cm^2 is cast into the bottom of the crucible. The sparging gas is delivered to the plenum beneath the sparger plate at a known flow rate. Melts are generated within the crucible using an induction heating unit. The temperature of the melt is monitored using eight alumina-sheathed, type S thermocouples.

In the WITCH-LINER experiments, 45 kg of mild steel was inductively melted within the crucible. Instrumented probes were then inserted into the steel melt to investigate heat transfer from the gas sparged melt to the probe. A schematic diagram of the instrumented probes is shown in Figure 4. The probes were mild steel tubes with an outside diameter of 5.08 cm and an inside diameter of 2.54 cm. The inside surface of the probes was instrumented using 1/16 inch, Type K thermocouples which were peened into 1.5 mm deep holes. (The locations of these thermocouples are shown in Figure 4.) The interior of the probes were then filled with a castable alumina ceramic to provide structural support and thermal insulation. A 1.27 cm thickness of alumina ceramic was also cast around the upper portion of the probe to eliminate axial heating due to thermal radiation and splashing of the melt. The radiation shield also eliminates uncertainties due to variation in the insertion depth of the probe.

Four instrumented probes were utilized in the experiments to examine heat transfer at four different gas sparging rates. The gas sparging rates corresponded to superficial gas velocities of 5.5, 11.6, 21.0, and 33.0 cm/s. These gas sparging rates were selected because they are comparable to the gas generation rates calculated by the CORCON-Mod2 code [17] for core debris interactions with concrete during a reactor accident. The probes were inserted into the melt for approximately one minute and then removed. During this time, the induction power supply was turned off and the melt cooled from an initial temperature of 1850 K to approximately 1800 K. At the end of this period, the steel surface of the probe had completely melted and only the castable alumina remained.

Dummy probes were used to study the transient growth and remelting of the crust that formed on the surface of the probe. These probes were constructed in the same manner as the instrumented probes, except that they were not instrumented with thermocouples. Four dummy probes were inserted into the melt for times ranging from 6 to 45 seconds, and then withdrawn. The gas sparging rate was held constant at 5.5 cm/s during insertion of the dummy probes. As with the instrumented probes, the initial temperature of the melt was 1850 K at the time the probes were inserted.

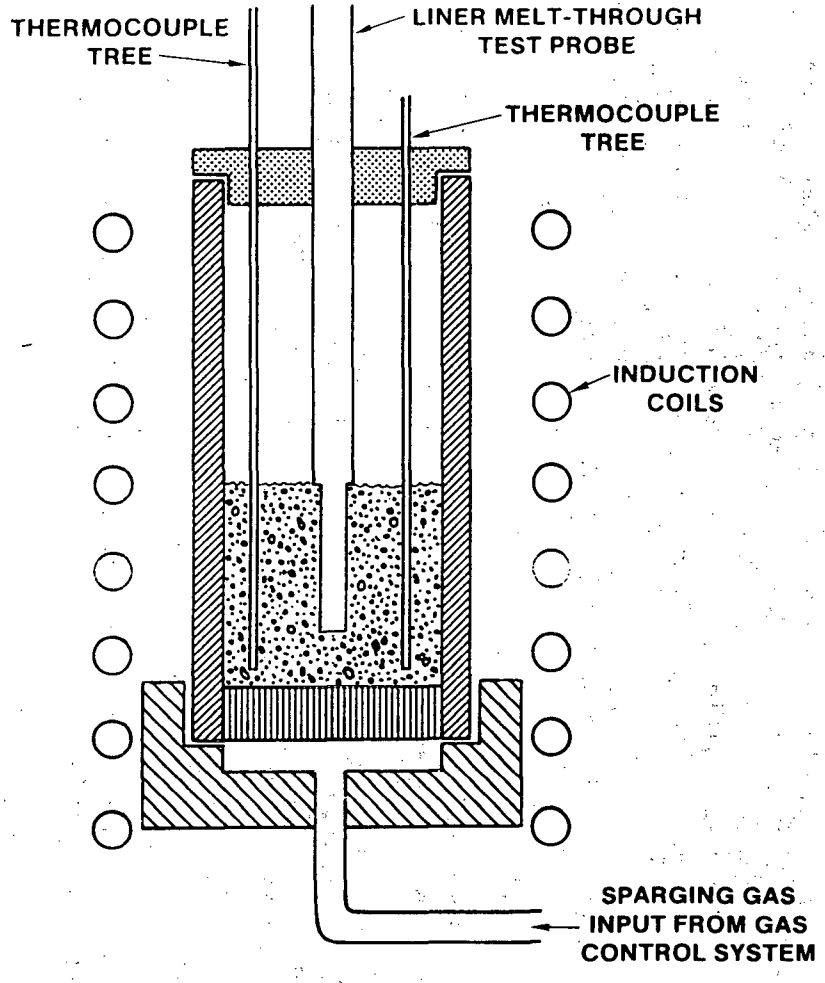


Figure 3. Schematic Diagram of the WITCH-LINER Apparatus

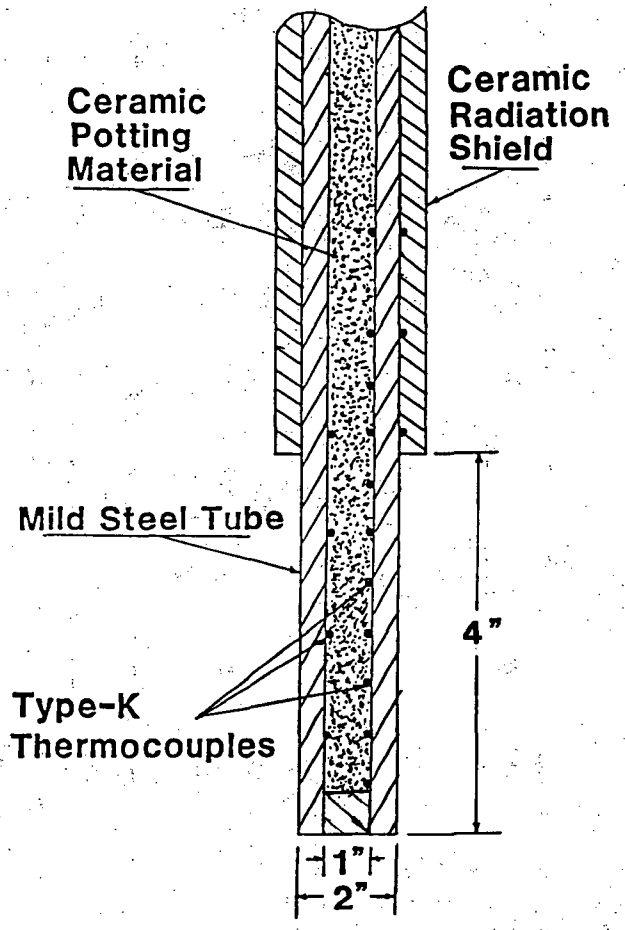


Figure 4. Schematic Diagram of the WITCH-LINER Instrumented Probes

RESULTS FROM THE EXPERIMENTS

LINERQT Results:

The thermocouple results from the four LINERQT experiments show the same general behavior. In each experiment, the measured temperatures increase rapidly during the first 30 to 60 seconds following initiation of the pour. The temperatures then level off, and after about 120 seconds, begin a slow decline. The initial period of rapid heating corresponds approximately to the time that the steel melt was predominantly molten. In each experiment, the maximum temperature was recorded by the thermocouple placed near the axial midpoint of the melt. The maximum temperatures for the four experiments were: LINERQT-1, 1160 K; LINERQT-1A, 870 K; LINERQT-2, 950 K; and LINERQT-3, 1210 K. The following discussion will focus on the results from LINERQT-1. The conclusions that are derived for this test are equally applicable to the other tests.

The temperatures recorded by the thermocouples located at the midpoint of the melt are shown in Figure 5. Two thermocouple traces are shown in the figure: one from the array located 90 degrees to the right of the pour direction and one from the array located 90 degrees to the left of the pour direction. The figure shows that the thermal response of the steel pipe was essentially the same for both arrays.

The thermocouple responses shown in Figure 5 have been used as input to a computer code, IHCP [18], which solves the ill-posed, inverse heat conduction problem. IHCP uses Beck's method [19] to calculate the heat flux required to produce a given thermocouple response. The time-dependent heat fluxes calculated for the left-side and right-side thermocouple locations are presented in Figure 6. For both locations, the heat flux is calculated to decrease rapidly from an initial value of 220 to 270 W/cm^2 to approximately 10 W/cm^2 in 40 seconds. The observed decrease in the heat flux is probably due to 1) crust formation on the surface of the steel pipe and eventual bulk freezing of the steel melt, and 2) heating of the surface of the pipe which reduces the temperature difference driving the heat transfer.

WITCH-LINER Results:

Typical thermocouple responses for the four instrumented probes are shown in Figure 7. Note that during the first fifteen seconds following insertion into the melt, the measured temperatures were nearly the same -- the only exception being the highest gas velocity probe. Apparently, the mechanism controlling heat transfer during this initial phase was independent of the gas velocity. After this initial period, a transition occurred and the heatup of the probe was sensitive to the gas velocity.

The transition in behavior is even more pronounced in the heat fluxes calculated from the thermocouple responses. These heat fluxes are displayed in Figure 8. As would be expected based on the similarity in the temperature results, the heat fluxes were almost the same early in the experiments. Again, the lone exception to this is the test at the highest superficial gas

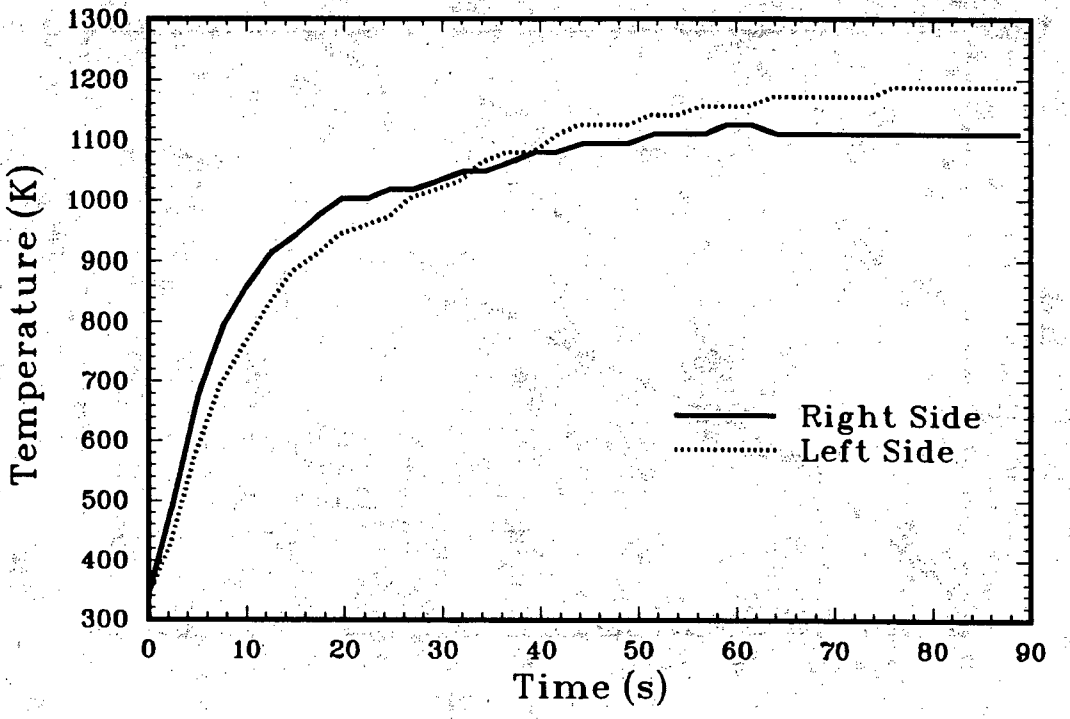


Figure 5. Temperatures Recorded By Backside Thermocouples in the LINERQT-1 Test

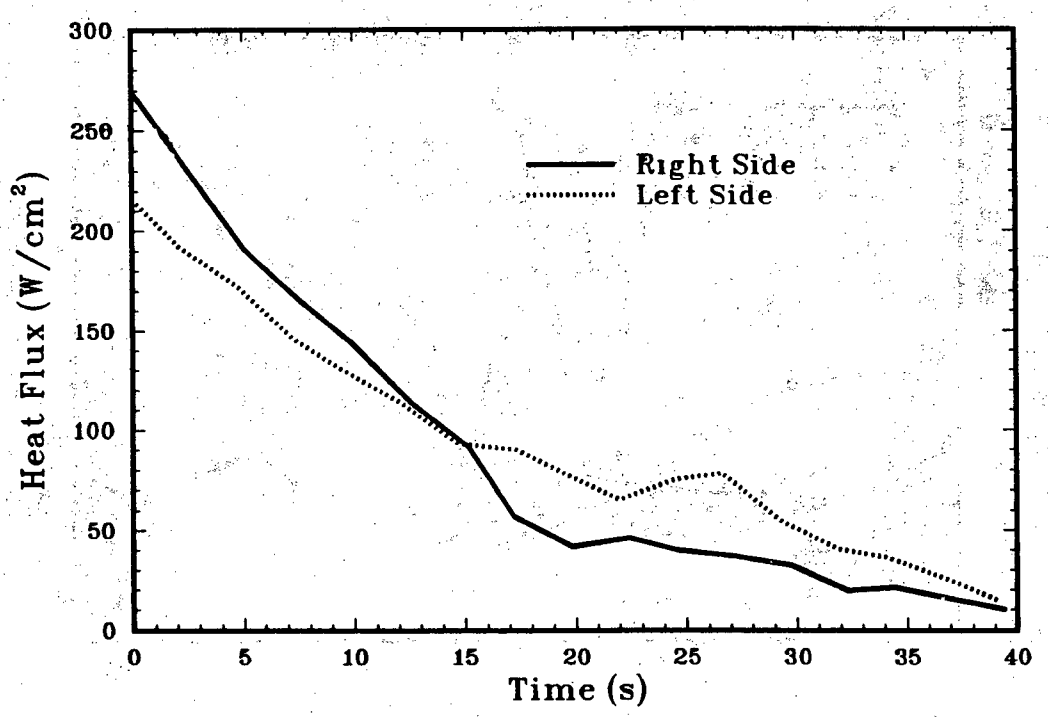


Figure 6. Heat Fluxes Determined From the LINERQT-1 Thermocouple Data

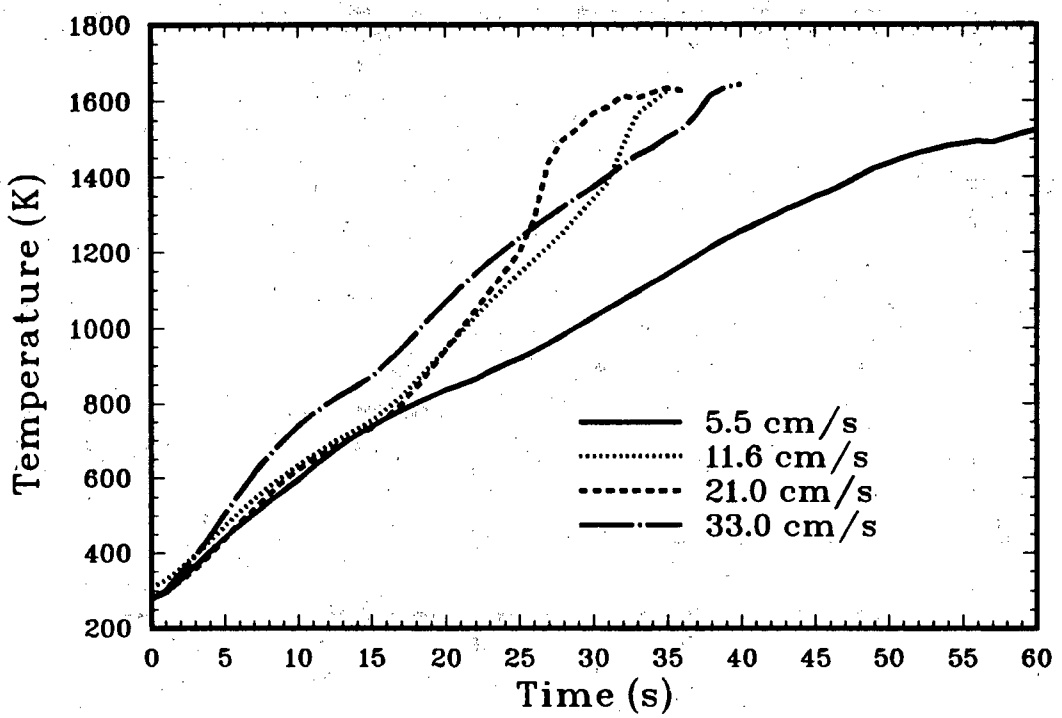


Figure 7. Inside Surface Temperatures Measured in the WITCH-LINER Tests

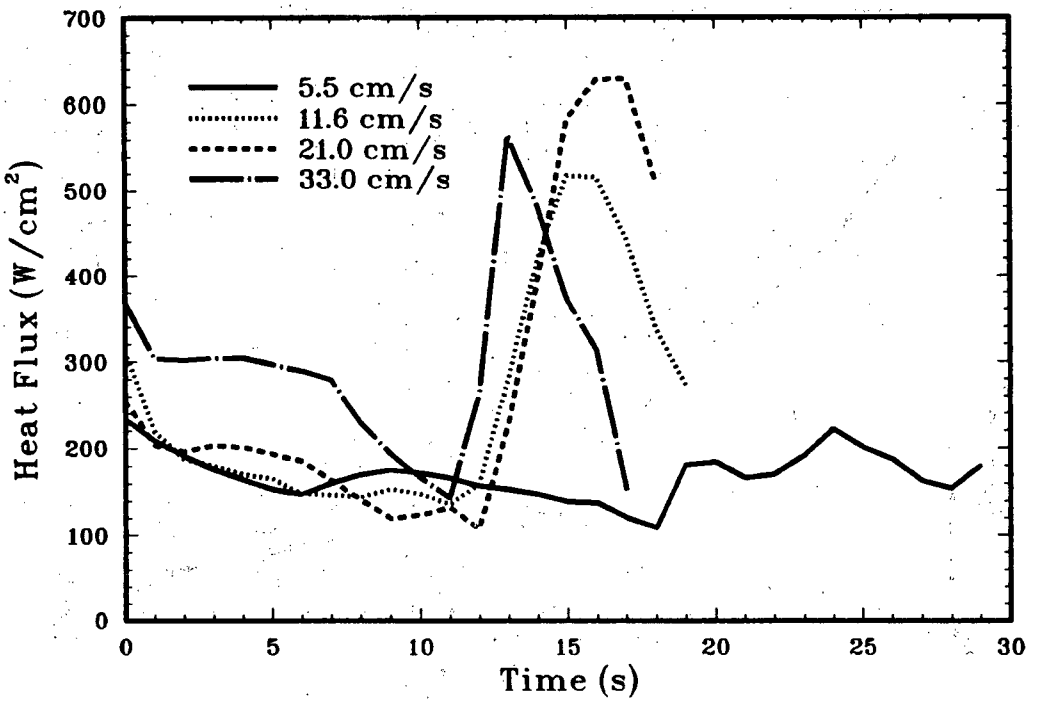


Figure 8. Heat Fluxes Determined From the WITCH-LINER Thermocouple Data

velocity. (Interestingly, the heat fluxes during the early phase of the WITCH-LINER tests were also approximately the same as the heat fluxes early in the LINERQT tests.) At about twelve seconds after insertion of the probe, the heat flux very rapidly increased to a peak value of greater than 500 W/cm^2. Soon after this, the surface of the probe was calculated to begin melting and the heat flux calculation was terminated.

Insight into the mechanisms controlling heat transfer during the experiments was provided by insertion of the dummy probes. Though quantitative results are not yet available for crust growth on the surface of the dummy probes, several qualitative observations can be made. First, rapid crust formation was apparent during the first few seconds following probe insertion. A crust of approximately one centimeter thickness had formed on the first dummy probe, which was inserted into the melt for only six seconds. Another probe, which was inserted for 15 seconds, had a crust of approximately the same thickness. Significant remelting of the crust and some melting of the original probe surface were evident in a third probe, which was inserted for 30 seconds. Substantial melting of the probe was evident in a fourth probe, which was inserted for approximately 45 seconds.

We conclude from the WITCH-LINER results that heat transfer in the experiments was initially controlled by the formation of a crust on the probe surface. This was also true in the LINERQT tests. Later, gas driven convection controlled heat transfer and remelting of the crust began. This was not observed in the LINERQT tests because the melt rapidly solidified, and gas flow was not sustained.

In the following section, a model is presented to describe initial crust formation and resulting heat transfer to the probe.

A MODEL FOR CRUST FORMATION

A model has been developed to describe the formation of a crust on the surface of the steel shell during the first few seconds following contact by molten core debris. The model considers the melt pool and the steel shell to be semi-infinite bodies which are suddenly brought into contact with one another. Immediately upon contact, the interface between the melt and the shell is assumed to reach an intermediate temperature which is commonly referred to as the "contact temperature". If the contact temperature is below the freezing temperature of the melt, a crust will begin to form at the interface. Simultaneous melting of the surface is also possible if the contact temperature is above the melting temperature of the solid steel surface.

To describe these processes and the heat transfer that results, an analytic solution technique is employed which is a generalization of Neumann's solution for one-dimensional melting or solidification [20]. The approach used here is similar to the analytical techniques employed by Epstein [21] and Bradley [22] to analyze similar problems. Epstein examined freezing of molten uranium dioxide on the surface of stainless steel cladding, while Bradley modelled heat transfer from molten core debris to concrete. The details of

the solution approach are provided below.

In the most general case, four regions are possible: the initially molten phase, the solid substrate, the solidified molten phase crust, and the layer of melting substrate. The energy equation in each of these four regions has the form

$$\frac{\partial^2 T_i}{\partial x^2} = \frac{1}{\alpha_i} \frac{\partial T_i}{\partial t} \tag{1}$$

where T_i is the temperature in region i, α_i is the thermal diffusivity of region i, x is the spatial location, and t is the time. Note that internal heating in the molten phase due to decay of fission products or chemical reactions has been neglected. It can be easily shown that during the short time period of interest for crust formation, internal energy generation can be neglected.

Designating the initially molten material as material 1, the solid substrate as material 2, and the positions of the solidification and melting fronts (relative to the coordinate system origin located at the interface between the two materials) as X_1 and X_2, the following boundary conditions apply:

$$T_{1s}(X_1,t) = T_{1m}(X_1,t) = T_{1mp} \tag{2a}$$

$$T_{2s}(-X_2,t) = T_{sm}(-X_2,t) = T_{2mp} \tag{2b}$$

$$k_{1s} \frac{\partial T_{1s}}{\partial x} - k_{1m} \frac{\partial T_{1m}}{\partial x} = L_1 \rho_1 \frac{\partial X_1}{\partial t} \quad \text{at } x = X_1(t) \tag{2c}$$

$$k_{2s} \frac{\partial T_{2s}}{\partial x} - k_{2m} \frac{\partial T_{2m}}{\partial x} = -L_2 \rho_2 \frac{\partial X_2}{\partial t} \quad \text{at } x = -X_2(t) \tag{2d}$$

$$T_{1s}(0,t) = T_{2m}(0,t) = T_i \tag{2e}$$

$$k_{1s} \frac{\partial T_{1s}}{\partial x} = k_{2m} \frac{\partial T_{2m}}{\partial x} \quad \text{at } x = 0 \tag{2f}$$

$$T_{1m}(\infty,t) = T_{10} \tag{2g}$$

$$T_{2s}(-\infty,t) = T_{20} \tag{2h}$$

where the subscripts s and m refer to the solid and molten phases, respectively, of materials 1 and 2; T_{10} and T_{20} are the initial temperatures of materials 1 and 2; and k, ρ, and L are the thermal conductivity, density, and enthalpy of fusion for the material or region of interest.

Solutions for the four possible regions have the general form [17]:

$$T_{1s} = A_1 + B_1 \mathrm{erf}\left(\frac{x}{2(\alpha_{1s}t)^{1/2}}\right) \qquad 0 < x < X_1(t) \qquad (3)$$

$$T_{1m} = T_{10} - C_1 \mathrm{erfc}\left(\frac{x}{2(\alpha_{1m}t)^{1/2}}\right) \qquad X_1(t) < x < \infty \qquad (4)$$

$$T_{2m} = A_2 + B_2 \mathrm{erf}\left(\frac{-x}{2(\alpha_{2m}t)^{1/2}}\right) \qquad -X_2(t) < x < 0 \qquad (5)$$

$$T_{2s} = T_{20} + C_2 \mathrm{erfc}\left(\frac{-x}{2(\alpha_{2s}t)^{1/2}}\right) \qquad -\infty < x < -X_2(t) \qquad (6)$$

with the positions of the solidification and melting fronts given by

$$X_1(t) = 2\lambda_1(\alpha_{1s}t)^{1/2} \qquad (7)$$

and

$$X_2(t) = 2\lambda_2(\alpha_{2m}t)^{1/2} \qquad (8)$$

The eight constants, A_1, B_1, C_1, A_2, B_2, C_2, λ_1, and λ_2, are determined by applying the eight boundary conditions given above.

Application of these boundary conditions results in a set of algebraic equations for the eight constants. By algebraic manipulation, this set of equations is reduced to two simultaneous transcendental equations for λ_1 and λ_2, which can then be solved numerically. The two equations for λ_1 and λ_2 are:

$$\frac{\sigma}{\exp(\lambda_1^2)\mathrm{erf}(\lambda_2) + \sigma\exp(\lambda_1^2)\mathrm{erf}(\lambda_1)} - \frac{\theta_1}{\exp(\beta_1^2\lambda_1^2)\mathrm{erfc}(\beta_1\lambda_1)} = \lambda_1\Lambda_1 \qquad (9)$$

and

$$\frac{1}{\sigma\exp(\lambda_2^2)\mathrm{erf}(\lambda_1) + \exp(\lambda_2^2)\mathrm{erf}(\lambda_2)} - \frac{\theta_2}{\exp(\beta_2^2\lambda_2^2)\mathrm{erfc}(\beta_2\lambda_2)} = \lambda_2\Lambda_2 \qquad (10)$$

where

$$\sigma = \left(\frac{\alpha_{1s}}{\alpha_{2m}}\right)^{1/2} \frac{k_{2m}}{k_{1s}}$$

$$\beta_1 = \left(\frac{\alpha_{1s}}{\alpha_{1m}}\right)^{1/2}$$

$$\beta_2 = \left(\frac{\alpha_{2m}}{\alpha_{2s}}\right)^{1/2}$$

$$\theta_1 = \frac{\beta_1 k_{1m}}{k_{1s}} \left(\frac{T_{10} - T_{1mp}}{T_{1mp} - T_{2mp}}\right)$$

$$\theta_2 = \frac{\beta_2 k_{2s}}{k_{2m}} \left(\frac{T_{2mp} - T_{20}}{T_{1mp} - T_{2mp}}\right)$$

$$\Lambda_1 = \frac{\pi^{1/2} L_1}{c_{1s}(T_{1mp} - T_{2mp})}$$

and

$$\Lambda_2 = \frac{\pi^{1/2} L_2}{c_{2m}(T_{1mp} - T_{2mp})}$$

After λ_1 and λ_2 have been determined, the contact temperature is calculated from

$$\frac{T_i - T_{2mp}}{T_{1mp} - T_{2mp}} = \frac{\text{erf}(\lambda_2)}{\text{erf}(\lambda_2) + \sigma\text{erf}(\lambda_1)} \qquad (11)$$

This compares to the simple equation for T_i in the absence of phase changes:

$$\frac{T_i - T_{20}}{T_{10} - T_{20}} = \frac{1}{1 + \sigma} \qquad (12)$$

If solidification of the molten layer occurs but no melting of the solid substrate, the governing equations are slightly different. Using the same general approach as outlined above, the following equation for the crust growth constant, λ_1, is derived:

$$\frac{\sigma}{\sigma\exp(\lambda_1^2)\text{erf}(\lambda_1) + \exp(\lambda_1^2)} - \frac{\theta_1}{\exp(\beta_1^2\lambda_1^2)\text{erfc}(\beta_1\lambda_1)} = \lambda_1\Lambda_1 \qquad (13)$$

while the contact temperature, T_i, is given by

$$\frac{T_i - T_{20}}{T_{1mp} - T_{20}} = \frac{1}{\sigma + \text{erf}(\lambda_1)} \qquad (14)$$

In these equations, σ is defined by

$$\sigma = \left(\frac{\alpha_{1s}}{\alpha_2}\right)^{1/2} \frac{k_2}{k_{1s}}$$

The method discussed above has been incorporated into a computer program which solves for the contact temperature given the thermophysical properties of the four possible regions and the initial temperatures of the molten phase and solid substrate. The program first determines whether melting of the substrate occurs. If melting occurs, the four-region solution is used. If no melting occurs, the three-region solution is used. For the current application to steel melts contacting a cold steel surface, melting of the steel substrate is not calculated to occur -- a result that is consistent with the observations from the LINERQT and WITCH-LINER experiments.

Given the calculated contact temperature and crust growth constant, the time-dependent temperature profile in the solid substrate and the heat flux at the surface of the substrate are determined from:

$$T_2(x,t) = T_{20} + \frac{(T_{1mp} - T_{20})}{1 + \sigma \mathrm{erf}\lambda_1} \mathrm{erfc}\left(-\frac{x}{2(\alpha_2 t)^{1/2}}\right) \qquad (15)$$

and

$$q_2(0,t) = k_2 \frac{\delta T}{\delta x}(0,t)$$

$$= k_2 \frac{(T_{1mp} - T_{20})}{1 + \sigma \mathrm{erf}\lambda_1} \frac{1}{(\pi \alpha_2 t)^{1/2}} \qquad (16)$$

The model discussed above has been applied to the analysis of crust growth and heat transfer during the initial period of the LINERQT and WITCH-LINER experiments. The results of these calculations and comparisons to the results from the experiments are shown in Figures 9 and 10.

In general, the time-dependent heat flux calculated using the crust formation model compares favorably with the results of the LINERQT experiments (see Figure 9). The crust model appears to significantly overpredict the heat flux during the first five seconds of the experiment. However, some of this difference is due to the limitations of the inverse heat conduction code, IHCP, which was used to determine the experiment heat flux. Given the thermocouple placement nearly a centimeter from the heated surface, the code required that the heat flux be averaged over a three second period. Hence, resolution in the early time heat flux was lost. Had this limitation not been imposed, the heat flux determined for the experiment would have been much closer to that predicted by the crust model. The late-time deviation between the prediction of the crust model and the result from the experiment is probably due to bulk freezing of the steel melt. The crust model assumes that

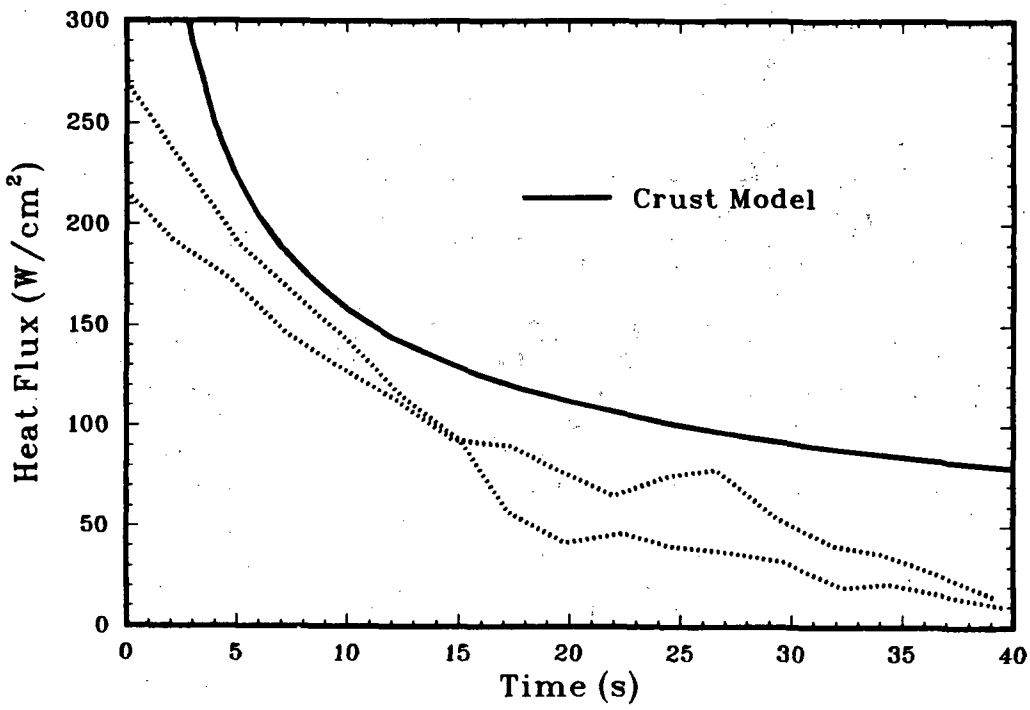


Figure 9. Comparison of LINERQT-1 Heat Fluxes to the Prediction Using the Crust Model

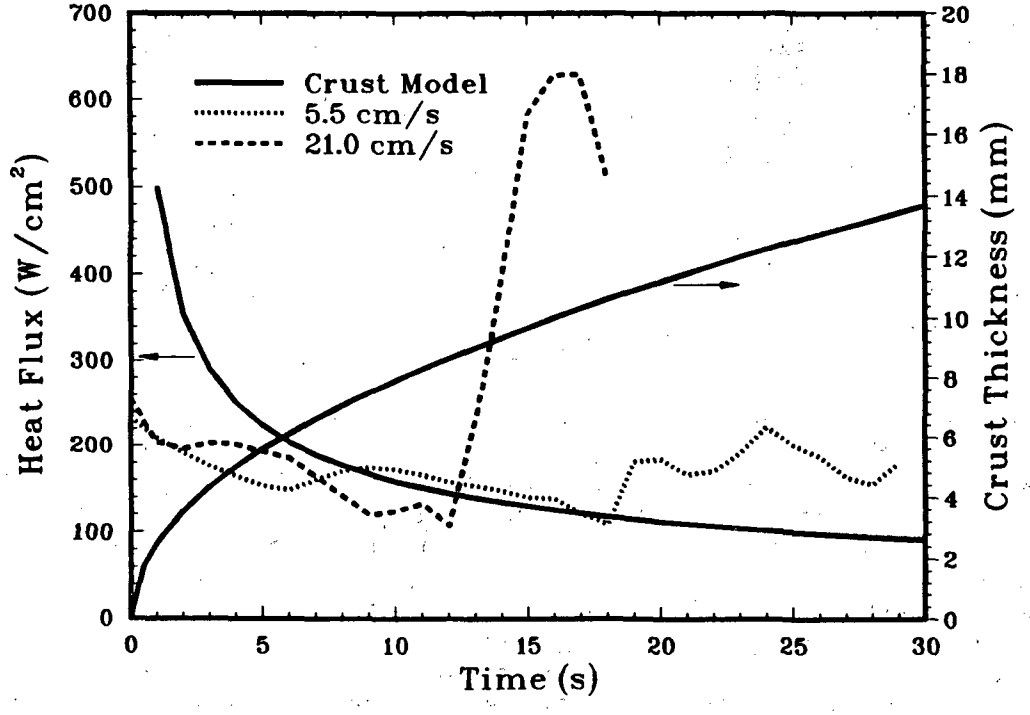


Figure 10. Comparison of the WITCH-LINER Heat Fluxes to the Prediction Using the Crust Model

the bulk temperature of the melt remains constant during crust formation.

Figure 10 shows a comparison of the heat flux calculated using the crust model to the heat flux determined for two of the WITCH-LINER probes. Again, the model appears to significantly overpredict the experiment heat fluxes early in the tests. As before, this is caused primarily by the time-averaging required by the IHCP code. After the first five seconds and prior to the time that convective heat transfer becomes important, the agreement between the model predictions and the experiment results is quite good.

Also shown on Figure 10 is the calculated crust thickness as a function of time. The calculated rapid growth of the crust to a thickness on the order of one centimeter is consistent with the observed crust growth on the dummy probes.

Based on the WITCH-LINER heat flux results, approximate values for the convective heat transfer coefficients during the convection-limited period of the experiments can be determined. To do this, a surface temperature must be assumed for the steel probes. Given the heat fluxes calculated for the WITCH-LINER probes, the surface temperature of the probes is estimated to be 500 K to 700 K higher than the temperature measured by the interior thermocouples. Using the average of these two values (600 K), the heat transfer coefficients shown in Table 2 are calculated.

Table 2.
Heat Transfer Coefficients Estimated From the WITCH-LINER Heat Fluxes

Superficial Gas Velocity (cm/s)	Heat Transfer Coefficient (W/m^2 K)
5.5	4400 - 6400
11.6	9200 - 10600
21.0	13700 - 14400
33.0	10500 - 13400

Summary and Conclusions

Based on the results from the LINERQT and WITCH-LINER experiments, we have identified two different mechanisms controlling heat transfer to the steel surface. Initially, heat transfer in the experiments was controlled by the formation of a crust on the surface of the steel. In the WITCH-LINER experiments, which had a sustained gas sparging rate, heat transfer was controlled by gas-driven convection after a period of only 12 to 18 seconds. The convective heat transfer coefficients estimated for this latter phase were in the range of 4000 to 14000 W/m^2 K. A transition to convection-limited heat transfer was not observed in the LINERQT experiments since the steel melt rapidly cooled and solidified, and gas flow was not sustained.

15. R. E. Henry, et al., "Experiments Relating to Drywell Shell-Core Debris Interactions," 16th Water Reactor Safety Information Meeting, Gaithersburg, MD, 1988.

16. J. E. Brockmann and F. E. Arellano, The WITCH-GHOST Program Plan, Sandia National Laboratories, Albuquerque, NM, to be published.

17. R. K. Cole, D. P. Kelly, and M. A. Ellis, CORCON-Mod2: A Computer Program for Analysis of Molten-Core Concrete Interactions, NUREG/CR-3920, SAND84-1246, Sandia National Laboratories, Albuquerque, NM, 1984.

18. J. E. Gronager, et al., TURC1: Large Scale Metallic Melt-Concrete Interaction Experiments and Analysis, NUREG/CR-4420, SAND85-0707, Sandia National Laboratories, Albuquerque, NM, 1986.

19. J. V. Beck, B. F. Blackwell, and C. R. St. Clair, Inverse Heat Conduction: Ill-Posed Problems, John Wiley and Sons, New York, 1985.

20. H. S. Carslaw and J. C. Jaeger, Conduction of Heat in Solids, Clarendon Press, Oxford, 1959, pp. 282-290.

21. M. Epstein, "Heat Conduction in the UO_2-Cladding Composite Body with Simultaneous Solidification and Melting," Nuclear Science and Engineering, Vol. 51, No. 84, 1973.

22. D. R. Bradley, "Modelling of Heat Transfer Between Core Debris and Concrete," Proceedings of the 25th National Heat Transfer Conference, Houston, TX, August, 1988.

NRC FORM 335 (8-87) NRCM 1102, 3201, 3202

U.S. NUCLEAR REGULATORY COMMISSION

BIBLIOGRAPHIC DATA SHEET

SEE INSTRUCTIONS ON THE REVERSE

1. REPORT NUMBER (Assigned by PPMB: DPS, add Vol. No., if any)
NUREG/CP-0097
Vol. 5

2. TITLE AND SUBTITLE
Proceedings of the Sixteenth Water Reactor Safety Information Meeting

3. LEAVE BLANK

4. DATE REPORT COMPLETED
MONTH: February YEAR: 1989

5. AUTHOR(S)
Compiled by Allen J. Weiss, BNL

6. DATE REPORT ISSUED
MONTH: March YEAR: 1989

7. PERFORMING ORGANIZATION NAME AND MAILING ADDRESS (Include Zip Code)
Office of Nuclear Regulatory Research
U. S. Nuclear Regulatory Commission
Washington, D. C. 20555

8. PROJECT/TASK/WORK UNIT NUMBER

9. FIN OR GRANT NUMBER
A-3282

10. SPONSORING ORGANIZATION NAME AND MAILING ADDRESS (Include Zip Code)
Same as Item 7 above

11a. TYPE OF REPORT
Proceedings of conference on safety research

b. PERIOD COVERED (Inclusive dates)
October 24-27, 1988

12 SUPPLEMENTARY NOTES
Proceedings prepared by Brookhaven National Laboratory

13. ABSTRACT (200 words or less)

This five-volume report contains 141 papers out of the 175 that were presented at the Sixteenth Water Reactor Safety Information Meeting held at the National Institute of Standards and Technology, Gaithersburg, Maryland, during the week of October 24-27, 1988. The papers are printed in the order of their presentation in each session and describe progress and results of programs in nuclear safety research conducted in this country and abroad. Foreign participation in the meeting included twenty different papers presented by researchers from Germany, Italy, Japan, Sweden, Switzerland, Taiwan and the United Kingdom. The titles of the papers and the names of the authors have been updated and may differ from those that appeared in the final program of the meeting.

14 DOCUMENT ANALYSIS - a. KEYWORDS/DESCRIPTORS
reactor safety research
nuclear safety research
decontamination and decommissioning

b. IDENTIFIERS/OPEN-ENDED TERMS

15. AVAILABILITY STATEMENT
Unlimited

16. SECURITY CLASSIFICATION
(This page) Unclassified
(This report) Unclassified

17. NUMBER OF PAGES

18 PRICE